UNIVERSITE BRETAGNE LOIRE / SCIENCES POUR L'INGENIEUR

CENTRALE NANTES

THESE DE DOCTORAT DE

L'ÉCOLE CENTRALE DE NANTES
COMUE UNIVERSITE BRETAGNE LOIRE

ECOLE DOCTORALE N° 602
Sciences pour l'Ingénieur
Spécialité : Mécanique des solides, des matériaux, des structures et des surfaces

Par
Chady KHALIL

Développement du procédé de soudage par impulsion magnétique pour soudage hétérogène bimétallique et pour assemblage hybride métal / composite

Thèse présentée et soutenue à Nantes, le 22-10-2018
Unité de recherche : Institut de Recherche en Génie Civil et Mécanique (GeM) – UMR 6183

Rapporteurs avant soutenance :

Mohamed RACHIK   Maitre de Conférences HDR - Université de technologie de Compiègne

Aude SIMAR   Professeur des Universités – Université Catholique de Louvain

Composition du Jury :

Président :
Christophe BINETRUY   Professeur des Universités – Ecole Centrale de Nantes

Aude SIMAR   Professeur des Universités – Université Catholique de Louvain

Marie-Noëlle AVETTAND FENOEL   Maitre de Conférences – Université Lilles 1

Mohamed RACHIK   Maitre de Conférences HDR - Université de technologie de Compiègne

Directeur de thèse :
Guillaume RACINEUX   Professeur des Universités – Ecole Centrale de Nantes

Co-encadrant de thèse :
Chrsitian BURTIN   Maitre de Conférences – Ecole Centrale de Nantes

Invité
Yannick AMOSSE   Directeur de la Recherche - FAURECIA

Development of Magnetic Pulse Welding process for welding dissimilar metals and joining polymeric composites to metals

Chady Khalil

FAURECIA - Centrale Nantes Chair

Research Institute in Civil and Mechanical Engineering - GeM

Processes and Mechanics of Materials Research Group

This dissertation is submitted for the degree of
Doctor of Philosophy in Mechanics of solids, materials, structures and surfaces

2018

"He who would accomplish little must sacrifice little; he who would achieve much must sacrifice much; he who would attain highly must sacrifice greatly."

James Allen

à ma source de support inconditionnel...mon frère Fady
à mes chers parents... Fadia et Elia
à ma chère Mère spirituelle... Soeur Salwa EL HAYEK
à ma chère Marraine... Ursüla
à mon cher petit frère... Hady

C'est grâce à vous que je suis là aujourd'hui...

"Stay away from negative people. They have a problem for every solution."

Albert Einstein

Acknowledgements

Résumé

La réduction des émissions CO2 et l'amélioration de la performance restent toujours les grands objectifs de l'industrie automobile. Pour atteindre ces objectif, les équipementiers automobiles cherchent toujours à alléger les structures à travers l'emploie des matériaux hétérogènes qui a évolué au cours des dernières décennies où nous trouvons aujourd'hui à la fois des aciers doux, des aciers à très hautes résistances, des alliages légers tels que les alliages d'aluminium et de magnésium ainsi que des composites à fibre de verre ou de carbone.

Cette tendance pose aujourd'hui plusieurs défis concernant à la fois l'assemblage bimétallique et l'assemblage hybride métal/composite. Les difficultés de réaliser ce type d'assemblage est lié surtout à la différence des propriétés mécaniques, thermiques et chimiques des divers matériaux. Ces différences limitent l'utilisation des techniques d'assemblage traditionnelles, c'est-à-dire l'assemblage mécanique, le soudage par fusion et le collage, et nécessitent ainsi le développement de nouvelles solutions d'assemblage.

Dans ce contexte, cette étude vise à répondre aux défis des soudages hétérogènes ainsi qu' à développer deux nouvelles solutions originales d'assemblage hybride métal/composite en utilisant le procédé de soudage par impulsion magnétique.

Abstract

Reducing CO2 emissions and improving performance are still the main goals of the automotive industry. To achieve these objectives, automotive suppliers are still seeking to lighten the structures through the use of heterogeneous materials that has evolved in recent decades. We find today in one vehicle mild steels, very high strength steels, light alloys such as aluminum and magnesium alloys as well as fiber reinforces polymeric composites.

The presence of dissimilar materials arises several challenges regarding both the heteregeneous metal assemblies and hybrid metal / composites assemblies. The differences in the mechanical, thermal and chemical properties of the various materials limit the use of traditional assembly techniques, i.e. mechanical assembly, fusion welding and adhesive bonding, and thus the development of new assembly solutions is required.

In this context, this study aims to meet the challenges of heterogeneous metal welding and aims to develop two new original hybrid metal / composite assembly solutions using the magnetic pulse welding process.

Contents

Nomenclature

Roman Symbols

AHSS Advanced high strength steels

DP Dual phase steels

EXW Explosive welding

MPSW Magnetic Pulse Spot Welding

MPW Magnetic Pulse Welding

R stress ratio

List of Figures

List of Tables

Introduction

The increasing stringency of the environmental norms to reduce pollution and CO_2 emission as well as improving fuel economy present today the most important challenges for the automotive industry. To meet these challenges, the OEMs have a must to produce much lighter vehicles for the future. In order to achieve this goal, the materials used in the construction of automobiles have changed significantly in the last decades and today a combination of low carbon steels, high strength steels, light alloys, such as aluminum and magnesium alloys, and fiber reinforced polymer composites (FRPC) are used in one vehicle.

These varieties of materials combinations, and which will have tendency to increase more and more in the near future, arise the issues of joining dissimilar metals and of hybrid joining between metals and FRPC. The problems in achieving dissimilar joints are related to dissimilarities in mechanical, thermal and chemical properties. These differences have limited the use of the traditional joining techniques, i.e. mechanical joining, fusion welding and adhesive bonding, and made the development of new joining solutions a major concern for the industry especially in the case of FRPC to metals joining.

In the automotive industry, every new joining method should minimize the limitations faced in traditional techniques and at the same time it should be applicable under mass production conditions that is high productivity, high reliability, cost effectiveness, recyclability and with less damage on joining partners.

In this context, this study aims to develop new solutions for joining FRPC to metals using the magnetic pulse welding (MPW) / spot welding (MPSW) technology. This technology has been successfully applied for joining similar and dissimilar metals [77, 132, 149, 199, 239, 241] (aluminum to aluminum, aluminum to steel, aluminum to magnesium...) and consequently, extending its use for joining metals to FRPC makes it a multi-use solution.

MPW is a high-velocity impact welding method that consists in accelerating one metal, using magnetic diffusion phenomenon, at very high velocities against another fixed metal where the impact between the two metals creates the weld. It is classified as solid state welding process which means that there will be no heat generation during the welding and therefore thermal damages on the FRPC could be avoided. At the same time, MPW is a very fast process (few microseconds) and it could be robotized which means that it can be applied under mass production conditions.

For all these reasons, two solutions for joining metals to FRPC were developed using the MPW technology and they are based on two principles that take into account different possible applications. Both solutions were the subject for two patents [101, 175].
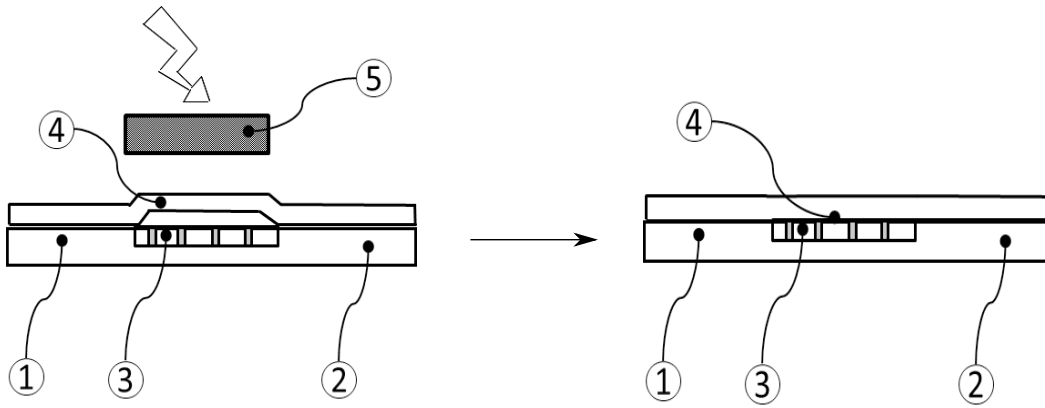
Figure 1: first joining principle
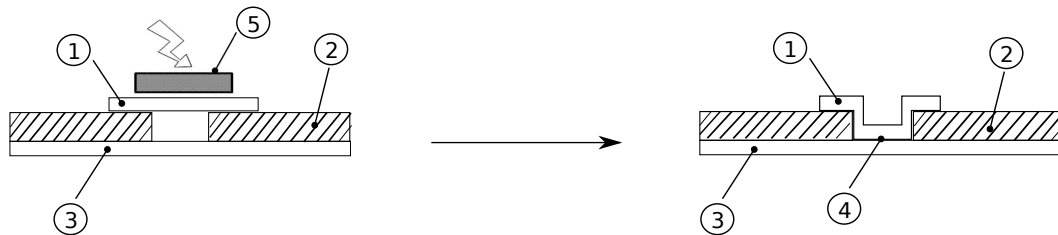
Figure 2: second joining method principle

The first principle (Fig.1) consists in introducing a thin metallic insert (made of aluminum or steel) in the intended joining areas of the FRPC and to weld after that the metallic part on this insert using MPW / MPSW creating then the joint between the two pieces.

The second principle (Fig.2) consists in leaving a hole inside the FRPC in the intended joining areas through which a metallic patch, positioned above it, will be welded to the metallic part using MPW / MPSW.

Looking at the proposed solutions, one can clearly see their multi-physical aspect as well as the large amount of questions that should be asked in order to have a full control of the proposed processes. These questions can be divided into three big areas which will constitute the work outline of this thesis:

- first and since the welding occur between the metal part (aluminum or steel) and another metal component (insert or patch), the development of the proposed solutions goes through the development of the MPW / MPSW process for metal to metal welding. An important point here to mention is that this development will also benefit to the MPW technology on the subject of the aluminum to steel welding;

- the second point to consider is the design and introduction of metallic inserts in the FRPC in order to test and validate the first principle;

- and finally comes the testing and validation of the second principle.

In order to try to advance the comprehension of different involved topics, this dissertation will be divided into five main chapters:

Chapter 1 focuses on a litterature review about different involved subjects. It will include a summary about the joining techniques used and always under development for assemblies between metals and FRPC and a review on the dissimilar welding challenges between aluminum and steel. After that, a detailed presentation of the MPW / MPSW process will be exposed to present next the numerical simulation review of the process.

Chapter 2 will interpret the tooling design for the MPW. It will discuss first the electromagnetic phenomenon involved in the MPW processes from a physical point of view in order to clear physical understanding of the electromagnetic phenomena and to apply them on the coil design and the mounting system considerations. Then we will present the numerical model developed using the commercial FEM-BEM code of LS-DYNA that will be used next to study the effect of different parameters of the process on the impact phenomenon between metals in both MPW and MPSW cases.

Chapter 3 investigates the development of the metal to metal MPW/MPSW. The experimental setup and welding parameters of a combination of aluminum alloys with low carbon and dual phase steels will be presented: 5754 with DC04, 5182 with DC04, 5182 with DP450, 6016 with DC04 and 6013-T4 with DP1000. Mechanical testing and microscopic observations and analyses of the joints will be afterward discussed. Also, within this chapter a special attention will be given to the applicability of MPSW for welding aluminum to zinc coated steels where a full section discusses the effect of galvanizing on mechanical performance and microstructure of the welds.

Chapter 4 details the innovative solutions proposed for joining FRPC to metals. Within this chapter, the concept feasibility tests for both principles will be presented: metallic inserts design, patch and holes in FRPC and examining the transition from the metal/metal MPW parameters to metal/FRPC hybrid joining parameters. Different mechanical testing results as well as micrsocopic observations and analysis of the joints will be discussed.

Chapter 5 concerns the development of a simplified model for constructing welding windows. In this chapter, a method using the numerical simulation will be proposed with the aim of defining a path from the process parameters to the physical parameters to be able to predict whether we will have a good quality weld or not. The model will be linked with the experimental results and discussed.

Introduction

L'industrie automobile subie aujourd'hui d'un côté des normes environnementales de plus en plus sévères pour réduire la pollution et les émissions CO2 et de l'autre côté une demande de la clientèle pour des voitures de moins en moins consommatrices de carburant. Pour relever ces défis, les équipementiers doivent impérativement produire des véhicules beaucoup plus légers. Pour atteindre cet objectif, l'emploi des matériaux hétérogènes dans le monde de l'automobile a considérablement augmenté au cours des dernières décennies et nous trouvons aujourd'hui à la fois des aciers doux, des aciers à très hautes résistances, des alliages légers tels que les alliages d'aluminium et de magnésium ainsi que des composites à fibre de verre ou de carbone.

La multiplication des matériaux utilisés dans les véhicules pose aujourd'hui plusieurs défis concer-

nant à la fois l'assemblage bimétallique et l'assemblage hybride métal/composite. Les difficultés pour réaliser ce type d'assemblages sont essentiellement liées à la différence des propriétés mécaniques, thermiques et chimiques des divers matériaux. Ces différences limitent l'utilisation des techniques d'assemblage traditionnelles, c'est-à-dire l'assemblage mécanique, le soudage par fusion et le collage, et nécessitent ainsi le développement de nouvelles solutions d'assemblage.

Dans l'industrie automobile, chaque nouvelle méthode d'assemblage doit minimiser les difficultés rencontrées avec les procédés traditionnelles tout en respectant la cadence de production, la rentabilité, la recyclabilité et en minimisant les risques de dommages sur les pièces à assembler.

Dans ce contexte, cette étude vise à développer de nouvelles solutions d'assemblage hybride métal/composite en utilisant la technologie de soudage par impulsion magnétique / soudage par point par impulsion magnétique. Le soudage par impulsion magnétique a démontré son intérêt pour souder des métaux homogènes et hétérogènes [77, 132, 149, 199, 239, 241] (aluminium/ aluminium, aluminium/ acier, aluminium/ magnésium, ...) et, par conséquent, étendre son application pour des assemblages hybrides métal/composite ferait de cette technologie une solution d'assemblage multi-matériaux et multi-usage.

Le soudage par impulsion magnétique est un procédé d'assemblage à l'état solide qui consiste à accélérer une pièce métallique électriquement conductrice en utilisant le phénomène de diffusion magnétique ; cette pièce impactera une pièce fixe créant ainsi une soudure entre les deux pièces. Puisque le procédé se fait sans une source de chaleur, il n'aura pas des effets thermiques sur la pièce composite. En outre, ce procédé est très rapide et susceptible d'être robotisé donc il peut être bien adapté à une cadence de production automobile.

Pour toutes ces raisons, deux solutions innovantes utilisant le soudage par impulsion magnétique ont été développée en tenant compte de tout type d'application possible. Les deux solutions ont été sujet de deux brevets [101, 175].

La première solution (Fig.1) consiste à introduire un insert métallique de faible épaisseur dans la zone d'assemblage de la pièce composite et à venir souder après par impulsion magnétique la pièce métallique sur cet insert créant ainsi une jonction entre les deux pièces.

La deuxième solution (Fig.2) consiste à laisser un trou dans la pièce composite dans la zone d'assemblage au travers lequel un patch métallique sera soudé à la pièce métallique par impulsion magnétique.

Comme nous pouvons voir dans les deux solutions, nous sommes devant des procédés multiphysiques qui nécessitent de répondre à plusieurs questions afin de pouvoir maitriser les procédés. Ces questions définissent les trois axes de travail de cette étude :

- comme l'assemblage nécessite le soudage entre deux composants métalliques, il est nécessaire de travailler au préalable sur le développement du procédé de soudage par impulsion imagnétique pour les applications bimétalliques. Ce développement sera aussi d'un très grand intérêt pour les applications métal/métal ;

- le second axe est celui de la conception des inserts métalliques et de l'étude de faisabilité de la première configuration d'assemblage métal / composite ;

- le troisième axe concerne l'étude de faisabilité de la seconde solution d'assemblage métal / composite.

Pour répondre aux différents défis de cette étude, le mémoire est structuré en cinq chapitres :

Le **Chapitre 1** se concentre sur la revue bibliographique de différents aspects techniques et scientifiques liés à divers sujets. Une revue des assemblages hybrides métal/composite en cours d'utilisation et en cours de développement sera donnée. De même pour le soudage hétérogène aluminium/acier nous discuterons des difficultés concernant ce sujet. Ensuite, une présentation détaillée du procédé de soudage par impulsion magnétique sera donnée ainsi que la simulation numérique associée.

Le **Chapitre 2** se concentrera sur la compréhension physique du problème électromagnétique pour pouvoir bien assimiler les différents phénomènes observés dans les procédés d'impulsion magnétique. Cette compréhension approfondie a pour but de déterminer des règles de conception pour les inducteurs et des systèmes de montage pour une meilleur efficacité. Dans ce chapitre, nous présenterons également le développement d'un modèle numérique pour le procédé en utilisant le logiciel LS-DYNA afin d'étudier l'effet des différents paramètres du procédé sur les conditions d'impact dans les deux cas de soudage par impulsion magnétique et de soudage par point par impulsion magnétique.

Le **Chapitre 3** traitera du développement du procédé de soudage par impulsion magnétique pour les applications métal/métal. Une étude expérimentale complète sera donnée pour des soudures entre différents couples d'alliages utilisés dans l'automobile: 5754/DC04, 5182/DC04, 5182/DP450, 6016/DC04, 6013-T4/DP1000. Les essais mécaniques et les caractérisations métallurgiques seront également présentées. Dans ce chapitre, nous traiterons également du soudage d'aluminium avec les aciers revêtus et les effets de revêtements sur les soudures par impulsion magnétique.

Le **Chapitre 4** présentera en détails les deux solutions d'assemblage métal/composite. Les études de faisabilité des deux solutions seront présentées : conception des inserts métalliques, patch et trous dans les composites ainsi que le report des paramètres de soudages métal/métal pour application à l'assemblage métal / composite. Des essais mécaniques sur les assemblages et des analyses microscopiques seront également présentés.

Le **Chapitre 5** présentera le développement d'une méthode simplifiée pour la construction d'une fenêtre de soudabilité physique. Cette méthode a pour but de lier les paramètres procédés aux paramètres physiques de soudure pour pouvoir prédire la qualité de la soudure obtenue.

Chapter 1

Literature Review

1.1 Résumé

Ce chapitre présente une étude bibliographique complète de divers sujets liés au travail de développement de cette étude.

La première partie de la revue bibliographique est consacrée au sujet des assemblages hybrides métal/composite qui est aujourd'hui au centre de l'intérêt de l'industrie automobile. Les procédés traditionnels que ce soit les assemblages mécaniques ou le collage restent toujours les plus utilisés puisqu'ils sont bien connus dans l'industrie et leurs différents outils côté applications ou côté théoriques sont bien établis. Les assemblages mécaniques sont bien connus pour leur capabilité d'assemblage de n'importe quel types de matériaux ensembles, ils sont faciles à démonter si besoin, les différentes technologies et machines liées à ces types d'assemblage sont bien développées et les modèles numériques ont un très bon niveau de précision. Pourtant, ce type d'assemblage présente quelques inconvénients côtés composites : la concentration des contraintes, le risque d'infiltration d'eau à l'intérieur des fibres, de laminage et le risque de rupture des fibres. Côté collage c'est surtout la longue durée de préparation des surfaces des pièces ainsi que les questions de sécurité liées aux produits chimiques utilisés et les limitations de performance mécanique qui posent problème.

D'autres techniques ont également été développées qui combinent les deux et qui ont présentés de meilleures performances mécaniques mais en même temps elles augmentent énormément le temps de production. Parmi les autres techniques qui sont toujours en cours de développement, nous pouvons dire qu'elles sont presque toutes basées sur des procédés employant la fusion du plastique. On peut citer : le soudage ultrasonique par point, l'assemblage par laser, l'assemblage par friction ou le soudage par recouvrement par friction.

Par la suite, le sujet des soudures hétérogènes aluminium/acier est présenté en détail en mettant l'accent sur les difficultés liées à ce type de soudure surtout qu'il y a des grandes différences dans les propriétés physiques, thermiques et métallurgiques qui nécessitent une manipulation et une optimisation des procédés pour éviter les effets de dégradation que nous pouvons avoir dans les pièces à assembler. Il faut aussi éviter la formation de couches épaisses d'intermétalliques qui dégradent la tenue mécanique des soudures. Ces risques peuvent être évités en employant des procédés de soudure à l'état solide pour lesquels il y a eu beaucoup de développement durant les

dernières années. On peut citer le procédé de soudage par friction malaxage (FSW) pour plusieurs applications qui sont déjà utilisées en série.

Les autres procédés de soudure à l'état solide qui ont démontré qu'ils permettent de s'affranchir des différences de propriétés des matériaux hétérogènes, sont les soudure par impact dont la soudure par explosion est la plus ancienne par exemple. La difficulté avec la soudure par explosion est qu'elle n'est pas adaptée aux conditions de grande cadence industrielle et en plus elle présente de grandes difficultés de sécurité. En revanche, la soudure par impulsion magnétique qui a aussi démontré sa capacité à souder divers alliages métalliques hétérogènes, est mieux adaptée d'un point de vue ergonomie et possibilité de robotisation.

Le procédé de soudure par impulsion magnétique est un procédé basé sur le principe de diffusion magnétique (Fig. 1.37): un courant intense et variable dans le temps est déchargé dans un inducteur ; cet inducteur génère un champ magnétique variable dans le temps qui diffuse dans la pièce conductrice placée à proximité de cet inducteur ; ce champ va induire des courants à l'intérieur de cette pièce conduisant ainsi à d'importantes forces électromagnétiques qui vont pousser la pièce à de très grandes vitesses. Celle-ci va impacter la pièce fixe et créer une soudure. Pour cela, nous avons besoin : d'un générateur d'impulsion, d'un inducteur et d'une pièce conductrice électriquement. L'ensemble peut être considéré comme un circuit RLC (Fig. 1.38).

Les paramètres du procédé sont à la fois géométriques, électriques et physiques et bien entendu liés aux propriétés des matériaux formant les pièces. Parmi ces paramètres: l'énergie de décharge (Eq. 1.1) et le courant de décharge (Eq. 1.2), l'épaisseur de peau (Eq. 1.8), la pression magnétique (Eq. 1.9), la distance séparant les deux pièces (Fig. 1.39), la géométrie de l'inducteur, le comportement dynamique de la pièce induite, l'angle d'impact et la vitesse d'impact (Fig. 1.44).

D'un point de vue opérationnel, comme nous pouvons le remarquer, un jeu entre les deux pièces est indispensable pour accélérer la pièce projectile à la vitesse nécessaire pour la soudure. Pour une application plus pratique industriellement, Manogaran et al. [131] ont développé le procédé de soudage par point par impulsion magnétique qui évite les problèmes de positionnement des pièces. Cette méthode consiste à créer un bossage sur la pièce conductrice dans la zone où la soudure prendra place (Fig. 1.45) et d'accélérer juste cette bosse de telle manière à obtenir un point de soudure entre les deux pièces (Fig. 1.46).

Voyons maintenant les différentes théories qui expliquent la formation des soudures à l'interface entre les deux pièces. Ces théories ont été établies durant le développement du procédé de soudage par explosion et adoptées pour les soudages par impulsion magnétique du fait des grandes similitudes de l'allure ondulatoires de l'interface de soudage. Ces théories peuvent être classées en quatre catégories : mécanisme d'indentation du jet formé lors de l'impact progressif [1, 18, 28, 181] (Fig. 1.50), instabilité de Kelvin-Helmholtz [28, 86, 161, 181, 183, 184], mécanisme de formation de tourbillons [28, 49, 58, 113, 181, 182] (Fig. 1.51) et le mécanisme d'intéraction d'ondes de choc à l'interface [18, 25, 109, 112, 181, 182] (Fig. 1.52).

Nous avons également vu que malgré la ressemblance entre la technique traditionnelle de soudage par explosion et le soudage par impulsion magnétique, nous ne pouvons pas considérer que les deux procédés sont à 100% identiques. Si nous considérons le mode opératoire et la manière dont les pièces sont accélérées dans le cas du soudage par explosion (Fig. 1.54): les explosives couvrent

toute la surface de la pièce et agissent sur toute cette surface, l'angle d'impact est constant tout le long de la formation de la soudure qui à son tour est continue sur toute la surface accélérée. Cela n'est pas le cas en impulsion magnétique. Après nos recherches dans le domaine du soudage par explosion, la grande ressemblance peut être établie avec le procédé développé par la NASA (Fig. 1.55, Fig. 1.56) et pour lequel nous ne trouvons que peu de littérature accessible sur les détails techniques.

Ensuite, nous avons regardé la simulation numérique du procédé. Le grand nombre de paramètres et de phénomènes physiques impliqués dans ce type de procédé rend la simulation numérique nécessaire pour pouvoir comprendre les différentes interactions. Pour les personnes qui sont spécialisées dans la mécanique et les matériaux, la première chose à faire est de comprendre la formulation des équations électromagnétiques et comment elles sont liées aux équations mécaniques et thermiques dans les codes de simulation. Le point de départ de toute résolution mathématique des problèmes électromagnétiques ce sont les fameuses équations de Maxwell (Eq. 1.11 à l'Eq. 1.14) qui couplées avec les équations de continuité (Eq. 1.15), les équations constitutives (Eq. 1.16, Eq. 1.17), de la loi d'Ohm (Eq. 1.18) et des forces de Lorentz (Eq. 1.23) couvrent toutes les interactions électrique-mécanique et thermique. Dans le cadre des procédés d'impulsion magnétique, nous sommes dans l'approximation quasi-statique. Les équations sont présentées dans le système d'Eq. 1.43 et les conditions aux limites de passage entre deux milieux sont présentées de l'Eq. 1.25 à l'Eq. 1.28. La formulation typique de problème est présentée dans la section 1.6.4 ainsi que la méthode de résolution utilisée par le logiciel LS-DYNA que nous allons utiliser tout le long de ce travail. L'intéraction entre les différents solveurs du logiciel est présentée dans la Fig. 1.58. Finalement, nous avons discuté les méthodes de simulation en cours de développement et visant à simuler la formation de l'interface de soudure ainsi que la définition des bons paramètres de soudure ([53, 54, 63, 155, 189]).

Suite à cette étude bibliographique, notre objectif principal est d'étendre le domaine d'application du soudage par impulsion magnétique à des applications non-métalliques permettant ainsi d'avoir un procédé capable avec les mêmes installations de réaliser des soudures homogènes, hétérogènes ainsi que des assemblages métal/composite. Tout cela passe par plusieurs vagues de développement du procédé et des solutions d'assemblage proposées qui seront traités dans les différents chapitres de cette thèse.

1.2 Introduction

As it is now clear, the main interest of this study is to respond to the challenge of dissimilar joining with a special attention for the assemblies between FRPC and metals especially in the planar sheet applications. The proposed solutions uses the MPW/MPSW which occurs between the metal part (aluminum or steel) and another metal component (insert or patch) creating the assembly between the FRPC and the metal. Hence, the MPW/MPSW development for metal to metal welding is an essential point in the study and which at the same time will be an opportunity to develop the MPW technology for the dissimilar welding of aluminum alloys to steel alloys in the automotive industry.

In this context, this chapter will present a full review of different revealed points. We will start

first by the hybrid joining techniques between the metals and FRPC. After that, a review on the dissimilar welding between aluminum and steel alloys will also be given to understand difficulties and challenges related to this topic. Thereafter, the detailed presentation of MPW and MPSW processes will be given: principle, equipement, advantages and limitations. In addition, the numerical modeling and simulation of the MPW problem will be presented. Finally, a conclusion will recapitulate the whole picture in order to define on what should the study concentrate.

1.3 FRPC to Metals Joining

In this section a review for the assembling methods of polymer composites to metals used nowadays will be presented starting with the traditional most used joining techniques, i.e. mechanical joining and adhesive bonding, and continuing through new techniques, which are always under investigation and development. Their main characteristics, advantages and limitations will be discussed.

1.3.1 Mechanical joining

The term *mechanical joining* refers to technologies and processes that allow to have permanent connections between two or multiple workpieces by transforming at least one of these pieces or by using an additional fastener such as bolts, nuts, cap screws, setscrews, rivets, spring retainers, locking devices, pins and keys [37, 77]. In the case of composite-metal hybrid structures, the most used methods are those that employs additional fasteners, i.e. mechanical fastening processes, since the forming processes are limited by the thickness and formability of the composites and the metals to join.

1.3.1.1 Mechanical fastening

Riveting, bolting, pinning and bonding are all possible where the composite part can be drilled, countersunk and joined with a fastener: rivets, pins, two-piece bolts and blind fasteners made of aluminum, titanium and stainless steel [82]. This kind of joining is widely used, well established in the market and cost-effective means of joining in all industrial fields since it represents some important advantages [2, 12]:

- Joining of dissimilar materials

- Ease of disassembling when required

- Easy technology and machinery

- Well-known prediction methods and analysis

- Fast surface preparation and cleaning

- Easy repair and replacement
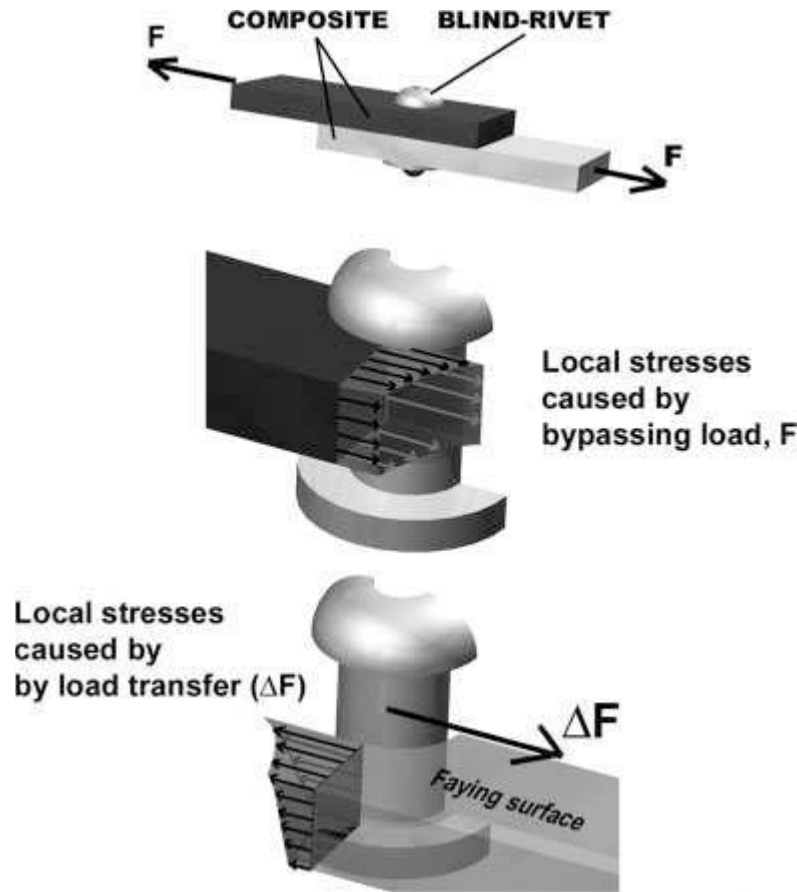
Figure 1.1: Nonuniform distribution of local peak bearing stress-Blind Rivet Case [12]

Despite all the advantages cited before, several factors limit the mechanical fastening processes and should be considered. The common problem for both composites and metals in this type of assemblies, is the stress concentration caused by holes and nonuniform distribution of local peak bearing stress due to interaction between the fastener and the parts in the joining region (Fig. 1.1).

Another effect during drilling and machining of the composite is the damage caused by these processes where they can cause delamination and exposure of the fibers so that the intrusion of water between the fastener and composite will weaken the material [12, 82]. In addition, the metallic fasteners used can expand and contract when changes in temperature occur which leads to relative motion between the joined parts and hence changes in clamping load where the pressure within the joint is often critical[82, 164]. The other point to reveal in this case is also the difference in the thermal expansion coefficient between the metallic and composite partners which may increase the residual stresses in the joining area [12, 164]. Furthermore, the galvanic corrosion is an additional factor to take into consideration due to the chemical reaction of the fastener material and the composite fibers as in the case of an aluminum fasteners and carbon fibers since the aluminum and carbon can chemically react together producing a corrosion product, the aluminum carbide ($4Al + 3C \rightarrow Al_4C_3$). Coating the fasteners can reduce this effect but increases the cost and time to assembly [82]. Nonmetallic fasteners exist also and are typically made of fiber reinforced plastic composites; they are used in secondary or tertiary structures due to their low elastic modulus without forgetting that they are lighter, more electromagnetically transparent and have a better

11
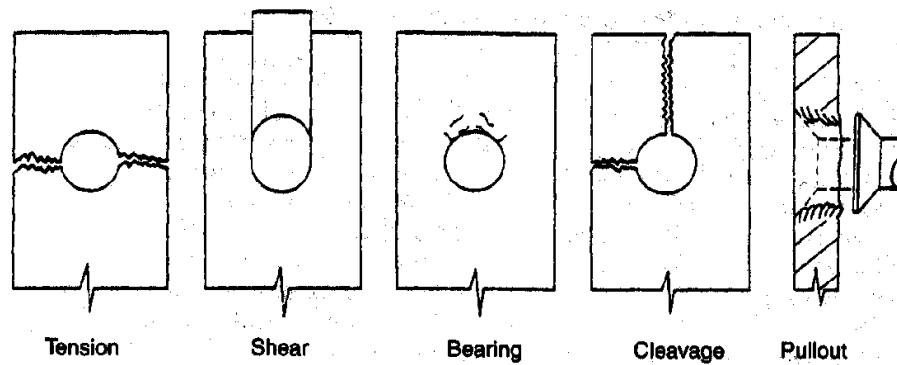
Figure 1.2: modes of failure for mechanical joints in composites [82]

corrosion resistance than metallic fasteners [12, 65].

An important consideration should also be given to both kinds of creep in the joined partners, i.e. creep of the fastener hole and the long-term material compression, as well as for the environmental factors (wet, heat...) that can cause degradation of the shear and bearing strength properties. For example, for fiber reinforced epoxies, the presence of wet at high temperatures (above 100°C) can cause a strength loss that can reach 40% [2, 12, 82]. When it comes to the failure modes, and because of the complex failure mechanisms of composites, two additional modes other than those existing in the case of fastened metal structures become possible: cleavage and pullout. Hence, the possible failure modes are five: tension, shear, bearing, cleavage and pullout (Fig. 1.2). Moreover, an important aspect to consider is the increase in weight of the structures due to the addition of the fasteners and from an industrial point of view, more steps are required in the production cycle where also the properties of the composites and metals play an important role in the used techniques and equipments for producing quality holes and in choosing the type of fasteners and their material.

All of the discussed aspects should be taken into consideration for designing the mechanical fastening processes and try to limit the negative influences on the joint's quality and to reduce the required cycle time.

1.3.1.2 Hole-Clinching process

Joining methods based on forming technology, which creates connection between the metals without any fastener, presents a high economical efficiency because of the saved costs of additional parts and the automatic feeding system of fasteners. For this reason, their manufacturing is interesting for industrial applications and where clinching process is one of the most applied technology of this kind [77]. The traditional application of this process consists in pressing a local limited area of the materials to join using a punch and die in order to form a protrusion that creates a mechanical interlocking between the two materials (Fig. 1.3). Joining of more than two parts in one step is possible.

In the case where the metals have low ductility like composites, it is difficult to achieve geometrical interlocking using this process. [120] Lee et al. developed a new mechanical clinching process called "hole-clinching" which enables the joining of a ductile material to low-ductility material.
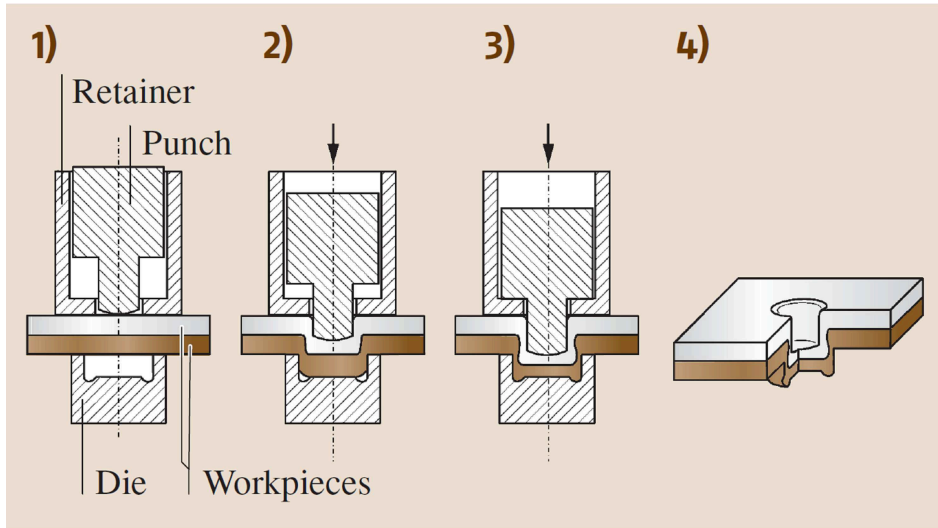
Figure 1.3: process steps of clinching [77]
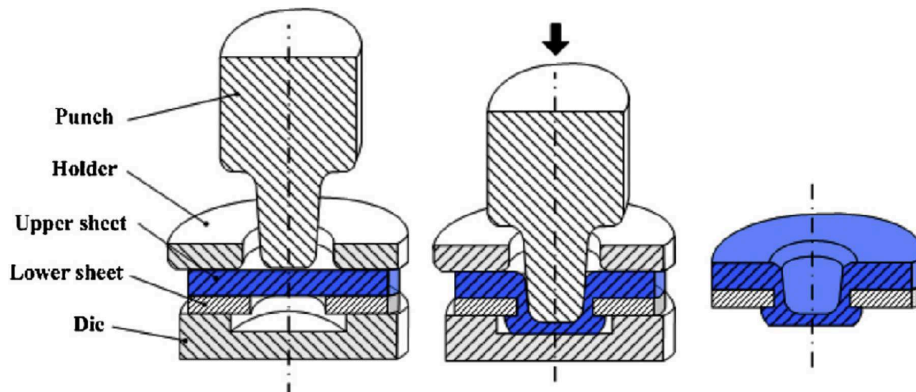
Figure 1.4: schematic of hole-clinching process [120]

In this process, the low-ductility material was used as the lower sheet into which a hole is formed and the ductile material as the upper sheet which will be indented by the punch into the die cavity through the hole made inside the lower sheet to form an undercut that realizes the geometrical interlocking (Fig. 1.4). The lower sheet is not deformed by the punch and does not affect the deformation of the upper sheet when the geometrical interlocking is formed as it is seen in the Fig. 1.5 where the process variables are presented also.

The process was tested on the joining between Al6061-T4 and a carbon fiber reinforced polymer CFRP (Fig. 1.6) where they reported that the upper sheet dragged the composite sheet into the die cavity due to friction between the two sheets. This dragging and the compression load resulting from the spreading of the upper sheet material caused delamination inside the composite (Fig. 1.7). The pieces underwent a single-lap shear test where the average shear fracture load is evaluated as being 3.155 kN as it seen from the Fig. 1.8.

1.3.2 Adhesive bonding

The use and development of polymeric adhesive bonding in joining structural, semi-structural and non-structural components was employed at a time to meet the complexity of modern structures
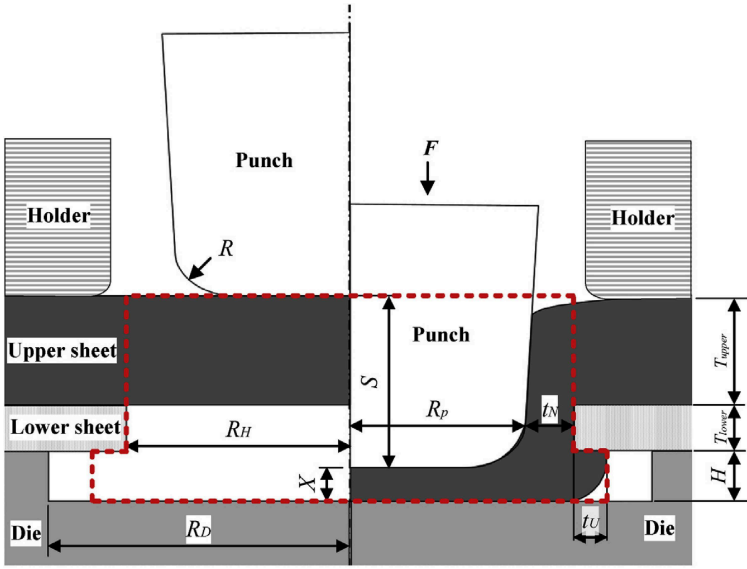
Figure 1.5: hole-clinching process variables [120]

Figure 1.6: Al6061-T4 and CFRP joining by hole-clinching process [120]
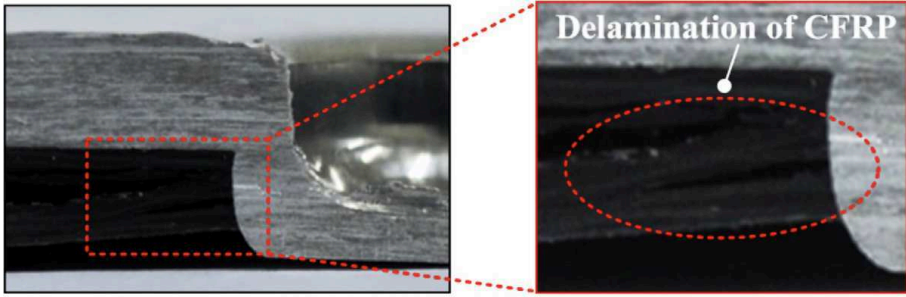
Figure 1.7: delamination of the composite in hole-clinching process [120]
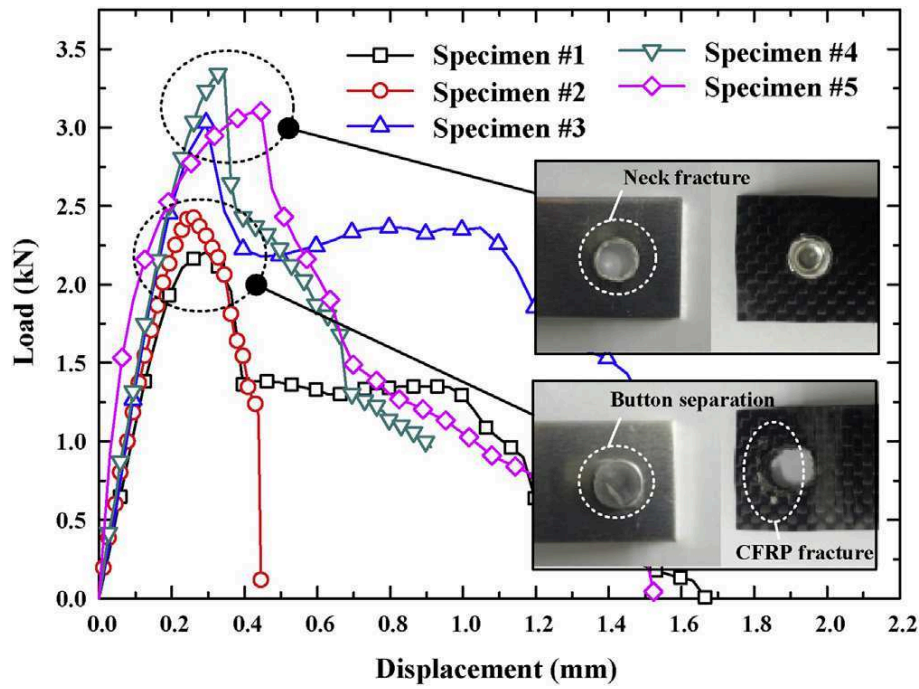
Figure 1.8: load-displacement curves for a single-lap shear test of hole-clinched joint between Al6061-T4 and CFRP [120]
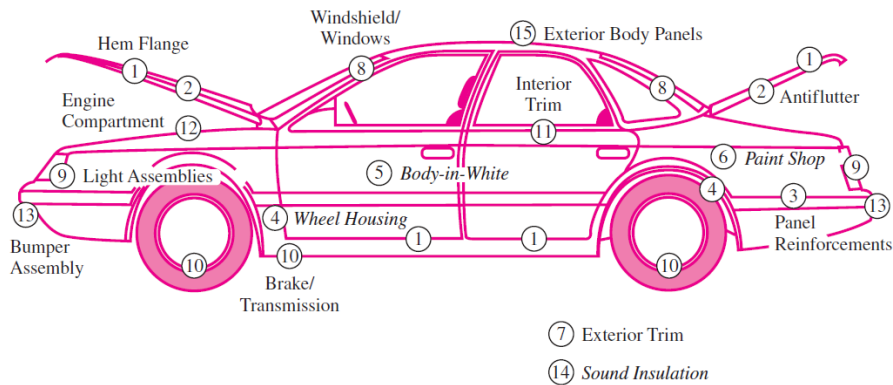
Figure 1.9: adhesives in modern automobile [37]

as well as the diverse types of materials involved and to overcome the disadvantages presented by mechanical fastening processes. It presents the possibility of joining any combination of similar and dissimilar material, minimizes or prevents galvanic corrosion in dissimilarities cases, reduces weight of the assembly and it is often less expensive and faster than mechanical fastening [37, 82]. Adhesives provide large stress-bearing area and excellent fatigue strength and they have good vibrational damping and shock absorbing properties [2, 12, 186]. The Fig. 1.9 illustrates the application of adhesives in a modern automobile where it is seen the large number of applications of adhesives.

In adhesive joints, solid materials other than the adhesive are known as the adherends and the phenomenon, which allows the adhesive to transfer a load from the adherend to the adhesive joint, is called adhesion . There is also the phenomenon of abhesion , which is the condition of having minimal adhesion [167]. To have a good bond, basic steps are required: proper joint design and

15
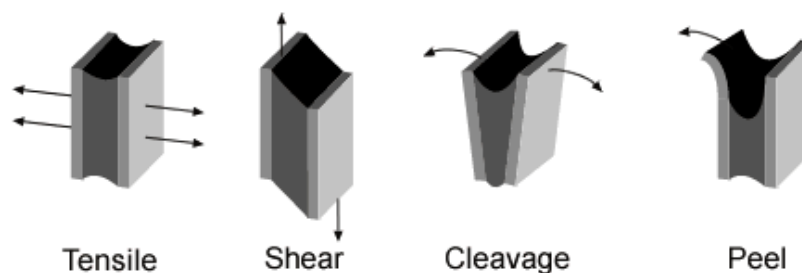
Figure 1.10: types of possible stresses in bonded joints

selection of adhesive, surface cleanliness, wetting of the surface by the adhesive and the cure or solidification of the adhesive [37, 82, 167, 205].

The joint design should take into consideration the four basic types of possible loading stress in a bonded structure (Fig. 1.10):

- Tensile stresses: when the acting forces are uniformly distributed over the bonded area and are perpendicular to the plane of the joint

- Shear stresses: when the acting forces tend to separate the adherends

- Cleavage stresses: when the acting forces are at one end of a rigid bonded assembly and tend to split the adherends apart

- Peel stresses: similar to cleavage but in this case one or both of adherends are flexible

Good design requires that adhesive joints are constructed in a manner that the adhesive carries the load in shear rather than tension and avoids peel and cleavage stresses that can be also a result of the tension stresses since in practical, loads are rarely axial to have only tension. An exception is to make in the case of tough flexible adhesives where the peeling stresses are distributed over a wider bond area and present greater resistance to peel than to shear [37, 82]. Also, the distribution of the stress should be as much as possible uniform over the bonding area to maximize the joint efficiency.

Other design parameters to take into consideration are the bond width and the overlap depth as well as the adherends thicknesses. The adhesive strength is directly proportional to the width of the joint but it is not the case when it comes to the overlap depth where the relation between the two is not linear since excessively heavy adhesive-film thickness can cause greater internal stresses during cure and concentration of stresses at the ends of a joint. Optimum adhesive thickness for maximum shear strength is generally between 2 and 8 millimeters [82]. Considering the adherends thicknesses, a phenomena should be paid attention: the distortion in the case of relatively thin flexible adherends which causes cleavage stress at the ends of joint (Fig. 1.11).

The selection of adhesives is a second very important step in the adhesive bonding procedure and there are several important influencing factors that can be summarized in the Table 1.1[82].

These factors are important since they affect physical and chemical properties of both adhesives and plastic substrates which will have a great influence on the bonded joint. The thermal expansion
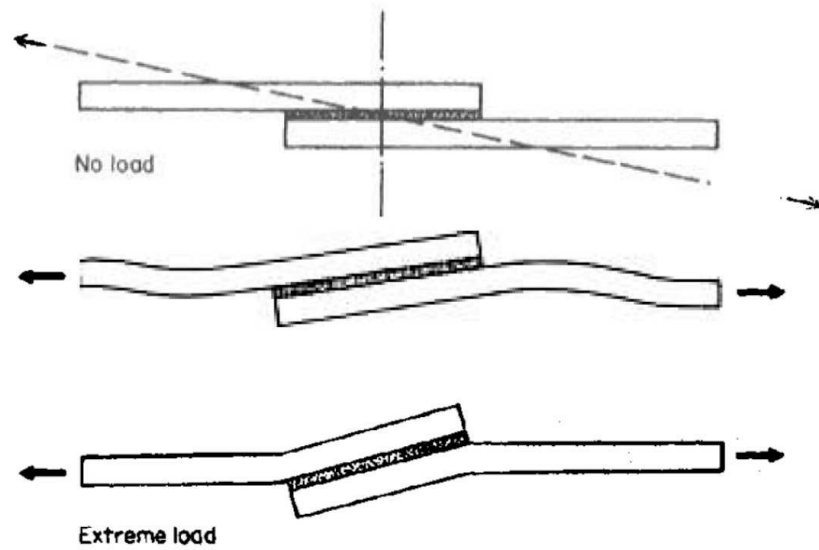
Figure 1.11: distortion in thin adherends case [82]

Stress	Tension
	Shear
	Peel
	Cleavage
	Impact
	Fatigue
Chemical	External (service-related)
	Internal (effect of adherend on adhesives)
Exposure	Weathering
	Light
	Oxidation
	Moisture
	Salt spray
Temperature	High
	Low
	Cycling
Biological factors	Bacteria or mold
	Rodents or vermin
Working properties	Application
	Bonding time and temperature range
	Tackiness
	Curing rate
	Storage stability
	Coverage

Table 1.1: factors influencing adhesive selection

and glass transition temperature of the substrate relative to the adhesive present major concerns as well as the polymeric surface changes due to aging and the environmental conditions. In fact, a big difference in thermal expansion between the adhesive and the substrates will lead to increasing stresses at the interface. Also, the operating temperature should be lower than the glass transition temperature to prevent weak bond and possible creep problems. Furthermore, brittleness of the adhesive at low temperature can be a limitation for the joint strength[82].

The classification of adhesives to choose from can be done in various manner depending on their function (i.e load carrying capability), chemical composition and type. First, the functional classification defines the adhesives as structural, semi-structural or non-structural. Structural adhesives are relatively strong, i.e shear strengths greater than 6.9 MPa ([82, 167]), and permanent where their role is to hold structures together and resist high loads. These properties are common for epoxies and some acrylics. Semi-structural adhesives are adhesives where the failure would be less critical while non-structural adhesives, that are sometimes referred as holding adhesives, have just to hold lightweight materials in place. Then, the chemical composition classification divides the adhesives into four big groups ([37, 82]: thermosetting adhesives (epoxies, polyimides,acrylic...), thermoplastic adhesives (Ethylene-vinyl acetate, polyamide adhesives...), elastomeric-type adhesives (natural rubber, butyl, silicone...) and adhesive alloys or hybrids which are made by combining thermosetting, thermoplastic and elastomeric adhesives (epoxy-phenolic, epoxy-nylon, vinyl-phenolic...). Finally, the type composition is related to the way they cure or solidify. They can be hot melt, reactive hot melt, pressure sensitive, contact or anaerobic adhesives.

Once the adhesive is chosen, the surface cleanliness of plastics prior to bonding is important to eliminate dirt, oil, mold release agents, water or polishing compounds. This step is to avoid the bonding between the adhesive and these weak boundary layers than to actual substrate and it is achieved usually by applying solvents or detergents (acetone, methyl ethyl ketone...). In addition, many plastics requires surface treatments before joining to provide a good surface roughness and to increase surface energy which will allow better wetting and hence better joining strength. These surface preparations can go from a simple mechanical abrasion to physical or chemical modification of the polymeric surface such in crystalline thermoplastics where several methods are used to improve the bonding characteristics of these surfaces: oxidation via chemical treatment or flame treatment, electrical discharge to leave a more reactive surface, plasma treatment and metal-ion treatment. A very important point to involve here is that these treatments decrease with time and it is necessary to bond soon after applying them [82].

After the surface preparations, the wetting of the surface by the adhesive takes place depending on their viscosity. The low viscosity adhesives can be sprayed on, brushed on or applied with a trowel and the heavily bodied adhesive pastes and mastics are applied by syringe, caulking gun or pneumatic pumping equipment [82]. After this phase, the cure of the adhesive takes place. This process can be done depending on the adhesive type where it can be done through a chemical reaction by any combination of heat, pressure and curing agent (epoxies, cyanoacrylates, anaerobic, urethanes, acrylics...) or by a cooling from a molten liquid to a solid state (hot melts adhesives) or by drying due to solvent evaporation (contact adhesives) [82].

Despite of the advantages that adhesive bonding presents, there is some important limitations. The

Adhesive Type	Lap Shear Strength (MPa)	Peel Strength (kN/m)
Pressure Sensitive	0.01-0.07	0.18-0.88
Starch-based	0.07-0.7	0.18-0.88
Cellosics	0.35-3.5	0.18-1.8
Rubber-based	0.35-3.5	1.8-7
Formulated hot melt	0.35-4.8	0.88-3.5
Synthetically designed hot melt	0.7-6.9	0.88-3.5
PVAc emulsion (white glue)	1.4-6.9	0.88-1.8
Cyanoacrylate	6.9-13.8	0.18-3.5
Protein-based	6.9-13.8	0.18-1.8
Anaerobic acrylic	6.9-13.8	0.18-1.8
Urethane	6.9-17.2	1.8-8.8
Rubber-modified acrylic	13.8-24.1	1.8-8.8
Modified phenolic	13.8-27.6	3.6-7
Unmodified epoxy	10.3-27.6	0.35-0.18
Bis-maleimide	13.8-27.6	0.18-3.5
Polyimide	13.8-27.6	0.18-0.88
Rubber-modified epoxy	20.7-41.4	4.4-14

Table 1.2: mechanical performance of various types of adhesives

good mechanical performance is limited to shear resistance where also it does not exceed the 40 MPa in the best case as it can be clear from Table 1.2[37].

The extreme surface preparations, the long cure times in some cases, and the special training requirements to handle hazardous chemicals and solvents present a deceleration for the production cycle time and an increase in costs. Another important disadvantage is the uncertainty in bond's failure prediction. To these it can be added the temperature sensitivity of the adhesives where they cannot perform in a very high temperature environments and VOC emission that present a serious danger on health [2, 12, 82, 205].

1.3.3 Hybrid joints processes

The hybrid joints present a combination of a mechanical joint (riveted, bolted, screwed...) with an adhesive and they are used in many industrial sectors such as aeronautics, automotive and naval industry [70]. The idea of the use of this kind of processes is to combine the advantages of each kind of joint and hence get better properties than those obtained from simple joints [70]: high static strength and better resistance to peeling and fatigue, stiffer structures, sealed joints and better resistance to corrosion, no need for additional fastening while the adhesive is being cured, a two-stage cracking process that makes it easier and safer to detect before the joint breaks.

Investigations on this kind of joining have been done in the case of composite/composite joining [39, 66, 70, 83, 99, 100] as well as in the case of composite/metal joining where [118] investigated failure loads of the bonded/bolted hybrid joints between carbon/epoxy composite and aluminum alloy 7075-T62 (Fig. 1.12) and found that the hybrid joining improves joint strength when the mechanical fastening is stronger than the bonding. However, fiber damage and delamination is still
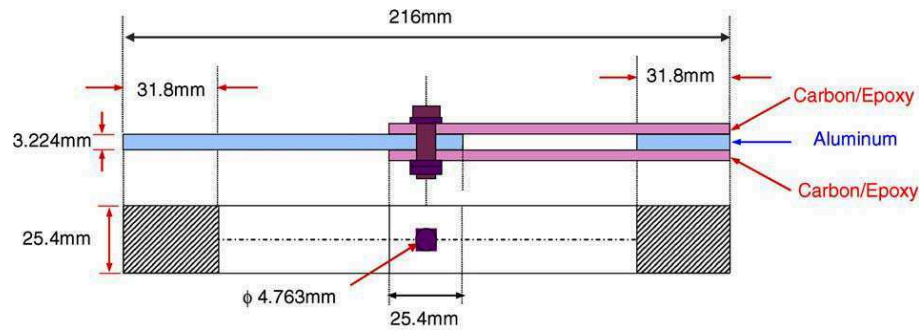
Figure 1.12: bonded/bolted hybrid joint CFRP/Al 7075-T62 [118]
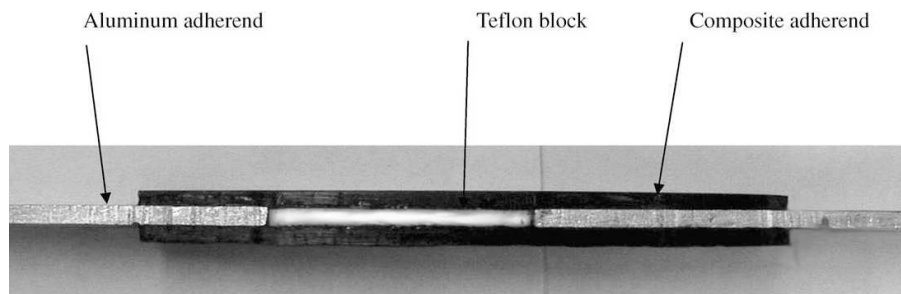
Figure 1.13: co-cured joint between composite and aluminum [163]

a problem for the composite and the manufacturing time has increased due to the curing time of the adhesive that will be added to the mechanical fastening process time in addition to the thermal damage that can be caused to the composite when curing requires elevated temperatures[139].

For all the mentioned reasons, another hybrid joint process was developed: co-curing [85, 102, 103, 163, 195, 196]. In this case, the excessive resin of the composite acts as adhesive (Fig. 1.13) and hence both the curing of the composite and the joining can be achieved simultaneously. This process is used generally to mold a metallic edge into the composite and then weld this assembly to the metal structure via the edge [142]. Despite the reduction of the additional curing time process, the increase in strength's joining was not interesting in comparison with the conventional adhesively bonded joint. As a result, improvement for the process were proposed: [142] suggested the use of perforated metallic parts (Fig. 1.14) on the edge where they will be molded into the composite as well as tongue-and-groove methods [143] (Fig. 1.15). [138] proposed dimple treatment for glass fiber reinforced polymer/aluminum co-cured joints. These solutions consist in complex
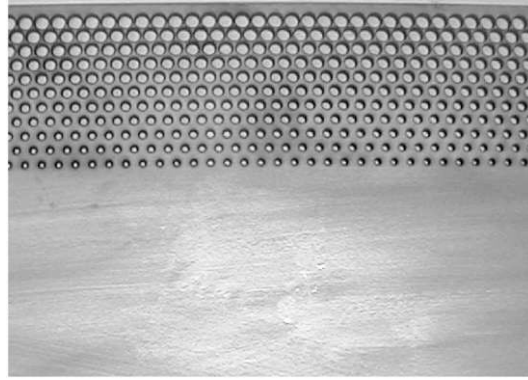
Figure 1.14: Perforated steel sheet for co-curing process [142]
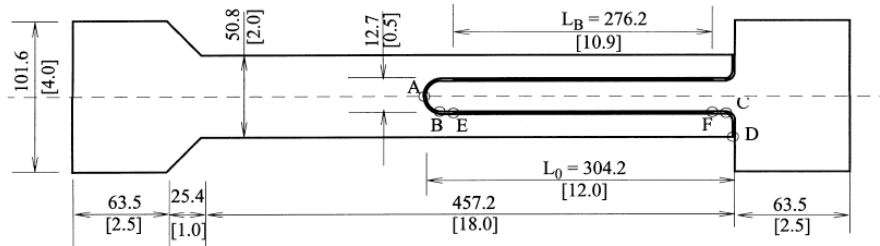
Figure 1.15: tongue-and-groove method [143]

geometries design and require special skills to create perforations, tongue-and-groove and dimples and finally they are still affected by the adherend surface conditions which make them a little bit complicated for application[139].

Another hybrid joint technique was thus introduced by [139] called bolted/co-cured hybrid joining method and which combines co-cured adhesive joints and bolted joints. Here, bolts are inserted in the dry glass fiber composite laminate and aluminum alloy A5052-F before the co-curing process so that the glass fibers are not broken and remain continuous around the bolt holes (Fig. 1.16). The shear tests shows that this method has 1.84 times higher maximum shear strength and a quarter of the standard deviation compared with the co-cured process. Also, the fatigue strength was higher than that of the bolted joint and which was explained as a result of less stress concentration and undamaged glass fibers since the clearance between the bolts and bolt holes is filled with resin.
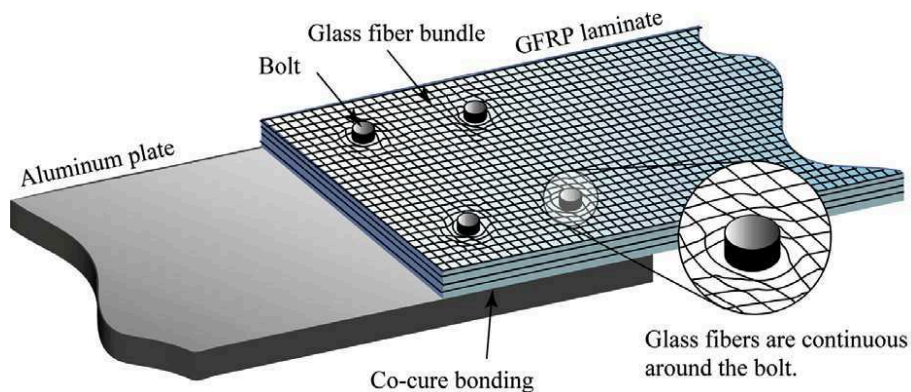
Figure 1.16: bolted/co-cured hybrid joint between aluminum and GFRP laminate [139]

21
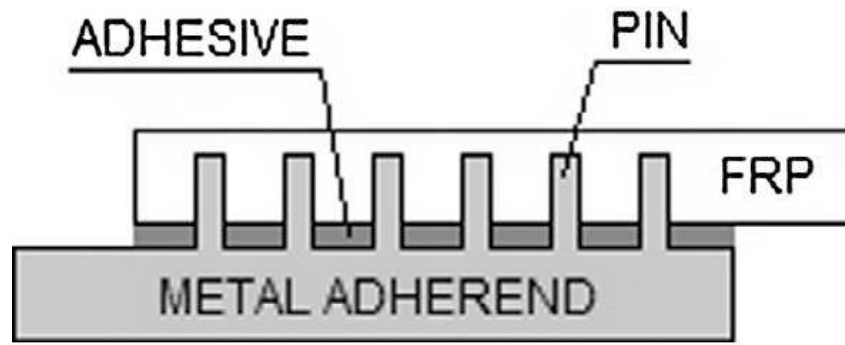
Figure 1.17: section view of an advanced hybrid single lap joint's schematic [73]

Furthermore, the bolts were covered with resin during the curing process which will improve the corrosion resistance.

The complexity of these particular hybrid technique due to the additional weight associated with the fixings and the complexity of the manufacturing process was the motivation to introduce the so-called advanced pinned hybrid joints that combine adhesive bonding with an interlocking array of mechanical reinforcement (Fig. 1.17). The mechanical strength of this type of joints is dependent most on the pins creating and attaching method to the composite and the interaction of these pins with the composite component [73]. To produce the pins on the metallic part (possible for a range of material including steel, aluminum and titanium), surface restructuring processes or additive layer processes can be used. Surface restructuring consists in creating protrusions and intrusions by using an electron beam across the material surface but it presents some disadvantages [73]: high costs because of the beam use, it can cause excessive damage to the metal surface and it is limited in controlling the pin's geometry. This technique was used in the work of [98] where it was demonstrated that this type of joining had greater strength than equivalent bonded joints and a better mechanical energy absorption during failure.

The other techniques called additive layer processes have all the same principle which is adding layers on the material surface to create the required pins. Two common techniques based on metal-powder processing are used and allow reasonable control of pin geometry without causing high damage for the material surface: selective laser melting (SLM) and laser metal deposition (LMD) The first one uses a metal powder bed over which a laser spot is focused to permit full melting (welding) of the particles to form solid shape and hence layer after layer the pins shape is formed. The LMD process uses a laser beam to form a melt pool on the metallic substrate, into which powder is fed to melt after that forming a deposit that is fusion bonded to the substrate and the required geometry is built up layer by layer. The disadvantage of these techniques is the elevated costs for industry [73]. Ucsnik et al. [211] proposed to use the cold metal transfer (CMT) technique to create the pins. This relative new technique allows droplets of molten metal wire to be welded on the metal surface in progressive layers to form small spikes of different shapes and dimensions (Fig. 1.18).

Once the array of pins is created, they are penetrated in the textile leading to a mechanical interlocking between the metal structure and dry laminate to be co-cured with the composite after that. In their work, Ucsnik et al. [211] compared the specimens using this pinned hybrid joint technique
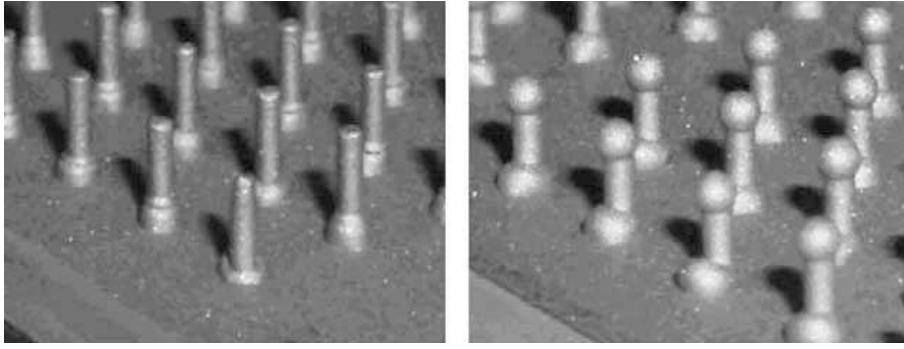
Figure 1.18: pins geometries in advanced hybrid joint technique [211]

with an epoxy bonded reference pieces and found then to have better strength of the joint (reached +52.3% in case of ball pins), higher mean local strains at maximum force (about 1000% in case of ball pins) and an increase in energy absorption capacity (with a factor of 30 in case of ball pins). Graham et al. [73] compared their specimen with what they called co-cured control specimens, i.e. using co-cured joint technique, and have also found better strength, higher energy absorption capacity, and better fatigue durability.

All these hybrid joining techniques are still under experimental and modeling investigation for a detailed understanding of performance, failure as well as geometric and material sensitivity.

1.3.4 Thermoplastics as melt adhesives

Because of the limitations imposed by the traditional joining techniques, the use of thermoplastics as melt adhesives for joining composites to metals was proposed . This method consists in applying a thin layer of thermoplastic material to the metal surface prior to joining and where a major advantage unlike the adhesive bonding is that this application can be done well before joining and can be stored for a long period before joining step ([2, 222]). The fusion bonding methods used in this case are resistance welding [222, 223], ultrasonic welding [179, 222] induction welding [31, 179] and hot press welding [141].

The main advantages of the hot melt thermoplastic adhesives are [2, 32]: infinite shelf life, rapid bonding process, repairs and replacements are possible, and recycle possibility. When it comes to constraints, we can say that they require higher temperature and pressure than thermosetting adhesives [32].

This method was investigated for several combination of aluminum/composite were the three fusion bonding methods were applied. The lap shear strength of the joining reached 20 MPa ([3]).

1.3.5 Ultrasonic spot welding

The ultrasonic welding of similar materials is already established in industrial manufacturing since it is characterized by a low energy input and short welding times ([19, 78]). The ultrasonic plastic welding and ultrasonic metal welding are used with a significant difference between both welding
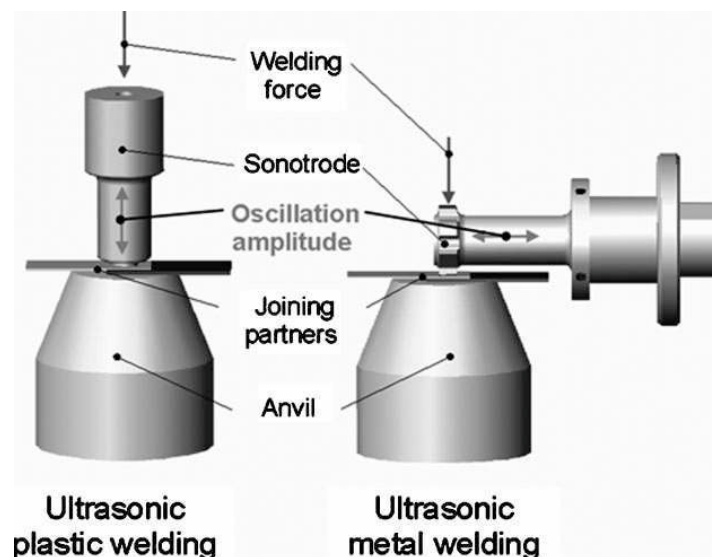
Figure 1.19: ultrasonic spot welding principle [20]
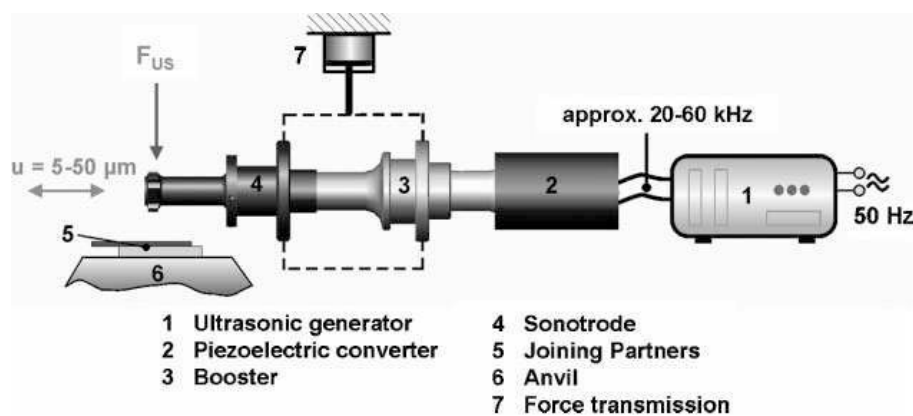
Figure 1.20: ultrasonic spot welding system components [20]

techniques is that, in the first case the ultrasonic oscillation is perpendicular to the weld area while in the second it is parallel to the weld area (Fig. 1.19).

Recent studies showed that the two techniques can be used also to join glass fiber and carbon fiber-reinforced polymer with metal sheets such as aluminum alloys, but the parallel oscillation presents a greater advantage which is, the possibility of a direct contact with fibers without destroying it ([19, 78]). This process consists of two steps: softening and displacement of the polymer matrix out of the welding zone and then direct weld between fibers of the composite and the metal is established.

The components of the ultrasonic spot welding system are shown in Fig. 1.20 where the joining partners are pressed on the anvil with a force F perpendicular to the welding zone: this force presents the first important parameter of the process. The generator converts the main voltage frequency (50 Hz) into a high frequency alternating voltage ($\approx$20 kHz) which is again converted into mechanical oscillation of the same frequency in the convertor. This oscillation's amplitude, u, presents the second important parameter and it is related to the design of the booster and sonotrode. The range of the amplitude is between 5 and 50 μm. The third important parameter of the process
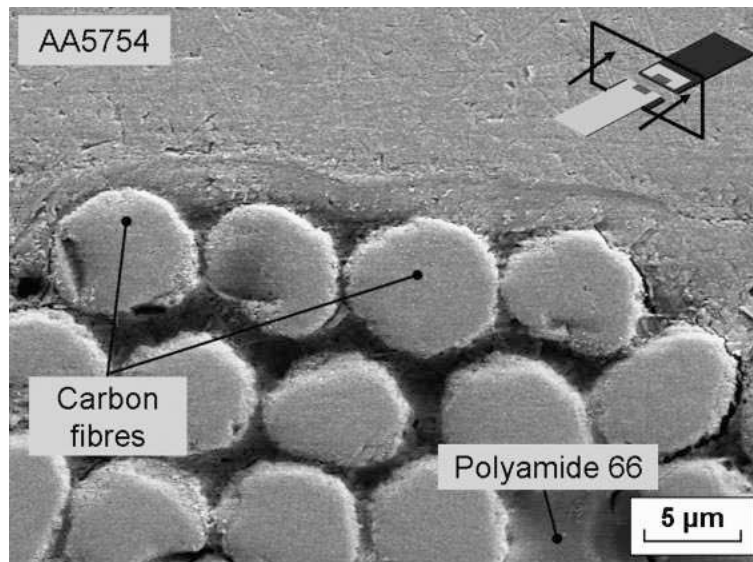
Figure 1.21: SEM micrograph of a AA5754/CF-PA66-joint ([20])
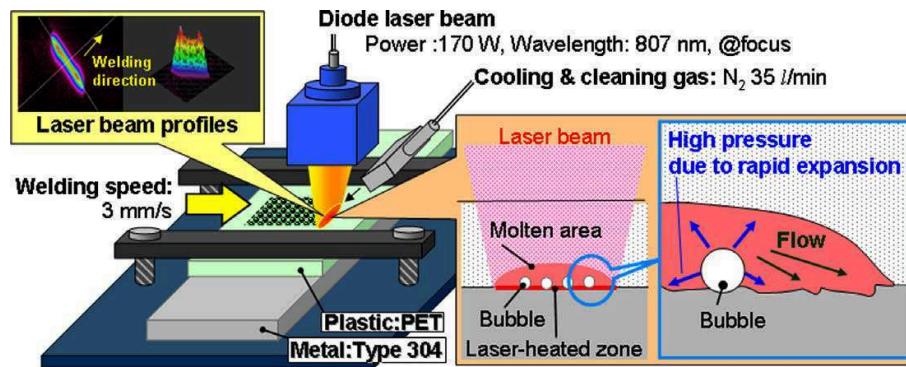
Figure 1.22: laser direct joining process principle [96]

is the specific welding energy. Also, the material parameters have a significant effect, specially the upper joining partner's thickness due to the energy absorption in the material and the roughness of the surfaces which needs to be well chosen in order to prevent the gliding of the partners in the case of low roughness and extreme temperature gradients leading brittle materials to a fracture when roughness is high. The joint created develops both an intermolecular contact and a mechanical interlocking (Fig. 1.21) and the tensile shear stresses at failure are between 20 and 40 MPa where a cohesive failure takes place.

1.3.6 Laser direct joining

Laser welding is an effective technique for joining metals since a laser beam has sufficient power density to melt metals at high speed, and for joining plastics because of their transparency or ability of absorption to a laser beam. However, this process has been investigated by [96], [93] and [185] for joining metals to plastics (including composites) and demonstrated a strong joint.

The process principle is showed in Fig. 1.22: a line beam from a diode laser is irradiated onto a plastic sheet overlapped on a metal plate under a shielding gas to cool and clean the surface.

25

Figure 1.23: FSpJ tool system [72]

Hence, the metal surface is heated to melt and partially decompose the plastic which goes in contact with laser-heated metal surface as a result of the high pressure caused by the bubbles' generation and rapid expansion. This mechanism produces a chemical and physical bonding (Van der Waals interaction forces) between the melted base plastic and an oxide film existing on the metal surface at the atomic-molecular scale and a mechanical bonding, anchor effect, related to the metal surface's roughness. The tensile shear test in the work of [93] demonstrated a failure load of 3300 N (bonding area 20×10 mm²) between a CFRP and zinc-coated steel.

In the same context and to increase the joint performance, generating a micro pattern on the metal surface to provide an extra mechanical interlock was proposed: stamping using a metal plate with protruding peaks and sandblasting the metal surface and hence increasing the roughness ([26]), creating protrusions on the metal's surface ([43]) or a micro-structuring using a laser ([185]).

This method is still in its beginning phase and its development is always under investigation because of the large number of parameters which makes it complicated. In fact, to have a good welding quality, laser power, welding speed, pulse mode, focus shape and size, beam quality, polarization and shielding gas should be taken into consideration.

1.3.7 Friction spot joining (FSpJ)

The FSpJ is a three-piece tool system (Fig. 1.23) used to generate frictional heat: a clamping ring to hold the parts to be joined together during process, a sleeve and a pin to produce the required heat through the friction between them and the work piece. The sleeve and the pin can rotate independently. The three parts are mounted coaxially and can be moved independently of each other. The metal overlaps the composite material and the two are clamped together, where the tool approaches the metal. There are two variants for this process: Pin plunge and sleeve plunge. Considering the sleeve plunge variant, the rotating sleeve goes to a pre-defined depth inside the metallic sheet without reaching the composite to avoid possible damages, while the pin retracts upwards. The friction between the sleeve and the metal, increase the temperature to below the melting point of the metal used. This temperature is enough to soften and to plasticize the metal which flows in the gap left by the retraction of the pin (Fig. 1.24 (1)). The retracted softened metal is pushed then by the pin and fills the hole created in the metallic sheet (Fig. 1.24 (2)) to remove the tool after that and leave the joint to consolidate under pressure (Fig. 1.24 (3)).
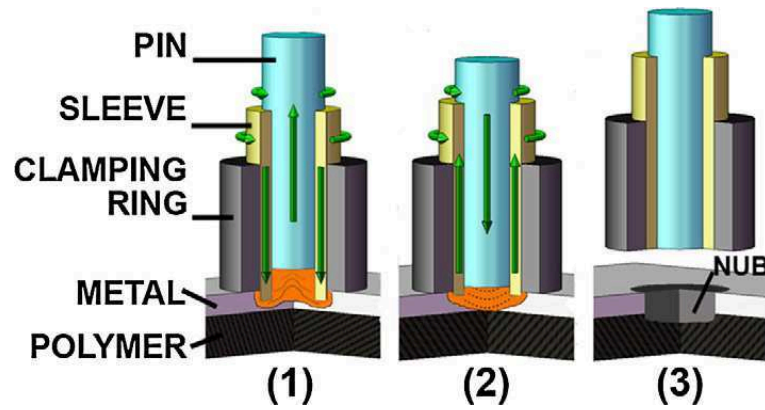
Figure 1.24: FSpJ process principle [72]
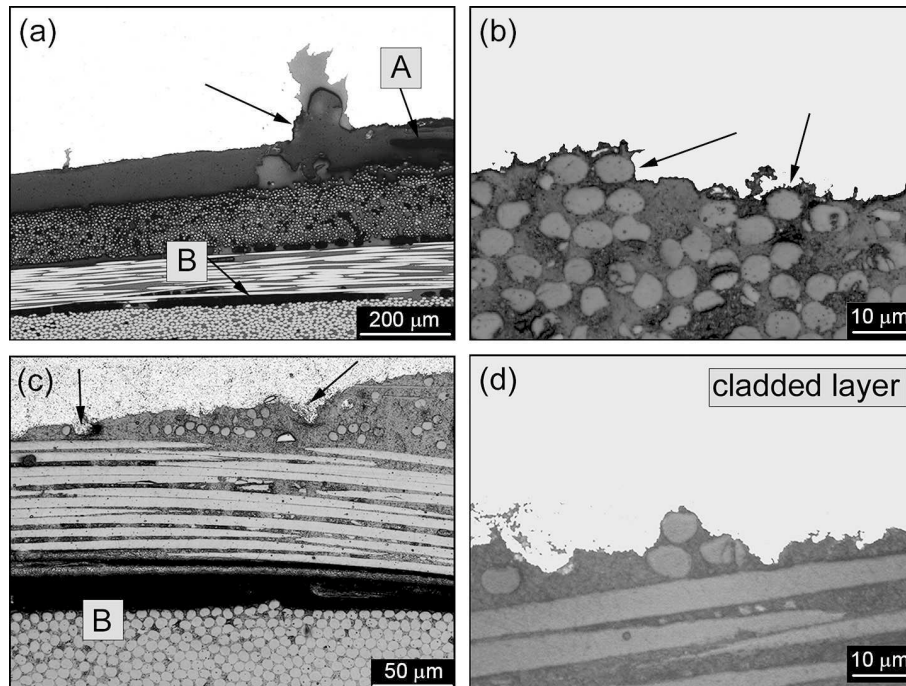
Figure 1.25: FSpJ microscopic bonding state [72]

The bonding mechanisms between the metal and the composite are: mechanical interlocking: due to the deformed metal by the plunging motion under heat which creates a kind of nub inside the composite (Fig. 1.25 (b) and (d)) adhesion forces caused by the heat transfer from metal to composite via conduction enough to melt the polymer in the spot area. The pressure during consolidation induces adhesion forces between the composite and the metal (Fig. 1.25 (a) and (c)).

The main advantages of this technique consist in: the short joining cycles, absence of emissions, operation simplicity, availability of commercial equipment and good mechanical performance since shear strength between 20 and 30 MPa ([13]) were attend , which is better compared to adhesive joining, while the main limitations are in overlap configurations and spot geometry joint design.
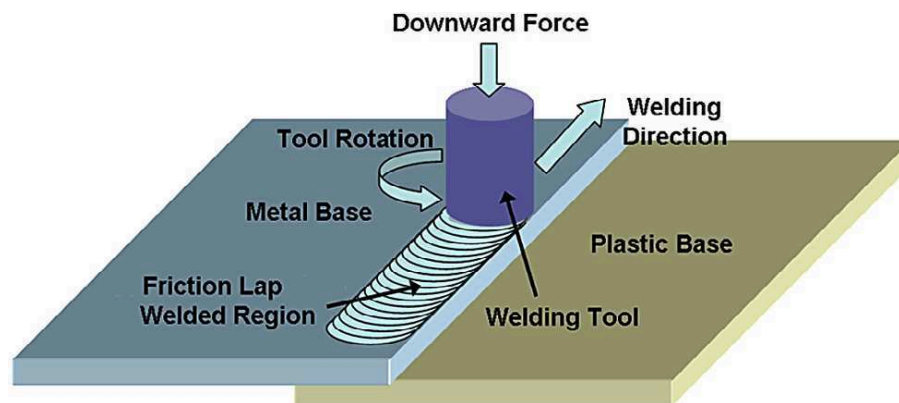
Figure 1.26: FLW process principle [126]

1.3.8 Friction Lap Welding (FLW)

The friction lap welding shown in Fig. 1.26 is a similar process to the friction stir welding (FSW) with one difference in the non-consumable rotation tool which is without a stir pin since the function needed is not to cause the material flow as it is in FSW. In this technique, the rotation tool aims to press and heat the metal part by friction. This heated part and by conduction, melts the plastic component at interface between the joining partners and under a provided pressure by the metal component, the plastic solidifies creating a bond.

The main parameters of this process are the tool dimension, rotation rate, welding speed and plunge depth. This method was investigated by [126] for joining between MC Nylon-6 and AA6061 and demonstrated several advantages: high quality joining can be obtained where nominal shear strength (maximum load divided by lapped area) 5-8 MPa was attempted without any surface preparation, it can be achieved at high welding speeds, it is an energy saving and environmental friendly technique and present fewer parameters in comparison to friction spot joining.

1.3.9 Conclusion

The various joining techniques presented show that the processes for assemblies between FRPC and metals are always in active development and the search for new techniques that combine the advantages of the processes is always ongoing.
The traditional mechanical joining and the adhesives remain always the most used since they are the most well-known historically and their tools whether theoretical or technical are developed to a high accuracy. In the mechanical joints as we have seen the main limitations stay the additional weight and the additional steps during manufacturing as well as their effect on the FRPC especially: risk of water intrusion, lamination in the joining area, fibers breakage and the high stress concentration. In the adhesive bonding case, the main limitations remain the long surface preparation and long cure times which can increase the production time, the safety conditions for the operators, the environmental impact and finally the limitation of the joint mechanical performance. The next techniques are the combination of the two previous traditional ones which called the hybrid joints processes which represent several advantages especially in improving mechanical performances but the big limitation is the processes duration which will highly increase the

production time rate.

Finally, the most of the new miscellaneous techniques which are under development use heating as a main source to create the joints which increase the risk to have thermal damages on the FRPC and are limited to the thermoplastics most of the time.

After this extensive overview of the FRPC/metal joining techniques, we will move to our next main interest concerning the dissimilar joining topics in the automotive industry: aluminum to steel.

1.4 Aluminum to Steel dissimilar welding

The heteregeneous welding between two dissimilar metal alloys has several difficulties due to the differences in thermal, metallurgical and mechanical properties of the concerned materials. These differences cause voids, residual stresses and distorsions when introducing heating into the joining partners causing microstructural changes in the weld bead and in the heat affected zone (HAZ) which leads to weakening the joint's strength [114, 131]. In addition, generally the two dissimilar metals are not totally soluble into each other and consequently in the transition zone at the interfaces of the welding, one or several intermediate compounds are formed which are dependent on the temperature flows during the welding as well as the cooling rates after. These intermediate compounds have different microscopic structures from the base metals as well as different mechanical and physical properties and they can have a drastic effect on the welding strength. In fact, these compounds are in general brittle and the discontinuity in the mechanical properties due to their presence will create high stress concentrations and distortions causing weakening in the weld strength [4, 34, 68, 200].

From here, the challenges in the case of aluminum to steel welding are so many. To have an overview, we will start first by listing the physical properties differences of the two base materials to go through the intermetallic compounds present in the Al/Fe system and present the main processes used nowadays for this kind of dissimilar welding.

1.4.1 Physical properties differences between Al and Fe

The main physical properties of both Al and Fe are represented in Table 1.3. The melting temperature of the steel is so much higher than that of the aluminum ($T_{m_{Fe}} > 2.3 T_{m_{Al}}$). The difference in thermal expansion coefficient will lead during the cooling to high internal stresses in the welding zone as well as at the interface between the HAZ and the base metals. Therefore, the residual stresses will be high in the welding joint which can cause micro-cracks initiation. In addition, the thermal diffusivity of Al is about 4.5 times of that of Fe which means that the fusion pool on the aluminum side will be bigger and hence the HAZ will be also bigger in the aluminum.

1.4.2 Fe-Al intermetallic compounds: properties and effect on welds mechanical properties

In Fig. 1.27 the Fe-Al binary phase diagram is represented. The intermetallic compounds can be grouped under two categories:

Property	Symbol	Unit	Fe	Al
Melting temperature	T_m	°C	1535	660.37
Density	ρ	kg$\cdot m^{-3}$	7870	2699
Heat capacity	C_p	J$\cdot$kg$^{-1}\cdot K^{-1}$	440	897
Thermal conductivity	k	W$\cdot m^{-1}\cdot K^{-1}$	75	237
Thermal diffusivity	D_T	$m^2\cdot s^{-1}$	2.2×10^{-5}	9.8×10^{-5}
Linear coefficient of thermal expansion	α	μm$\cdot m^{-1}\cdot °C^{-1}$	12.2	24
Young's modulus	E	GPa	200	68
Poisson's ratio	ν	-	0.291	0.36
Crystal structure	-	-	CC	CFC

Table 1.3: physical properties of Al and Fe

Phase	Symbol	Crystal structure	Composition	Density [-]
α-Fe (Al)	$\alpha - Fe$	BCC	0 - 45	7.8
γ-Fe	$\gamma - Fe$	FCC	0 - 1.3	7.8
FeAl	β_1	BCC	23 - 55	5.58
Fe$_3$Al	β_2	BCC	23 - 34	6.72
Fe$_2$Al$_3$	ε	Cubic (complex)	58 - 65	-
FeAl$_2$	ζ	Triclinic	66 - 66.9	-
Fe$_2$Al$_5$	η	Orthorhombic	70 - 73	4.11
FeAl$_3$	θ	Monoclinic	74.5 - 76.5	3.9
Al (Fe)		FCC	99.998 - 100	2.69

Table 1.4: phases compositions and crystal structures [194]

- one for those which are rich in iron (FeAl, Fe$_3$Al)

- and one for those rich in aluminum (FeAl$_2$, Fe$_2$Al$_5$, FeAl$_3$).

In Table 1.4 we can find their compositions and the crystal structure for each of them.

In addition to these stable compounds, other metastable compounds can be detected:

- FeAl$_6$ having a orthombic crystal structure with 74.5 %at. of Al

- Fe$_2$Al$_9$having a monoclinic crystal structure with 68.6 %at. of Al

The mechanical properties of aluminum rich intermetallic compounds (Fig. 1.28 and Table 1.5) have shown higher hardness than that of the iron rich compounds. Also, the aluminum rich compounds showed purely brittle behaviour while the iron rich compounds showed some plastic deformation before failure. The iron rich compounds showed in addition better strength in compression than that of aluminum rich compounds.

As it can be seen from the characteristics and the mechanical properties of the IMC, there are lot of differences between the IMC themselves and at the same time with the base materials. These IMC showed during previous studies high influence on the mechanical strength of the welds [84, 116, 208, 227]. In Fig. 1.29, the results of tensile tests on dissimilar aluminum to steel welds are represented as a function of the IMC layers thicknesses. In Kuroda et al. [116] and Hirosa et al.
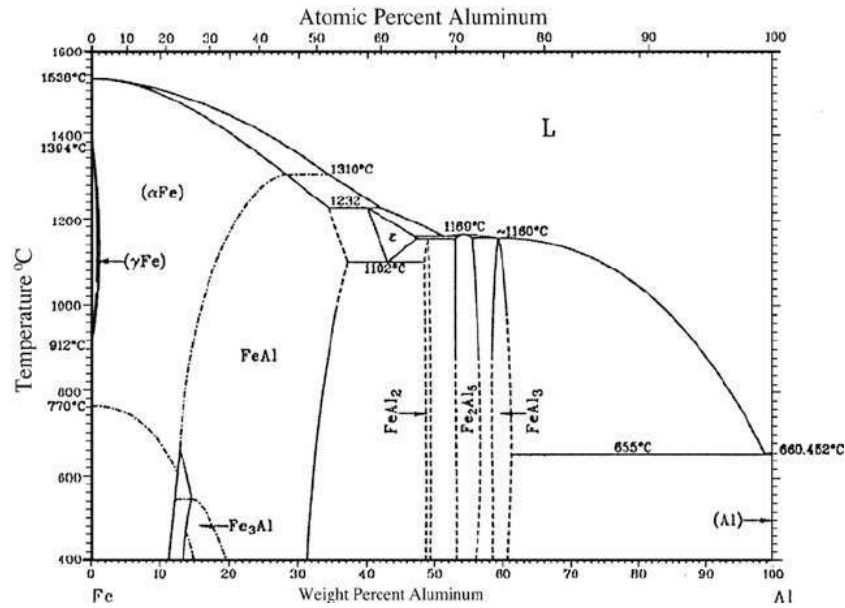
Figure 1.27: Fe-Al equilibrium phase diagram [194]
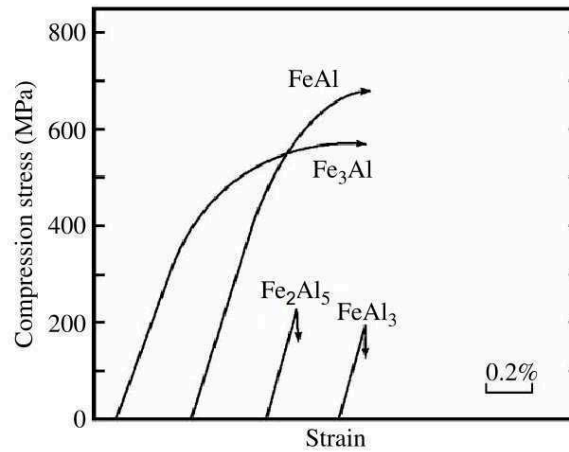
Figure 1.28: strain-stress curves for compression tests on Fe-Al intermetallic compounds [226]

Phase	HV	Tenacity $(MPa\cdot\sqrt{m})$	Yield compressive strength (MPa)	Plastic deformation in compression (%)
FeAl	470	-	670	0.45
Fe$_3$Al	330	-	540	0.80
FeAl$_2$	1000-1050	-	-	-
Fe$_2$Al$_5$	1013	2.3	240	0
FeAl$_3$	892	2.15	200	0

Table 1.5: mechanical properties of Fe-Al intermetallic compounds [35, 180, 226]
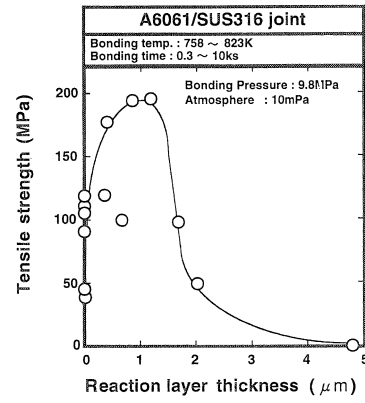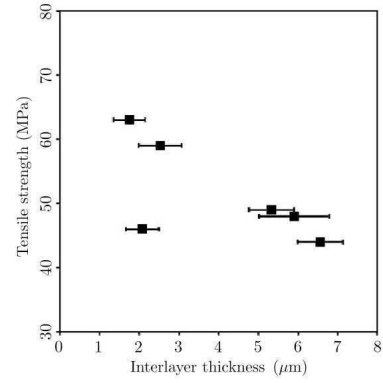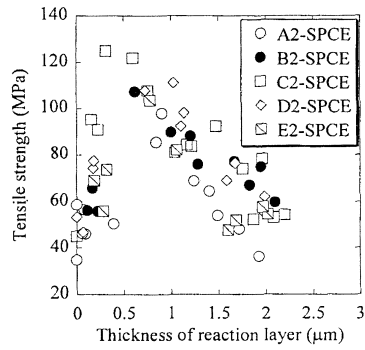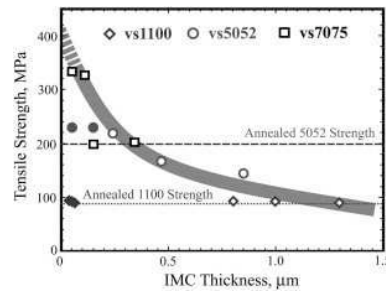
Figure 1.29: IMC thicknesses effect on mechanical strength of dissimilar Fe/Al welds (a) Kuroda et al. [116], (b) Yilmaz et al. [227], (c) Hirose et al. [84] and (d) Tanaka et al. [208]

[84] the aluminum is a 6xxx and in Yilmaz et al. [227] it is a 1xxx aluminum. Tanaka et al. [208] took into consideration several aluminum alloys. These studies cover multiple types of welding processes and show less strength of the joints when the layer of the IMC is less than hundreds of nanometers. The maximum strengths are reached when these layers are between 0.2 and 1 μm and the mechanical strength decreases the more the IMC layer thickness increases after that. The decrease however is not the same for all and it can be seen that on the case of aluminum 6xxx it is faster than it is in the 1xxx case.

1.4.3 Review of the welding technologies applied for joining aluminum to steel alloys

The welding technologies for dissimilar aluminum to steel joints can be divided into fusion-based, semi-solid state and solid state technologies. In the former, we can find metal arc joining [60, 88, 148, 154, 203, 233, 234], cold metal transfer [5, 40], electron beam welding [76, 231], laser brazing [11, 59, 137, 192, 235], furnace brazing [165, 187], and the resistance spot welding [159, 171–174, 206, 226, 237] which is always the dominant joining technology in automotive industry [71]. The semi-solid state best example is the friction stir brazing [212, 232].

Since all of these processes heat the metals up to their liquid state, they lead to a rapid formation of IMC at the interface of the welds increasing the risk of deteriorating the mechanical properties of the joints. To limit the formation of IMCs during the joining, various solutions have been investigated: optimizing the welding parameters to limit the heat input at the interface [30, 200], reducing the welding time by preheating the steel [119, 193] and changing the chemical composition of the interface [23, 159, 193, 200].

Keeping the materials at their solid state and reducing the time of welding give rise to the use of another kind of welding processes and which showed their applicability for very wide dissimilar range of metals [77, 150, 199, 240, 241]: the solid state welding processes. Among these technologies, we can find the friction stir welding [33, 44–46, 48, 55, 56, 79, 89, 104, 105, 115, 117, 127, 153, 178, 201, 204, 208], the explosive welding [28, 80, 125, 188], laser impact welding [218], the vaporizing foil actuator welding [216] and the magnetic pulse welding [75, 77, 152]. These techniques take place in some microseconds which minimize the chances of formation of intermetallics and no significant HAZ is present [8, 95, 151].

1.4.4 Conclusion

In this section, we have discussed the challenges related to weld Al- to Fe- alloys. As we have seen, the large differences in the physical, thermal and metallurgical properties of both alloys require special manipulation and optimization of the fusion technologies to avoid the damage on the joining partners and to limit the formation of thick IMC which decrease the mechanical strength of the joints. To avoid these risks, the solid-state welding techniques were extensively developed during the last years especially the FSW which have already several applications in the automotive industry.

The other solid-state welding techniques that showed their efficiency in joining dissimilar metals

and were able to bypass the physical differences are the high-velocity impact welding techniques where the explosive welding is the oldest one. The big limitation of explosive welding in the application for high volume production industries is the safety and the handle of the technique under high production rates conditions. The MPW showed the same joining capabilities for metals where very large similar and dissimilar metal alloys were welded using this technology. Also, the MPW can be automated and the ergonomics on manufacturing sites can be respected using the tools of the MPW. From here, the MPW is the most suitable to apply and will be detailed in the next section.

1.5 Magnetic Pulse Welding

1.5.1 Introduction

In the previous section we discussed the welding processes for joining Al/Fe and we have mentionned the MPW between the solid state welding processes. The MPW is a high-velocity impact welding having analogy with the father of all the similar welding process: the explosive welding (EXW). In this type of processes, one metal called the flyer is accelerated at very high velocities towards another fixed metal called the parent metal causing an impact that will create the bonding between the two materials. As their names indicate, the EXW uses the detonation of explosives as an accelerator for the flyer while the MPW uses the electromagnetic driving forces [69, 95, 135, 150, 239].

The process was developed by Kurchatov Institute of Nuclear Physics in the late 1960's for both tubes and sheets application [130] but the industrialization of the process took place only at the end of the twentieth century. In Kapil et al. [95], a very interesting graph is represented showing this fact through the year wise number of scientific and technical papers dealing with EXW and MPW (Fig. 1.30).

The application on tubes was the most used and developed in the MPW field and from the year 2000 more focus was given to the sheet metal applications. In the latter, additional process was developped by Manogaran et al. [132]: the magnetic pulse spot welding. This process aimed to facilitate the automation of this kind of processes and proposed hence solution mainly aiming the automotive industry.

From an industrial point of view, MPW was restricted first to the nuclear field for welding closing caps and end closers of nuclear fuel rods (Fig. 1.31). Nowadays we can find also other applications in aerospace, energy, construction, heat exchangers, packaging, electronics and automotive industry: space frame structures [108], flange mufflers in the exhaust system [90], drive-shafts (Fig. 1.32 (a) and (b)), components of air conditioners (Fig. 1.33), tubular seats, components of fuel filters (Fig. 1.34) automotive earth connector (Fig. 1.35), assembling air brake hoses [152], attaching reinforcing bands on oil filters and clamping rings over sleeves on shock absorbers [62], aircraft control tubes welded through MPW (Fig. 1.36), flexible printed circuit boards (FPCB) [9], joining of high voltage cables, metal fittings onto ceramic insulators and swaging of copper tubes to coaxial cables [152].
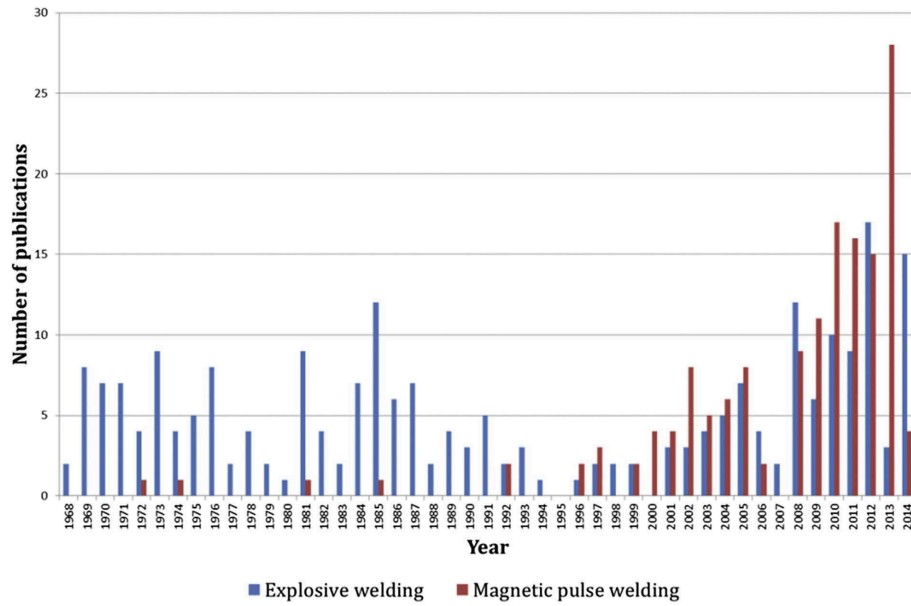
Figure 1.30: research publications related with MPW and EXW studies [95]
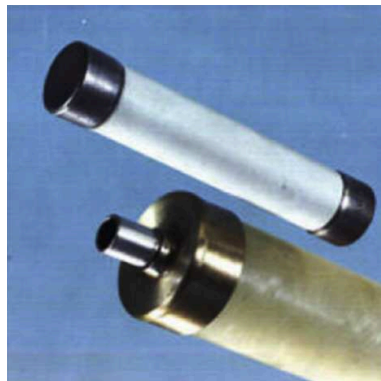
Figure 1.31: end enclosures for nuclear fuel rods [210]

(a)	(b)

Figure 1.32: MPW application for drive-shafts (a) aluminum to steel (b) aluminum to aluminum [62]

35

Figure 1.33: MPW application for automotive A/C receiver-dryer [62]
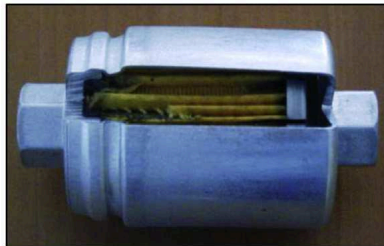
Figure 1.34: MPW application for fuel filter [62]
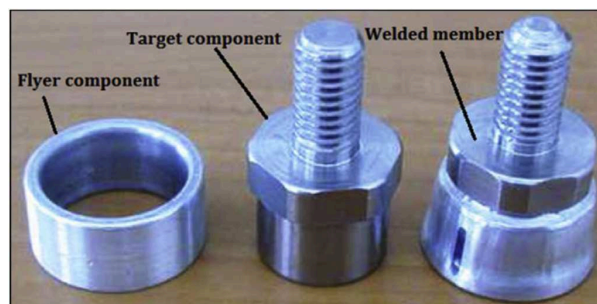
Figure 1.35: MPW application for automotive earth connector [62]

Figure 1.36: MPW application for aircraft flight control tubes [241]
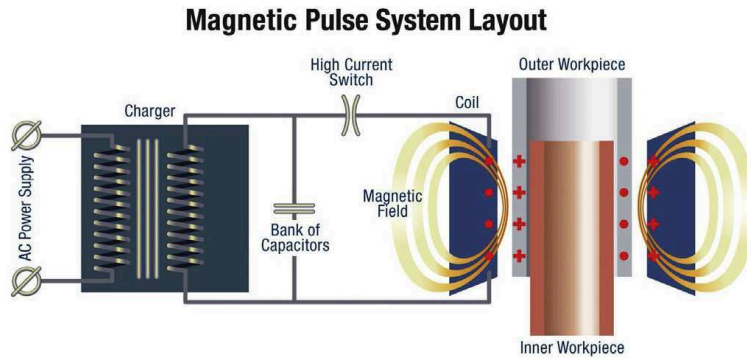
Figure 1.37: schematic of the MPW set up [197]

The increase of demand on solutions for dissimilar joining in various applications makes the MPW an important field to further explore, extend its scope of applications and to do so further understanding of the phenomena realted to this process is needed. Up to this day, the major researches in MPW are experimental with some increasing interest during the last years on modelling and simulation [95, 131]. This fact is related to the complexity of the process physics and interdependency between different phenomena.

In order to understand this complexity, this section will discuss in details the MPW: we will begin by presenting the process and its parameters in order to be able to list the different physics involved. We will also include a section to present the MPSW process with its main differences and advantages in comparison with the MPW. Afterward we will discuss the welding formation mechanism to be able finally to present the overview on the modelling and simulation of the process.

1.5.2 MPW: process and parameters

1.5.2.1 Equipment

As it was mentioned in the introduction of this section, the MPW uses magnetic driving forces to accelerate the so-called flyer metal. The principle is based on the Laplace force law: the presence of a current-carrying conductive metal in a time-varying magnetic field generates Laplace forces on this metal. Therefore and to achieve large amounts of Laplace forces, the MPW processes use:

1. high pulse generator capable of generating intense time-varying current that will be the source of the time-varying magnetic field,

2. a coil capable of producing the magnetic field due to the discharged current delivered by the generator,

3. and a conductive metal in the vicinity of the coil in which the magnetic field penetrates and induces currents leading to the generation of large amounts of Laplace forces of it leading to its acceleration.

The schematic of the MPW process is represented in Fig. 1.37 for a tubular geometry.
The pulse generator contains a high voltage power supply, capacitor banks and high current switches able to open and close rapidly for charging and discharging the capacitor banks. The control unit
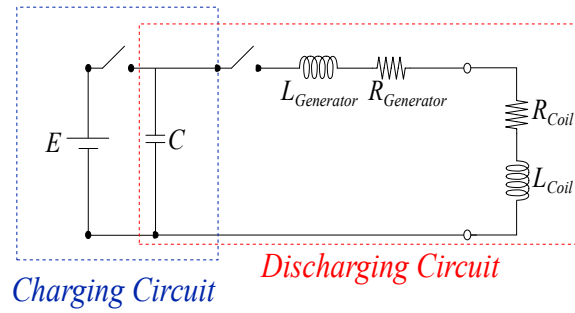
Figure 1.38: RLC analogy for MPW
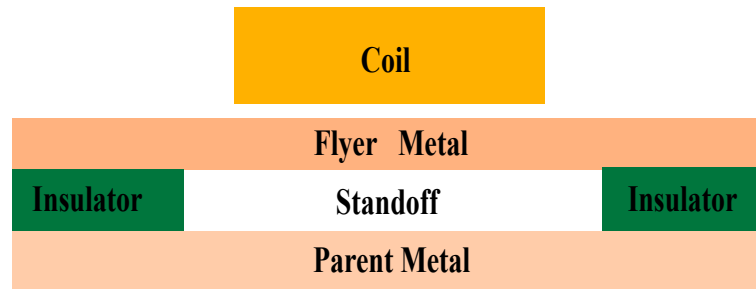
Figure 1.39: MPW operational positionning

of the generator is outside the working area. This working area consists of the coil, its mounting system and the joining partners. The pulse generator with the coil setup corresponds to a resonant circuit RLC as represented in Fig. 1.38.

1.5.2.2 Principle and operation

The first step is to position the parts in the workstation properly in vicinity of the coil as it can be seen in Fig. 1.39. After that, the capacitor bank is charged to the desired energy level. Then, the high current switch is closed and current flows rapidly from the stored capacitor bank through the inductor. Considering the basic principle that a current-carrying wire produces a magnetic field in the area around it (Ampere's Law), a primary changing magnetic field is therefore produced around the coil. When the time-varying magnetic field diffuses inside the flyer metal which should be an electrically conducting material, a secondary current will be induced in the flyer which by its turn will create a secondary magnetic field in the opposite direction to the primary magnetic field (Lenz's Law). The eddy current, i.e. the secondary current, is now subjected to this opposing magnetic field which generates large amount of the so called Lorentz forces on the surface of the metal sheet leading to the acceleration at a very high speed away from the inductor to get in contact with the stationary parent metal. The power of this impact under defined proper conditions will cause the welding between the two parts.

From the principle of operation we can deduce that we will have electrical and geometrical parameters related to the process and physical parameters related to the workpiece and the impact between the materials. Of course, we should not forget that all of the parameters will be interdependent and will influence one-another. Hence, these parameters will be detailed next.

1.5.2.3 Parameters

1.5.2.3.1 Discharge energy and discharge current

The source electrical energy that will be converted to a mechanical energy is the energy that will be discharged in the coil from the capacitor bank. Hence, this discharge energy E is depending on the voltage that is charging the capacitors and it can be expressed by:

$$E_{discharge} = \frac{1}{2} C V_0^2 \tag{1.1}$$

where C is the capacitance and V_0 is the charging voltage.
The resulting discharge current in the coil which is a highly damped sinusoidal as presented before due to the RLC equivalence is:

$$I(t) = I_0 e^{\frac{-t}{\tau}} \sin(\omega t) \tag{1.2}$$

where :

$$I_0 = V_0 \sqrt{\frac{C}{L}} \tag{1.3}$$

$$\tau = \frac{2L}{R} \tag{1.4}$$

$$\omega = \frac{1}{\sqrt{LC}} = \frac{f}{2\pi} \tag{1.5}$$

with L and R the equivalent inductance and resistance of the system respectively:

$$L = L_{Generator} + L_{Coil} \tag{1.6}$$

$$R = R_{Generator} + R_{Coil} \tag{1.7}$$

A typical discharge current curve is represented in Fig. 1.40 which was recorded during a MPW application.

1.5.2.3.2 Skin depth (δ)

At high frequencies, the magnetic field does not penetrate completely into the interior of a conductor. The skin depth describes the degree of penetration of a conductor by the magnetic flux and the eddy current. In other words, the skin depth is the distance at which the amplitude of the electromagnetic wave traveling in a lossy conductor is reduced to $1/e$ of its original value. Due to this skin effect phenomenon, the repulsive magnetic field produces electromagnetic forces that exert the requisite pressure on the workpiece (flyer) that will accelerate it away from the coil. The skin depth is mathematically approximated by:

$$\delta = \frac{1}{\sqrt{\pi \mu \sigma f}} \tag{1.8}$$
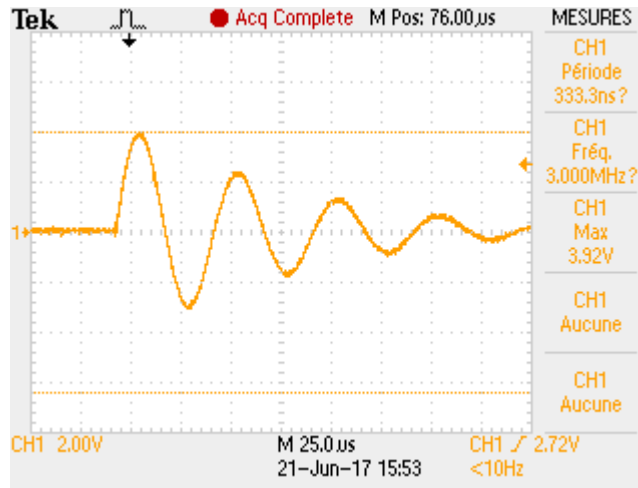
Figure 1.40: typical discharge current measured during MPW

where μ is the electrical permeability of the workpiece, σ is the electrical conductivity (S/m) and f is the frequency of the discharge current (Hz).

Therefore, to use effectively all the magnetic field produced by the coil, the skin depth should be less than the thickness of the flyer metal. Otherwise, only a part of the magnetic field will diffuse inside the flyer which will lead to less generated forces and hence decreased acceleration of the flyer metal. In the case of less conductive materials, the frequency of the discharge currents should then be increased in order to compensate the decrease in conductivity.

1.5.2.3.3 Magnetic pressure

Magnetic pressure is one of the parameters responsible of driving the flyer metal to the parent metal. This pressure is the one that will oppose the magnetic field from the coil and will make the flyer metal gain velocity until collision. The magnetic pressure is expressed by:

$$P = \frac{\mu}{2}H^2 = \frac{B^2}{2\mu} \tag{1.9}$$

where H is the magnetic field intensity (Amper-turns per meter), B is the magnetic flux density (Tesla) and μ is the magnetic permeability of the material (H/m). A high magnetic pressure is therefore required to have a successful bonding since the tensile strength was found to increase for increasing the magnetic pressure [191]. This high pressure can be obtained with high discharge energy or high frequency current.

1.5.2.3.4 Standoff distance

The standoff distance or gap is the distance between the two joining partners prior to welding. This distance is so important because an enough space is needed to gain velocity and acquire kinetic energy which will be transformed to impact energy creating the welding. Several studies showed that there is an optimum value for this distance: a lower distance makes the flyer plate unable to reach the needed velocity and a higher distance drops the velocity at collision (Fig. 1.41).

Fig. 1.42 shows the behavior of bonding between aluminum and titanium. The standoff distance
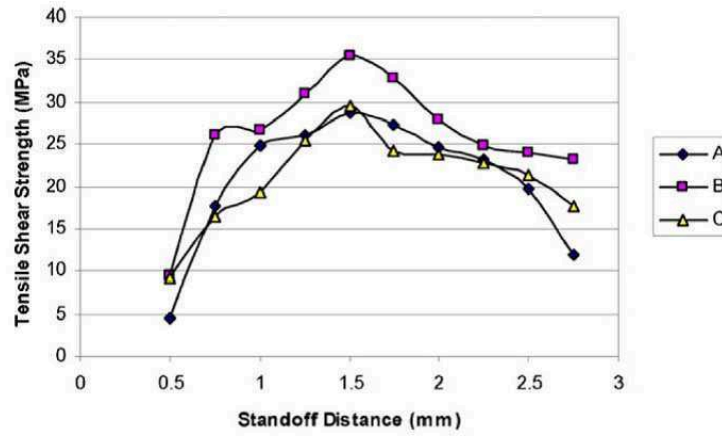
Figure 1.41: standoff distance effect on the welding quality between aluminum and stainless steel sheet [111]
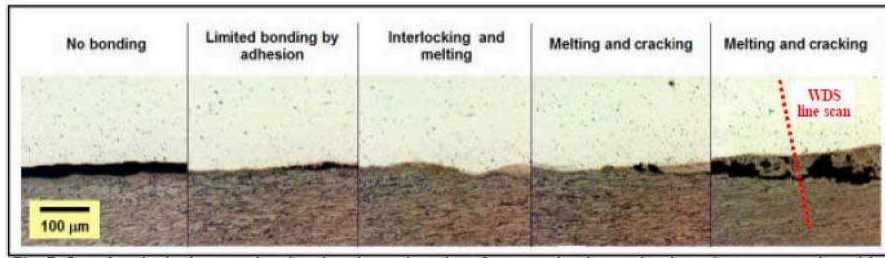
Figure 1.42: bonding interface between aluminum and titanium welded using MPW [77]

and discharge energy increase from the left to the right. It is clear that the third picture presents the optimum value: the first and second pictures present a lower standoff distance where no bonding occurred and in the fourth and the fifth pictures, the standoff distance is high so intermetallic formation and cracks are observed.

1.5.2.3.5 Coil

The coil geometries depend on the application. In the case of the tubular applications, we can find helical coil and round coils [95, 123]. In the sheet metal applications, it is especially the flat coils that were applied: I-shape, H-shape and E-shape [6–9]. When it comes to the material of the coils, the most used coils are copper based alloys: copper-chromium, copper-beryllium... Other coils in aluminum were also used.

1.5.2.3.6 Flyer metal dynamic behaviour

Since the electromagnetic forces are at very high levels and are experienced by the flyer metal in some microseconds, the deformation of the metal is then at very high strain rates. As the behaviour of almost all the metals becomes sensitives to strain rates above 10^{-4} s^{-1}, a constitutive law including the strain and strain-rate is needed. In addition, the joule heating due to the induced current inside the flyer metal and the plastic deformation will be sources of heating for the metal and then the constitutive law should take into consideration the material temperature sensitivity.
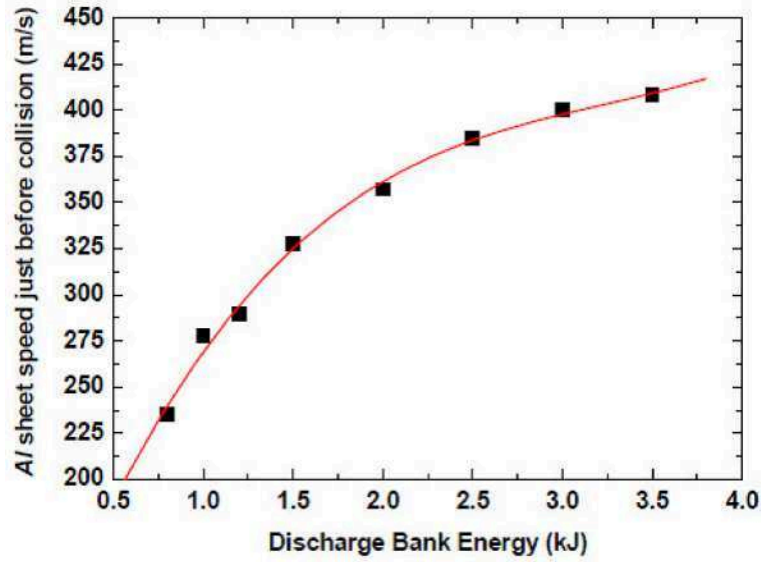
Figure 1.43: flyer metal velocity just before collision [10]

The commonly used constitutive law for MPW is the Johnson-Cook model that can be expressed as [62, 81, 92, 95]:

$$\sigma_p = [A + B \cdot \varepsilon_p^n][1 + C \cdot \ln(\dot{\varepsilon}^*)][1 - T^{*m}] \qquad (1.10)$$

where σ_p is the von Mises tensile flow stress, ε_p is the equivalent plastic strain, $\dot{\varepsilon} = \frac{\dot{\varepsilon}_p}{\varepsilon_{p0}}$ is the dimensionless plastic strain rate for $\dot{\varepsilon}_{p0} = 1.0 \ s^{-1}$ and $T^* = \frac{T - T_{room}}{T_{melt} - T_{room}}$ is the homologous temperature. A, B, C, n and m are five material constants.

1.5.2.3.7 Impact velocity and angle

The impact velocity is directly dependent on energy and time of discharge from the capacitor through the coil into the flyer metal (Fig. 1.43, Fig. 1.44) as well as on the impact angle since when it increases the velocity increases also [239]. Once the impact angle is fixed, if this velocity is low, no bonding will occur and if it is excessive, damage can appear. The other importance of this velocity is that its high value creates a jet that will remove contaminants or oxidation particles from both contact surfaces and it ensures by this way two clean surfaces ready for welding without pre-treatment. The creation of the jet acquires then a sufficient high velocity with oblique collision [110, 131]. The elimination of these impurities is important to avoid the intermetallic formations during the welding time.

The impact angle is the angle formed by the target plate and the flyer plate at the impact moment. For MPW the angle starts small and ends big for a parallel setup of the tubes. The impact angle normally is somewhere between 3° and 30° [77, 95, 214].
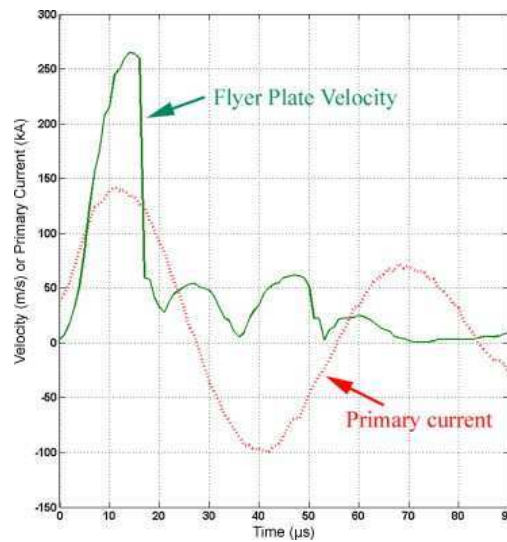
Figure 1.44: impact velocity as a function of discharge time [239]
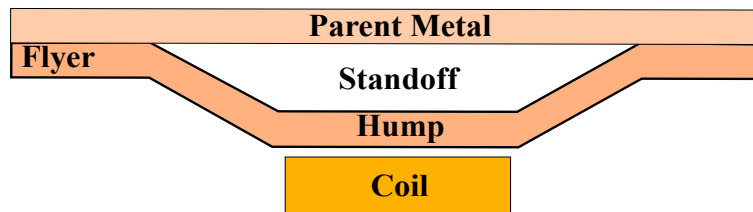
Figure 1.45: MPSW configuration

1.5.3 Magnetic pulse spot welding (MPSW)

We have seen that having a standoff distance between the flyer and the parent metal is one essential condition for the accelerating the flyer to the required velocity during MPW process. When considering the industrial automation of this process, we will have then two difficulties: positioning the two insulators with the required distance between them and then positioning the flyer at the good required standoff distance accordingly. To overcome this overlapping difficulties and to have a better control for the intended welding area, Manogaran et al. [131] proposed a new concept: create a prior local stamping on the intended spot welding location in the flyer metal creating hence a hump (Fig. 1.45); this hump will ensure the required standoff distance and the flyer could be directly placed on the parent metal and it will be accelerated by the magnetic pulse and create a spot weld after impact (Fig. 1.46).

This method of course will have in addition to the MPW parameters, the hump design parameters. The hump geometry should take into consideration four important criterions:

- The necessary air gap to create the welding

- The required collision angle on impact to form the spot weld

- A proper shape to expulse the surface impurities along with the jet

- Assure attached flat surface with the stationary part after welding without having protrusions
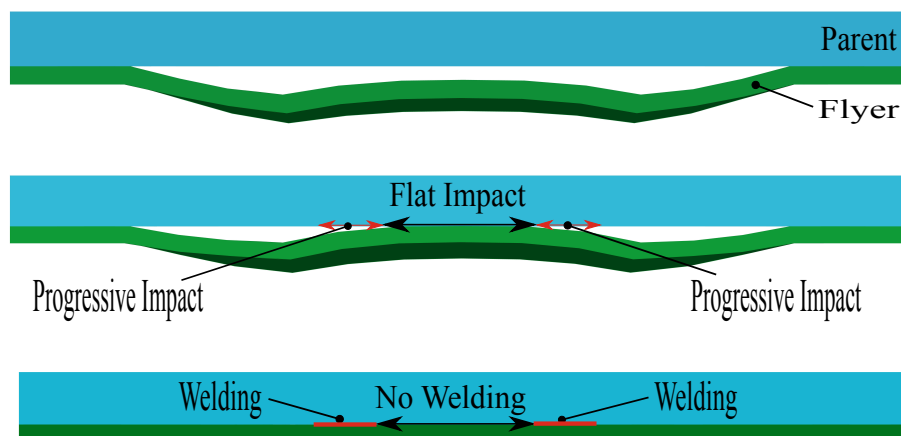
Figure 1.46: impact between the hump and the parent metal during MPSW
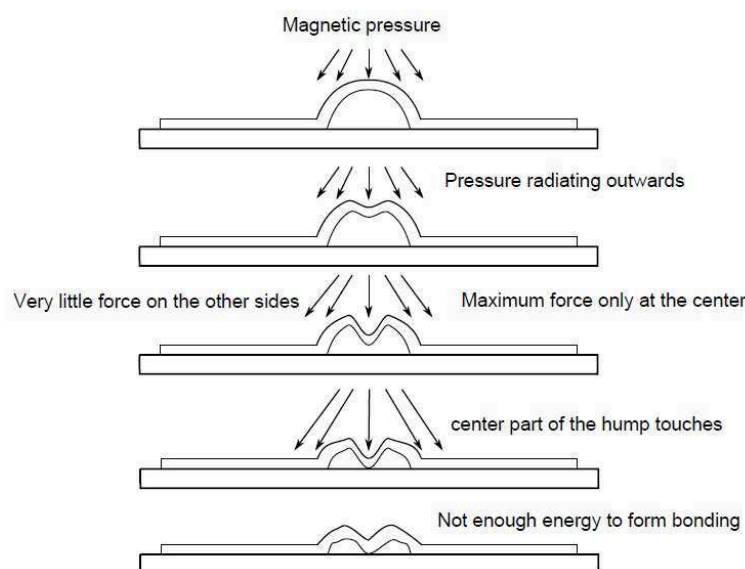
Figure 1.47: circular hump deformation during MPSW [131]

The first comment to do is that the hump geometry will be better when it is similar to the inductor geometry since the distribution of the force will be more adequate to the hump surface creating higher impact velocity. In Manogaran et al. [131] series of experiment trials was undergone where several geometries of the hump were investigated: rectangular, elliptical , triangular and circular. it was found that the rectangular geometry is the best one to use since the forces will be uniformly distributed on the surface of the hump. To illustrate this fact, Fig. 1.47 and Fig. 1.48 show the circular hump and rectangular hump deformation during MPSW respectively.

After these introductions to the MPW and MPSW processes, we will now go over the welding formation mechanism topic and various explanations present in the high velocity impact welding litterature.
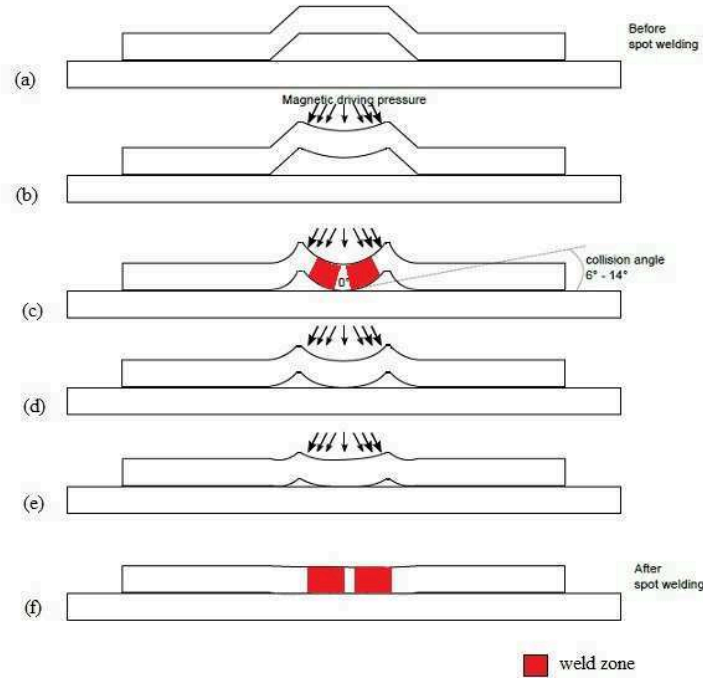
Figure 1.48: rectangular hump deformation during MPSW [131]

1.5.4 Weld formation mechanism in MPW

1.5.4.1 Welding interface: review of theories and analogies with EXW

The first process in the area of impact welding is the EXW and its researches are used as the reference for explaining physics behind the welding formation. At early stages of development, some studies considered that it is a fusion welding process [51] due to the dissipation of the kinetic energy as a source of heat activating the diffusion at the interface of the two joining partners. Other investigators considered it as a pressure welding process [28]. Another theory attributed the weld to the shearing at the interface as a heating source for the boundary layers [158]. These proposed theories were considered inadequate since they ignored the existence of the jet phenomenon that takes place during oblique impacts [17]. From experimental observations, two distinct interfaces can be observed: whether a wavy one or a straight/waveless one (Fig. 1.49); and the strongest joints will be in the former case [22]. Based on these experimental facts, several researches accepted the jet formation at the collision point as an essential condition for welding [50, 51, 145, 158]. This is because in fact, it is the jet that leaves virgin surfaces clean and free of films and contaminants which make possible for the atoms of two materials to meet at interatomic distances under the high pressure caused by the impact.

The presence of this jet, the observation of waves at the welding interfaces and considering the "wavy interface" as a good quality weld indicator, have led many investigators to seek an explanation and a characterisation of these waves in terms of a flow mechanism [49, 61, 217]. This fact shows that today when we talk about the impact welding processes we see more in the litterature the term "wave formation mechanism" instead of "weld formation mechanism". The similarities between the interfaces of EXW and the other impact welding processes including the MPW, were
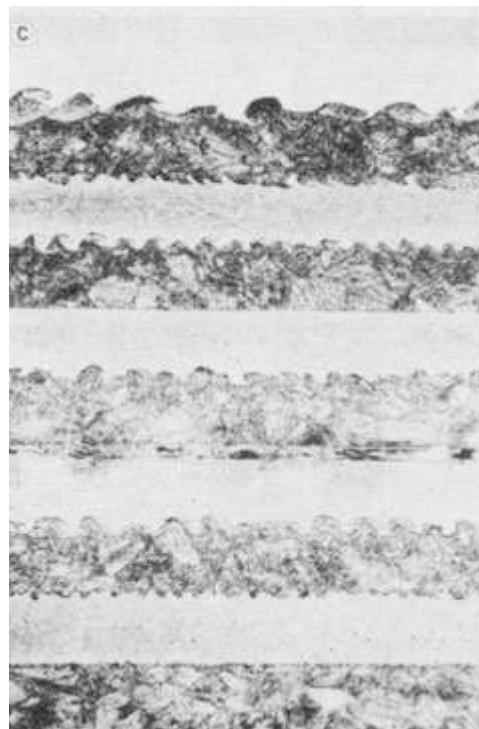
Figure 1.49: types of multiple welding interfaces observed during impact welding [28]

the reason to adopt the analogy with EXW considering that the same mechanism explanation developed for EXW can be carried-over for the other. From here, we can explain why only few researches attempted to develop specific model for the wave formation in MPW [95, 220, 221].

The explanations of the wave formation mechanism present multiple theories which can be classified under four main categories:

1. Jet indentation mechanism [1, 18, 28, 181]: waves are the result of the indentation action of the salient jet on the base plate and the periodic release of the hump formed ahead of the collision point by the material removed by indentation. Another explanation attributing the indentation to the re-entrant jet and the vortices formation to the trapping of this re-entrant jet material between the hump and the salient jets (Fig. 1.50).

2. Flow/Helmholtz instability mechanism [28, 86, 161, 181, 183, 184]: in the indentation mechanisms we saw that waves are considered to be formed essentially within the collision zone; the flow instability mechanisms suggest that they are created ahead of the collision point or behind the collision point relating this to the discontinuity of the velocity across the interface. This theory involves the re-entrant jet and salient jet respectively and it is treated as a Helmholz instability.

3. Vortex shedding mechanism [28, 49, 58, 113, 181, 182]: in this theory the stagnation point is considered as a solid obstacle. The waves are formed due to a vortex shedding mechanism starting at the stagnation point and continuing to grow behind the collision zone (Fig. 1.51).

4. Rarefaction wave mechanism [18, 25, 109, 112, 181, 182]: in this theory it is considered that
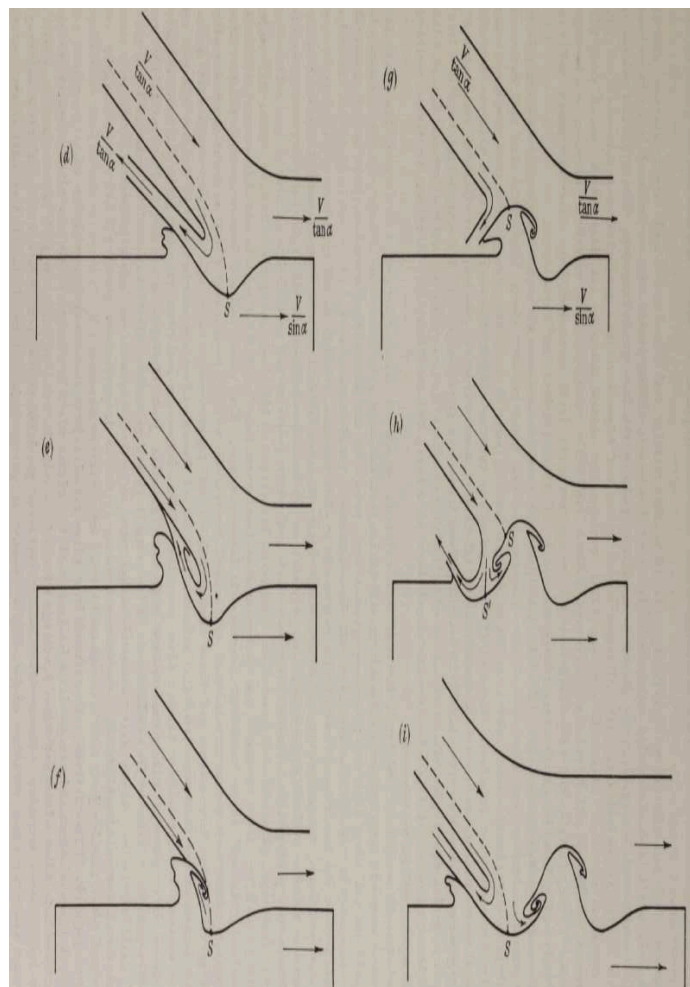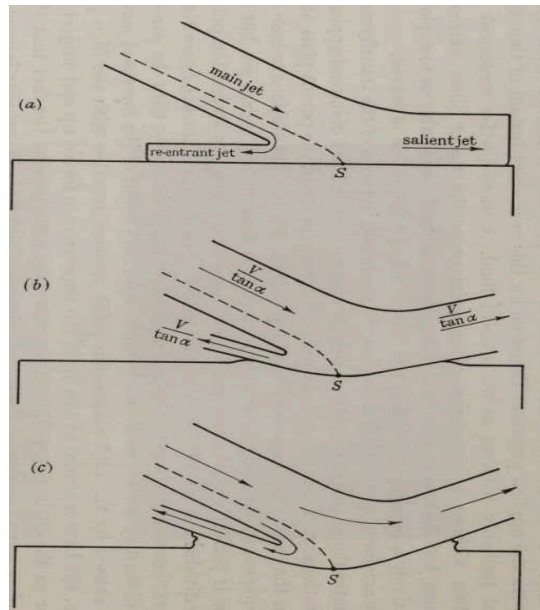
Figure 1.50: formation of waves per indentation mechanism [18]
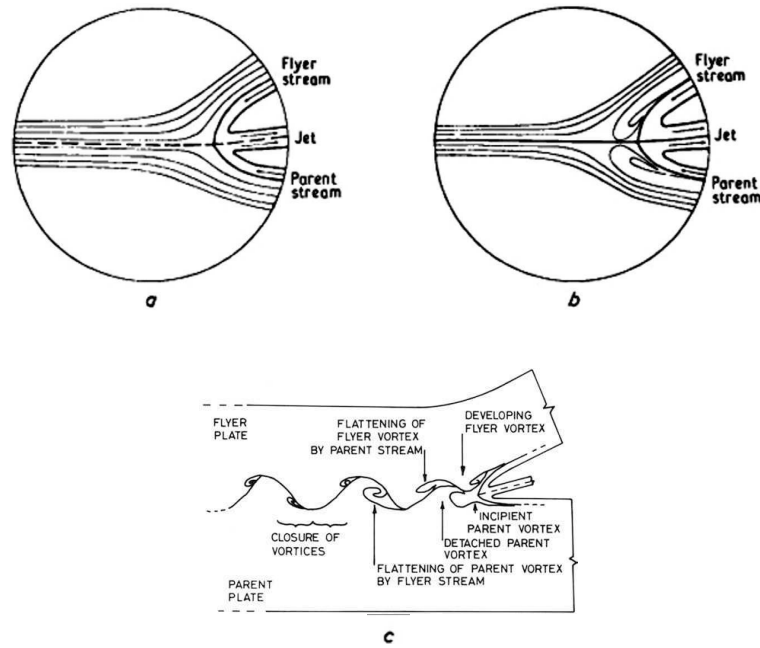
Figure 1.51: vortex shedding mechanism [182]
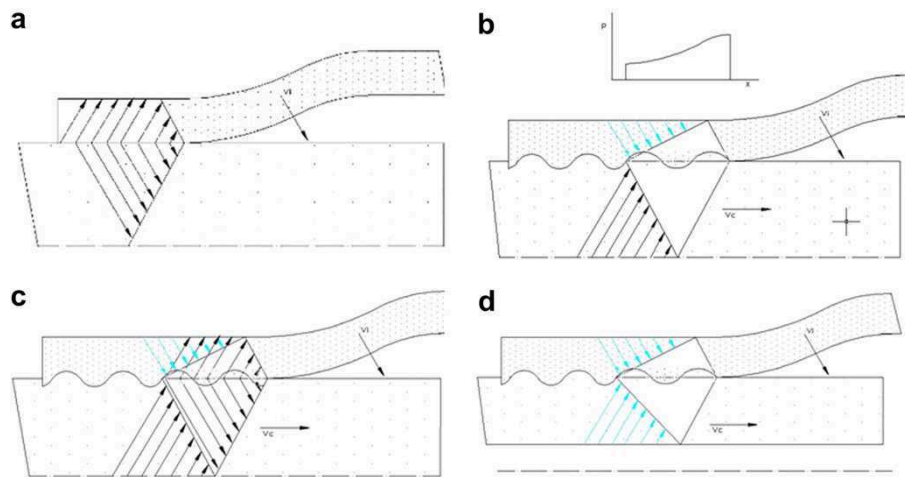
Figure 1.52: rarefaction wave mechanism [25]

the Helmholtz instability is initiated by the shock waves caused by the impact. These shock waves are generated at the impact point and travel in both metals with a radial front (Fig. 1.52 (a)). The compression waves are then reflected from the back surface as refraction waves (gray arrows in Fig. 1.52 (b)) with assorted periodic time. The compression waves in the parent metal meet their corresponding waves at the rigid fixture holding the parent and are reflected as compression waves towards the interface (black arrows in Fig. 1.52 (b)). The pressure peak is always at the collision point, since the speed is higher at that point and decreases retrogressively. Each new impact point creates new shock waves and a superposition of this phenomenon is represented in Fig. 1.52 (c). The interaction of the compression and refraction waves, that generate interface waves, must occur at the collision point and in its vicinity and it can be only the case if their periods match. Since the collision point is under extreme pressure and heat, the interaction of the shock waves, in combination with mutual
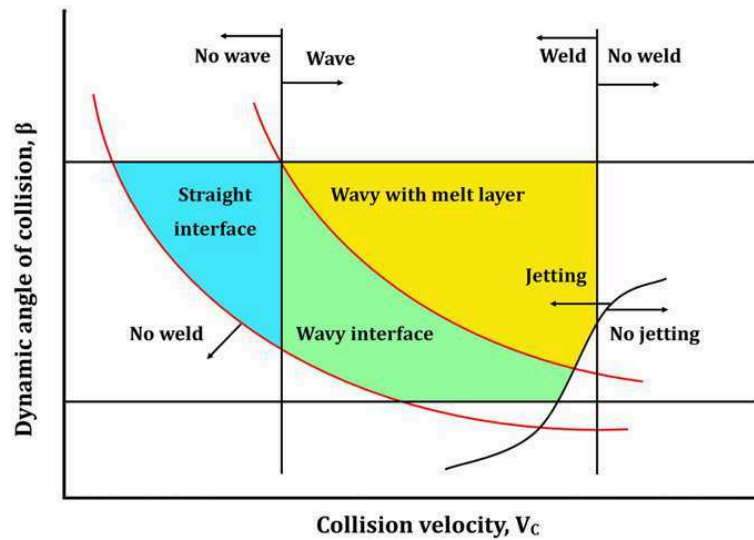
Figure 1.53: welding window schematic [15]

movement of the metals, is the source of interface waves. The wavelength is proportional to the parent metal thickness, since the radius of the pressure front of the reflected shock wave increases with the propagation distance. In cases where the inner welded part is a tube (Fig. 1.52 (d)), the compression waves are reflected from the free surface of the hole as refraction waves and interact with refraction waves at the interface to create interface interferences.

The presence of so much "theories" clearly shows that up to this day we don't have one and only one scientific physical explanation for the wave formation phenomena. In other words, we can say that today we have simple assertions used to explain the observed facts in terms of such theories.

Despite all that and while waiting to have clearer picture, we cannot ommit the advantage of the impact welding processes in direct joining dissimilar metals and having a working range of welding parameters from a process technological point of view is very important. Based on this fact, several researchers from the EXW suggested the construction of a graphical diagram relating the large numbers of parameters involved. This diagram is the well-known "welding window" and which gives the range of upper and lower limits of each physical parameter within which an acceptable weld can be achieved [42, 47, 57, 224] and it is represented in Fig. 1.53. The critical parameters used to construct this window are the collision angle for jet formation, the collision point velocity, the kinetic energy and impact pressure in the collision region associated with the impact velocity. This welding window was also used in the MPW applications successfully according to several studies [95, 198].

1.5.4.2 Discussion

After viewing the principle of functionning of both EXW and MPW and despite of big similarities between the two processes, they cannot be totally treated in the same manner. If we start from the traditional setup of the EXW presented in Fig. 1.54, the explosives cover all the area of the flyer and lead to continuous weld lines on all the traveling distance of the explosives. Concerning the impact angle, it is a constant in EXW whereas in the MPW it is not the case.

(a)

(b)
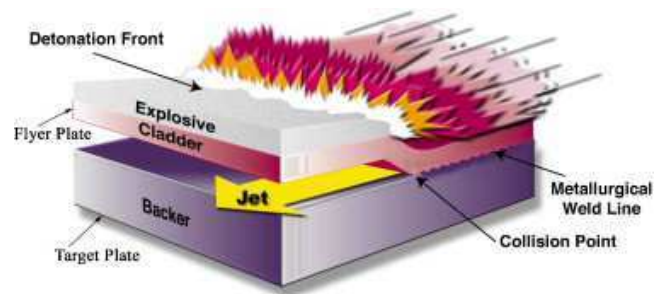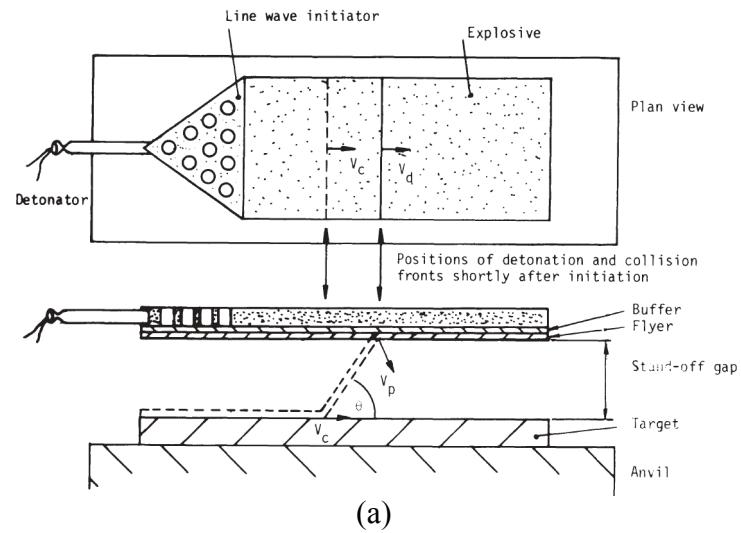
Figure 1.54: EXW setup for planar applications (a) plan view [28](b) schematic 3D presentation [238]
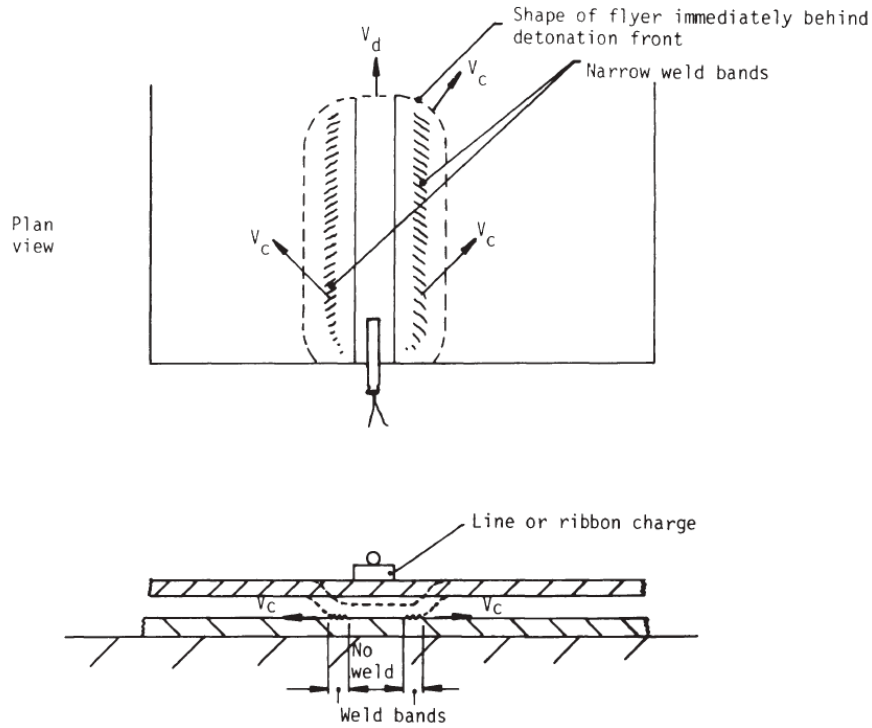
Figure 1.55: NASA's explosive seam welding technique producing welding conditions transiently [28]

After studying the EXW techniques and different applications, the EXW application that have the striking ressemblance with MPW is not the EXW traditional parallel plate configuration but the NASA's explosive seam welding technique presented in Fig. 1.55 and Fig. 1.56. In this application, the explosive loading is confined to an area which is small in comparison to the total area of the flyer metal. Under the detonation area no welding is obtained and over a small distance the transient impact velocities and angles are suitable for welding giving two weld bands and elliptical seam weld just like in the MPW.

Unfortunately, the available litterature about this technique is very limited and contains no deep theoretical analysis.

1.5.5   Conclusion

After this full review of the MPW going from the process principle and operation up to the bonding formation analysis, we can see that in the last thirty years a huge volume of research effort has been done and very interesting results were obtained. The MPW parameters are various, interdependent and require special handling to achieve good quality welds. The main parameters are: the discharge energy which is the source electrical energy that will be transformed into mechanical energy responsible of accelerating the flyer metal; the standoff distance or gap between the flyer and the parent metals and which is the distance that will permit the flyer metal to attain the required level of velocity for impact; and the coil design which will define how the magnetic field and the induced currents will be distributed. All these parameters will define the physical parameters conditions (impact velocity and impact angle at the interface) and by that the welding or non-welding.

(a)

(b)
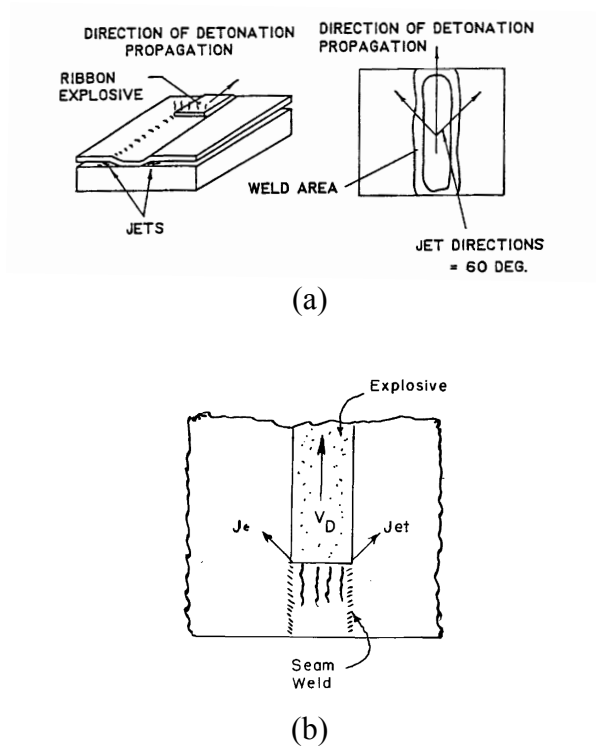
Figure 1.56: NASA's explosive seam welding technique presentation (a) [24] (b) [162]

These physical parameters are also related to the materials electrical and mechanical properties as well as thermal properties due to the plastic deformation and the joule effect.

The MPW efficiency in welding dissimilar materials gains lot of interest in different industries and during the last years especially in the automotive industry and to take into consideration the process automation at long term, we have also seen the magnetic pulse spot welding process which consists in avoiding the overlapping difficulties by creating a local hump in the intended welding area ; this hump will be accelerated to impact the parent metal and creates consequently a spot weld.

Another important point discussed during this section is the welding formation mechanisms where we have seen that the wavy interface was adopted by most of researchers in the impact welding processes field as the indicator of a good welding. Multiple assertions for wave formation were presented and it is important to remember that they were all established while developing the EXW process and carried-over to the MPW. Between these we can find four main mechanisms: jet indentation mechanism, flow/Helmholtz instability mechanism, vortex shedding mechanism and rarefaction wave mechanism. We have also discussed the welding window concept which stays the most used and considered as giving reasonable results for defining welding parameters.

Finally, we have seen that carrying-over all the concepts from the traditional parallel configuration EXW to MPW cannot be at 100% true since we are not in the same physical context and that the explosive seam welding process is closer to the MPW but it presents big lack of information in the accessible litterature.

After this extensive presentation of the MPW, we can say that due to the large number of parameters and their complex dependency, the need of numerical quantitative modelling is of great importance

to be able to link all that. In the next section, we will have a review of the numerical simulation of the process and the developments related to its modelling during the last years.

1.6 Magnetic Pulse Processes Simulation

1.6.1 Introduction

The MPW is a combination of different physical fields: electromagnetics, dynamic mechanics and thermal. These fields in the MPW are independent and any change in one of them affect the two others. From here, to be able to predict the electromagnetic fields, their simultaneous interaction with the flyer metal as well as the behaviour of the flyer under these dynamic conditions and after that the impact conditions, coupled mechanical-thermal-electromagnetic simulations have been developed during the last years.

For people coming from mechanical and materials engineering background, the first thing to understand is how the electromagnetic problem is formulated, what numerical solutions can be applied to the electromagnetic equations and how they can be linked to the other mechanical and thermal fields which we are familiar with.

Hence, our first aim during this section will be to present the mathematical problem formulation and the numerical solutions used for electromagnetics and where a focus will be given to the solver of LS-DYNA which is the multiphysics code that we will be using during the whole study.

1.6.2 Notations and physical variables

Table 1.6 provides the meaning of each symbol and the SI unit that will be used later on in this document.

1.6.3 Electromagnetic problem formulation

1.6.3.1 Maxwell equations

Maxwell equations are a set of four complicated equations that unify Ampère, Faraday and Gauss laws (for electric and magnetic fields) and describe how electric and magnetic fields propagate, interact and how they are influenced by surrounding objects. They provide a quantitative and qualitative description of static and dynamic electromagnetic fields and hence they can be used to explain and predict electromagnetic phenomena [97].

They are given in differential (point or microscopic) forms in the time domain at any point and any time t :

$$\overrightarrow{\nabla} \times \overrightarrow{H} = \overrightarrow{J} + \frac{\partial \overrightarrow{D}}{\partial t} \tag{1.11}$$

$$\overrightarrow{\nabla} \times \overrightarrow{E} = -\frac{\partial \overrightarrow{B}}{\partial t} \tag{1.12}$$

Symbol	Meaning	Units (S.I.)
$\overrightarrow{E}$	Electric field	Volt per meter (V/m)
$\overrightarrow{B}$	Magnetic flux density	Tesla (T)
$\overrightarrow{H}$	Magnetic flux intensity	Amperes per meter (A/m)
$\overrightarrow{J}$	Current density	Amperes per square meter (A/m²)
$\overrightarrow{D}$	Electric flux density	Coulombs per square meters (C/m^2)
Φ	Scalar potential	Volt
$\overrightarrow{A}$	Vector potential	Tesla meters (T.m)
σ	Electrical conductivity	Siemens per meter (S/m)
μ	Magnetic permeability	Henries per meter (H/m)
μ_0	Permeability of free space	$4\pi \cdot 10^{-7}$ H/m
ε	Permittivity	Farads per meter (F/m)
ε_0	Permittivity of free space	$\dfrac{1}{36\pi \cdot 10^9}$ F/m
ρ	Total charge density	oulombs per cubic meters (C/m^3)
V	Voltage	Volt (V)
I	Current	Ampere (A)
C	Capacitance	Farad (F)
q	Charge	Coulomb (C)
R	Resistance	Ohm
L	Inductance	Henry (H)

Table 1.6: variables and constant of the electromagnetic equations

$$\nabla \bullet \overrightarrow{D} = \rho \qquad (1.13)$$

$$\nabla \bullet \overrightarrow{B} = 0 \qquad (1.14)$$

The Maxwell-Ampère's (Eq. (1.11)) explains that the sources of the electromagnetic fields $(\overrightarrow{H}, \overrightarrow{E}, \overrightarrow{B})$ are conduction currents, $\overrightarrow{J}$, corresponding to the motion of charge and/or displacement current, $\overrightarrow{J_D} = \frac{\partial \overrightarrow{D}}{\partial t}$ which is a term added by Maxwell to the Ampère's Law in order to explain magnetic fields that are produced by a changing electric field [157]. The Maxwell-Faraday's (Eq. (1.12)) dictates that a time-changing magnetic field gives rise to an electric field circulating around it and that a circulating electric field in time gives rise to a magnetic field changing in time. The Maxwell-Gauss equation (Eq. (1.13)) states that electric charges, ρ, act as sources or sinks for electric fields. Finally, the Gauss's Magnetic Law (Eq. (1.14), called also Maxwell-Thomson Law) says that magnetic monopoles does not exist and that the magnetic fields tend to form closed loops.

To these equations, the law of conservation of charge (the continuity equation) is added to express the fact that a charge can neither be created or destroyed and which is a fundamental equation for electromagnetic problems and it is expressed by the local form:

$$\overrightarrow{\nabla} \bullet \overrightarrow{J} = -\frac{\partial \overrightarrow{\rho}}{\partial t} \qquad (1.15)$$

These five equations form a foundation of a unified and coherent theory of electricity and magnetism [97].

1.6.3.2 Constitutive relationships and quantities

The relation between different quantities of the Maxwell equations are made by the constitutive relationships:

$$\overrightarrow{D} = \varepsilon \overrightarrow{E} = \varepsilon_0 \varepsilon_r \overrightarrow{E} \tag{1.16}$$

$$\overrightarrow{B} = \mu \overrightarrow{H} = \mu_0 \mu_r \overrightarrow{H} \tag{1.17}$$

$$\overrightarrow{J} = \sigma \overrightarrow{E} \tag{1.18}$$

where ε presents the permittivity which is a measure of how much the molecules of a material oppose an external electric field, $\varepsilon_r > 1$ is the relative permittivity of a medium, μ is the permeability of the medium which is a measure of how easily a magnetic field can pass through this medium, μ_r is the relative permeability: $\mu_r < 1$ for diamagnet materials, $\mu_r > 1$ for paramagnet materials, $\mu_r >> 1$ for ferromagnet materials and σ is the electrical conductivity. Eq. (1.18) present the Ohm's Law.

The mentioned quantities present the constitutive quantities of a medium and can be scalars in isotropic materials, functions of space coordinates in heterogeneous materials, a matrix of nine components in the case of anisotropy (ferrite or birefringent...), dependent of the fields change i.e. non-linear mediums as ferromagnetic materials, dependent of time as in the non-stationary cases and in some complex mediums they can combine multiple aspects form the mentioned cases or even all these characteristics [157]. They also depend on frequency, temperature and humidity.

1.6.3.3 Lorentz force and Lorentz force density

The Lorentz force is the combination of electric and magnetic force on a point charge due to electromagnetic fields: a particle of charge q moving with velocity $\overrightarrow{v}$ in the presence of an electric field $\overrightarrow{E}$ and a magnetic field $\overrightarrow{B}$, will experience a force. This force is called Lorentz Force and is given by:

$$\overrightarrow{f} = q(\overrightarrow{E} + \overrightarrow{v} \times \overrightarrow{B}) \tag{1.19}$$

Considering a magneto-quasistatic case, since the charge density is negligible then the Lorentz Force exerted will be only associated to the magnetic field and hence:

$$\overrightarrow{f} = q\overrightarrow{v} \times \overrightarrow{B} \tag{1.20}$$

Considering a number n of moving charges q with a velocity $\overrightarrow{v}$ inside an arbitrary volume V.

The total charge inside an elementary volume dV will be:

$$dq = n \cdot q \cdot dV \tag{1.21}$$

In the presence of a magnetic field $\vec{B}$, the exerted force $d\vec{f}$ on dq will be:

$$d\vec{f} = dq \cdot \vec{v} \times \vec{B} = n \cdot q \cdot \vec{v} \times \vec{B} \, dV = \vec{J} \times \vec{B} \, dV \tag{1.22}$$

So the force density is:

$$\vec{F} = \frac{d\vec{f}}{dV} = \vec{J} \times \vec{B} \tag{1.23}$$

The total force over a volume is hence the volume integral of Eq. (1.23).

Combining Eq. (1.11) and Eq. (1.23):

$$\vec{F} = \frac{1}{\mu}(\nabla \times \vec{B}) \times \vec{B} = \frac{1}{\mu}(\vec{B} \bullet \nabla)\vec{B} - \nabla(\frac{B^2}{2\mu}) \tag{1.24}$$

As a result, the Lorentz Force can be divided in two terms: a conservative term $-\nabla(\frac{B^2}{2\mu})$ that present a pressure, the so-called *magnetic pressure*, and a rotational term $\frac{1}{\mu}(\vec{B} \bullet \nabla)\vec{B}$ that can be interpreted as a force that acts tangentially and normal to the magnetic field lines the so-called tension forces that accelerates a conductive fluid in regions where the magnetic field is greater than zero ([106]).

We know from the form of the Lorentz force that it is perpendicular to $\vec{B}$. In general, both the magnetic pressure and tension forces have components parallel to $\vec{B}$. These are equal in magnitude but opposite in direction, so they cancel.

1.6.3.4 Boundary conditions

The fields $\vec{E}, \vec{B}, \vec{D}$ and $\vec{H}$ are discontinuous at points where ε, μ, and σ also are as it is seen from the equations Eq. (1.13), Eq. (1.11) and the constitutive equations. Therefore, the field vectors will be discontinuous at a boundary between two medias with different constitutive parameters.

To express boundary conditions in a magnetic problem, the integral form of Maxwell's equations are used to determine the relations of the normal and tangential components of the fields at the interface between two different medias, i.e. with different constitutive parameters, where surfaces density of sources may exist along the boundary.

For two different mediums 1 and 2, the general boundary conditions are [134, 157] :

$$\vec{n} \times (\vec{E_1} - \vec{E_2}) = 0 \tag{1.25}$$

$$\vec{n} \times (\vec{H_1} - \vec{H_2}) = \vec{J_S} \tag{1.26}$$

$$\vec{n} \cdot (\vec{D_1} - \vec{D_2}) = \rho_S \tag{1.27}$$

$$\overrightarrow{n} \cdot (\overrightarrow{B_1} - \overrightarrow{B_2}) = 0 \tag{1.28}$$

The Eq. (1.25) and the Eq. (1.28) express respectively the continuity of tangential components of $\overrightarrow{E}$ and the normal components of $\overrightarrow{B}$ across interface while the Eq. (1.26) and the Eq. (1.27) express the interface continuity dependence of the tangential components of $\overrightarrow{H}$ on the free charge surface density ρ_S and the normal components of $\overrightarrow{D}$ on the surface current density $\overrightarrow{J_S}$. For finite conductivity, the tangential magnetic field is continuous across the boundary.

1.6.3.5 Electromagnetic potential

After the presentation of the Maxwell's equations, it is important to say that these equations are not so easy to solve. To facilitate the calculation of the fields created by a bounded source distribution, scalar electric potential Φ and magnetic vector potential $\overrightarrow{A}$ as magnitudes were introduced. These potentials present the first two auxiliary functions that once they are obtained, it will be easier to calculate the fields from them.

According to Eq. (1.14), the divergence of the magnetic field $\overrightarrow{B}$ is always zero so using the mathematical property $div(\overrightarrow{curl}) = 0$, it exists then some vector potential such as:

$$\overrightarrow{B} = \nabla \times \overrightarrow{A} \tag{1.29}$$

Combining this equation with Faraday's Law (Eq. (1.12)) :

$$\nabla \times (\overrightarrow{E} + \frac{\partial \overrightarrow{A}}{\partial t}) = 0 \tag{1.30}$$

Using the mathematical property $\overrightarrow{curl}(\overrightarrow{grad}) = 0$, which dictates that any zero curl can be expressed as the gradient of a scalar function Φ, we can conclude form Eq. (1.30) that:

$$\overrightarrow{E} + \frac{\partial \overrightarrow{A}}{\partial t} = -\nabla\Phi \Leftrightarrow \overrightarrow{E} = -\frac{\partial \overrightarrow{A}}{\partial t} - \nabla\Phi \tag{1.31}$$

where $\frac{\partial \overrightarrow{A}}{\partial t}$ is the non-conservative part of the electric field with a non-vanishing curl.

Eq. (1.30) and Eq. (1.31) determine completely the fields $\overrightarrow{B}$ and $\overrightarrow{E}$ but looking at $\overrightarrow{A}$ and Φ, it is clear that there is infinite potentials giving the same $\overrightarrow{E}$ and $\overrightarrow{B}$:

Considering any arbitrary, single valued, continuously differentiable, scalar function of position and time Ψ such as:

$$\overrightarrow{A} = \overrightarrow{A'} + \nabla\Psi \tag{1.32}$$

will lead to:

$$\overrightarrow{B} = \nabla \times \overrightarrow{A} = \nabla \times \overrightarrow{A'} + \nabla \times \nabla\Psi = \nabla \times \overrightarrow{A'} \tag{1.33}$$

Inserting Eq. (1.32) into Eq. (1.31):

$$\overrightarrow{E} = -\frac{\partial \overrightarrow{A'}}{\partial t} - \nabla(\Phi + \frac{\partial \Psi}{\partial t}) \tag{1.34}$$

so that the value of $\overrightarrow{E}$ obtained from $\overrightarrow{A'}$ will remain the same on the condition that Φ is replaced by the scalar potential:

$$\Phi' = \Phi + \frac{\partial \Psi}{\partial t} \tag{1.35}$$

Consequently and in order to make the electromagnetic potentials unique, a particular choice of the scalar and vector potentials is needed. In order to get to this purpose, the spatial behavior of $\overrightarrow{A}$ should be completely determined through the definition of $\nabla \bullet \overrightarrow{A}$ (Helmholtz's Theorem), this procedure is called gauging and the function Ψ is called gauge function.

1.6.3.6 Magnetic pulse processes - Magnetoquasistationary approximation

A simple, linear, homogeneous and isotropic conductive medium present constant conductivity $\sigma > 0$, permeability $\mu > 0$ and permittivity $\varepsilon > 0$ which is the case of the non-ferromagnetic materials like aluminum, copper, silver...

In the case of good conductors, i.e. $\sigma >> \omega\varepsilon$, the displacement current $\overrightarrow{J_D}$ is negligible when compared to the conduction current $\overrightarrow{J}$. In fact, Combining the phasor form of the Maxwell-Amper's equation, i.e. Eq. (1.11), with constitutive equations, the Eq. (1.36) is obtained:

$$\overrightarrow{\nabla} \times \overrightarrow{H} = \overrightarrow{J} + \overrightarrow{J_D} = \overrightarrow{J} + j\omega\overrightarrow{D} = \sigma\overrightarrow{E} + j\omega\varepsilon\overrightarrow{E} = (\sigma + j\omega\varepsilon)\overrightarrow{E} \tag{1.36}$$

If the frequency of the sources needed to have $J = J_D$, i.e. $\sigma = \omega\varepsilon = 2\pi f \varepsilon$, in the copper's, aluminum's and steel's case is computed:

$$\left. \begin{cases} \sigma_{Copper} = 5.88 \times 10^7 \, S/m \\ \varepsilon_{Copper} = \varepsilon_0 = \frac{1}{36\pi \times 10^9} \, F/m \end{cases} \right\} \Rightarrow f_{Copper} = 1.00441 \times 10^{18} Hz$$

$$\left. \begin{cases} \sigma_{Aluminum} = 3.65 \times 10^7 \, S/m \\ \varepsilon_{Aluminum} = \varepsilon_0 = \frac{1}{36\pi \times 10^9} \, F/m \end{cases} \right\} \Rightarrow f_{Aluminum} = 6.57 \times 10^{17} Hz$$

$$\left. \begin{cases} \sigma_{Steel} = 1.32 \times 10^6 \, S/m \\ \varepsilon_{Steel} = \varepsilon_0 = \frac{1}{36\pi \times 10^9} \, F/m \end{cases} \right\} \Rightarrow f_{Steel} = 2.376 \times 10^{16} Hz$$

In the EMF case, the frequencies reached by the pulse generator are in orders of KHz and hence they are about $10^{-14}\%$ of the needed frequencies to reach a reasonable value for the displacement currents. Hence, in the case of good conductors materials, the Eq. (1.11) can be written:

$$\overrightarrow{\nabla} \times \overrightarrow{H} = \mu\nabla \times \overrightarrow{B} = \overrightarrow{J} \tag{1.37}$$

This is the so-called *magneto-quasistatic case*.

On the other side and since the constitutive parameters are constants, then the continuity equation,

Eq. (1.15), combined with the constitutive relations Eq. (1.16) and Eq. (1.17) can be expressed by:

$$\nabla \bullet \overrightarrow{J} = \nabla \bullet (\sigma \overrightarrow{E}) = \sigma \nabla \bullet \overrightarrow{E} = \frac{\sigma}{\varepsilon} \nabla \bullet \overrightarrow{D} \tag{1.38}$$

Eq. (1.38) and Gauss's Law (Eq. (1.13)) will lead to:

$$\frac{\sigma}{\varepsilon}\rho = -\frac{\partial \rho}{\partial t} \Rightarrow \frac{\partial \rho}{\partial t} + \frac{\sigma}{\varepsilon}\rho = 0 \Rightarrow \rho = \rho_0^{-\frac{\sigma}{\varepsilon}t} \tag{1.39}$$

where ρ_0 is the charge density at time $t = 0$. To reach the steady state, the conductor material will hence need $t' = 5\tau$ where τ presents the characteristic time (relaxation time) needed for the charge at any point to decay to $\frac{1}{e}$ from its original value and its given by:

$$\tau = \frac{\varepsilon}{\sigma} \tag{1.40}$$

Computing again the value for copper, aluminum and steel :

$$t'_{Copper} = 7.55 \times 10^{-19}s$$
$$t'_{Aluminum} = 1.215 \times 10^{-18}s$$
$$t'_{Steel} = 6.698 \times 10^{-18}s$$

Thus, the charge distribution decays exponentially so quickly that it may be assumed that $\rho = 0$ and as a result, the Maxwell-Gauss law, i.e. Eq. (1.13), and the continuity equation can be written respectively:

$$\nabla \bullet \overrightarrow{E} = 0 \tag{1.41}$$

$$\nabla \bullet \overrightarrow{J} = 0 \tag{1.42}$$

Finally, the electromagnetic equations in the case of simple, linear, homogeneous and isotropic good conductors in magneto-quasistatic case are:

$$\begin{aligned} \overrightarrow{\nabla} \times \overrightarrow{H} &= \overrightarrow{J} \\ \overrightarrow{\nabla} \times \overrightarrow{E} &= -\frac{\partial \overrightarrow{B}}{\partial t} \\ \nabla \bullet \overrightarrow{E} &= 0 \\ \nabla \bullet \overrightarrow{J} &= 0 \\ \nabla \bullet \overrightarrow{B} &= 0 \end{aligned} \tag{1.43}$$

The magneto-quasistatic case also called low-frequency or eddy-current approximation, is the case of the magnetic pulse processes.

A typical eddy current problem (Fig. 1.57) consists of a region $\Omega = \Omega_1 \cup \Omega_2$ where Ω_1 is an eddy current region with non-zero conductivity (metallic pieces) and Ω_2 a surrounding region free of eddy currents ($\sigma = 0$, air) which may, however, contain source currents.

The boundary of Ω_2 and hence of Ω is divided into two parts in accordance of the boundary conditions presented in Eq. (1.25) till Eq. (1.28): Γ_B where the normal component of magnetic
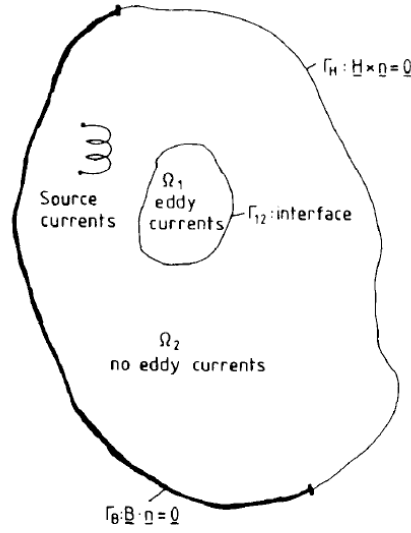
Figure 1.57: typical eddy current problem [27]

flux density is prescribed and Γ_H where the tangential component of magnetic field is given. The boundary Γ_{12} of Ω_1 presents the interface between the conducting and nonconducting regions where the continuity conditions of the normal component of magnetic field density and of the tangential component of magnetic field intensity should be respected also.

Hence, the differential equations as well as the boundary and interface conditions can be summarized as follow [27]:

$$
\text{in } \Omega_1: \begin{cases} \vec{\nabla} \times \vec{H} &= \sigma \vec{E} \\ \vec{\nabla} \times \vec{E} &= -\frac{\partial \vec{B}}{\partial t} \\ \nabla \bullet \vec{B} &= 0 \end{cases} \tag{1.44}
$$

$$
\text{in } \Omega_2: \begin{cases} \vec{\nabla} \times \vec{H} &= \vec{J_S} \\ \nabla \bullet \vec{B} &= 0 \end{cases} \tag{1.45}
$$

$$
\text{on } \Gamma_B: \vec{B} \cdot \vec{n} = 0 \tag{1.46}
$$

$$
\text{on } \Gamma_H: \vec{H} \times \vec{n} = \vec{0} \tag{1.47}
$$

$$
\text{on } \Gamma_{12}: \begin{cases} \vec{B_1} \cdot \vec{n_1} + \vec{B_2} \cdot \vec{n_2} &= 0 \\ \vec{H_1} \times \vec{n_1} + \vec{H_2} \times \vec{n_2} &= 0 \end{cases} \tag{1.48}
$$

where $\vec{J_S}$ denotes the source current density, $\vec{n}$ the outer normal on the corresponding surface and subscripts 1 and 2 the quantities in the regions Ω_1 and Ω_2 respectively.

The introduction of magnetic vector potential $\vec{A}$ in $\Omega = \Omega_1 \cup \Omega_2$ and a scalar electric potential Φ in Ω_1, allow the description of the fields quantities as in Eq. (1.29) and Eq. (1.31). In order to

ensure the uniqueness of the potentials, the general Coulomb gauge condition is used:

$$\nabla \bullet (\sigma \overrightarrow{A}) = 0 \tag{1.49}$$

The use of the Maxwell equations in terms of potentials and respecting the uniqueness condition (1.49) will lead us to a boundary value problem with the two unknowns $\overrightarrow{A}$ and Φ[27] :

$$\text{in } \Omega_1: \begin{cases} \overrightarrow{\nabla} \times \frac{1}{\mu} \overrightarrow{\nabla} \times \overrightarrow{A} - \overrightarrow{\nabla} \frac{1}{\mu} \nabla \bullet \overrightarrow{A} + \sigma \frac{\partial \overrightarrow{A}}{\partial t} + \sigma \overrightarrow{\nabla} \Phi & = & \overrightarrow{0} \\ \nabla \bullet (-\sigma \frac{\partial \overrightarrow{A}}{\partial t} - \sigma \overrightarrow{\nabla} \Phi) & = & 0 \end{cases} \tag{1.50}$$

$$\text{in } \Omega_2: \left\{ \begin{array}{l} \overrightarrow{\nabla} \times \frac{1}{\mu} \overrightarrow{\nabla} \times \overrightarrow{A} - \overrightarrow{\nabla} \frac{1}{\mu} \nabla \bullet \overrightarrow{A} & = & \overrightarrow{J_S} \end{array} \right. \tag{1.51}$$

$$\text{on } \Gamma_B: \begin{cases} \overrightarrow{n} & \times & \overrightarrow{A} & = & \overrightarrow{0} \\ \frac{1}{\mu} \nabla & \bullet & \overrightarrow{A} & = & 0 \end{cases} \tag{1.52}$$

$$\text{on } \Gamma_H: \begin{cases} \frac{1}{\mu} \overrightarrow{\nabla} \times \overrightarrow{A} & \times & \overrightarrow{n} & = & \overrightarrow{0} \\ \overrightarrow{n} & \cdot & \overrightarrow{A} & = & 0 \end{cases} \tag{1.53}$$

$$\text{in } \Omega_1: \begin{cases} \overrightarrow{A_1} & = & \overrightarrow{A_2} \\ \frac{1}{\mu_1} \overrightarrow{\nabla} \times \overrightarrow{A_1} \times \overrightarrow{n_1} + \frac{1}{\mu_2} \overrightarrow{\nabla} \times \overrightarrow{A_2} \times \overrightarrow{n_2} & = & \overrightarrow{0} \\ \overrightarrow{n} \cdot (-\sigma \frac{\partial \overrightarrow{A}}{\partial t} - \sigma \overrightarrow{\nabla} \Phi) & = & 0 \end{cases} \tag{1.54}$$

Once these two unknowns are solved, the fields can be hence calculated and the Lorentz force as well as Joule power heating term can be deduced.

1.6.4 Numerical Solutions and Multiphysics Codes

In the simulation field of electromagnetic forming processes, there is a variety of commercial codes which are used today: ABAQUS, COMSOL, ANSYS as well as LS-DYNA [21]. LS-DYNA presents advanced capacities in coupling automatically mechanical, thermal and electromagnetic solvers. For this reason, it will be used during this study.

LS-DYNA is a general purpose finite element code for analyzing the large deformation static and dynamic response of structures including fluids and thermal interactions [128]. In the recent years, a new electromagnetism module was added to the code for solving coupled mechanical - thermal - electromagnetic simulations [122]. This module allows to introduce source electrical currents into solid conductors, and to compute the associated magnetic and electric fields as well as induced currents. The computation is done by solving the Maxwell equations in the magneto-quasistatic approximation as presented in 1.6.3.6. The software uses a coupled FEM-BEM approach where both are based on discrete differential forms (Nedelec-like elements [156]).

The boundary element method uses analytical free space solutions of the governing differential equations under the action of a point source and presents some important advantages: discretisation of the boundary only, improved accuracy for secondary variables and simple accurate modelling
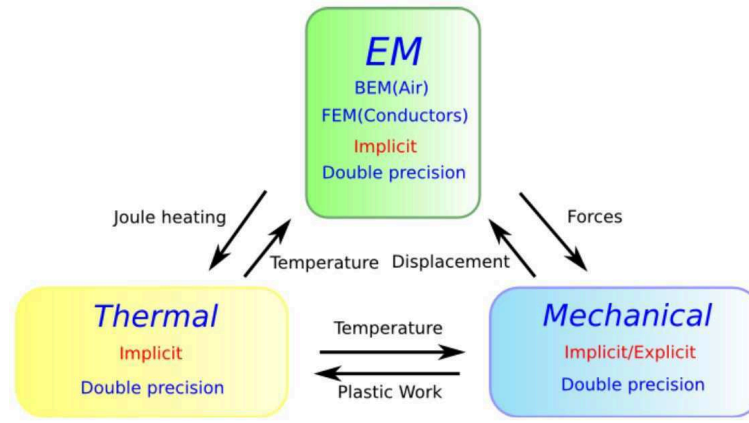
Figure 1.58: interactions between different solvers in LS-DYNA [128]

of problems involving infinite and semi-infinite domains, a typical situation in electromagnetism [67]. Since the BEM takes into account the behaviour of the solution in external region, it is used for the approximation in the complement of a smaller bounded domain (i.e. the conductors) in which the solution is approximated using the FEM.

At each electromagnetic time step, the electromagnetism solver and mechanical solver will interact where the EM solver will communicate the Lorentz force described in Eq. (1.23) to the mechanical solver resulting in an extra force in the mechanical model :

$$\rho \frac{du}{dt} = \nabla \bullet \sigma + f_{ext} + F_{Lorentz} \tag{1.55}$$

where u is the velocity vector and σ is the Cauchy stress tensor.

In the same manner, at each EM time step, the electromagnetism solver will communicate the extra Joule heating power term and the thermal solver will communicate the temperature. The interaction between different solvers in LS-DYNA is illustrated in the Fig. 1.58.

1.6.5 Welding interface simulation

Due to the development of the simulation capability, several studies discussed some methods in order to try to predict welding numerically. These methods go from processing the impact conditions to using Lagrangian - Eulerian and Eulerian simulations of the welding interface and recently molecular dynamics modeling of atomic diffusion was also used.

Cuq-Lelandais et al. [53, 54] used the LS-DYNA coupled simulation to extract the impact conditions. They proposed to use an estimated analytical welding window using the equations of EXW window (Fig. 1.59 (a)) and then to plot the collision angle versus the normal impact velocity and to follow the ballistic path evolution in order to explain the causes of non-weldability (Fig. 1.59 (b)). Several 2D median cross section analysis have been done and compared to experimental welding lines for aluminum/steel joints (Fig. 1.59 (c) and (d)).

Nassiri et al. [155] focused more on the interface welding formation of high velocity impact welding in general. They varied the impact conditions (Fig. 1.60), i.e. impact velocity and angles, and
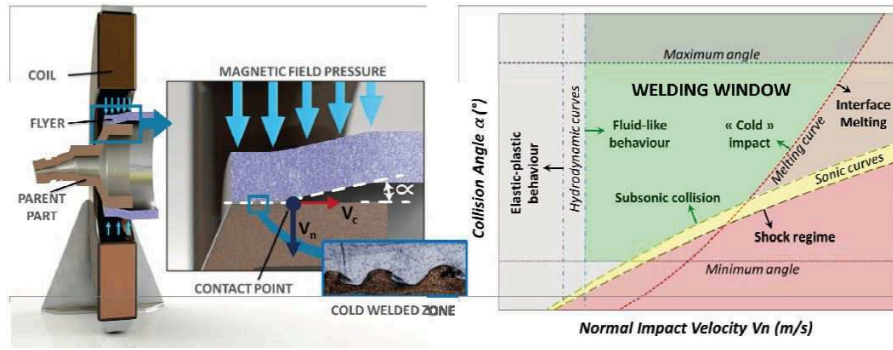
(a)
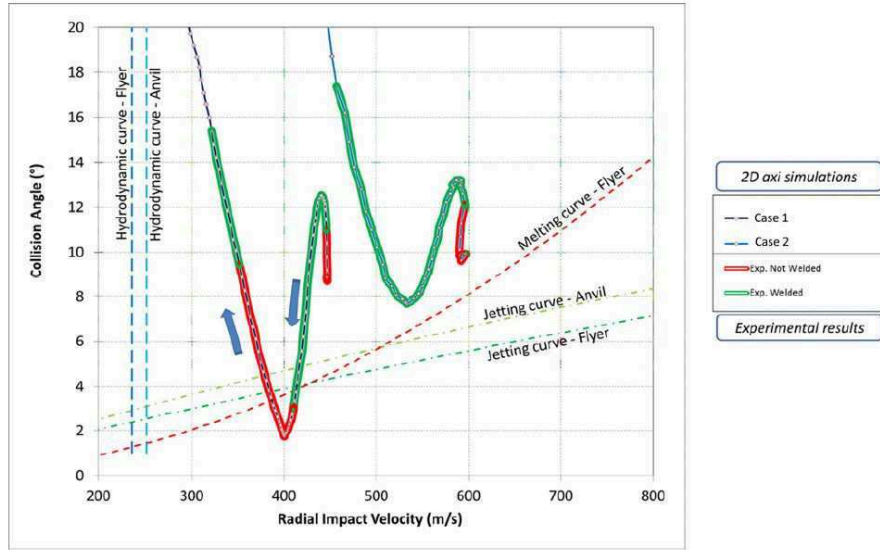
(b)
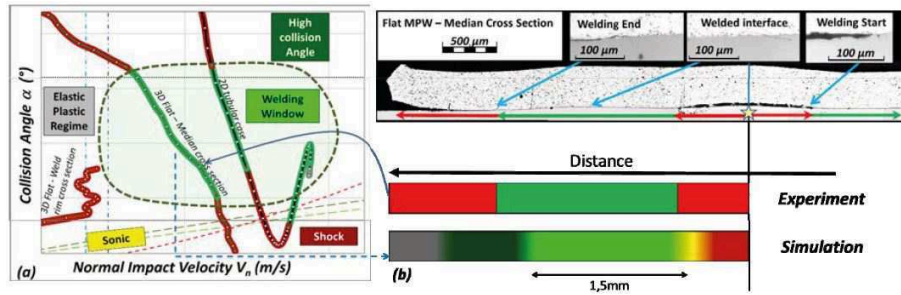
(c)
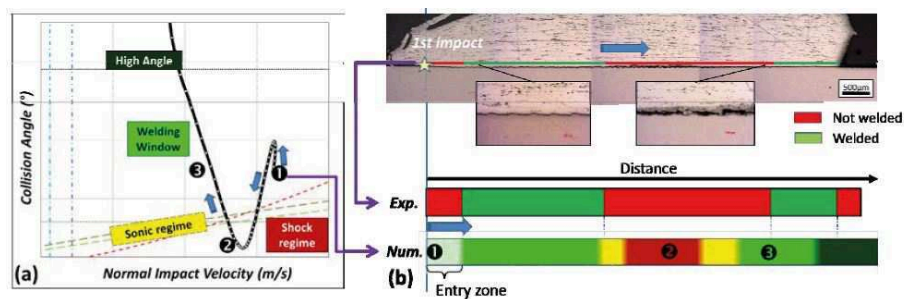
(d)

Figure 1.59: impact conditions processing [53, 54]: (a) analytical welding window deduced from EXW (b) ballistic path evolution (c) and (d) experimental/numerical comparison on MPW aluminum/steel joints

63
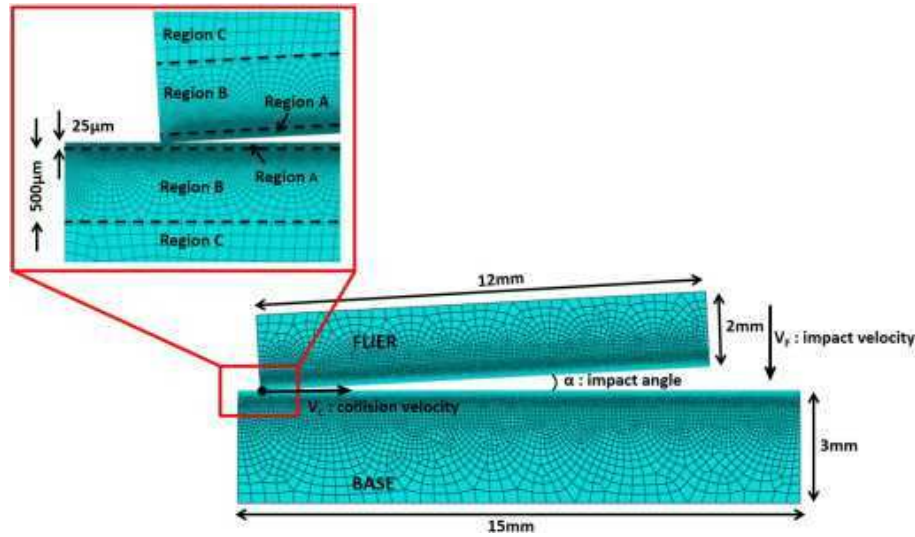
Figure 1.60: mesh and collision parameters in ABAQUS [155]

they used Arbitrary Lagrangian-Euler (ALE) in ABAQUS to numerically predict the temperature at the interface as well as the necessary process parameters to achieve a wavy morphology at the interface which is assumed to be a characteristic of a quality impact weld. This allowed the prediction of a weldability window of similar Al6061-T6 welding using the vaporizing foil actuator impact welding technique (Fig. 1.61), including separate regions for melting and purely solid state welds. The method also allowed the prediction of molten layer at the interface (Fig. 1.62).

Sapanathan et al. [189] also focused on the interface welding formation in general. They compared ALE and Eulerian computations and concluded that ALE simulations cannot accurately capture thermophological transition toward a wavy shape and cannot compute the successive jet formation from the interface (Fig. 1.63). The Eulerian method becomes a good alternative to overcome those limitations of the ALE method. They computed interfacial features using Eulerian simulations and compared it with experimental observations of various interfacial phenomena (Fig. 1.64) and claimed that the Eulerian simulation provides understanding for the potential cause of defects that corresponds to the experimental observations, in terms of morphology and site occurrence (Fig. 1.65). Zhang et al. [236] presented also Eulerian computation using LS-DYNA to study the interfacial morphology of impact welding between Cu110 and CP-Ti.

Fan et al. [63] used molecular dynamics modeling for simulating atomic diffusion behaviour during MPW between Al and Fe. They used the Large-scale Atomic/Molecular Massively Parallel Simulator (LAMMPS) and they worked on the prediction of the interfacial region evolution through the diffusion layer thickness. They compared the results to experimental data and claimed to have good accuracy.

1.7   Conclusion

At the end of this chapter and after this extensive litterature review of all the points that may be involved during this study, several conclusions can be made simultaneously concerning the dissimilar welding, the multi-material joining and the MPW process.
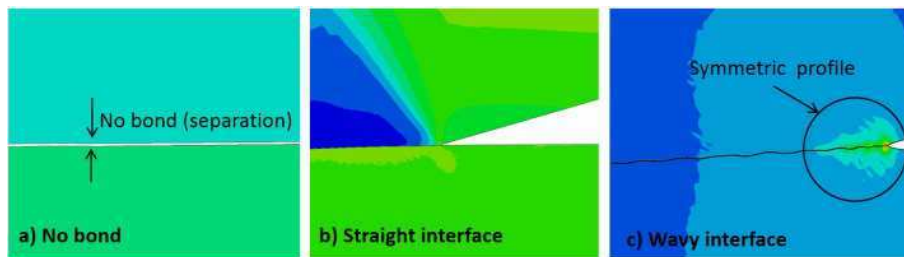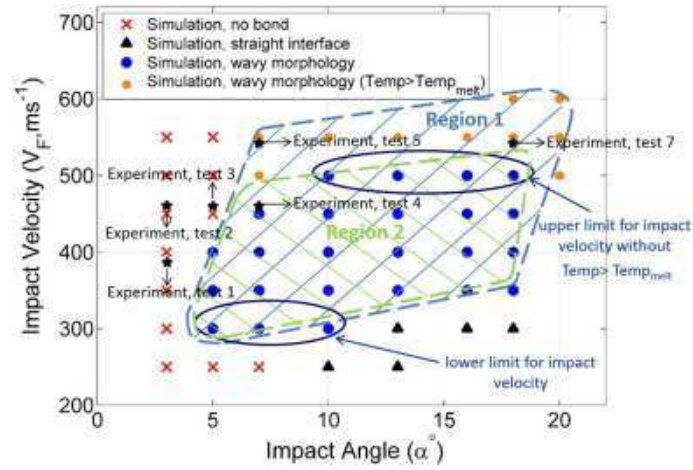
Figure 1.61: wavy pattern window for Al6061-T6 with shape of the interface [155]
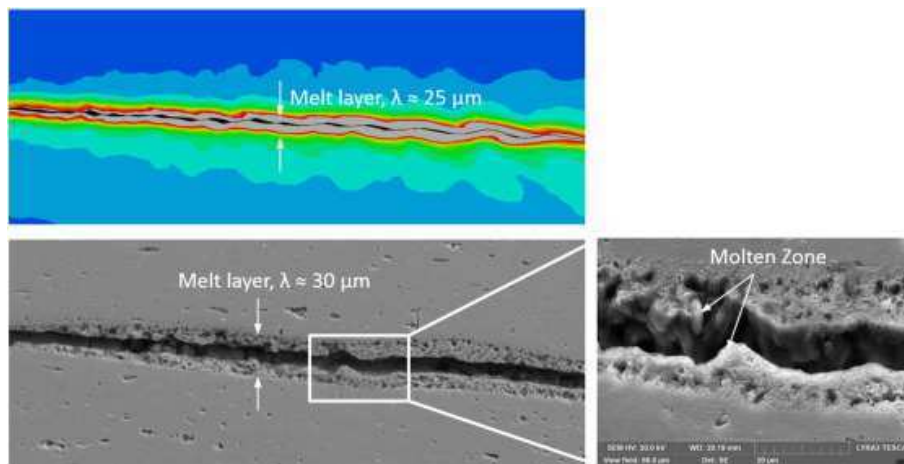
Figure 1.62: melt interlayer prediction for Al6061-T6 similar welding using VFAW [155]
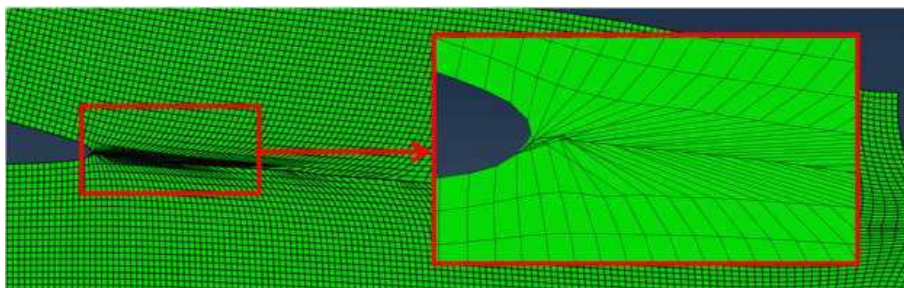
Figure 1.63: ALE limitation due to excessive interfacial shearing [189]

(a)

(b)
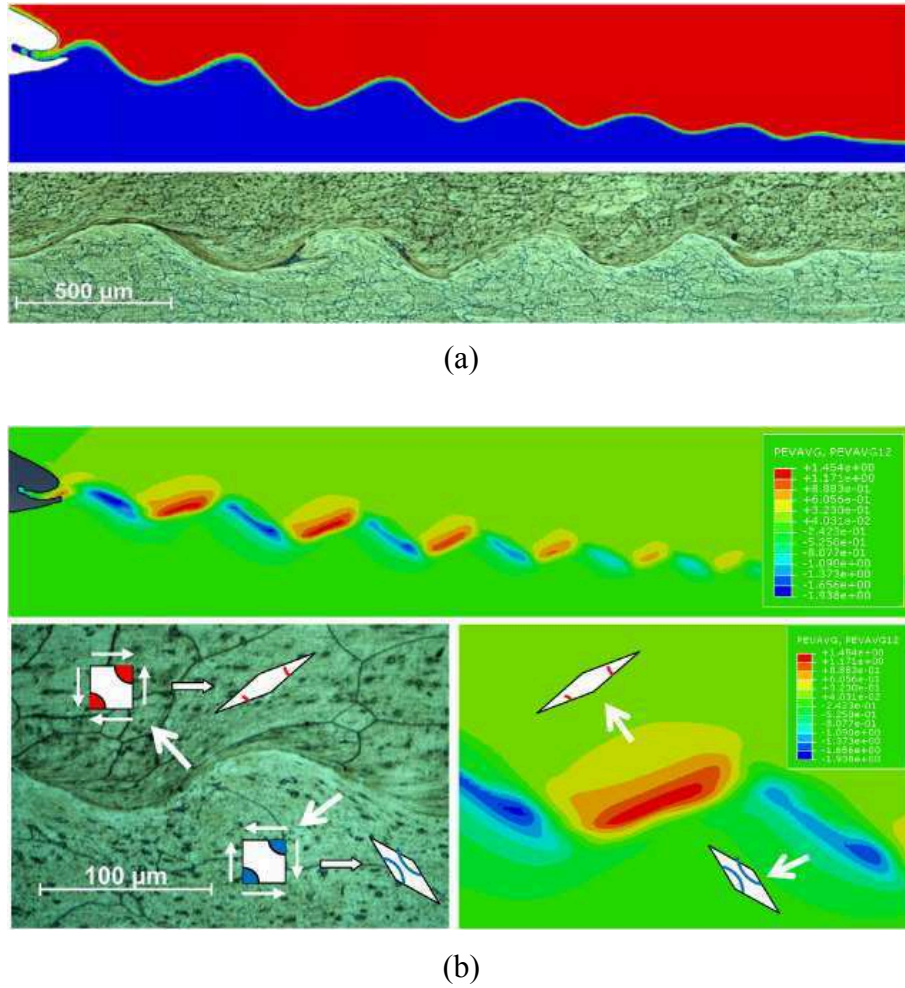
Figure 1.64: comparison of experimental and numerical results for the accuracy of Eulerian method [189]: (a) interfacial kinematics and wave formation (b) interfacial shearing
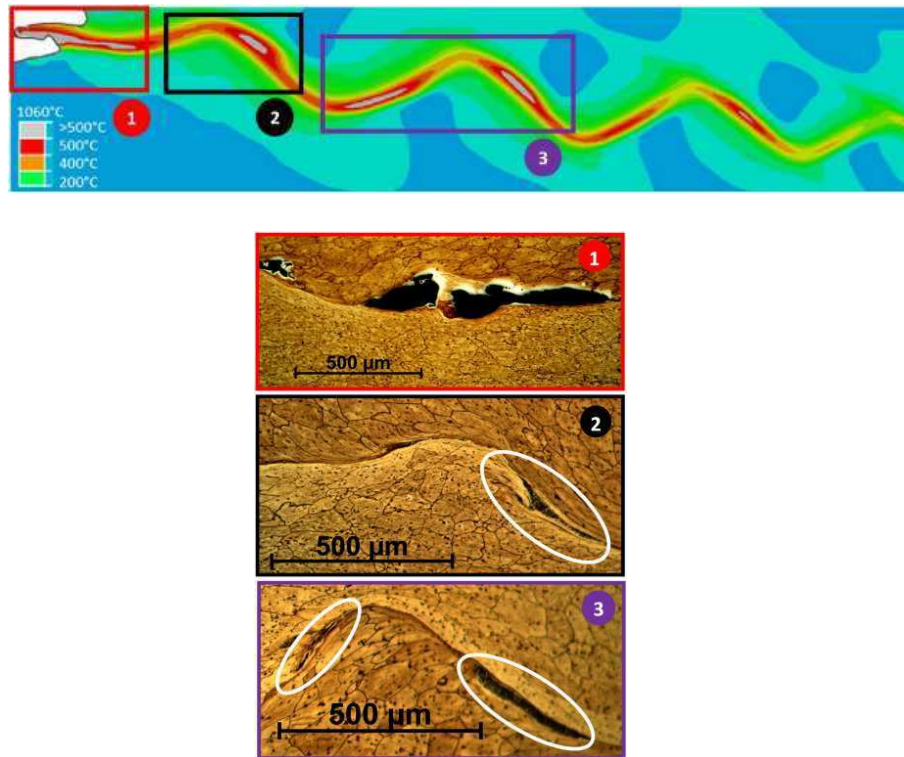
Figure 1.65: numerical and experimental comparison for interfacial defects due to significant heating [189]

Let's start with dissimilar welding and multi-material joining. First, the joining between FRPC and metal remains always a big challenge for various industries and more specific for the automotive industry since we are talking about high volumes production rates. The traditional techniques are far from being replaced today due to their historical advantages but however they still have several limitations from a technical and more from an operational point of view. When taking a look at the joining processes used and under development, every process has its own tools and equipments and also sometimes it is limited to one kind of application whether related to geometrical or materials. Here, we can think especially about the heat based technique which are always the most proposed in joining FRPCs to metals. Therefore, the most important point to take into consideration when developing a new solution is to try to limit all the technical difficulties especially avoid heating on FRPCs and at the same time to develop solutions able to be automated and respect the production rates in the automotive industry.

Second, the dissimilar joining of aluminum to steel is also another challenge from a technical and industrial point of view. In the former, we have seen that fusion based processes are very difficult to apply for heteregeneous aluminum/steel application due to the large differences of the physical properties leading to several risks on the welding quality where we can mention the HAZ and the IMCs formation. From an industrial point of view, we know that the switching from steel to aluminum in some automotive components has already started and a full transition is far from being realistic due to economical and technical reasons and if it will happen, it will not be some "overnight" process. This fact applies not only for aluminum but also for the newly rising candidate as a lightweight alloy: the magnesium.

Consequently, joining processes capable of being multi-tasking and able to be automated are the

best solutions that the industries are seeking for.

While presenting the solid-state welding techniques, we have seen that all the dissimilarities that we have in the heteregenous welding can be overcame using high velocity impact solid-state welding which already demonstrated their efficiency through the large combinations that have been applied whether in EXW, MPW/MPSW or other similar processes. In addition, we have discussed that the MPW is the most approporiate from an ergonomy and robotization point of view.

Although the researches about the MPW increased a lot during the last decades and presented interesting results towards deeper understanding of the process, we have seen in the litterature review that a great deal of work still needed to reach a unique comprehensive qualitative and quantitative theory able to explain and predict the welding formation. In fact, we have seen that there are different mechanisms theories for the welding interface formation. All of them try to explain the waviness at the interface considered as the indicator of a good welding. However, the big advantages of the MPW are unquestionable and the benefits that we can have from this process are worth to be explored.

For all of these reasons, the main aim of this study was to try to extend the field of applications of the MPW particularly in planar sheets configurations to the FRPC. By that, we will have a multi-tasking solution able to join similar and dissimilar metals as well as plastics/FRPC to metals and all that using same tools and equipment. To do so, we have thought about the two solutions presented in the introduction of this study and for which we will have to focus on several open points concerning the MPW processes. These open points with the two joining solutions propositions gave rise to lots of questions which constituted the roadmap of our investigations:

The first wave of questions that we asked ourselves and where we found a lack of litterature about it, is the electromagnetic problem presentation from a physical point of view that makes clear the physical principles to any new arriver into this field of research. Also, this presentation is needed to clarify how the design of coils should be thought and how to qualitatively know how it will induce the currents in the flyer metal and finally all that with its positioning how they will affect its efficiency. The other important consequence from this understanding will be clarifying to the designers how they should design the mounting system accordingly.

On the other hand, the influence of the geometrical and process parameters of the MPW/MPSW and the forces distribution on the flyer metal is of main interest and defining some qualitative rules to find rapidly the welding parameters in function of flyer thickness and strength could be an important time saver for the application on new couples.

These questions will be the concern of the Chapter 2 and they will include the development of 3D coupled numerical model using the multiphysics code LS-Dyna.

The second wave of interrogations was concerning the metal/metal MPW. In the automotive industry, the most used aluminum sheet alloys belong to the 5xxx and 6xxx families and having thicknesses that can reach 2 mm. In the litterature of the MPW, another lack concerning these alloys and thicker sheets was also found and to be able to check whether the automotive aluminum grades going from thin to thick are able also to be welded using MPW. Within the same context, the other investigation that we should do is the weldability of these grades not only with low carbon

deep drawing well-known steels but also with the new multi-phase generations steels which are more and more used in the automotive. The mechanical behaviour of these joints under different types of loads and their metallurgical characteristics should be also examined. Finally, one of the very rare discussion in the litterature is the weldability on coated steels and some investigations are also needed.

All of these interrogations are treated in Chapter 3.

After all the above waves of questions, the Chapter 4 will focus on extending the application of the MPW/MPSW to the FRPC/metal hybrid joints: the two solutions feasibility study, the mechanical behaviour of the joints, the control of the process and the transition possibility from the metal/metal to FRPC/metal joints.

Once all that is done and in the last part of this study, we will use the experimental results and the numerical model obtained to propose a method to construct the welding window by linking the process parameters to the physical parameters.

Chapter 2

Tooling design for magnetic pulse welding

2.1 Résumé

Une meilleure maitrise du procédé de soudage par impulsion magnétique nécessite la compréhension des différents facteurs qui peuvent influencer les paramètres physiques de ce procédé c.-à-d. les conditions d'impact entre les deux pièces. Ces facteurs sont les paramètres procédé qui sont eux-mêmes liés et interdépendants.

Le premier point à évoquer ici est l'inducteur qui est l'outil le plus important du procédé. Cet inducteur va géner les champs magnétiques et induire ainsi les courants dans la pièce métallique à proximité. Sa géometrie va influencer à la fois sa résistance, son inductance ainsi que la distribution des courants induits dans la pièce à proximité. La résistance et l'inductance vont influencer la fréquence qui ensemble auront une influence sur l'épaisseur de peau de l'inducteur et de la pièce métallique à accélérer.

Le second point concerne le mécanisme d'impact entre les deux pièces à assembler qui est lié à la fois à la réponse dynamique des pièces en question ainsi qu'aux paramètres géométriques du procédé (Fig. 2.26, Fig. 2.27).

Dans ce chapitre, nous allons ainsi traiter le sujet des phénomènes électromagnétiques d'un point de vue physique et nous allons présenter les modèles numériques développés dans le logiciel LS-DYNA dans le but de pouvoir analyser l'influence des différents paramètres sur les conditions d'impact.

La première partie de ce chapitre a été ainsi totalement consacrée à présenter les lois de l'électromagnétisme en utilisant une approche physique permettant de comprendre les principes et les interactions entre différentes grandeurs : les forces électromagnétiques (Section 2.3.1.1), les densités des courants et les courants (Section 2.3.1.2), la résistivité et la conductivité électrique (Section 2.3.1.3), la force de Laplace (Section 2.3.1.4), la signification physique des équations de Maxwell (Section 2.3.1.5) et les interactions électromagnétiques au sein d'un conducteur ainsi qu'avec son entourage (Section 2.3.1.6). Cette compréhension nous a permis ensuite de passer à l'analyse des points importants à prendre en considération dans la conception des outils pour le procédé d'impulsion magnétique : l'inducteur (Section 2.3.2) ainsi que son système de montage (Section 2.3.3). Ces analyses ont permis d'évaluer les inducteurs linéaires (Section 2.3.2.1) utilisés souvent

dans les soudures des tôles ainsi que de développer une nouvelle géométrie d'inducteur dit en "O" (Section 2.3.2.2) qui a une meilleure efficacité. Ces analyses ont également montré l'importance de la position des inducteurs par rapport à la pièce métallique (Fig. 3.6, Fig. 3.7) ainsi que l'influence du système de montage sur la durée de vie des inducteurs et sur l'efficacité générale du procédé.

Dans un second temps, le modèle numérique développé a été présenté : préparation du modèle (Fig. 2.24), propriétés des matériaux et conditions aux limites (Table 2.1, Table 2.2, Table 2.3) ainsi que le choix du maillage et du pas de temps (Section 2.4.2). Ce modèle a servi par la suite à étudier les conditions d'impact dans les deux configurations de soudage (normal et par point) pour faire aboutir à des règles qualitatives présentées dans la Fig. 2.42: en général, la fenêtre procédé peut être divisée en quatre parties:

- une première où la distance séparant les deux pièces (h) est inférieure à 1,3 mm: l'augmentation de l'énergie de décharge (E) et de h n'ont pas d'effet significatif sur les conditions d'impact.

- une deuxième région où la distance de sécurité est comprise entre 1,3 et 2,3 mm: L'énergie de décharge E, pour une valeur de h donnée, n'a d'influence que sur la vitesse d'impact mais, lorsqu'elle change, elle influe à la fois la vitesse d'impact et l'angle.

- une troisième région où la distance de sécurité est entre 2,3 et 2,8 mm: L'énergie de décharge E, pour une valeur donnée de h, n'a plus d'effet sur la vitesse d'impact par contre h continue d'influencer à la fois la vitesse et l'angle.

- une quatrième région où h est supérieure à 2,8 mm: On commence à amincir et à déchirer le métal sur les bords de la partie déformée.

Aussi et dans une conclusion générale, la vitesse d'impact dans la région 1 est inférieure à la vitesse d'impact dans la région 2 pour un même h. La vitesse maximale dans la région 2 pour un même h est égale à la vitesse dans la région 3. Par contre, les angles augmentent toujours lorsque l'on se déplace de la région 1 à la région 3. On peut en conclure que rester dans la région 2 , où les distances de départ sont comprises entre 1,3 et 2,3 mm, est le point de départ le plus efficace pour trouver les bons paramètres de soudage puisque les vitesses sont à des hauts niveaux et les angles d'impact ne sont ni très faibles ni très élevés. Ce modèle nous a également permis de démontrer le meilleur rendement de l'inducteur en format de O, même s'il est fabriqué en acier, qui donne des vitesses 1,55 fois plus élevées que les inducteurs linéaires en cuivre.

2.2 Introduction

A better control of the MPW process requires the understanding of the major factors influencing the physical parameters i.e. impact conditions. These factors are the process parameters and they are varied, interdependent and linked to different equipments and tools in the system.

The first important point to talk about is the coil which is the most important tool of the process. The coil will generate the magnetic fields required for inducing currents in the flyer metal where

necessary. These induced currents in the presence of the magnetic field generated by the coil will allow the generation of the magnetic forces that will deform the material up to high velocities. The inductor electrical resistance and inductance will affect the frequency, the current rise time and its peak value and hence the skin depth and the magnetic forces magnitude.

The other important point to understand is the way the flyer impacts the parent metal which, beside the inductor, is related to the configuration conditions and the behaviour of the material at high speed deformations under these conditions. These conditions are the gap and the distance seperating the insulators in the MPW overlapping case and the hump design in the MPSW case.

In this chapter, the first part will be fully devoted to the coil design considerations. After that, the implementation of a numerical model developed using LS-Dyna will be detailed. This model will be used thereafter to study the MPW and MPSW configurations, the impact phenomenon in both cases and the influence of the configurations conditions on the impact.

2.3 Coil design considerations

2.3.1 Physical approach for electromagnetics problem

In order to understand how a coil should be designed for the magnetic pulse processes, it is necessary to have first a physical approach for different electromagnetic phenomena. This physical approach has for purpose linking the microscopic comprehension of these phenomena to the macroscopic effects observed. To do that, the basic concepts in electromagnetics [36, 74, 87, 97, 107, 170, 230] will be revisited here from a qualitatively physical point of view in order to understand the electromagnetic part which is the basis of the MP processes.

2.3.1.1 The Lorentz force law

The Lorentz force law is a fundamental axiom of the electromagnetic theory whose justification was found experimentally:

$$\vec{F} = q(\vec{E} + \vec{v} \times \vec{B}) \tag{2.1}$$

It expresses the entire net force exerted on a particle carrying charge q, moving with velocity $\vec{v}$ in a magnetic field $\vec{B}$ and in the presence of an electric field $\vec{E}$. In metallic conductors, the free electrons called also the conductive electrons can move freely through the whole solid and hence each free electron with a charge q obeys this law. Looking at the Eq. 2.1, several observations can be done:

- the electric force $(q\vec{E})$ is aligned with the electric field;

- the electric field power $(q\vec{E} \cdot \vec{v})$ is different from zero and by considering the kinetic energy theorem, this power can modify the kinetic energy of the electron and hence the magnitude of its velocity;

- the magnetic force i.e. velocity-dependent part of the Lorentz force is orthogonal to the magnetic field and to the electron's velocity. The force direction can hence be found using the simple right hand rule;

- the magnetic forces being perpendicular to the electron velocity, they do no work and hence all they can do to a charge is to alter the direction in which it moves but they cannot speed it up or slow it down.

2.3.1.2 Current density and currents

An electric current is charge in motion. Every particle having some charge q_K moving at some velocity $\vec{v}_K$ will constitute then a current element $q_K \vec{v}_K$. If we have in a some small volume dV different particles types q_i (Coulombs) having each a concentration of c_i (particles per cubic meter) and moving at an average velocity $< \vec{v}_i >$ (meter per second), the current density through the surface of dV will be:

$$\vec{J} = \sum_i c_i q_i < \vec{v}_i > \tag{2.2}$$

At a macroscopic level, we have to speak about macroscopic averaging of the quantities in the last equation leading to the equation of the macroscopic current density which is a general idea of current or charge transport involving charge carriers moving around in three dimensional space:

$$\vec{J} = \sum_i \rho_i < \vec{v}_i > \tag{2.3}$$

where ρ_i is the macroscopic charge density of moving particles (C/m^3) and $< \vec{v}_i >$ is the macroscopic spatial average of velocity $\vec{v}_i$ (m/s). The magnitude of $\vec{J}$ is in $A/m²$ and it expresses the distribution of charge flowing at a specific position at a specific time.

The current is defined as the flow of electric charges across a surface:

$$I = \int_S \vec{J} \cdot \vec{ds} \tag{2.4}$$

It is a measurable quantity which is expressed in coulombs per second (C/s) or ampere (A). In a metallic conductor, the charge carriers being the free electrons having a random distribution of velocities varying in direction and magnitude, the current density will be expressed by:

$$\vec{J} = (-q) c_{e^-} < \vec{v_{e^-}} > \tag{2.5}$$

where q is the elementary charge of the electron $(1.60218 \times 10^{-19} C)$, c_{e^-} is the macroscopic concentration of electrons (e^-/m^3) and $< \vec{v_{e^-}} >$ is the macroscopic average velocity of all the electrons. The current in this case will correspond to the flow of free electrons.

To make a current flow, a push on the charges should be applied and how fast they move, in response to this push, depends on the nature of material. Using the definition of the current density

$\vec{J}$ and for most substances, the current density is proportional to this push-force per unit charge:

$$\vec{J} = \sigma \vec{f} \tag{2.6}$$

This factor σ is the so-called the electrical conductivity of the material and which varies from one material to the other and $\vec{f}$ is nothing but the electromagnetic forces that drives the charges to produce the current and hence Eq. 2.6 becomes:

$$\vec{J} = \sigma(\vec{E} + \vec{v} \times \vec{B}) \tag{2.7}$$

The velocity of the charges is sufficiently small in ordinary cases[1] that the second term can be ignored giving the equation:

$$\vec{J} = \sigma \vec{E} \tag{2.8}$$

This last equation is the statement of Ohm's law which is an empirical law[2].

As a conclusion from the definition of the current density and the relation between the current density and the electric field:

- the highest the applied electric field is, the highest the flow of charges will be and hence the highest the electric current I is.

- the more we have charge carriers; the higher the carryed current will be.

2.3.1.3 Electrical resistivity and conductivity

The resistivity ρ ($\Omega.meter$) which is the inverse of conductivity σ (S/m) depends on the number of electrons in the valence shell. Good conductors have from one to three valence electrons (Ag, Cu, Au, Al...). Valence electrons can become easily free electrons at room temperature and because they are movable charges therefore they become current carriers.

The resitivity is proportional to the temperature and it is inversely proportional to the mean length of free path of electrons between the collisions and to the square of the amplitude of vibrations. Thus, the more the temperature T increases, the more collisions between electrons occur and the less is the mobility of these electrons which result in an increase in the resistivity.

As a conclusion:

- the higher is the resistivity of the material, the less the flow of charges will be when the material is subjected to the electric field

- the higher is the temperature of the conductor, the higher its resistivity will be resulting in a less flow of charges.

---

[1]The plasmas are the good example where the magnetic contribution to $\vec{f}$ becomes significant

[2]Since Ohm's law is an empirical one, it will fail at very strong electric fields but these electric fields are far beyond of our field of application. They correspond to current densities above $10^9 A/cm^2$
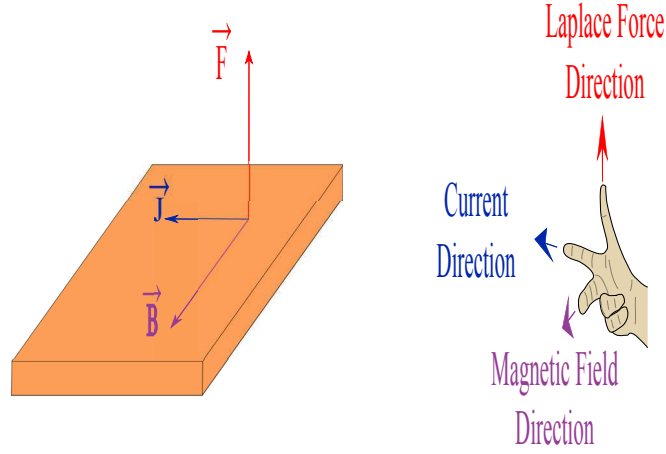
Figure 2.1: force on a current-carrying conductor placed in a magnetic field

2.3.1.4 The Laplace force

When a current-carrying conductor is placed in a magnetic field, each moving charge (i.e. free electron in metals) experiences the magnetic part of Lorentz forces ($\vec{v} \times \vec{B}$ in Eq. 2.1). All these individual microscopic forces on charges together will result in a macroscopic force on the conductor called the Laplace force. In other words, the Laplace force provides a continuum representation of the magnetic part of the Lorentz force law. The elementary Laplace force acting on an elementary volume dV is expressed by:

$$d\vec{F} = \rho\,(\vec{v} \times \vec{B})\,dV = \vec{J} \times \vec{B}\,dV \tag{2.9}$$

where $\vec{J}$ is the current density in the conductor and $\vec{B}$ the magnetic field exterior to this conductor. Same expressions can be expressed for line ($\vec{I}$) and surface ($\vec{K}$) currents respectively:

$$d\vec{F} = \lambda\,(\vec{v} \times \vec{B})\,dl = \vec{I} \times \vec{B}\,dl \tag{2.10}$$

$$d\vec{F} = \sigma_K\,(\vec{v} \times \vec{B})\,ds = \vec{K} \times \vec{B}\,ds \tag{2.11}$$

where λ and σ_K are the line charge and the surface charge density respectively.

The direction of this force is determined using the right-hand rule. Fig. 2.1 presents a current-carrying conductor placed in a magnetic field resulting in a Laplace force $\vec{F}$.

2.3.1.5 Maxwell equations

The four well-known Maxwell equations (Eq. 2.12 to Eq. 2.15) together with the Lorentz force law form the foundation of the unified electromagnetic theory: the Maxwell equations tell how fields are produced and reciprocally the force law tells how fields affect charges.

$$\nabla \cdot \vec{E} = \frac{\rho}{\varepsilon}\ (Maxwell - Gauss) \tag{2.12}$$
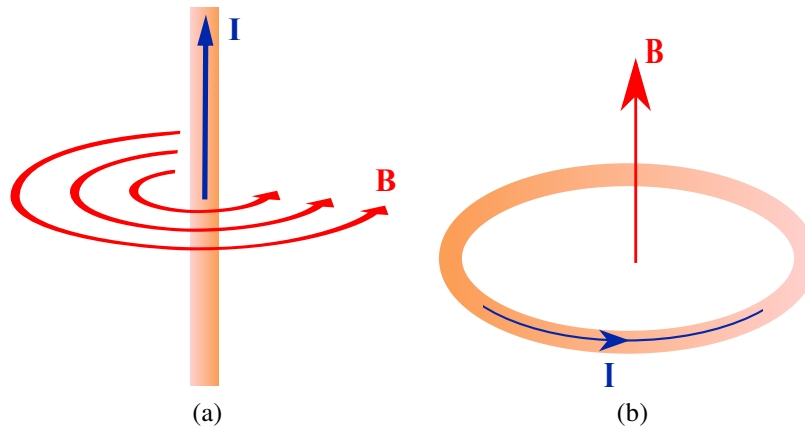
Figure 2.2: magnetic field generated by (*a*) a line current and (*b*) a loop current

$$\nabla \cdot \vec{B} = 0 \; (Maxwell - Thomson) \tag{2.13}$$

$$\nabla \times \vec{B} = \mu \vec{J} + \mu \varepsilon \frac{\partial \vec{E}}{\partial t} \; (Maxwell - Amp\grave{e}re) \tag{2.14}$$

$$\nabla \times \vec{E} = -\frac{\partial \vec{B}}{\partial t} \; (Maxwell - Faraday) \tag{2.15}$$

These four equations remind that electric fields can be produced either by charges or by changing magnetic fields; and magnetic fields can be produced either by currents or by changing electric fields. μ and ε are respectively the magnetic permeability and the electric permittivity of the medium.

The Maxwell-Gauss equation (Eq. 2.12) states that charges are the source of electric field and this electric field diverges from this source and it is proportional to the distribution of the charges.

The Maxwell-Thomson equation (Eq. 2.13) called also Gauss' magnetic law expresses the fact that there is no magnetic sources or sinks and magnetic flux lines close upon themselves (magnetic fields are divergenceless) .

The Maxwell-Ampère equation (Eq. 2.14) shows the dependence of the magnetic field on the conduction current density (rate of motion of charges) and on the rate of change of electric field (displacement current density). In other words, a magnetic field is due to the presence of an electrical current and to a changing electric field. The magnetic field direction for conduction current sources is determined in a practical manner using the right-hand curl rule. Fig. 2.2 illustrate the direction of magnetic fields around a segment of linear current-carrying conductor and a current loop.

The Maxwell-Faraday equation (Eq. 2.15) is the universal law of induction. It illustrates the fact that a non-uniform magnetic field causes a generation of an electric field (electromotive force) which make the charges circulate around a closed path (i.e. creating induced eddy-current loops) in a way to counteract the flux change. This counteraction which is expressed in the minus sign in the equation, is an interpretation of the essential physical fact: the tendency of systems to resist change
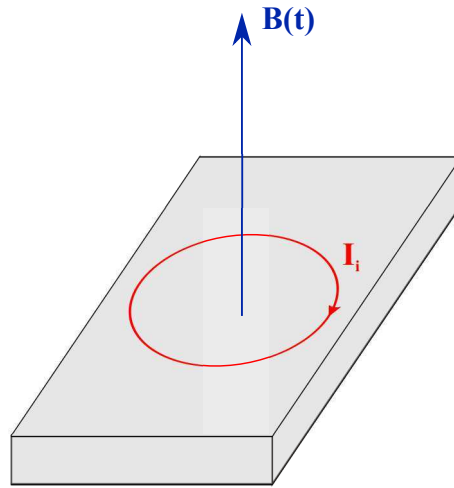
Figure 2.3: conductor in a changing magnetic field

which is in this context called the Lenz's law. Fig. 2.3 illustrates the Faraday's law for a conductor material within a changing magnetic field: $\vec{B}(t)$ being in positive z-direction, the generated electric field will circulate the charges and hence creates an induced current loop in such a manner that this induced current will generate a magnetic field in the negative z-direction.

The Maxwell-Ampère (Eq. 2.14) and the Maxwell-Faraday (Eq. 2.15) equations show the interdependence between the magnetic fields and electric fields and how the variation of one is proportional to the magnitude of the other.

2.3.1.6 Fields - conductors interaction

A system where we have time-varying current conductor with other conductor in its vicinity corresponds to the case of the MP processes where we have the coil with a conductive sheet metal in its proximity. According to Maxwell-Ampère law, the time-varrying current in the coil will generate a time-varying magnetic field. According to Maxwell-Faraday, this field will induce electromotive forces resulting in eddy-currents in the conductors which are: (1) internal to the coil due to its internal magnetic fields and (2) induced currents in the sheet metal due to the external magnetic field generated by the coil. Having currents and magnetic fields will generate Laplace forces according to the Lorentz force law (Eq. 2.1). Thus, the MP processes require the combination between the Maxwell equations and the Lorentz force law to understand different interactions and effects observed in the system.

2.3.1.6.1 Internal fields-coil interaction

A conductor carrying time-varying current $I(t)$ induces a time-varying magnetic field $B(t)$ both inside and outside of it and hence the coil will be subjected also to its own varying magnetic fields. These magnetic fields will induce eddy current loops $di_e(t)$ inside the conductor itself which, according to Maxwell-Faraday, will tend to counteract the internal magnetic fields.

The elementary eddy current loops will form big closed loops that adds to the applied current $I(t)$ in the area close to the surface and substract from it in the middle of the conductor (Fig. 2.4).
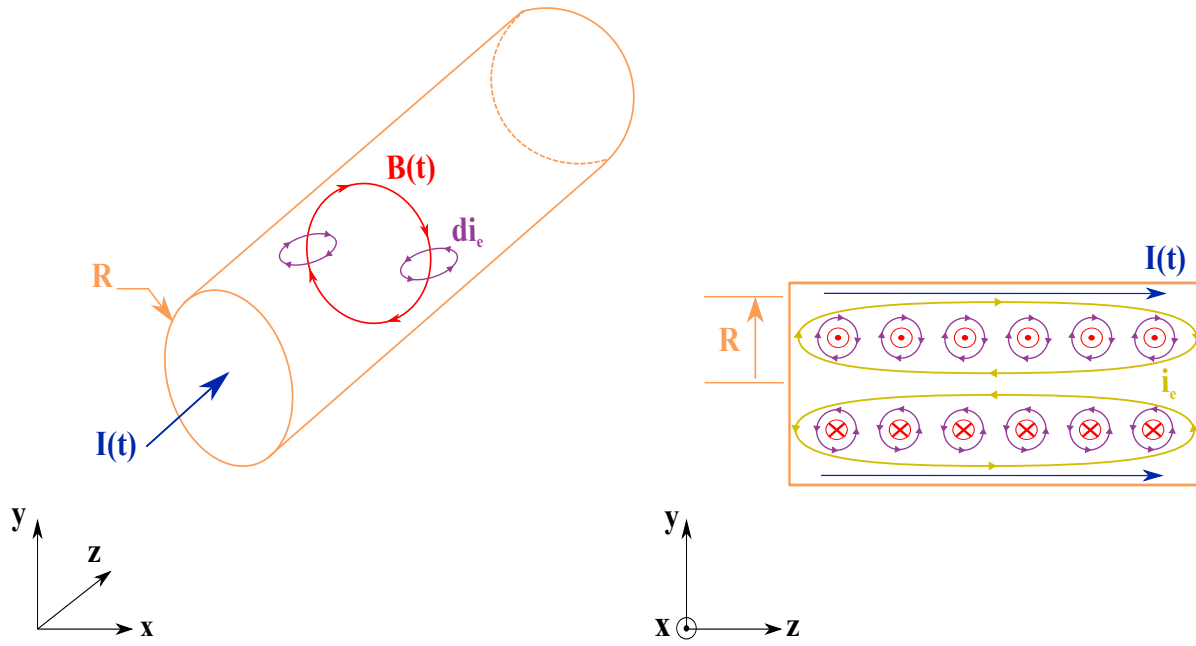
Figure 2.4: skin effect in a long straight round conductor at high frequency

The net current $I(t)$ remains unchanged but the current density is not uniform. The higher the frequency of the external current $I(t)$ is, the higher is the frequency of the generated magnetic field $\vec{B}(t)$ and hence the higher are the counter electromotive forces inside the coil (Maxwell-Faraday) leading to increasing the nonuniformity of the current density. As a result, the current tends to flow near the surface and the current density decreases from the surface to the center of the coil. This phenomenon is the so-called skin effect. The current density decreases from the conductor surface and at a depth δ, which is the skin depth, it is reduced to $1/e$ of the value at the conductor surface. The skin depth is approximated by the Eq. 1.8 presented in Section 1.5.2.3.2 and it is a function of the permeability, conductivity and the frequency. The skin effect is only negligible when the skin depth δ is much greater than the conductor thickness.

The fact that the current circulates on a confined thickness of the coil's surface causes also higher joule effects in this region and hence higher temperatures at the surface.

When approaching the MP processes, the conclusions to be made:

- the interaction between the internal magnetic fields and the time-varying source current will define the path of the latter;

- the skin effect will confine this path in an area close to the surface causing higher thermal fatigue in these regions than in the core of the coil.

2.3.1.6.2   External fields - conductors interaction

After discussing the internal magnetic field effect on the coil itself, we will discuss here the effects of the interaction between external fields generated by current-carrying conductors. To do so, we will start by the two simple illustrations given in Fig. 2.5 : (a) two conductors carrying currents in the same direction will generate attractive forces and (b) two conductors carrying currents in
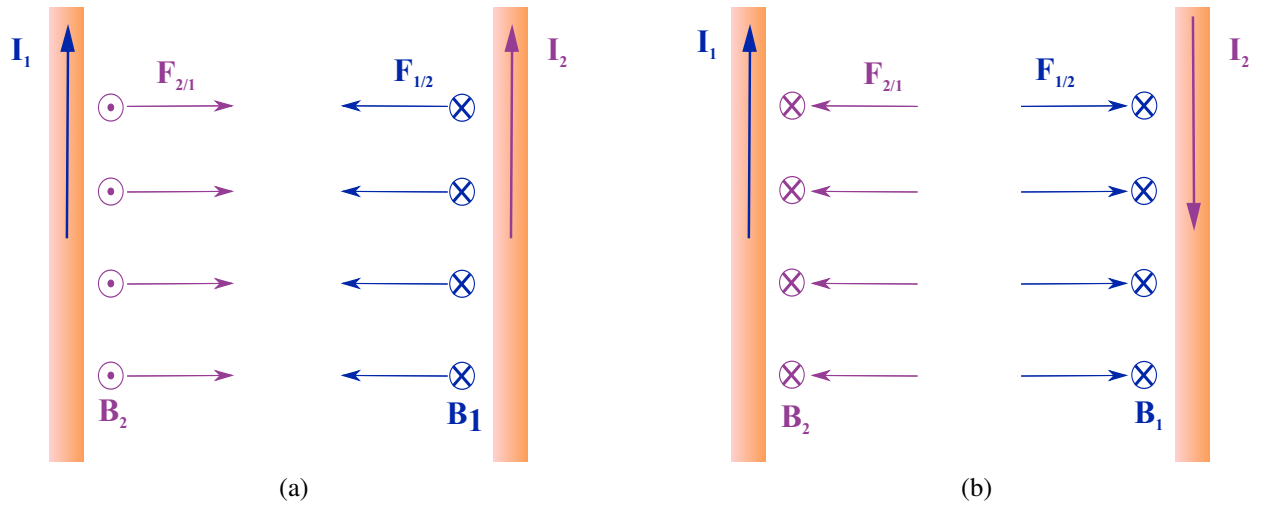
Figure 2.5: forces between current-carrying conductors (a) currents in the same direction and (b) currents in opposite directions

opposite directions will generate repulsive forces. The forces on each conductor are due to current of the conductor itself and to the magnetic field generated by the other conductor.

Therefore, if we consider a current I_1 varying in time is passing through a conductor wire 1 which is in the proximity of another conductor wire 2 with no currents inside it, according to Maxwell - Ampères law (Eq. 2.14) a magnetic field varying in time $\vec{B}_1$ will be generated by I_1. Once it penetrates the other conductor and according to Maxwell - Faraday law (Eq. 2.15), it will induce a current I_2 in the opposite direction of I_1. As a result, we will have two current-carrying conductors with currents in opposite directions and hence the forces between them will be repulsive.

Another important case to analyze is when a conductor wire 1 with a time-varying current I_1 (Fig. 2.6) is placed vis-a-vis a conductive sheet metal. I_1 will generate circle loops of magnetic fields according to Maxwell - Ampère (Eq. 2.14) and Maxwell - Thomson (Eq. 2.13) that will penetrate the sheet metal and will induce a current I_i according to Maxwell - Faraday (2.15). How will this induced current circulate in the sheet metal and how the forces will be between the two conductors? The induced current will be the sum of all elementary currents dI_i in the sheet which each one of them forms a current loop that will tend to oppose the external magnetic field according to Lenz's law (the minus sign in Eq. 2.15). The boundary sections of these loops in the x-direction will cancel each other forming two big loops having an opposite direction to the primary currents just above the wire. In this area, the primary magnetic field is tangential to the sheet metal in the negative x-direction and since a current I_i is present now in the metal sheet, according to Laplace force (Eq. 2.9) a force $\vec{F}$ will be acting on the sheet metal in this area. Similarly, the secondary magnetic field $\vec{B}_i$ poduced by the induced current I_i is tangential in the negative x-direction to the current-carrying wire therefore according to Laplace force principle a force $\vec{F}_i$ will be acting on the wire. I_1 and I_i being in two opposite directions, the forces as presented in Fig. 2.6 are repulsive. From these two simple examples, two conclusions can be made when approaching the MP processes:

- intense magnetic forces are not only applied on the flyer metal but also on the coil in the
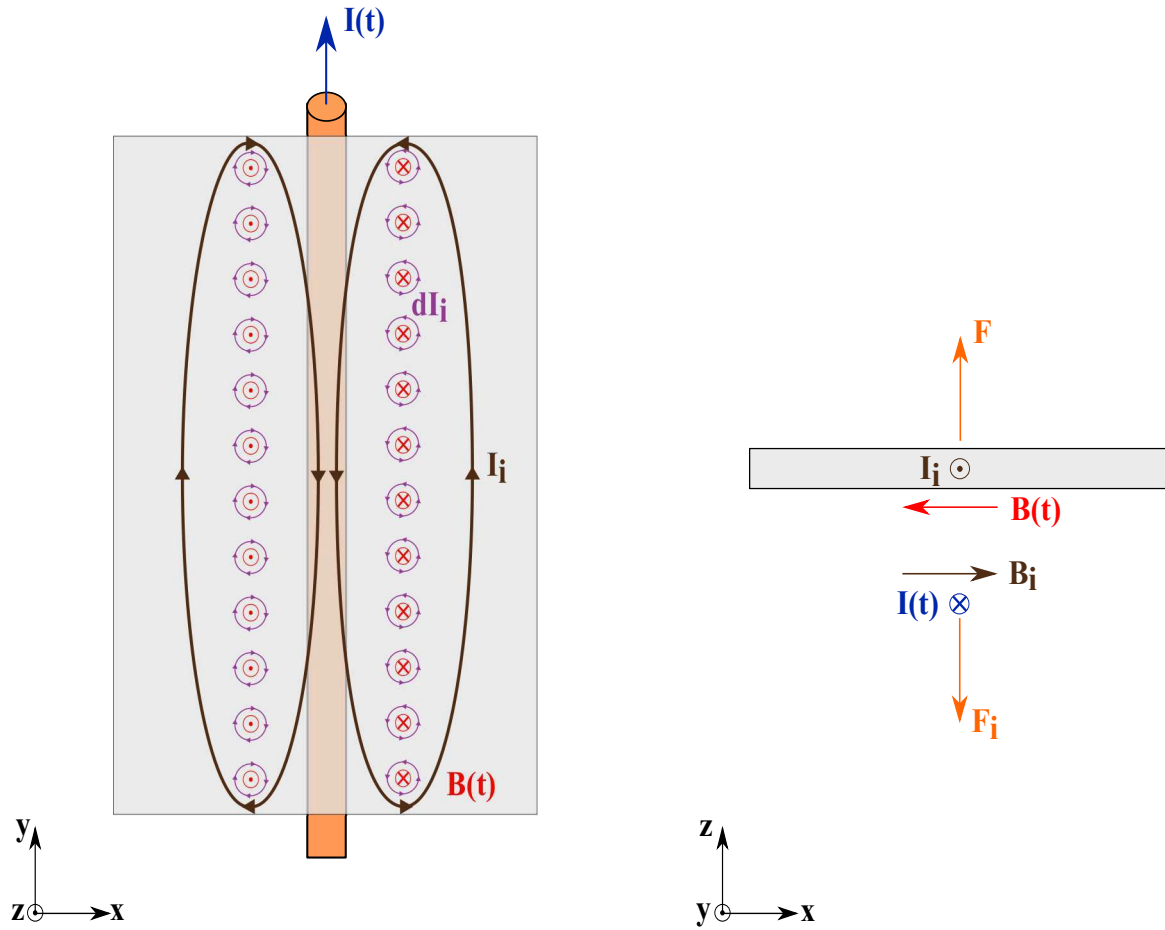
Figure 2.6: interaction between infinite line current-carrying conductor and a sheet metal

region where both conductors interact;

- the position of the coil regarding the flyer metal will define the way the induced currents are distributed within the flyer and hence the way the forces will be applied.

2.3.2 Coil design

After the presentation of different electromagnetic principles in relation with the MP processes, we will present now the procedure of coil design selection used during this study. The principle of the MPW (Section 1.5) requires the acceleration of the flyer metal with a progressive impact phenomenon between the latter and the parent metal in the intended welding region. Therefore, the coil design should permit the generation of the forces where it is necessary and that these forces ensure obtaining the required progressive impact. Two coil shapes were used in this study that we will present next.

2.3.2.1 Linear rectangular cross-section coil

Linear rectangular cross-section coils have been the first coils used for sheet metal welding and presented good efficiency to simplicity ratio [7, 132]. The first coil shape used during this study was also a linear rectangular cross-section coil and it is represented in Fig. 2.7 . The measured in-
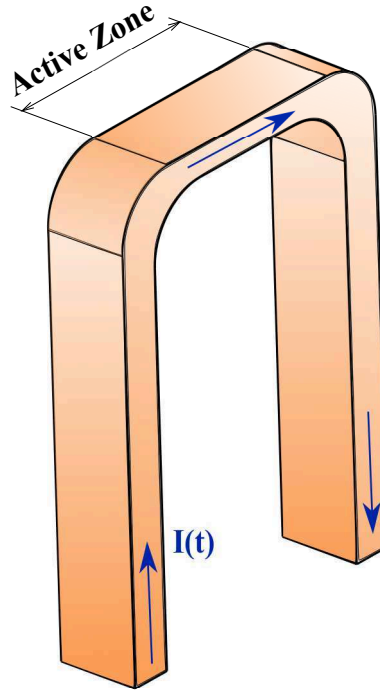
Figure 2.7: linear rectangular cross-section coil

ductance of the coil L_{Linear} presented a value equal to 81% of the generator's inductance $L_{Generator}$:

$$L_{Linear} = 0.81 L_{Generator} \tag{2.16}$$

giving a system total inductance L_1 (Eq. 1.6):

$$L_1 = 1.81 L_{Generator} \tag{2.17}$$

The active zone is the zone that will be facing the flyer metal and hence the interaction between the coil and the sheet metal will be restricted to this zone. The interaction between the magnetic field generated by the discharge current of the coil (in the active zone) and the sheet metal can be therefore simplified to a linear bar facing the sheet metal. Fig. 2.8 represents the shape of the magnetic field $\vec{B}(t)$ generated by the rectangular cross-section of the coil: as discussed in Section 2.3.1.6.1, the current will flow near the surface which according to Maxwell-Ampère will generate divergenceless magnetic fields and the resultant generated external field will be in x-direction just above the conductor and in xy-direction near the corners.

Fig. 2.9 represents the interaction between the linear bar (i.e. active zone) and the sheet: the generated magnetic field $\vec{B}(t)$ is entering from one side and leaving from the other creating induced current loops I_i having an opposite direction to the discharge current $I(t)$ just above the active zone. According to the Laplace force equation (Eq. 2.9), the presence of the sheet metal with a current I_i flowing inside placed in a magnetic field $\vec{B}(t)$ will generate a repulsive force $\vec{F}$.

The profile of the Laplace force generated on the sheet is represented in Fig. 2.10 : the forces applied in the area where the magnetic field is purely tangential to the surface to the sheet will produce forces only in y-direction and near the corners, where the tangential component of the magnetic field is less than the magnetic field itself, the force y-direction component will be lower.
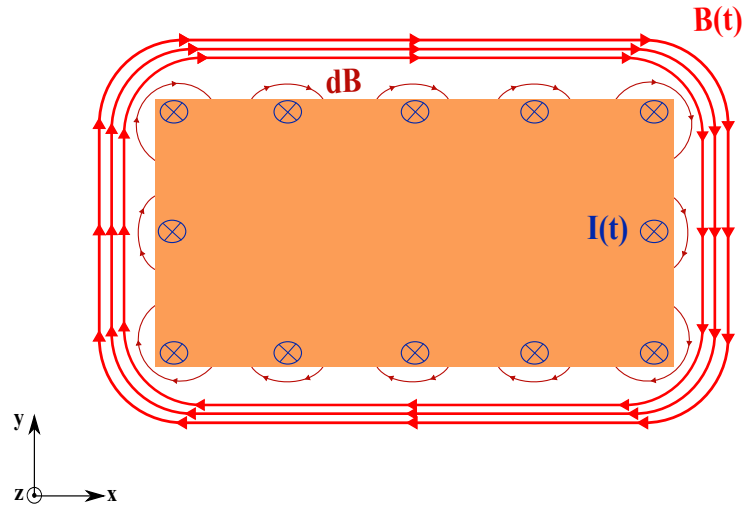
Figure 2.8: magnetic field around rectangular cross section time-varying current carrying conductor
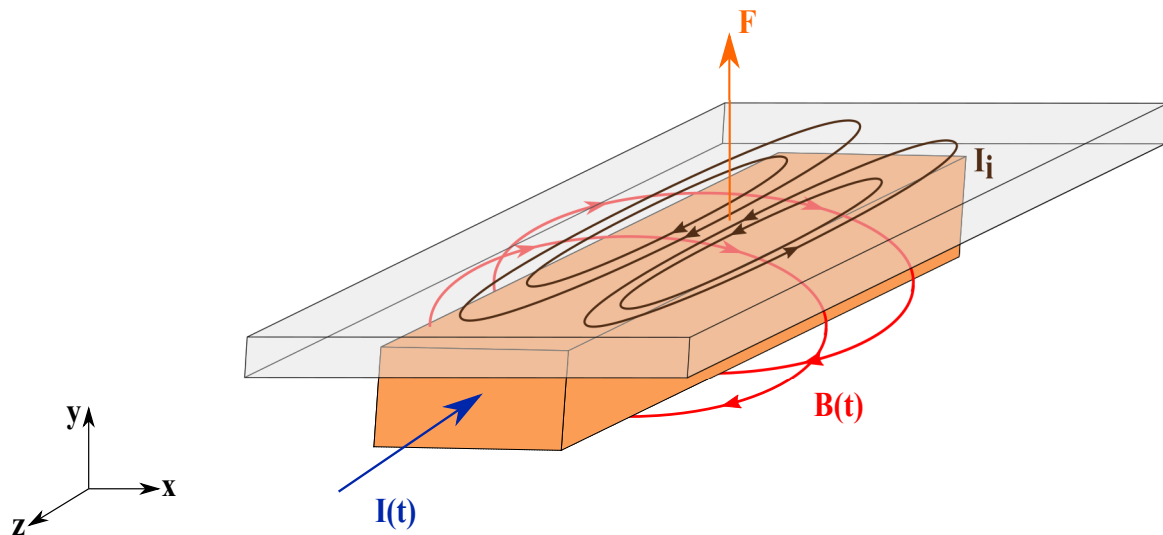
Figure 2.9: active zone of the linear coil with the sheet metal interaction
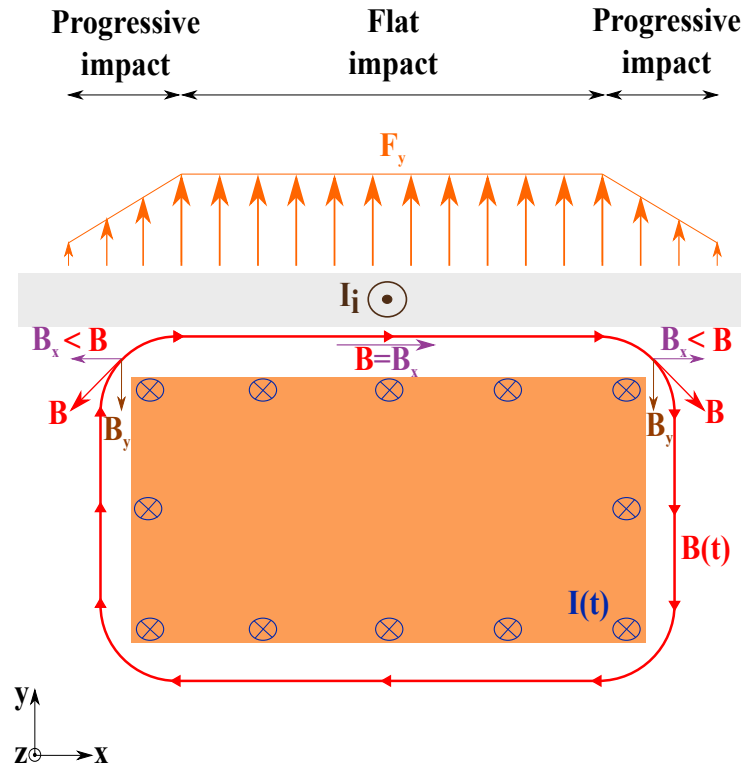
Figure 2.10: Laplace force in the case of the linear coil
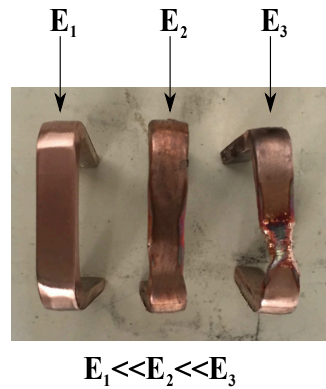
Figure 2.11: linear coil thermomechanical failure due to increasing the discharge energy

This will lead to a flat normal impact in the middle area between the flyer and the parent metal with a progressive impact symmetrically from both sides which is the requirement for a welding to occur.

The magnetic forces applied on the flyer metal will lead to its acceleration and therefore the more this metal harder and/or thicker is, the higher the required forces are. To increase these forces in the case of the linear coils we have to increase the discharge currents by even decreasing the cross-section of the linear coil (i.e. increase the current density leading to higher currents) and/or increase the discharge energy from the generator. The coil will then itself experiment higher thermo-mechanical stresses because of the action-interaction properties of magnetic forces (Section 2.3.1.6.2) and the significant temperature increase due to the skin effect (Section 2.3.1.6.1) leading to faster failure (Fig. 2.11). The use of the linear shape coils arrives then to its limitations when very high magnetic forces are required and new design concept for the coil was used and it
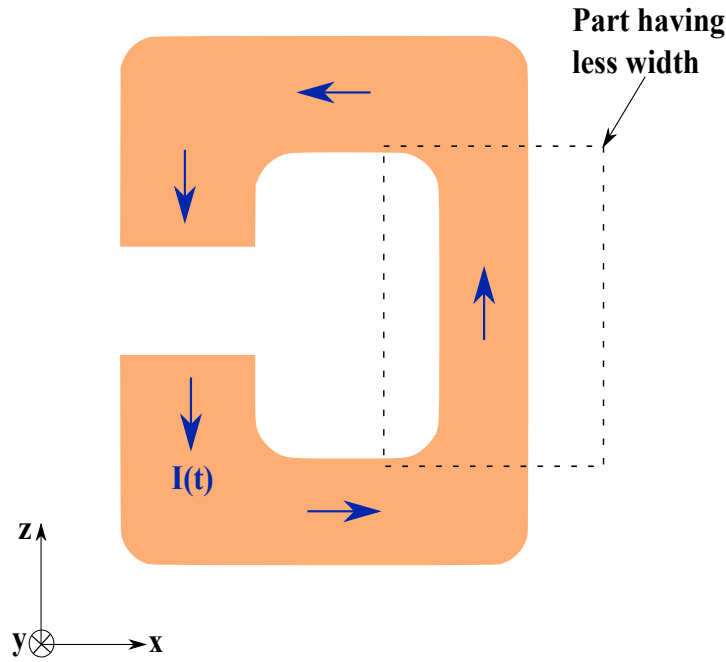
Figure 2.12: O-shape rectangular cross-section coil

will be presented next.

2.3.2.2 O-Shape rectangular cross-section coil

From the Laplace force equation (Eq. 2.9), the forces on the flyer metal are related to the magnetic field generated by the discharge current and to the induced currents in the flyer metal. The new coil design is based on the idea of improving the efficiency by having higher discharge currents and induced currents at the same levels of energies based on:

1. reducing the inductance of the coil to increase the peak currents (Eq. 1.3; Fig. 1.40);

2. putting more charge carriers on the flyer metal in movement to increase the induced currents magnitude and increasing at the same time the current density in the area where the material should be accelerated (Section 2.3.1.2).

These two points were achieved by using an O-shape rectangular cross-section coil represented in Fig. 2.12 : the part were the flyer metal is to be accelerated has smaller cross section than the other parts.

The measured inductance of the coil $L_{O-shape}$ presented a value equal to 49% of the generator's inductance $L_{Generator}$:

$$L_{O-shape} = 0.49 L_{Generator} \tag{2.18}$$

The system total inductance (Eq. 1.6) will be then:

$$L_2 = 1.49 L_{Generator} \tag{2.19}$$
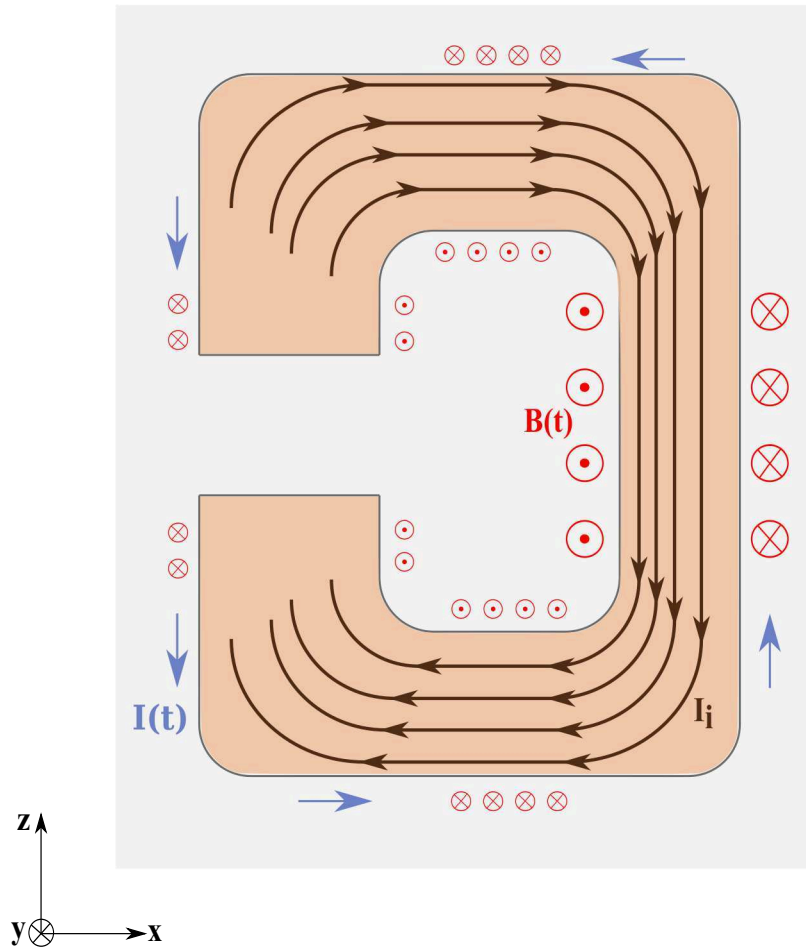
Figure 2.13: magnetic fields penetration and induced currents in the flyer metal with an O-shape coil

Comparing the total inductance of the system between this coil and the linear coil case by dividing the Eq. 2.19 and the Eq. 2.17:

$$\frac{L_2}{L_1} = 0.823 \tag{2.20}$$

leading to an increase of about 10% of the peak current and the frequency for the same discharge voltage:

$$\frac{I_{02}}{I_{01}} = \frac{\omega_2}{\omega_1} = 1.1 \tag{2.21}$$

The flyer metal covers all the coil so that the paths of induced currents are longer carrying with them more charges inside the flyer metal (Fig. 2.13): the fact that the magnetic fields are entering and leaving the sheet metal from all sides of the coil will create loops of induced currents along all the area above the coil creating long paths and these paths are more dense in the area where the width of the coil is smaller.

The distribution of the forces on the flyer in this case are presented in Fig. 2.14 : the magnetic field in the areas just above the coil are tangential to the flyer metal creating repulsive forces according to Laplace force law (Eq. 2.9) that are the highest in the area of the thinner part of the coil. However the smaller forces existing on the other parts of the flyer require blocking the movement
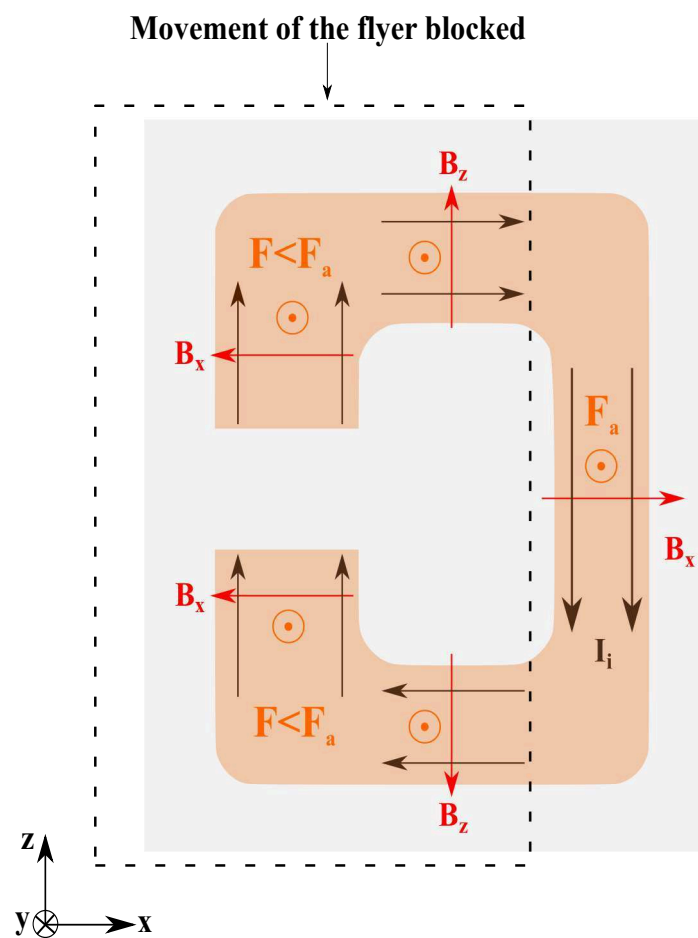
Figure 2.14: forces distribution on the flyer in the O-shape coil case
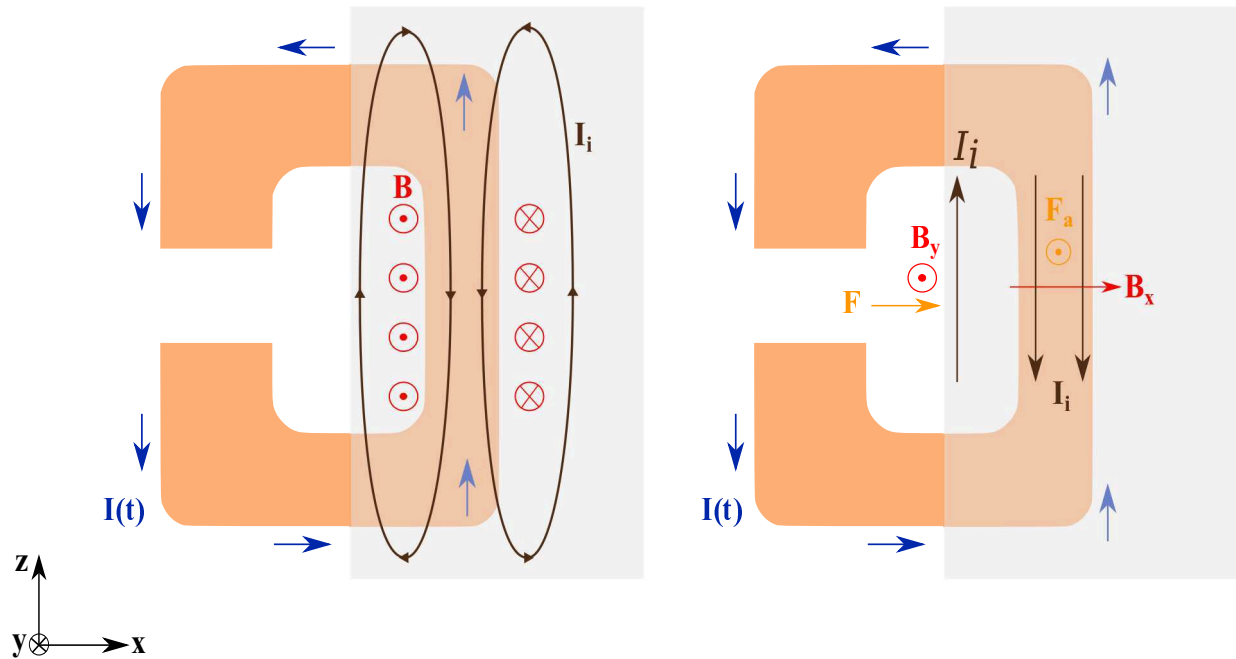
Figure 2.15: flyer metal not covering all the O-shape coil area

of the flyer in these areas and which is done ordinarily by using a massive die on this area. The rectangular cross section of the coil where the flyer metal is allowed to move will give a look-alike distribution of the forces as it was represented in Fig. 2.10 allowing a progressive impact required for the welding.

The position of the coil regarding the flyer metal is very important to have the full efficiency of the coil. In fact, if the flyer metal does not cover all the coil the way the currents are induced in the flyer and the way the forces are generated will not be the same leading to loose the coil's efficiency (Fig. 2.15): the induced currents in this case will form as it was a simple linear coil and in addition, in the middle region of the coil since the magnetic field is in y-direction and having the induced current in z-direction, Laplace forces in x-direction will develop leading to a sort of smashing the flyer in that direction as shown in Fig. 2.16.

2.3.3 Mounting system considerations

The mounting system should be able to stand the shock forces upon impacts between the flyer metal and the parent metal to block the movement of the latter. Also, it has to maintain the coil in its place during the process by counteracting the magnetic forces experimented by the coil due to their action-reaction nature (Section 2.3.1.6.2). These magnetic forces does not only occur between the flyer and the coil but also between the internal parts of the coil itself. If it is not the case, the magnetic forces will generate undesired large deformation in the coil leading to a faster failure.

In the case of the linear shape rectangular cross section, the forces experienced by different coil parts are presented in Fig. 2.17 : in addition to the force appplied downward in the active zone due to the flyer metal reaction magnetic forces, the side parts of the coil interact and create repulsive forces between them. Hence, the maintain of this coil should block its movement downward in the active zone and the movement on each side of part 1 and part 2. The clamping system for the
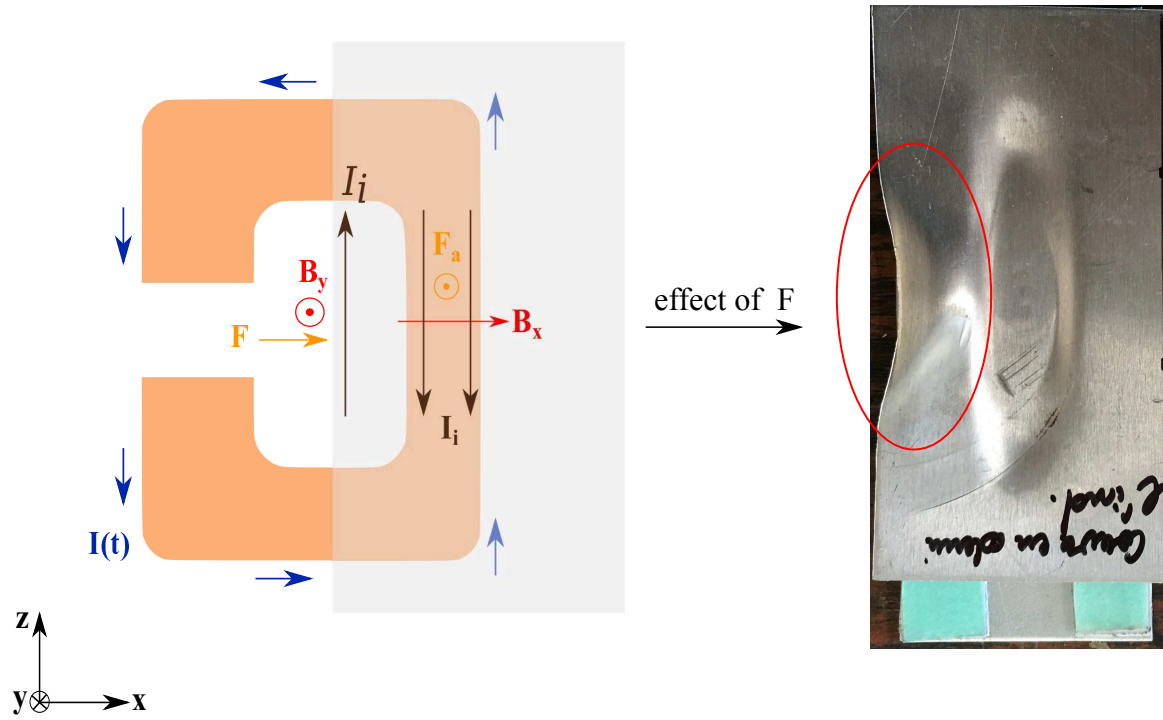
Figure 2.16: experimental illustration of the flyer metal not covering all the O-shape coil area
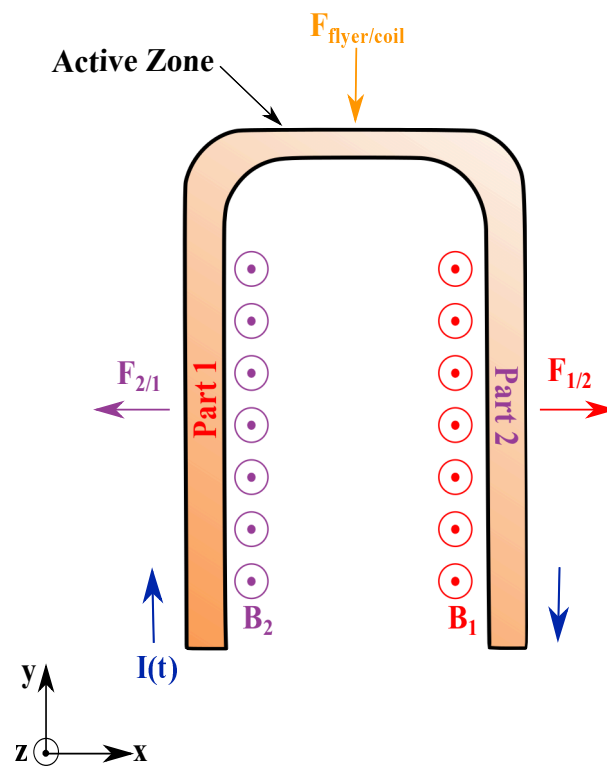
Figure 2.17: forces experienced by the linear coil
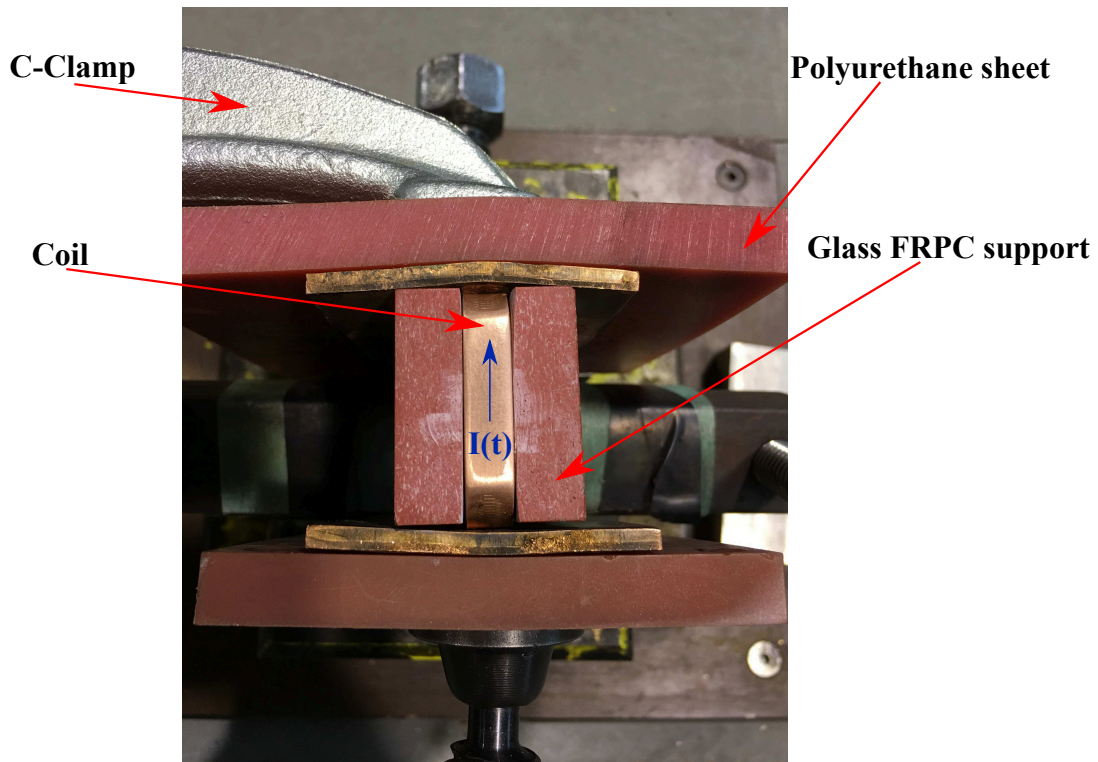
Figure 2.18: linear coil clamping system

coil is presented in Fig. 2.18 and the whole mounting system in Fig. 2.19 . The movement on the side of the coil is blocked using a C-clamp with thick PU plastic sheets to prevent electrical conduction between the discharge current and the metallic C-clamp. The coil is placed in an electrical nonconductive glass FRPC support. A massive steel die is placed above the parent metal to absorb the shock during impact and a steel structure clamping system prevents the movement of the assembly.

The different metallic parts of this structure are isolated eletrically from one another as we can see from Fig. 2.19. This is a crucial point for the efficiency of the MP processes whatever the application is. To understand why, we need first to remind the physical concept of intrinsic electrical quantities inductance (i.e. self inductance) and mutual inductance. They are consequences from the Maxwell-Faraday law. As it was said earlier in Section 2.3.1.6.1, a time-varying current induces not only an electromotive force in nearby conductors but also in the source itself that opposes this change and the self inductance is nothing than a measure of the resistance of the current-carrying conductor to the change of its own current. It plays the same role in an electric circuit that mass plays in mechanical systems: the greater L is, the harder it is to change the current, just as the larger the mass, the harder is to change an object's velocity.

To understand the mutual inductance, we will consider two loops of conductive materials fixed in position relative to one another (Fig. 2.20) where Loop 1 carries a time-varying current $I_1(t)$. This current will generate a magnetic field $\vec{B}_1$ according to Maxwell-Ampère. According to Maxwell-Faraday, $\vec{B}_1$ will induce an electromotive force in the Loop 2 proportional to the rate of change of the magnetic field $\vec{B}_1$. The ratio of the electromotive force in Loop 2, caused by changing current in Loop 1, to the rate of change of the current $\frac{dI_1}{dt}$ is called the mutual inductance M_{21} (same unit
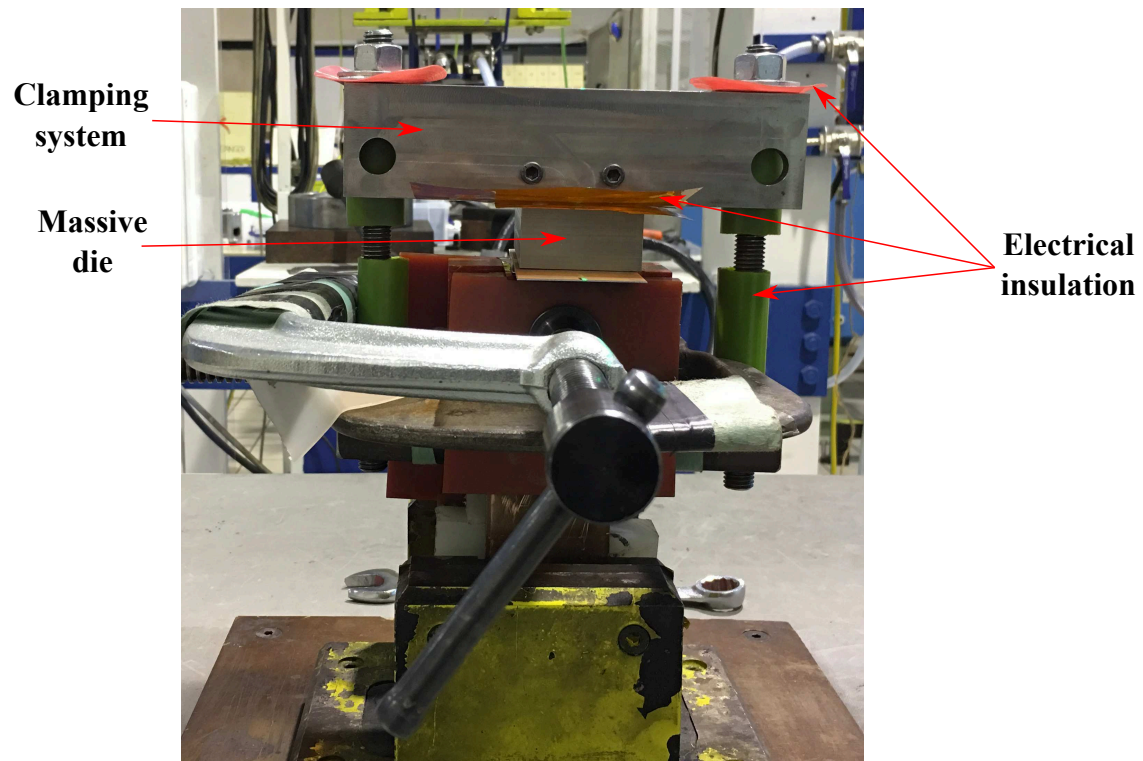
Figure 2.19: mounting system in the linear coil case
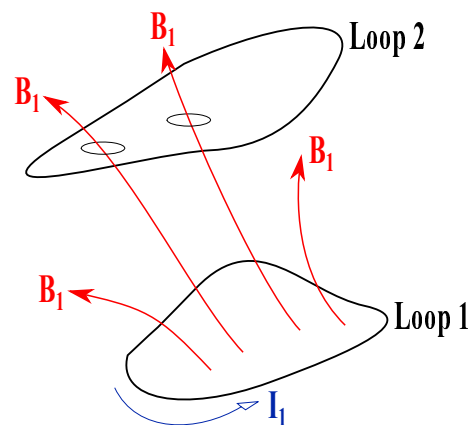
Figure 2.20: mutual inductance between two loops of conductive materials
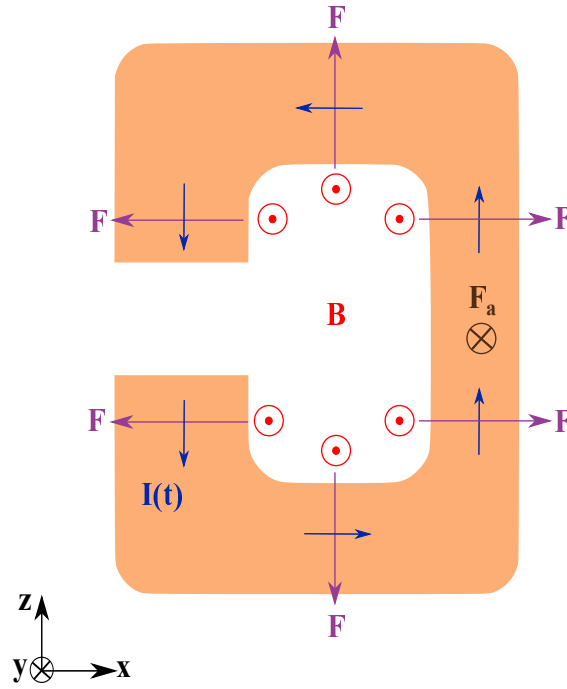
Figure 2.21: forces experienced by the O-shape coil

as inductance H) expressed by:

$$M_{21} = \frac{\xi_{21}}{\frac{dI_1}{dt}} \qquad (2.22)$$

where ξ_{21} is the magnitude of electromotive force induced in Loop 2 due to the current in Loop 1. Similarly, if the Loop 2 was carrying an equal time-varying current instead of Loop 1, it would has generated an electromotive force in Loop 1 leading to a mutual inductance M_{12} equal to M_{21}. The total inductance in an electric system is determined by the sum of self inductances and mutual inductances. Both depends only on the geometry of the system in the magnetoquasistationary approximation.

Going back to our problem, the importance of isolating electrically the metallic parts of the clamping system has for purpose to cut any possibility of the induced currents to form closed loops all around the mounting system. Because if it is the case, the induced currents in components will lead to undesired mutual inductances that will increase the total inductance in the region of the coil and the flyer and reducing hence the rate of change in electromagnetic fields which will limit the efficiency of the system.

In the case of the O-shape coil, the forces experienced are presented in Fig. 2.21 : in addition to the reaction force from the flyer on the coil $\vec{F}_a$, the parts of the coil will generate repulsive forces $\vec{F}$ on each other due to the fact that magnetic fields inside the coil are in y-direction. The movement of the coil in this case should be then blocked in all directions from all sides. Fig. 2.22 presents the clamping system of the coil: component 1 presents the glass FRPC support for the coil, component 2 has for purpose to block the movement in positive z- as well as positive and negative x-directions, component 3 blocks the movement in negative z-direction and component 4 is the enforcement for the y-direction forces and it will serve as the link part with the assembly mounting system which
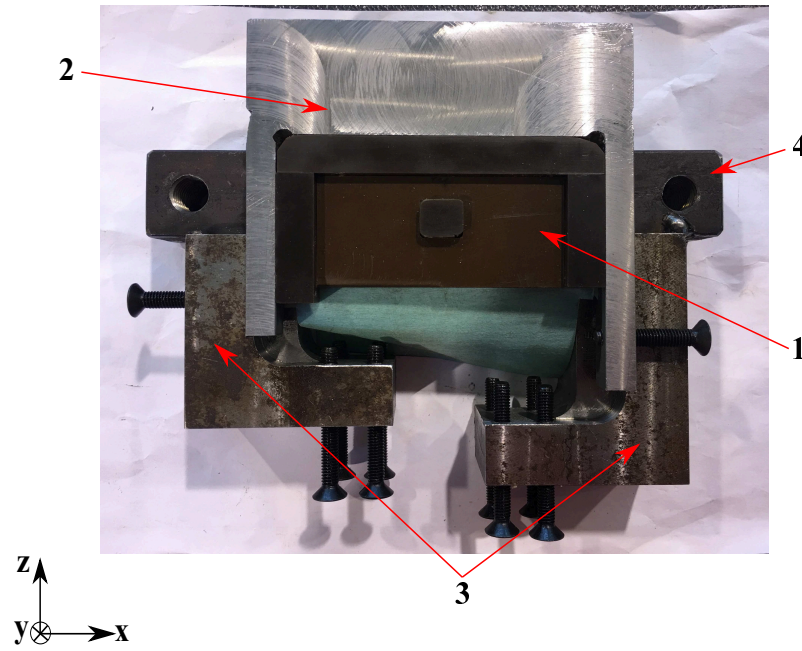
Figure 2.22: clamping system for the O-shape coil

is presented in Fig. 2.23 .

2.4 Numerical model presentation

In the last section, the physical explanation for the electromagnetic problem to understand physiscally different interactions in the process as well as how to design the coils were given. In this section, we will be interested in the numerical simulation of the MPW using the 3D FEM-BEM code LS-DYNA. The developed model has for purposes to determine the deformation profile of the flyer metal, the impact conditions at which it will collide with the parent metal and to visualize the progressive impact phenomenon.

As it was introduced in the litterature review, an important advantage of the use of BEM is that the air region has not to be meshed (see Section 1.6.4) and hence three parts only need to be prepared and meshed for the simulation: the inductor, the flyer and the parent metal. The meshed parts together with the materials parameters, boundary conditions and initial conditions present the input data for LS-Dyna and they will be presented in the next sections. In Fig.2.24 the model preparation steps are summarized with the software used for each one.

The simulations during this study were performed by using HPC resources of the Centrale Nantes Supercomputing Centre on the cluster Liger, granted and identified gem-mptc by the High Performance Computing Institute (ICI).

2.4.1 Material properties and boundary conditions

In order to solve the coupled electromagnetic - mechanical - thermal problem, the three properties for each part should be defined.
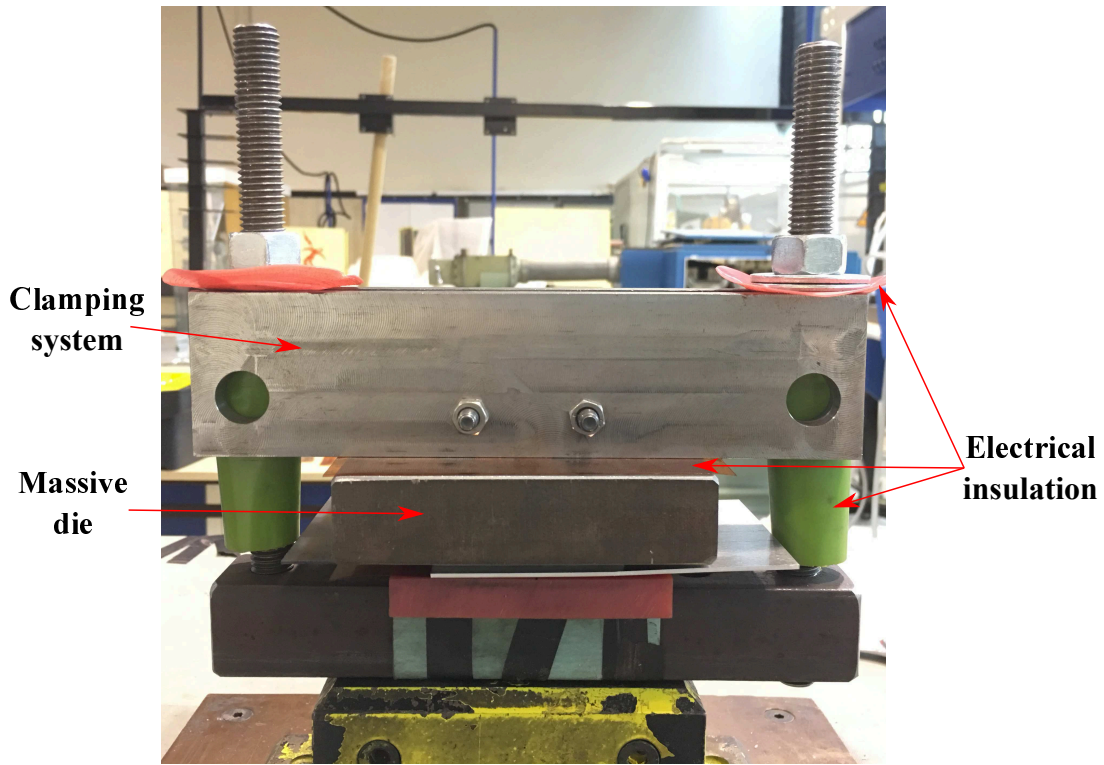
Figure 2.23: assembled mounting system in the O-shape coil case

		A (MPa)	B (MPa)	n	C	m
Copper	OFHC	90	292	0.31	0.025	1.09
Aluminum Alloys	5754	67.456	471.242	0.424	0.003	2.519
	5182	106.737	569.120	0.485	−0.001	3.261
Steel Alloys	ASTM A36	286.1	500.1	0.2282	0.022	0.917
	DC04	162	598	0.6	2.623	0.009

Table 2.1: Johnson-Cook constitutive model parameters for various alloys

The coils materials used in this study are OFHC copper and ASTM A36 steel. The flyer metals used in the models are the aluminum alloys 5754 and 5182. The parent metal was the DC04 deep drawing low carbon steel.

A Johnson-Cook constitutive model was used (Eq. 1.10) for the mechanical solver and the parameters for all materials are taken from litterature [91, 190, 202, 213] and they are presented in Table 2.1 .

The thermal parameters of different materials are presented in Table 2.2 and they are also taken from the litterature [91, 190, 202, 213]. The initial room temperature T_{RT} was set at 293 K.

As it was discussed in the Section 2.3.1.3, the electrical conductivities of different materials are function of the temperature. Electrical conductivities for the used materials in the simulation at room temperature are presented in Table 2.3. The variation of the electrical conductivity with temperature for the copper and aluminum are based on the Meadon model which is a simplified Burgess model [38] and it gives the conductivity as a function of temperature and density at solid

CATIA

Hypermesh

LS-DYNA

LS-PrePost

CAD

Mesh

| Material Properties | Boundary Conditions | Initial Conditions |

EM / Mechanical / Thermal Solvers

Post - Processing
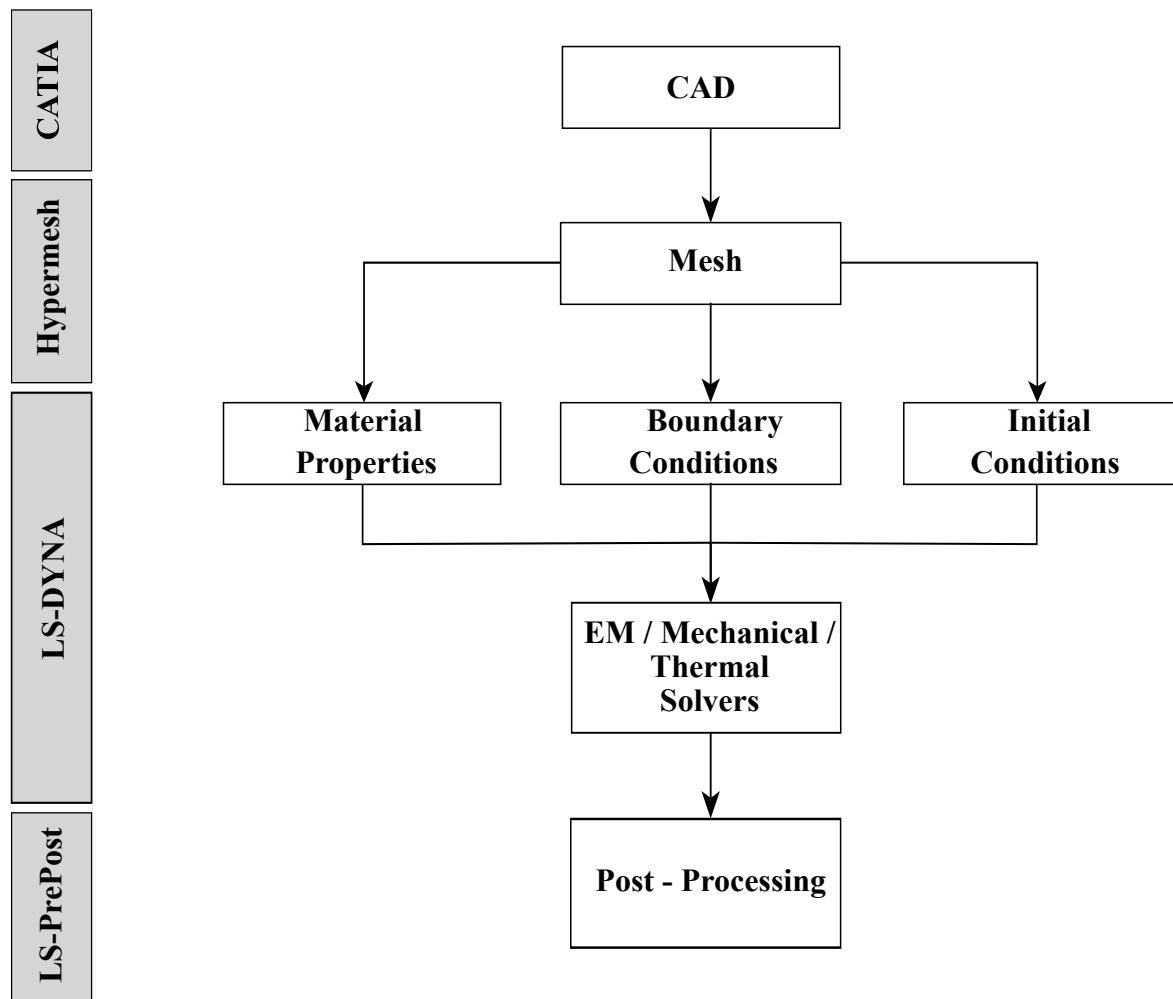
Figure 2.24: model preparation

		Thermal Conductivity (W/mK)	Specific Heat Capacity (J/kgK)
Copper	OFHC	386	383
Aluminum Alloys	5754	130	897
	5182	123	902
Steel Alloys	ASTM A36	50	450
	DC04	52	470

Table 2.2: thermal properties

		Electrical Conductivity	
		%IACS[3]	(S/m)
Copper	OFHC	100	5.8001×10^7
Aluminum Alloys	5754	33	1.9140×10^7
	5182	28	1.6240×10^7
Steel Alloys	ASTM A36	12	6.9600×10^6
	DC04	13	7.5400×10^6

Table 2.3: electrical properties

Parameter	Cu	Al
$V_0 \, (cm^3/g)$	0.112	0.370
γ_0	2	2.13
C_1	-4.12×10^{-5}	-5.35×10^{-5}
C_2	0.113	0.233
C_3	1.145	1.210

Table 2.4: Meadon-Burgess parameters

phase [129]:

$$\rho = (C_1 + C_2 T^{C_3}) f_C(\frac{V}{V_0}) \tag{2.23}$$

where T is the temperature, V is the specific volume and V_0 is the reference specific volume (zero pressure, solid phase):

$$f_C(\frac{V}{V_0}) = (\frac{V}{V_0})^{2\gamma-1}$$

where γ is the Gruneisen value given by:

$$\gamma = \gamma_0 - (\gamma_0 - \frac{1}{2})(1 - \frac{V}{V_0})$$

with γ_0 the reference Gruneisen value. In Table. 2.4, the set of parameters for aluminum and copper from Burgess paper [38, 129] are given.

For the steel case, a simple linear model was used:

$$\rho = \rho_0[1 + \alpha_0(T - T_{RT})] \tag{2.24}$$

where ρ is the electrical resistivity at the actual temperature T, ρ_0 is the electrical resistivity at the reference temperature T_{RT} and α_0 is the temperature coefficient of resistivity for the taken T_{RT} reference temperature. The values of α_0 for steel, aluminum and copper are given in Table 2.5 .

The source currents in the coil are due to the imposition of boundary conditions where it is possible to have an imposed current or an imposed voltage (see Section 1.6.4). In our case, the voltage $V(t)$ is imposed through an equation depending on the charging voltage V_0 (Eq. 1.1), the R, L and C of the generator (Table 2.6) as well as the mesh resistance and inductance (Fig. 2.25). Dirichlet and Newman boundary conditions are applied and no further constraint is applied on the BEM [128].

Metal	α_0 at $293\,K(10^{-3}\,K^{-1})$
Steel	6
Copper	3.9
Aluminum	4

Table 2.5: Temperature coefficient of resistivity for some common metals

	R(mΩ)	L(nH)	C (μF)
Electric B.C.	14	100	408

Table 2.6: RLC properties of the generator
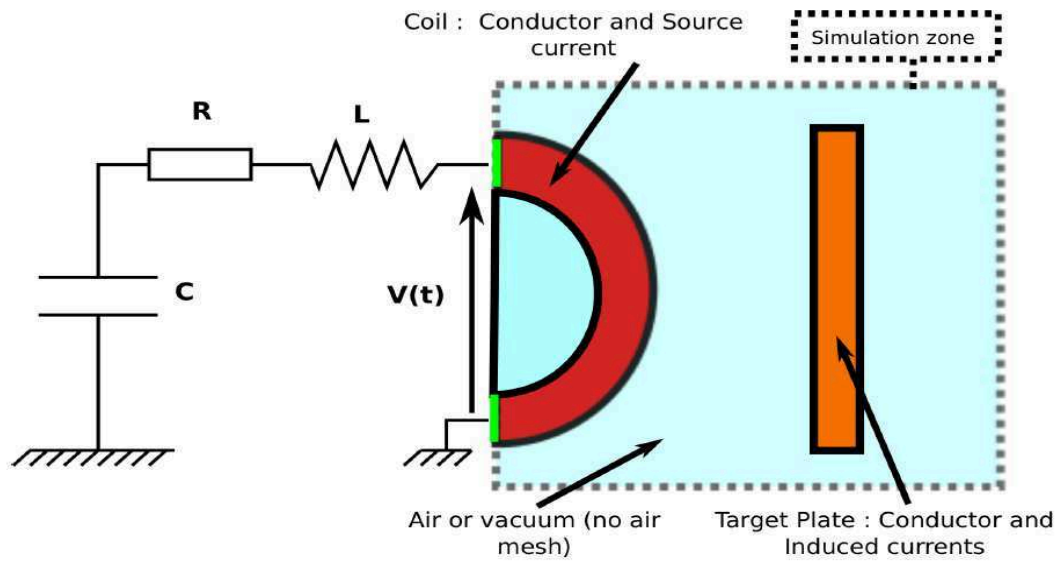
Figure 2.25: problem with (R,L,C) imposed voltage on the coil [128]
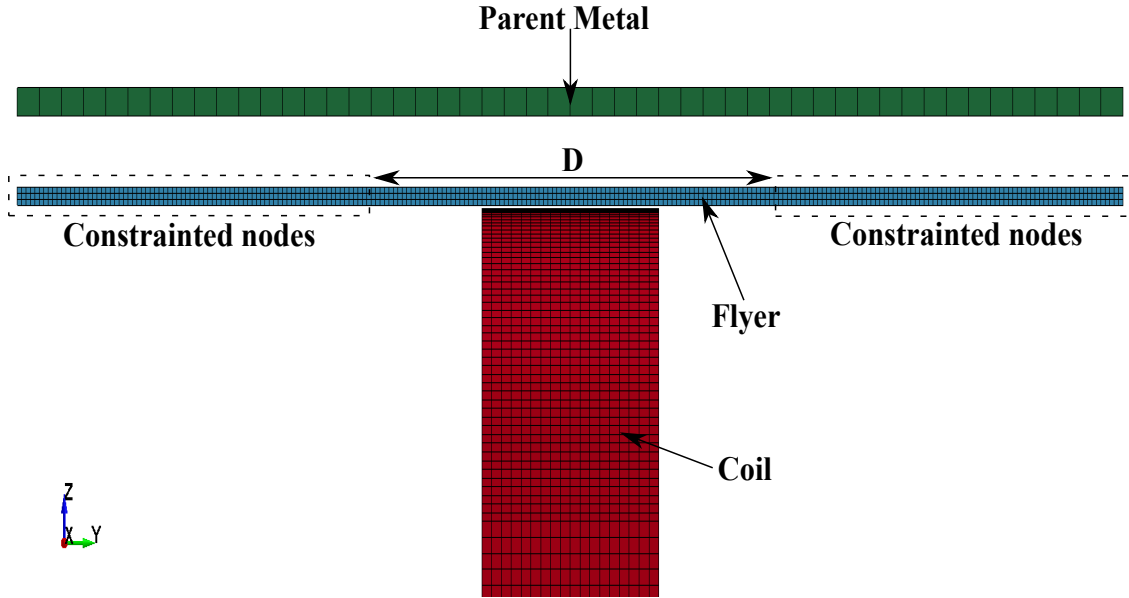
Figure 2.26: model in the MPW overlapping configuration

The inductor nodes movement was constrained in all directions (translation and rotation) since in the MPW applications the coils are fixed in a way to prevent their movement. It is the same for the parent metal nodes. The flyer sheet nodes movement in MPW overlapping case (Fig. 2.26) were blocked outside the distance D that represents the distance between the insulator. In the case of the MPSW (Fig. 2.27) and since the hump is the only part that will be accelerated from the flyer (Section 1.5.3), all the other nodes were also constrained.

2.4.2 Mesh and time step

The electromagnetic solver uses 8 nodes brick elements only and hence the mesh was controlled to not have any other type of elements in the model. Since we are in a 3D full coupled simulation and to avoid very long simulation times, the length of one element edge l_e in the non-active zones was equal to the skin depth δ and in the active zones it was smaller to have accurate numerical results:

$$l_e = \frac{\delta}{3} \tag{2.25}$$

Where l_e is the edge element length and δ the skin depth of the corresponding material. In Fig 2.28 , the variation of the skin depths of the coils and flyer metals are presented as a function of the frequency.

The time-step dt for the electromagnetic solver is computed as the minimal elemental diffusion time step over the elements [128]:

$$dt = \frac{\mu_0 \sigma}{2} l_e^2 \tag{2.26}$$

where μ_0 is the magnetic permeability of the material and σ its electrical conductivity.
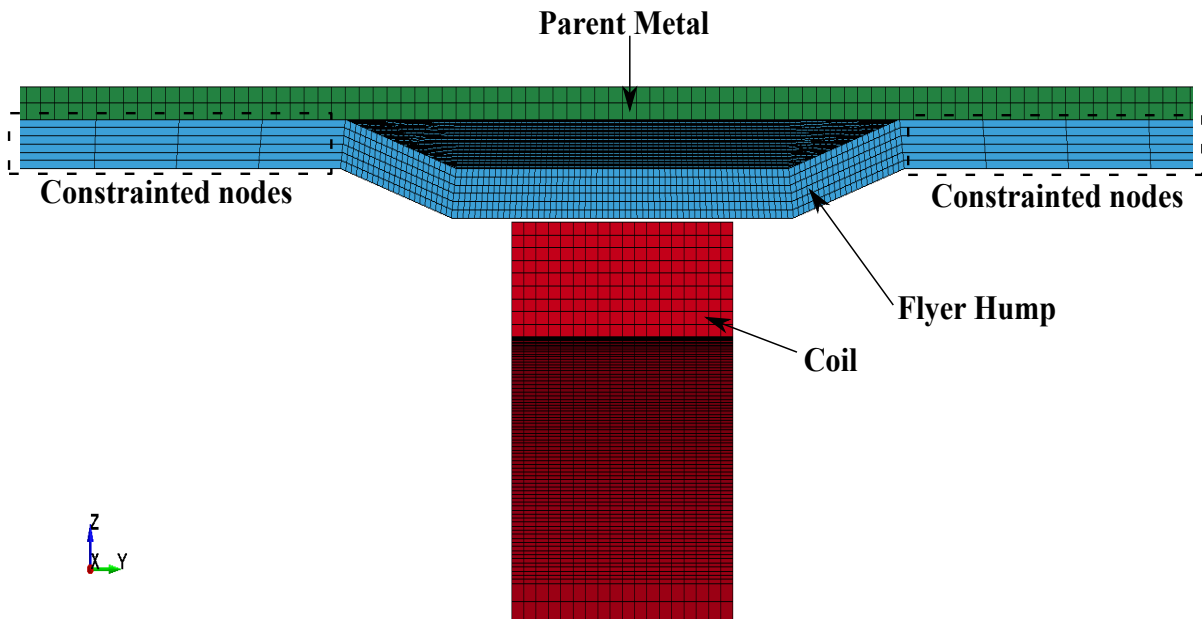
Figure 2.27: model cross section view in the MPSW configuration
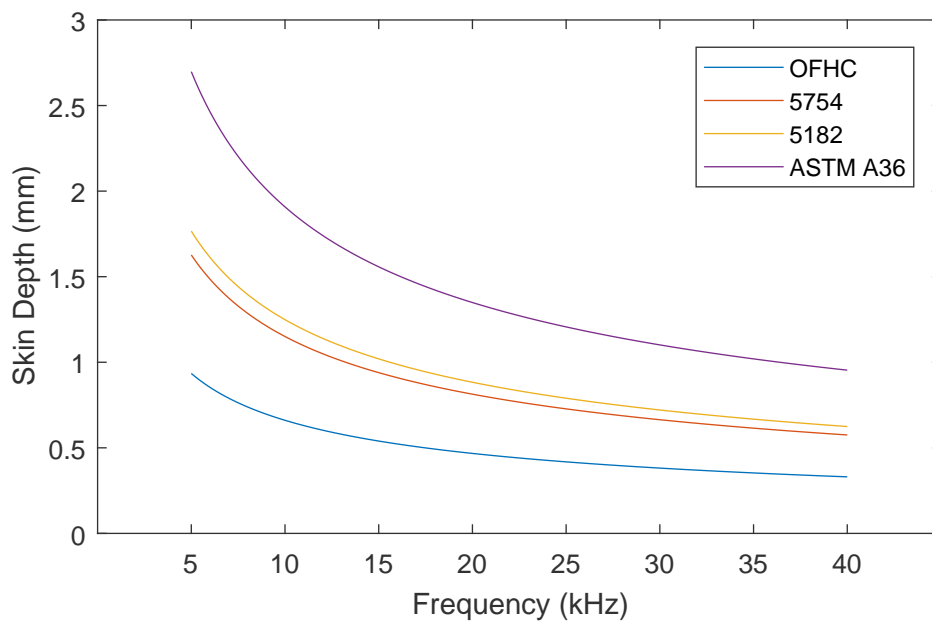
Figure 2.28: skin depth variation as a function of frequency for the used metals

(a) MPW   (b) MPSW
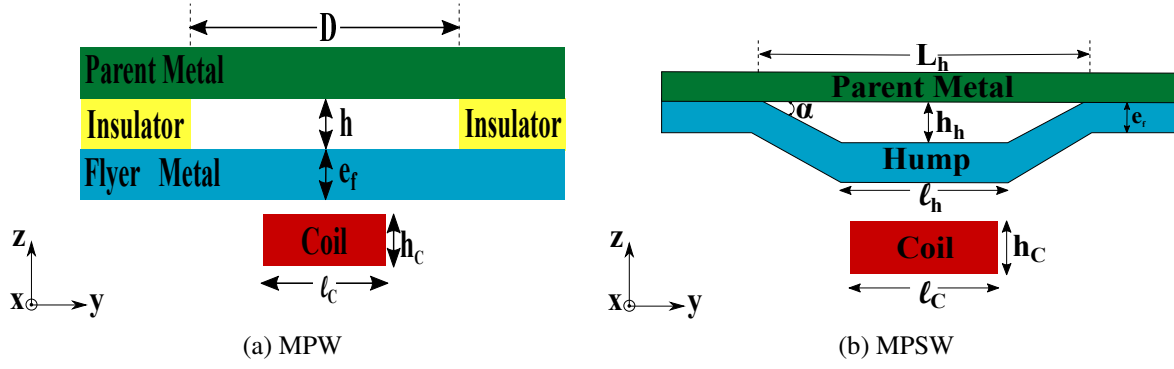
Figure 2.29: welding configurations parameters

2.5 Magnetic pulse welding configurations analyses

After the presentation of the implementation of the numerical model in LS-Dyna, this model will be used now to analyze the impact kinematics in the MPW and MPSW cases.

As it was presented in the litterature review of the MPW / MPSW processes, the two physical parameters for the welding are the impact velocity and the impact angle. These physical parameters are related to and conditioned by the process operational parameters i.e. the electrical coil's geometry, the configurations' geometrical parameters and the discharge energy. The aim of this section is to present and analyze the effect of the configurations' geometrical parameters on the deformation profile of the flyer metal at the impact moment. These analysis of the deformation profiles at different set of parameters, in both MPW and MPSW cases, are essential to obtain some "right hand rules" of choosing convenient welding parameters in general when trying to weld new combination of metals and reduce then the trial and error experiments for finding these parameters.

In order to have the same electromagnetic conditions of the problem, a linear rectangular cross section coil with fixed dimensions was used for all analyses and the flyer metal is an aluminum 5754-H111. We will start by introducing the geometric parameters for both configurations and then explain the procedure of analyses in each case.

2.5.1 Process's operational parameters

The configuration's geometric parameters which may influence the flyer metal deformation profile in the MPW case are: the standoff distance h, the distance between the insulators D and the flyer metal thickness e_f (Fig. 2.29a). In the case of MPSW they are: the standoff distance h_h, the width of the hump l_h , the base length of the hump L_h and the flyer metal thickness e_f. The angle α is directly related to these parameters by the relation $\alpha = \tan^{-1}(\frac{2h_h}{L_h - l_h})$.

The coil used is a linear rectangular cross section (Fig. 2.7) having the dimensions $l_C = 2.8$ mm and $h_C = 8$ mm and made of OFHC copper. The total corresponding inductance of the system is 181 nH which gives a total frequency of 20.83 kHz. At this frequency, the coil has a skin depth $\delta_{OFHC} = 0.46$ mm and the flyer metal has a skin depth $\delta_{5754} = 0.8$ mm.

The flyer metal, for both MPW and MPSW analyses, was considered in two cases:
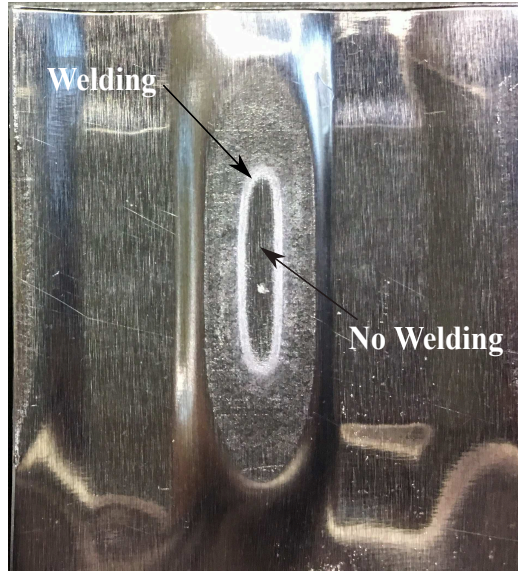
Figure 2.30: MPW welding shape

1. thin sheet metal with $e_f = 0.5\,\text{mm}$;

2. thick sheet metal with $e_f = 1.2\,\text{mm}$;

The idea from choosing a thin and a thick sheet metal is to include the strength of the sheet metal to be deformed in the analysis. In this manner, the conclusions on the qualitative choice method for the welding parameters will include the two levels of strengths for the sheet metals. The discharge energies where varied between 10 kJ and 16 kJ (discharge currents peaks between 290 kA and 360 kA).

After this presentation of the operational parameters, we will start by analyzing the impact between the flyer and the parent metal and the effect of the configurations' geometric parameters on the impact conditions in each case.

2.5.2 Impact between the flyer and the parent metals

2.5.2.1 MPW overlapping case

In the physical analysis presented in Section 2.3.2, it was shown that the applied magnetic forces on the flyer should be symmetrical in respect to the coil cross-section axis that should give an area of flat impact between both metals where no welding occurs and two symmetric areas of progressive impact where welding will take place.

In Fig. 2.30, the form of the welding between two metals is shown. As indicated, the welding takes place within the elliptical ring. When looking to the deformation profile of the flyer metal using the 3D-simulation developped model (Fig. 2.31), a part of the flyer just above the coil has an elliptical form and it has higher displacements than the other elliptical rings around it. In the cross section view at the impact moment and which is presented in Fig. 2.32 , the impact between the flyer and the parent is totally symmetric in respect to the coil cross-section axis where it is clearly seen the flat impact zone and the two progressive impact symmetrical zones. The velocities $\vec{V}_f$ within the
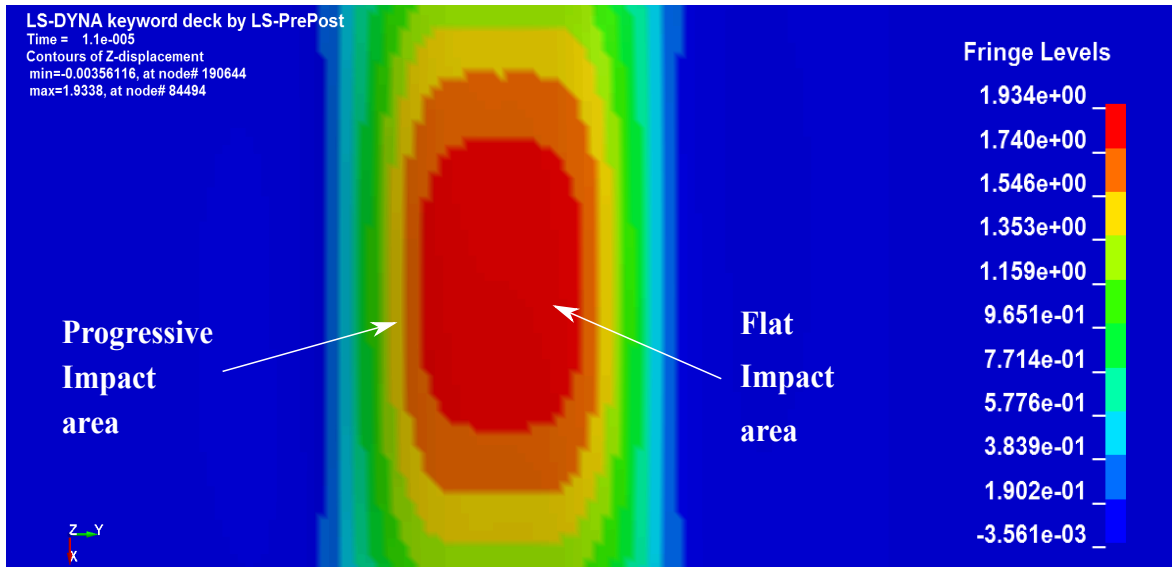
Figure 2.31: flyer metal displacement zones in MPW overlapping case
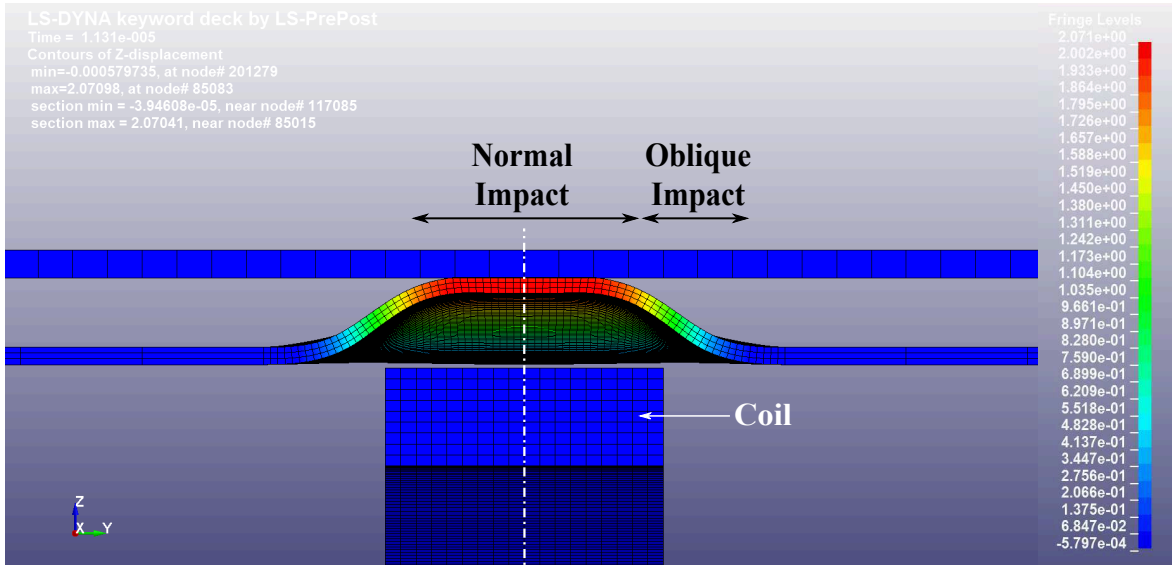
Figure 2.32: impact moment between flyer and parent metals in MPW case

flat impact area are totally normal to the surface of the parent metal (they have only z-direction component) and they have similar values. In the progressive impact areas, the velocities $\vec{V_i}$ have y-components V_{i_Y} (Fig. 2.33).

When looking to the deformation profile of the material at the impact moment, it can be seen that the analysis could be reduced to one side from the coil cross-section axis due to the symmetry of the profile. The bulge formed at the impact moment is schematically represented in Fig. 2.34 : in addition to the process's operational parameters represented in the previous section, l_f represents the flat impact length, V_i represent the velocities of the flyer at the impact moment and β_i represent the angles of the tangents to the normalized shape with the horizontal level of the parent metal. β_i will prescribe how sharp is the deformation profile shape which will give an idea about the evolution of the impact angles during the collision.
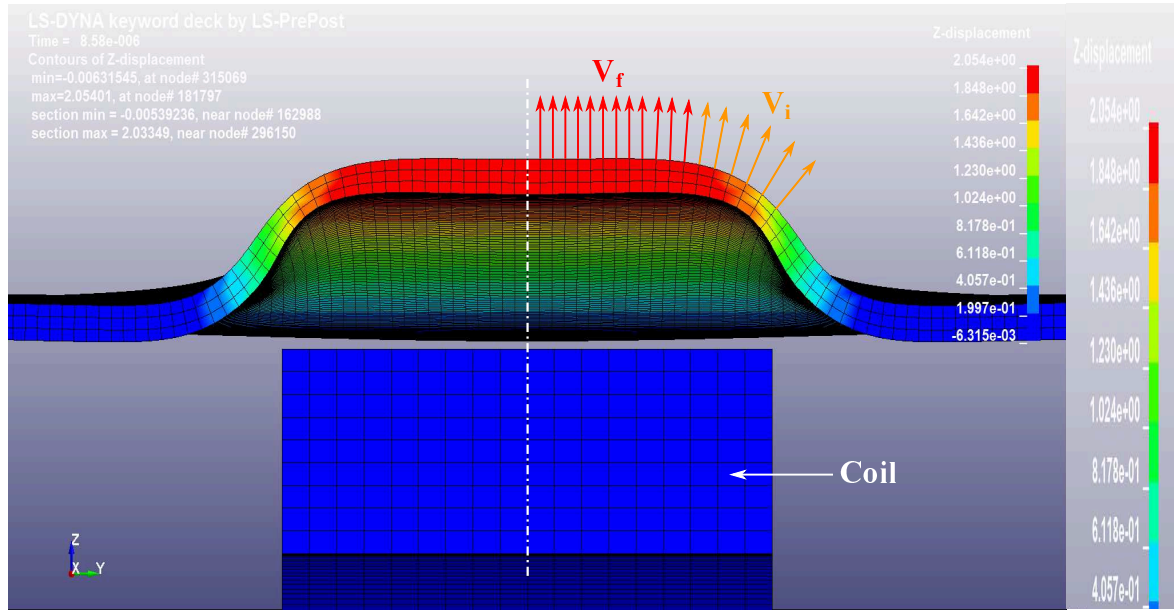
Figure 2.33: velocities in the MPW overlapping case
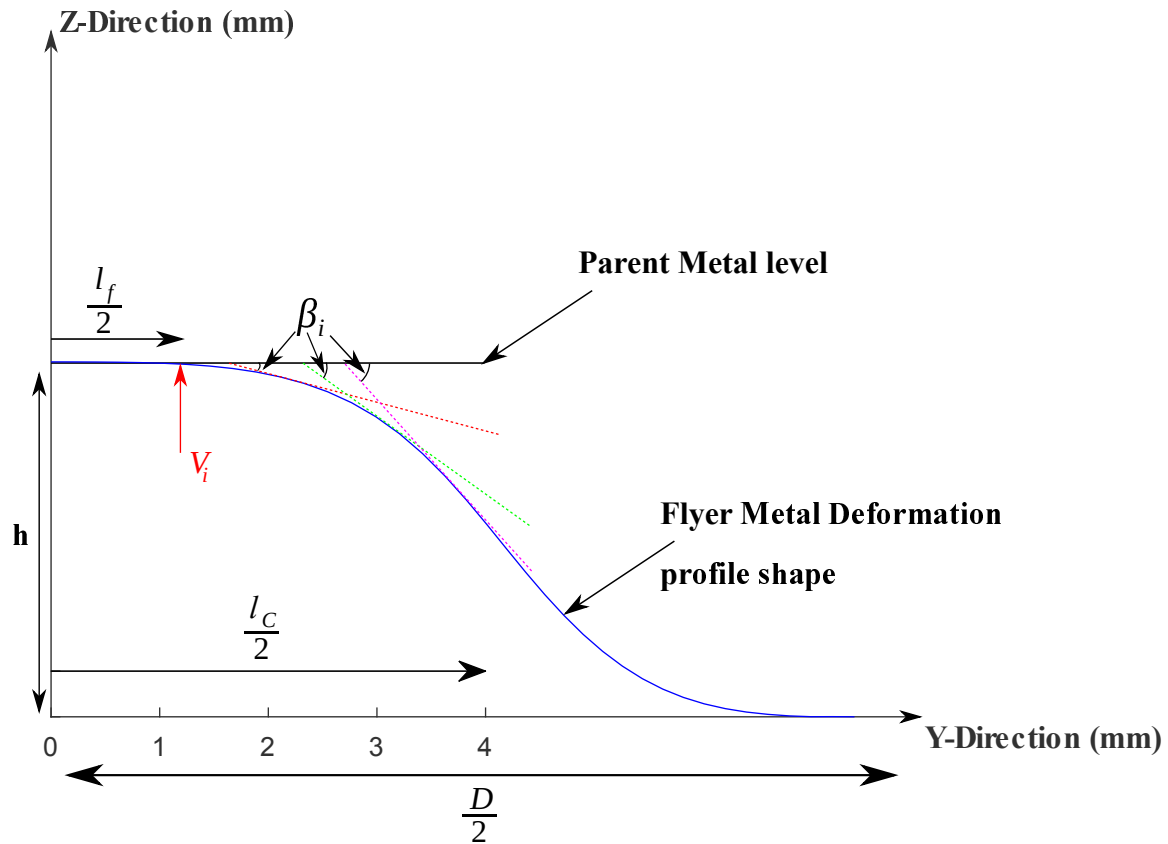
Figure 2.34: schematic of the deformation profile general shape at the impact moment in the MPW overlapping case

2.5.2.1.1 Thin sheet metal Case ($e_f = 0.5$ mm)

In this case the distance D between the insulators has shown no effect on the deformed part of the flyer metal where in general it is equal to $2(\frac{l_c}{2} + 3)$ mm. In Fig. A.1, Fig. A.2 and Fig. A.3, the deformation profiles at different standoff distances and discharge energies for both $D = 15$ mm and $D = 25$ mm are presented.

The velocity of the flyer at impact moment as a function of the discharge energy and the standoff distances are represented in Fig. A.4 and Fig. A.5 for both $D = 15$ mm and $D = 25$ mm. The velocities values and their variation are very similar in both cases and hence the influence of D is not very high on the impact velocity values.

At low standoff distances ($h \leq 1.2$ mm), increasing the discharge energy does not have a high influence on the velocities values where the difference stays less than 50 m/s. When $h > 1.2$ mm, the velocity increases in a considerable way when the energy is increased.

Another thing to notice is that the velocities increase when increasing the standoff distances up to some limit around $h \approx 2.2$ mm where above this standoff distance the velocities stop increasing significantly and this is the case for all the energy levels.

When it comes to β_i, the influence of the standoff distances on its values are presented from Fig. A.6 to Fig. A.11 for both $D = 15$ mm and $D = 25$ mm respectively at different energy levels. The value 4 mm in Y-Direction represents the limit of the coil. In both cases the values of β_i at the first impact points are almost the same and have values between 1.5 and 3 degrees. When moving away from the axis of the coil's cross-section, these values increase more rapidly when the standoff distances increase. Thus, when increasing the standoff distance the deformed part of the flyer metal has sharper form and this will lead to higher impact angles along the progressive impact.

The Fig. A.12 through Fig. A.19 represent the influence of the energy levels on β_i for both cases $D = 15$ mm and $D = 25$ mm. The discharge energy has negligible effect for $h \leq 1.6$ mm but when h becomes greater than 2 mm, the influence of the discharge energy becomes important for the deformed part of the flyer metal near the coil's end and hence the deformation profile becomes in this case very sharp at this region.

The last point to talk about is the influence of D on the values of β_i and which is presented for different energy levels and standoff distances from Fig. A.20 to Fig. A.31. The values of β_i are less in the case where $D = 25$ mm. This difference shows that in the case where $D = 15$ mm the deformation profiles of the flyer metal will result in higher impact angles.

2.5.2.1.2 Thick sheet metal ($e_f = 1.2$ mm)

The distance D between the insulators has here a clear effect on the deformed part. From Fig. A.32 to Fig. A.34, the deformation profiles for different standoff distances and discharge energies at $D = 15$ mm and $D = 25$ mm are represented. The deformed part in the case of $D = 15$ mm is equal to $2(\frac{l_c}{2} + 3.5)$ and in the case of $D = 25$ mm it is $2(\frac{l_c}{2} + 6)$.

The velocity of the flyer at impact moment as a function of the discharge energy and the standoff distances are represented in Fig. A.35 and Fig. A.36 for both cases $D = 15$ mm and $D = 25$ mm.

The values of the impact velocities for both are similar and hence the influence of D is not very significant on the impact velocities.

The discharge energies here have influence on the velocities values at low standoff distances. At low and medium energies, the increase rates of the velocities start to have some limit after a standoff distance $h \approx 2.2$ mm. At high energy levels the velocities have almost a linear increase with the standoff distance.

The variations of β_i due to changes in the standoff distance are presented in Fig. A.37 through Fig. A.42 for both $D = 15$ mm and $D = 25$ mm. At all energy levels, the evolution of β_i is higher when the standoff distances are higher. Another thing to notice is that when $h > 1.6$ mm, the evolution continues to be linear when moving away from the coil's cross-section axis but when $h \leq 1.6$ mm, the evolution tends to have some limit less than $20°$.

From Fig. A.43 to Fig. A.50 the influence of the energy levels on β_i are represented for both cases $D = 15$ mm and $D = 25$ mm respectively. The evolution of β_i values are very similar when increasing the discharge energy with a slight difference when approaching the coil end where the values of β_i are a bit higher for higher energy levels.

The influence of D on the values of β_i and which is presented for different energy levels and standoff distances from Fig. A.51 through Fig. A.62. The values of β_i are higher in the case of $D = 15$ mm when approaching the end limit of the coil. Consequently, the deformation shape of the deformed part of the flyer metal has sharper form and the angles at impact will be higher in the case where D is small.

2.5.2.1.3   Conclusion and discussion

After analyzing the influence of different geometric parameters on the velocity and the shape of the flyer metal deformation for thin and thick , i.e. harder, sheet metal different conclusions can be made. First, the velocity at the impact moment V_i of the flyer metal is affected mainly by both the discharge energy E and standoff distance h and the evolution of the impact angle expressed by β_i is more related to the distance between the insulators D and to the standoff distance h.

Since the D parameter have mainly an influence on the impact angles evolution, it should be chosen not very small where it has been remarked that the angles become higher in that case so having $D > 15$ mm will give less sharp deformation profile and this is the case for both thin and thick metal case.

When it comes to the choice of the standoff distance in the thin sheet metal case it is better to have h between 1.4 and 2 mm so that, at the same time, the velocities (Fig. A.4) will be high enough (450 m/s $< V_i < 720$ m/s) and the impact angles evolution does not excessively exceed the $30°$ (Fig. A.37 to Fig. A.42).

In the case of the thick sheet metal, a smooth evolution of β_i is obtained for $h \leq 1.6$ mm (Fig. A.40) and then choosing a standoff distance between 1 and 1.6 mm will lead to a better impact angles conditions. On the other hand, the velocities at these standoff distances vary between 240 m/s for $h = 1$ mm up to 380 m/s for $h = 1.6$ mm which are sufficient when referring to the conditions for
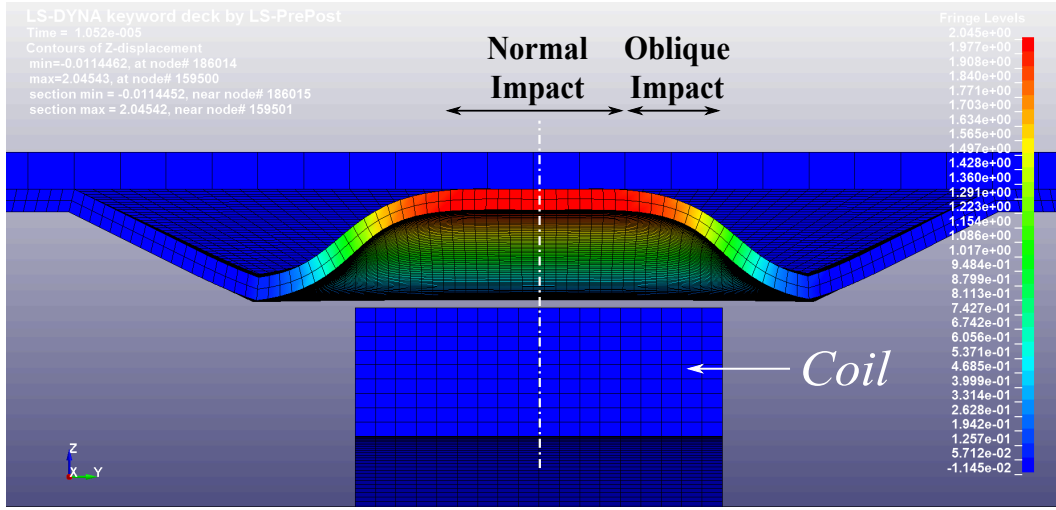
Figure 2.35: Impact moment between flyer and parent metals in MPSW case

impact velocities ($V_i > 200$ m/s) found in litterature [152, 215]. However, comparing the velocities in the thick sheet metal case with the thin sheet metal case shows that in the former the velocities are on average 40% less at different energy levels.

2.5.2.2 MPSW case

Similarly to the MPW case, the welding in the MPSW application occurs within an elliptical ring and the deformation of the hump is totally symmetrical to the coil axis (Fig. 2.35). The analysis then can also be reduced to one side of the symmetry axis of the coil (Fig. 2.34).

The idea behind the development of the MPSW is to have a spot weld similar in size to the traditional resistance spot welding and to avoid the overlapping problem existing in MPW case. The dimensions of the hump are then in this case: $l_h = 12$ mm and $L_h = 20$ mm in a way that the width of the hump l_h stays small and the angle α varies between 10° and 35° when changing the hump's height h_h between 1 and 2.8 mm.

2.5.2.2.1 Thin sheet metal ($e_f = 0.5$ mm)

The deformation profiles at different h_h and discharge energies E are represented in Fig. A.63 through Fig. A.65. The first thing to notice is that the deformed part of the hump at the impact moment is limited to the l_h dimension where the value 6 mm in Y-Direction presents its end limit. When it comes to the velocities of the flyer metal at the impact moment which are presented in Fig. 2.36, at low standoff distances ($h_h < 1.2$ mm) the energy does not have important influence on the velocities values. In addition, the velocity at low discharge energy levels varies linearly in function of h_h and the difference between low and high standoff distances does not exceed 120 m/s. Also, the velocities when $h_h \geq 2.2$ mm attain some limit at medium and high energy levels.

The variations of β_i as function of the standoff distances at different energy levels are presented in Fig. A.66 through Fig. A.68. The values of the angles at the first points of impact are similar and are between 2° and 5° but once moving away the angles become higher when h_h increases which
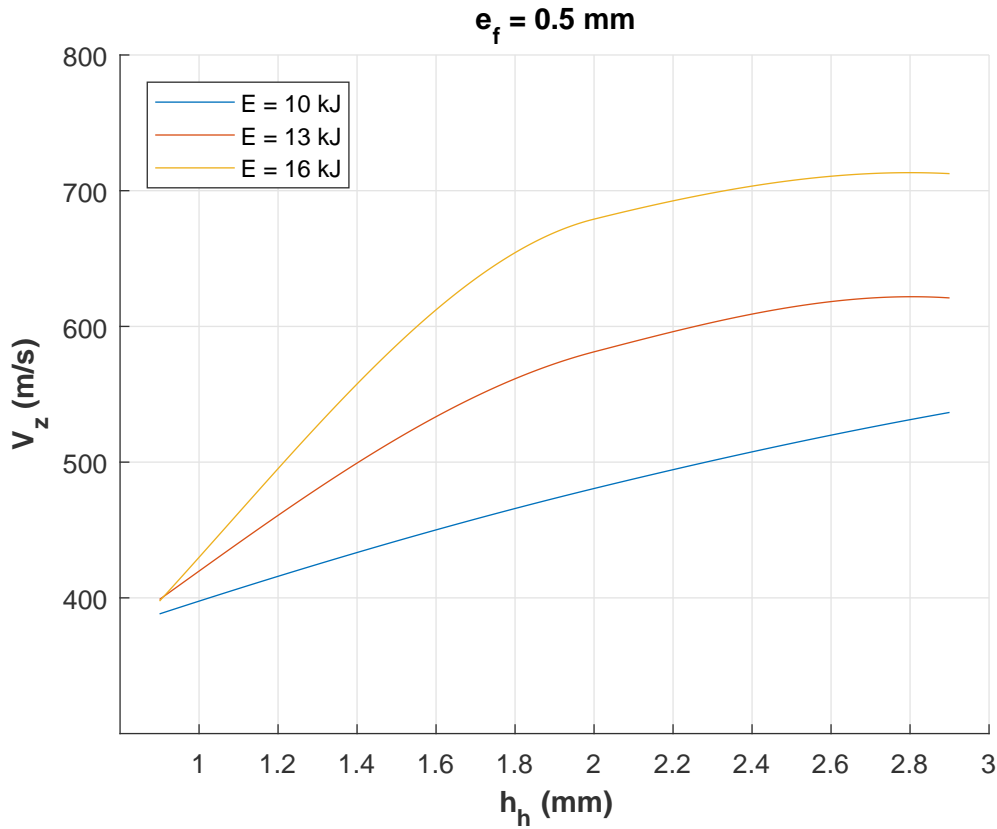
Figure 2.36: Velocity at impact moment of thin aluminum 5754-H111 ($e_f = 0.5$ mm) for different standoff distances at various discharge energies in the MPSW configuration

means that the deformation shape is more sharp in this case and then the resulting impact angles will be higher during the progressive impact.

2.5.2.2.2 Thick sheet metal ($e_f = 1.2$ mm)

The deformation profile at different h_h and discharge energies E are represented from Fig. A.69 to Fig. A.71. The velocities presented in Fig. 2.37 show that the discharge energy have influence on the velocity even at small standoff distances. At low energy levels, the velocities attain some limit when h_h exceeds 1.8 mm and at high energy levels the evolution of the velocities is almost linear with the increase of h_h.

The variations of β_i are presented from Fig. A.72 to Fig. A.74. The angles at the first impact points are similar (between 2° and 5°) and when moving away the angles become higher the more h_h increases. Once again, the increase of h_h will result in the increase of the impact angles during the progressive impact.

2.5.2.2.3 Conclusion and discussion

In the case of the thin aluminum sheet, the combination between high velocities and smooth angles evolution will lead to standoff distances between 1.2 and 2 mm (Fig. 2.36 and Fig. A.66). On the other hand, for the thick aluminum case, the same conclusion in this case can be done (Fig. 2.37 and Fig. A.72). Also, in this case the lost of velocities between the thin aluminum case and the thick sheet case is around 40% on average.
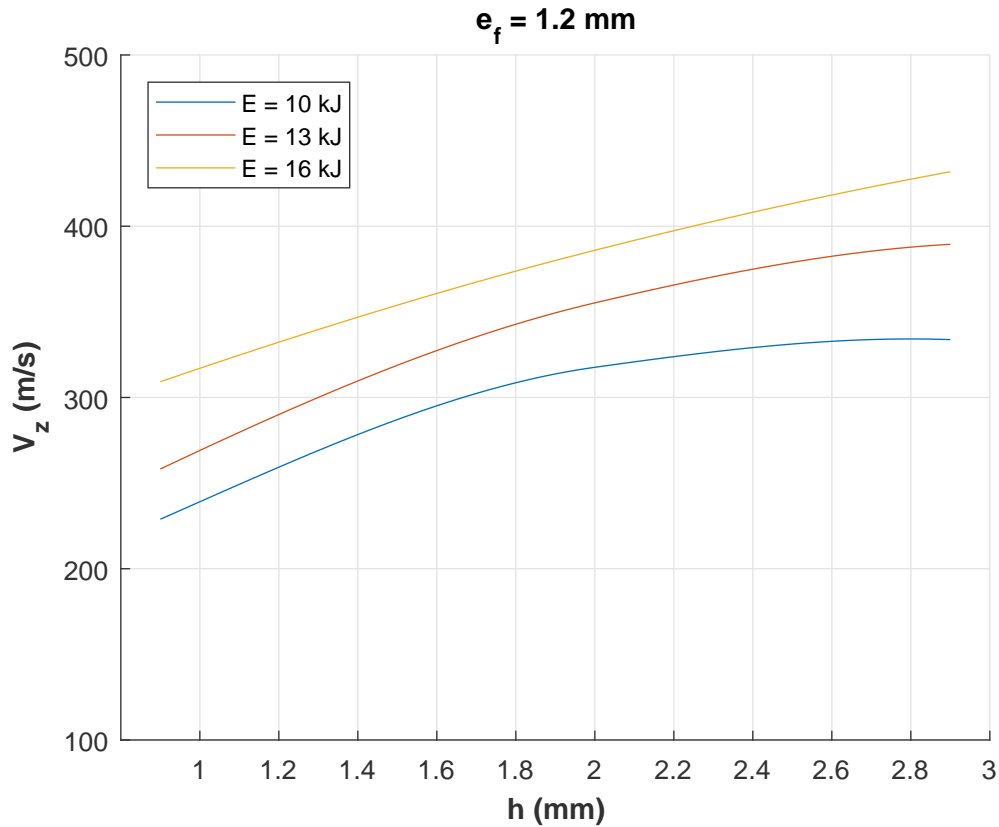
Figure 2.37: Velocity at impact moment of thick aluminum 5754-H111 ($e_f = 1.2$ mm) for different standoff distances at various discharge energies in the MPSW configuration

When comparing the velocities in the case of the MPSW and MPW at the same standoff distances (Fig. 2.38) , it can be seen that in the latter they are higher in the thin aluminum case at low and medium energy levels while at higher energy levels there is no difference for standoff distances less than 1.8 mm. In the thick aluminum case (Fig. 2.39), the difference is not observed between both configuration at lower energy levels but when increasing the discharge energy, the flyer have higher velocities in the MPW case. The MPSW configuration will lead then to a slight loss in velocity comparing with the MPW case when applied to the same metal.

2.5.3 O-shape and linear coils comparison

As it was pointed in Section 2.3.2, the linear rectangular cross-section coil shows some limitations in the case of higher strength flyer metals where, consequently, the O-shape coil design was developed to improve the efficiency in that case. This limitation was also seen in the previous analysis of the process's operational parameters where the lost in the velocities levels was about 40% when applying the same discharge energy for a higher thickness sheets using a linear coil.

To validate the fact that the O-shape coil design has higher efficiency, the developed numerical model was used to compare the flyer velocities in the MPW configuration case for the thick aluminum 5754-H111 ($e_f = 1.2$ mm). Since the discharge currents are higher in O-shape coil case, the mechanical strength of the coil should be higher and hence two approches were considered. In the first, the material of the coil is kept an OFHC copper but the thickness was increased to 4 mm (i.e. 1.4 times the thickness in the linear coil case). The second approach involves the use of
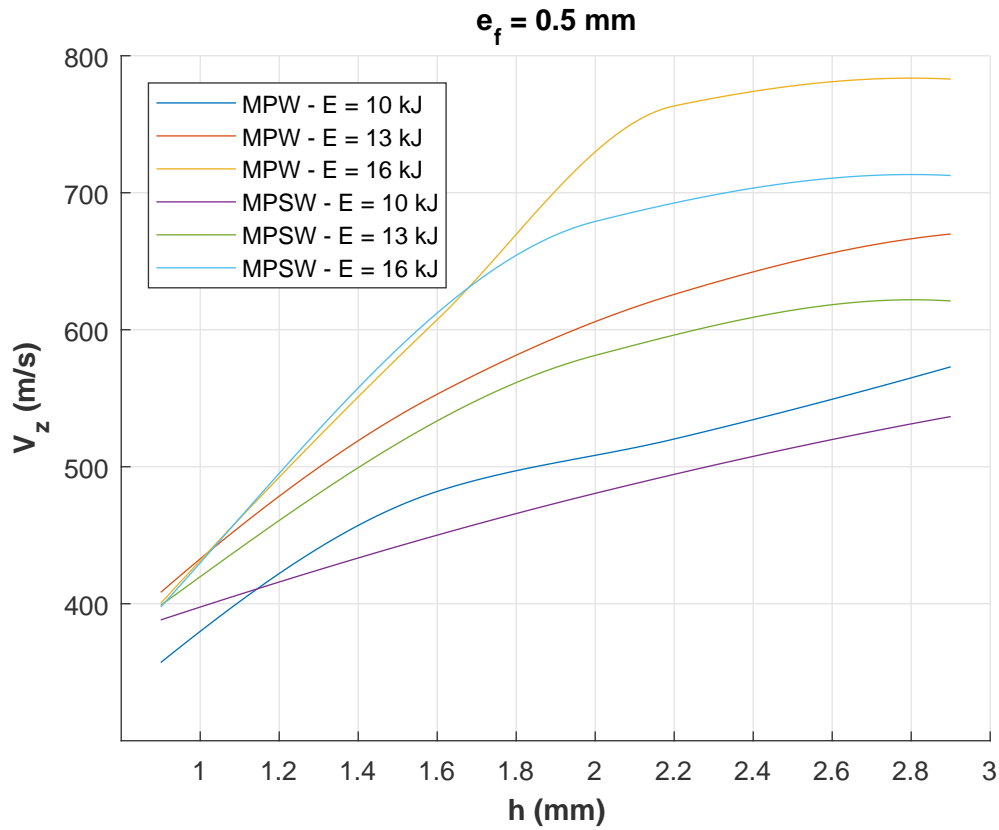
Figure 2.38: comparison of the flyer velocity at the impact moment between MPW and MPSW configuration for thin aluminum case ($e_f = 0.5$ mm) at different standoff distances
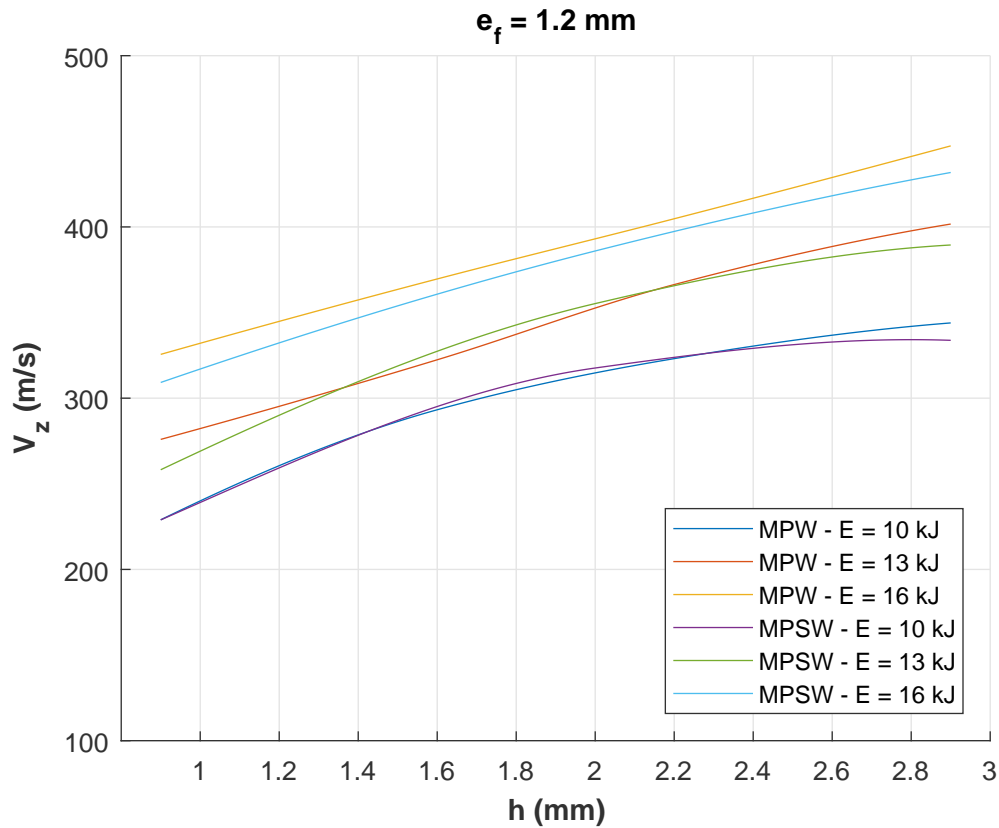
Figure 2.39: comparison of the flyer velocity at the impact moment between MPW and MPSW configuration for thick aluminum case ($e_f = 1.2$ mm) at different standoff distances
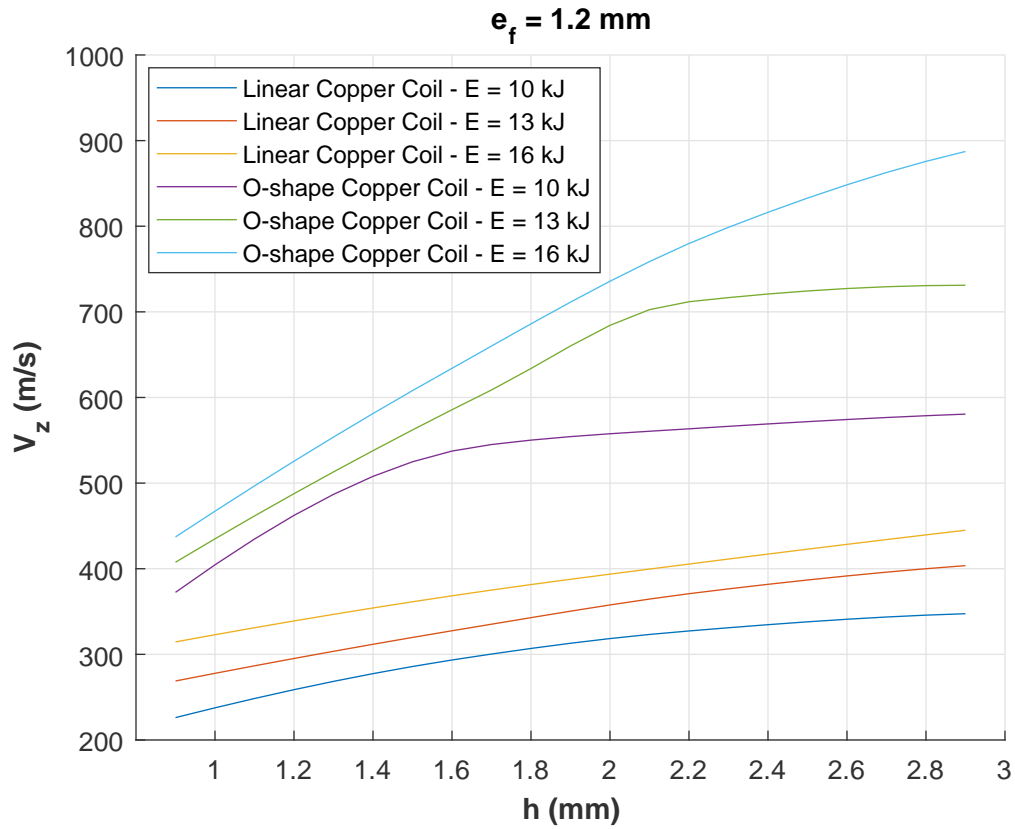
Figure 2.40: impact velocities comparison between the OFHC O-shape and linear coils ($e_f = 1.2$ mm)

a 4 mm thickness coil made of steel ASTM A36 which has better mechanical properties and see wether the loss in electrical conductivity will have high influence on its global efficiency.

Fig. 2.40 represents a comparison between impact velocities for the cases of use of a OFHC copper O-shape and a linear OFHC copper coil. The velocities at $E = 10$ kJ in the O-shape coil case are much higher than these at $E = 16$ kJ in the linear case. The velocity in the O-shape case is on average 1.75 times the velocity in the linear coil shape.

When using a steel O-shape coil, the velocities are 1.55 times the velocities in the linear coil case. The velocities curves at different standoff distances in both cases are presented in Fig. 2.41 .

The data presented in the previous two figures shows clearly that the O-shape coil is far better than the linear coil and even when the steel is used for the coil it still has higher efficiency than the linear coil.

2.6   Conclusion

This chapter presented first a very important detailed physical analysis for the whole magnetic pulse processes which, to our knowledge, have been never presented as a whole package in the litterature. The electromagnetic principles and the interaction of different physical phenomenon involved in the magnetic pulse processes were presented using an extensive physical approach allowing the understanding of the principles, of how to design different components and of how to
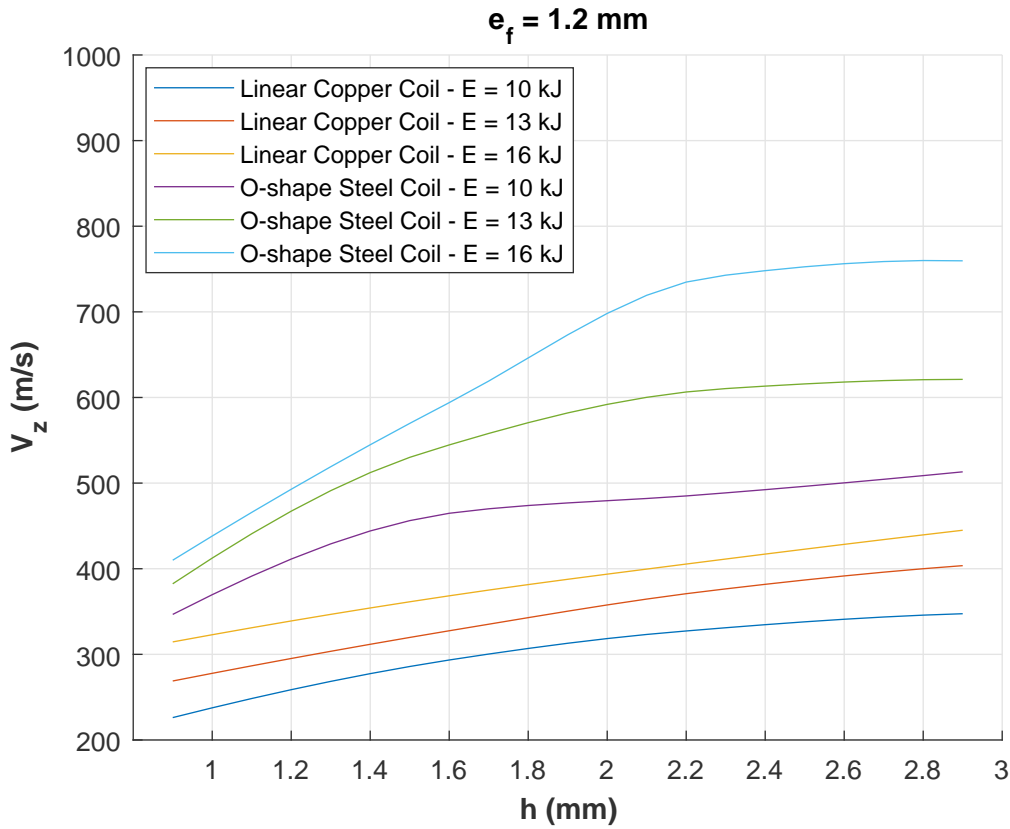
Figure 2.41: impact velocities comparison between the steel O-shape coil and linear copper coil ($e_f = 1.2$ mm)

think the systems in the magnetic pulse field (not only for the MPW but it can also be extended to the magnetic pulse forming). This comprehension helps the reader to have a qualitative approach on the way a coil should be designed, on the importance of its position vis-a-vis the flyer metal and the considerations to be taken when designing the mounting systems. One important result of these analysis is the presentation of the design of O-shapes coils (or closed shapes) and why they have higher efficiency.

The second important point presented in this chapter is the development of numerical models for both MPW and MPSW using a commercial code that serves in analyzing the effect of different MPW configuration parameters. These analysis showed the effect of process's operational parameters on the impact conditions between flyer and parent metals. Using these models and from a simple free forming analysis of the flyer metal, qualitative conclusions can be drawn which allows to find qualitatively the region of parameters for a succesfull welding. Fig. 2.42 presents some general conclusions from these analysis. In general, the process window can be divided into four regions. The first where the standoff distance is less than about 1.3 mm, the increasing of energy and of standoff distance has no significant effect on the impact conditions. In the second region, where the standoff distance is between 1.3 and 2.3 mm, the energy at a specific standoff distance has an influence only on the impact velocity but on the other hand, changing the standoff distance has influence on both impact velocity and angle. In the third region, where the standoff distance is up to 2.8 mm, the energy here at a specific standoff distance has no more effect on the impact velocity but the standoff distance continues to have influence on both impact velocity and angle.
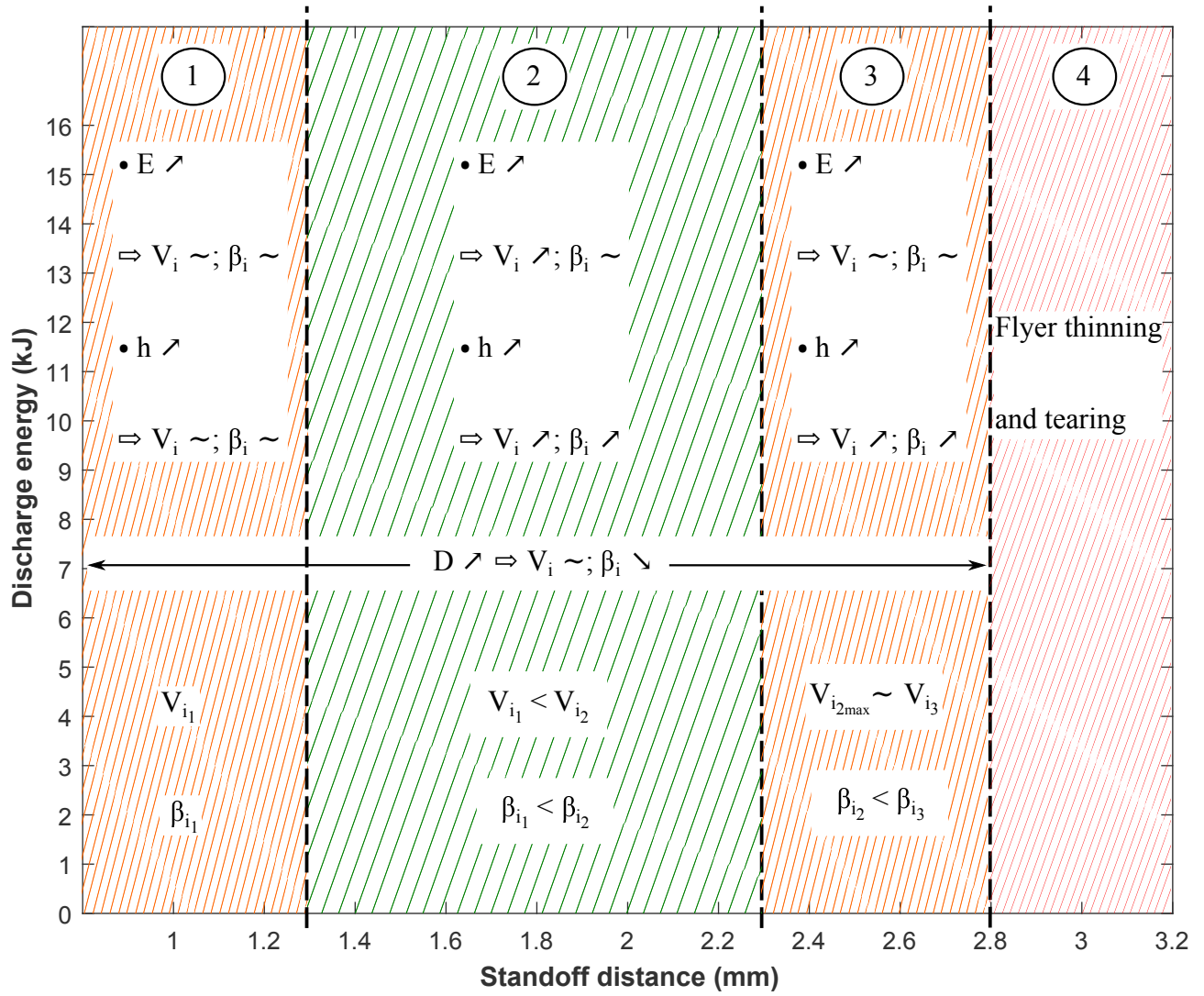
Figure 2.42: impact conditions dependence on the process parameter

Above a standoff distance of 2.8 mm i.e. in region 4, the flyer metal begins to have thinning and tearing is observed on the edges of the deformed distance. Also and in a general conclusions, the impact velocity in region 1 is less than the impact velocity in region 2 at every specific standoff distance. The maximum velocity in region 2 at every standoff distance is equal to the velocity in region 3. On the other hand, the angles are always increasing when moving from region 1 to region 3. The conclusion that can be made is that staying in region 2, where the standoff distances are between 1.3 and 2.3 mm, is the most effective start for finding the welding parameters:

- the velocities are high enough: higher than region 1 and their maximums are similar to region 3

- the angles are at medium levels: not low as they are in region 1 and not increasing as in region 3 with a velocity similar to region 2.

The last conclusion that can be done is also that the influence of the controlled distance that will be deformed of the flyer metal, i.e. D in MPW case or l_h in MPSW case, have only influence on the angles and non-significant on the velocities.

In addition, this model allowed us to validate the fact that the O-shape coils are more efficient than the linear coils since the velocities in the former are more than 1.55 times higher even when using a steel coil and for the application on a thick flyer metal. The importance of the possibility of using a steel coil will have first benefits on the mechanical stength of the coils and second from an economic point of view where the prices of steels are on average three times less than that of the copper. In the same context, it is very important to mention that it is the first time that a coil made of steel is used for welding applications.

All these numerical/theoretical analysis and conclusions done during this chapter will now be investigated experimentally in the next chapter where the focus will be given to the application of the MPW/MPSW on different combination of aluminum and steel alloys.

Chapter 3

Magnetic pulse welding development for metallic alloys applications

3.1 Résumé

L'utilisation des alliages d'aluminium séries 5000 et 6000 dans l'automobile est de plus en plus importante (panneaux de carrosserie, structures de sièges, éléments de renforcement, ...). Du côté de l'acier, les aciers doux ont historiquement été utilisés pour divers composants et, au cours des 30 dernières années, les développements des aciers avancés à haute résistance (AHSS) ont entraîné une augmentation de l'utilisation des aciers multi-phases. Ces composants fabriqués en acier lorsqu'ils sont utilisés dans un environnement corrosif nécessitent des revêtements qui posent un autre problème à considérer lors de l'étude de la soudabilité de métaux différents : l'effet des revêtements sur le procédé de soudage ainsi que sur les performances mécaniques et la microstructure de la soudure.

Dans le cas du soudage par impulsion magnétique et afin d'étudier la soudabilité des différents couples métalliques, une combinaison de différents alliages, en particulier ceux utilisés dans l'industrie automobile, sera envisagée dans ce chapitre, y compris les cas homogènes des alliages d'aluminium et les cas hétérogènes des alliages d'aluminium / acier dissemblables. En outre, pour étudier l'effet des revêtements sur le procédé, la soudure entre l'alliage d'aluminium 1050 et les aciers revêtus de zinc a également été étudiée.

Nous présentons en un premier temps l'équipement utilisé (Sections 3.3.1, 3.3.2), les différents compositions et propriétés des matériaux utilisés (Tables: 3.1, 3.2, 3.3, 3.4, 3.5), le montage et la procédure expérimentale pour le MPW (Section 3.3.4.1) et MPSW (Section 3.3.4.2). Ensuite, nous présentons la stratégie adoptée pour les essais qui est constituée de six phases (Section 3.3.4.3):

- une phase zéro qui consiste à définir les besoins en termes de soudure hétérogène ;

- une phase 1, pour étudier la soudabilité entre différents couples définis ;

- une phase 2, pour la construction des fenêtres de soudabilité expérimentales pour les deux couples utilisés dans la simulation numérique dans le chapitre précédent afin de valider les conclusions théoriques et pouvoir appliquer ces conclusions dans d'autre cas ;

- une phase 3 d'applications du MPW et MPSW sur différentes combinaisons des alliages d'aluminium et des aciers ;

- une phase 4 pour étudier la tenue mécanique des soudures sous différents types de chargement (quasi-statique, dynamique et fatigue) ;

- une phase 5 pour des analyses microscopiques des soudures ainsi que les surfaces de rupture.

A partir de ce travail expérimental plusieurs conclusions ont été tirées. Commençons par la procédure expérimentale qui a montré l'importance de respecter les étapes mentionnées lors de l'applicat- ion du processus :

- le décapage de l'huile qui, si elle n'est pas enlevée, empêche la soudure ;

- le contrôle du positionnement de la tôle par rapport à la bobine qui joue un rôle important dans la façon dont le courant induit sera distribué et qui va donc affecter l'efficacité du procédé ;

- l'utilisation d'un couple de serrage correct dans la configuration MPW (max. 40 N.m) pour ne pas sur-compresser les isolants et modifier la distance de sécurité souhaitée ; et dans la configuration MPSW, le serrage correct (35 Nm) a un rôle important pour ne pas déformer le bossage et changer la distance de sécurité.

Concernant les fenêtres de soudabilité construites expérimentalement pour différents couples de matériaux et combinées aux études numériques (Fig. 3.25), elles ont montré que lorsque le métal de la pièce projectile est plus mince / moins rigide, la fenêtre de soudage est très grande et la distance entre les isolants présente moins d'influence sur le soudage. D'autre part, lorsque l'épaisseur / la résistance du métal de la pièce projectile augmente, la fenêtre de soudage se rétrécit et des énergies de décharge plus élevées sont requises ; la distance entre les isolant doit être plus grandes et influe de manière significative sur la qualité des soudures (Fig. 3.21 et Fig. 3.22).

Les résultats expérimentaux ont validé aussi le fait que l'inducteur en forme de O a un meilleur rendement que les inducteurs linéaires (Table 3.7). Un important point à mentionner ici est que les différentes nuances d'aluminium et d'acier soudés ensemble dans ce chapitre n'ont jamais été soudées, à notre connaissance, en utilisant le procédé de soudage par impulsion magnétique. En plus, le soudage entre l'aluminium et les aciers revêtus ainsi que l'aluminium avec le zinc pur ont montré encore plus le large domaine d'applications de la technologie non restreinte à des alliages métalliques spécifiques. Ce fait est appuyé encore plus quand nous regardons la résistance mécanique des différentes soudures (Table 3.10) montrant que la liaison entre différentes combinaisons est loin d'être faible:

- pour les essais quasi statiques, les tenues mécaniques dépassent les 6 kN et atteignent 9 kN dans le cas de la soudure 5182 / DC04.

- le comportement quasi-statique des soudures a montré une similitude lorsque la pièce fixe est semblable: Fig. 3.39, Fig. 3.45 et Fig. 3.43 pour les aciers DP; Fig. 3.36 et Fig. 3.41 pour l'acier DC04.

- lorsque l'on compare la configuration de soudage (MPW) et celle du soudage par point (MPSW) pour une même combinaison de 6013-T4 / DP1000, cette dernière présente une soudure moins performante à la fois en quasi-statique et en dynamique ;

- durant les essais dynamiques, les soudures des alliages d'aluminium 6xxx avec différentes nuances d'aciers présentaient une meilleure résistance où, dans le cas 6013-T4 / DP1000, la charge dynamique moyenne est de 14 kN ;

- le comportement en fatigue des différents couples montre également un nombre de cycles plus élevé pour les alliages 6xxx dépassant les 40000 cycles, avec un nombre de cycles plus élevé pour la configuration MPW. En ce qui concerne l'analyse microscopique, dans la configuration MPSW, divers composés intermétalliques ont été détectés tandis que dans les soudures MPW, le seul composé intermétallique détecté est un composé riche en aluminium qui peut expliquer le meilleur comportement dans le cas du MPW ;

- durant les essais quasi-statiques des soudures entre l'aluminium 1050 et les aciers revêtus (DC04 + ZE et DP450 + ZE), la rupture était dans la tôle d'aluminium. Cependant, la soudure s'est rupturé dans certains cas ce qui peut être liée à l'irrégularité de la couche de zinc sur la surface de l'acier.

D'un point de vue microscopique (Section 3.4.5), les interfaces de soudures ont des aspects ondulatoires et présentent différents types de couches fines intermétalliques en fonction des couples. En outre, les surfaces de rupture ont également montré que la rupture peut se produire dans le matériau de base lui-même ou dans la soudure. En ce qui concerne les soudures avec l'acier revêtu, deux couches sont apparues à l'interface : une solution solide (Al)Zn et une couche biphasée (Al + Zn); la couche de Zn permet d'éviter la formation des intermétalliques type Fe_xAl_y à l'interface aluminium-acier.

3.2 Introduction

The use of 5000- and 6000- series aluminum alloys in automotive applications is very wide (body panels, seat structures, reinforcement members...). From the steel side, the low carbon drawing steels were historically used for various components and during the last 30 years, the developments of the advanced high stregnth steels (AHSS) led to the increase in use of the dual phase steels (DP) in different parts of a vehicle [166]. The steel components when used in a corrosive environment require coatings for protection which arise another problem to consider when studying weldability of dissimilar metals: the effect of the coatings on the welding process as well as on the mechanical performance and the microstructure of the weld.

In the case of the MPW and in order to study the weldability of the different metal couples, a combination of different alloys, especially the one used in the automotive industry, will be considered during this chapter including similar aluminum alloys and dissimilar aluminum/steel alloys. In addition, and to study the effect of the coating in the MPW process, the welding between aluminum alloy 1050 and zinc coated steels was also investigated.

Figure 3.1: 50 kJ pulse generator at ECN

We will start first by presenting the equipment used, the experimental setup and procedure. After that, we will present the experimental design strategy and the results obtained for different couples in order to discuss them: weldability, mechanical tests and microscopic observations. Finally, the application of the MPW in the case of zinc coated steels will be presented and discussed.

3.3   Equipment and experimental procedure

3.3.1   Pulse Generator

The pulse generator used is a 50 kJ developed at ECN (Fig. 3.1) which has the below characteristics:

$$C = 408\,\mu\text{F}, L_{Generator} = 0.1\,\mu\text{H}, R_{Generator} = 14\,\text{m}\Omega$$

$$V_{max} = 15000\,\text{V}, I_{max} = 500\,\text{kA}, f_{short} = 25\,\text{kHz}$$

The higher limit for the discharge energy is hence fixed at 16 kJ so that the discharge current does not exceed 80% of the maximum allowable current for the generator:

$$I_{operation_{max}} = 0.8 \times I_{max} = 400\,\text{kA}$$

3.3.2   Coils

The coils used during this study, as discussed in the previous chapter (Section 2.3.2), are a linear rectangular cross-section coil and an O-shape rectangular cross-section coil. The dimensions of both coils are presented in Fig. 3.2 and Fig. 3.3 respectively.

Isometric view   Side view
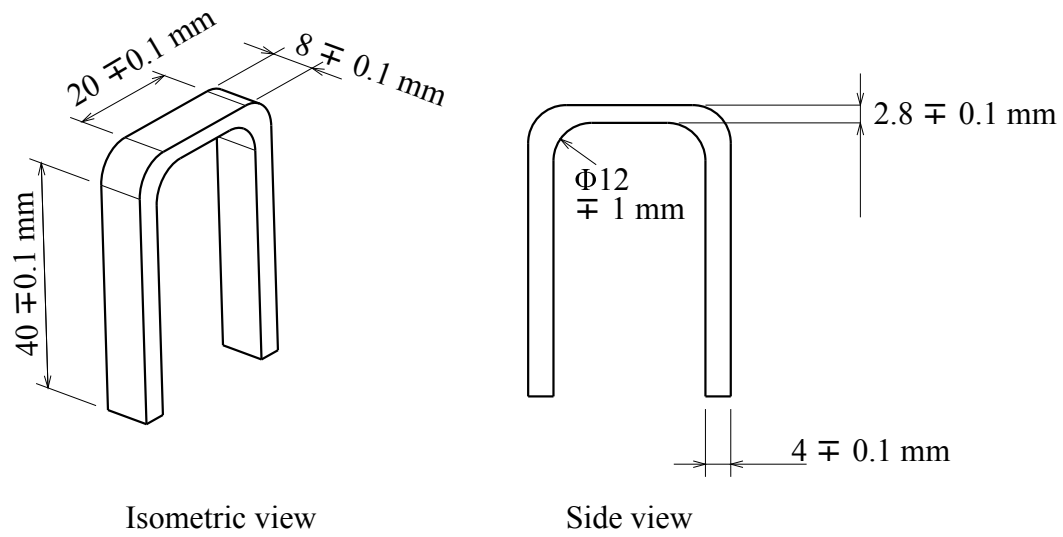
Figure 3.2: linear rectangular cross-section coil

Units	mm
Tolerances	∓ 0.1

Top view   Side view
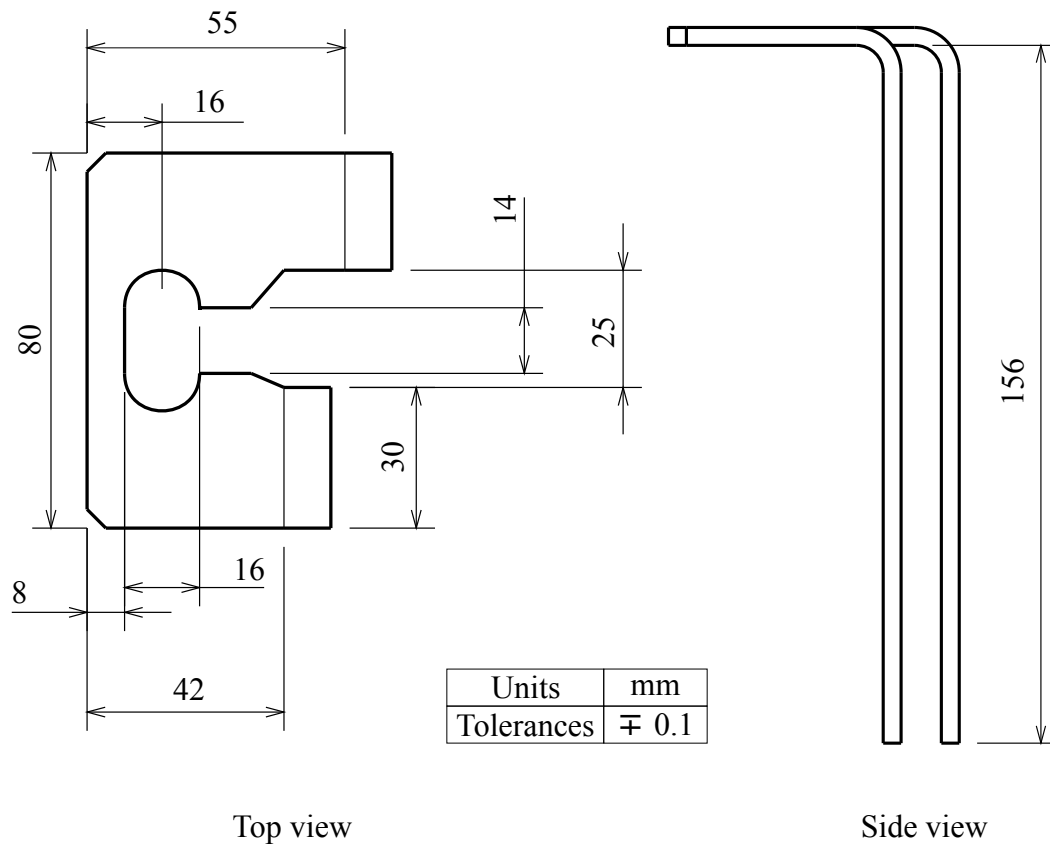
Figure 3.3: O-shape coil dimensions

	Si max	Fe max	Cu max	Mn max	Mg max	Cr max	Zn max	Ti max	Other max
1050	0.25	0.40	0.05	0.05	0.05	-	0.07	0.05	0.03
5182	0.20	0.35	0.15	0.50	4.00 5.00	0.10	0.25	0.10	0.15
5754	0.40	0.40	0.10	0.50	2.6 3.6	0.30	0.20	0.15	-
6013	0.78	0.28	0.97	0.40	1.02	0.06	0.10	0.05	0.15
6016	0.5 1.5	0.50	0.20	0.20	0.25 0.70	0.10	0.20	0.15	0.15

Table 3.1: aluminum alloys chemical compositions (% at.)

	C max	Mn max	Si max	P max	S max	Al max
DC04	0.08	0.40	0.10	0.025	0.025	0.020

Table 3.2: DC04 steel chemical composition (% at.)

3.3.3   Materials

The aluminum and steel alloys chemical compositions used during this study are presented in Table 3.1 , Table 3.2 and Table 3.3 . Their mechanical properties are given in Tables 3.4 and 3.5 .

3.3.4   Experimental procedure and design

The MPW and MPSW configurations require two different procedures for preparing every test. Each procedure is detailed next.

3.3.4.1   MPW configuration

The MPW configuration involves the use of insulators to create the needed airgap between the two metals (Fig. 2.29). The insulators are made of PE and PVC and they are designed to have the same thickness of the required standoff distance between metals. They are fixed on the flyer metal using adhesive tapes. In Fig. 3.4 and Fig. 3.5, the flyer metals with insulators are represented for both cases I-shape and O-shape respectively. In Fig. 3.6 and Fig. 3.7 the positioning of the flyer metal regarding both coils is represented.

	C max	Mn max	Si max	P max	S max	Al max	Ti + Nb max	V max	Cr max	Mo max	B max	N max	Ni max	Nb max
DP 450	0.10	0.16	0.4	0.04	0.015	0.015 0.08	0.05	0.01	0.8	0.3	0.005	0.008	-	-
DP 1000	0.139	1.50	0.21	0.009	0.002	0.046	-	0.01	0.02	-	0.0002	0.003	0.03	0.015

Table 3.3: DP steels chemical compositions (%at.)

	$R_{p_{0.2}}$ (MPa)	R_m (MPa)	A% ISO 20x80
DC04	160	280	37
(e≤ 1.47 mm)	200	340	
DP450	290	460	27
	340	560	
DP1000	787	1059	8.5

Table 3.4: steels mechanical properties

	$R_{p_{0.2}}$ (MPa)	R_m (MPa)	A% ISO 20x80
1050	85	105	4
5754-H111	90	200	21
(e ≤ 1.5 mm)	130	240	
5182	120	260	23
(e ≤ 1.5 mm)	160	310	
6013 - T4	174	310	26
6016 - T4	110	220	23
	150	270	

Table 3.5: aluminum alloys mechanical properties
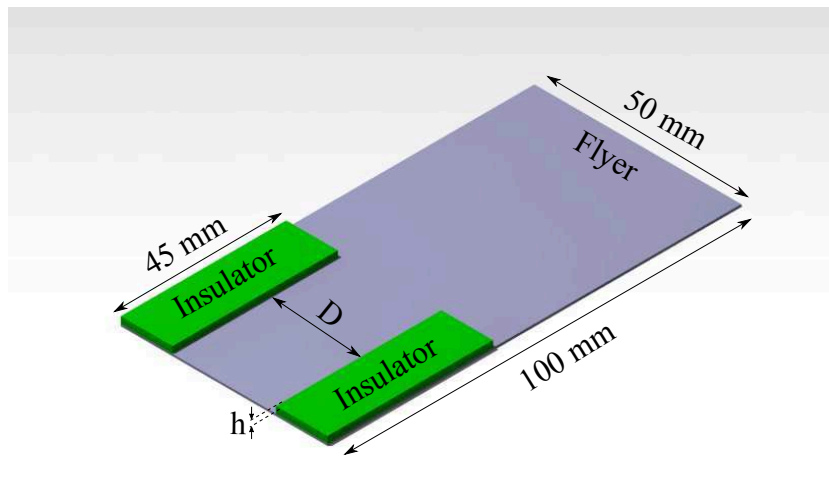
Figure 3.4: flyer with insulators in the case of linear coil use
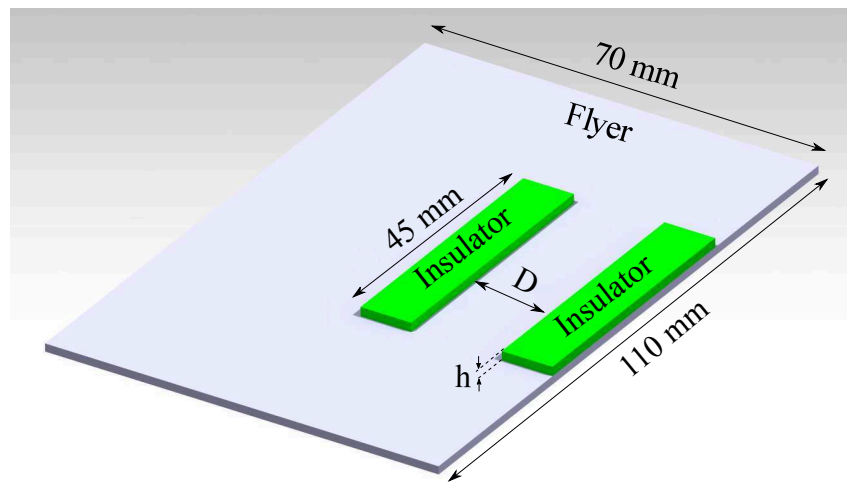
Figure 3.5: flyer with insulators in the O-shape coil use
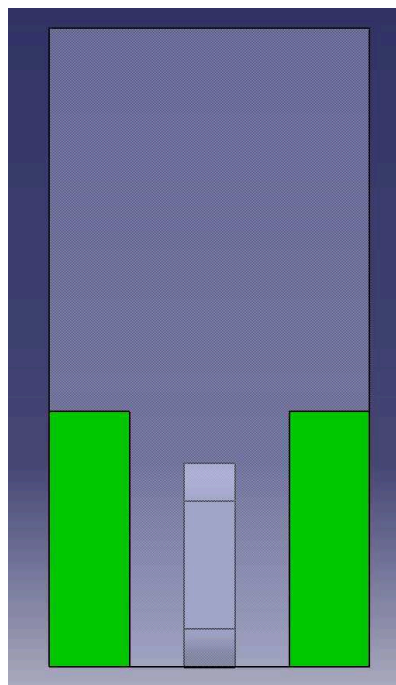
Figure 3.6: flyer metal positioning regarding the linear coil
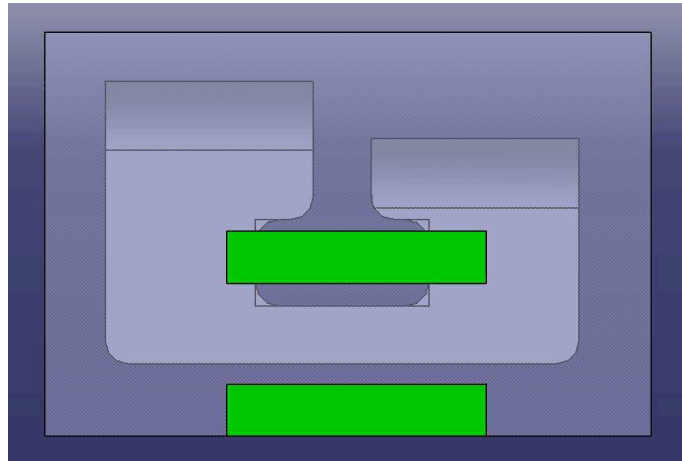
Figure 3.7: flyer metal positioning regarding the O-shape coil
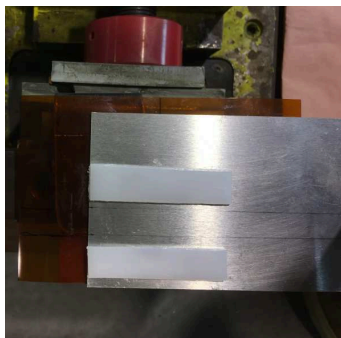
step 1

step 2
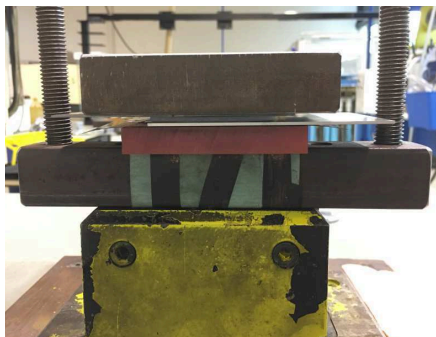
step 3
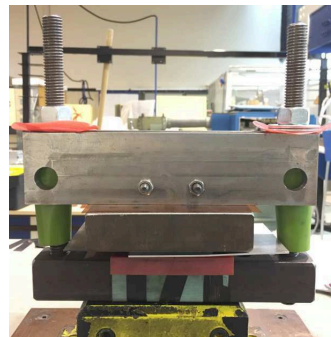
step 4

Figure 3.8: MPW experimental procedure
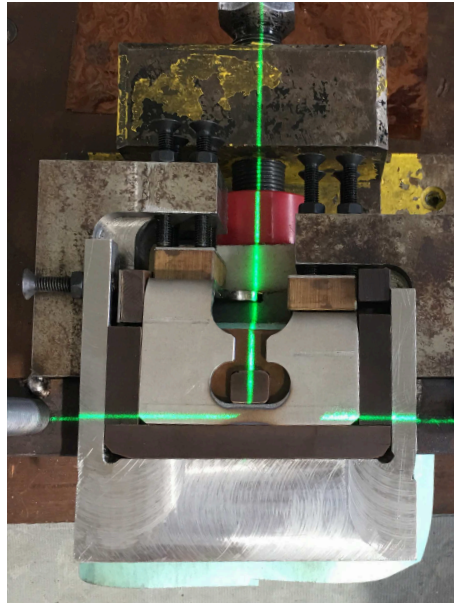
Figure 3.9: positioning control using a laser

A very important step is cleaning the flyer and parent metals surfaces from oil using acetone solution. In fact, we always saw in the litterature that there is no need to clean the metal surfaces when using MPW processes but during experimental investigation we noticed that the presence of some oil on any of the sheet metals surfaces (flyer or parent), prevents the welding from occuring. After the cleaning step, the flyer metal is positioned facing the coil where a Kapton insulation sheet with a 0.1 mm thickness is used to separate it from the coil. The positioning is controlled by a laser so that the part of the flyer metal to be deformed is centered regarding the coil's active area (Fig. 3.9). The parent metal is then positioned on the insulators, over it a massive steel die and finally the whole system is clamped using a special system designed to avoid any displacement during the welding process (Fig. 3.8). The clamp torque is not exceeding the 40 N.m so that the height of the standoff distance does not change due to the compression of the plastic insulators. The standoff distance is controlled using a feeler gauge before every test.

3.3.4.2 MPSW configuration

In this case, the first step of the process is to create the hump in the flyer metal. The general geometry of the hump chosen is a rectangular one. This geometry was chosen based on the previous study done by Arun et al. [131] during which different geometries were tested and it was proven that the rectangular one is the more efficient. Fig. 3.10 presents this general geometry with different dimensions. The hump is stamped in the flyer metal using a hydraulic press die and the pressure used does not exceed 6 tones (Fig. 3.11).

After cleaning the metal surfaces from oil using acetone solution, the flyer metal is then positioned in such way the hump is guided by a plastic insulator (Fig. 3.12) and the laser so that it is facing and centered on the coil's active area. The parent metal is then positioned above the flyer metal with the massive die on and finally the system is clamped similar to the MPW case. The clamping torque is 35 N.m and it was selected in a way so that the hump will not be deformed due to clamping.
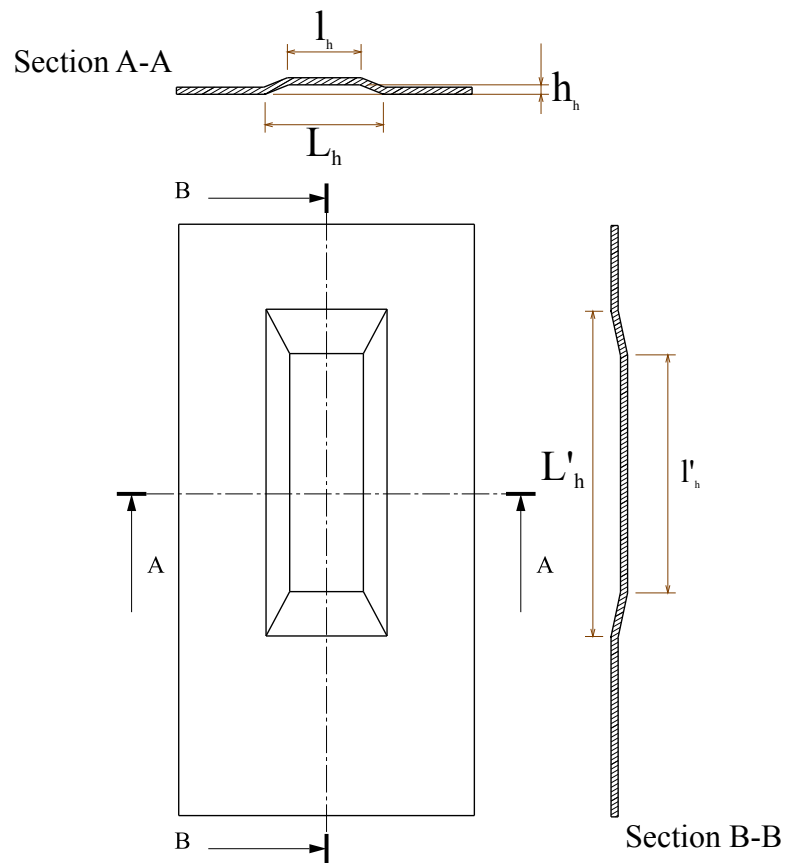
Figure 3.10: hump geometry
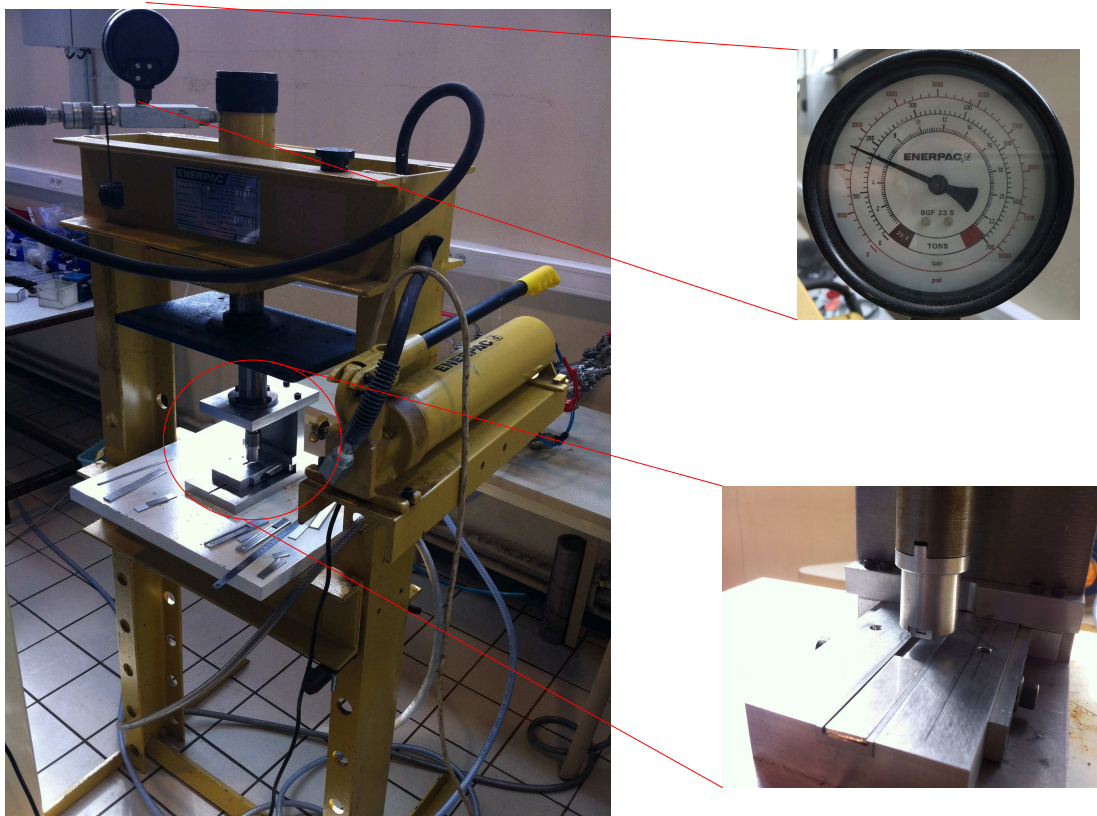
Figure 3.11: hydraulic press die

125
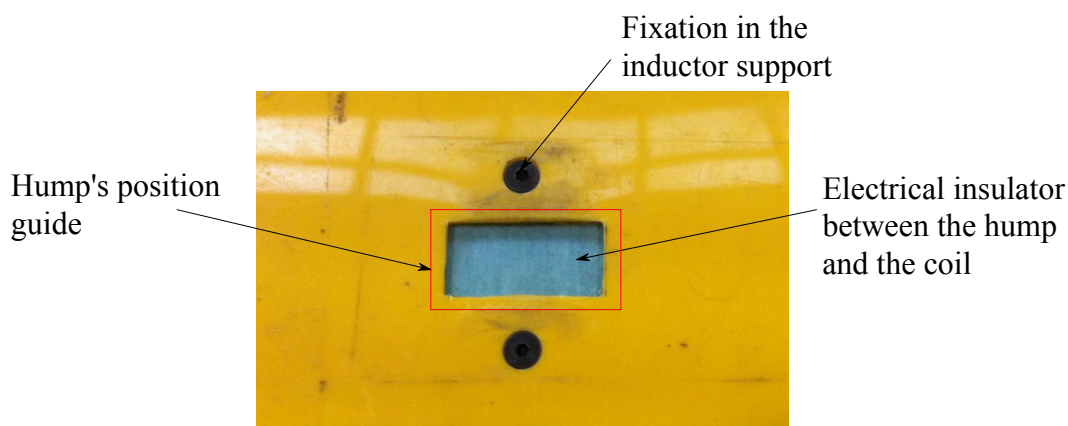
Figure 3.12: hump position guide

3.3.4.3 Experimental design strategy

The most of the metal couples investigated in this study have never been welded together using MPW to our knowledge specifically when it comes to dissimilar couples case. Hence the experiments were designed using a 6-Phases strategy:

- **Phase 0 - Needs identification**

The needs were defined based on the main purpose of the study which is the assembly between FRPC and metals and, at the same time, industrial applications involving dissimilar metals joining. In a general context, the aluminum alloys to consider belong to 5xxx and 6xxx series. The steel alloys are low carbon deep drawing steels (DCxx) and dual phase steels (DPxxxx).

- **Phase 1 - Explore weldability between different types of alloys**

The early study was dedicated to explore weldability of aluminum with different steel alloys using the MPW process. Therefore, the aluminum 1050, which belongs to the "commercially pure" wrought alloys family 1xxx, has been chosen first to validate the fact that aluminum is weldable with different steel alloys using this technology. After that, the study was focused on exploring the weldability of the 5xxx and 6xxx alloys with aluminum alloys as well as with steel alloys. These tests include different thicknesses of the flyer metal in some cases in order to define the limitations of the used coil as well as the technology itself where these limitations exist.

- **Phase 2 - Build experimentally the process welding windows for two couples of interest to compare them to the theoretical/numerical conclusions**

Once the last phase was accomplished, the focus was given to build experimentally the process welding window with different discharge energies and standoff distances for two dissimilar couples: 0.5 mm thickness 5754 aluminum with low carbon DC04 steel and 1.2 mm thickness 5182 with low carbon DC04 steel. The choice of these two couples is to validate the theoretical/numerical conclusions made in the previous chapter. Therefore, after the process window are built, the specimens were tested in quasi-static lap shear condition to have an idea about the optimal welding conditions. These data will provide experimental feedback for later development of theoretical methods for predicting welding parameters.

- **Phase 3 - Application to similar and dissimilar welding combinations**

In this phase, the focus was given to weld different combinations in a manner to include similar aluminum alloys together and dissimilar aluminum/steel combinations from different families of alloys and in different MPW/MPSW combinations.

- **Phase 4 - Study the mechanical strength of welding under different loading conditions**

The specimens for various dissimilar magnetic pulse welded couples were tested in the mechanical test center CRED of GeM at Ecole Centrale de Nantes: quasi-static lap shear, dynamic and cyclic tests. The results are then analyzed and compared for different couple of materials.

- **Phase 5 - Microscopic analysis of welding and failure surfaces**

Finally, microscopic analysis for welding interfaces as well as for failure surfaces were done using SEM and EDX.

3.4 Results

3.4.1 Weldability between different alloys

To explore weldability of aluminum with different alloys, the aluminum 1050 was tested in the MPSW configuration. The thickness of the 1050-sheet is 0.5 mm. The coil used is a linear copper coil (Fig. 3.2). The hump dimensions (Fig. 3.10) are: $l_h = 8$ mm, $L_h = 12$ mm, $l'_h = 10$ mm, $L'_h = 18$ mm and $h_h = 1.6$ mm. Table 3.6 lists the minimum discharge energy needed for a welding to occur regarding each parent metal and also includes all the information about the thicknesses of each.

The next phase of exploring weldability was by exploring the 5xxx and 6xxx with aluminum alloys as well as with both low carbon and AHSS DP steel. The materials strength and thicknesses of the flyer metals in this case are higher. As it was presented during the numerical analyses in the previous chapter for the thick flyer metal sheets, the lost in velocity using the linear coil was significant (Section 2.5.2). This was clear while exploring the weldability of different couples where the limitation of the linear coil was detected when the flyer is thicker. Table 3.7 summarizes different weldability results in this case. The successful combinations between different similar and dissimilar alloys show that the pulse welding technology has large scopes of applications for both similar and dissimilar metal alloys. Now that the weldability has been proven for all the combination, attention is given to specific couples of interest.

3.4.2 Experimental process welding windows for aluminum 5xxx with DC04 steel

3.4.2.1 Aluminum 5754 ($e_f = 0.5$ mm) to steel DC04 ($e_p = 0.8$ mm) welding

The configuration tested is the MPW with a linear copper coil (Fig. 3.2). The thicknesses of the flyer 5754 and the parent DC04 are 0.5 and 0.8 mm respectively. The experimental welding windows were built for the distances between the insulators $D_1 = 15$ mm and $D_2 = 25$ mm.

Parent metal	E_{min}(kJ)	h_h(mm)
1050 (0.5 mm)	4	1.6
5754 (0.5 mm)	6	1.6
5182 (1.2 mm)	6	1.6
6016 (1 mm)	6	1.6
DP450 (1.2 mm)	7	1.6
DP450+ZE (1.2 mm)	9	1.6
DP980 (1 mm)	7	1.6
DP980+ZE (1 mm)	9	1.6
DP1180 (1 mm)	7	1.6
DC04 (0.62 mm)	4	1.6
DC04+ZE (0.67 mm)	6	1.6
DC01 (0.8 mm)	4	1.6

Table 3.6: weldability tests between aluminum 1050 and different aluminum and steel alloys using a linear coil in MPSW configuration
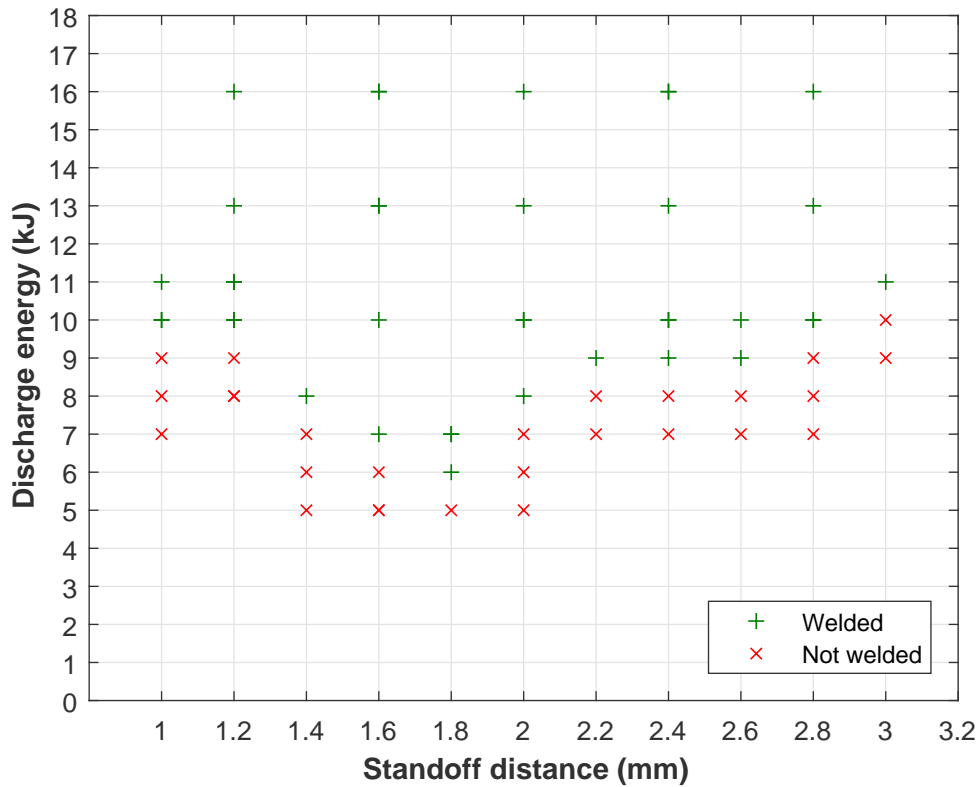
Figure 3.13: MPW experimental welding window for 5754 aluminum ($e_f = 0.5$ mm) with DC04 steel; $D = 15$ mm

These welding windows are presented in Fig. 3.13 and Fig. 3.14. These experimental welding windows show that the required discharge energies to achieve welding is higher when having low standoff distances (less than 1.4 mm when $D = 15$ mm and less than 1.2 mm when $D = 25$ mm) and when having higher distances (higher than 2.2 mm for both D).

Welded specimens were tested in quasi-static lap shear conditions for standoff distances at 1.2, 1.6, 2 and 2.4 mm and for each at 3 energy levels 10, 13 and 16 kJ respectively. The maximum load results are presented in Fig. 3.15 and Fig. 3.16. The failure for maximum load values less than 2500 N was occured in the welding and for higher than 2500 N no failure has occured in welding, it is the aluminum sheet that was teared (Fig. 3.17). The welding strength is the highest in the middle ranges of standoff distances i.e. $1.2 < h < 2.4$ and they are higher when the distance D is higher i.e. $D = 25$ mm.

3.4.2.2 Aluminum 5182 ($e_f = 1.2$ mm) to steel DC04 ($e_p = 0.8$ mm) welding

The configuration tested is also the MPW where first investigations were achieved using the same linear coil. The thicknesses of the flyer 5182 and the parent DC04 are 1.2 and 0.8 mm respectively. The discharge energies needed to achieve welding were over 13 kJ and the coil lifetime was so bad (not more than 8 shots) due to high thermomechanical stresses developed within the active length of the coil facing the flyer metal (Fig. 3.18) . Also, the welds were so weak that they broke at very low loads (not exceeding the 600N) in the quasi-static lap shear tests. Once again the limitation of the linear coils is reached and an O-shape steel coil was used instead (Fig. 3.3). The experimental welding window were then built using this coil for distances between insulators $D_1 = 15$ mm and

	5754	5754	5182	5182	6016	6016	DP 450	DP 450	DP 1000	DP 1000	DC04	DC04
5754 (0.5 mm)	✓	✓	✓	✓	✓	✓	✓	✓	✓	✓	✓	✓
5182 (1 mm)	✓	✓	−	−	−	−	✓	✓	−	−	✓	✓
5182 (1.2 mm)	✓	✓	−	−	−	−	✓	✓	−	−	✓	✓
5182 (1.4 mm)	×	✓	−	−	−	−	×	✓	−	−	×	✓
5182 (2 mm)	×	✓	−	−	−	−	×	✓	−	−	×	✓
6013 (1.4 mm)	−	−	−	−	−	−	−	−	×	✓	×	✓
6016 (1 mm)	✓	✓	−	−	−	−	−	−	−	−	✓	✓
	L	**O**	**L**	**O**	**L**	**O**	**L**	**O**	**L**	**O**	**L**	**O**

×: Not welded; ✓: Welded; −: Not tested; L: Linear coil; O: O-shape coil

Table 3.7: weldability of different metals combination

Figure 3.14: MPW experimental welding window for 5754 aluminum ($e_f = 0.5$ mm) with DC04 steel; $D = 25$ mm

Figure 3.15: quasi-static lap shear maximum load for MP welded 5754 aluminum ($e_f = 0.5$ mm) with DC04 steel; $D = 15$ mm

Figure 3.16: quasi-static lap shear maximum load for MP welded 5754 aluminum ($e_f = 0.5$ mm) with DC04 steel; $D = 25$ mm

Figure 3.17: 5754 sheet teared during quasi-static lap shear test

Top view   Side view
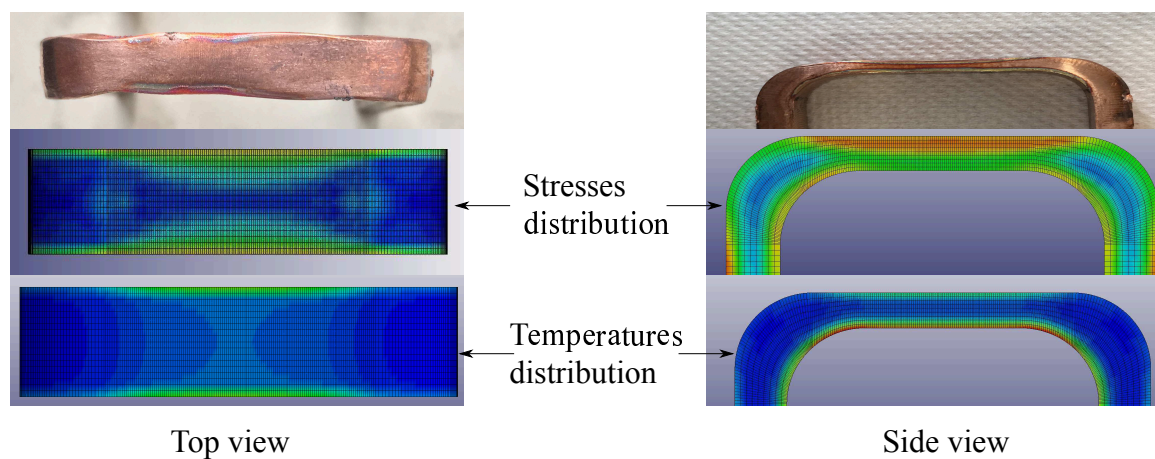
Figure 3.18: stresses and temperatures distribution in linear coil
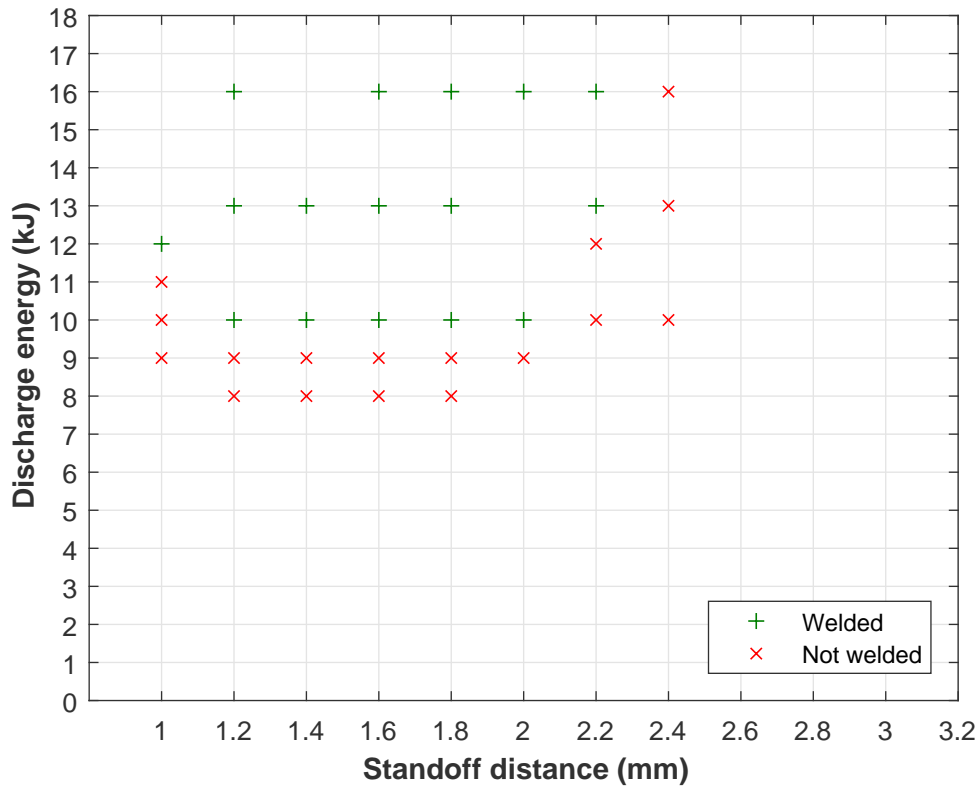
Figure 3.19: MPW experimental welding window for 5182 aluminum ($e_f = 1.2$ mm) with DC04 steel; $D = 15$ mm

$D_2 = 25$ mm and they are presented in Fig. 3.19 and Fig. 3.20 . As a first analysis, the welding window is smaller than it was in the thin aluminum case since welding started to become difficult from a 2 mm standoff distance and no welding was obtained for $h \geq 2.4$ mm when $D = 15$ mm and for $h \geq 2.6$ when $D = 25$ mm. The discharge energy required for welding at small distances (for $h < 1.2$ mm) is also higher than that required for average standoff ranges (1.2 mm$\leq h \leq 2$ mm).

To analyze the strength of the welds, quasi-static lap shear tests were done for standoff distances at 1.2, 1.6, 2 and 2.4 mm and for each at 3 energy levels 10, 13 and 16 kJ respectively (Fig. 3.21 and Fig. 3.22). The first important conclusion is that the welds with low distance D (maximum load less than 2 kN) are very weak when compared to the welds with higher D (maximum load higher than 6 kN). Also, the weld strength is higher at the low range of the medium standoff distances i.e. from 1.2 to 1.6 mm. The strength of the welds decreases rapidly when having $h > 1.6$ mm. In all cases, the failures occured in the weld line (Fig. 3.23) .

3.4.2.3 Discussion - Combination between experimental results and numerical conclusions

In Fig. 3.24 the welding windows are superposed together. The first conclusion that can be made is that the harder is the material, the smaller the welding window is even when using higher efficiency coil. The second conclusion is concerning D where in both cases the smaller the D, the smaller is the welding window. When comparing the strength of welding, the effect of D is insignificant in the thin case but in the case of the thick metal, the maximum load from lap shear tests is so much higher in the case where D is high. The lap shear tests showed that in the case of the thin sheet metal, the strength is high on large standoff ranges (from 1.2 mm up to 2.4 mm) and starts

133
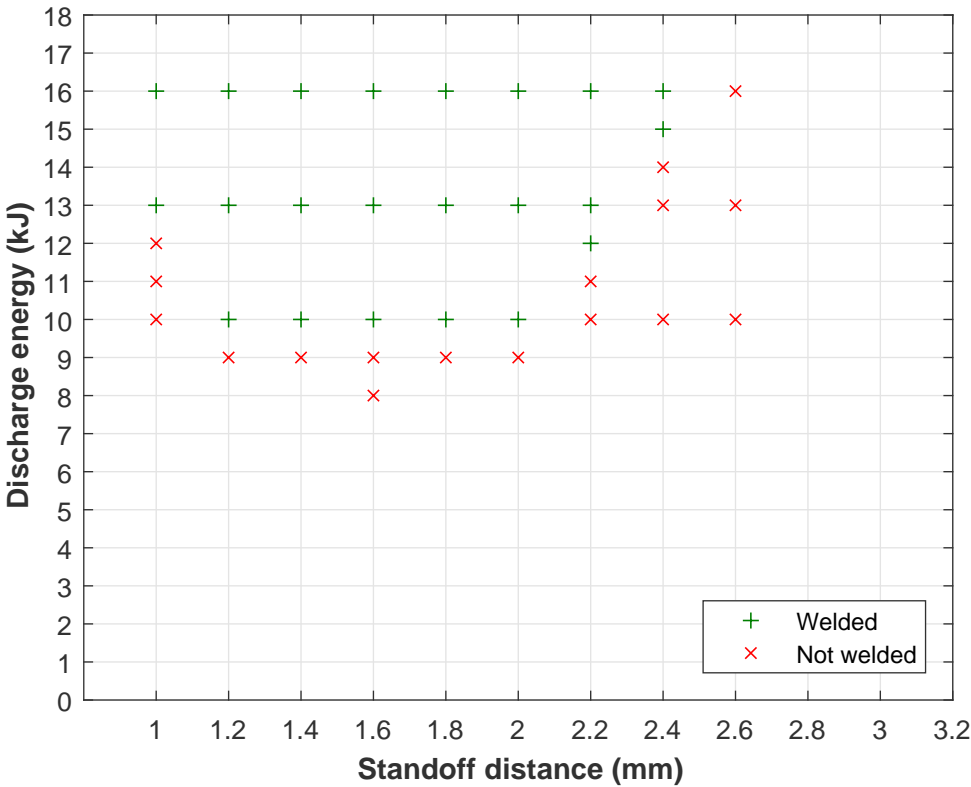
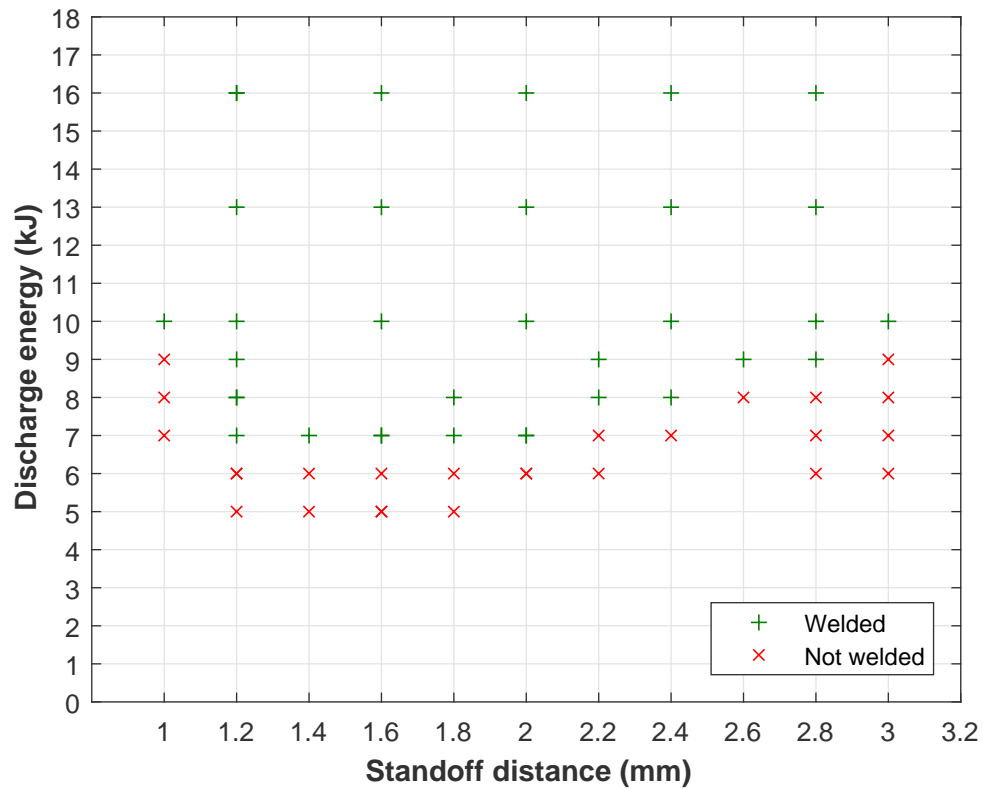Figure 3.20: MPW experimental welding window for 5182 aluminum ($e_f = 1.2$ mm) with DC04 steel; $D = 25$ mm
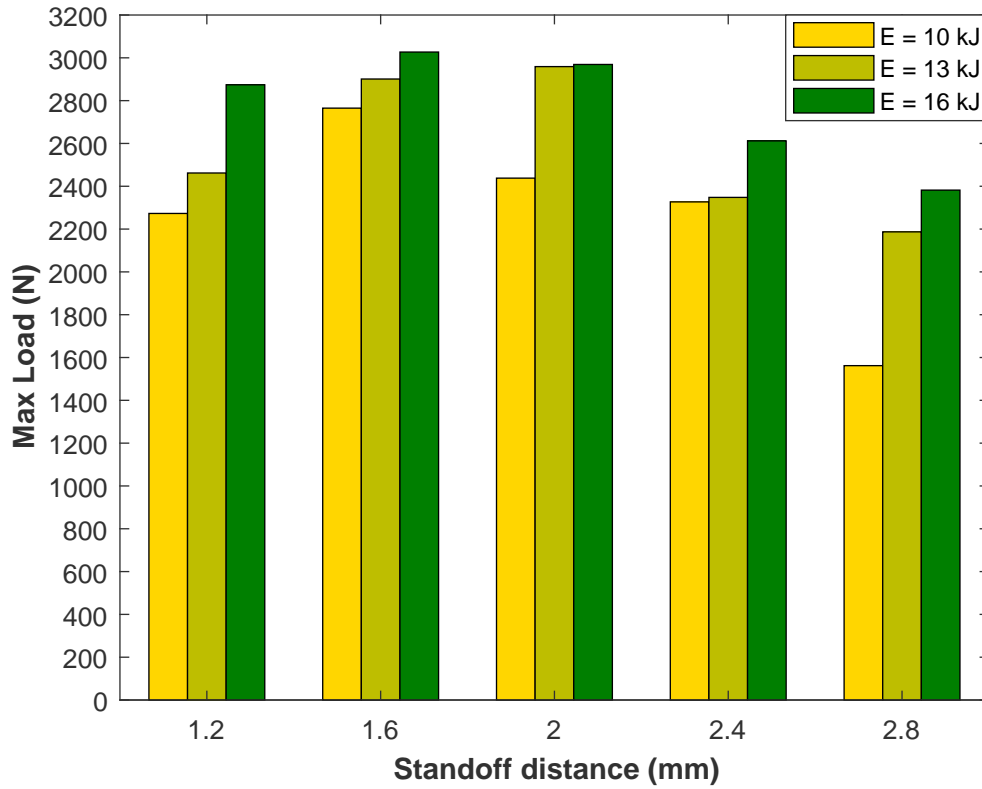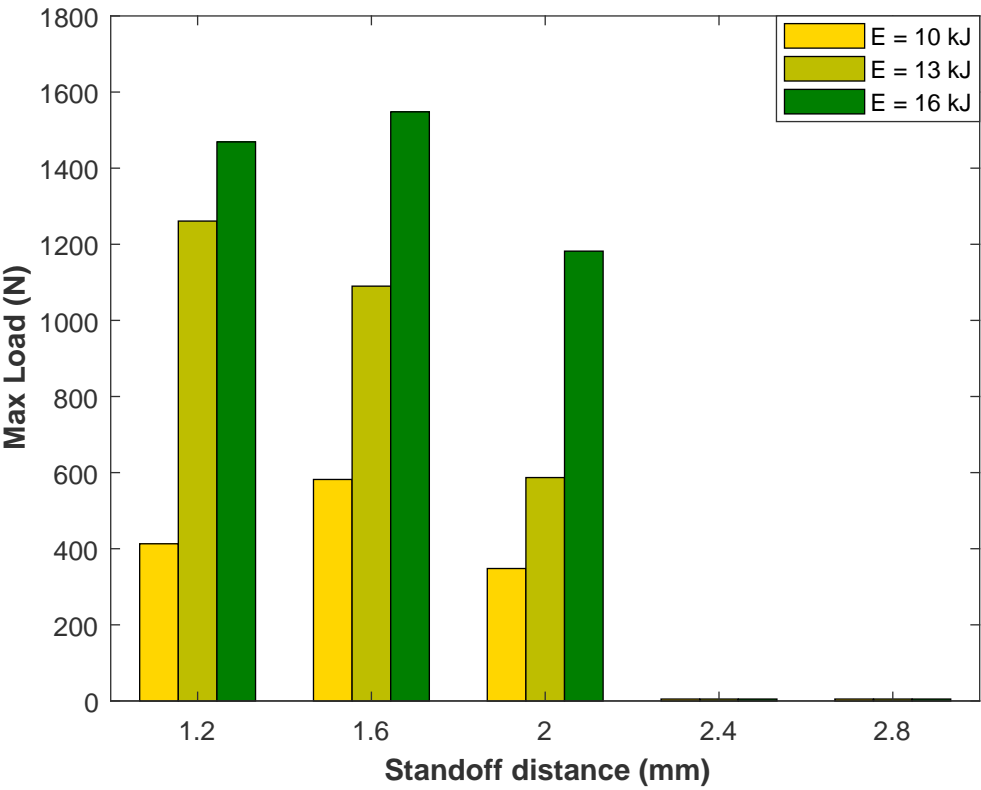

Figure 3.21: quasi-static lap shear maximum load for MP welded 5182 aluminum ($e_f = 1.2$ mm) with DC04 steel; $D = 15$ mm
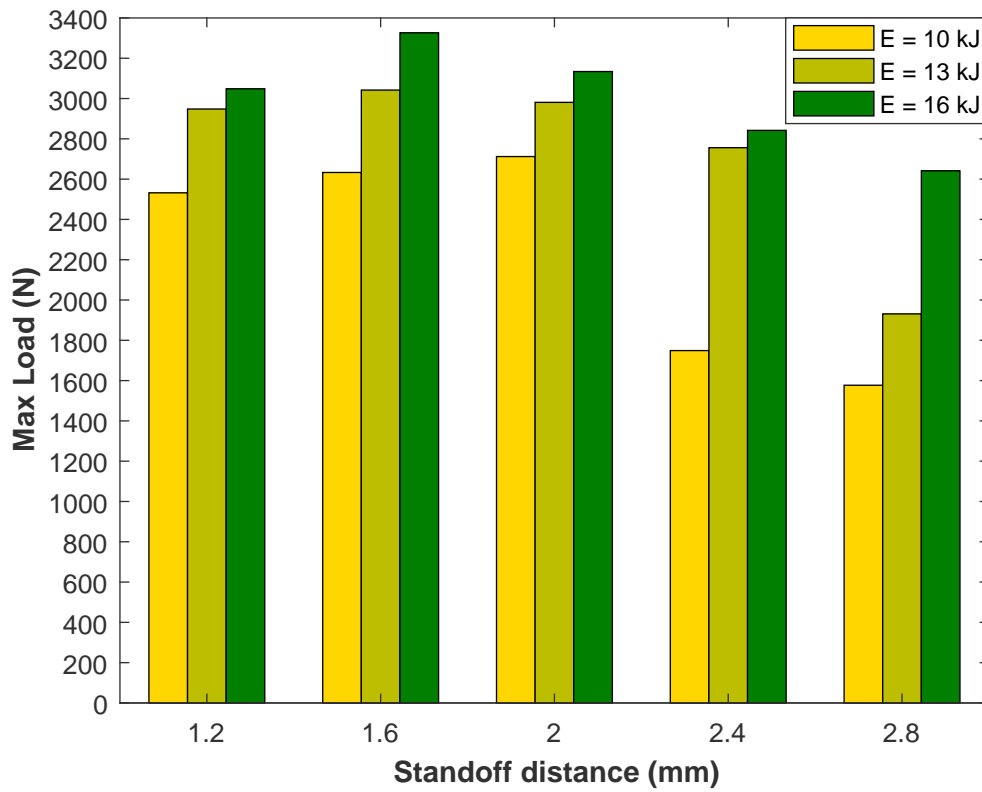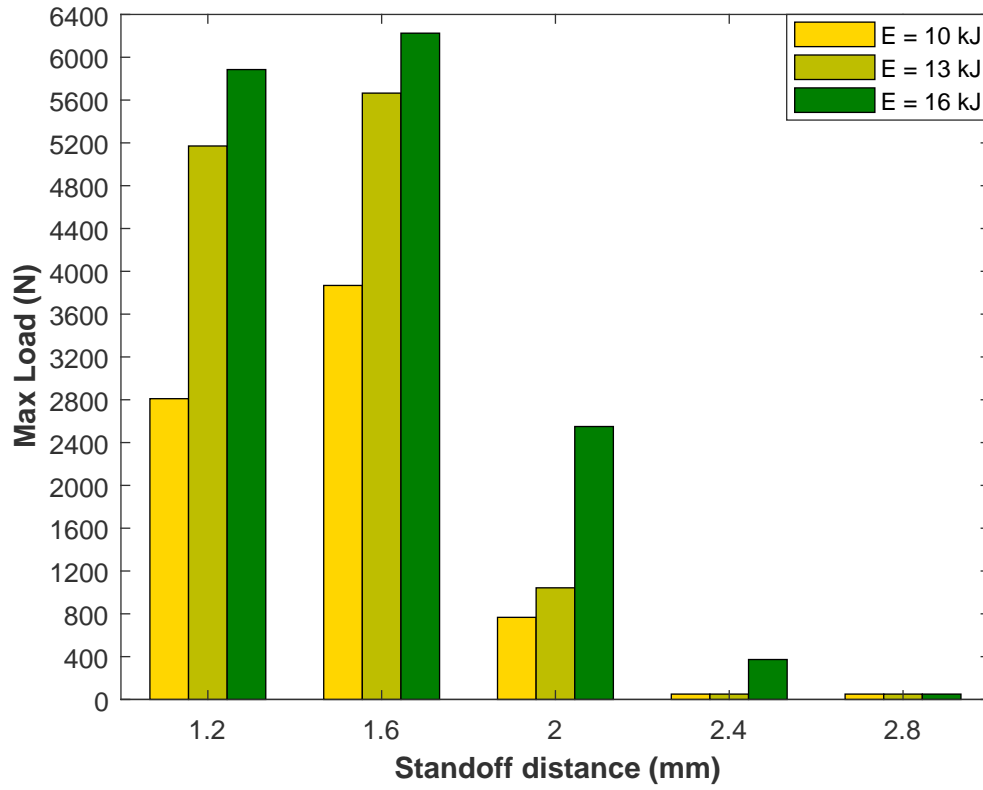
Figure 3.22: quasi-static lap shear maximum load for MP welded 5182 aluminum ($e_f = 1.2$ mm) with DC04 steel; $D = 25$ mm
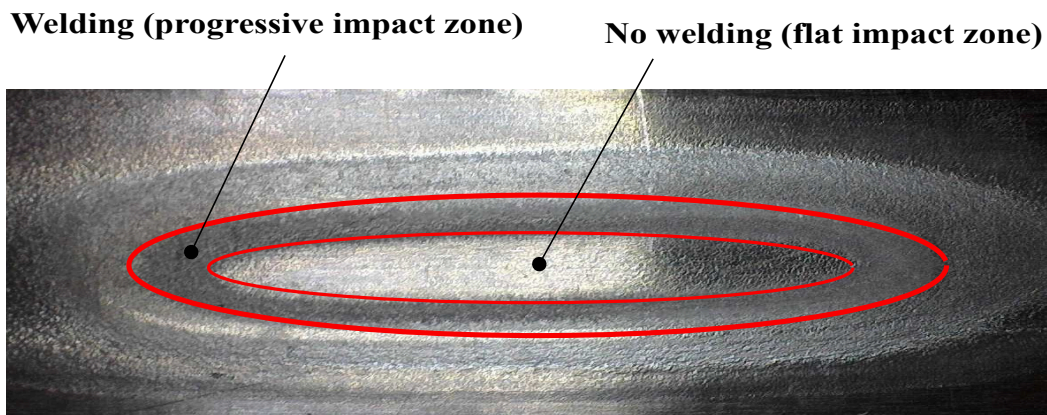
Figure 3.23: elliptical weld line after failure
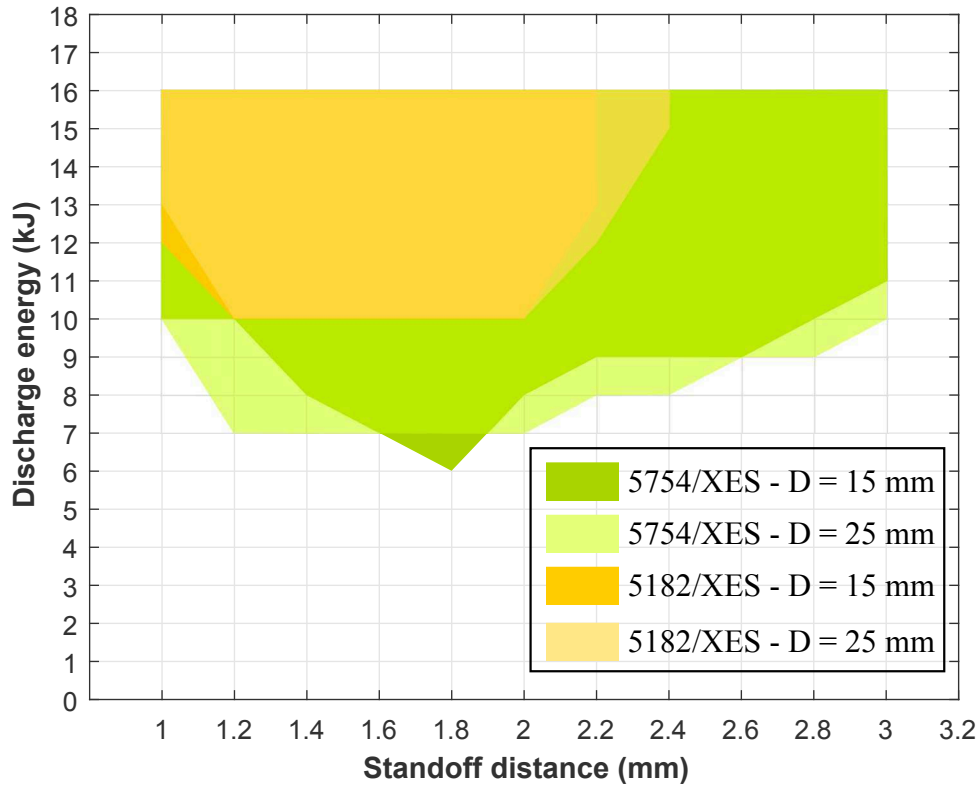
Figure 3.24: experimental welding windows superposition

to decrease after that. In the thick sheet metal case, the welding strength is high for low standoff distances (from 1.2 mm to 1.6 mm) and decreases rapidly after that. In addition to all this, the energy influence on the welding strength is less remarkable in the thin aluminum case than it is in the thick aluminum case.

According to the welding achieved and the strength in lap shear testing, it will be important now to show the optimal experimental parameters for both thin and thick flyer regarding the four region that were concluded from the previous chapter numerical analysis (Fig. 2.42). This is done in Fig. 3.25. The optimal welding conditions are in the region 2 and at the interface of region 1 - region 2 for both thin and thick metal case where in the latter the minimal energy required is higher and the standoff distances ranges are smaller than the former. In both cases, the distance D as it was concluded is better when having $D = 25$ mm.

These optimal welding windows deduced from the welds strength, allow to superpose the velocities values and the angles in these ranges and which are given also in Fig. 3.25. The velocities are deduced from the velocities graphs of numerical model developed in the previous chapter for the corresponding standoff distances and the discharge energies ranges. For the thin aluminum sheet case, these velocities are between 425 and 780 m/s and for the thick aluminum sheet they are between 470 and 700 m/s. Somehow, the ranges are not so far one from the other. Concerning the angles, the first thing was to do measurements on the welding ellipse on the specimens so that the welding can be defined regarding the coil symmetrical axis (Fig. 3.26) . The measurements of the lower and higher limit of the optimal welding window are listed in Table 3.8. These values are
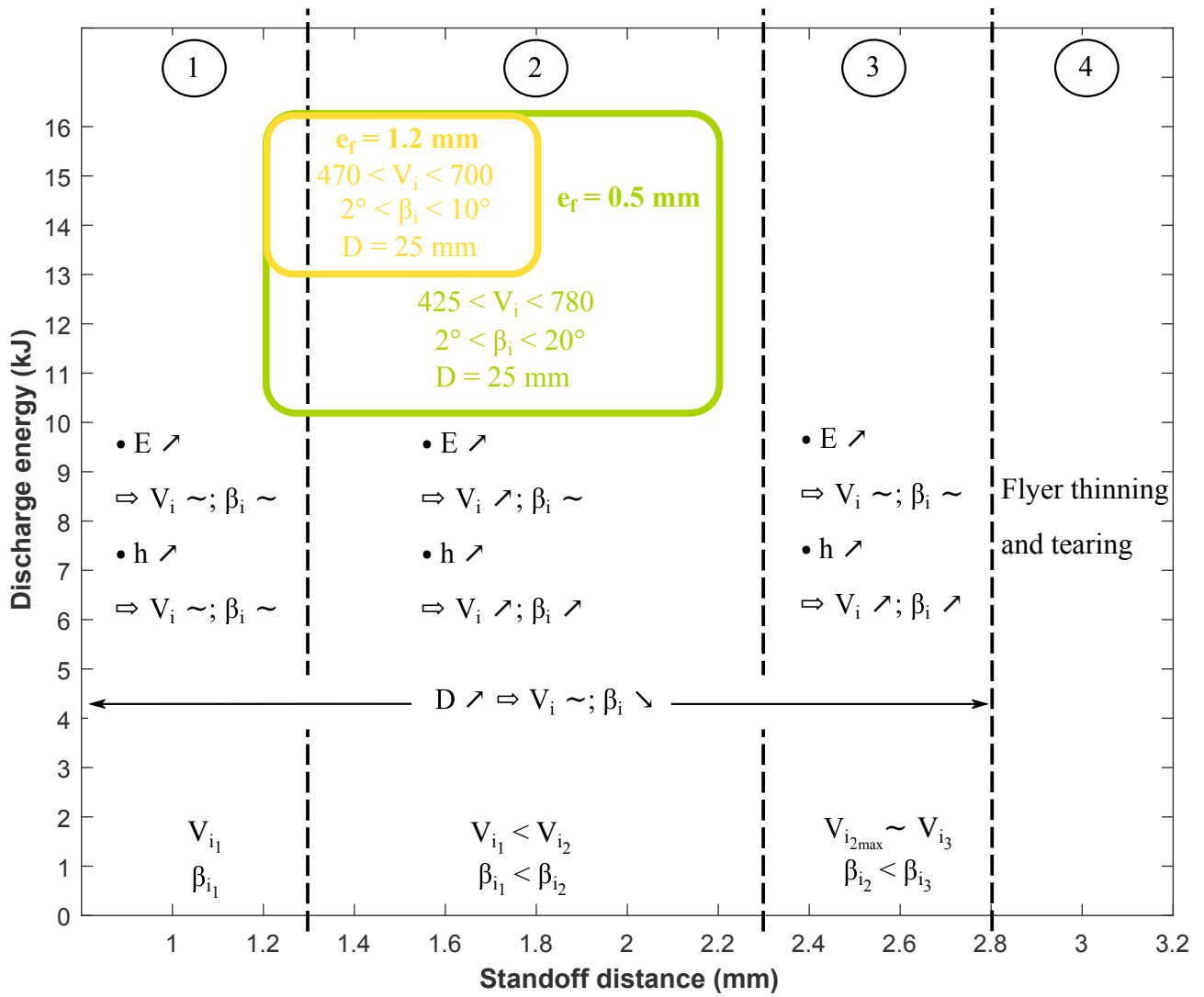
Figure 3.25: optimal welding conditions on the numerical conclusion graph

	$e_f = 0.5$ mm				$e_f = 1.2$ mm			
	E = 10 kJ		E = 16 kJ		E = 13 kJ		E = 16 kJ	
	h (mm)		h (mm)		h (mm)		h (mm)	
	1.2	2.2	1.2	2.2	1.2	1.8	1.2	1.8
$l_f/2$ (mm)	1.35	1	1.75	1.55	0.6	0.4	0.9	0.5
l_w (mm)	1	1	1.1	1.5	1.2	1.2	1.2	1.6

Table 3.8: measurements on the welding ellipse
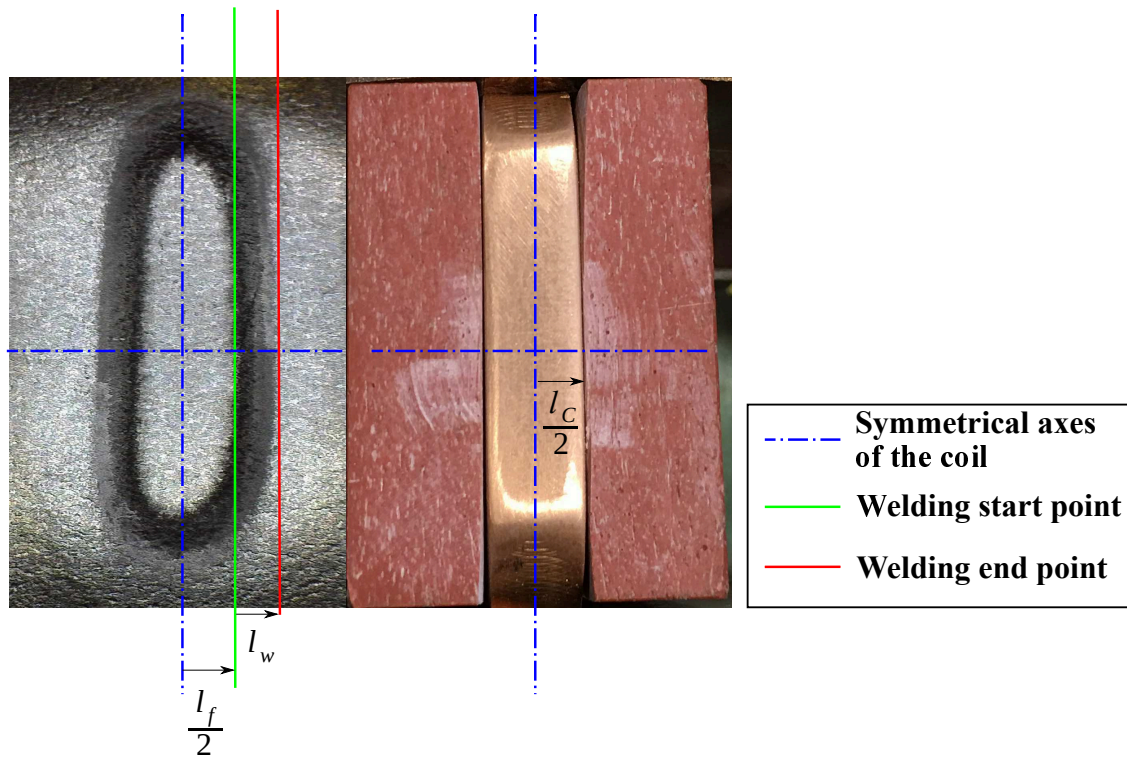
Figure 3.26: welding ellipse measurements

then superposed with the numerical graphs of β_i as it is represented in Fig. 3.27 and Fig. 3.28 and hence showed values between 2° and 20° for the thin sheet metal case and between 2° and 10° for the thick metal case.

When looking to the complete welding windows in Fig. 3.24 and at the optimal welding windows, qualitative analysis can be done:

- at the interface of 1-2 regions and in the region 2, the standoff distance allows the sheet metals to attain high enough impact velocities values at different discharge energy levels. The required energy levels are higher of course for the thicker sheet metals;

- the standoff distances which allows to increase the velocity, they also increase the angles up to a limit where this increase affect the progressive impact phenomenon so that the degradation of welding strength is observed;

- when having a small D (15 mm in our case), the angles are higher and then β_i increases faster which gives a smaller welding window. So, increasing the standoff distance distance D (25 mm for instance), which decreases angles, allows having some equilibrium with the increase in angle due to the increase of standoff distances up to some limit where the increase in angle due to h becomes dominant; this compensation effect leads to a bigger welding window in higher D case.

A good combination between these parameters is then required in a way that the velocity stays sufficient and the increase in angle stays in an acceptable range. This combination is more easy to have in the thin aluminum flyer case where the welding window is large enough to have a variety

(a)

(b)
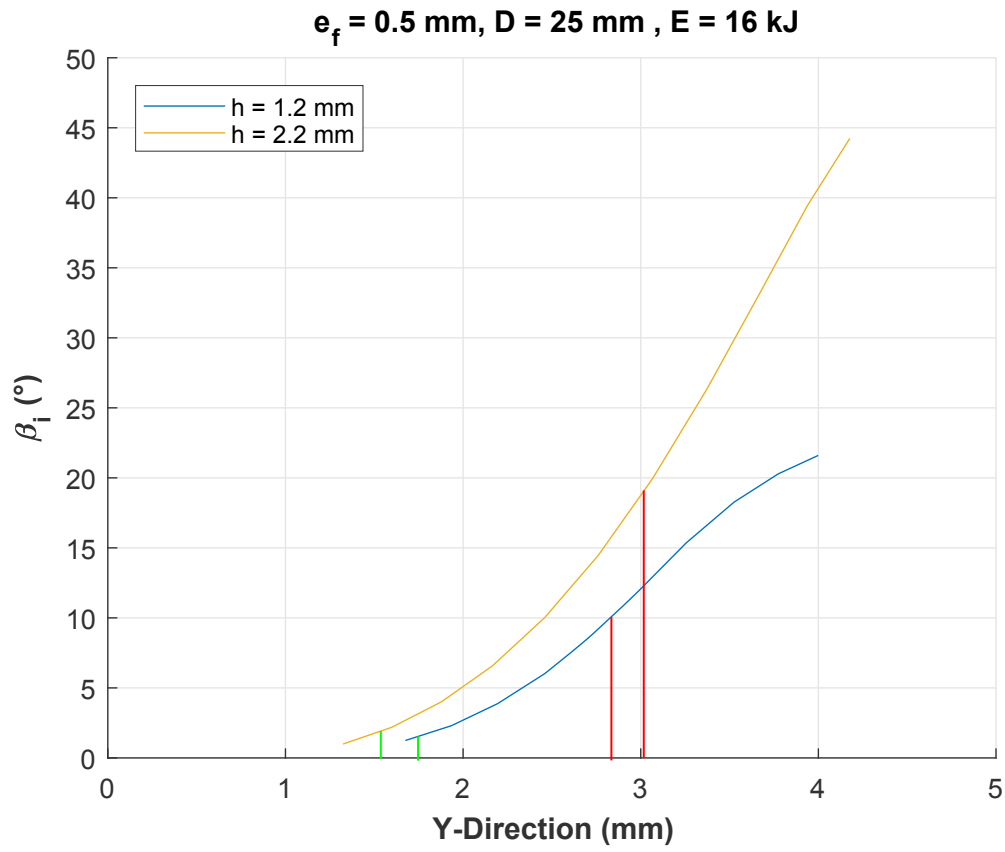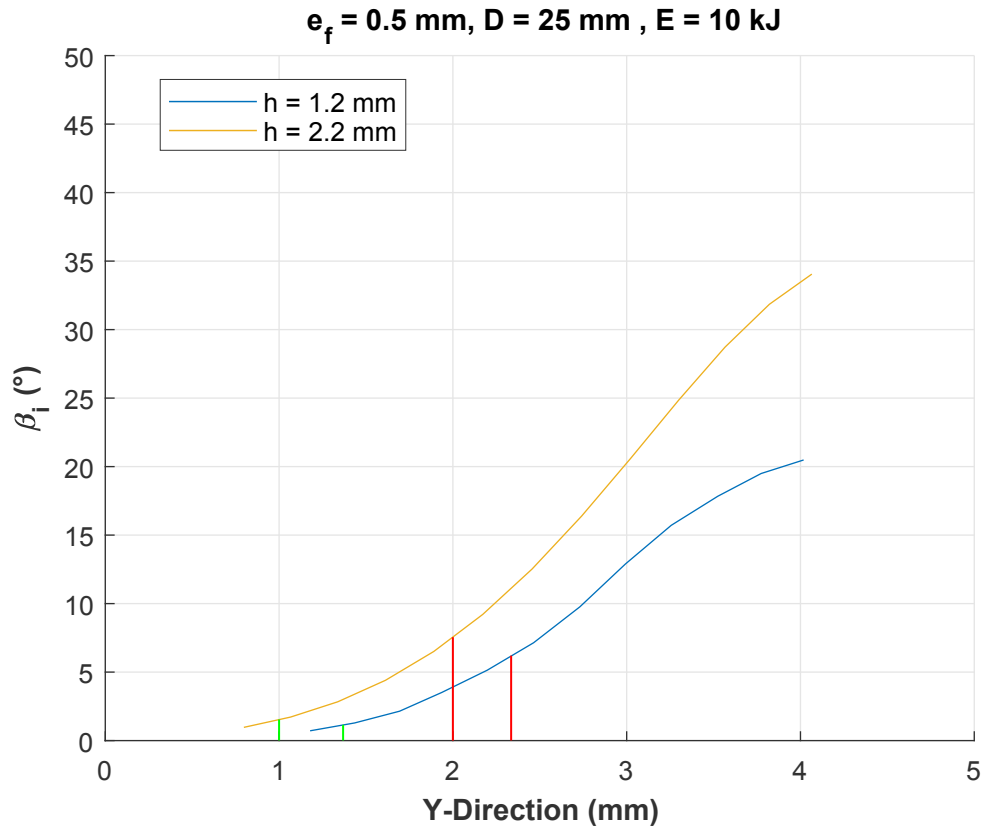
Figure 3.27: β_i for optimal welding in thin aluminum sheet case

e_f = 1.2 mm, D = 25 mm , E = 13 kJ

(a)

e_f = 1.2 mm, D = 25 mm , E = 16 kJ

(b)
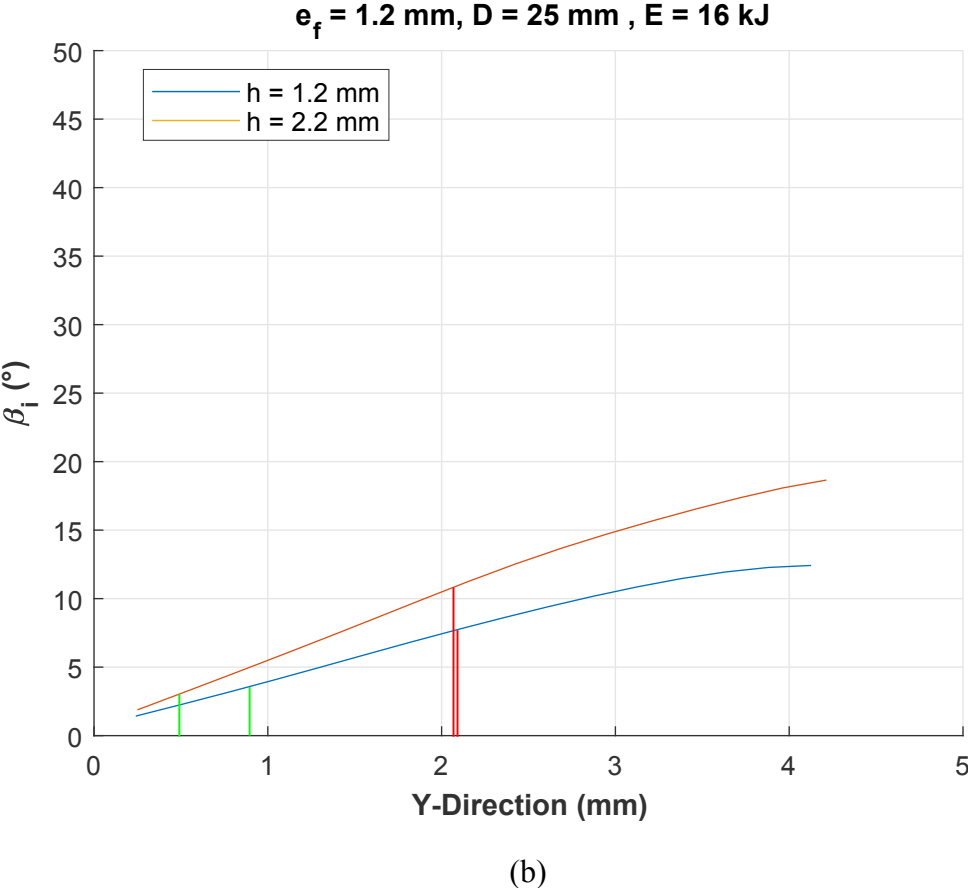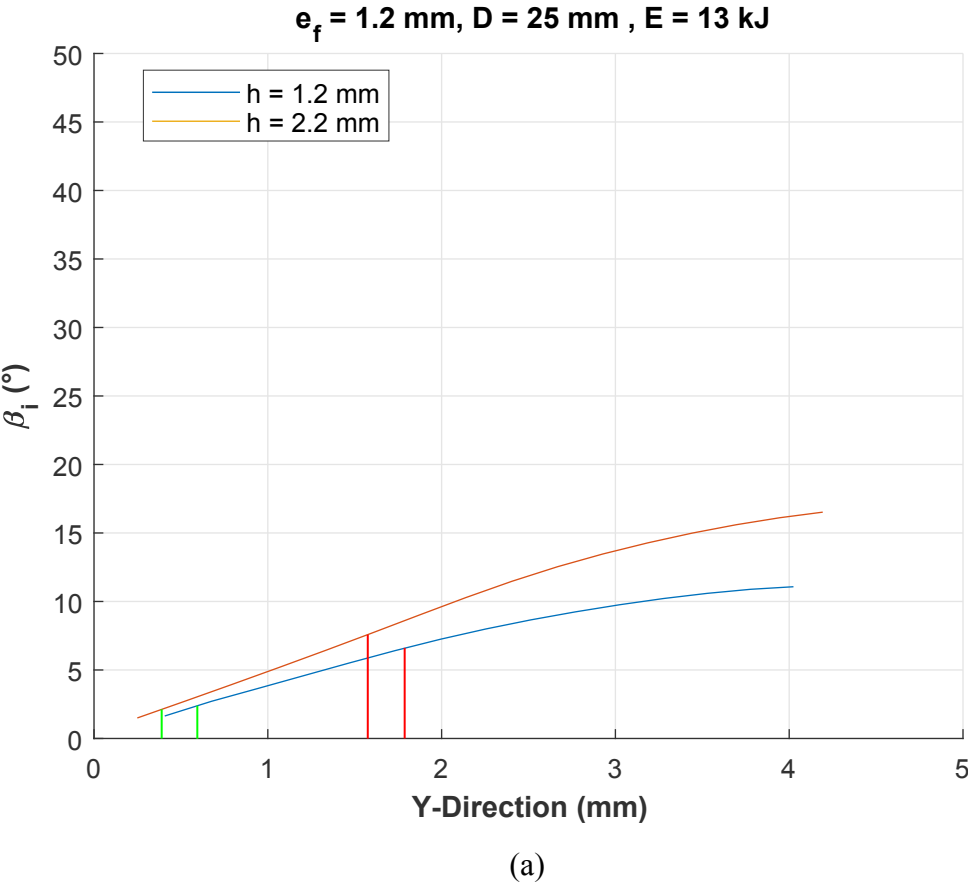
Figure 3.28: β_i for thick aluminum sheet case
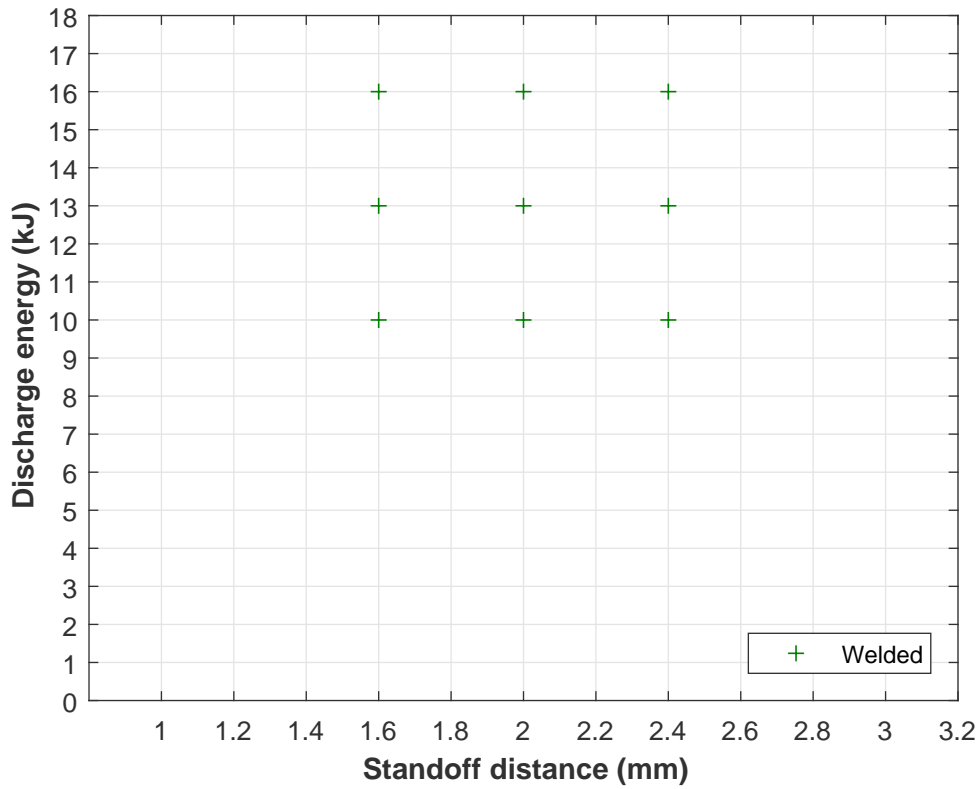
Figure 3.29: MPW experimental welding for 5182 aluminum ($e_f = 1.2$ mm) with aluminum 5754 ($e_f = 0.5$ mm); $D = 15$ mm

of possible standoff distances to use. In the thick sheet metal case, the best is to use low ranges to middle ranges standoff distances with a higher discharge energy.

3.4.3 Experimental welding windows for two other combinations

3.4.3.1 Similar MPW and MPSW between aluminum 5182 ($e_f = 1.2$ mm) and aluminum 5754 ($e_p = 0.5$ mm)

As said in the introduction of this dissertation, the main purpose of the study is to use the MPW/MPSW as a solution for joining metals with FRPC and the first configuration presented in Fig. 1 may include aluminum or steel metallic inserts. For this purpose, the investigation of the welding between the 5182 and 5754 was also included during this phase. This investigation was done using an O-shape steel coil.

In the MPW configuration, the worst case for the distance between the insulators was chosen, i.e. $D = 15$ mm, in order to see the behavior of the similar welding case. The standoff distances are 1.6, 2 and 2.4 mm and for each case three levels of discharge energies were applied: 10, 13 and 16 kJ. In all of these cases (Fig. 3.29), successful welding were obtained and then three specimens for each case were tested in quasi-static lap shear condition to evaluate the welding strength and the average values of maximum loads are presented in Fig 3.30. .

In the MPSW configuration, the hump dimensions (Fig. 3.10) were $l_h = 12$ mm, $L_h = 20$ mm, $l'_h = 40$ mm and $L'_h = 55$ mm.
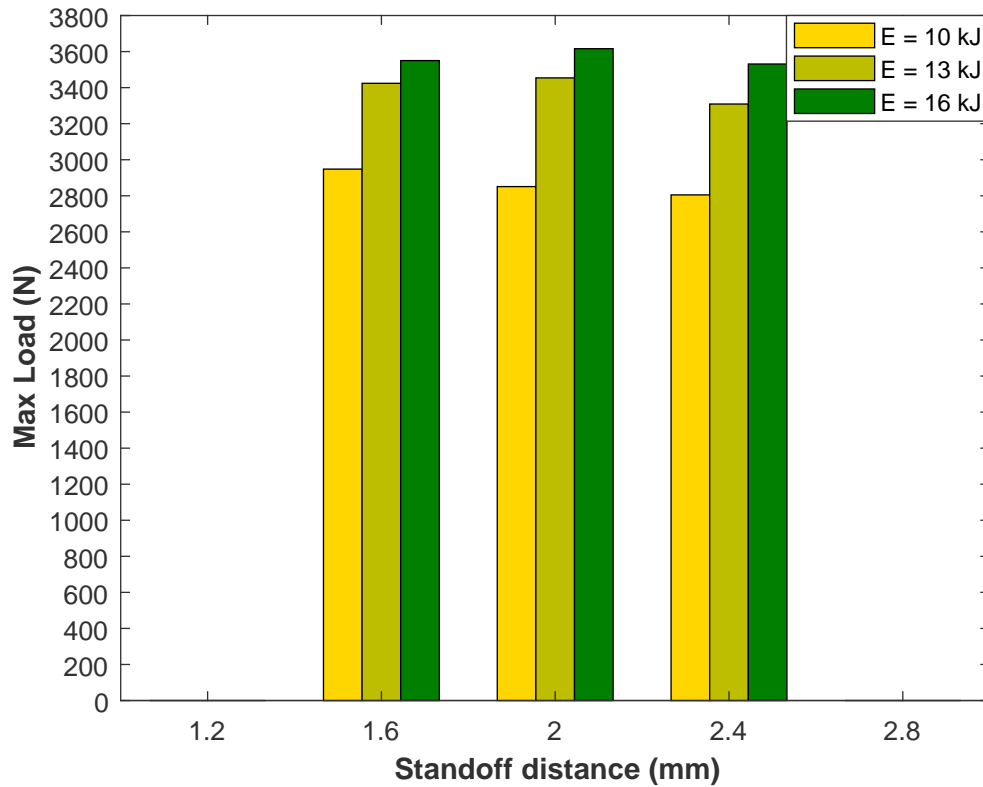
Figure 3.30: quasi-static lap shear maximum load for MP welded 5182 aluminum ($e_f = 1.2$ mm) with aluminum 5754 ($e_f = 0.5$ mm); $D = 15$ mm

At different energies and different standoff distances the failure was occuring in the aluminum 5754 sheets as it was presented in Fig. 3.17.

3.4.3.2 Dissimilar MPW between aluminum 6013-T4 ($e_f = 1.4$ mm) and steel DP1000 ($e_p = 1$ mm)

The aluminum 6013-T4 is gaining attention in automotive because of its superior strength in service and its good corrosion resistance. One of the candidate application is the automotive seat frames where Faurecia Seating is one of the worldwide leader in this field. The introduction of the 6013-T4 will mean a combination between it and other steels widely used in automotive seats where DP1000 is one of these. Therefore, an investigation for the joining between these two materials using magnetic pulse technologies will be interesting. The thickness of the 6013-T4 is 1.4 mm and for the DP1000 it is 1 mm. In the MPW configuration, the distance between the insulators D is 18 mm in a way to have a middle range between the 15 and 25 mm. The experimental results are represented in Fig. 3.31. The specimens were then tested in lap-shear and the loads are represented in Fig. 3.32.

3.4.4 Mechanical testing for the welding joints

Now that the weldability of a variety of combinations is proven, the next step will be to investigate the strength of dissimilar joints between aluminum alloys and steels. To do so, each of the next MPSW combinations was tested in quasi-static lap-shear, dynamic lap-shear as well as fatigue
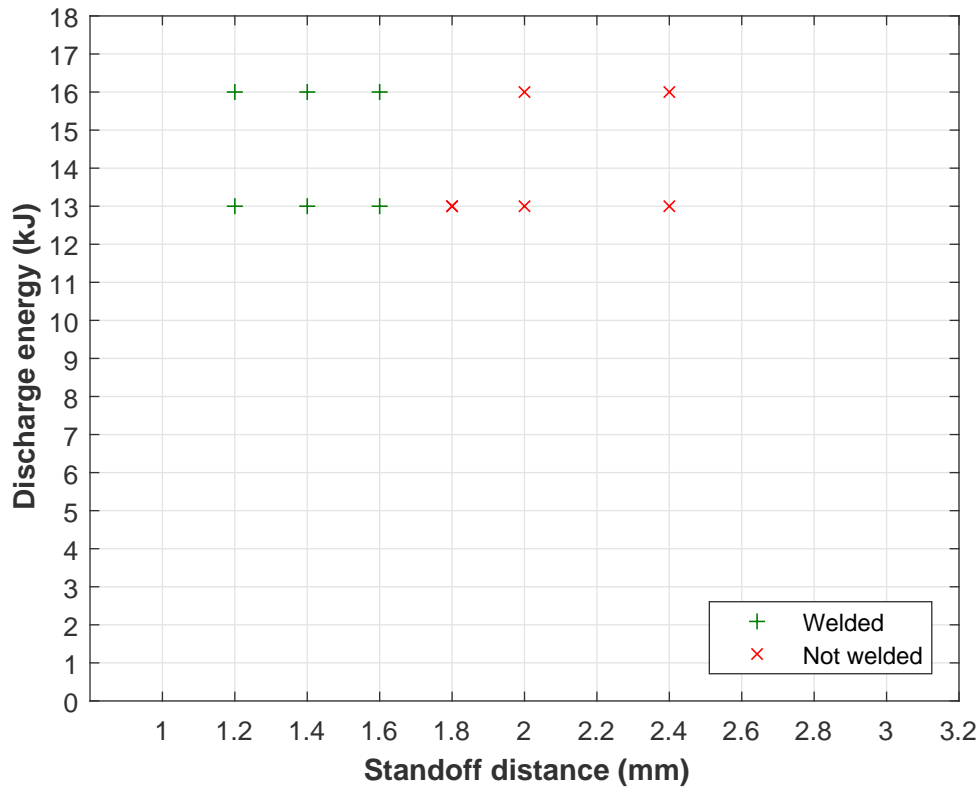
Figure 3.31: MPW between 6013-T4 ($e_f = 1.4$ mm) and steel DP1000 ($e_f = 1$ mm)
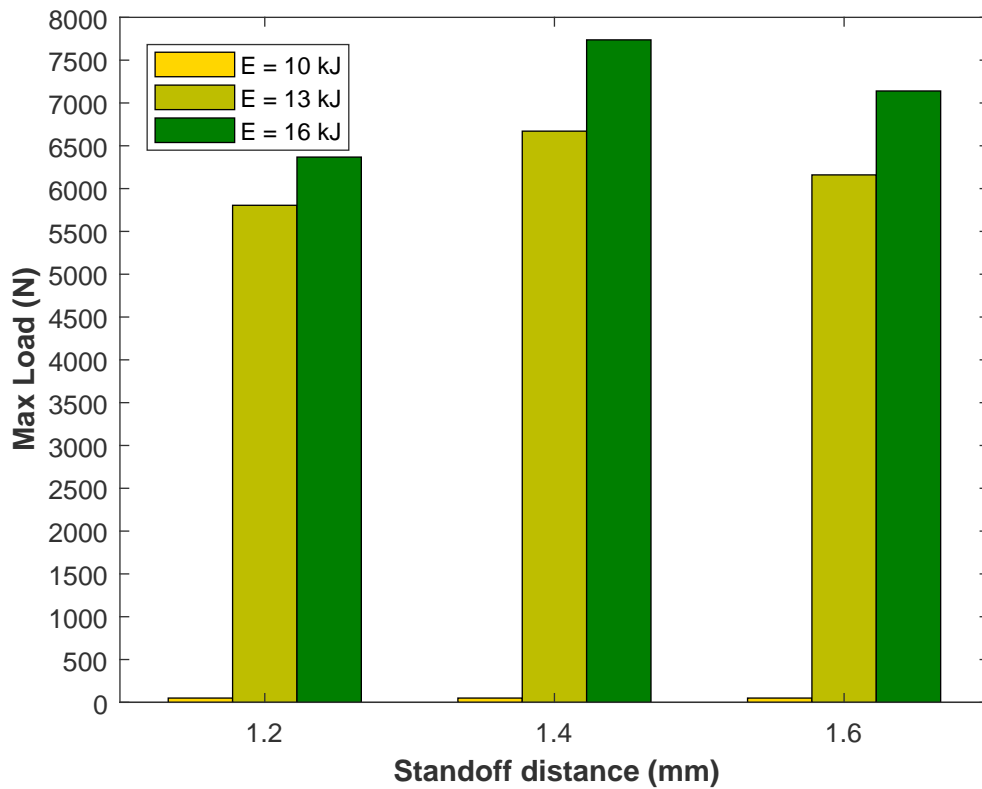
Figure 3.32: quasi-static lap shear maximum load for MP welded 6013-T4 aluminum ($e_f = 1.4$ mm) with DP1000 steel; $D = 18$ mm
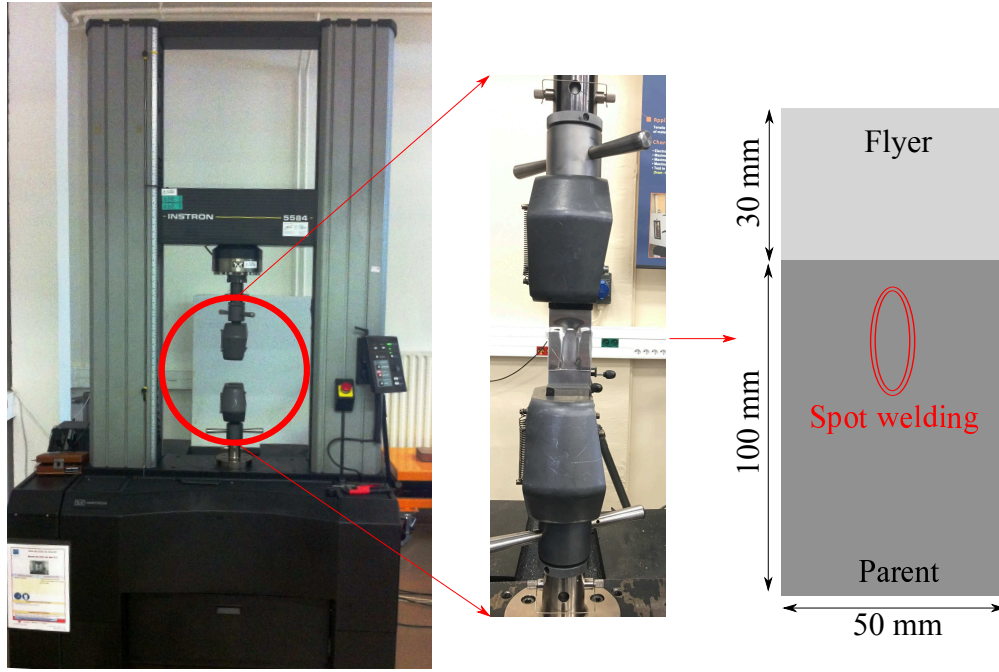
Figure 3.33: quasi-static lap-shear test

lap-shear:

- 5182 ($e_f = 1.2$ mm) with DC04 ($e_p = 0.8$ mm)

- 5182 ($e_f = 1.2$ mm) with DP450 ($e_p = 1.17$ mm)

- 6013-T4 ($e_f = 1.4$ mm) with DP1000 ($e_p = 1$ mm)

- 6016 ($e_f = 1$ mm) with DC04 ($e_p = 0.8$ mm)

In each test three specimens were tested.

The focus on the MPSW comes from the fact of being easier for industrial application as it was presented in the litterature review. The inductor used is a steel O-shape (Fig. 3.3).

The last important points to mention are:

- the same hump was used to weld different tested combinations: $l_h = 12$ mm, $L_h = 20$ mm, $l'_h = 40$ mm and $L'_h = 55$ mm;

- the same discharge energy was used 16 kJ to achieve all weld joints.

For the 6013-T4 to DP1000 welding case, the MPW configuration was also tested and the parameters for welding were $D = 18$ mm and $h = 1.4$ mm (the optimum point found in the experimental welding window).

All the tests were performed in the Dynamic and static test centre - CRED of GeM at ECN. For the quasi-static lap-shear an INSTRON 5584 (150 kN) machine was used and the velocity was of 10^{-2} mm/s (Fig. 3.33). For the dynamic tests, a MTS 20 kN machine was used and the velocity was of 614 mm/s (Fig. 3.34). For the fatigue tests, an INSTRON E10000 (linear-torsion 10 kN-150
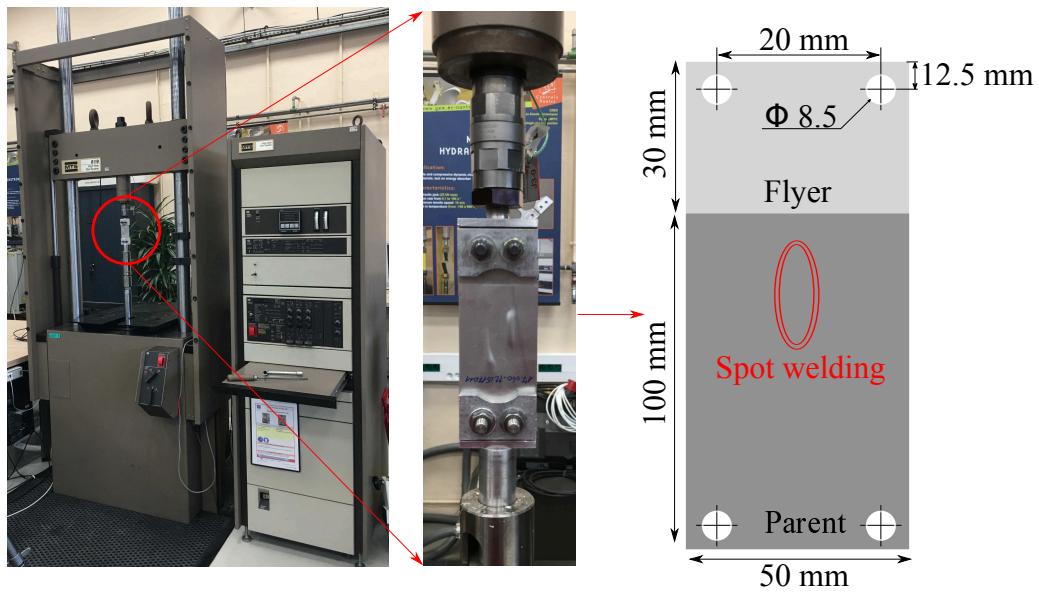
Figure 3.34: dynamic lap-shear test
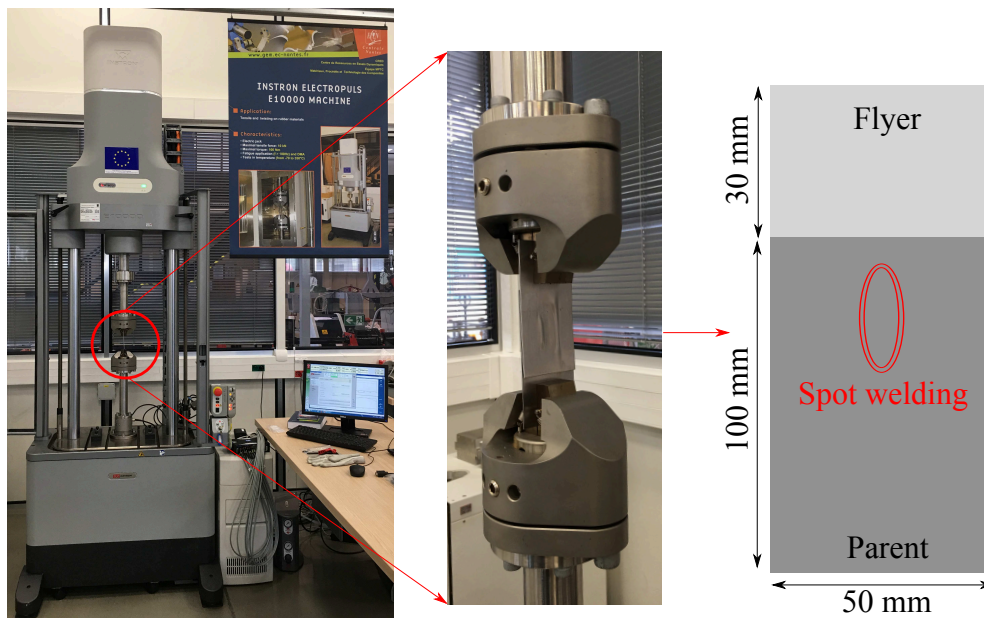
Figure 3.35: fatigue lap-shear test
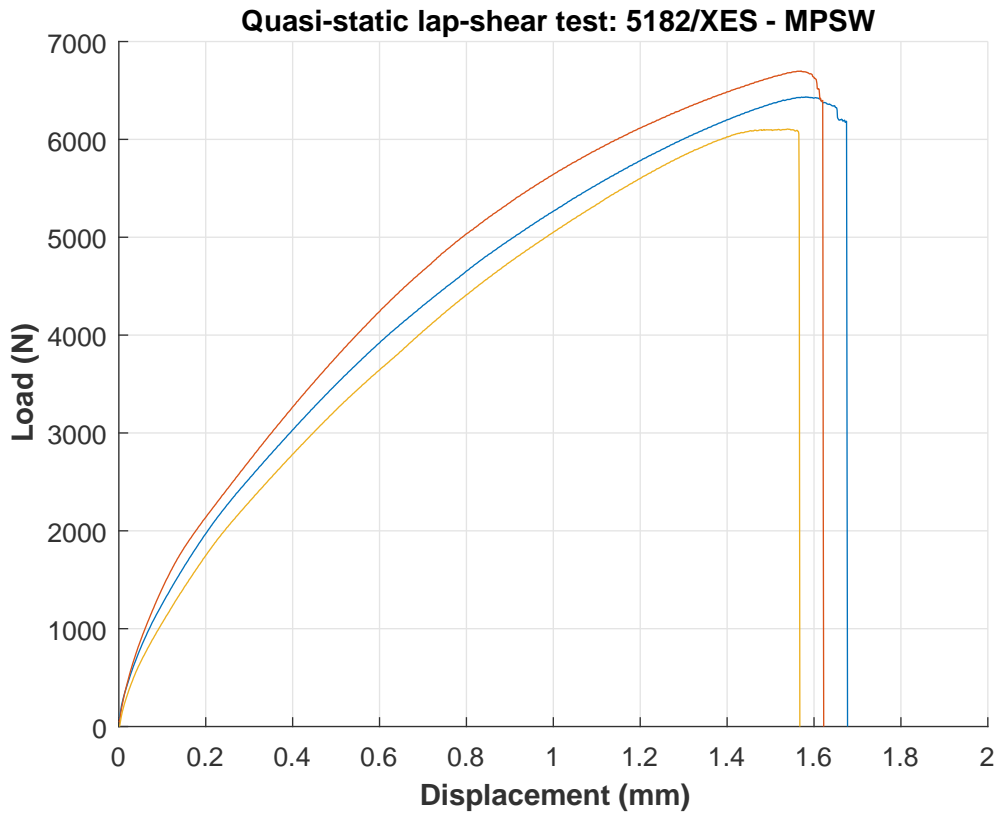
Figure 3.36: quasi-static lap-shear test for MPS welded 5182 ($e_f = 1.2$ mm) with DC04 ($e_p = 0.8$ mm)

Flyer	Parent	Configuration	F_{max} (kN)	Number of cycles		
				Test 1	Test 2	Test 3
5182	DC04	MPSW	4	26000	28000	25000
5182	DP450	MPSW	5	21000	24000	22000
6016	DC04	MPSW	4.4	44000	42000	43000
6013-T4	DP1000	MPSW	4.4	32000	30000	31000
6013-T4	DP1000	MPW	5	61000	69000	63000

Table 3.9: fatigue tests results for different combinations ($R = 0$; $f = 20$ Hz)

Nm) machine was used and the tests were performed under undirectional conditions ($R = 0$) and at a frequence of 20 Hz (Fig. 3.35). The maximum load for fatigue tests is for each couple equal to 60% of the highest quasi-static lap-shear failure load.

3.4.4.1 MPSW of 5182 ($e_f = 1.2$ mm) with DC04 ($e_p = 0.8$ mm)

The quasi-static lap shear tests are given in Fig. 3.36 and the dynamic tests are represented in Fig. 3.37. The fatigue tests results are represented in Table 3.9.

In the quasi-static lap shear tests the maximum force is between 6000 and 7000 N with a displacement between 1.62 and 1.75 mm. The failure was in the weld and a deformation of the steel in the welding area was observed. The maximum dynamic loads that the weld attained were between 7500 and 8900 N with a displacement between 1.37 and 1.52 mm and the failure occured in the welding also. Finally, the number of cycles reached during the fatigue tests were between 25000
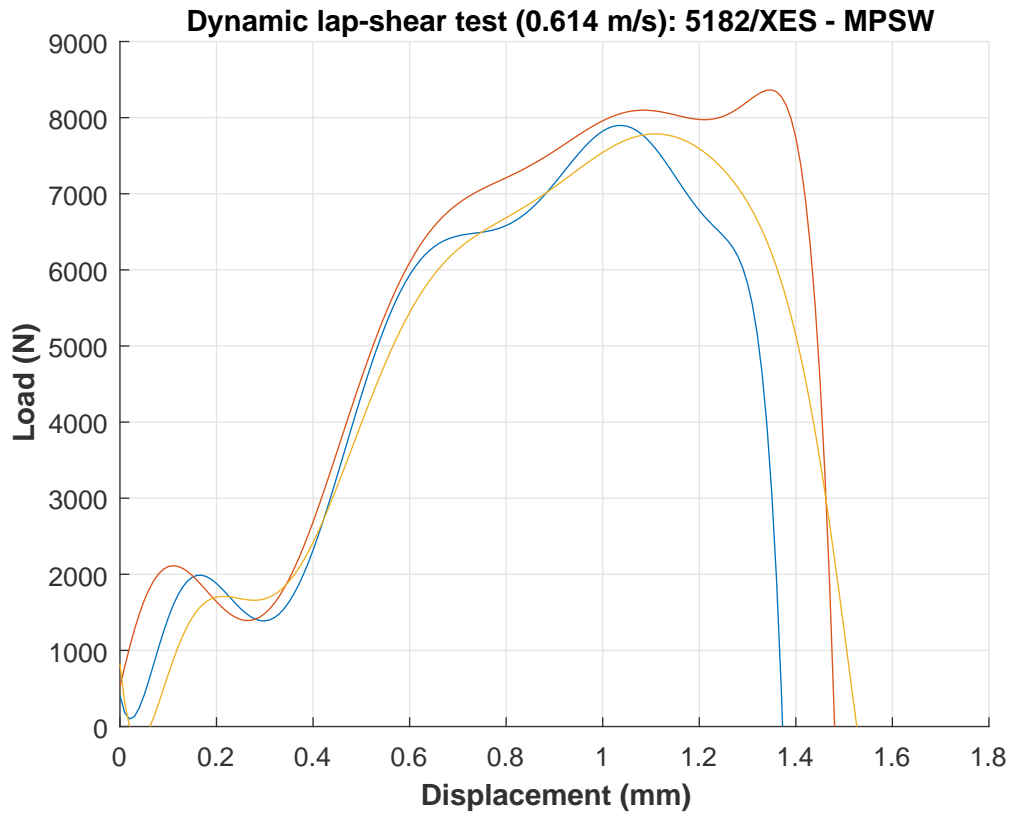
Figure 3.37: dynamic lap-shear test for MPS welded 5182 aluminum ($e_f = 1.2$ mm) with DC04 steel ($e_p = 0.8$ mm)

and 28000 cycles where tearing was observed in both aluminum and steel plates during the test (Fig. 3.38).

3.4.4.2 MPSW of 5182 ($e_f = 1.2$ mm) with DP450 ($e_p = 1.17$ mm)

The quasi-static lap shear tests are presented in Fig. 3.39 and the dynamic tests are represented in Fig. 3.40. The fatigue tests results are represented in Table 3.9.

The quasi-static lap shear maximum loads are between 8200 and 10000 N and the displacements are between 1.37 and 1.92 mm. The failure occured in the welds in all the 3 tests. The maximum dynamic loads were between 6125 and 8183 N and the displacements were between 1.1 and 2.1 mm. The fatigue tests showed that the number of cycles are between 21000 and 24000 cycles.

3.4.4.3 MPSW of 6016 ($e_f = 1$ mm) with DC04 ($e_p = 0.8$ mm)

The quasi-static lap shear tests are represented in Fig. 3.41. Concerning the dynamic test in this case and for all tested specimens the failure occured at the aluminum fixation holes at 9000 N without any failure in the welding. The fatigue tests results are listed in Table 3.9.

The quasi-static lap shear maximum loads are between 7000 and 8400 N and the displacements are between 2 and 3 mm. The fatigue tests showed a number of cycles between 42000 and 44000 and tearing was observed in both aluminum and steel sheets (Fig. 3.42).
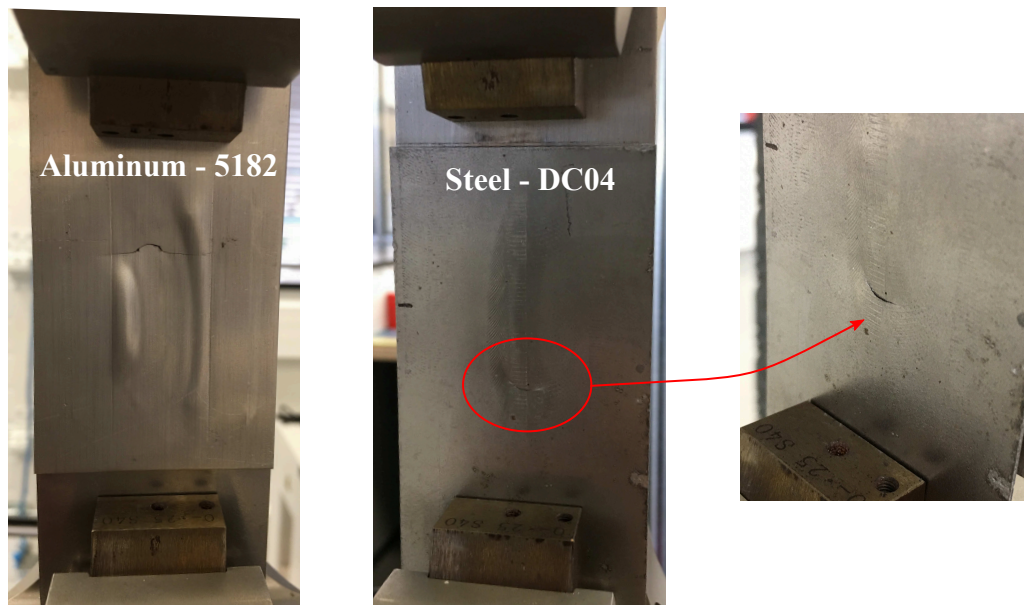
Figure 3.38: aluminum 5182 and steel DC04 tearing during fatigue tests
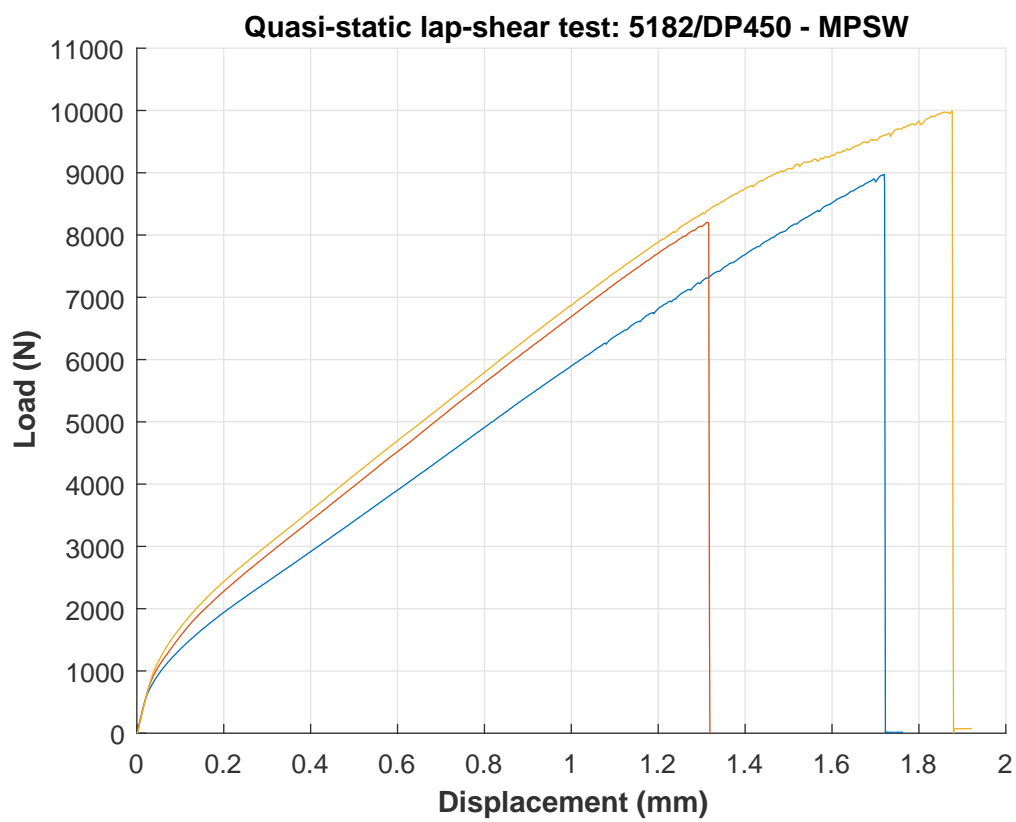
Figure 3.39: quasi-static lap-shear test for MPS welded 5182 ($e_f = 1.2$ mm) with DP450 ($e_p = 1.17$ mm)
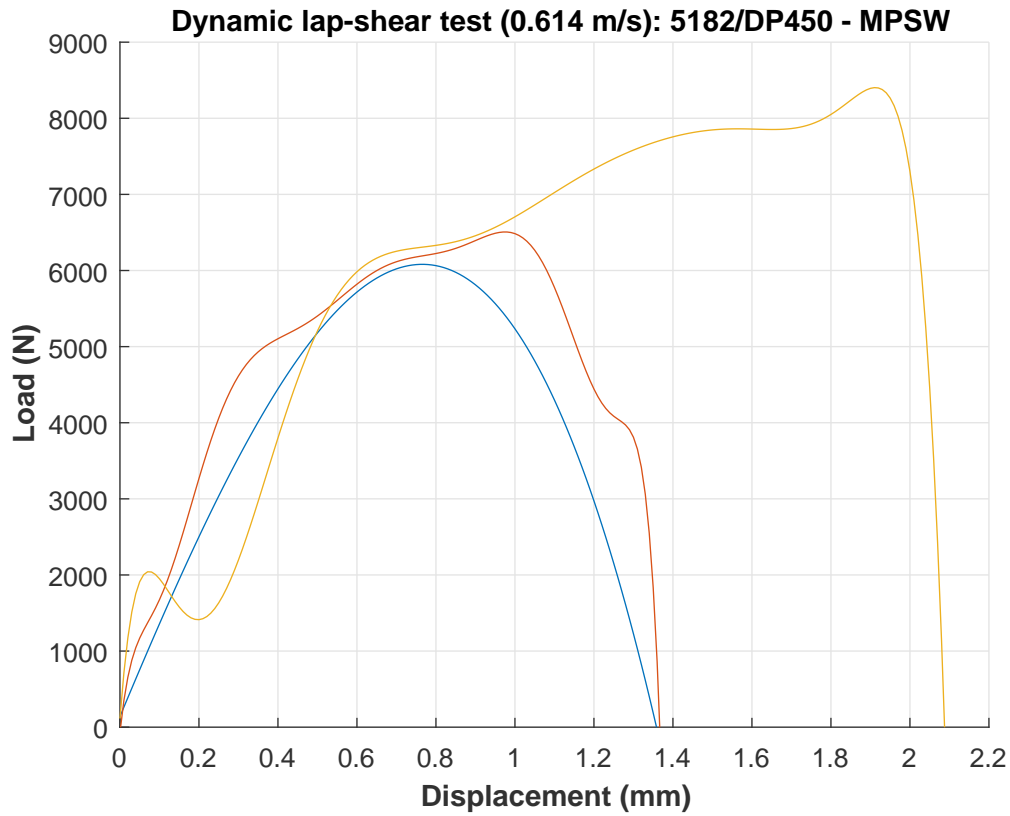
Figure 3.40: dynamic lap-shear test for MPS welded 5182 aluminum ($e_f = 1.2$ mm) with DP450 steel ($e_p = 1.17$ mm)
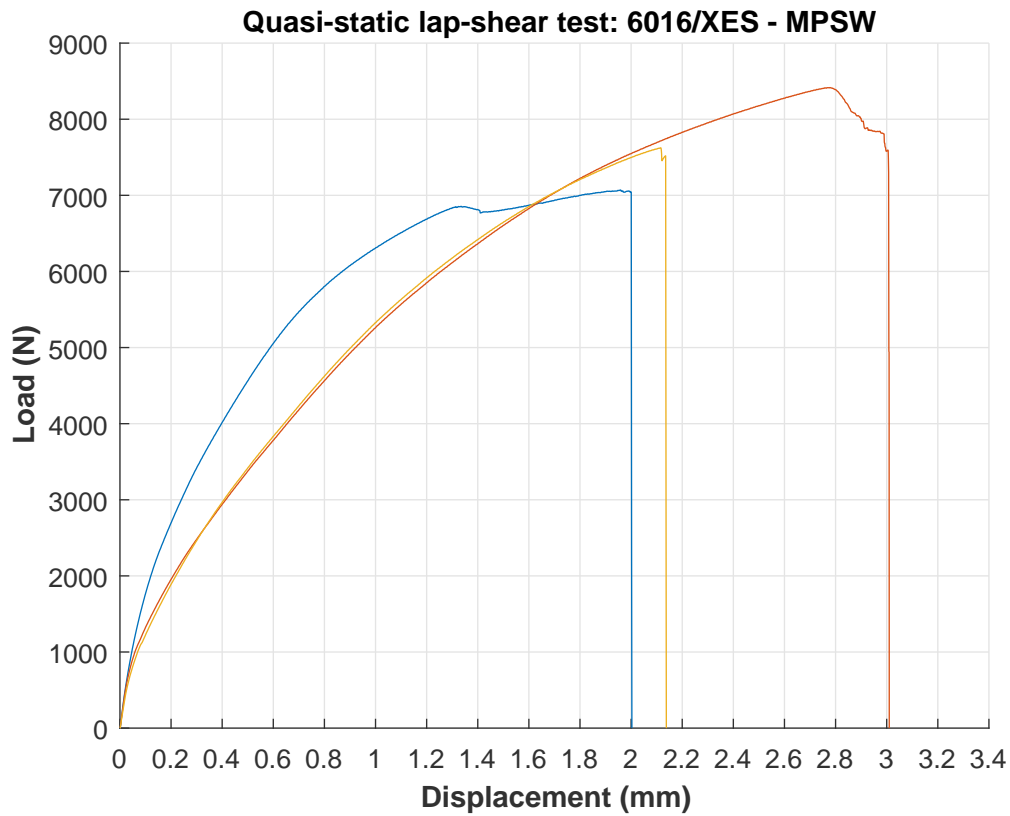
Figure 3.41: quasi-static lap-shear test for MPS welded 6016 ($e_f = 1$ mm) with DC04 ($e_p = 0.8$ mm)
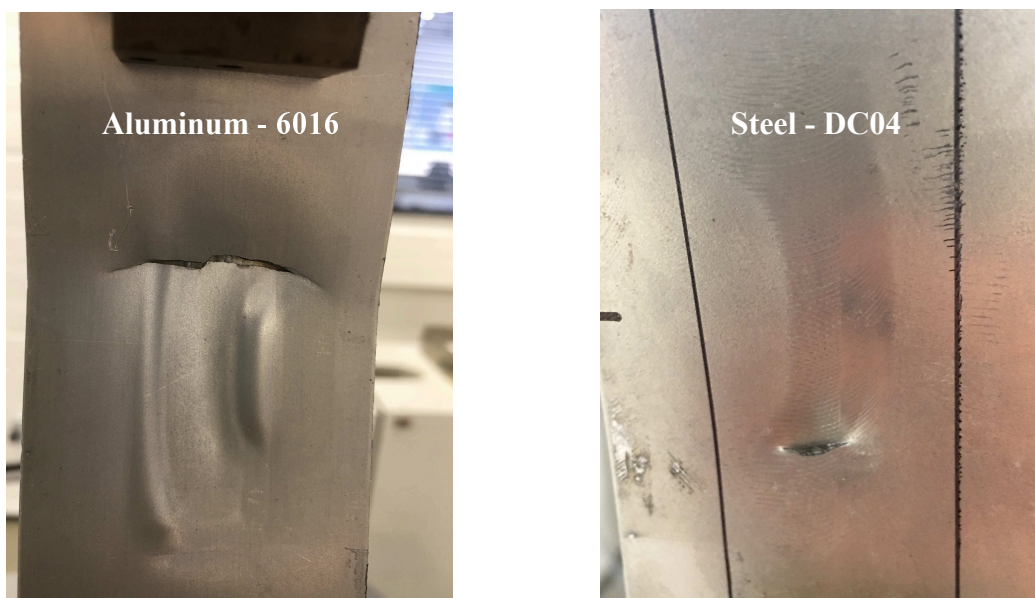
Figure 3.42: aluminum 6016 and steel DC04 tearing during fatigue tests

3.4.4.4 MPW and MPSW of 6013-T4 ($e_f = 1.4$ mm) with DP1000 ($e_p = 1$ mm)

In this case both configuration, MPW and MPSW, were tested. For the MPW case, the quasi-static tests are presented in Fig. 3.43 and the dynamic results are shown in Fig. 3.44. The quasi-static maximum loads are between 7500 and 9500 N with displacements between 0.78 and 1.1 mm. The dynamic loads are between 13247 and 14251 N and the corresponding displacements are between 2.7 and 5.2 mm. The fatigue results which are represented in Table 3.9 showed number of cycles oscillating between 40000 and 89000.

For the MPSW configuration, the quasi-static results are presented in Fig. 3.45 and the dynamic results in Fig. 3.46. The quasi-static maximum loads in this case were between 7380 and 8400 N and the displacements between 0.85 and 1.1 mm. The dynamic loads attained were between 6500 and 9022 N and the displacements between 0.78 and 2.3 mm respectively. The fatigue tests results presented in Table 3.9 showed a number of cycles between 30000 and 32000.

3.4.5 Microscopic and metallurgical analysis

3.4.5.1 Welding interface

The welded specimen for observation were cutted to be observed as indicated in Fig. 3.47. The cuts are then coated in hot carbon filled resin and after that they are polished using a diamond strip (1 μm).

The welding interface between different couples showed a wavy interface especially in the middle area of the welding (Fig. 3.48). The waves length and amplitudes vary a lot within one welding (Fig. 3.49): for the wave lengths, it can vary between 8 up to 32 μm at the same interface and for the amplitudes, it is between 1 and 5 μm.

Several intermetallic layers were observed at the interfaces:
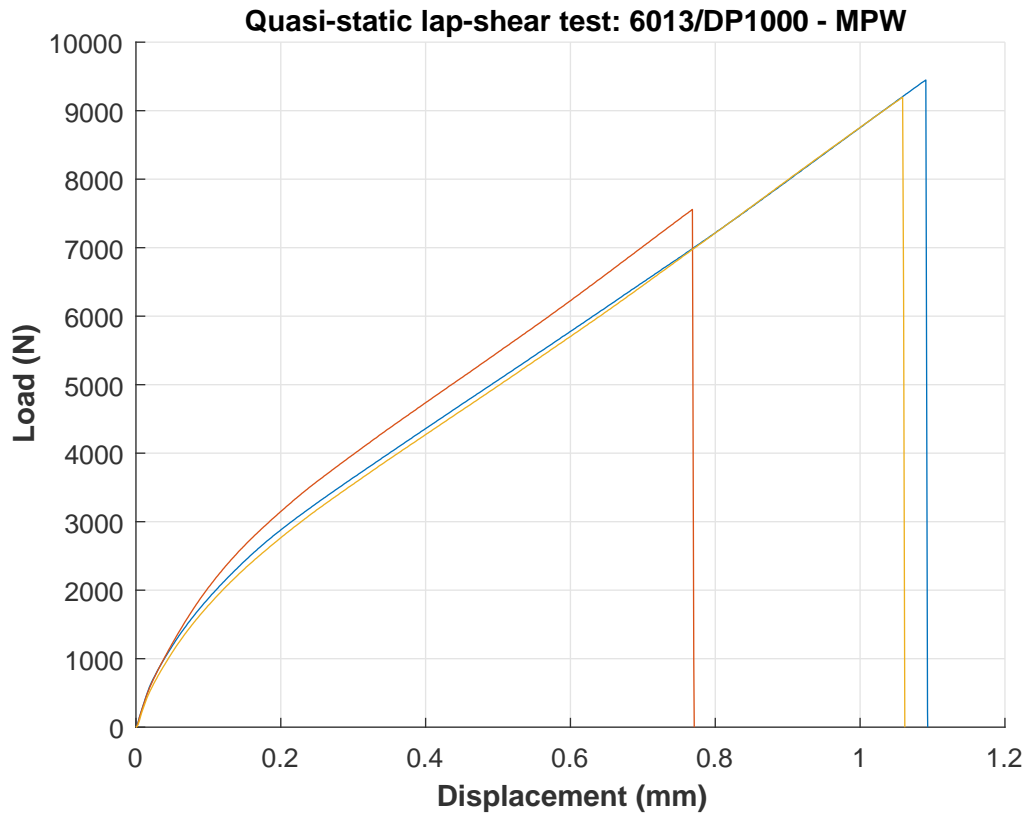
Figure 3.43: quasi-static lap-shear test for MP welded 6013-T4 ($e_f = 1.4$ mm) with DP1000 ($e_p = 1$ mm)
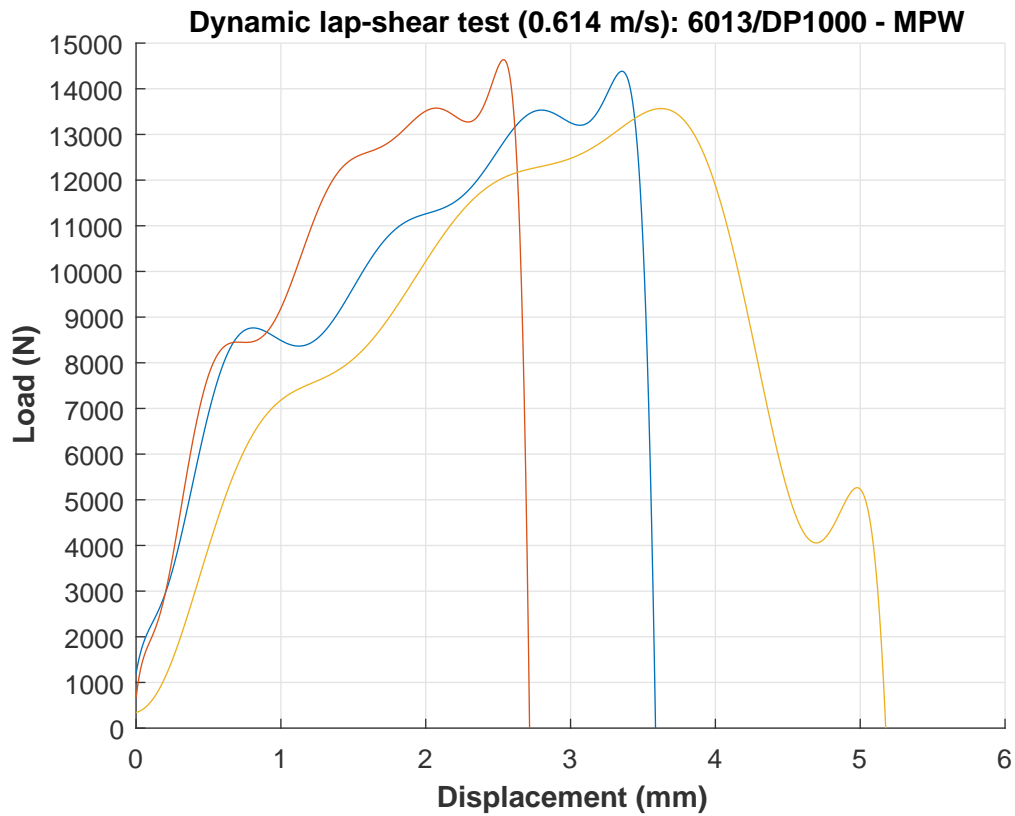
Figure 3.44: dynamic lap-shear test for MP welded 6013-T4 aluminum ($e_f = 1.4$ mm) with DP1000 steel ($e_p = 1$ mm)
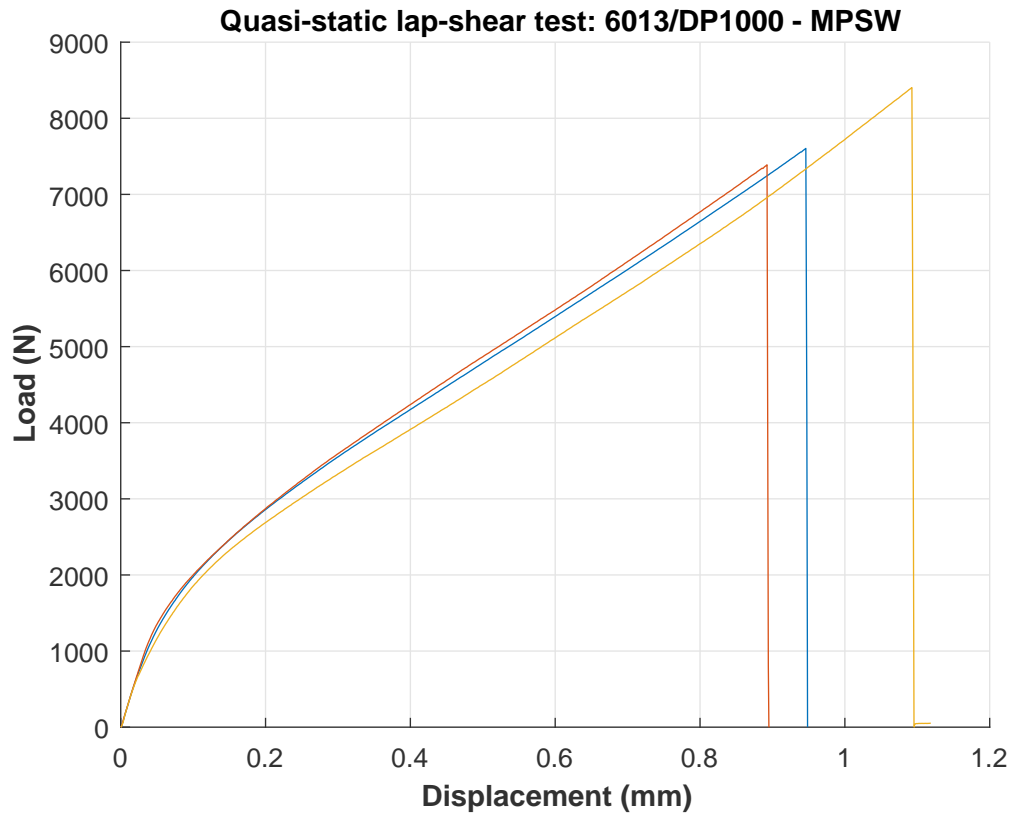
Figure 3.45: quasi-static lap-shear test for MPS welded 6013-T4 ($e_f = 1.4$ mm) with DP1000 ($e_p = 1$ mm)
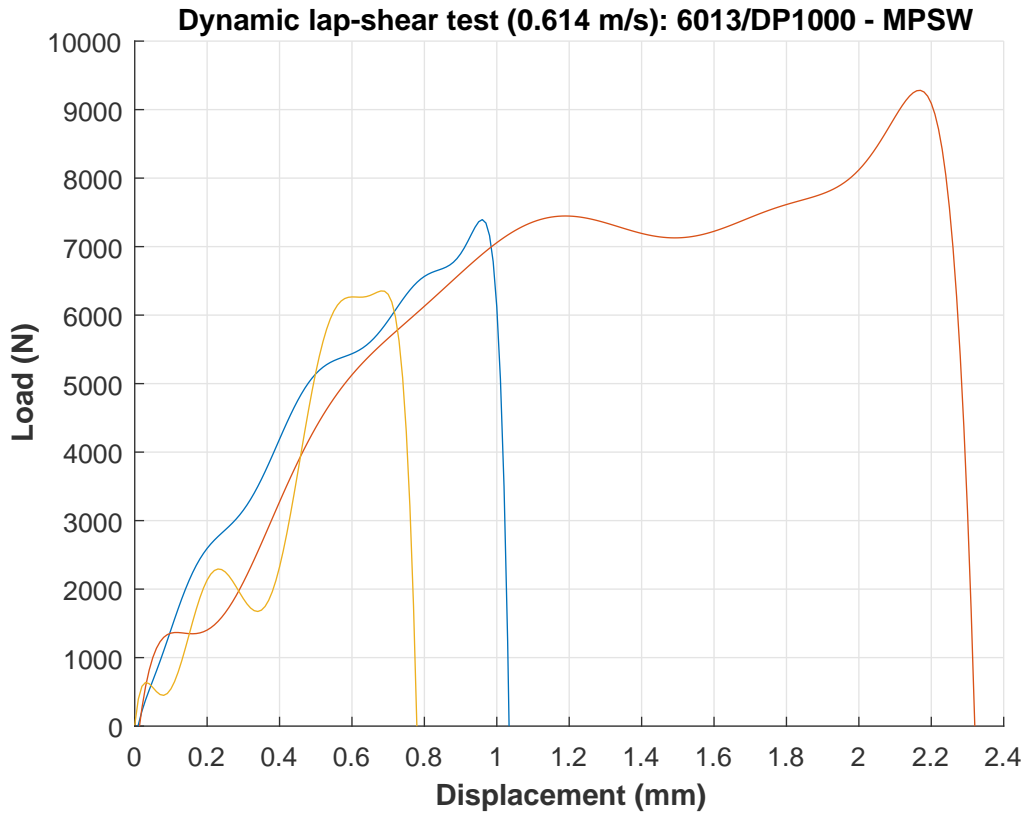
Figure 3.46: dynamic lap-shear test for MP welded 6013-T4 aluminum ($e_f = 1.4$ mm) with DP1000 steel ($e_p = 1$ mm)
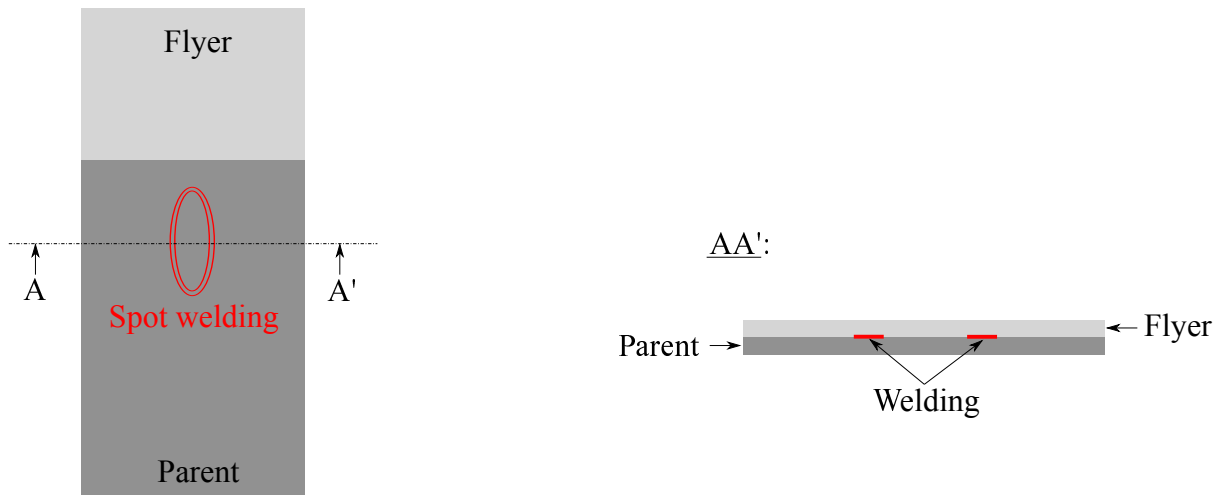
Figure 3.47: SEM observation direction
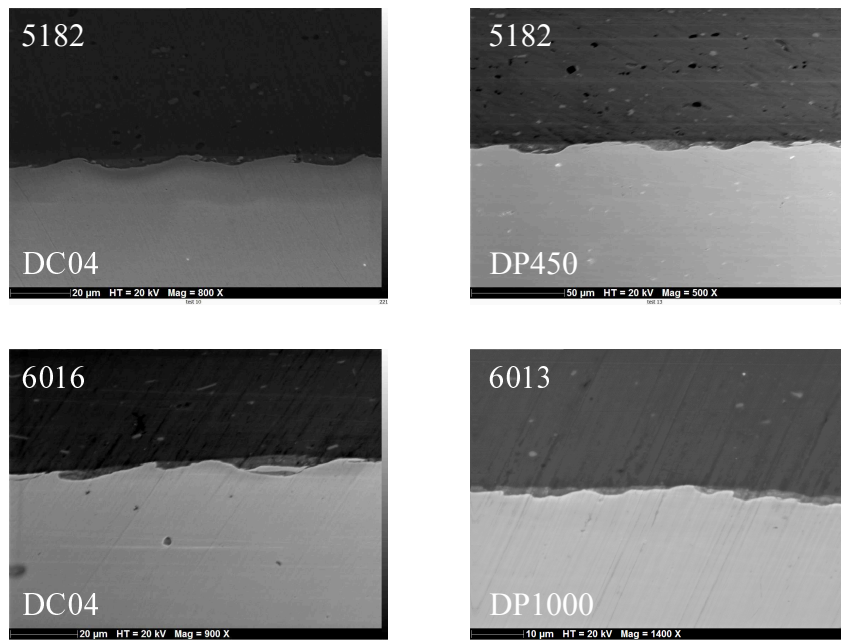
Figure 3.48: wavy interface in different combinations of materials

Impact progression

Impact progression

Impact progression
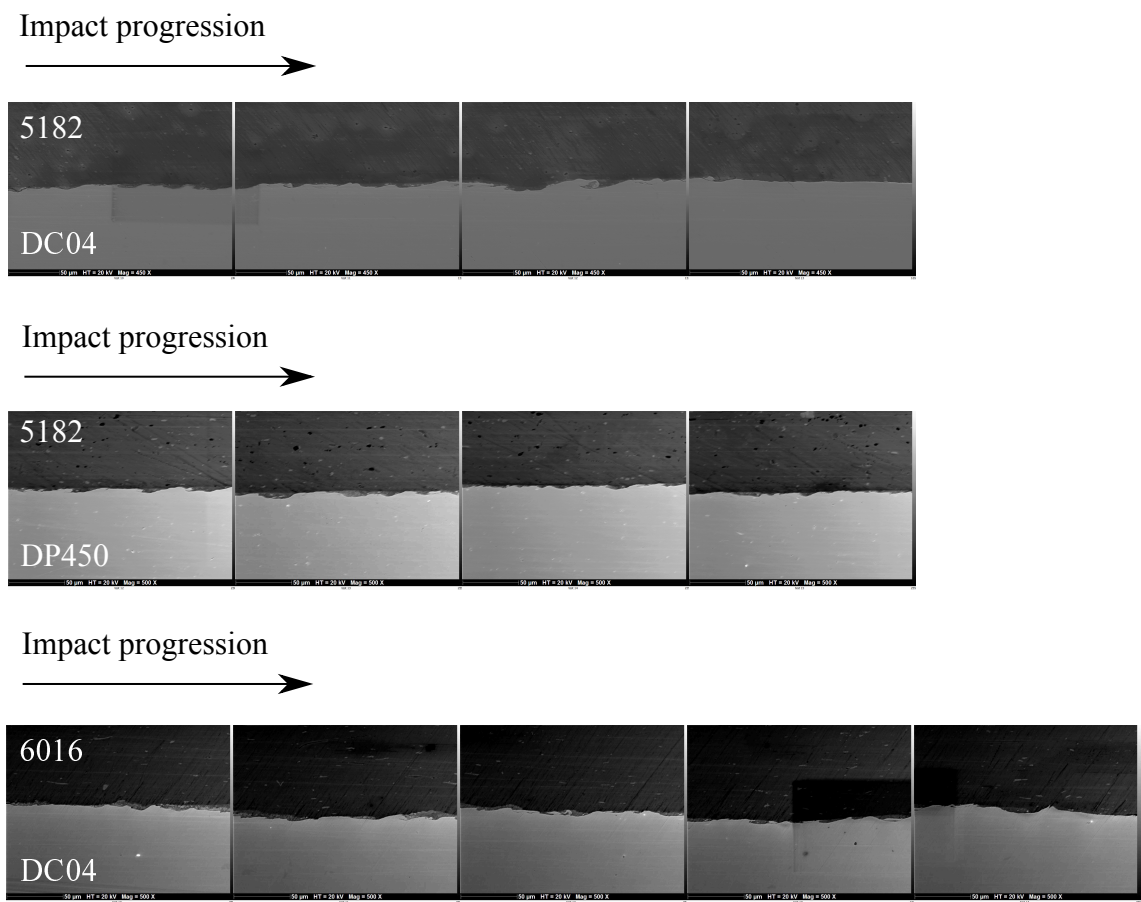
Figure 3.49: chaotic wavy interface for different couples welding interface
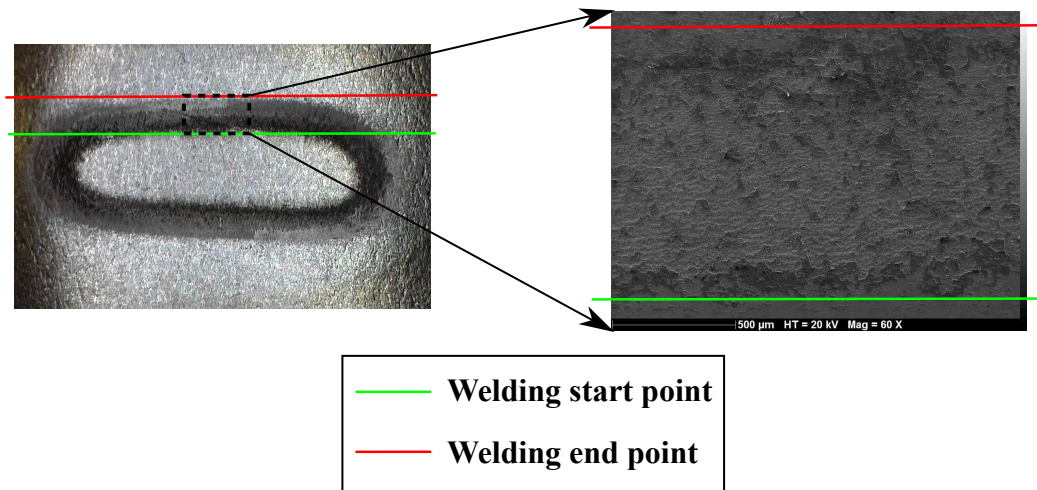
Figure 3.50: observation area of the welding lines

At the 5182/DC04 interfaces, the intermetallic compounds detected were *FeAl* and two other compounds: the first with 80% at. of aluminum and the second with 94% at. of aluminum. These layer thicknesses are varying between 0.8 and 2 μm.

At the 5182/DP450 interface, very thin layers of Fe_2Al_5 were detected and two other compounds with 79% at. of aluminium and 89% at. of aluminum respectively.

In the case of the 6016/DC04, layers of Fe_2Al_5, Fe_2Al_3, *FeAl* as well as two other compounds with 79% at. and 86% at. of aluminum respectively were detected. The thickness of these layers were between 2 and 4 μm.

In 6013/DP1000 and for the MPW configuration, the intermetallics compounds observed are with 90% at. of aluminum with thicknesses between 0.8 and 2.35 μm. When it comes to the MPSW, the intermetallic compounds observed were Fe_2Al_3, $FeAl_3$, *FeAl*, Fe_2Al_5 varying from 0.5 μm up to 2.8 μm.

This high variety of intermetallics presence at the interface shows the brutality of the impact phenomenon and the very local heat increase variation between the different interface points that leads to different intermetallic compounds formation within the same welding.

3.4.5.2 Failure surfaces analysis

The welding as it was represented previously occurs in a look-like elliptical line shape and during the observations the focus was along the width of this line from the start of the weld up to its limit (Fig. 3.50) . These observations were done on both the flyer and the parent correspondingly (Fig. 3.51) . The presence of different areas with different combinations along the weld width were observed: areas of pure aluminum were observed in the failure zones on the boundaries and also in the middle area of the welding width where islands of pure alumunium were also observed in different combinations of materials on the steel side (Fig. 3.52) . On the aluminum side, these teared parts of the pure aluminum can be observed in the middle of different areas were it is seen voids in the welding and the aluminum plate can be seen (Fig. 3.52).

In the middle regions of the welding, both aluminum and iron presence is detected as we can see in Fig. 3.51. In different combinations and across the width different compositions were detected
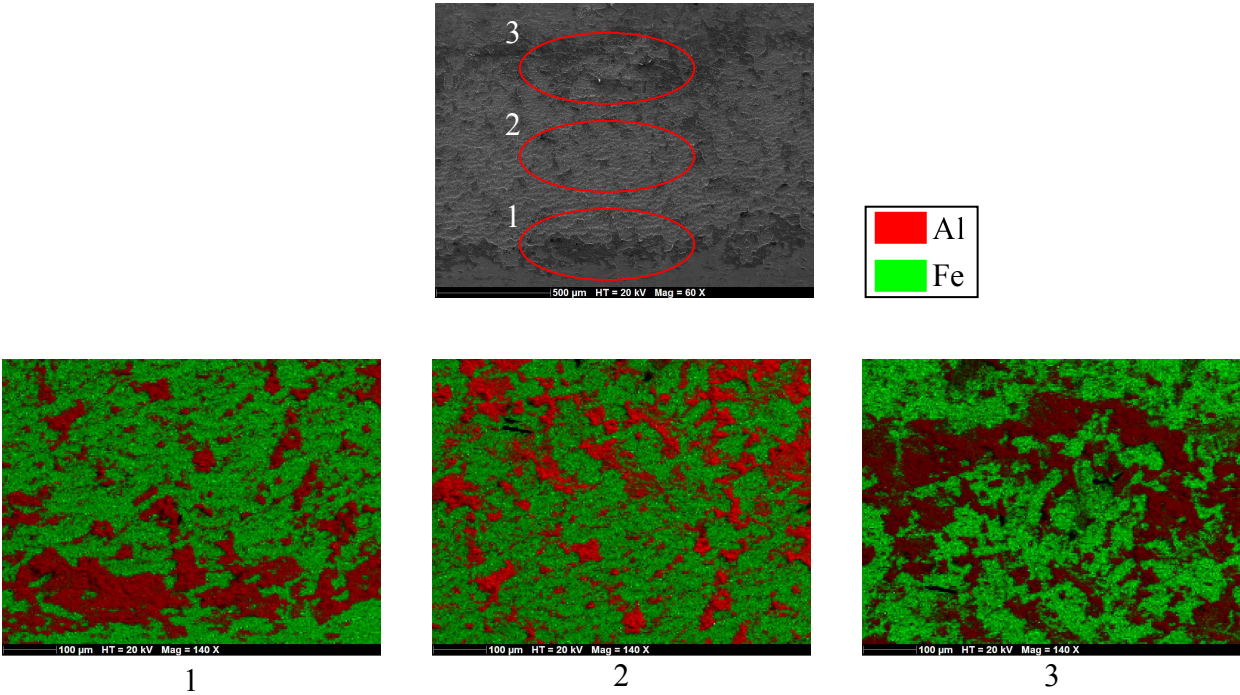
(a) steel side
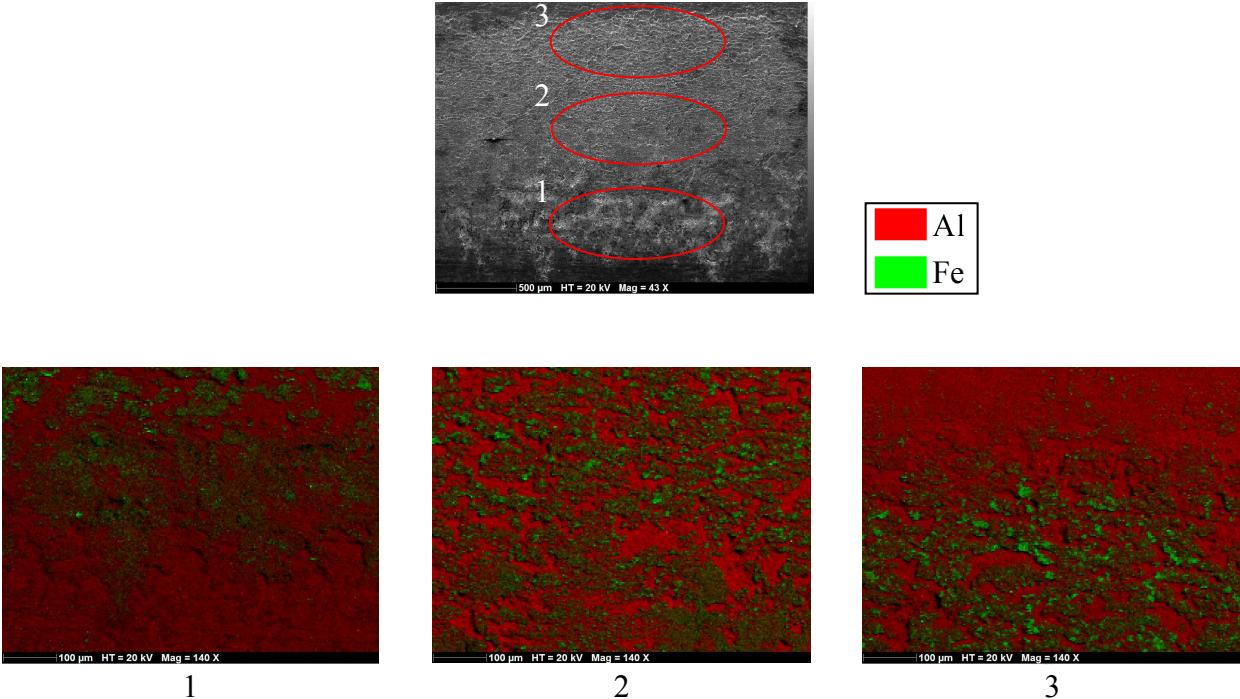
(b) aluminum side

Figure 3.51: failure surfaces on both (a) parent/steel and (b) flyer/aluminum sides

steel side:
pure aluminum islands

aluminum side:
voids in welding width
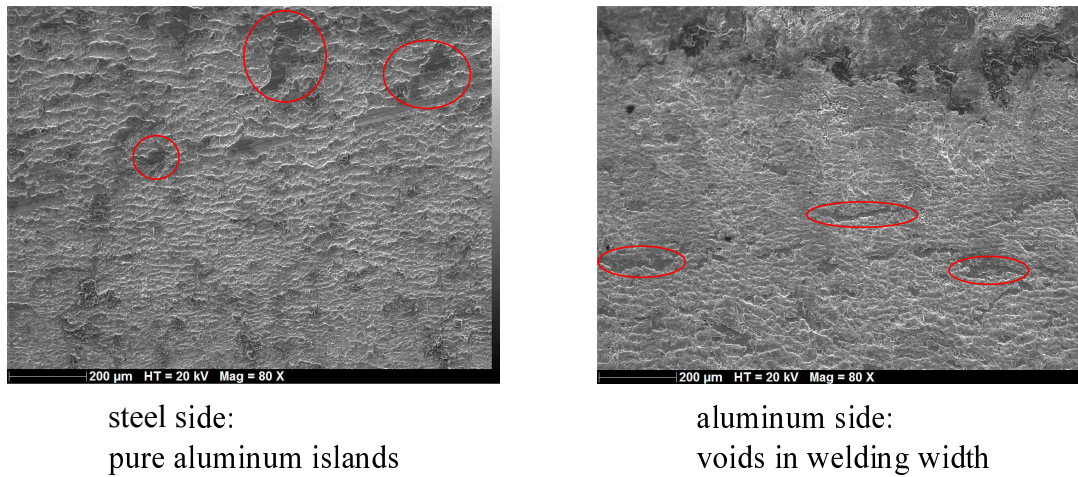
Figure 3.52: islands of pure aluminum on steel side
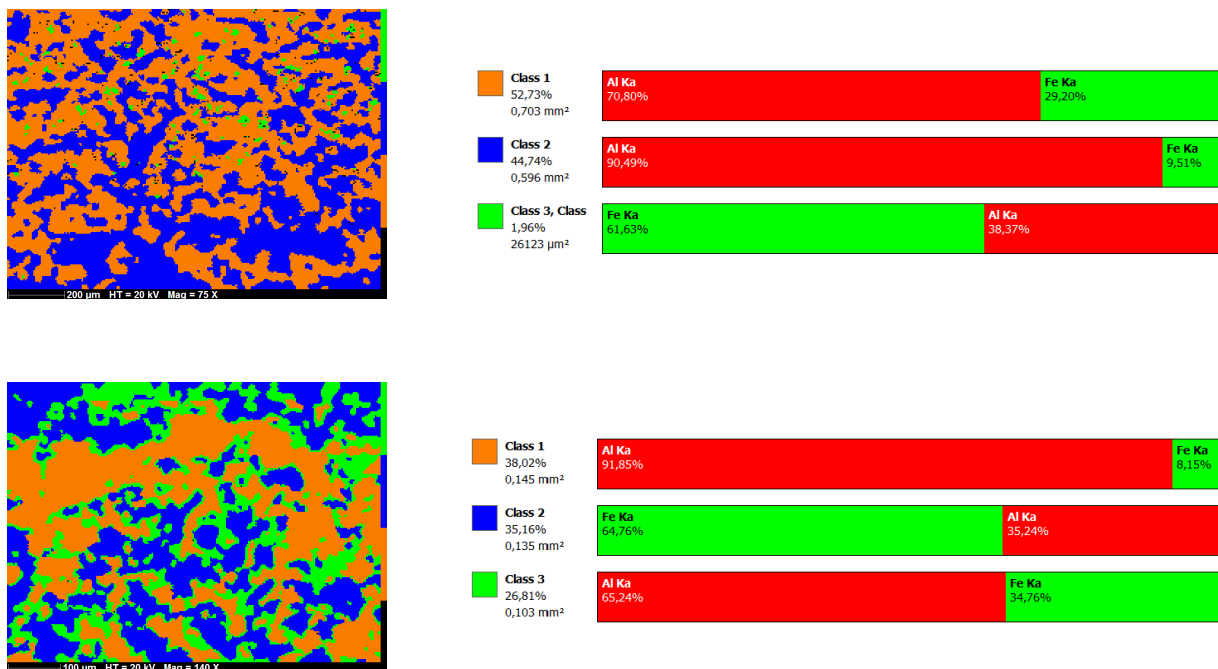
Figure 3.53: example of atomic distribution of Al and Fe on the failure surfaces

including the different intermetallics observed at the wavy interfaces presented in the previous section. However, when analyzing the failure surfaces on the aluminum and the steel sides, the most present areas are those with the Al-rich intermetallics (Fig. 3.53) .

Concerning the specimens from the fatigue tests in the case of the 5182 to DC04 and 6016 to DC04 where cracks where observed in the flyer and in the parent metal during the test (Fig. 3.38 and Fig. 3.42): the microscopic observation showed a combination of cohesive and substrate failure. On the aluminum side and at the boundary of the welding a clear substrate failure was detected (Fig. 3.54) and when looking on the steel side, the aluminum strip remaining on the corresponding steel area confirms that the failure happened in the aluminum side in this area. In addition, also in the teared region of the steel plate during the test, a similar band of aluminum was observed (Fig. 3.55) . The cohesive failure was confirmed through the observation of different areas on the welding line where, and in the same area, the presence of pure material and mixed zones of materials were

157
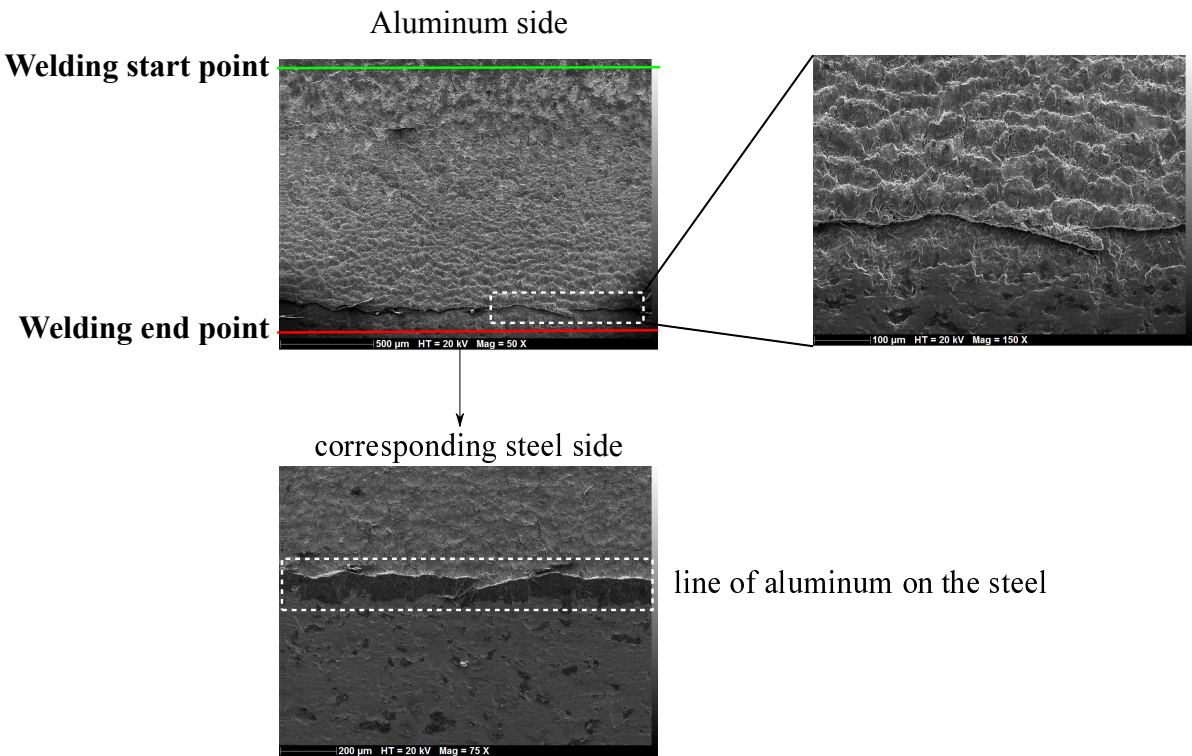
Figure 3.54: substrate failure during fatigue test
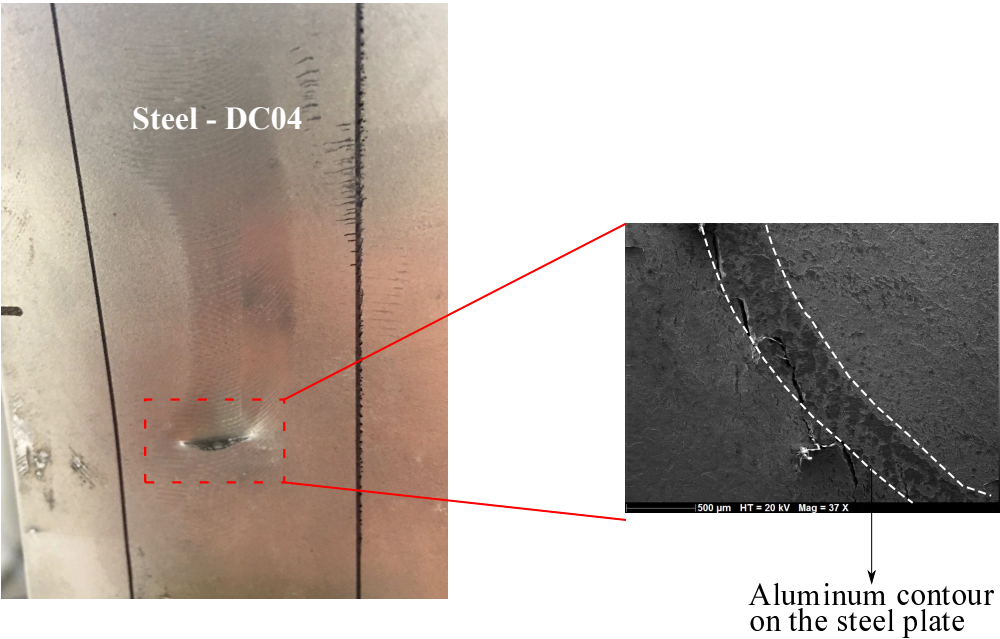
Figure 3.55: aluminum strip on the steel in the tearing area
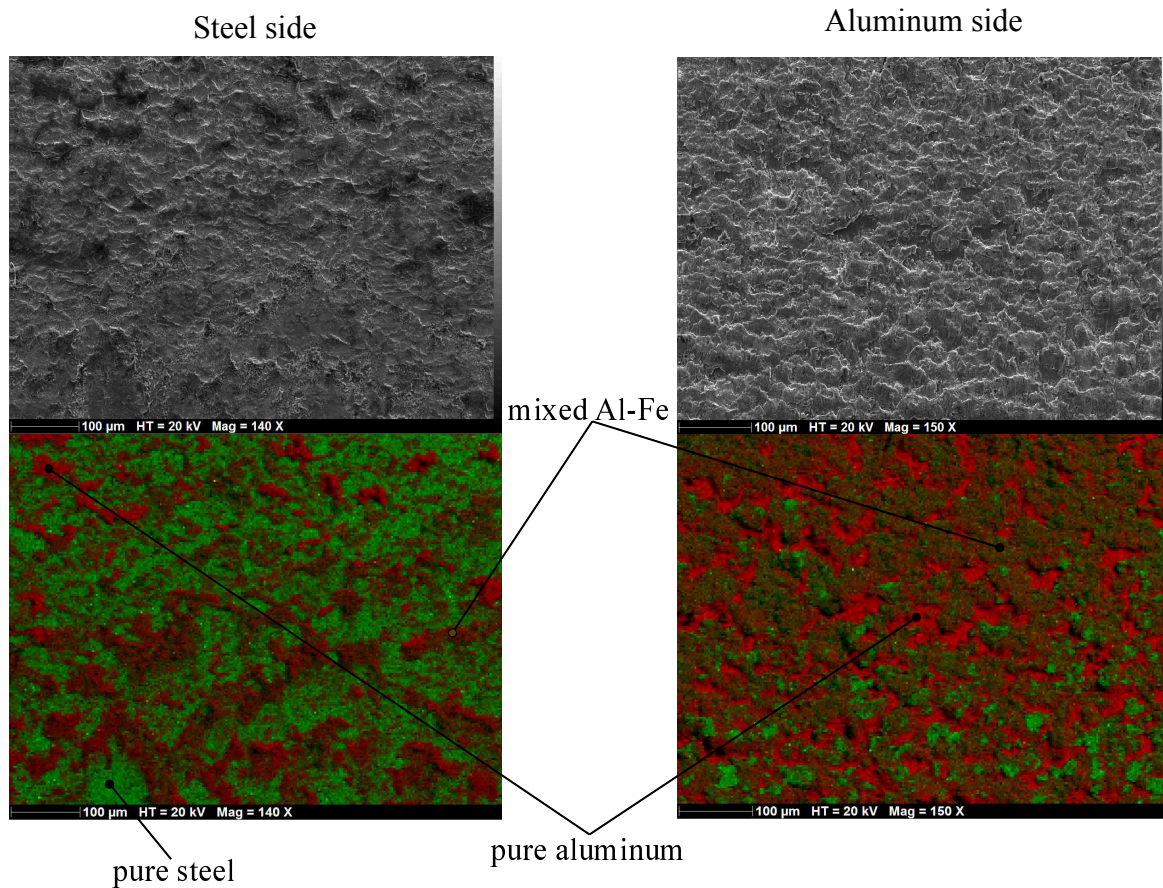
Figure 3.56: fatigue surface failure analysis

noticed (Fig. 3.56).

3.5 MPSW applicability for welding aluminum to zinc coated steel

3.5.1 Feasibility study

In the previous section the focus was on the weldability of different aluminum to steel alloys. In this section, the main problematic is the MPSW applicability for welding aluminum to zinc-coated steels since the industrial application of the coated steels is very wide and in different fields. The first two questions that arised were: is it possible to have a MPS welding in the first place? If yes, is the progressive impact of the aluminum sheet able to remove the coating layer and create the bonding between the aluminum and the steel? or how will the welding establish?

The first thing to do was to observe microscopically the layer of coating on the steels. Two steels used in automotive applications were considered: the DC04 +ZE deep drawing coated steel and DP450 +ZE dual phase coated steel. The layer shows at microscopic scale irregularities in its thickness (Fig. 3.57) and even on a very small length the variation of the thickness can be up to 2 μm. In addition, the thickness itself of this layer of coating is higher than 6 μm and when looking at the total welding interface dimensions in MPW/MPSW applications (Fig. 3.49), the

159
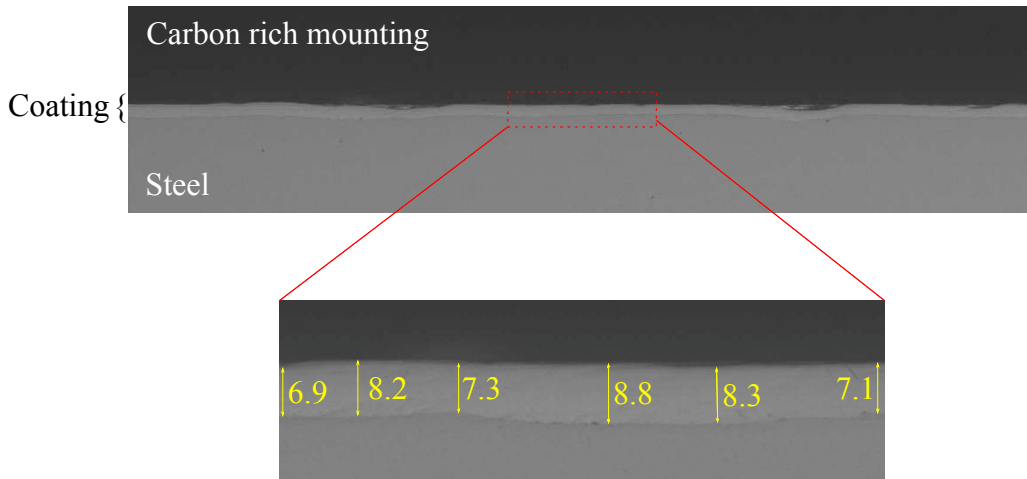
Figure 3.57: zinc coating thickness irregularities on steel surface (measurements in μm)
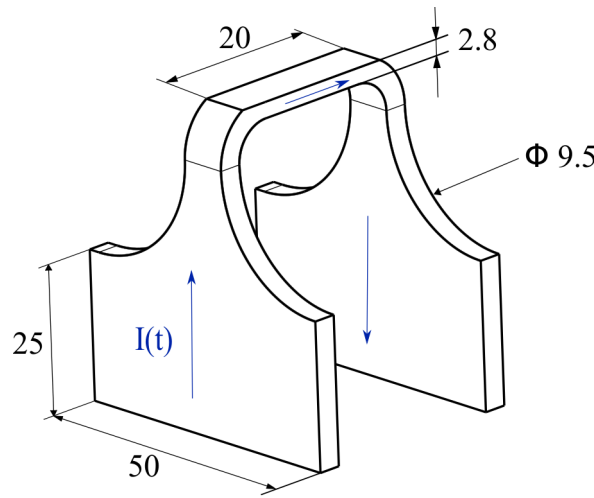
Figure 3.58: linear coil with rectangular cross-sectional area for aluminum to coated steel application (dimensions in mm)

wave amplitudes are not more than 5 μm. Therefore saying that the progressive impact will remove the coating could be an irrealistic hypothesis.

To validate this, the first experimental investigation was done between the 1050 aluminum (e_f =0.5 mm) and DC04 + ZE (e_p =0.62 mm) steel. The dimensions of both are 90 mm length and 40 mm width. The coil used is a linear rectangular cross-section coil presented in Fig. 3.58 and the hump dimensions deep drawn on the aluminum flyer plate (Fig. 3.10) were: $l_h = 8$ mm, $L_h = 14$ mm, $l'_h = 14$ mm and L'_h =27 mm; with a standoff distance h =1.5 mm. The discharge energy applied to achieve the weld is 10 kJ.

To evaluate the strength of the weld, lap shear quasi-static tests for 3 specimens were done (Fig. 3.59) and the failure occured in the flyer metal sheet and not in the welding (Fig. 3.60). To answer how the welding occured on a microscopic level, specimens were cutted and prepared as explained before (Fig. 3.47). The result which is presented in Fig. 3.61 validates the fact that the welding has occured in fact between the aluminum sheet and the zinc coat layer with a wavy welding interface.

Since the welding occured between the aluminum and the zinc coating layer, several questions
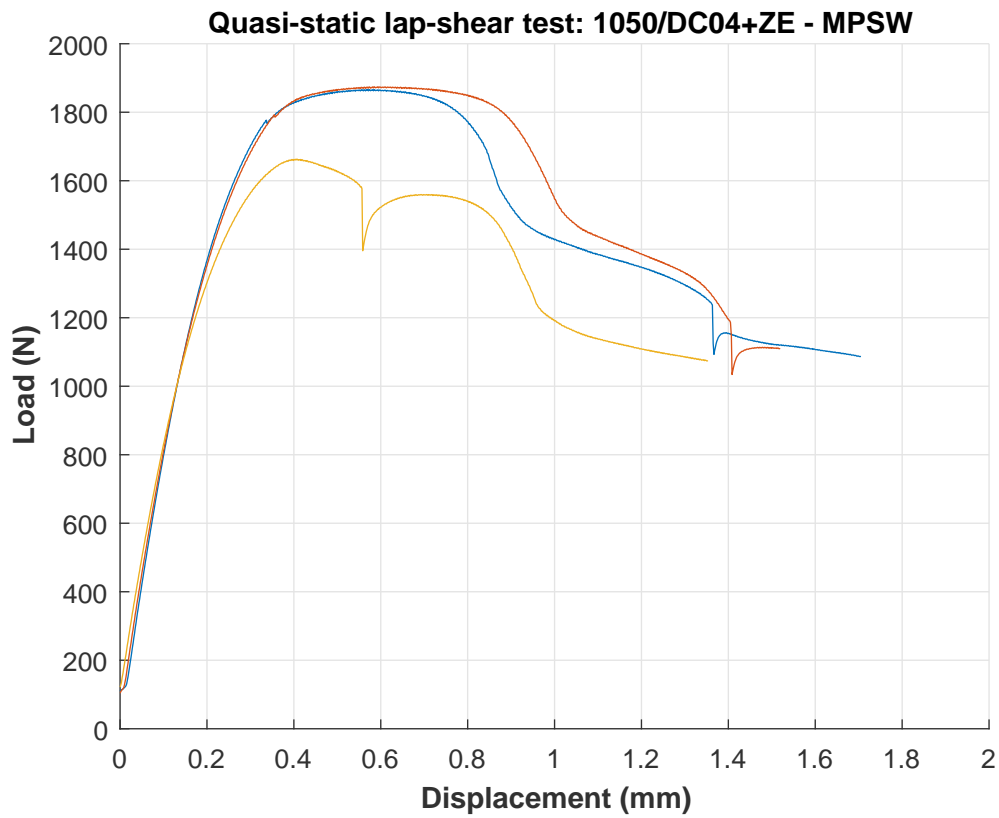
Figure 3.59: typical lap-shear quasi-static test for MPSW of 1050 to DC04 +ZE
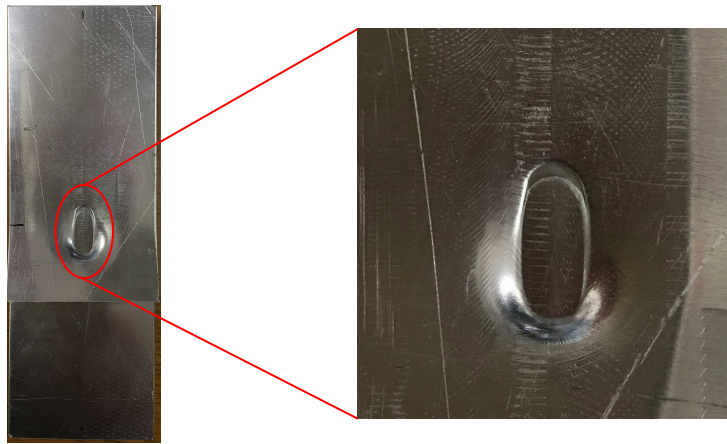
Figure 3.60: aluminum failure in 1050 to DC04 +ZE MPSW during lap-shear test
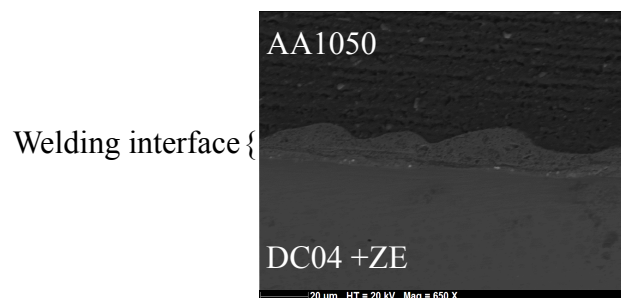
Figure 3.61: welding interface between 1050 and DC04 +ZE showing that the welding occured between the flyer and the zinc coat layer
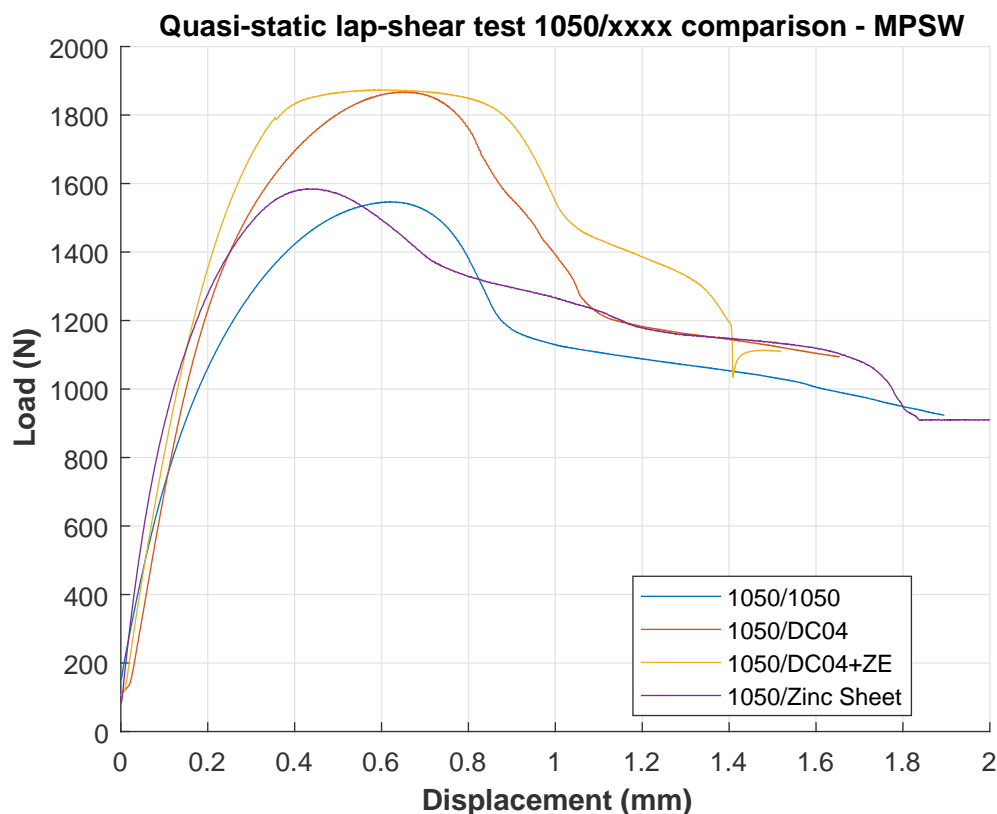
Figure 3.62: comparison between typical lap-shear quasi-static behaviour of the MPS welded specimens: 1050 with 1050, 1050 with DC04, 1050 with DC04 +ZE and 1050 with a pure zinc sheet metal

Figure 3.63: welding interface for (a) 1050 and pure zinc sheet; (b) 1050 and DC04

arised: what is the behaviour of this welding in comparison with the welding of 1050 to 1050 similar welding? What is the difference between this welding and a MPSW between the 1050 aluminum with the uncoated DC04 steel? If we apply the MPSW between a 1050 aluminum sheet and a pure zinc metal sheet, will it also lead to a welding? In order to have clear answers, experimental application of the MPSW were done with the same conditions as before (same discharge energy, same hump dimensions and standoff distance). All welding were successfull and the specimens were tested under lap-shear quasi-static condition. The results are presented in Fig. 3.62 and the failure occured always in the flyer aluminum sheet as it was presented in Fig. 3.60.

The behaviour of the welding is similar for all the couples welded as it can be seen in Fig. 3.62 and when looking at a microscopic level also the welding in both cases with DC04 and pure zinc sheet showed a wavy interface (Fig. 3.63) with amplitudes varying between 1and 5 μm (less the thickness of the zinc layer).

This experimental investigation demonstrates first that the MPSW is also applicable to weld dissimilar aluminum to zinc-coated steel alloys. Besides, it allow us to say that this coating layer

can be considered as the parent material itself as well as to claim that the progressive impact will not remove the coating layer and have the weld directly between the steel and the aluminum, but, instead, it will weld directly on the zinc layer keeping its function as a corrosive protection layer. Further, the weldability of aluminum and the zinc using MPSW is an additional proof that the scope of application of the MPSW itself is not limited to some dissimilar alloys only.

Now that the feasibility of using the MPSW also for dissimilar application with coated steel was proven, the aim was to go further with metallurgical analysis by studying the effect of a galvanized steel coating at various length scales on the microstructure of the welding interface. For this purpose, the extended study on this topic was conducted in collaboration with Dr. M. N. Avettand Fenoel from UMET CNRS 8207 laboratory at Université de Lille 1 in France which is specialized in materials science and which will be presented next.

3.5.2 Effect of steel coating on the microstructure of the dissimilar aluminum to steel MPSW (in collaboration with UMET Lille 1)

3.5.2.1 Experimental procedure

The materials investigated are AA1050 and coated and uncoated cold-rolled DP450 steel. The dimensions of the plates are 40 x 90 mm² for the aluminum and 40 x 110 mm² for the steel and the dimensions of the hump are the same as before as well as for the discharge energy (10kJ). Successful welding was obtained between the 1050 and DP450 as well as for 1050 with DP450 +ZE.

Hereafter, transverse cross sections of the joints were diamond polished to 1 μm and characterized by light microscopy, scanning electron microscopy, and X-ray energy dispersive spectroscopy (EDX/SEM) with the secondary electron (SE) or back-scattering electron (BSE) mode.

For the (scanning) transmission electron microscopy ((S)TEM)/EDX) and electron diffraction investigations, thin foils were prepared using the focused ionic dual beam (FIB) technique. During cutting, the thin foil edge facing the ion beam was protected by a 3.5-μm-thick deposit of platinum. A 300-pA beam intensity was applied for final thinning.

X-ray diffractometry (XRD) was performed on the transverse cross section of the weld using a Bragg-Brentano configuration and a cobalt anticathode [λ_{Co} ($K_{\alpha 1}$) = 1.78901 Å].

Vickers microhardness tests were performed under a 50 g load with a 15-second dwell time along the MPW joint in the transverse cross section. Three to four tensile shear lap tests were finally performed on each kind of full weld along the length of the rectangular joint at a rate of 1 mm/min.

3.5.2.2 Results

3.5.2.2.1 Base materials microscopic observations

The DP450 steel has a dual-phase structure (Fig. 3.64) composed of both equiaxed grains of ferrite with a 10 μm mean size and allotriomorphic martensite-austenite compounds (MACs), which are characteristic of thermomechanical steels [207]. The Al 1050 alloy exhibits finer and rather equiaxed grains with a size close to 1 μm in diameter. The hot-dip coating of the galvanized DP450
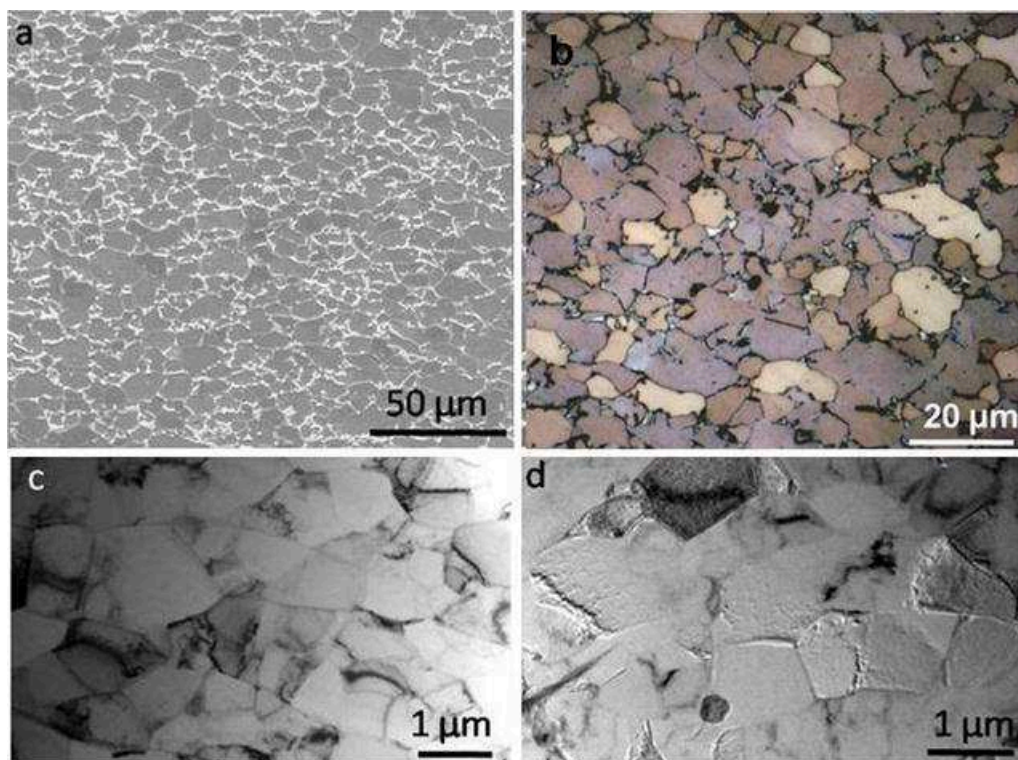
Figure 3.64: transverse cross section of the DP450 steel after either 2 pct nital etching (SE/SEM) (a) or Marder–Benscoter etching (b), and aluminum structure (TEM) (c, d). In micrograph b, austenite is white, ferrite is off-white, blocky martensite is black, and pearlite is black and white [16]

Figure 3.65: transverse cross section of the galvanized DP450 steel (light microscopy) [16]

steel comprises two layers including, from the steel surface, a 150-nm-thick inhibition layer (Fig. 3.71) covered by a 6- to 10-µm-thick Zn layer (Fig. 3.65). The formation of the thin layer of $FeAl_3$, Fe_4Al_{13}, and $Fe_2Al_5Zn_x$ is the rule when steel is hot-dipped in a Zn melt enriched in Al [133].

3.5.2.2.2 Microstructure of the joint

Fig. 3.66 shows that at the bonded interface, the steel microstructure is not modified at the mesoscopic scale by magnetic pulse welding. This result is consistent with some previous studies [121][150]. Otherwise, the Al grains are rather equiaxed with a size close to 1 µm. In addition, the steel grains contain dislocation cells close to 0.7 µm in size, whereas the Al grains are dislocation free and contain some second phases composed of 70% at., 25% at. Fe, and 5% at. Si at first sight (Fig. 3.66 (b) and (d)). Such an uncommon chemical composition is very likely overestimated in Al due to the overly large extent of the X-ray source region. The presence of particles that are more enriched in Fe and Si is indeed the rule in raw Al 1050 alloys [14]. In addition, regardless of the joint, i.e., with or without the galvanized layer, the interface has the same wavy shape, which results from the pulsed waves generated during welding (Fig. 3.67). Fig. 3.67 further displays the
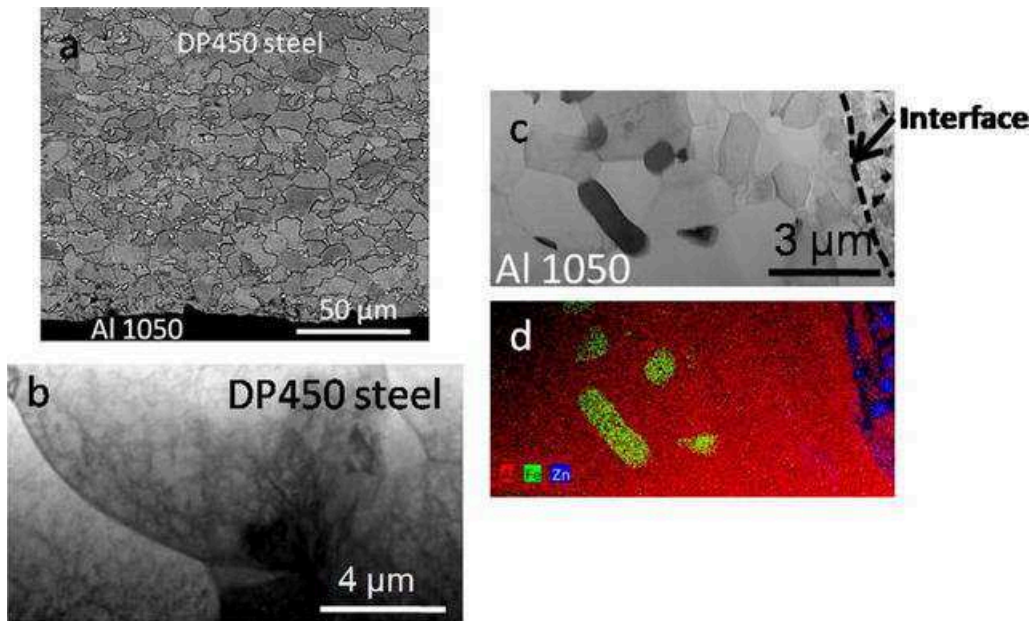
Figure 3.66: Al 1050-coated DP450 steel joint: (a) Transverse cross section of the joint (BSE/SEM). The steel was etched with 2 pct nital. (b) The steel grains in close contact with the interface contain dislocations cells (TEM). (c and d) Al grains near the interface and X-ray $Al-K_\alpha$ (red),$Fe-K_\alpha$ (green), and $Zn-K_\alpha$ (blue) composite map (EDX/STEM)[16]
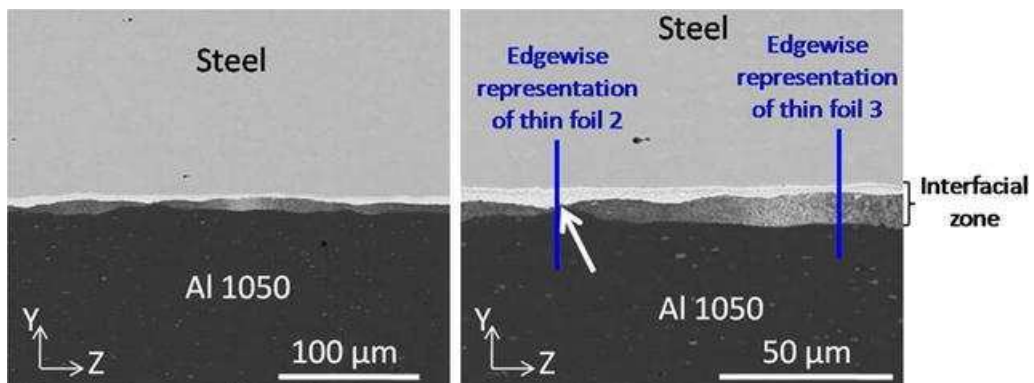
Figure 3.67: interfacial zone of the Al 1050-galvanized steel joint in the X-Y transverse section (BSE/SEM). In the interfacial zone, Zn is the brightest phase [16]

165
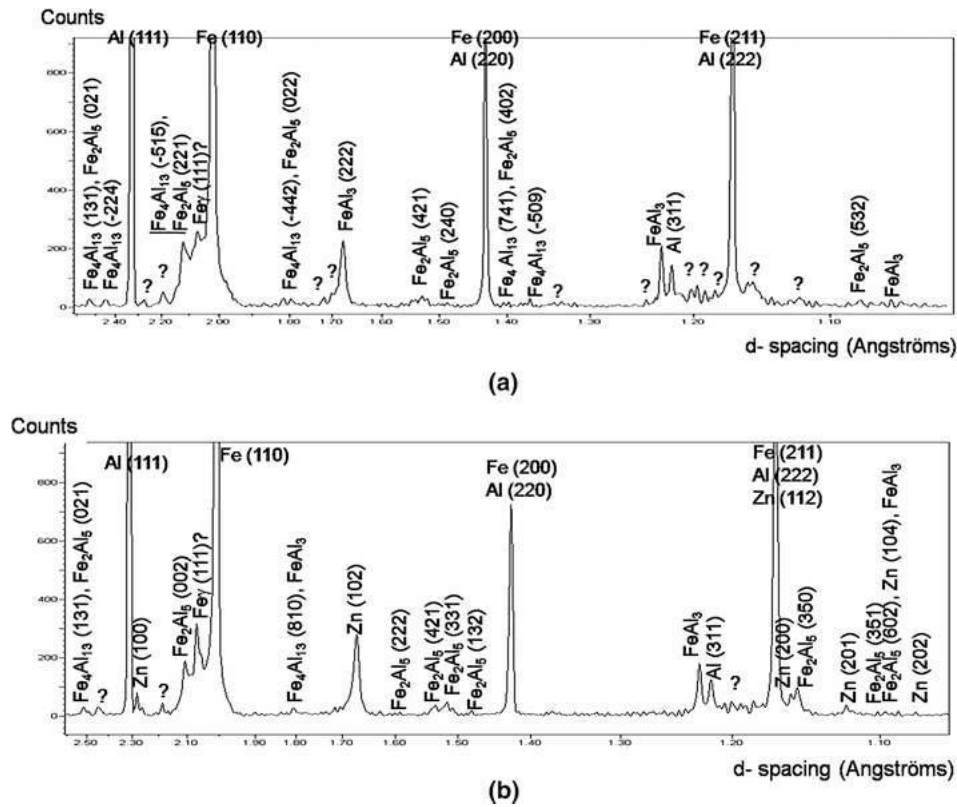
Figure 3.68: X-ray diffraction patterns of (a) the Al 1050-DP450 steel joint and (b) the Al 1050-galvanized DP450 steel joint [16]

variability of the transition zone width which can extend up to 2 μm in steel. In relationship with the impact symmetry and the planar joint configuration, the slope of the waves is reversed from one side of the central unbonded zone to the opposite side.

The chemical analysis of the joint interface using the X-ray diffractomery showed in the case of the uncoated steel that the $FeAl_3$ compound is predominantly detected together with small amounts of the Fe_2Al_5 and Fe_4Al_{13} phases (Fig. 3.68(a)) . In the coated steel case, some pure Zn, Fe_2Al_5, $FeAl_3$, and Fe_4Al_{13}compounds are observed, which is very likely due to the presence of the inhibation layer in the galvanized layer (Fig. 3.68 (b)).

In addition, most of the small intensity peaks and those marked by question marks in Fig. 3.68 may correspond either to cementite or to the $Al_xFe_ySi_z$ compounds observed in Fig. 3.66.

The transverse cross sections of both joints were also investigated at the finer length scale of TEM. In the case of the Al 1050-uncoated steel weld, some discrete intermetallic compounds with a maximum thickness of approximately 2.5 μm are detected in the interfacial zone (Fig. 3.69). In accordance with the XRD analyses (Fig. 3.68), their chemical composition determined by STEM/EDX is approximately 75% at. Al and 25% at. Fe, which corresponds to $FeAl_3$ (Fig. 3.70). At the interface, some harder Fe-rich convoluted lamellae are further detected within the softer Al part and inside the mixed zone (Fig. 3.69 and Fig. 3.70). They are composed of grains that are nearly 100 nm in size which is approximately 100 times smaller than the grains of the base steel. These grains result either from the dynamic recrystallization of Fe during MPW or from recrystallization due to heating during thin foil preparation by FIB.

For the Al 1050-galvanized steel weld, it is worth noting the irregular thickness of the interfacial
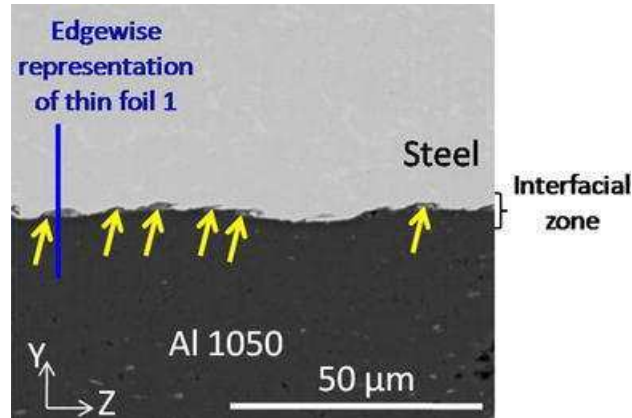
Figure 3.69: pockets (indicated by yellow arrows) containing thick IMCs along the interface of the Al 1050-uncoated steel joint observed in the X-Y transverse section (BSE/SEM) [16]
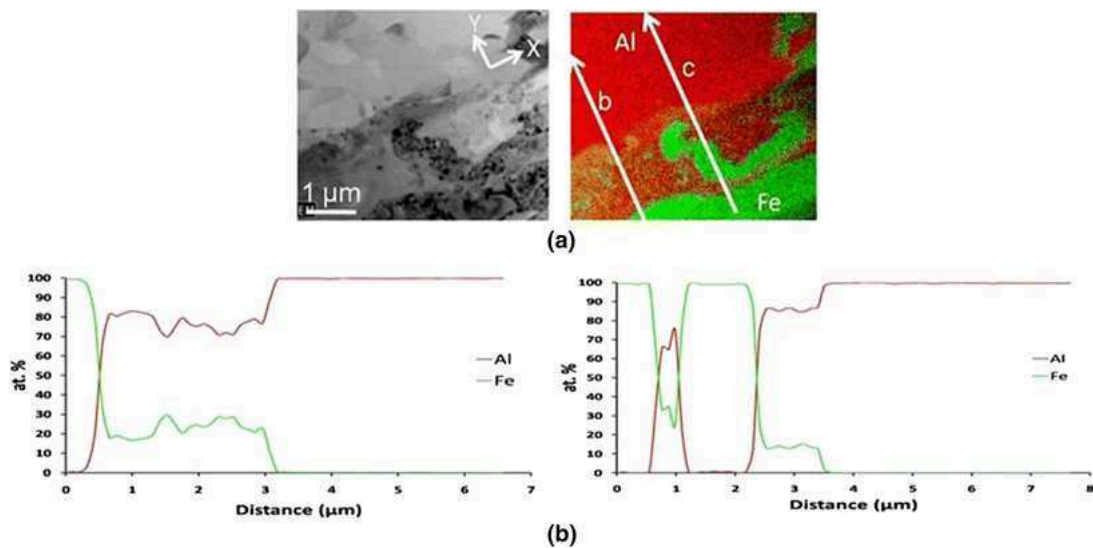
Figure 3.70: thin foil 1 (see its location in Fig. 3.69). (a) Interfacial zone of the Al 1050-uncoated steel joint in the X-Y transverse section (bright field-STEM) and combined Al-Fe X-ray map (EDX) [Al is colored in red and Fe in green]; (b) and (c): Al and Fe quantitative profiles along the lines (b) and (c) drawn in panel (a)[16]
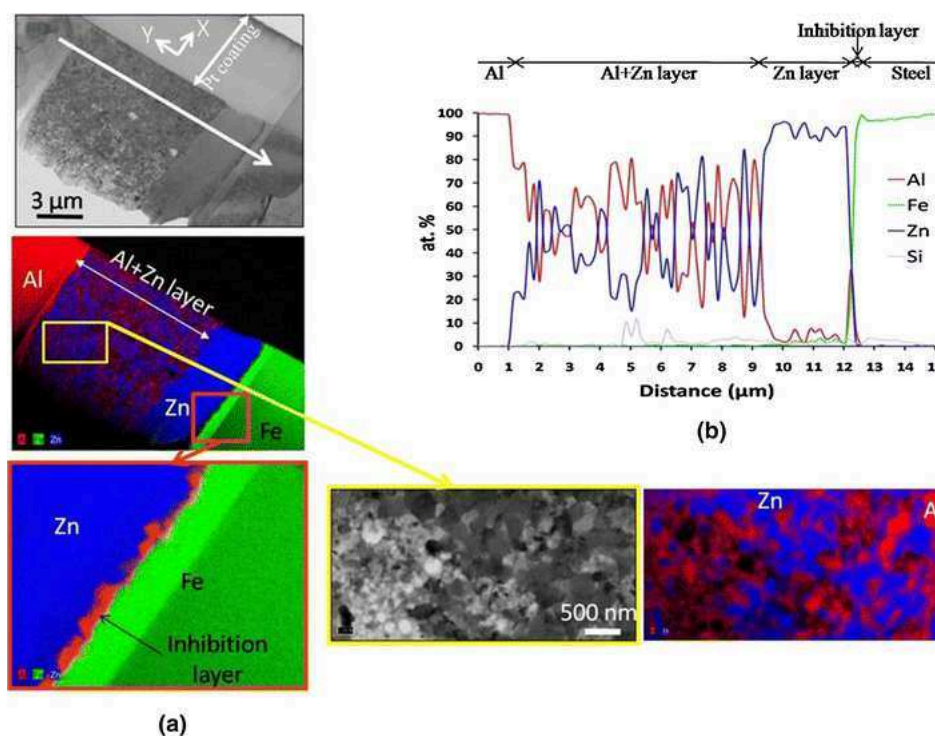
Figure 3.71: thin foil 2 (see its location in Fig. 3.67). (a) X-Y transverse section of the Al 1050-galvanized steel joint (bright field-STEM) and combined Al-Zn-Fe X-ray map (EDX) [Al is colored in red, Fe in green, and Zn in blue]; (b) Al, Fe, Si, and Zn quantitative profiles along the heavy white arrow drawn in panel a. The brightest green band is due to a zone that was less thinned during the preparation of the thin foil by FIB (Color figure online).[16]

zone (Fig. 3.67). In addition, going from steel to aluminum, the interfacial zone is composed of an inhibition layer, a zinc layer, and an Al+Zn bi-phased layer (Fig. 3.71) . This observation agrees with the XRD results (Fig. 3.68(b)) obtained at the mesoscopic scale. In the following, the Al+Zn bi-phased layer will be called the extra layer because, contrary to the other layers, it does not take part in the original steel coating. The flatness of the galvanized interface between steel and Zn contrasts with the unevenness of the Zn/extra layer and extra layer/Al interfaces. In addition, two types of waviness that are differentiated by both their periodicity along the joint and their amplitude of oscillation can be noted along the zinc/extra layer and extra layer/Al interfaces. According to the location along the joint, the respective thicknesses of both the zinc and the extra layer may significantly change, but their total thickness remains less than 12 μm (Fig. 3.67). At the location of thin foil 2, an 8-μm-thick extra layer composed of equiaxed grains with a diameter between 50 and 450 nm is formed (Fig. 3.71). This extra layer can be thinner (1 μm) (Fig. 3.72) , for instance at the constricted place marked by a white arrow in Fig. 3.67. The Zn layer is approximately 2.3 and 7 μm thick in the first (thin foil 2) and second (thin foil 3) cases, respectively. Compared to the [6 to 10 μm] initial thickness of the Zn coating, the pure Zn layer thickness can thus be divided by a factor of 5 at places where the (Al+Zn) layer is thick.

At the constricted parts of the interfacial zone (exemplified by the location of thin foil 3 in Fig. 3.67), an additional (Al)Zn, Al-10% at. Zn, solid solution is observed adjacent to Al (Fig. 3.72). The width of this layer is approximately 200 nm (Fig. 3.72).

Another observation is the waviness of the interface: a comparison of Fig. 3.69 and Fig. 3.67
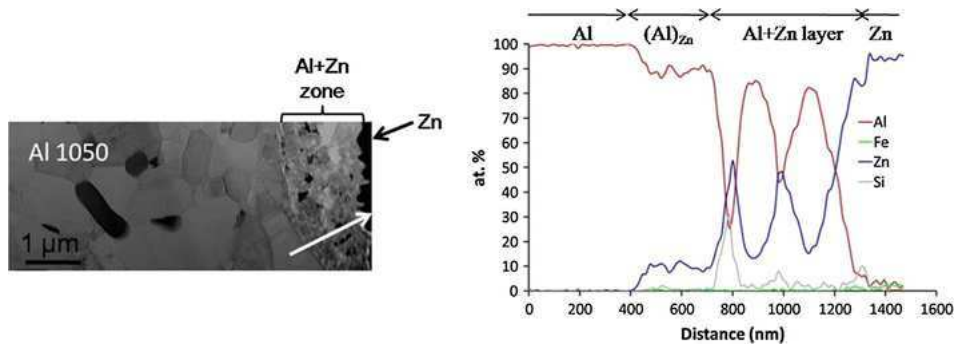
Figure 3.72: thin foil 3 (see its location in Fig. 3.67). Al side of the X-Y transverse section of the interfacial zone in the Al 1050-galvanized steel joint (bright field-STEM) and Al, Fe, Si, and Zn quantitative profiles along the white arrow drawn in the micrograph [16]
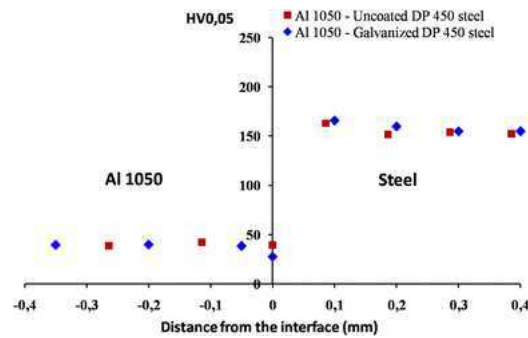
Figure 3.73: hardness profiles along the plate thickness (Y direction) for the Al 1050-DP 450 steel and Al 1050-galvanized DP 450 steel joints [16]

shows that the waviness of the interface is more pronounced for the uncoated steel. This observation is very interesting because both kinds of welds were obtained with the same process settings. This suggests that waviness is promoted by the ease of plastic deformation of the two base materials. Indeed, Zn presents fewer slip systems than steel or aluminum. In addition, in the case of the Al-uncoated steel joint, the waviness is further amplified by the insertion of hard Fe fragments, expelled by the spallation of the steel surface into softer Al during impact.

3.5.2.2.3 Mechanical properties of the joint

The hardness profiles across the interface and along the Y normal direction of both joints are depicted inFig. 3.73 . On the Al side, no softening originating from an extended heat-affected zone (HAZ) is observed, which is consistent with the absence of this zone. The latter deduction is confirmed by the invariability of the grain size and shape compared to those in the base material. The absence of an HAZ also agrees with both the high thermal conductivity of Al and the very short welding time. In the case of the joint with the coated steel, softening is observed close to the interface, which is very likely due to the presence of the Zn and (Zn+Al) layers (Fig. 3.73).

It is worth noting that the microhardness profiles presented here are similar to other results [160], but they differ from those of Yu et al., who noted hardening over a distance of 50 μm from the AA3003-low-carbon steel joint interface because at once of the presence of IMCs at the interface, of grain size refinement and of strain hardening on both sides of the interface [228]. In the current case of the joint formed with the uncoated steel, the lack of detection of hardening close to the
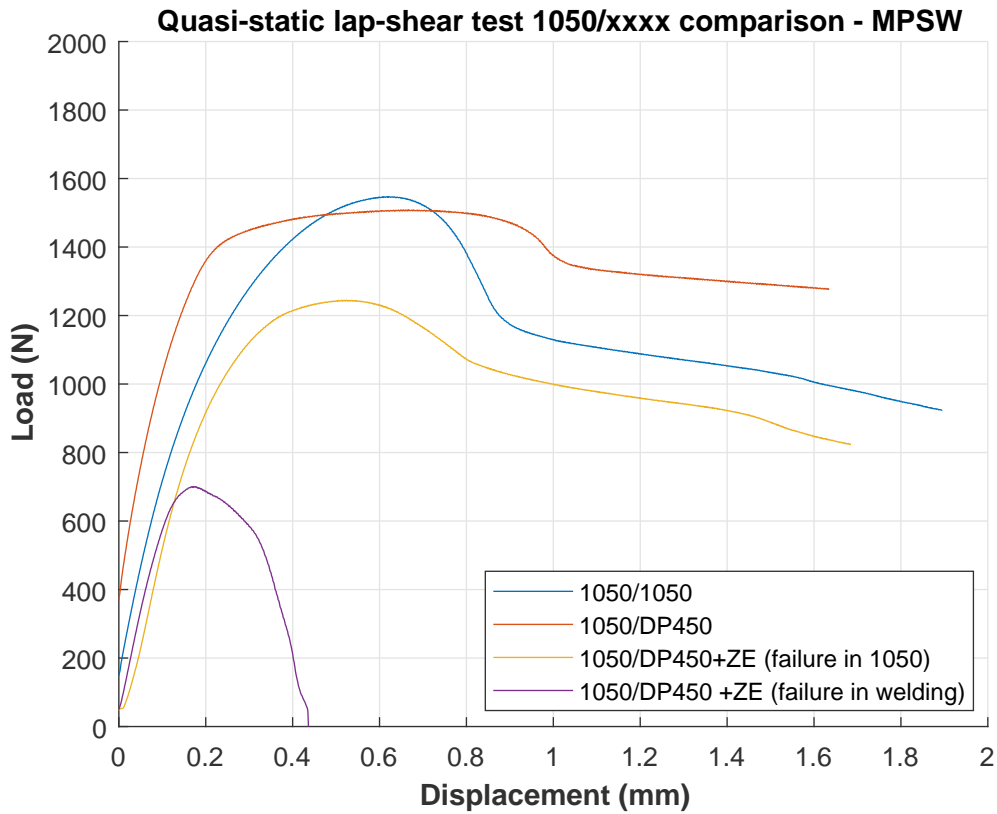
Figure 3.74: comparison between typical lap-shear quasi-static behaviour of the MPS welded specimens: 1050 with 1050, 1050 with DP450, 1050 with DP450 +ZE

interface is very likely due to the use of an important load for indentation and to an overly large measurement interspacing. Strengthening due to the presence of both hard $FeAl_3$ IMCs and fine recrystallized grains is expected on the Al side of the interface. According to the Hall–Petch relationship, the grain size effect must be significant in aluminum as it should lead to 30 MPa hardening compared to the one close to 85 MPa yield strength of the base material. In contrast to the previous interpretation of Yu et al. [228], strain hardening is not efficient in the present case, as suggested by the low density of dislocations on the Al side close to the interface (Fig. 3.66(c)).

Fig. 3.74 presents the lap-shear quasi-static test results for the joints between the aluminum and both coated and uncoated steel where the curve of the 1050 to 1050 was also included. The failure in the case of 1050-DP450 +ZE joints was not always the same: in most cases, the failure occurred in the 1050 sheet metal where the aluminum was teared; in some rare cases, the failure occured in the welding itself. When looking to the continuity of the load-displacement curves, there is no shift between the joining partners before reaching the peak strength and the ultimate tensile force is higher for the joint with the uncoated steel. The maximum displacement is rather low, independently of the joint type. However, the shear lap behavior of the joint with the uncoated steel is very similar to that of Al 1050-Al 1050 prepared with the same conditions.

Sound, i.e., not macroscopically damaged, joints were obtained when fracture occurred by ductile tearing in the Al base material and in front of the transverse part of the joint. The latter joints are characterized by a progressive decrease of the load with displacement. In contrast, for the joint with the galvanized steel where the failure occured in the welding, the load dropped rapidly after

its peak, as fracture occurred in the transverse part of the weld around the C zone denoted in Fig. 3.75 . Fig. 3.75(a) and (b) display the general character of both sides of the fracture surface. The fracture area on the galvanized steel side is essentially enriched in Zn, whereas some parts are Al-rich (Fig. 3.75 A, B, and C). The latter islands are obviously plastered in the shear direction over the Zn layer (Fig. 3.75(D)), which indicates that they were the last zones to break during testing.

3.5.2.3   Discussion

The first worth noting point is that with the present process parameters, the microstructure of the magnetic pulsed joints is defect-free in both cases i.e. with or without coating on the steel.

3.5.2.3.1   Joints with uncoated steel

In the absence of Zn and in accordance with data from the litterature [8] [121], intermetallic compounds are formed at the Al–steel interface. Some $FeAl_3$ compounds up to 2.5 μm thick are predominantly found on the Al side of the interface as shown by XRD and TEM analyses (Fig. 3.68(a) and Fig. 3.69). These IMCs are more specifically located in pockets distributed along the wavy interface and in close contact with the steel fragments that are torn and spread into the softer Al during impact. Such observations are consistent with previous works [121] [219]. A close examination of the literature data, not presented here to be concise, suggests that the discontinuity of the joint microstructure seems to result from a reduced input voltage and a low discharge energy. The IMC nature is consistent with a previous work [228], whereas other studies report the presence of discrete particles of both $FeAl_3$ and Fe_2Al_5 [132], Fe_4Al_{13} or Fe_2Al_5 [121] or continuous layers of Fe_4Al_{13} and $FeAl_3$ [228]. It is worth noting that neither a glassy (Al+Fe) zone [64] nor an oversaturated (Fe)Al solid solution was observed, which is in contrast to other studies [64, 132]. The observed discrepancies very likely result from differences in parameter settings. Process parameters are, however, often not reported in the literature, which makes the comparison difficult. In addition, the different natures of the steel used here compared to steel used by other authors may also explain the discrepancies in results because steels of different chemical compositions will have different material flow responses during MPW, exacerbating the variability of the microstructure.

In the current case, on the Al side of the interface, the predominant formation of $FeAl_3$ among all the Fe_xAl_y IMCs reported in the equilibrium phase diagram [34] can be questioned.

The formation of $FeAl_3$ and Fe_4Al_{13} generates a volume increase of 5764 pct vs 715 pct, 283 pct, and 4 pct for Fe_2Al_5, Fe_3Al, and $FeAl$, respectively, with respect to the Al matrix. Accordingly, the formation of $FeAl_3$ should not have been promoted because during MPW, the Al flyer piece is more plastically deformed than steel and compressive residual stresses are already constrained close to the interface. The formation of $FeAl_3$ is, however, aided by its compressibility, as it presents a lower bulk modulus than Fe_2Al_5, i.e., 284 GPa vs 475 GPa [140]. The latter argument is nevertheless doubtful because of the plastic nature of the lattice deformation.

In addition, according to the effective heat of formation model, the first intermetallic phase to nucleate would be Fe_2Al_5 which possesses the most negative heat of formation at the composition corresponding to the lowest temperature of the liquidus in the Al-Fe system [168]. In contrast, the
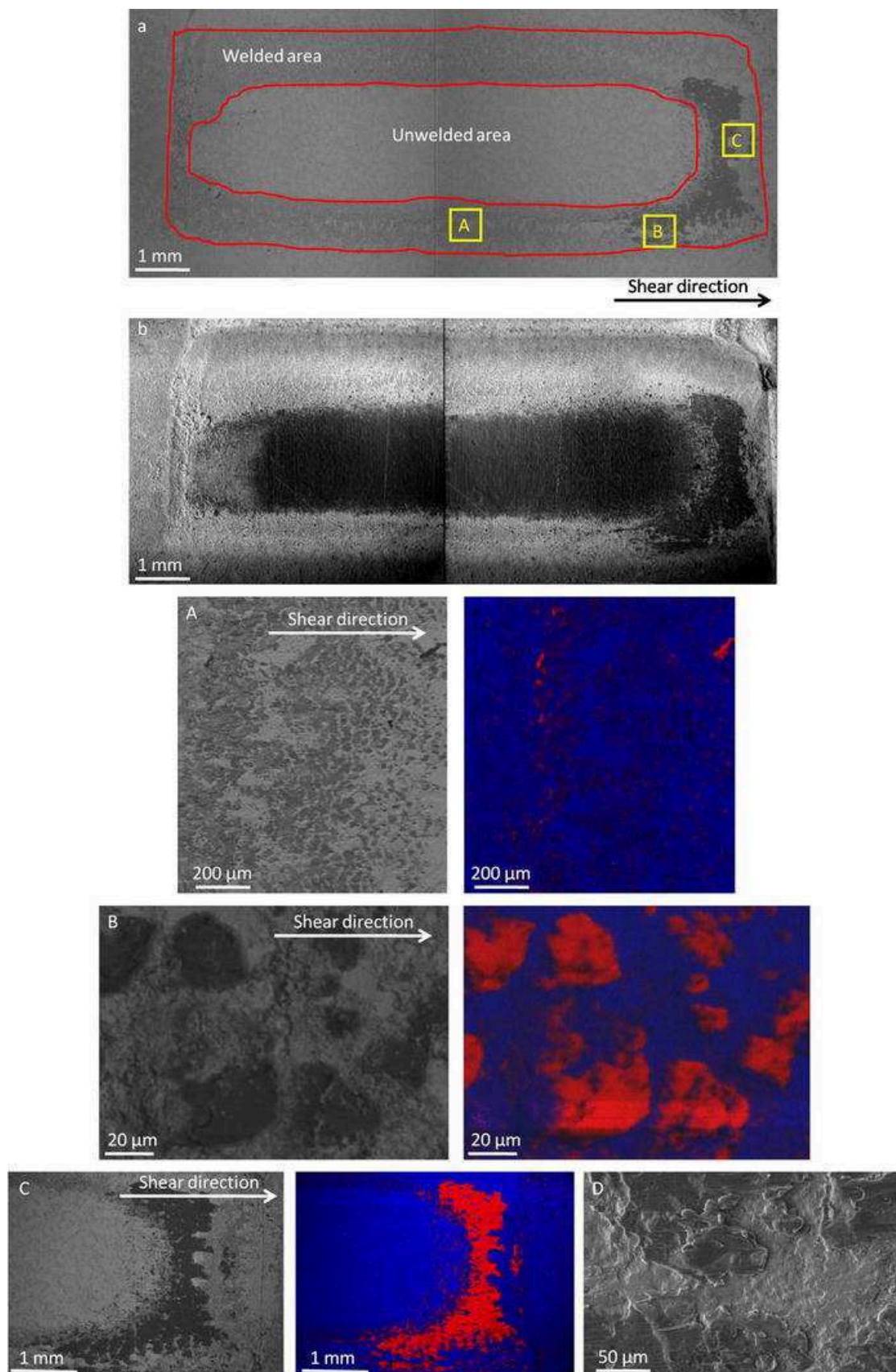
Figure 3.75: fracture surface of joint were the wleding failed: (a) galvanized steel side and (b) Al side, with A, B, and C being magnified views with corresponding combined Al-$K\alpha$ (red) and Zn-$K\alpha$ (blue) X-ray maps of the zones encircled in micrograph (a), and (D) a close-up of zone C [16]
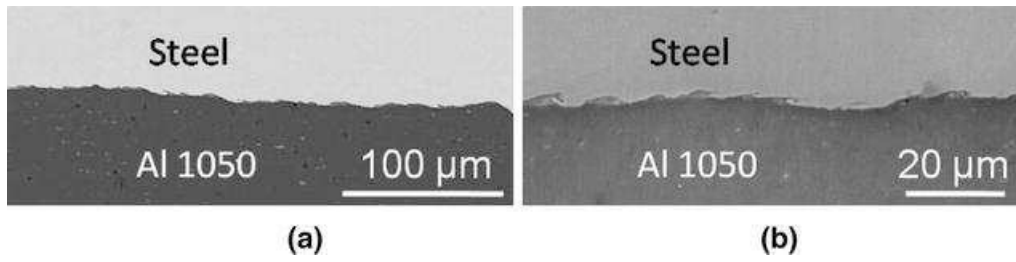
Figure 3.76: Aspect of the Al 1050-DP450 steel interface (a): BSE/SEM, (b): SE/SEM magnified view of figure (a)

Walser-Bene model predicts that the first phase to nucleate would be $FeAl_3$, which is the congruent phase immediately adjacent to the low-temperature eutectic phase in the Al-Fe phase diagram [209]. Another factor favorable for the preferential formation of $FeAl_3$ is the large extent of its composition range. Indeed the extent of composition is as efficient as diffusion for the growth of phases [94].

In addition, although the materials are not at equilibrium during MPW, the very low equilibrium solubility of Fe in Al (0.025 at. pct) [34] and the local chemical composition could also explain the preferential formation of $FeAl_3$, which is the most Al-rich Fe_xAl_y IMC on the Al side.

Finally, it is important to emphasize that some rather large IMC particles are formed in spite of the short (µs) welding time. The high kinetics of formation (some meters per second) is very likely assisted by the very high deformation rate. Two explanations are proposed. In the first hypothesis, welding proceeds in the solid state. Due to high strain rates and great pressures up to 105 MPa, Al would behave like a high velocity fluid, although it remains solid [169] [121] [198]. The viscous state would be induced by a high heat input and/ or by a great atomic disorder due to a high density of defects generated by the high strain rate at the interface. The high density of dislocations and the high oversaturation of vacancies [136] [147][146] [29] produced during impact should markedly increase the diffusion of elements. The dislocation density is, for instance, estimated at 1011 dislocations per cm² after explosion welding [146]. In the second assumption, the heating effect due to a high strain rate for a short time [189] may induce local melting followed by rapid solidification at the interface [169] [124] [64] [229]. In this case, diffusion is exacerbated during the process, which leads to the fast formation of IMCs. However, because of the absence of clue of solidification structures, the solid-state mechanism is the most likely mechanism in the present case. This contradicts assertions in the literature in which pockets at interfaces (see Fig. 3.76 and Fig. 3.69) should result from local melting [124].

3.5.2.3.2 Joints with coated steel

In the presence of the galvanized coating, except for the 150-nm-thick and continuous inhibition layer, no IMC is detected on either side of the joint interface. Instead, some pure zinc, with a thickness smaller than the primitive Zn coating, is observed together with a zone of interdiffusion.

A comparison with the 6 to 10 µm initial thickness of the Zn coating shows that, in the joint, the pure Zn layer thickness can be divided by 5 when the (Al+Zn) layer is thick (approximately 9 µm) (Fig. 3.71). Two assumptions can be made to explain this observation.

The first assumption would be that Al diffused into Zn over a distance greater than that over which

Zn migrated within Al. This explanation is indeed consistent with the different orders of magnitude of both diffusion coefficients. The diffusion coefficient of Zn in Al is 2.17×10^{-17}, 1.57×10^{-15}, and 3.63×10^{-10} cm²/s at 383 K (110 °C), 433 K (160 °C), and 688 K (415 °C), respectively [34], whereas the diffusion coefficient of Al in Zn is equal to 3.16×10^{-9} cm²/s at 573 K (300 °C) [52]. The deformation very likely further promotes the diffusion of Al in Zn since the distance covered by the elements during the process (i.e., in approximately 15 µs) is equal to a few micrometers, which is greater than the distance of 0.24 µm calculated by considering the previous diffusion coefficients measured in deformation-free samples. Only Al should diffuse in Zn since the original Zn coating thickness is very close to the total thickness of both the (Al+Zn) and Zn layers after welding.

A second explanation would be fracturing of the brittle zinc layer under the impact effect followed by filling of the empty spaces (let by the cracks) by viscous Al.

Moreover, as previously stated for the case of the Al-uncoated steel joint, the absence of clue of solidification structures suggests that joining very likely occurred in the solid state in spite of the easy melting of Zn with its low melting temperature, i.e., 419.5 °C.

3.5.2.3.3   Role and interest of the zinc layer

Without the galvanized coating, only discrete and thin Fe_xAl_y IMC particles are formed, whereas the presence of Zn contributes to the formation of both a bi-phased (Al+Zn) layer and an (Al)10% at. Zn solid solution. The comparison of both kinds of joints proves that the presence of Zn hinders the formation of Fe_xAl_y IMCs at the interface. Indeed, the presence of the $Fe_2Al_5Zn_x$ inhibition layer on the steel hinders the diffusion of Fe and, subsequently, the formation of both Fe_xZn_y and Fe_xAl_y IMCs.

From the mechanical point of view, the comparison between the results of the shear lap tensile tests suggests that the presence of a continuous Zn layer is more deleterious than that of discrete IMCs particles at the interface. Discrete IMC particles may not be redhibitory with regard to joint fracture [173] [232] [216]. Otherwise, it is worth noting the absence of the (Al+Zn) bi-phased layer over the fracture surface (Fig. 3.75). This observation may result from both the insufficient spatial resolution of the present SEM images and/or the high plasticity of the bi-phased layer. The latter hypothesis agrees with both the submicrometer size and the chemical composition of the grains. Superplasticity was observed in Zn-22 at. pct Al alloy at room temperature and at a similar strain rate [225].

3.6   Conclusion

In this chapter, we investigated deeply the development of the MPW/MPSW processes for welding metal alloys. The experimental procedure was presented first in a detailed manner to show the importance of respecting the mentionned steps during the application of the process:

- the cleaning of the metal sheets from oil which, if present, prevents the welding from occuring;

Couple (Flyer/Parent)	Configuration	QS load (N)	QS displacement (mm)	Dynamic load (N)	Dynamic displacement (mm)
5182/DC04	MPSW	6413	1.7	8142	1.44
5182/DP450	MPSW	9057	1.7	6949	1.5
6016/DC04	MPSW	7703	2.43	>9000	-
6013-T4/DP1000	MPSW	7799	1	7580.23	1.36
6013-T4/DP1000	MPW	8734	1	13808	3.52

Table 3.10: summary of quasi-static and dynamic average maximum loads for different dissimilar combinations

- the control of the sheet metal positionning regarding the coil which has an important role in the way that the induced current will be distributed and hence it will affect the efficiency of the process;

- the use of a proper clamping torque in the MPW configuration (max. 40 N.m) to not over-compress the insulators and change the intended standoff distance; and in the MPSW configuration the proper clamping (35 N.m) has an important role to not deform the hump and change hence the standoff distance.

The experimental constructed welding window for different couples of materials combined with the numerical studies (Fig. 3.25) showed that when the flyer metal is thinner/weaker the welding window is very large and the distance between the insulator has less influence on the welding behviour. On the other hand, when the thickness/strength of the flyer metal increases, the welding window decreases where higher discharge energies are required and the distance between the insulators should be higher and has crucial influence on the welding quality (Fig. 3.21 and Fig. 3.22). In addition, the experimental results validated the fact that the O-shape coil has higher efficiency than the linear typical coils (Table 3.7).

Further, the different dissimilar combinations of automotive aluminum and steel alloys investigated and presented in this chapter have never been welded together, to our knowledge, using MPW and MPSW. The presented results in Table 3.7, the welding between the aluminum and coated steels as well as the aluminum with the pure zinc showed the wide scope of application of this technology to different and not restricted types of dissimilar metal alloys wether new generations or traditional alloys. The mechanical strength of these different weldings showed also that the bonding between different dissimilar combinations is far from being weak. The Table 3.10 summarizes the average maximum loads of dissimilar aluminum to steel combinations under quasi-static and dynamic loads with the corresponding average displacements attained during these tests:

- In quasi-static tests, the average loads hold by a welding line exceed 6 kN and attain 9 kN in the 5182/DC04 case. The quasi-static behaviour of the welds showed similarity when the parent metal is from the same family of steels: Fig. 3.39, Fig. 3.43 and Fig. 3.45 for DP

steels; Fig. 3.36 and Fig. 3.41 for DC04 steel. When comparing the MPW and MPSW configuration for the same combination of 6013-T4/DP1000, the latter has less strong welding in both quasi-static and dynamic.

- In the dynamic loads, the aluminum 6xxx alloys showed higher strength with different alloys of steels where in the 6013-T4/DP1000 case, the dynamic load withstanded by the welding has an average of almost 14 kN.

- The fatigue behaviour of different couples showed also higher number of cycles for the 6xxx alloys exceeding the 40000 cycles with, once again, a higher number of cycles for the MPW configuration. When looking to the microscopic analysis, in the MPSW configuration various intermetallic compounds were detected while in the MPW the only detected intermetallic compound is an aluminum rich compound which can give an explanation of the better behaviour in the MPW case.

- In the welding between the 1050 aluminum and coated steels (DC04 +ZE and DP450 +ZE), it is the aluminum sheet which failed in the mechanical tests and the welds even showed in the DC04 steel case higher strength than the similar welds of the 1050 itself (Fig. 3.62). However, the weld failed in some cases and which can be related to the non-uniform zinc layer on the steel surface.

From a microscopic point of view (Section 3.4.5), the welds showed a variety of wavy interfaces as well as different types of IMCs depending on the joined partners. Besides, the fracture surfaces showed also that the failure of the welding can occur in the base material itself or within the welding. Regarding the joint with galvanized steel (Section 3.5), two interfacial layers occurred, namely, an (Al)Zn solid solution and an (Al+Zn) bi-phased layer; the Zn layer enables to avoid the formation of Fe_xAl_y intermetallic particles at the Al-steel interface.

Now that the applicability of the planar MPW/MPSW technologies to different combinations of sheet metal alloys is validated, the next step is to explore the extension of this application to dissimilar materials application where the main aim is the joining between FRPC and metals and for which the next chapter will be totally devoted.

Chapter 4

FRPC to metal joining: MPW and MPSW extended application

4.1 Résumé

Comme discuté au début de cette étude, le but principal de cette thèse est le développement de nouvelles solutions pour les assemblages hétérogènes et hybrides afin de répondre aux défis de l'allègement de l'automobile. Dans le chapitre précédent, le large domaine d'application du soudage par impulsion magnétique pour différents alliages automobiles a montré le potentiel de cette technologie. Par conséquent, nous sommes devant un procédé capable d'assembler différentes nuances de métaux homogènes ou hétérogènes en utilisant les mêmes équipements et sans changer le procédé pour chaque application spécifique. Cette caractéristique unique du soudage par impulsion magnétique, qui le différencie de tous les autres procédés d'assemblage, nous a poussé à penser comment étendre son application, en particulier pour les configurations planes, pour des matériaux non métalliques dans le but d'en faire une solution d'assemblage multi-matériaux-multi-usages.

Nous avons ainsi proposé des solutions innovantes pour assembler des pièces composites à des tôles métalliques et qui ont été brevetées par l'Ecole Centrale de Nantes et FAURECIA [101, 175, 177]. Ces nouvelles solutions proposées couvrent toutes les applications possibles en tenant compte des différentes configurations ainsi que des propriétés et des épaisseurs des matériaux. Les deux idées principales sont basées sur l'introduction d'un insert métallique fin dans le composite ou par l'utilisation d'un patch métallique à travers le composite pour créer la jonction. Les différentes configurations proposées peuvent être trouvées dans les Fig. 4.2 à Fig. 4.6.
La faisabilité de ces idées est étudiée expérimentalement au cours de ce chapitre. Dans la configuration de l'insert métallique, les conclusions les plus importantes pouvant être formulées sont:

- les inserts métalliques peuvent être en aluminium ou en acier;

- la conception des inserts métalliques a montré que l'insert avec des trous à brides permet une forte adhérence avec le composite et cela a été prouvé lors de divers essais mécaniques ;

- le nettoyage des résidus de polymères de la surface des inserts est très important puisque

les expériences ont montré que l'impact progressif ne pourrait pas éliminer ces résidus qui constituent alors un obstacle à la soudure ;

- les trous dans l'insert n'empêcheront pas le soudage, mais ils réduiront de manière significative les lignes de soudage effectives conduisant à des soudures plus faibles et durant la conception il faut donc bien veiller à éviter toute coïncidence entre la ligne de soudage et les trous à l'intérieur des inserts ;

- la transition entre les paramètres de soudage bimétalliques peut être utilisée avec une grande précision afin de créer le soudage entre la pièce métallique et l'insert se trouvant dans le composite ;

- les essais mécaniques ont montré qu'il n'y avait pas de perte significative de tenue mécanique entre les applications bimétalliques et la soudure avec l'insert à l'intérieur du composite ;

- les inserts en acier ont montré une meilleure résistance que ceux en aluminium puisque dans ce dernier cas, l'insert était toujours déchiré durant les essais mécaniques.

Dans l'application patch métallique, les principaux points qui peuvent être énoncés sont les suivants:

- un patch métallique mince risque de se déchirer sur les bords des trous dans le composite lors de l'application du soudage et il est donc préférable d'utiliser des pièces d'épaisseur supérieure à 1 mm ;

- les dimensions des trous doivent correspondre à la longueur de la zone active de l'inducteur en dépassant cette longueur de 5 mm minimum de chaque côté ;

- la géométrie du trou est importante pour maintenir plus longtemps le soudage pour augmenter la surface du trou remplie par le patch qui impliquera une meilleure tenue mécanique;

- l'écoulement du patch à travers les trous du composite ne remplit pas nécessairement les bords de ces trous et crée des risques de glissement selon le type de chargement;

- la transition entre les paramètres bimétalliques de soudure et l'assemblage métal/composite est possible ; l'épaisseur du composite représente une analogie avec le paramètre h;

- la configuration où le FRPC est pris en sandwich entre deux pièces métalliques a prouvé son efficacité et le comportement mécanique de la soudure est le même que dans les applications bimétalliques.

Un point important à mentionner ici est le fait que ces solutions utilisent le même équipement que celui utilisé pour les applications bimétalliques et sans aucune modification.

Enfin, deux points importants sont à mentionner avant de clore ce chapitre :

- le premier concernant les observations microscopiques pour les échantillons préparés pour la microtomographie, ces observations devraient être effectuées afin de voir l'influence des

assemblages sur la microstructure du composite, mais malheureusement le tomographe était hors service pendant cette période et donc les observations ont été reportées à des dates ultérieures à la date de clôture de l'étude;

- la seconde concernant un nouvel insert métallique que nous avons également commencé à tester. Il s'agit d'un 5052-H32 épinglé (Fig. 4.37). Cet insert a également été testé pour souder de l'aluminium 6013-T4 d'épaisseur de 1,4 mm. Des soudures ont été obtenues à partir d'une énergie de décharge de 13 kJ et les premiers essais quasi-statiques ont montré des tenues supérieures à 2,5 kN. Malheureusement, le générateur a été arrêté durant la phase finale de cette étude et toutes les actions prévues durant cette période finale ont été reportées à des dates ultérieures à la date de clôture de la thèse.

4.2 Introduction

As it was discussed in the begining of this study, the main aim of this dissertation is the development of new solutions for hybride FRPC to metals joining processes in order to meet the challenges in automotive lightweighting. In the previous chapter, the wide application scope of the MPW/MPSW for different metal automotive alloys showed the potential of this technology at the same time on the similar and dissimilar metals joining scope. Therefore, we can say that we are in front of a process which allows us using same equipments for various applications at once instead of changing the process for every and different joining application. This unique characteristic of the MPW which differentiates it from all the other joining processes, prompt us to ask ourselves: how can we extend the application scope of MPW/MPSW, especially for the planar configurations to include non-metallic sheet materials and make the technology a multi-material-multi-use joining solution?

To do so, we proposed innovative solutions for joining sheet metal to FRPC sheets and which were patented by Ecole Centrale de Nantes and FAURECIA [175–177]. These solutions will first be detailed to go after that through their experimental feasibility studies.

4.3 New assembly methods between metal and FRPC

The first step in proposing the new solutions was to take into consideration the multiple factors that may influence the FRPC to metals joining techniques:

- variable thicknesses of FRPC sheets;

- characteristics of the joining partners (metals and FRPC);

- geometrical design limitations of the intended applications;

- avoiding the damage in the assembly region as much as possible;

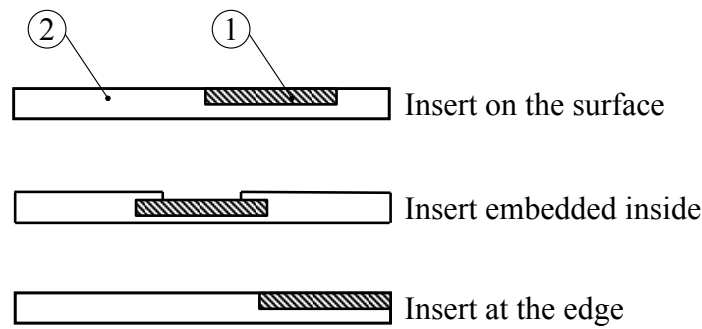- accessibility to the joining area on the assembly lines and

Figure 4.1: metallic insert embodying in the composite sheet

- reduction of the preparation phase time for the joining process.

Accordingly, the proposed solutions have been thought in a manner to cover all probable restrictions during applications and at the same time trying to benefit from the advantages that MPW/MPSW presents and taking into consideration the process main needed parameters especially the standoff distance.

4.3.1 Proposed solutions presentation

The first configurations have one common point which is the introduction of a thin metal insert with small dimensions in the FRPC sheet during the manufacturing phase where the polymer will act as an adhesive agent embodying this insert inside the composite (Fig. 4.1) . This metallic insert which is positioned at the intended joining zone will play two different roles depending on the application.

1. it will act as an intermediate metal on which the metallic partner can be welded using MPW or MPSW (Fig. 4.2) or,

2. it will be the flyer part which will be welded on a fixed metallic partner using the MPW (Fig. 4.3)

Configuration 1 can be used when even the metallic partner has a good electrical conductivity and relatively small yield strength (aluminum sheets for example) or FRPC sheets are thin (less than 1.6 mm) so that the metallic insert should be placed at the surface of the composite. It is suitable also in the case where the metallic partner is accessible for the robot welding gun holding the coil. On the other hand, this kind of configuration can be also used for applications were the joining is required at the edge of the FRPC sheets as represented in Fig. 4.4 and which can be used also for welding and as well as a clinching process at the same time.

Configuration 2 takes into consideration the case of thick composite sheets and where the accessibility of the welding gun is from the composite side only.

The second part of configurations takes into considerations the conditions where the metal partner could be a very high strength metal, or having high thickness or is an electrially less-conductive metal as an example ultra high strength steels. In this case, the solutions are represented in Fig. 4.5 and the principle is based on the use of a metallic patch which will have the role of a flyer metal that
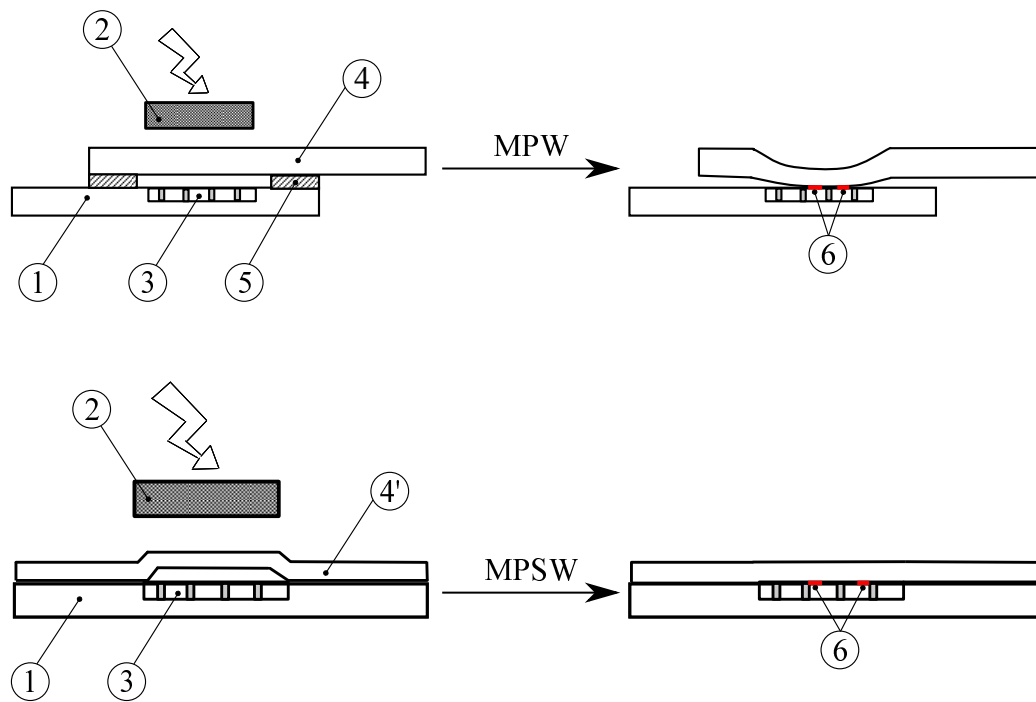
Figure 4.2: configuration 1 - 1: FRPC; 2: coil; 3: metallic insert; 4:flyer metal; 5: insulators; 6: welding
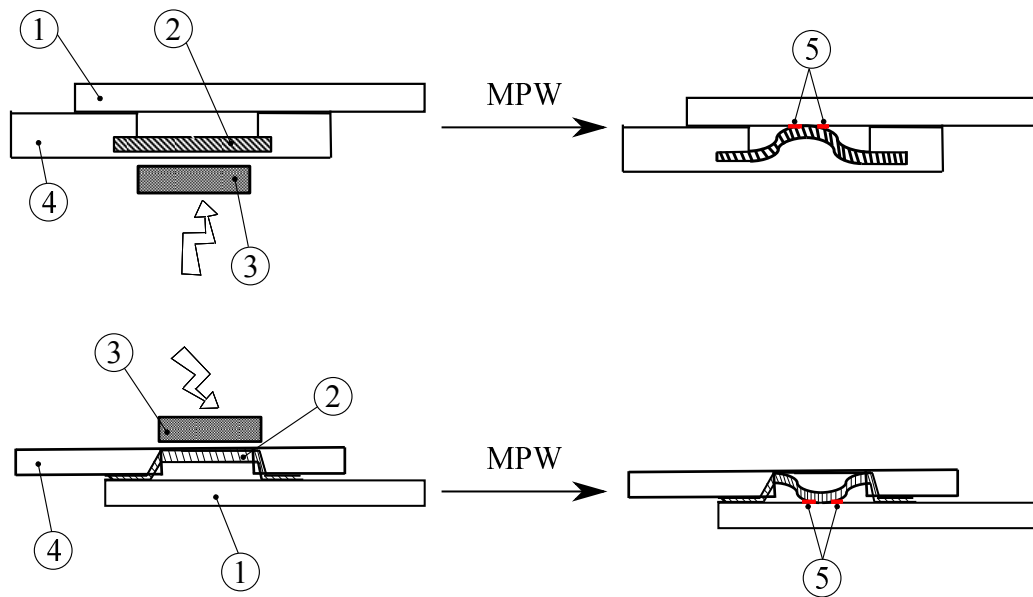
Figure 4.3: configuration 2 - 1:flyer metal; 2: metallic insert; 3: coil; 4: FRPC; 5: welding

181
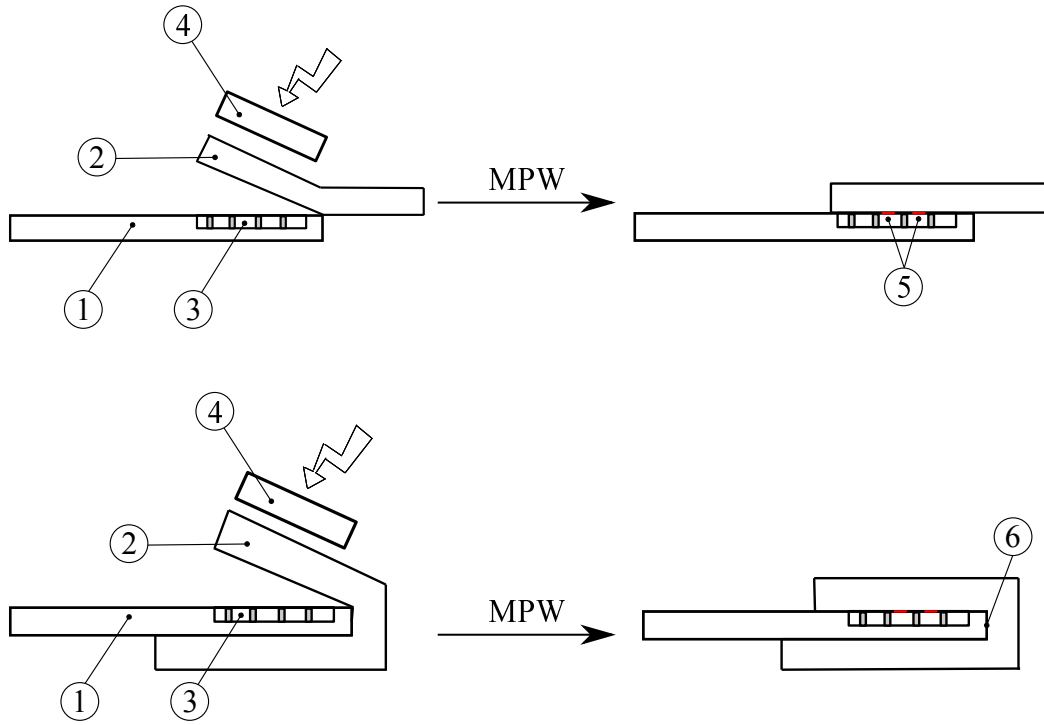
Figure 4.4: configuration 3 - 1:FRPC; 2: metal sheet; 3: metallic insert; 4:coil; 5: welding; 6:clinching area

once the MPW is applied, it will weld to the parent metal trapping the composite in-between and creating the joining. This application of course can be extended to create also sandwich structures of metallic and non-metallic sheets when needed (Fig. 4.6).

As it can be noticed, the ideas are based whether on MPW/MPSW of the sheet metal on a metallic insert inside the composite or using a metallic patch to apply the MPW/MPSW for joining between the materials. Hence, in the next section we will present the experimental feasibility study that was conducted using a metallic insert embedded in the composite and metallic patches to create this joining.

4.4 Equipment and experimental procedure

4.4.1 Pulse Generator

The pulse generator is the same one used during the metal/metal MPW/MPSW investigations and which has the below characteristics:

$$C = 408\,\mu\text{F}, L_{Generator} = 0.1\,\mu\text{H}, R_{Generator} = 14\,\text{m}\Omega$$

$$V_{max} = 15000\,\text{V}, I_{max} = 500\,\text{kA}, f_{short} = 25\,\text{kHz}$$

The higher limit for the discharge energy is hence fixed at 16 kJ so that the discharge current does not exceed 80% of the maximum allowable current for the generator:

Figure 4.5: configuration 4 - 1: metallic patch; 2: FRPC; 3: metal sheet; 4: welding

Figure 4.6: configuration 5 - 1: metal sheet; 2: FRPC; 3: fixed metal sheet; 4: welding

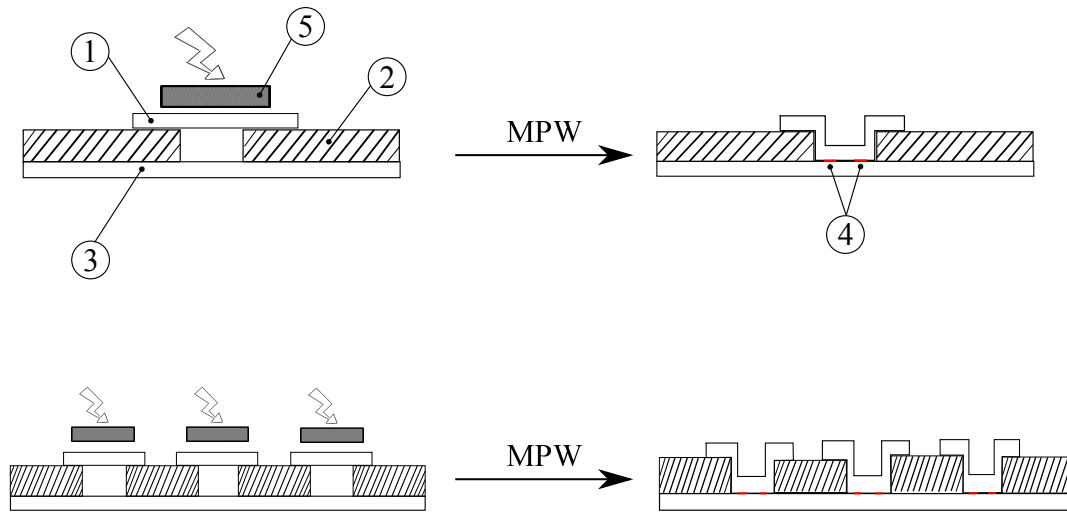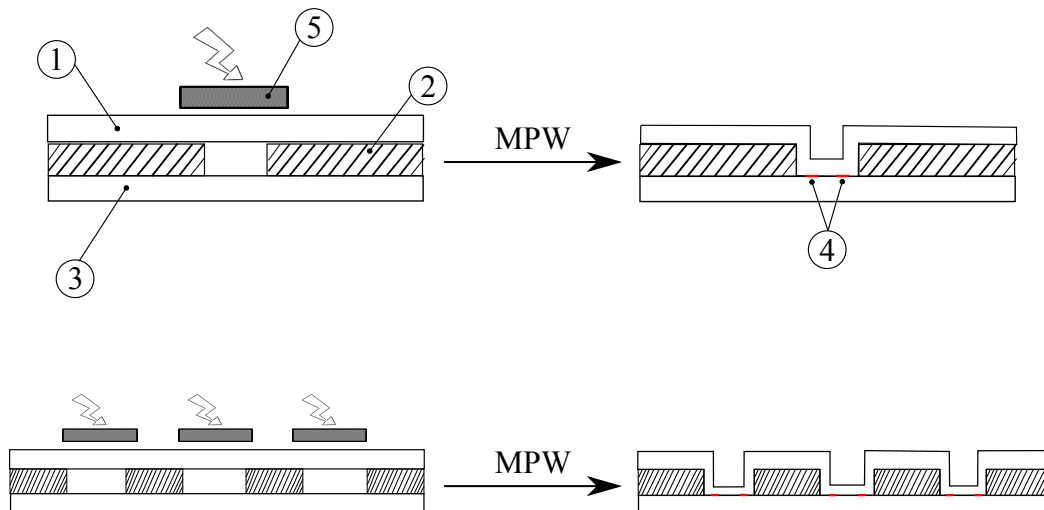| Property	Test Method	Units	Warp direction		Weft direction	
Reinforcement						
Fabric	-	-	2-2 Twill Weave Glass Fabric			
Warp to weft ratio	-	%	50		50	
Resin Composition	-	-	PA-GF75			
Sheet						
Thicknesses	-	[mm]	1.2 to 2			
Fiber Mass Fraction (M_f)	-	[%]	75			
Fiber Volume Fraction (V_f)	-	[%]	57			
Density	ISO 1183	[g/cm^3]	1.98			
Thermal						
Melting temperature	ISO 11357-1/-3	[°C]	260			
Mechanical			Dry	Cond.	Dry	Cond.
Tensile Modulus, 23°C	ISO 527-4	[GPa]	29	24	27	25
Tensile Stress at break, 23°C	ISO 527-4	[MPa]	491	399	504	411
Tensile Strain at break, 23°C	ISO 527-4	[%]	2.2	1.8	2.2	1.8

Table 4.1: DuPont-TM Vizilon™ SB75G1 thermoplastic composite sheet

$$I_{operation_{max}} = 0.8 \times I_{max} = 400\,\text{kA}$$

4.4.2 Coils

After the better efficiency that the O-shape coil showed, it will be used during this experimental feasiblity study in its steel version for the patches with higher thickness while the linear copper coil will be used for the patches with smaller thicknesses. Both coil dimensions are presented in Fig. 3.2 and Fig. 3.3.

4.4.3 Materials

As it is already known, the two basic ideas that will be tested are an application with a metallic insert and another using the metallic patches. In both cases, the FRPC chosen was a DuPont-Vizilon™ SB75G1 which is a heat stabilized, 2-2 Twill Weave Glass Fabric reinforced polyamide based thermoplastic composite sheet (Table 4.1) .

For the first configuration, i.e. with metallic inserts, the flyer metal was an aluminum-5182 (Table 3.1) having a thickness $e_f = 1.2$ mm. The metallic inserts were made of 5754 aluminum (Table 3.1) and DC04 steel (Table 3.1).

For the second configuration, i.e. with metallic patch, the metallic patches were 5754 and 5182 aluminums (Table 3.1) and the metallic partners tested are a DC04 steel with a thickness $e_p = 0.8$ mm and a DP450 steel with a thickness $e_p = 1.17$ mm.

4.4.4   Experimental setup

4.4.4.1   Experimental design strategy

The two main purposes of this experimental investigation are to proove the feasibility of the two principles on which the new proposed joining solutions are based, to have a first insight on the mechanical strength and some right hand rule for the design of these solutions. The experiments were designed then using a 6-Phase strategy:

- **Phase 0 - Define the configurations that allow to proove the feasibility of the solutions**

Based on the different solutions proposed, of course we will not have the time to test in details all the solutions so from here the idea was to test the two big principles:

1. one configuration with a metallic insert inside the FRPC using an automotive aluminum alloy as a flyer metal and where the MPSW is the joining process;

2. another configuration using the metallic patch principle and applying hence the MPW.

The configuration 1 using the MPSW as joining process (Fig. 4.2) was then chosen to validate the first principle and the configuration 4 (Fig. 4.5) was used to validate the second principle.

- **Phase 1 - Define the pre-joining steps to allow the application of the MPW/MPSW**

For the configuration using the metallic insert, the first thing to do was to define the insert design and the way of introducing it in the composite. For the design, it was very important to take into consideration to have a maximum adhesion between the insert and the composite and also to have an area where the application of the MPSW will lead to a good quality welding.

For the metallic patch configuration, the metallic patch material selection and its dimensions are to be considered. The other important preparation is the hole geometry and dimensions inside the FRPC.

- **Phase 2 - Experimental application for the metallic insert configuration**

The steps then in this case were:

1. define two designs of inserts and choose two different metal alloys;

2. define and optimize the process of introducing these inserts in the composite;

3. choose the MPSW process parameters from the lessons learned during the metal/metal MPSW development phase;

4. test the specimens in order to define the best design of the insert which led to a good adhesion in the composite;

5. prepare joints with this type of insert with two different types of materials for testing the mechanical strength of the joints under different loads (quasi-static, dynamic and fatigue);

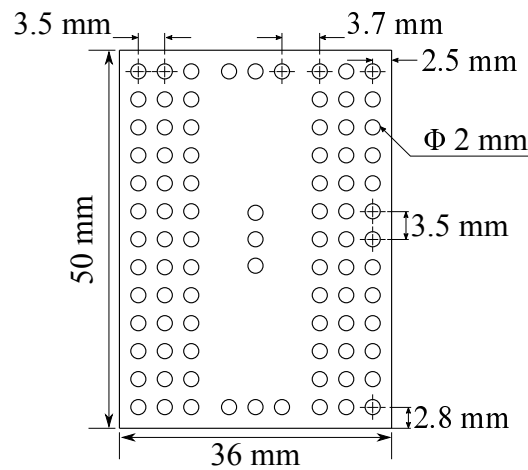6. analysis of the failures observed during the mechanical tests.

Figure 4.7: perforated metallic insert

- **Phase 3 - Experimental application for the metallic patch configuration**

In this case, the steps are:

1. define the dimensions of a metallic patch and a simple hole design by taking into consideration the coil active length to test as first feasibility of the principle;

2. test the specimen under quasi-static loading to observe the failure of the joint and understand how the patch flowed inside the hole;

3. define other holes design to improve the way how the patch will flow and to check how much does this influence the joint behaviour;

- **Phase 4 - Microscopic analysis of the joining surface**

Microscopic analyzes for the joints areas especially the influence of the process on the FRPC microstructure and if major damages are observed in these areas.

- **Phase 5 - Analyse the configurations**

Discuss the main observations during the experimental feasibility investigation to be able to conclude. In addition, this analysis will identify the main points to take into consideration for further development and also to consider the possibility of a transition from the metal/metal parameters to the metal/FRPC joining and the limitations for this transition.

4.4.4.2 Configuration with metallic insert

4.4.4.2.1 Metallic inserts

The metallic insert design focused on having the thinnest possible insert and a good adhesion with the composite. The materials of the inserts were aluminum 5754 and steel DC04 having thicknesses of 0.5 mm and 0.62 mm respectively.

The first design is perforated metallic inserts with perforation diameters of 2 mm (Fig. 4.7) and the inserts were sandblasted on the side in contact with the composite in order to increase the contact
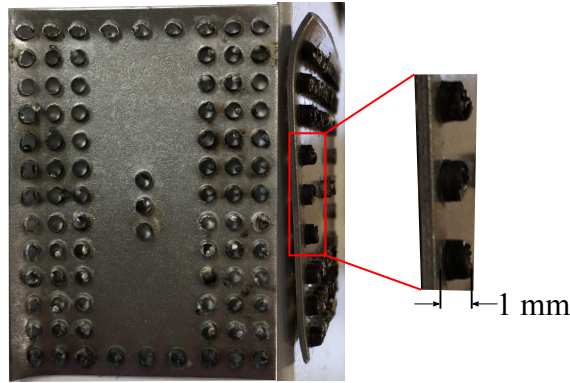
Figure 4.8: metallic insert with flanged holes

Figure 4.9: SCAMAX press

surface and improve the adhesion. At the same time the design took into consideration the fact that the area of the insert where the welding will take place needs to be free of any perforation. The second design is also perforated inserts with 2 mm diameters holes but with flanged holes having a depth of 1 mm (Fig. 4.8).

The inserts were embedded in the composite sheets by applying an over-molding thermo-compression process using a SCAMAX press consisting of two heating plates and a pressure cylinder (Fig. 4.9). The mold used is a steel one composed of two square plates having dimensions of 300×300 mm² (Fig. 4.10). The metallic inserts were then positionned on the composite sheet to be processed after that as presented in Fig. 4.11 and finally the FRPC sheet was cutted into the desired experimental specimens (Fig. 4.12).

4.4.4.2.2   Setup for MPSW application

As it was noticed in the previous chapter, the hump with the dimensions $l_h = 12$ mm, $L_h = 20$ mm, $l'_h = 40$ mm and $L'_h = 55$ mm, showed a good universal use on different alloys of flyer metals and hence it is chosen in this experimental phase also. It is stamped in the flyer metal using a hydraulic press die and the pressure used does not exceed 6 tones.
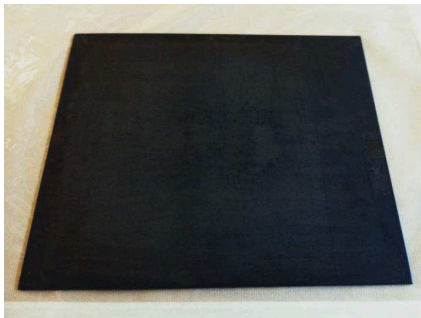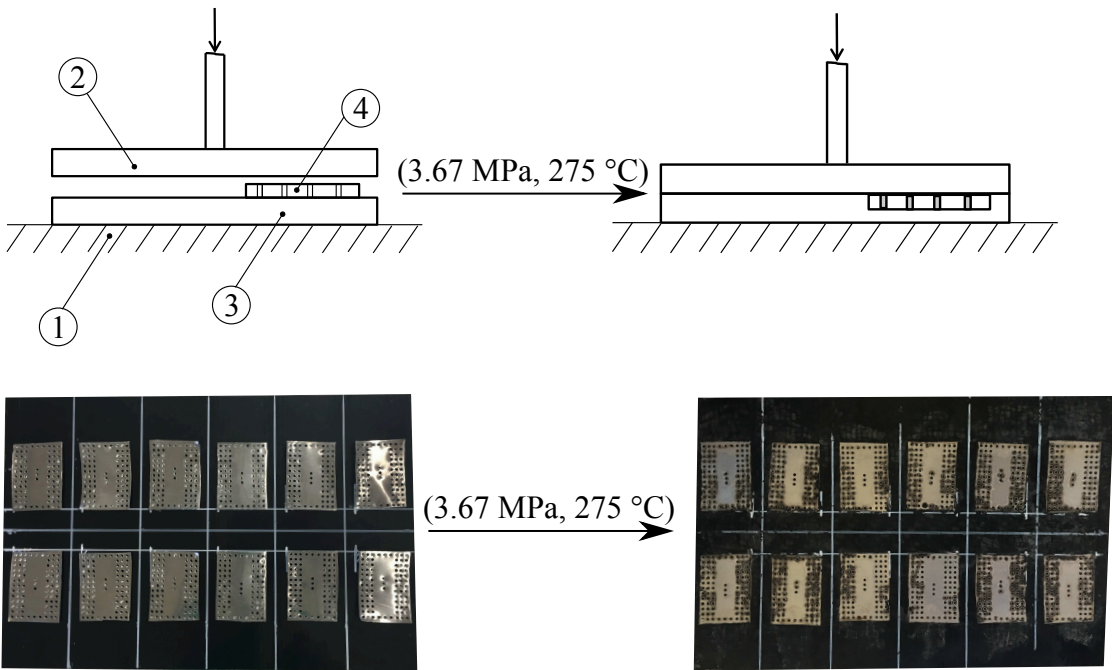
Figure 4.10: steel mold

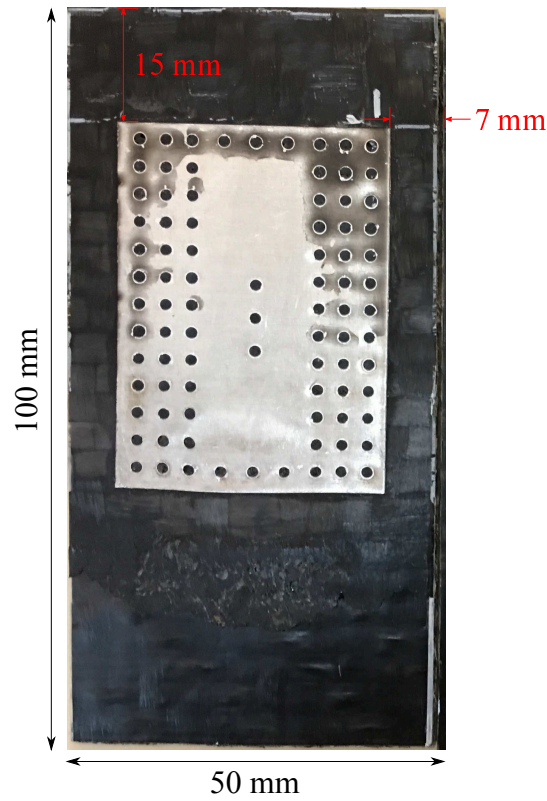Figure 4.11: metallic inserts over-molding

Figure 4.12: FRPC single specimen with metallic insert

The first cleaning step in this case is the metal insert surface that will serve for welding where the polymer film created during the overmolding needs to be removed (Fig. 4.13) and the second cleaning step is the hump surface oil removing by using an acetone solution. Here we need to mention that cleaning the metallic insert surface is crucial for the welding: in fact, we tested some specimens with and without cleaning and in the latter case no welding occured where polymer traces were observed on the flyer metal in the progressive impact region (Fig. 4.14) after the application of the MPSW. Hence, the progressive impact during the MPSW is not able to remove this thin film of polymers and the cleaning step becomes once more essential for the welding/joining to occur.

The flyer metal is then positioned in such way the hump is guided by a plastic insulator (Fig. 3.12) and the laser so that it is facing and centered on the coil's active area. The parent metal is then positioned above the flyer metal with the massive die on and finally the system is clamped similar to the MPW case. The clamping torque is 35 N. m and it was selected in a way so that the hump will not be deformed due to clamping.

4.4.4.3 Configuration with metallic patch

4.4.4.3.1 Metallic patches

The metallic patches were made of aluminum 5754 (thicknesses: $e_{f_1} = 0.5$ mm and $e_{f_2} = 1$ mm) and aluminum 5182 (thickness $e_f = 1.2$ mm). They have dimensions of 50×50 mm². The use of different thicknesses of patches will be detailed during the experimental test.
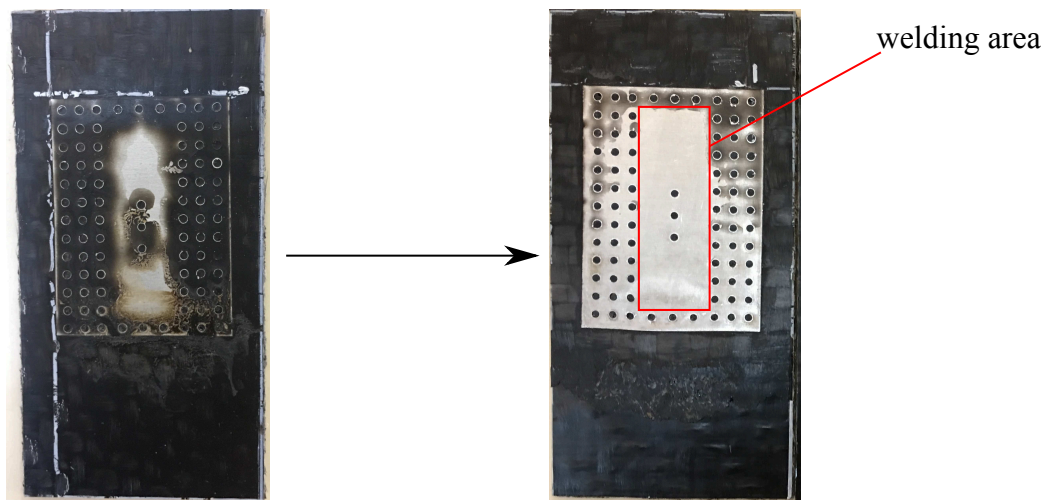
Figure 4.13: metallic insert surface cleaning from polymer film created during the over-molding process
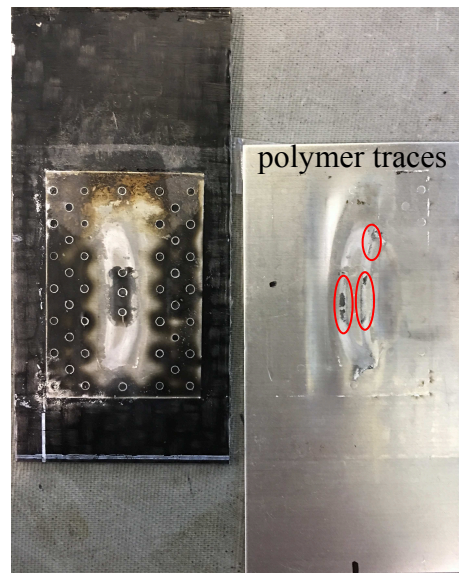

Figure 4.14: polymer traces on the flyer metal when the metallic insert surface is not cleaned prior to MPSW
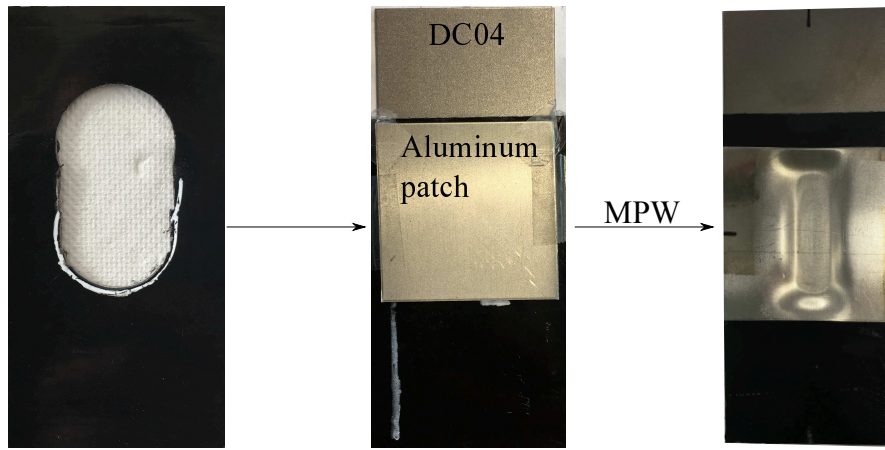
Figure 4.15: metallic patch configuration setup

4.4.4.3.2 Holes inside the FRPC sheets

The holes in the composite were chosen based on the results from the last chapter with the MPW configuration regarding the width and the length was also chosen such as it is equal to exceed the coil active length by 10 mm i.e. +5 mm on each side. Concerning the geometries of these holes inside the composite, they will be detailed later on in the results section.

4.4.4.3.3 Setup for MPW application

The metallic patch was first cleaned with acetone solution and centered on the hole in the composite. The parent metal i.e. DC04 was also cleaned using an acetone solution and then positionned regarding the composite as it is presented in Fig. 4.15. The flyer which is here the aluminum patch is positioned facing the coil where a Kapton insulation sheet with a 0.1 mm thickness is used to separate it from the coil. The positioning is controlled by a laser so that the part of the patch to be deformed is centered regarding the coil's active area. Over the steel part, a massive steel die is then placed and finally the whole system is clamped using the special system designed to avoid any displacement during the welding process (Fig. 3.8).

4.5 Results and analysis

4.5.1 Configuration with metallic insert

4.5.1.1 Configuration with 5754 aluminum metallic insert

The first welding tests were done using the first design of aluminum 5754 perforated inserts (Fig. 4.7). The discharge energies between 10 and 16 kJ using the O-shape coil lead to successful welding. The specimens were tested under quasi-static lap-shear tests and the average maximum load attained were between 1.9 and 2.5 kN. Different failure mechanisms were observed during the tests:

- at lower discharge energies, failure occured in the welding and a small part of the insert was detached from the composite (Fig. 4.16(a));
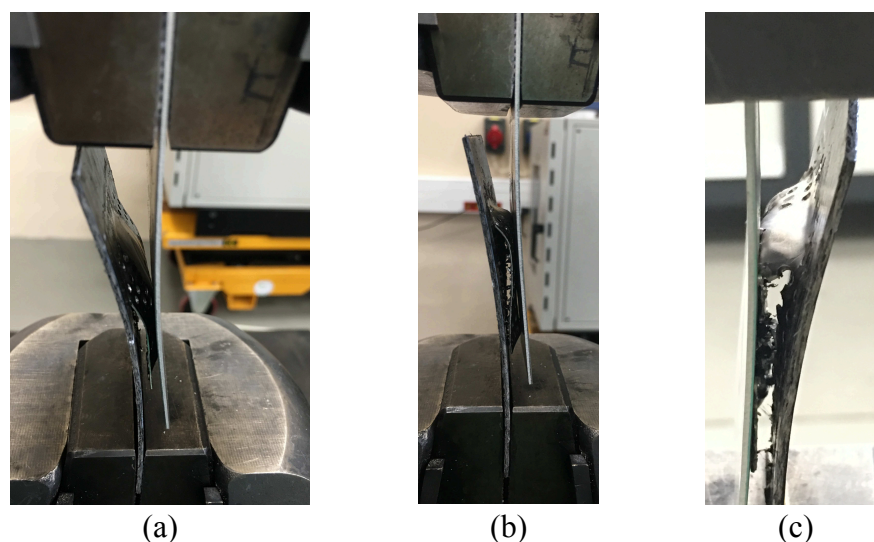
Figure 4.16: failure of the perforated aluminum 5754 insert during lap-shear tests

- at higher discharge energies, either the insert was totally detached from the composite (Fig. 4.16(b)) or tearing occured in the insert while a part of the insert was detached from the composite (Fig. 4.16(c)).

The second design of inserts, i.e. flanged holes perforated inserts (Fig. 4.8), was tested with the same energies. For the aluminum inserts and when testing the specimens under lap-shear quasi-static condition, the failure mode was the tearing of the insert. In the steel version of the insert it is the welding which failed.

These first tests had the aim to define the best design of the inserts which stands in the composite. As per the results, the steel insert stands the best in the composite in both cases and the flanged holes perforated insert also showed more adherence with the composite. Hence, to test the joining strength under different loads, the flanged holes perforated insert was chosen. Three sets of five specimens were prepared using a discharge energy of 16 kJ. Each set was then used for quasi-static, dynamic and fatigue tests.

For the aluminum metallic inserts, the results of the quasi-static lap-shear tests are represented in Fig. 4.17 and the dynamic tests are represented in Fig. 4.18. As can be seen in both cases, there is one specimen that stands less and in both the failure occured in the welding and not in the insert. When taking a closer look at these 2 specimens, a part of the welding coincided with the middle holes of the insert as represented in Fig. 4.19. In the dynamic tests other cases the failure occured in the insert and it is represented in Fig. 4.20 where the tearing of the aluminum insert is clear.

For the fatigue tests and as in the previous metal/metal joining case, the tests were performed under undirectional conditions ($R = 0$) and at a frequence of 20 Hz and the maximum load for fatigue tests is for each couple equal to 60% of the highest quasi-static lap-shear failure load. The results are given in Table 4.2. The failures during the fatigue tests was a combination between a tearing in the metallic insert and detachment of the insert from the composite (Fig. 4.21).

Figure 4.17: quasi-static lap-shear tests for joints between 5182 and FRPC with aluminum metallic insert
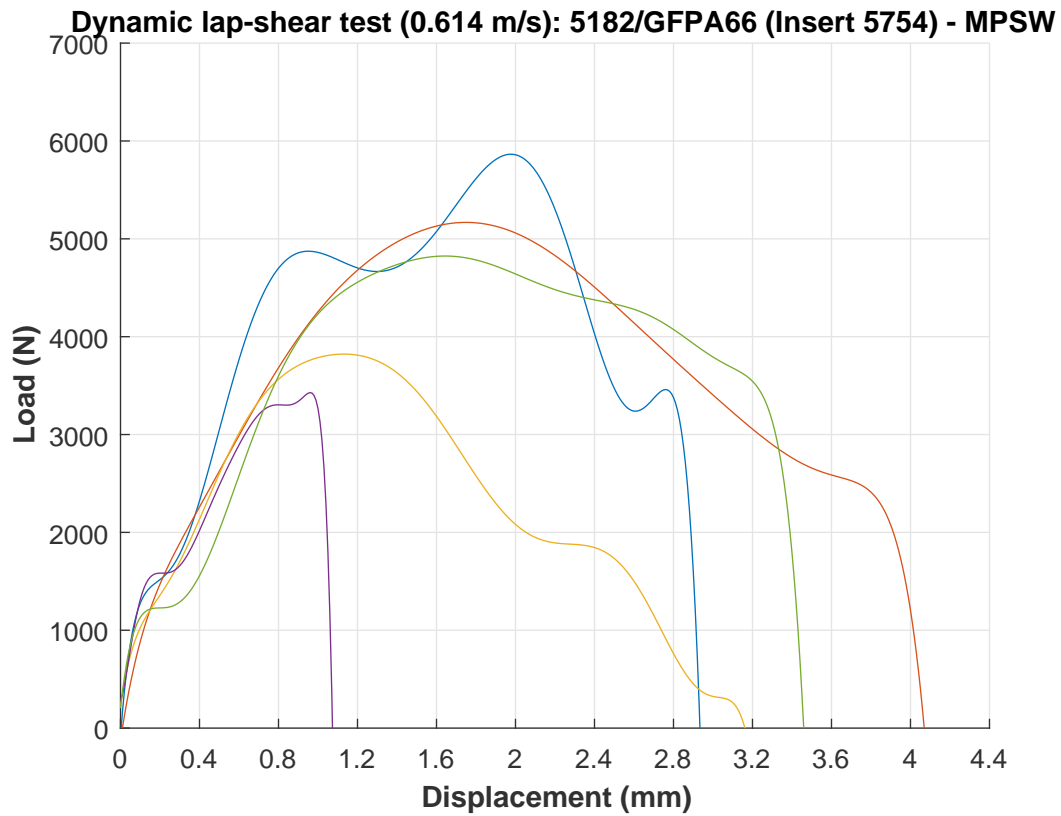
Figure 4.18: dynamic lap-shear tests for joints between 5182 and FRPC with aluminum metallic insert
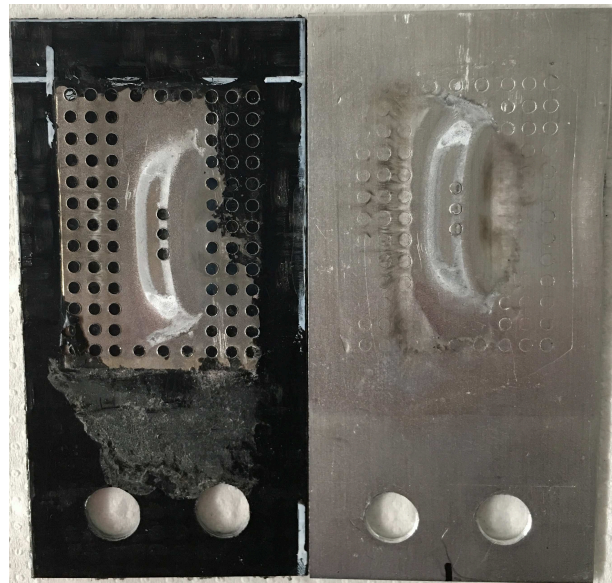
Figure 4.19: welding coincidence with the holes of the metallic insert
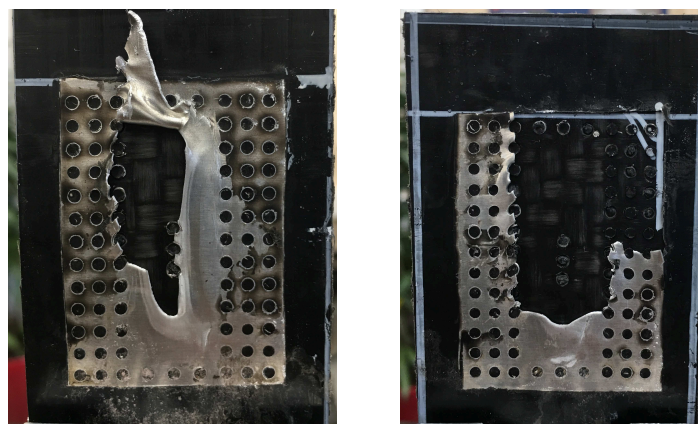
Figure 4.20: tearing in aluminum metallic insert during dynamic tests

Flyer	Parent	Metallic insert	F_{max} (kN)	Number of cycles				
				Test 1	Test 2	Test 3	Test 4	Test 5
5182	FRPC	5754	2	41000	35000	36000	42000	45000
5182	FRPC	DC04	2.88	45000	41000	24000	29000	34000

Table 4.2: fatigue tests results for metallic insert configuration
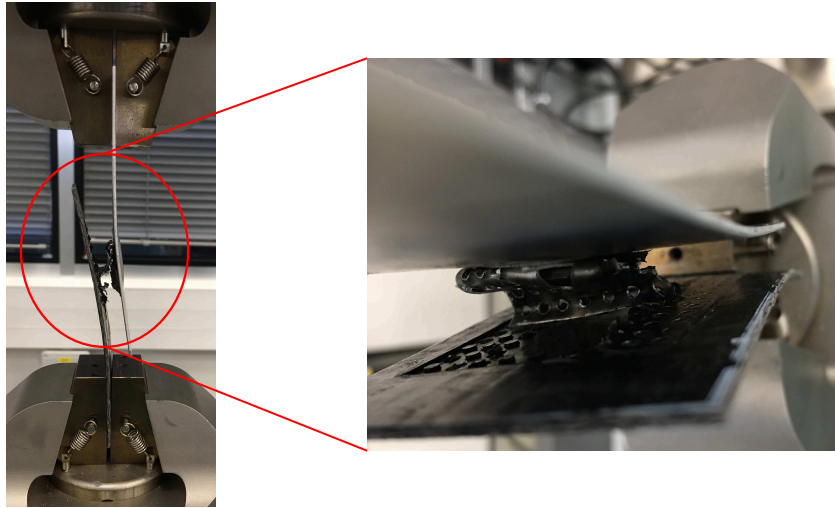
Figure 4.21: failure during fatigue test of the joining between the 5182 and aluminum 5754 insert

4.5.1.2 Configuration with DC04 steel metallic insert

Using the first insert design and the second design in its steel DC04 version, the welding also occured when applying discharge energies between 10 and 16 kJ. When the specimens were tested, the average maximum loads were between 2.9 and 5.3 kN for 10 and 16 kJ respectively. In both inserts design cases, the failure only occured in the welding.

The flanged holes perforated insert showed in the aluminum case a better adhesion in the composite and they will be used also in the steel insert case to be tested under different conditions. The results of the quasi-static lap-shear tests and dynamic tests are given respectively in Fig. 4.22 and Fig. 4.23. The failure always occured in this case in the welding itself.

The fatigue tests results are listed in Table 4.2. The failure also occured in the wleding itself and as in the metal/metal joints case between the 5182 and the DC04, a tearing was observed in the flyer metal (Fig. 4.24).

4.5.1.3 Analysis and discussion

As a first observation, the application of the MPSW to weld a metallic sheet on a metallic insert embedded inside a composite is possible using either aluminum or steel inserts. These inserts showed better adhesion in the composite in the case of the flanged holes inserts. On the other hand, the joints had higher strength in the steel metallic insert case since in the aluminum inserts the holes lead to concentration of the stresses around the holes which were not able to stand the efforts and this was observed through the tearing during different mechanical tests.

The other important point to reveal is that the use of the parameters as concluded from the metal/metal applications lead to successful welds in both aluminum and steel inserts cases showing the possibility for a transition from the bimetallic applications to joints using the inserts configuration. The next point to talk about is the similarity between the welding behaviour in the metal to FRPC joints and when we apply the same welding conditions between the same metallic sheet and another sheet having the same alloy of the insert. This fact is illustrated in Fig. 4.25 and in Fig. 4.26 where two
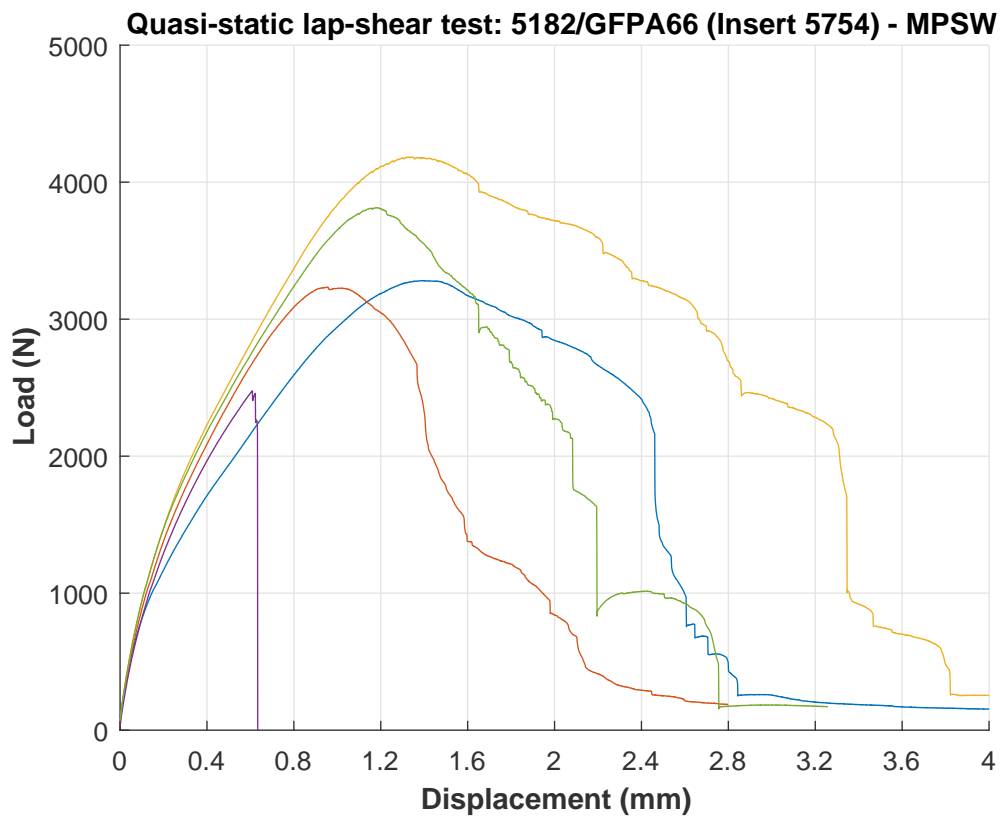
Figure 4.22: quasi-static lap-shear tests for joints between 5182 and FRPC with steel metallic insert

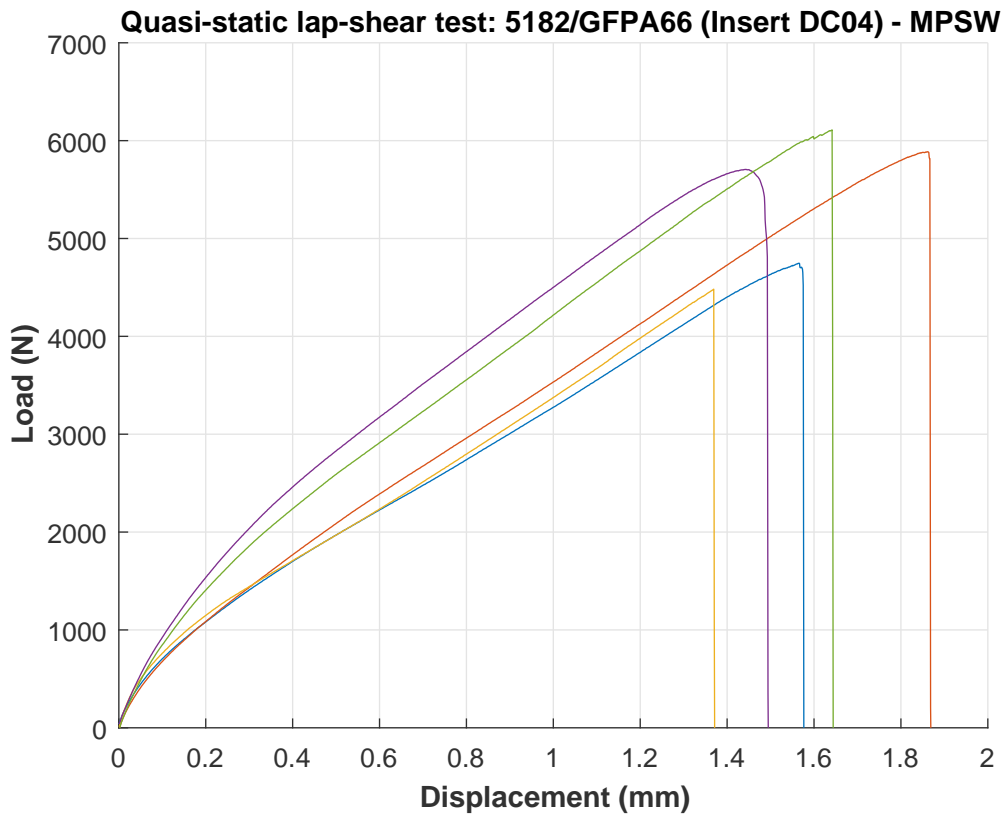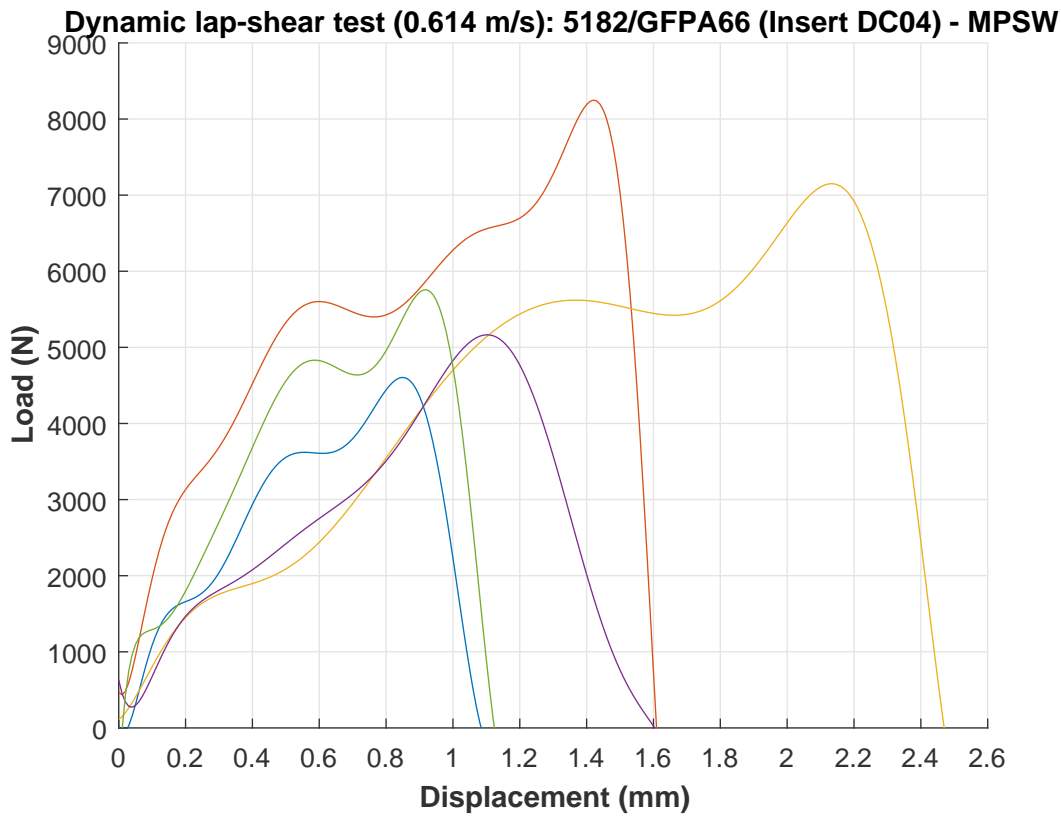Figure 4.23: dynamic lap-shear tests for joints between 5182 and FRPC with steel metallic insert

Figure 4.24: 5182 flyer metal tearing during fatigue test for the joint with FRPC using the steel DC04 metallic insert

Couple (Flyer/Parent)	Metallic insert	Configuration	QS load (N)	QS displacement (mm)	Dynamic load (N)	Dynamic displacement (mm)
5182/FRPC	5754	MPSW	3500	2.7	5050	3.2
5182/FRPC	DC04	MPSW	5400	1.64	6000	1.7

Table 4.3: summary of quasi-static and dynamic average maximum loads for both types of inserts

typical curves from quasi-static lap-shear configurations are represented: one in the case of the 5182/FRPC joint and the second for the 5182 MPS welded to a sheet metal having the same alloy as the insert used.

The average maximum loads and displacements during the quasi-static and dynamic tests are summarized in Table 4.3.

When the insert used is a 5754 aluminum, the maximum quasi-static load is exceeding the 3 kN and the dynamic load is around 5 kN. It is worth noting that the failure was always taking place due to the tearing of the insert during different loads applications. The fatigue cycles of the joints were in this case between 35000 and 45000 cycles and the failure mode was somehow more related to the insert since it was observed that the failure started always in the insert in the regions around the holes and then the tearing propagated leading finally to a total detachment of the insert from the composite as it was presented in Fig. 4.21.

On the other hand, when the insert is a steel DC04, the failure loads are exceeding 5 kN in quasi-static and 6 kN in the dynamic condition. In this insert case, the failure during different tests always occured in the welding itself. When comparing these values to the one we found in the previous chapter for the bimetallic applications, we can see that the average decrease in quasi-static is about 1 kN in the maximum loads while the displacement is almost the same. When it comes to the dynamic conditions, the lost in load is about 2 kN while the displacement is higher of 0.3 mm in average. The fatigue tests showed some disparities in the steel insert case but this was due to the fact that a part of the welding line coincided with the holes in the insert giving lower number of
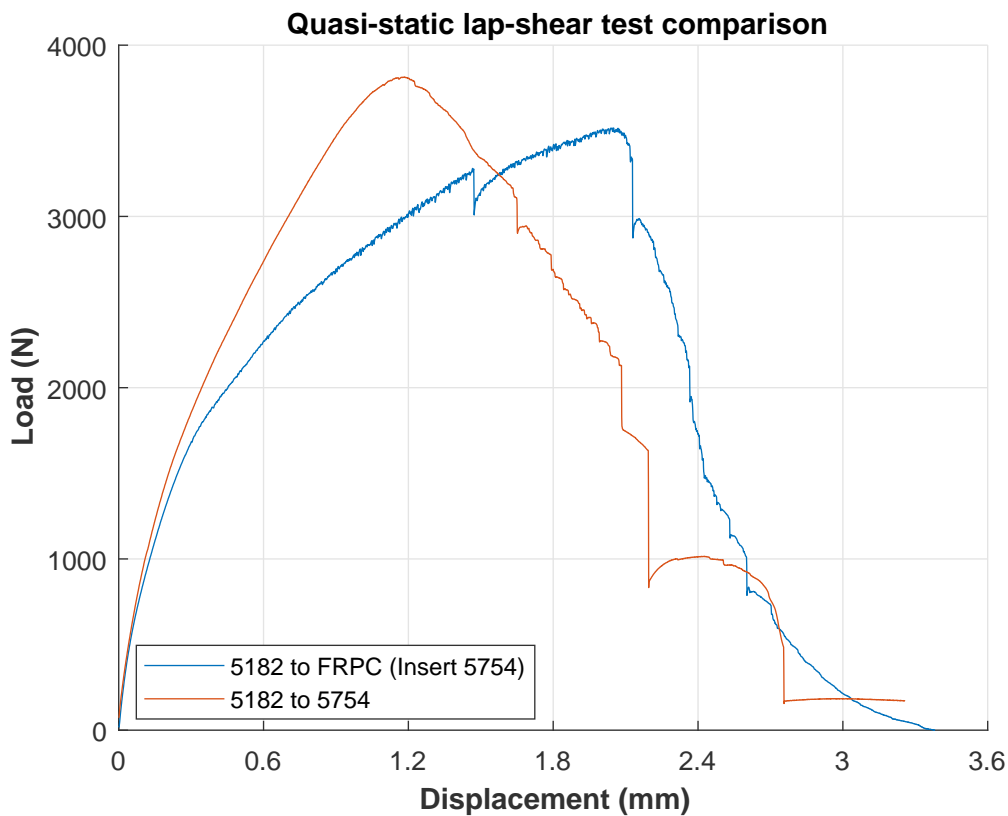
Figure 4.25: quasi-static lap shear typical curves comparison between joints of 5182/FRPC (insert 5754) and MPS welded 5182/5754 joints under the same conditions
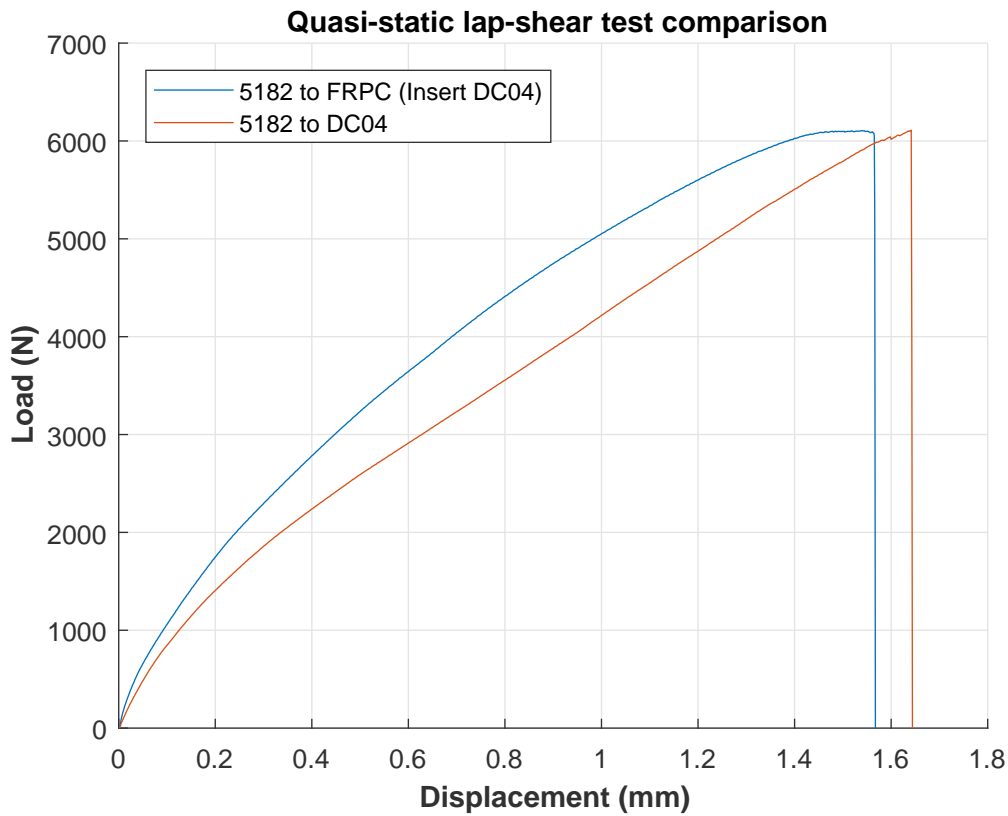

Figure 4.26: quasi-static lap shear typical curves comparison between joints of 5182/FRPC (insert DC04) and MPS welded 5182/DC04 joints under the same conditions
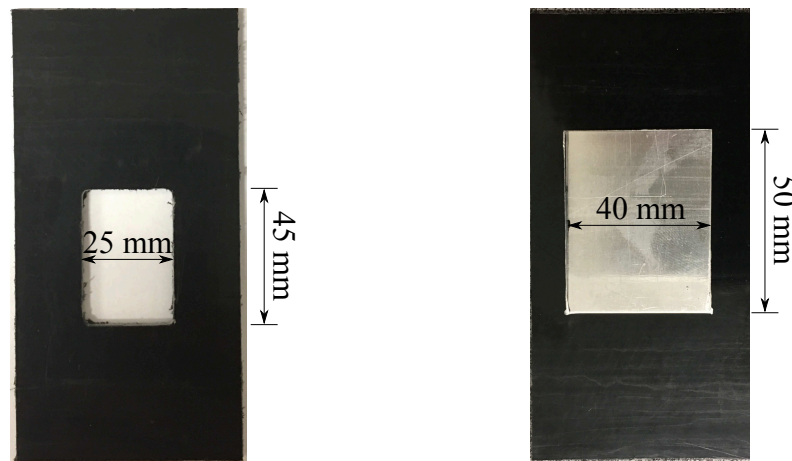
Figure 4.27: rectangular hole in the FRPC sheet and the 5754 aluminum patch used during the MPW application

cycles between 24000 and 29000 while the others were higher than 34000 and up to 45000 cycles. The other interesting observation and which was also seen in the bimetallic applications is the failure of the 5182 flyer metal aluminum during these cyclic tests.

4.5.2 Configuration with metallic patch

4.5.2.1 Principle feasibility validation

The very first step was to test the idea of the welding through a window inside the composite with another metal part using a metallic patch. Therefore, the first patch used was a simple 5754 aluminum patch of 50×40 mm² having a thickness of 0.5 mm. The hole in the composite is a rectangular hole having a width of 25 mm and a height of 50 mm (Fig. 4.27) and the coil is a linear copper coil. The configuration was tested on both a DC04 steel and a DP450 steel with discharge energies of 10, 13 and 16 kJ in both cases. The welding occured in the three cases and for both types of steels (Fig. 4.28).

The first observation noticed during this joining is in the thin 5754 aluminum patch: it was teared at the edges of the rectangular hole when applying an energy higher than 13 kJ (Fig. 4.29).
The use then of a thicker aluminum insert was tried to see if the tearing originated due to the sharp edges of the composite or it was more related to the thinness of the aluminum. Two trials were then done using the same 5754 aluminum but 1 mm thick and a patch of 5182 aluminum 1.2 mm thick. The coil used in this case is the O-shape steel coil since we have thicker sheets. The welding in both cases occured when applying energies between 10 and 16 kJ and no tearing at the rectangle edges was observed showing that it is better to go with patches having thicknesses higher than 1 mm to be able to stands the cutting edge of the holes inside the composite.

Now that the feasibility of the idea is prooved, the next questions to be answered were: how will the joining react under a quasi-static test? How did the patch flow inside the hole and how much will the hole geometry influence the joint strength? Answering these questions will guide us to define the best design practice when this type of joints is applicable that the designer should take into consideration when applying this type of processes for future use.
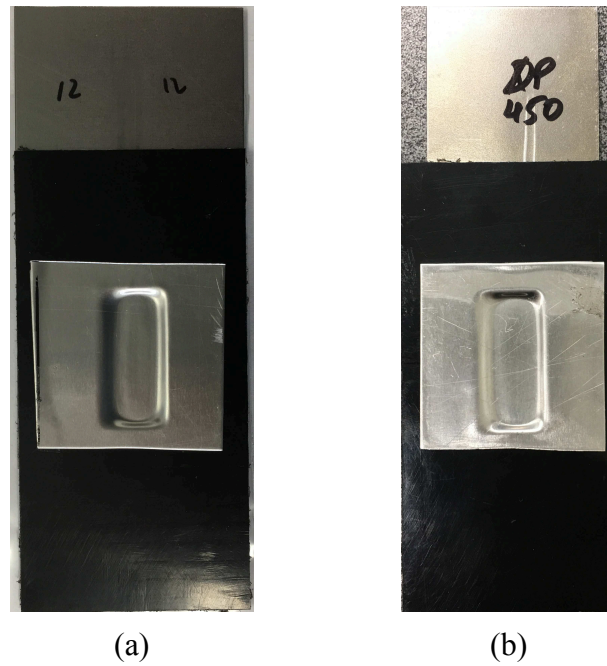
(a)   (b)

Figure 4.28: joining FRPC to (a) DC04 and (b) DP450 steels; in both cases the metallic patch is an aluminum 5754 ($e_f = 0.5$ mm)
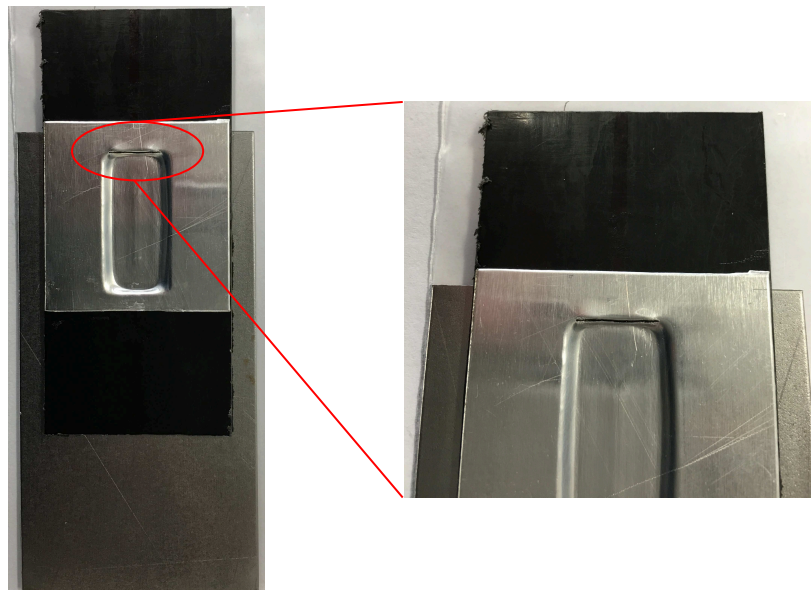

Figure 4.29: tearing in the thin 5754 aluminum patch at the upper edge at high discharge energies
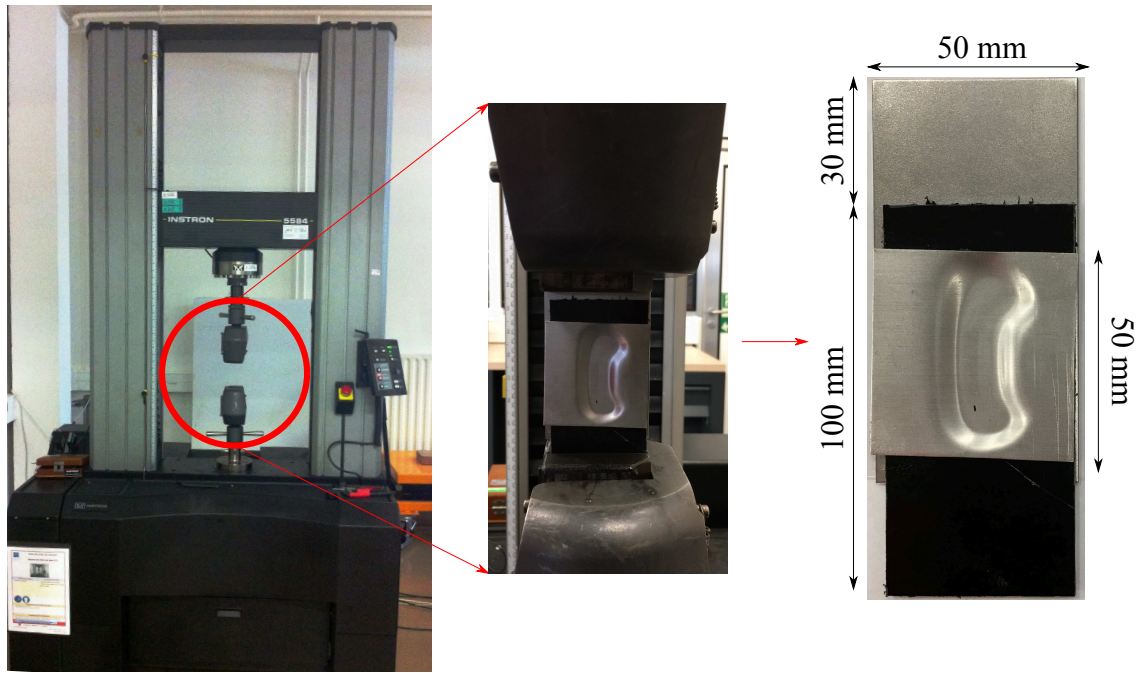
Figure 4.30: quasi-static test specimens with metallic patches

4.5.2.2 Analysis and discussion

The specimens were tested using the INSTRON 5584 (150 kN) machine and the velocity was of 10^{-2} mm/s (Fig. 4.30). First, it is very important to mention that even the testing looks like lap-shear configuration but in our case we cannot consider the test as lap shear since the loading will somehow be directly applied on the patch and there is some risk to have a peeling configuration in case where the patch does not fill at 100% all the composite hole. These hypothesis will be clearer after the first tests that will be performed and which will be presented next.

The maximum loads attained during the tests of 5754-patches are between 120 N and 680 N for the lower and the higher discharge energy level respectively. During the tests of 5182-patches, the maximum loads also varied between 120 N for lower discharge energy level and 600 N for the higher level. The first remarkable point is the failure in both cases that was due to the patch that jumped from its place and the second one is the relatively long time before the collapse of the insert which is about 2 min in average. In Fig. 4.31 and Fig. 4.32 typical curves of load vs. time and load vs. displacement are presented for both 5754- and 5182-patches respectively.

During the test, the composite sheet was slipping under the insert (Fig. 4.33) and hence the load was tearing the weld. When taking a look at a cut-section of the joining area (Fig. 4.34), the flow of the patch does not fill the corners and the slopes of the deformed patch observed confirm that. Therefore, the tests can be considered more as peeling tests than lap-shearing.

After this first observation and in order to prevent as much as possible this slipping effect and increase the zone of the welding that undergoes the loading, some other designs were thought for the holes. These geometries are represented in Fig. 4.35 and all the patches are 5182 having 1.2 mm thickness in order to avoid any risk of tearing at the corners of the holes. As it can be seen in the three cases we rotated the rectangular hole in a way that the load during the test will be

Figure 4.31: load vs. time curves of quasi-static tests for joints between composite and DC04 steel using the patch configuration
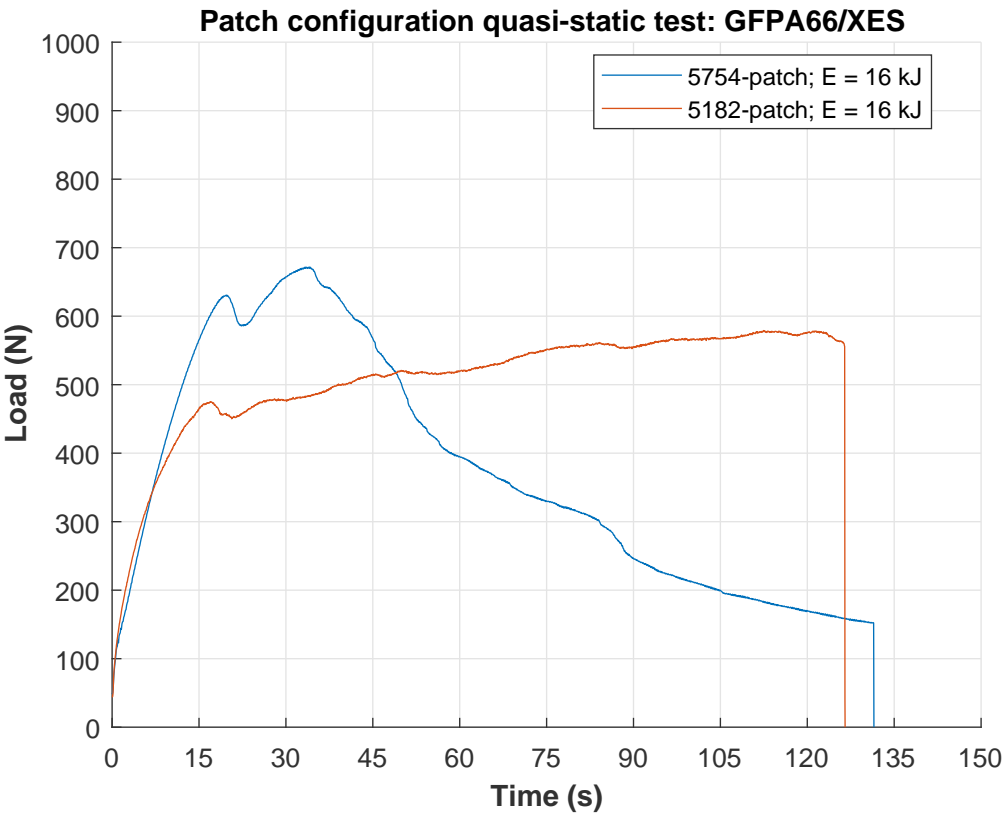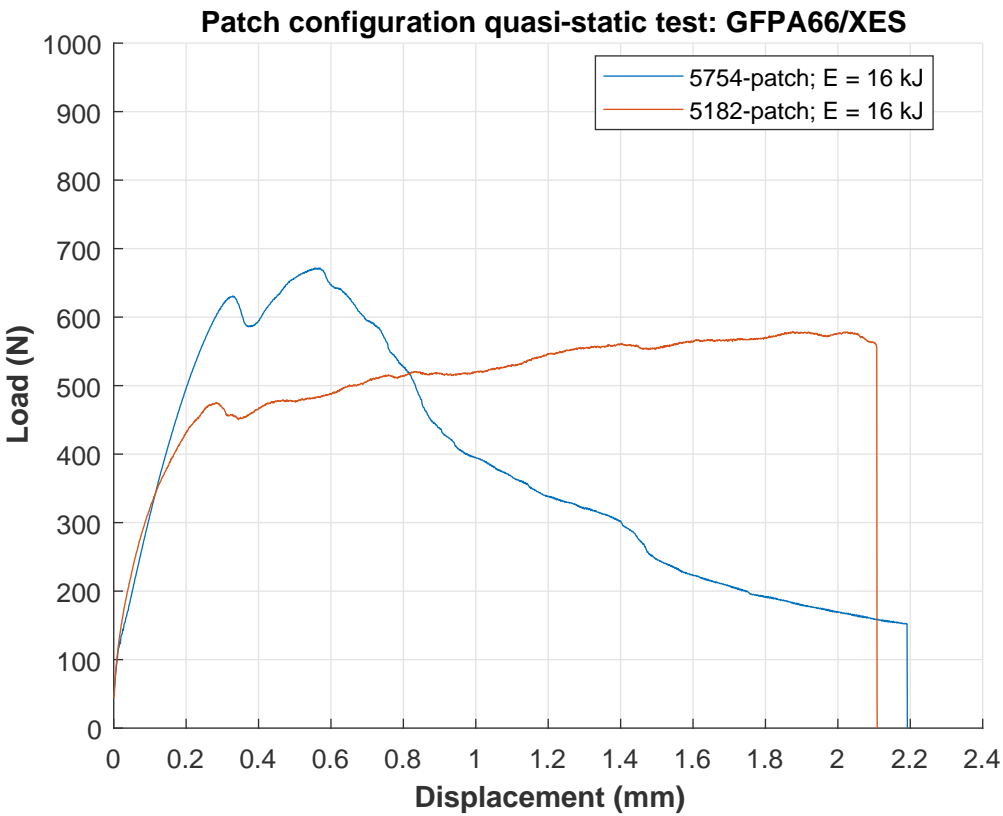

Figure 4.32: load vs. displacement curves of quasi-static tests for joints between composite and DC04 steel using the patch configuration

Composite tearing the
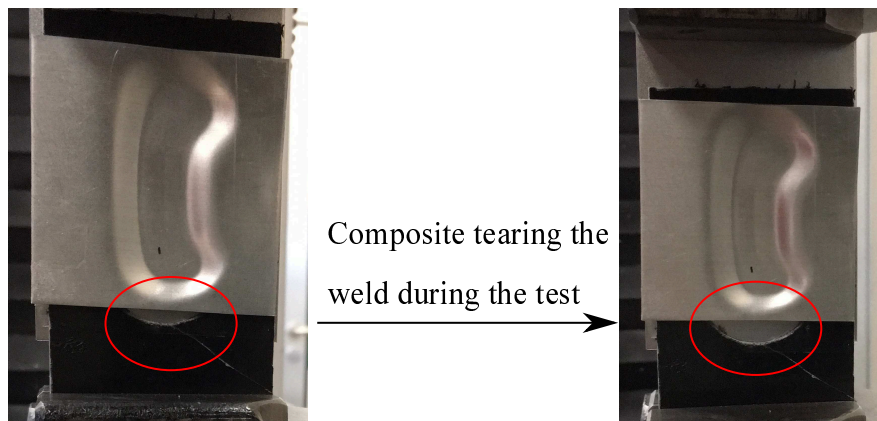weld during the test

Figure 4.33: composite sheet slipping under the metallic patch and tearing the welding
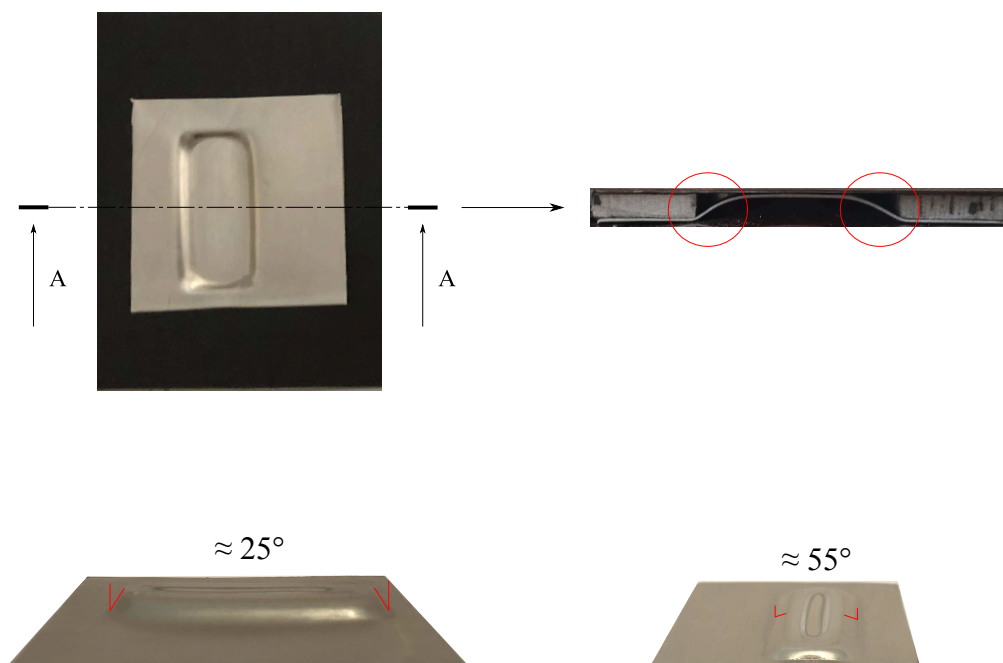

Figure 4.34: metallic patch flow in the rectangular hole showing that it does not fill the corners

applied on a higher surface of the welding and in the two last cases additional small graves were used at the holes corners so that the patch fills this additional areas to test if this will prevent the slipping effect directly on the patch. The specimens were then tested under the same conditions and the failure mode was always the patch that jumped from its place. However, the results which are presented in Fig. 4.36 showed that in the pure rectangular hole rotated, the maximum loading reached was higher than the previous tests and in the other two, where additional graves are used, the time before failure was almost 3 times higher.

As it can be seen in the last tests conditions, the welds undergoes peeling loading and adding the small graves tripled the time before the welding failure. To be in more real lap shearing test configuration in order to see what is the behaviour of the weld itself under quasi-static condition, the configuration 5 i.e. where the composite is taken into sandwich between the two metallic sheets should be tested (Fig. 4.6). In this case, a window in the composite was created in rectangular form and an aluminum 5754 sheet having a thickness of 0.5 mm was welded to the steel through this window using a discharge energy of 16 kJ. When testing the specimens under quasi-static lap-shear condition, we found the same behaviour as found during the MPW metal/metal case where the tearing happenned in the 5754 and the maximum loading exceeding 3500 N (Fig. 4.37).

The intention after that was to go further into our experimental investigation by applying other patches geometries and dimensions and to use some other coils geometries in order to improve the flow of the patch inside the holes but unfortunately the generator was in a shut down for 6 months during the final phase of the study and due to lack of time the further investigations were postponed for future time slots.

4.6 Conclusion

In this chapter, the main purpose was to develop new joining solutions based on the MPW technology in order to extend its application from planar dissimilar metal joining configuration into dissimilar materials involving FRPCs. The new proposed solutions covered all possible application taking into consideration different configurations as well as the materials properties and thicknesses. The two main ideas as it is now clear are based whether on introducing a thin metallic sheet in the composite or to use a metallic patch through the composite to create the join. The feasibility of these ideas was proven during this chapter by experimental application of both.

In the metallic insert configuration, the most important conclusions that can be stated are:

- metallic inserts material is not a limitation and it can be either aluminum or steel;

- the design of the metallic insert using flanged holes gave a high adherence with the composite and this was proven during various mechanical tests;

- cleaning the inserts from any slag of polymers is very important since the experiments showed that the progressive impact will not be able to remove any polymer residue which then will act as obstacle for the welding;
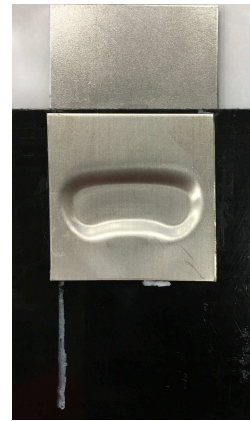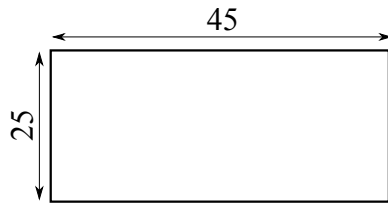
(a) hole 1
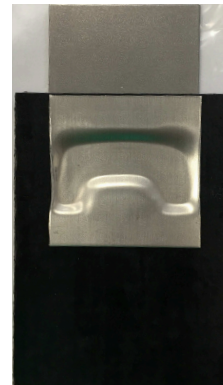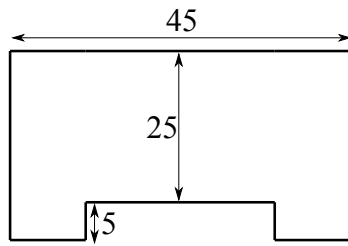
(b) hole 2
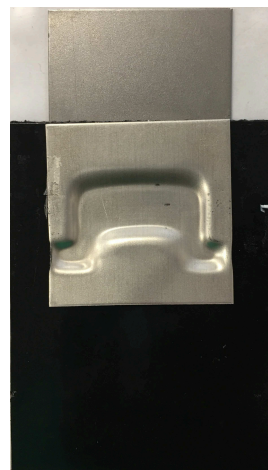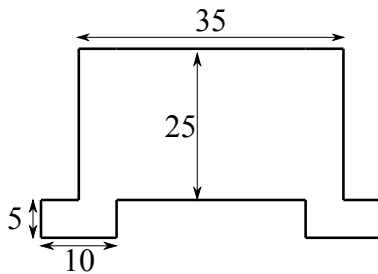
(c) hole 3

Figure 4.35: various holes geometries
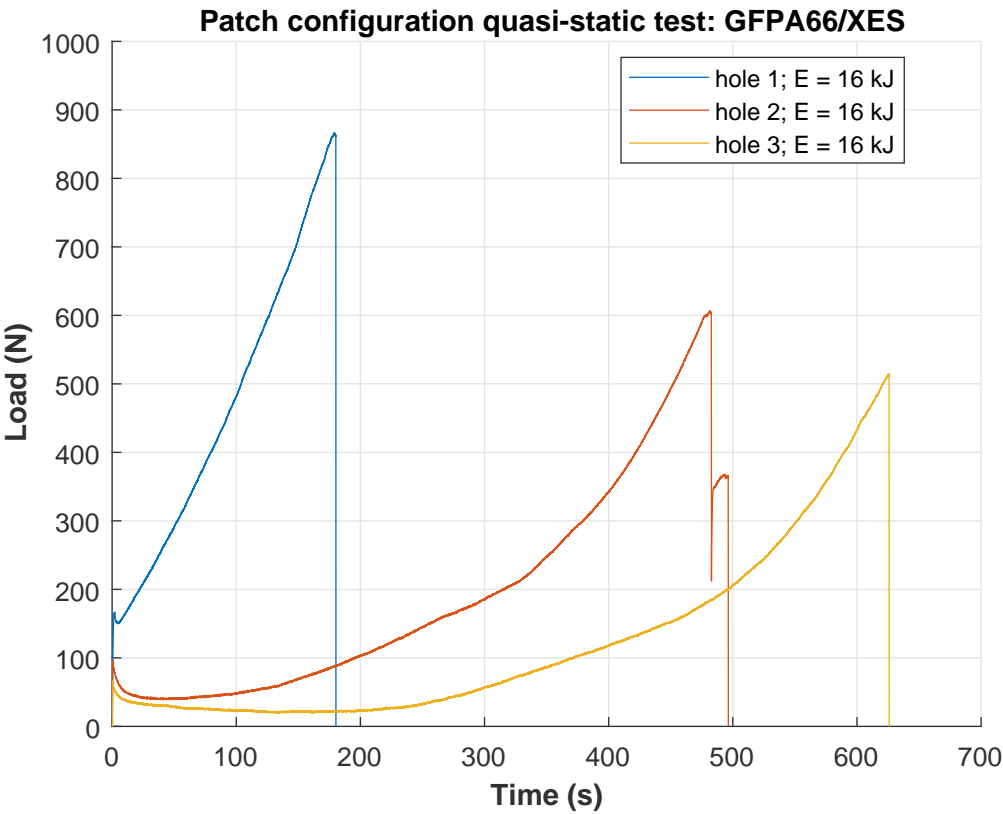
Figure 4.36: quasi-static tests for rotated holes inside composite for patch configurations
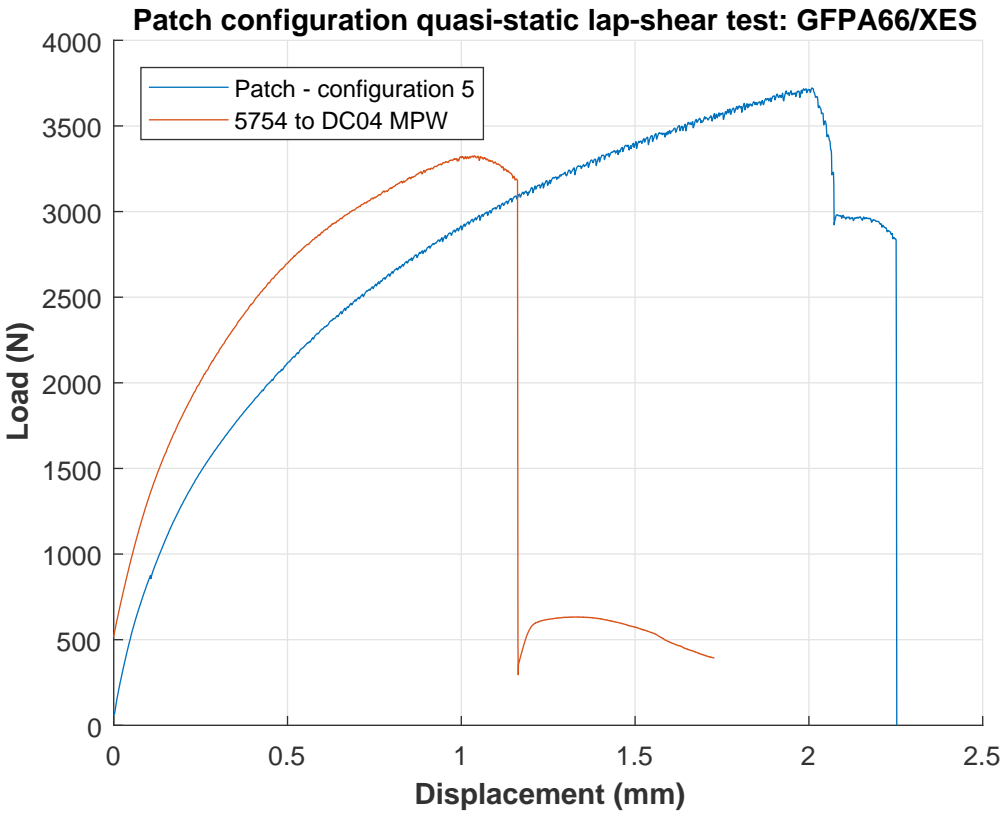
Figure 4.37: configuration 5 quasi-static lap-shear test typical curve

- the holes in the insert will not prevent the welding from occuring but they will decrease singnificantly the effective welding lines leading to weaker welds and hence the design should take into consideration avoiding any coincidence between the welding line and the holes inside the inserts;

- the transition from bimetallic MPSW parameters can be used with high accuracy in order to create the welding between the metallic partner and the insert embedded inside the composite;

- the mechanical tests showed that there is no significant loss in the welding strength when applying the MPSW on the insert as it has been seen in different mechanical tests;

- and the steel inserts showed better resistance than the aluminum ones during different tests since in the latter it was always the insert which teared.

Now when talking about the metallic patch, the main points that can be stated are:

- thin metallic patch will have the risk to tear on the borders of the holes in the composite during the application of the MPW and hence it is preferred to use patches having thicknesses higher than 1 mm;

- the hole dimensions should be consistent with the coil's active area length by exceeding this length of minimum 5 mm on each side;

- as it was noticed during the tests, the geometry of the hole is important to maintain longer the welding under peeling tests conditions and to increase the area filled by the patch during MPW;

- the flow of the patch through the holes in the composite does not necessarily fill the edges of the holes and hence creating slipping risks under loading conditions; these loading conditions, when possible, should be avoided by the design;

- the transition from MPW bimetallic parameters is also accurate and can be used according to the FRPC sheet thickness which will define the standoff distance to choose the good width of the hole active area in order to get good welding;

- the configuration where the FRPC is taken as sandwich between two metallic partners has proven its efficiency and the behaviour of the welding is the same as in the bimetallic case applications.

One additional point to mention is the fact that these solutions used the same equipment that were used for the bimetallic applications and without any modification. In addition, the accuracy between the transition of the parameters from bimetallic case to FRPC/metal case prooved that developing bimetallic MPW/MPSW for various alloys has benefits also for the extended new MPW/MPSW multi-material application.

Finally, two important points need to be clarified before closing this chapter:
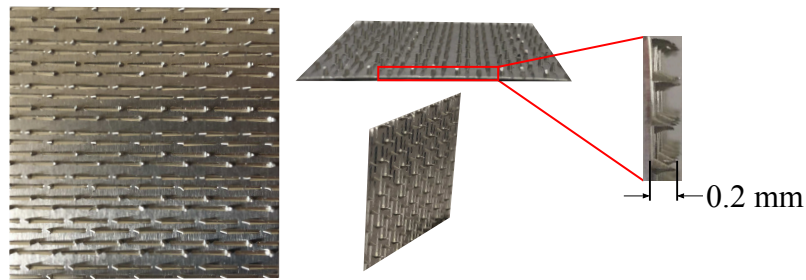
Figure 4.38: pinned 5052-H32 aluminum insert

- the first concerning the microscopic observations where the specimens were prepared for X-ray microtomography and the observations were scheduled to be done in order to see the influence of the joints on the microstructure of the FRPC but unfortunately the tomograph went out of service during this period and hence the observations were postponed for future time slots after the closure date of the study;

- the second concerning a new metallic insert that we also started to test: it is a pinned 5052-H32 (Fig. 4.38); this insert was also embedded inside the composite using the same thermo-compression cycle as the other inserts and the flyer material used was a 6013-T4 aluminum with a 1.4 mm thickness; the configuration tested was also MPSW and successful welds were obtained starting from a discharge energy of 13 kJ and the first quasi-static lap-shear tests showed maximum loads higher than 2.5 kN where the failure occured in the welding and the metallic insert withstands well the loading. Unfortunately as in the case of the patch configuration the generator was shut down for 6 months and further investigation were postponed for future time slots also.

After the last two chapters, we can claim that the MPW/MPSW technology has no limitations for applications going from similar to dissimilar welding and also for metallic to non-metallic joining applications. The next big discussion now and which will take place in the next and final chapter of this study: how can we build numerically a welding window for two different metals? In other words, we will try to find a path from the process parameters to the physical ones that will allow us to predict if we will have a welding or not.

Chapter 5

Towards the construction of physical welding windows

5.1 Résumé

La physique du soudage au cours des procédés d'impact à grande vitesse fait toujours débat au sein de la communauté scientifique et les théories sont multiples [28, 41, 51, 144, 158]: procédé de soudage par fusion, instabilité de Kelvin-Helmholtz, mécanisme de formation de tourbillons, cisaillement dynamique à l'interface, ... Bien que les discussions et les arguments philosop- hiques se poursuivent, la technologie de soudage par impulsion magnétique a démontré son utilité et une méthode / procédure basée sur des faits expérimentaux et capable de relier les paramètres du procédé aux paramètres physiques sera d'une grande utilité.

Cette méthode servira à constituer une fenêtre de soudure pour une combinaison de matériaux don- née. En se basant sur tout cela, la condition essentielle pour le soudage par impact et qui a été ex- périmentalement vérifiée à travers divers études est la formation de jets au point de collision. Cette condition est essentielle puisqu'elle assure l'obtention de surfaces propres sans aucuns résidus permettant aux deux matériaux en contact d'être capables de créer des liaisons interatomiques. Cette condition de formation de jet conduira aux paramètres physiques angle d'impact et vitesse d'impact. Le second critère de soudage consiste à maintenir ces deux surfaces propres sous une pression suffisamment élevée pour établir cette liaison interatomique donc le troisième paramètre physique important est la pression à l'interface. A partir de là, ces paramètres physiques doivent être liés aux paramètres du procédé et qui a fait l'objectif de la méthode qui est présentée dans ce chapitre.

Le modèle numérique macrosocopique développé au chapitre 2 va être utilisé dans ce chapitre. La largeur de la ligne de soudure selon les observations expérimentales varie entre 1 et 2 mm (Table 3.8). L'idée est d'évaluer l'évolution de l'angle d'impact et de la vitesse d'impact ainsi que la pression à l'interface à l'intérieur de cette surface de soudure.

Les valeurs (V_i, β_i) sont évaluées alors sur les bords et à l'intérieur de la largeur de soudage afin de pouvoir tracer les frontières de la fenêtre de soudure pour chaque cas (Fig. 5.2). Les deux fenêtres de soudage sont superposées tout d'abord pour vérifier que numériquement nous sommes sur les

mêmes paramètres physiques afin d'être sûr que même si un paramètre procédé change (ici D), les paramètres physiques restent similaires pour une soudure de bonne qualité. En évaluant la pression dans les deux cas, le profil de variation est déduit entre le point de départ et la fin d'une soudure (Fig. 5.3). Cela permet de voir comment cette pression est maintenue à l'interface lors de l'impact progressif d'une soudure de bonne qualité.

Pour cela, le couple de matériaux 5754 et DC04 a été choisi et l'évaluation a été faite dans la zone optimale de soudure trouvée expérimentalement dans le chapitre 3 (Fig. 3.25). Les valeurs pour les deux cas $D = 15$ et $D = 25$ mm sont représentées sur la Fig. 5.6 et montrent que les frontières des fenêtres de soudure sont presque les mêmes et les valeurs des vitesses varient entre 400 et 800 m/s ainsi que celles des angles entre 2° et 33°.

Quant aux profils des pressions qui sont présentés dans la Fig. 5.9, le maintien d'une pression supérieure à 1 GPa correspond presque à 80% de la largeur de soudage. Une première observation très importante est que, à la fin du soudage, la pression devient négative et que les ondes à l'interface deviennent répulsives. Le deuxième point est le maintien d'une pression élevée sur la plupart des zones à impact progressif. De plus, la variation de pression peut clairement prédire le point final du soudage probable car elle approche de zéro et devient même négative dans tous les cas.

Dans la Fig. 5.10, le (V_i, β_i) est représenté pour 3 cas de soudures de mauvaises qualités obtenues durant la phase expérimentale et comparé à la fenêtre de soudage numérique précédente. Dans les deux premiers cas, l'évolution de la vitesse est clairement en dehors de cette fenêtre et, dans le dernier cas, l'évolution de la vitesse est à l'intérieur de la limite de la fenêtre numérique (V_i, β_i). En examinant les profils de pression de ces soudures présentés dans la Fig. 5.11, le premier commentaire à faire est que les niveaux de pression sont inférieurs aux soudures optimales : dans le premier cas, il n'est que de 2,6 GPa ; dans le second, de 2,3 GPa et dans le troisième, le maximum est à 3,2 GPa. L'autre observation importante est que la pression est maintenue sur moins de 40% de la largeur des soudures dans les 2 premiers cas. Dans le troisième cas, elle augmente et diminue rapidement après presque 30% de la largeur totale. Par conséquent, même dans le troisième cas où le (V_i, β_i) est à l'intérieur de la fenêtre numérique, la pression à l'interface sera l'indicateur de la qualité de soudure puisqu'elle a une valeur faible et une période de maintien plus courte.

La première conclusion importante dans ce chapitre est que les paramètres physiques obtenus pour des paramètres de configuration de soudure différents sont très similaires, ce qui signifie que la construction d'une seule fenêtre de soudage expérimentale pour quelques matériaux suffit à évaluer numériquement les conditions physiques optimales de soudage et l'appliquer par la suite pour autres différents paramètres et configurations. De plus, la méthode a montré que l'utilisation de l'évolution de (V_i, β_i) comme seul critère ne suffit pas pour avoir une vision claire de la qualité de la soudure mais nous devons prendre en compte la pression à l'interface qui donnera l'information sur la qualité de soudage.

Les conditions présentées dans la Fig. 5.12 et la Fig. 5.13 pour (V_i, β_i) et le profil de pression respectivement peuvent être utilisées pour tout nouveau couple de matériaux pour trouver les premières conditions de soudage.

5.2   Introduction

The physics behind the welding formation during high velocity impact processes were from the beginning argued by the scientific community and there are multiple theories for the welding formation [28, 41, 51, 144, 158]: fusion welding process, Kelvin-Helmholtz instability, vortex shedding mechanism, jet indentation mechanism, stress wave pulsing and interfacial shearing. While the philosophical discussions and arguments continue, to be able to benefit from the MPW technology that showed through experimental proofs its various scope of applications, we need to adopt a method/procedure based on experimental facts and which is capable of linking the process parameters to physical parameters providing a welding window to any given material combination. Based on that, the mostly accepted essential condition for welding by so many investigators is: jet formation at the collision point. This condition is essential because it is the reason that chemically mating surfaces are produced, i.e. free of films and impurities, which allow the two materials to meet at interatomic level. This jet formation condition will lead to the physical parameters of the impact angles and the impact velocity. The second criterion of having a welding is to maintain these two clean surfaces under sufficant high pressure to produce the bond at the interface leading to the third important physical parameter. From here, these physical parameters need to be linked to the process parameters and this will be the aim of the method that will be presented next.

5.3   Method presentation

As it was mentionned in the introduction of this chapter, the jet formation which is linked to the impact velocity and the impact angle as well as the maintain of the pressure will allow the bonding to happen at the interface of the materials in question. In order to try to build a welding window for two couples of materials, the 3D simulation model developped in the Chapter 3 of this study will be used.

As it was observed in several studies, the angles that ensures the required progressive collision and the jet formation are in general between 6° and 30° [28, 215] and when it comes to velocities they are generally higher than 200 m/s [152, 215]. The other criterion which is very important and rarely taken into consideration in the litterature is the maintain of the pressure which is essential to keep the two surfaces in intimate contact. This dynamic pressure should be then compressive within the welding width in order to avoid any repelling wave at the interface during contact. The idea behind the method that is proposed here takes into consideration the three physical parameters at the interface during the progressive impact of the two metal sheets.

From our observation during the experimental applications, the elliptical welding line width varied between 1 and 2 mm (Table 3.8) and the idea was to evaluate the impact angle, the impact velocity and the pressure evolution within this l_w width of the welding during the progressive impact (Fig. 5.1).

In the model, the configuration of the MPW is adopted (Fig. 2.29a). The flyer metal is the aluminum 5754 and the parent is the DC04 steel with thicknesses $e_f = 0.5$ mm and $e_p = 0.8$ mm respectively. The coil is a linear rectangular cross-section one (Fig. 3.2). The 3D model param-
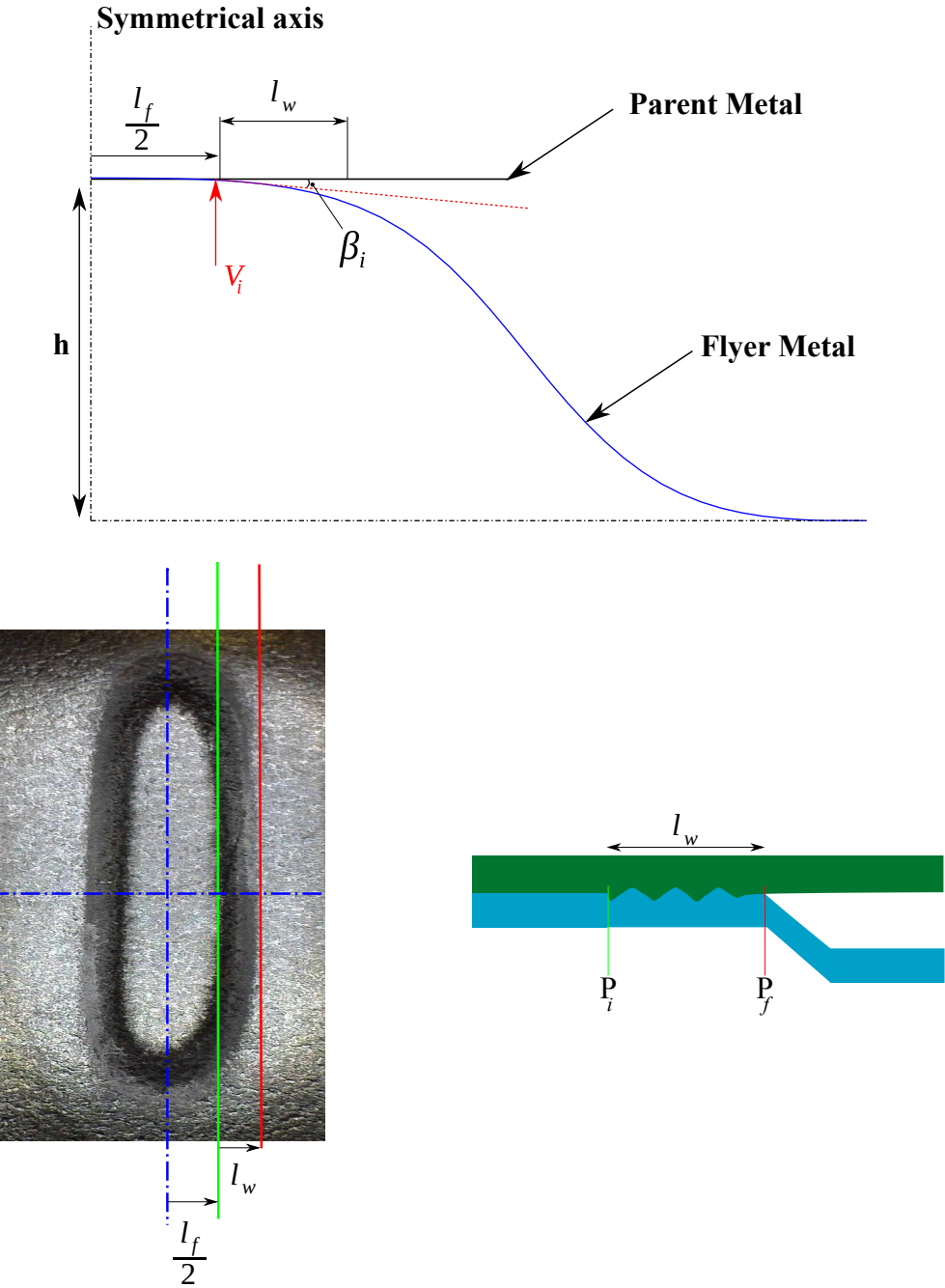
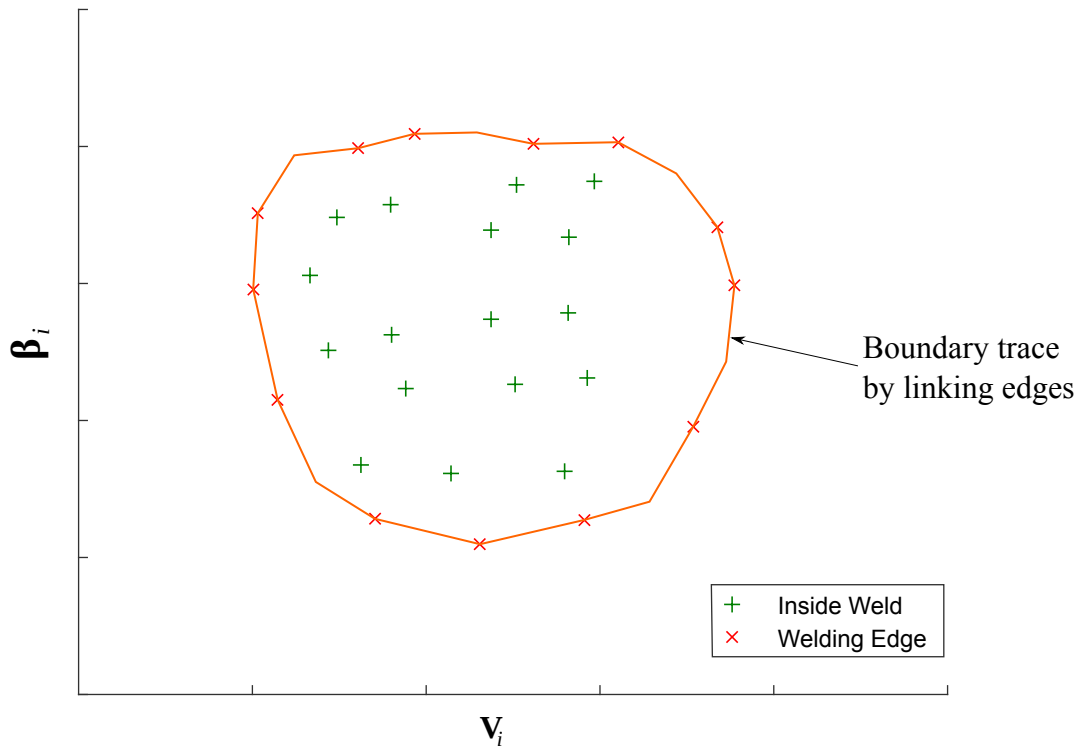Figure 5.1: progressive impact schematic physical parameters

Figure 5.2: schematic of the numerical (V_i, β_i) welding window

eters can be found in Chapter 2: Johnson-Cook model for mechanical materials properties (Table 2.1), electrical and thermal properties can be found in Table 2.2 and Table 2.3 respectively, mesh and time step based on Eq. 2.25 and Eq. 2.26.

According to the experimental datas from Chapter 3 (Fig. 3.25), the optimal welds between 5754 and DC04 were obtained for standoff distances between 1.2 and 2.2 mm using energies between 10 and 16 kJ so the numerical evaluation was done according to these results at $D = 15$ mm and $D = 25$ mm respectively.

The couple (V_i,β_i) will be evaluated at the edges and inside the welding width in order to be able to draw the welding window boundaries for each case (Fig. 5.2). After that, the two welding windows will be superposed to verify that numerically we will be in the same conditions for the physical parameters in order to be sure that even if a parameter changes (here it is D), the numerical physical parameters for a good welding will stay similar. On the other hand, by evaluating the pressure, the variation profile can be deduced between the start point and the end of a welding (Fig. 5.3). It is also done in both cases in order to see how this pressure is maintained at the interface during the progressive impact of a good quality welding.

5.4   Results and discussion

In Fig. 5.4 and Fig. 5.5 the values of (V_i,β_i) for $D = 15$ and $D = 25$ mm are represented respectively. In both cases, the values at the edges (red marks) and inside the welding area (green marks) are presented. A line linking the edges values is drawn to define the numerical welding boundaries. In order to compare both cases, the superposition for numerical (V_i,β_i) are represented in Fig. 5.6. As
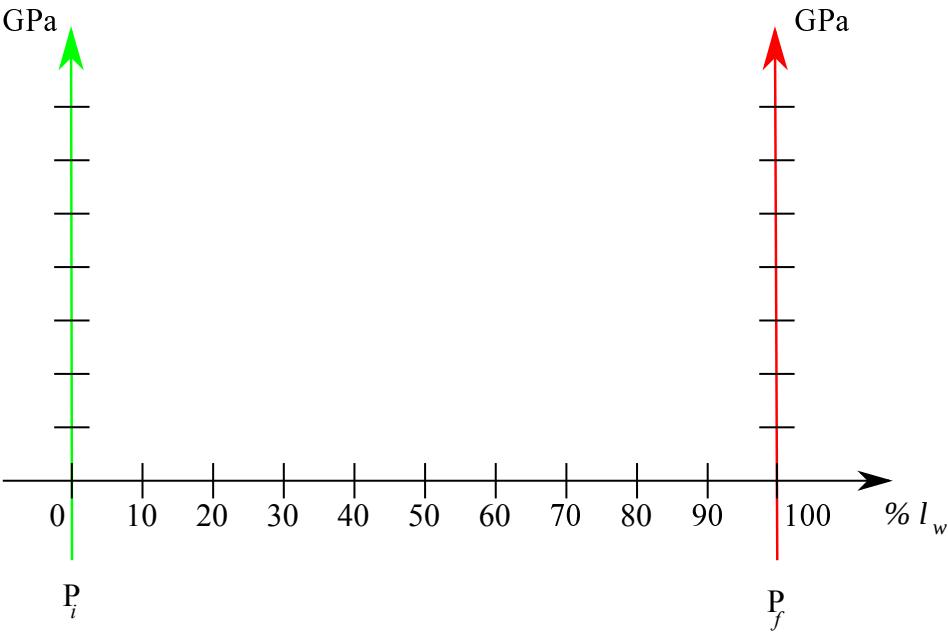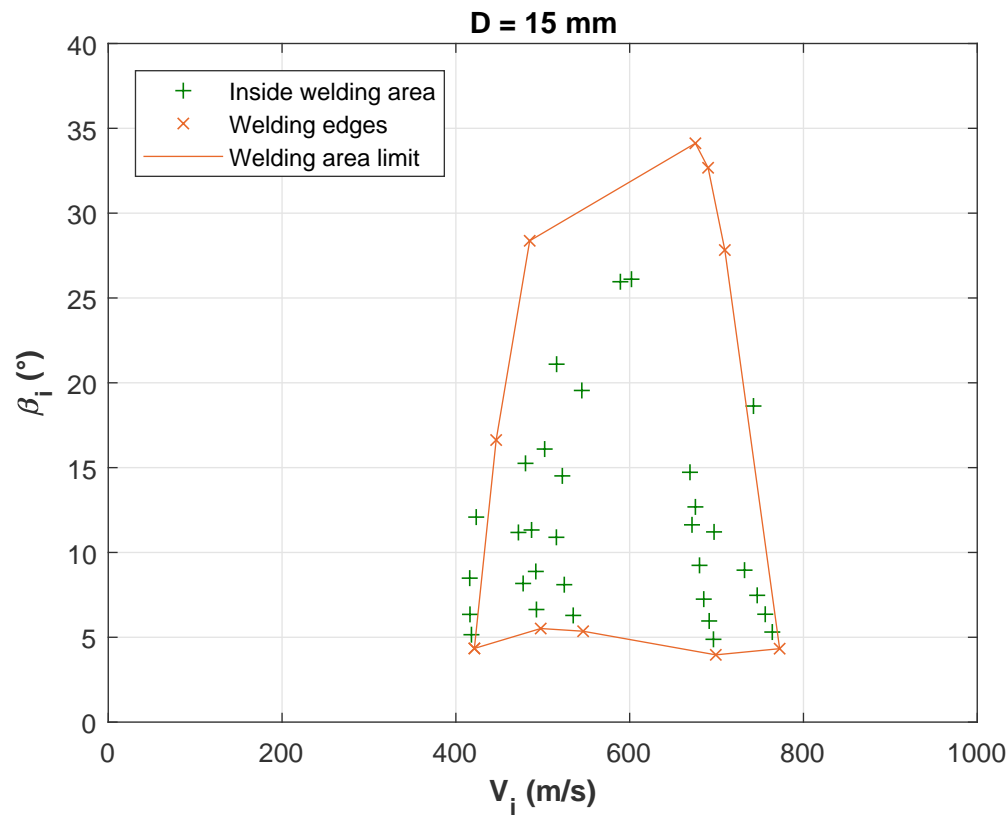
Figure 5.3: schematic of the pressure profile method between the start and the end point of a weld

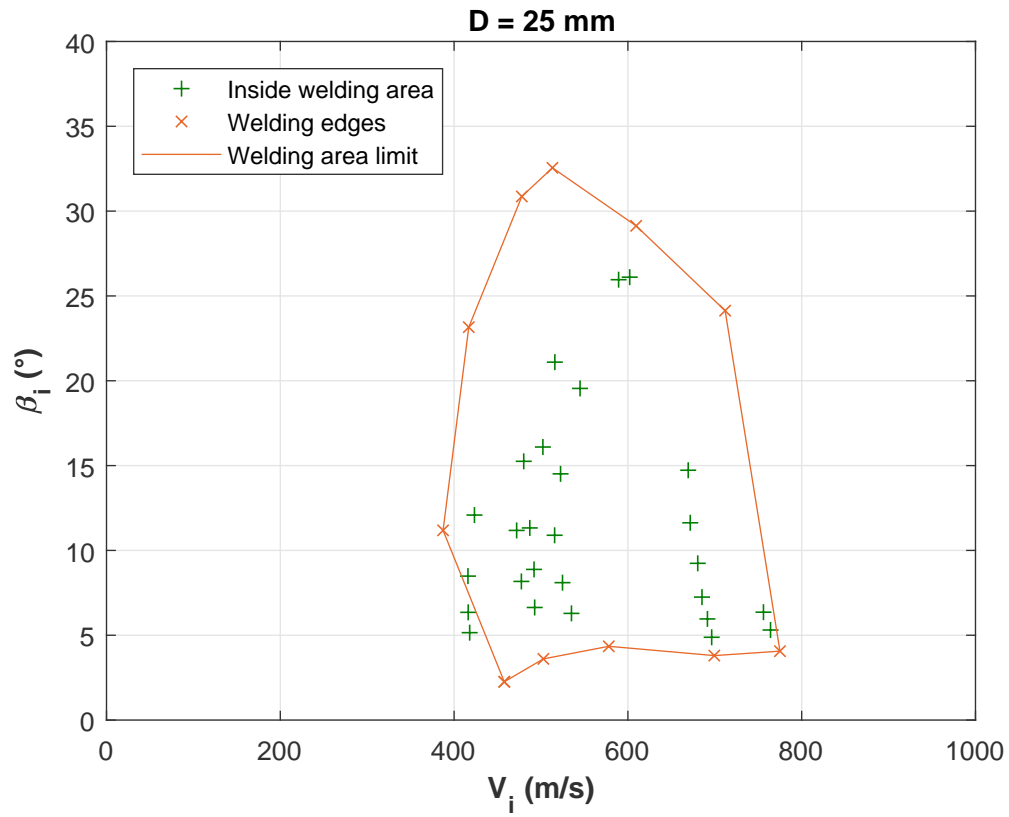Figure 5.4: (V_i, β_i) for material couple 5754/DC04: D = 15 mm

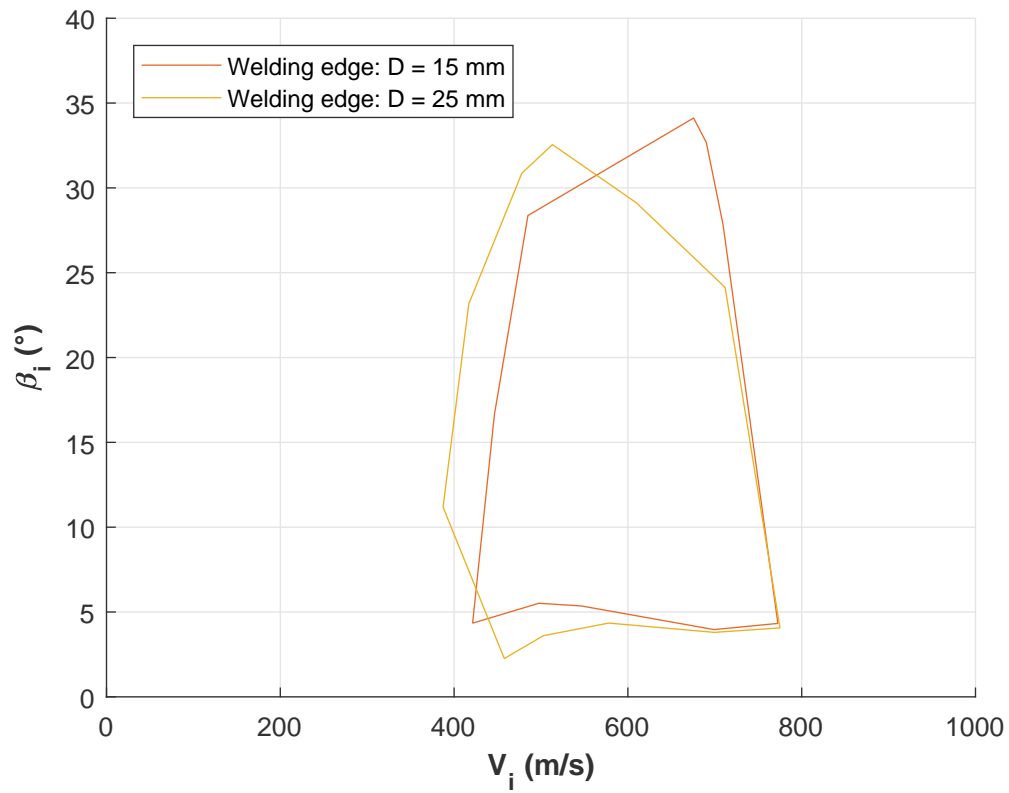Figure 5.5: (V_i, β_i) for material couple 5754/DC04: D = 25 mm

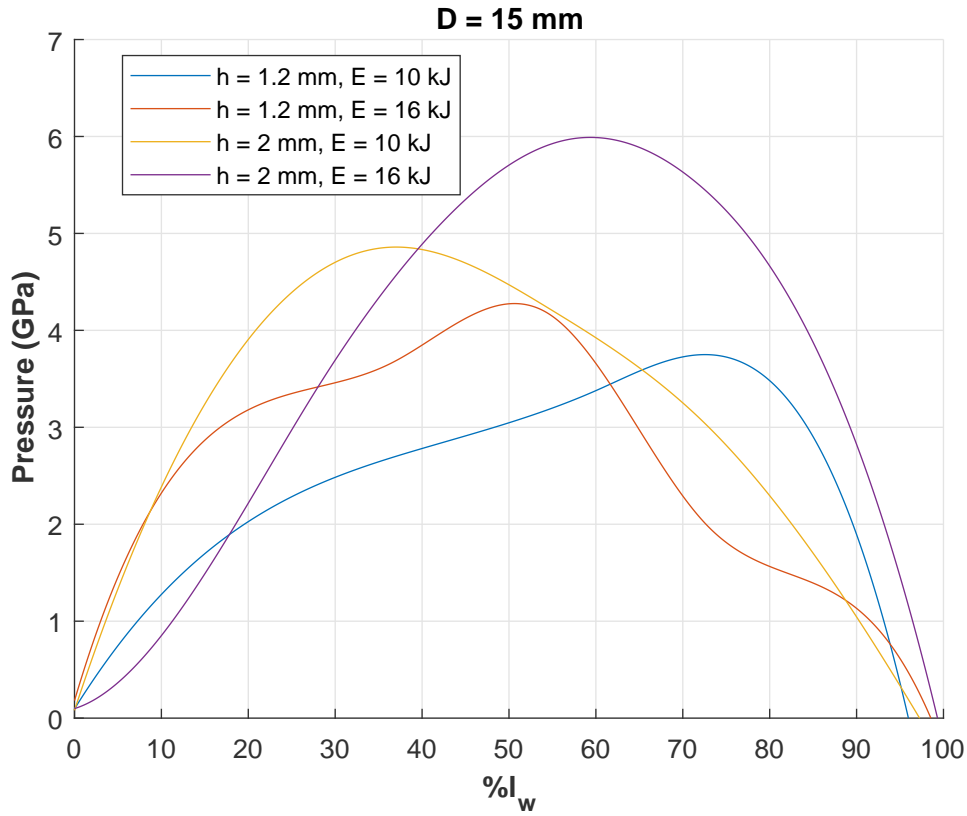Figure 5.6: (V_i, β_i) superposition for material couple 5754/DC04

Figure 5.7: pressure profiles for material couple 5754/DC04: D = 15 mm

it can be seen in both cases that the boundaries are very similar and varying between 400 and 800 m/s for angles between 2 and 33°.

When it comes to the pressure at the interface, Fig. 5.7 and Fig. 5.8 represent the profiles for both cases and the superposed results are represented in Fig. 5.9. The pressure is drawn as a function of the percentage of l_w. The pressures in both cases showed values at 10%-l_w higher than 0.5 GPa and after 90%-l_w a highly decrease rates to less than zero. The pressures between 10%- and 90%-l_w is increasing up to 4 GPa when we are at lower h where the difference between two discharge energies is not so high. This pressure in the case of intermediate standoff distance reaches 6 GPa for a discharge energy of 16 kJ. By combining the two profiles for both D, we can see that the maintain of a pressure higher than 1 GPa is almost on 80% of the welding width.

A very important first observation is that at the end of the welding, the pressure becomes negative and hence the waves at the interface is becoming repulsive at each end of the weld. The second point is the maintain of high pressure on most of the progressive impact area. In addition, the pressure variation can clearly then predict the end point of the probable welding since it approaches zero and even becomes negative in all cases.

The next thought that came to our head was: during the generation of the experimental welding windows, we have seen that there is less quality welds that occured at energies less than 10 kJ, are the numerical model for welding window and the corresponding pressure profiles conclusions able to tell us that this weld will be out of the optimal conditions? To answer this question, we considered three cases for $D = 25$ mm:

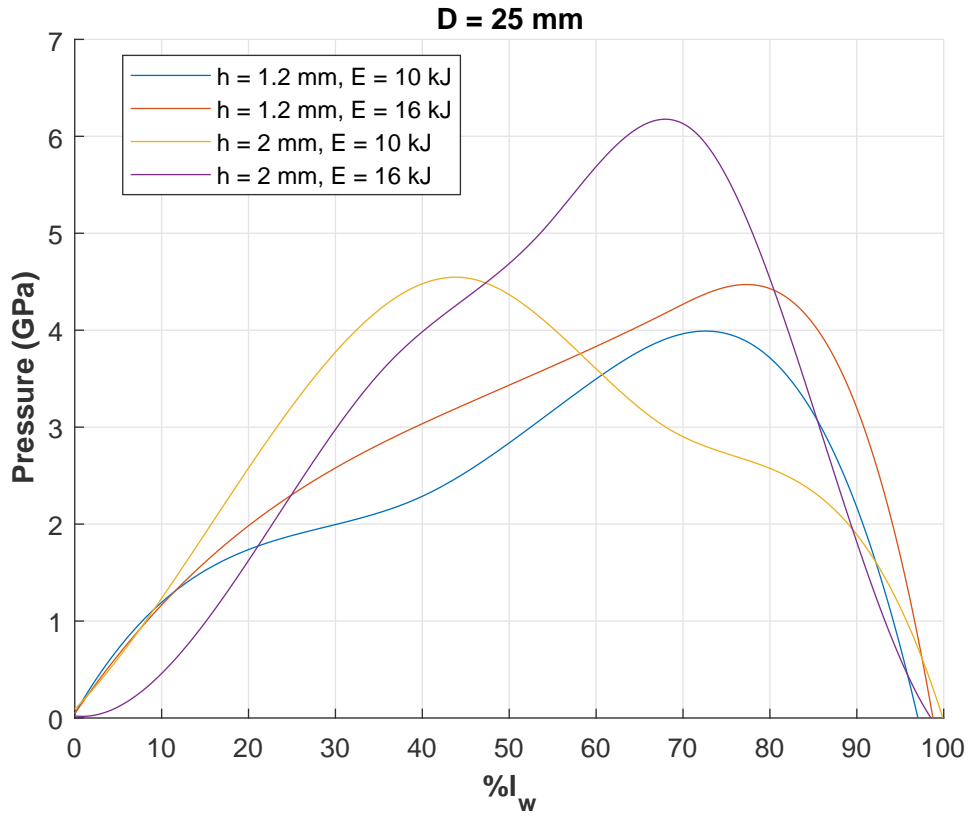- Case 1: $h = 1.2$ mm, $E = 8$ kJ

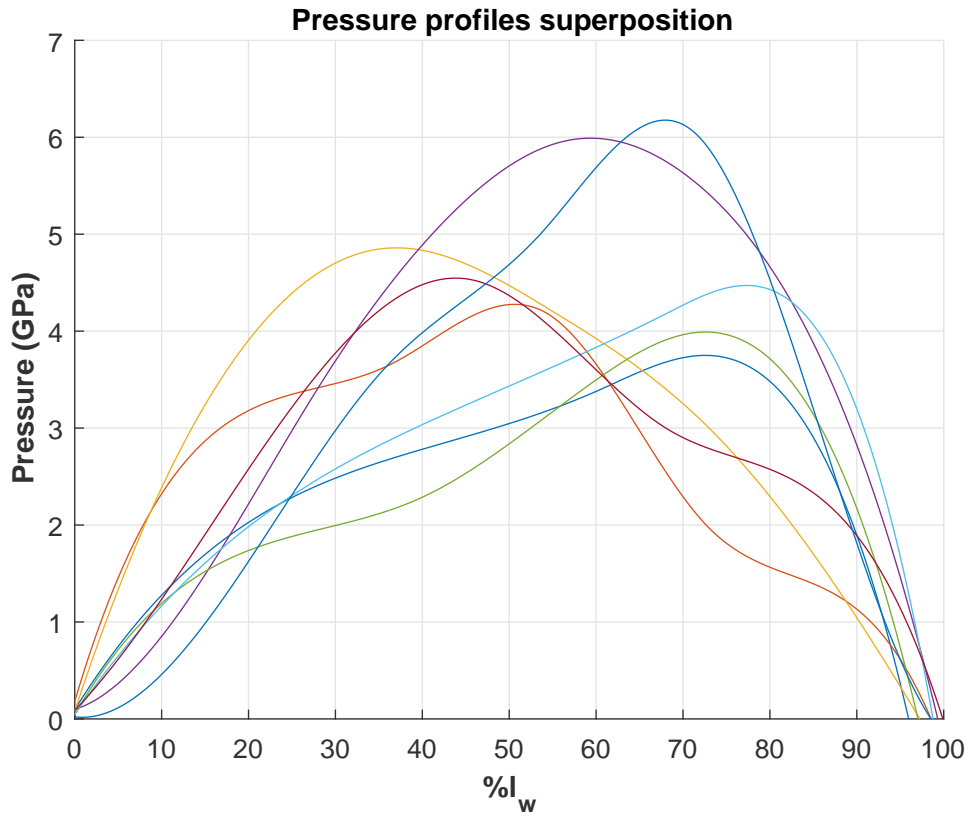Figure 5.8: pressure profile for material couple 5754/DC04: D = 25 mm

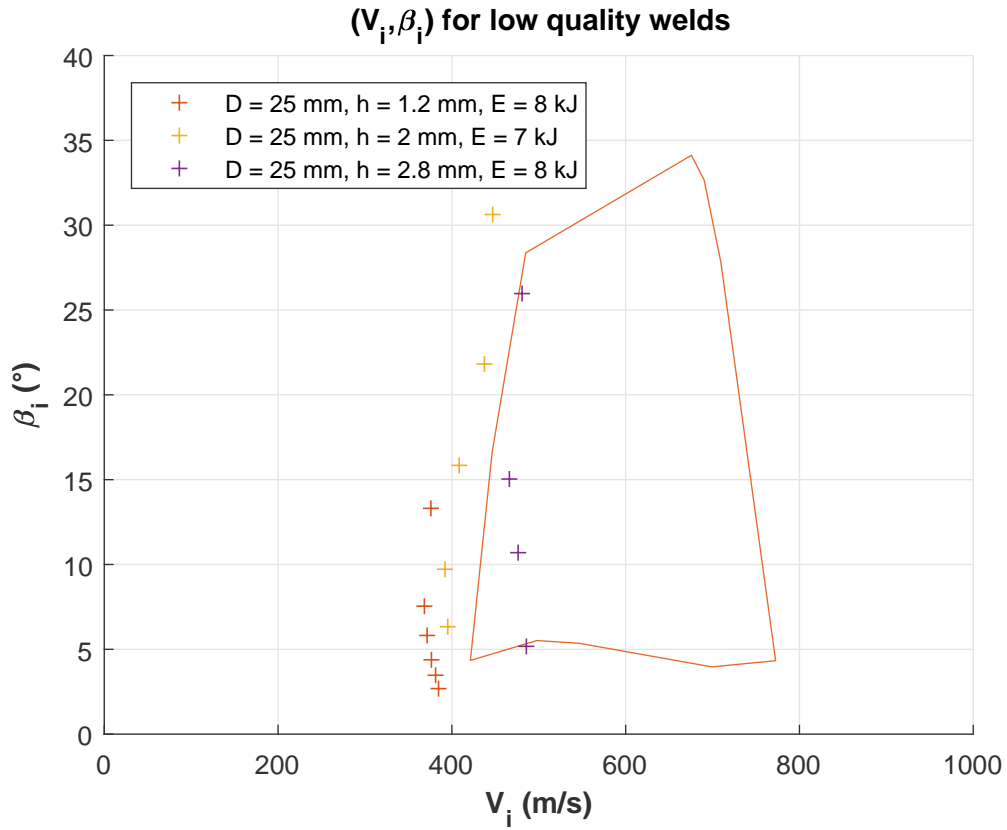Figure 5.9: pressure profiles superposition for material couple 5754/DC04

Figure 5.10: (V_i, β_i) of low quality welds for material couple 5754/DC04

- Case 2: $h = 2$ mm, $E = 7$ kJ

- Case 3: $h = 2.8$ mm, $E = 8$ kJ

In Fig. 5.10 the (V_i, β_i) are drawn together with the previous numerical welding windows boundary. In the first two cases, the evolution of the velocity is clearly outside this window and in the latest case the evolution of the velocity is inside close to the boundary of the (V_i, β_i) numerical window. When looking at the pressure profiles in Fig. 5.11, the first comment to say is that the pressure level is less than the optimal welds: in the first case it is only 2.6 GPa, in the second is 2.3 GPa and in the third one the maximum is at 3.2 GPa. The other important observation is that the pressure maitain is limited to less than 40% of the l_w in the first two cases and in the third case it is increases and then decreases rapidly after almost 30% of the l_w. Hence, even in the third case where the (V_i, β_i) are inside the numerical window, the pressure at the interface will be the indicator for the weld quality since it has low value and shorter maintain period.

After these analysis and if we want to conclude some preliminary indicators for a good welding to occur using a microscopic 3D dynamic code, we need to use not only the (V_i, β_i) evolution which are also an indicator but also the pressure at the interface which:

- will indicate the end of the weld when the wave at the interface becomes repulsive;

- will ensure that the maintain of the pressure for sufficient time during the progressive impact with values above 1 GPa and having peak values higher than 4 GPa.
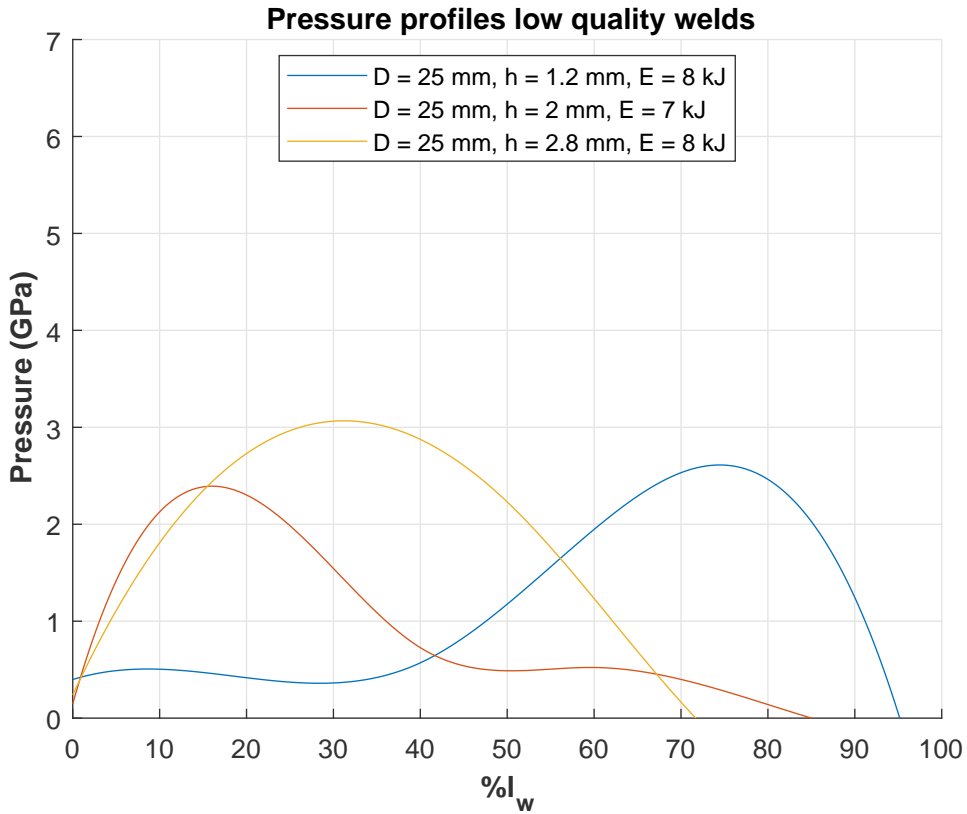
Figure 5.11: pressure profiles of low quality welds for material couple 5754/DC04

5.5 Conclusion

In this chapter, the main purpose was to initiate a macrosocopic numerical model able to predict basic information about the MPW parameters for joining two different materials. The first important conclusion is that the physical parameters obtained for two different MPW configuration parameters are very similar meaning that the construction of one experimental welding window for a couple of materials is sufficient to evaluate numerically the optimal physical welding conditions under different parameters and configurations.

In addition, the method showed that using the evolution of (V_i, β_i) as the only criterion is not sufficient to have clear view of the weld but we need to take into consideration the pressure at the interface which will give the information about the welding quality.

The conditions presented in Fig. 5.12 and Fig. 5.13 for the (V_i, β_i) and for the pressure profile conditions respectively can be used as an entry for any new couple of materials to find the first optimal welding conditions.
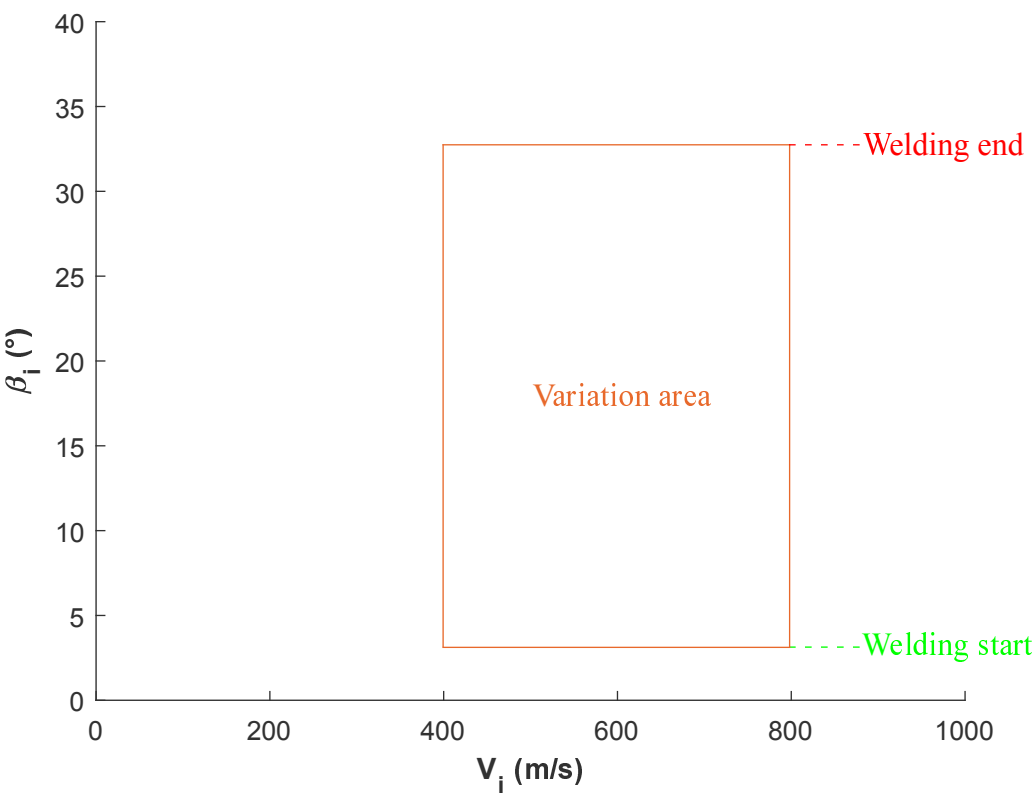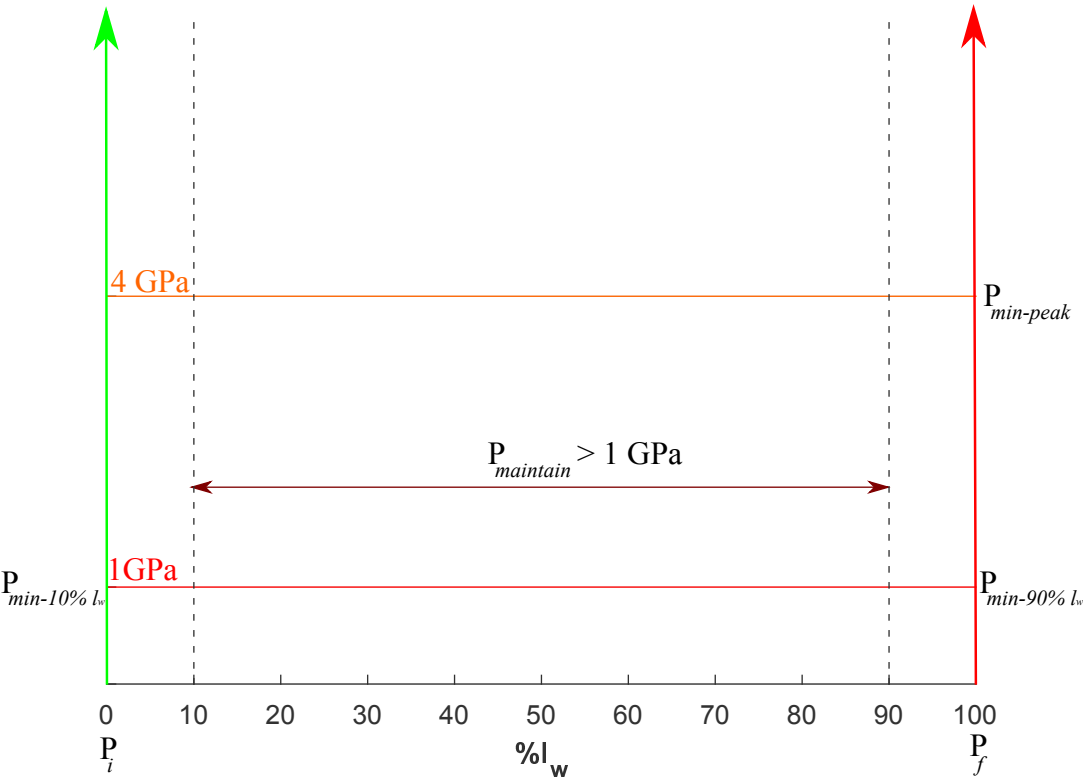
Figure 5.12: (V_i, β_i) conditions

Figure 5.13: pressure profile conditions

Conclusion

This study treats the general topic of multi-material joining field which remains one of the most biggest area of researches. The most important idea of this thesis was to extend the field of application of the MPW/MPSW to include hybrid joints between FRPC and metals. This extension resulted in the validation of two new solutions and it went through the development of the MPW which allowed improvements in the understanding of the coil design as well as achieved welds never done before using the MPW. Several important results and conclusions can be then deduced after the very large number of investigations conducted during this research work.

The physical approach of the all the electromagnetic phenomenon involved in the MPW present to any reader a one-whole-package that can be used to tackle the research field whether MPW or electromagnetic forming processes in general. It also allows to have the right analysis about the design of different components going from the coil geometry importance, its positioning influence on the efficiency and the importance of the mounting system considerations on increasing the efficiency of the process and at the same time on increasing the lifetime of the coil. One very important result of these analysis is the presentation of the design of O-shapes coils and demonstrate their higher efficiency than the linear coils. Also, it is worth mentioning that for the first time in the field of magnetic pulse welding process, a coil made of steel is used.

The development of numerical models during this study for both MPW and MPSW using a commercial code helped in analyzing the effect of different MPW configuration parameters. Using these analysis and from a simple free forming of the flyer metal, qualitative conclusions were done which allows to find qualitatively the region of parameters for a succesfull welding (Fig. 2.42).

In addition, the development of the metal/metal MPW showed the importance of the experimental procedure steps during the application of the process starting with making sure that the oil is removed from the surfaces to be joined then that the positioning of the coil will ensure the desired induced current distribution and that the whole system is clamped in a way to respect the conservation of the required standoff distance. This experimental investigation allowed also to show the weldability of different automotive aluminum alloys with different thicknesses to different steel alloys (Table 3.7). It is very important to mention that several combination were never welded using MPW. Also, several experimental welding windows were constructed during this investigation (5754/DC04; 5182/DC04; 6013-T4/DP1000) and the welds showed very good mechanical strength in various loading (quasi-static, dynamic and fatigue; Table 3.10). Another important application was also the process application between aluminum and coated steel where the welding showed good mechanical strength and that the weld is taking place with the coating layer. From a microscopic point of view (Section 3.4.5), the weldings showed a variety of wavy interfaces as

well as different types of IMCs depending on the joined partners.Their fracture surfaces showed that the failure of the welding can occur in the base material itself or within the welding.

When it comes to the new proposed solutions for joining FRPC to metals using the MPW, all possible application taking into consideration different configurations as well as the materials properties and thicknesses were covered. Their feasibility was proven by experimental application of both. In the metallic insert configuration, it was showed that there is no limitation on the insert material which can be either steel or aluminum. However, it is important to note that the adherence of flanged holes inserts was the best and that all the polymer residues should be removed because they act as obstacle of the welding. In the case of the metallic patch configuration, thin metallic patches showed risks to tear during the application of the MPW. The patches are not always able to fill completely the holes in the FRPC sheets and the flow of the patche's material should be better controlled through the coil design. Another important conclusion for both solutions is that the transition from metal/metal MPW to FRPC/metal joining can be done using the same parameters with high accuracy and that these solutions used the same equipments that were used for the bimetallic applications and without any modification.

Since all the above presents the wide scope of the process application, numerical prediction for welding depending on the application geometrical parameters will be very useful for future applications. The last chapter in this study initiated a macrosocpic numerical model able to predict basic information about the MPW parameters for joining two different materials. The physical parameters obtained for two different MPW configuration parameters are very similar meaning that the construction of one experimental welding window for a couple of materials is sufficient to evaluate numerically the optimal physical welding conditions under different parameters and configurations.

After this whole study, we can claim that the MPW/MPSW technology has no limitations for applications going from similar to dissimilar welding and also for metallic to non-metallic joining applications.

In addition, the efficiency of the steel inductors that we have used pushes us to wonder if we should think a little bit out of the box and to not just try to develop less resistant mechanical copper inductors but rethink the choice of inductors materials as well as their design.

All what has been said above shows that we still have a lot of work to do in order to master the MPW/MPSW and that we are still far from a complete single quantitative theory capable of giving a precise description for the welding and a prediction of the welding parameters. This multi-disciplinary process now makes the collaboration inevitable between different branches of engineering that it is the electromagnetic field, mechanical, metallurgical, ballistic and numerical. All these efforts are essential to answer all the big questions where the most vague for the moment remains: what is the physics behind magnetic pulse welding formation?

Conclusion

Cette étude s'inscrit dans le cadre général des assemblages multi-matériaux, qui reste l'un des domaines de recherche les plus importants. L'idée principale de cette thèse était d'étendre le domaine d'application du soudage par impulsion magnétique pour y inclure les assemlages hybrides métal/composite. Cette extension a abouti à la validation de deux nouvelles solutions et a permis en parallèle : le développement du procédé en lui même en améliorant la compréhension de la conception des inducteurs et d'obtenir des soudures jamais réalisées par impulsion magnétique. Plusieurs résultats et conclusions importants peuvent alors être déduits suite à ce travail de recherche.

L'approche physique des phénomènes électromagnétiques observés dans le procédé du soudage par impulsion magnétique présenté dans cette étude constitue un ensemble complet qui permettra la compréhension de ces phénomènes et de leurs interactions pas seulement pour le soudage mais aussi pour le magnétoformage. Cela permet également d'avoir la bonne analyse pour la conception des différents composants : la géométrie de l'inducteur, l'influence de son positionnement sur l'efficacité du procédé et les précautions à prendre dans les systèmes de montage pour maintenir cette efficacité et augmenter la durée de vie de l'inducteur. Un résultat très important de ces analyses est la présentation de l'inducteur en forme de O qui a montré une efficacité supérieure à celle des inducteurs linéaires. Il convient également de mentionner que pour la première fois dans le domaine des procédés à impulsions magnétiques, un inducteur en acier est utilisé pour souder des nuances plus ou moins rigides.

Le développement des modèles numériques au cours de cette étude pour le soudage et le soudage par point par impulsion magnétique en utilisant un code commercial a aidé à analyser les effets de différents paramètres procédé. À l'aide de ces analyses et d'une simple déformation libre de la pièce induite, des conclusions qualitatives ont été tirées qui permettent de trouver qualitativement la plage des paramètres pour une soudure réussie (Fig. 2.42).

En outre, le développement du procédé pour les applications métal/métal a montré l'importance des étapes de la procédure à respecter durant l'application du procédé en commençant par s'assurer qu'aucun résidu d'huile se trouve sur les surfaces à assembler, ensuite que le positionnement de l'inducteur va bien assurer la distribution du courant induit souhaitée et que tout le système soit bien serré tout en conservant la distance voulue entre les deux pièces. Cette étude expérimentale a également montré la soudabilité de différentes nuances d'aluminium de différentes épaisseurs avec différents aciers utilisés dans l'automobile (Table 3.7). Il est très important de mentionner que plusieurs combinaisons n'ont jamais été soudées avant avec du MPW. En outre, plusieurs fenêtres de soudage expérimentales ont été construites au cours de cette étude (5754 / DC04; 5182 / DC04; 6013-T4 / DP1000) et les soudures ont montré une très bonne résistance mécanique (quasi-statique, dynamique et fatigue). Une autre application importante était également l'utilisation du procédé pour souder l'aluminium et l'acier revêtu où la soudure se faisait avec la couche de revêtement et présentait une bonne résistance mécanique. D'un point de vue microscopique (Section 3.4.5), les soudures ont montré des interfaces ondulées ainsi que des fines couches d'intermétalliques dont la nature dépend des couples soudés. Leurs surfaces de rupture ont montré que la rupture du joint peut se produire dans le matériau de base lui-même ou dans la soudure.

En ce qui concerne les nouvelles solutions proposées pour les assemblages métal/composite utilisant le soudage par impulsion magnétique, les propositions prennent en compte divers configurations ainsi que les propriétés et les épaisseurs des matériaux à assembler. Leurs faisabilités ont été prouvées expérimentalement. Au niveau de la configuration utilisant l'insert métallique, il n'y a pas de limitation sur le matériau de l'insert qui peut être de l'acier ou de l'aluminium. Cependant, il est important de noter que les inserts ayant des trous à brides présentent la meilleure adhérence dans le composite et que tous les résidus de polymères doivent être éliminés car ils constituent un obstacle à la soudure. Dans le cas de la configuration des patchs métalliques, des patchs minces présentent des risques de déchirure lors de l'application du soudage. Les patchs ne sont pas toujours capables de remplir complètement les trous dans le composite et l'écoulement du matériau de la plaque doit être bien contrôlé grâce à la conception de l'inducteur. Une autre conclusion importante pour les deux solutions est que la transition entre les paramètres de soudure bimétalliques et les paramètres pour assemblage métal/composite peut être réalisée avec une grande cohérence et que ces solutions utilisent le même équipement sans rien changer entre les deux applications.

Étant donné tout ce qui précède, les avantages de la technologie de soudage par impulsion magnétique sont nombreuses et la prédiction numérique du soudage en fonction des paramètres géométriques sera très utile pour les applications futures. Le dernier chapitre de cette étude a initié un modèle numérique macroscopique capable de prédire les informations de base sur les paramètres MPW pour souder deux matériaux différents. Les paramètres physiques obtenus pour deux systèmes de paramètres différents conduisant à une bonne qualité de soudure sont très similaires, ce qui signifie que la construction d'une fenêtre de soudage expérimentale pour un couple suffit à évaluer numériquement les conditions physiques optimales de soudage et savoir en appliquant d'autres paramètres procédés si on obtient une soudure ou pas.

Après toute cette étude, nous pouvons affirmer que la technologie de soudage par impulsion magnétique n'a pas de limites pour les applications allant du soudage similaire à celui du soudage dissemblable, mais également pour les applications d'assemblage de pièces métalliques à des autres non métalliques.

En plus, l'efficacité des inducteurs en acier que nous avons utilisés nous pousse à se demander s'il ne faut pas sortir de la stratégie qui consiste à ne développer que des inducteurs en cuivre moins résistants mécaniquement et repenser ainsi le choix des matériaux des inducteurs ainsi que leur conception.

Tout ça aujourd'hui indique que nous avons encore énormément de travail pour maitriser le procédé d'impulsion magnétique et surtout que nous sommes encore loin d'une théorie unique quantitative complète capable de donner une description et une prédiction précises des paramètres de soudure. Cette pluridisciplinarité du procédé rend aujourd'hui inévitable la collaboration entre les différentes branches de l'ingénierie que ça soit du domaine électromagnétique, mécanique, métallurgique, balistique et numérique. Tous ces efforts sont indispensables pour répondre à toutes les grandes questions où la plus vague pour le moment reste: quelle est la physique derrière la formation de soudage par impulsion magnétique ?

References

[1] George Raymond Abrahamson. Permanent periodic surface deformations due to a traveling jet. *journal of applied mechanics*, 28(4):519–528, 1961.

[2] C Ageorges, L Ye, and M Hou. Advances in fusion bonding techniques for joining thermoplastic matrix composites: a review. *Composites Part A: applied science and manufacturing*, 32(6):839–857, 2001.

[3] Christophe Ageorges and Lin Ye. Resistance welding of metal/thermoplastic composite joints. *Journal of Thermoplastic Composite Materials*, 14(6):449–475, 2001.

[4] Leonardo Agudo, Dominique Eyidi, Christian H. Schmaranzer, Enno Arenholz, Nasrin Jank, Jürgen Bruckner, and Anke R. Pyzalla. Intermetallic Fe x Al y -phases in a steel/Al-alloy fusion weld. *Journal of Materials Science*, 42(12):4205–4214, jun 2007. ISSN 0022-2461.

[5] Leonardo Agudo, Dominique Eyidi, Christian H Schmaranzer, Enno Arenholz, Nasrin Jank, Jürgen Bruckner, and Anke R Pyzalla. Intermetallic fexaly-phases in a steel/al-alloy fusion weld. *Journal of materials science*, 42(12):4205–4214, 2007.

[6] T Aizawa and M Kashani. Magnetic pulse welding (MPW) method for dissimilar sheet metal joints. 2010.

[7] T Aizawa, K Okogawa, M Yoshizawa, and N Henmi. Impulse magnetic pressure seam welding of aluminium sheets. *Impact engineering and applications*, 2001.

[8] Tomokatsu Aizawa, Mehrdad Kashani, and Keigo Okagawa. Application of magnetic pulse welding for aluminum alloys and spcc steel sheet joints. *Welding Journal*, 86(5):119–124, 2007.

[9] Tomokatsu Aizawa, Keigo Okagawa, and Mehrdad Kashani. Application of magnetic pulse welding technique for flexible printed circuit boards (fpcb) lap joints. *Journal of Materials Processing Technology*, 213(7):1095–1102, 2013.

[10] M. Aizawa, T., Kashani. Magnetic Pulse Welding (MPW) Method for Dissimilar Sheet Metal Joints. *Tokyo Metropolitan college of Technology - Department of Electronic and Information Engineering*, 2004.

References

[11] Mathieu Alexander, Mattei Simone, and Viala Jean-Claude. Laser brazing welding using hot (88%-aluminum, 12%-silicon) filler material to join steel with aluminum. In *Laser materials processing conference, Proceeding of ICA-LEO*, volume 5, pages 985–991.

[12] S T Amancio-Filho and J F Dos Santos. Joining of polymers and polymer–metal hybrid structures: recent developments and trends. *Polymer Engineering & Science*, 49(8):1461–1476, 2009.

[13] S.T. Amancio-Filho, C. Bueno, J.F. dos Santos, N. Huber, and E. Hage. On the feasibility of friction spot joining in magnesium/fiber-reinforced polymer composite hybrid structures. *Materials Science and Engineering: A*, 528(10):3841–3848, 2011. ISSN 09215093.

[14] Adrian Anghelus, Marie-Noëlle Avettand-Fènoël, Catherine Cordier, and Roland Taillard. Microstructural evolution of aluminium/al–ni–sm glass forming alloy laminates obtained by controlled accumulative roll bonding. *Journal of Alloys and Compounds*, 631:209–218, 2015.

[15] MM Hoseini Athar and Behzad Tolaminejad. Weldability window and the effect of interface morphology on the properties of al/cu/al laminated composites fabricated by explosive welding. *Materials & Design*, 86:516–525, 2015.

[16] M-N Avettand-Fènoël, C Khalil, R Taillard, and G Racineux. Effect of steel galvanization on the microstructure and mechanical performances of planar magnetic pulse welds of aluminum and steel. *Metallurgical and Materials Transactions A*, pages 1–18.

[17] AS Bahrani and B Crossland. Explosive welding and cladding. *An Introductory Survey and Preliminary Results, Proc., . . .* , 1964.

[18] AS Bahrani, TJ Black, and Bernard Crossland. The mechanics of wave formation in explosive welding. *Proc. R. Soc. Lond. A*, 296(1445):123–136, 1967.

[19] F Balle, G Wagner, and D Eifler. Ultrasonic spot welding of aluminum sheet/carbon fiber reinforced polymer–joints. *Materialwissenschaft und Werkstofftechnik*, 38(11):934–938, 2007.

[20] F Balle, G Wagner, and D Eifler. Ultrasonic metal welding of aluminium sheets to carbon fibre reinforced thermoplastic composites. *Advanced Engineering Materials*, 2009.

[21] G. Bartels, W. Schätzing, H.P. Scheibe, and M. Leone. Models for Electromagnetic Metal Forming. In *3rd International Conference on High Speed Forming, ICHSF 2008*, pages 121–128, March 2008.

[22] SV Bazdenkov, VF Demichev, D Kh Morozov, and OP Pogutse. Possible mechanism of wave formation in explosive welding. *Combustion, Explosion and Shock Waves*, 21(1):124–130, 1985.

[23] GA Belchuk, VR Ryabov, and VI Yumatova. State of the art of argon-arc welding technology in joining aluminum and aluminum alloys to steel. Technical report, NAVAL INTELLIGENCE SUPPORT CENTER WASHINGTON DC TRANSLATION DIV, 1973.

[24] Laurence J Bement. Applying nasa's explosive seam welding. 1991.

[25] A Ben-Artzy, A Stern, and N Frage. Wave formation mechanism in magnetic pulse welding. *International Journal of . . .*, 2010.

[26] Jean Pierre Bergmann and Martin Stambke. Potential of laser-manufactured polymer-metal hybrid joints. *Physics Procedia*, 39:84–91, 2012.

[27] OP Biro. On the use of the magnetic vector potential in the finite-element analysis of three-dimensional eddy currents. 1989.

[28] TZ Blazynski. *Explosive welding, forming and compaction*. 2012.

[29] MP Bondar and VM Ogolikhin. Plastic deformation in bonding zone under explosive welding and its role in bonding formation. *Le Journal de Physique Colloques*, 46(C5):C5–379, 1985.

[30] Rattana Borrisutthekul, Taisei Yachi, Yukio Miyashita, and Yoshiharu Mutoh. Suppression of intermetallic reaction layer formation by controlling heat flow in dissimilar joining of steel and aluminum alloy. *Materials Science and Engineering: A*, 467(1-2):108–113, 2007.

[31] Pierre E Bourban, Erdal Karamuk, Roderic C Don, and John W Gillespie. Induction heating for rehabilitation of steel structures using composites. In *Infrastructure@ sNew Materials and Methods of Repair*, pages 287–294. ASCE, 1994.

[32] Pierre E Bourban, Steven H McKnight, Stacy B Shulley, Vistasp M Karbhari, and John W Gillespie. Durability of steel/composites bonds for rehabilitation of structural components. In *Infrastructure@ sNew Materials and Methods of Repair*, pages 295–302. ASCE, 1994.

[33] S Bozzi, AL Helbert-Etter, T Baudin, B Criqui, and JG Kerbiguet. Intermetallic compounds in al 6016/if-steel friction stir spot welds. *Materials Science and Engineering: A*, 527(16-17):4505–4509, 2010.

[34] Eric A Brandes and GB Brook. *Smithells metals reference book*. Elsevier, 2013.

[35] J Bruckner. Considering thermal processes for dissimilar metals: joining steel to aluminum in heat-intensive applications. *Fabricator*, 2003.

[36] John A. Buck and William H. Hayt. *Engineering Electromagnetics*. McGraw-Hill, sixth edit edition, 2001.

[37] Richard G. Budynas and J. Keith Nisbett. *Shigley's Mechanical Engineering Design*. McGraw-Hill, ninth edition, 2011.

References

[38] T.J. Burgess. Electrical resistivity model of metals. In *4th International Conference on Megagauss Magnetic-Field Generation and Related Topics*, Santa Fe, NM, USA, 1986.

[39] PP Camanho, CML Tavares, R De Oliveira, AT Marques, and AJM Ferreira. Increasing the efficiency of composite single-shear lap joints using bonded inserts. *Composites Part B: Engineering*, 36(5):372–383, 2005.

[40] R Cao, Gang Yu, JH Chen, and Pei-Chung Wang. Cold metal transfer joining aluminum alloys-to-galvanized mild steel. *Journal of materials processing technology*, 213(10):1753–1763, 2013.

[41] Leroy R. CARL. Brass welds, made by detonation impulse. *Metal Progress*, 46:102–103, 1944.

[42] SH Carpenter and RH Wittman. Explosion welding. *Annual review of materials science*, 5 (1):177–199, 1975.

[43] Asier Cenigaonaindia, Fernando Liébana, Aitzol Lamikiz, and Zelmar Echegoyen. Novel strategies for laser joining of polyamide and aisi 304. *Physics Procedia*, 39:92–99, 2012.

[44] CM Chen and R Kovacevic. Joining of al 6061 alloy to aisi 1018 steel by combined effects of fusion and solid state welding. *International Journal of Machine Tools and Manufacture*, 44(11):1205–1214, 2004.

[45] YC Chen, T Komazaki, YG Kim, T Tsumura, and K Nakata. Interface microstructure study of friction stir lap joint of ac4c cast aluminum alloy and zinc-coated steel. *Materials Chemistry and Physics*, 111(2-3):375–380, 2008.

[46] ZW Chen, S Yazdanian, and G Littlefair. Effects of tool positioning on joint interface microstructure and fracture strength of friction stir lap al-to-steel welds. *Journal of materials science*, 48(6):2624–2634, 2013.

[47] K.T. Christensen, N.S. Egly, and L. Alting. In *Proceedings of the 4th International Conference of the Center for High Energy Rate Forming*, Colorado, 1973. University of Denver.

[48] Rodrigo Santiago Coelho, Aleksander Kostka, Shahram Sheikhi, J Dos Santos, and Anke Rita Pyzalla. Microstructure and mechanical properties of an aa6181-t4 aluminium alloy to hc340la high strength steel friction stir overlap weld. *Advanced Engineering Materials*, 10(10):961–972, 2008.

[49] George R Cowan and Arnold H Holtzman. Flow configurations in colliding plates: explosive bonding. *Journal of applied physics*, 34(4):928–939, 1963.

[50] B Crossland. Development of exlosive welding and its application in engineering. *METALS MATERIALS*, 1971.

[51] B Crossland and JD Williams. Explosive welding. *Metallurgical Reviews*, 15(1):79–100, 1970.

[52] Senlin Cui, Yong Du, Lijun Zhang, Yajun Liu, and Honghui Xu. Assessment of atomic mobilities in fcc al-zn and ni-zn alloys. *Calphad*, 34(4):446–451, 2010.

[53] JP Cuq-Lelandais, S Ferreira, G Avrillaud, G Mazars, and B Rauffet. Magnetic pulse welding: welding windows and high velocity impact simulations. In *6th International Conference on High Speed Forming*, pages 199–206, 2014.

[54] JP Cuq-Lelandais, G Avrillaud, S Ferreira, G Mazars, A Nottebaert, G Teilla, and V Shribman. 3d impacts modeling of the magnetic pulse welding process and comparison to experimental data. In *7th International Conference on High Speed Forming*, pages 13–22, 2016.

[55] H Das, RN Ghosh, and TK Pal. Study on the formation and characterization of the intermetallics in friction stir welding of aluminum alloy to coated steel sheet lap joint. *Metallurgical and Materials Transactions A*, 45(11):5098–5106, 2014.

[56] H Das, SS Jana, TK Pal, and A De. Numerical and experimental investigation on friction stir lap welding of aluminium to steel. *Science and Technology of Welding and Joining*, 19 (1):69–75, 2014.

[57] AA Deribas. Physics of explosive hardening and welding. *Nanka, Novosibirsk*, 1980.

[58] AA Deribas, VM Kudinov, FI Matveenkov, and VA Simonov. Simulation of a wave formation process during explosion welding(detonation wave formation during explosion welding of plates analyzed by dimensionality theory). *FIZIKA GORENIIA I VZRYVA*, 4:100–107, 1968.

[59] C Dharmendra, KP Rao, J Wilden, and S Reich. Study on laser welding–brazing of zinc coated steel to aluminum alloy with a zinc based filler. *Materials Science and Engineering: A*, 528(3):1497–1503, 2011.

[60] Honggang Dong, Liqun Yang, Chuang Dong, and Sindo Kou. Arc joining of aluminum alloy to stainless steel with flux-cored zn-based filler metal. *Materials Science and Engineering: A*, 527(26):7151–7154, 2010.

[61] H. El-Sobky. *Mechanics of Explosive Welding*, pages 189–217. Springer Netherlands, Dordrecht, 1983. ISBN 978-94-011-9751-9.

[62] K Faes. Tube welding. *Belgian Welding Institute, St-Pietersnieuwstraat*, 41, 2011.

[63] Z Fan, H Yu, J Deng, and C Li. Molecular dynamics modeling of atomic diffusion across fe-al magnetic-pulse-welding interface. In *8th International Conference on High Speed Forming*, 2018.

[64] Zhisong Fan, Haiping Yu, and Chunfeng Li. Interface and grain-boundary amorphization in the al/fe bimetallic system during pulsed-magnetic-driven impact. *Scripta Materialia*, 110: 14–18, 2016.

References

[65] Paolo Feraboli and Attilio Masini. Development of carbon/epoxy structural components for a high performance vehicle. *Composites Part B: Engineering*, 35(4):323–330, 2004.

[66] Maofeng Fu and PK Mallick. Fatigue of hybrid (adhesive/bolted) joints in srim composites. *International Journal of Adhesion and Adhesives*, 21(2):145–159, 2001.

[67] L. Gaul, M. Kögl, and M. Wagner. *Boundary Element Methods for Engineers and Scientists, An Introductory Course with Advanced Topics*. Springer-Verlag Berlin Heidelberg, 2003. doi: 10.1007/978-3-662-05136-8.

[68] Marion Girard. *Soudage-diffusion hétérogène assisté par friction malaxage: cas du couple Al/Fe*. PhD thesis, Ecole Centrale de Nantes, 2010.

[69] Gunther Göbel, Eckard Beyer, Jörg Kaspar, and Berndt Brenner. Dissimilar metal joining: macro-and microscopic effects of mpw. In *5th International Conference on High Speed Forming*, pages 179–188, 2012.

[70] S Gomez, J Onoro, and J Pecharroman. A simple mechanical model of a structural hybrid adhesive/riveted single lap joint. *International journal of adhesion and . . .*, 2007.

[71] JE Gould. Joining aluminum sheet in the automotive industry - a 30 year history. *Weld. J*, 91:23–34, 2012.

[72] S.M. Goushegir, J.F. dos Santos, and S.T. Amancio-Filho. Friction Spot Joining of aluminum AA2024/carbon-fiber reinforced poly(phenylene sulfide) composite single lap joints: Microstructure and mechanical performance. *Materials & Design (1980-2015)*, 54: 196–206, 2014. ISSN 02613069. doi: 10.1016/j.matdes.2013.08.034.

[73] D.P. Graham, A. Rezai, D. Baker, P.A. Smith, and J.F. Watts. The development and scalability of a high strength, damage tolerant, hybrid joining scheme for composite and metal structures. *Composites Part A: Applied Science and Manufacturing*, 64:11–24, 2014.

[74] DJ Griffiths. *Introduction to electrodynamics*. Prentice-Hall, Inc., third edition, 1999.

[75] P Groche, S Wohletz, and M Brenneis. Joining by forming - a review on joint mechanisms, applications and future trends. *Journal of Materials . . .*, 2014.

[76] A Grodzinski, J Senkara, and M Kozlowski. Duralumin-stainless steel joint: structure and mechanism of forming by means of electron beam welding and ag-2mg filler metal shim. *Journal of materials science*, 31(18):4967–4973, 1996.

[77] Karl-Heinrich Grote and Erik K Antonsson. *Springer handbook of mechanical engineering*, volume 10. Springer Science & Business Media, 2009.

[78] M Gutensohn. FACHBEITRAGE-Ultraschallschweissen von Aluminiumlitzen. . . . *Schneiden*, 2007.

[79] M Haghshenas, A Abdel-Gwad, AM Omran, B Gökçe, S Sahraeinejad, and AP Gerlich. Friction stir weld assisted diffusion bonding of 5754 aluminum alloy to coated high strength steels. *Materials & Design*, 55:442–449, 2014.

[80] Jun Hyun Han, Jae Pyoung Ahn, and Myung Chul Shin. Effect of interlayer thickness on shear deformation behavior of aa5083 aluminum alloy/ss41 steel plates manufactured by explosive welding. *Journal of Materials Science*, 38(1):13–18, 2003.

[81] ASM Handbook. *Volume 14B Metalworking: Sheet Forming*, volume 924. 2006.

[82] Charles A Harper and A Charles. *Modern plastics handbook*, volume 1. McGraw-Hill New York, 2000.

[83] L_J HART-SMITH. Bonded-bolted composite joints. *Journal of Aircraft*, 22(11):993–1000, 1985.

[84] Akio Hirose, Hirotaka Imaeda, Miki Kondo, and Kojiro F Kobayashi. Influence of alloying elements on interfacial reaction and strength of aluminum/steel dissimilar joints for light weight car body. In *Materials science forum*, volume 539, pages 3888–3893. Trans Tech Publ, 2007.

[85] CK Huang. Study on co-cured composite panels with blade-shaped stiffeners. *Composites Part A: applied science and manufacturing*, 34(5):403–410, 2003.

[86] JN Hunt. Wave formation in explosive welding. *Philosophical magazine*, 17(148):669–680, 1968.

[87] JD Jackson. *Classical electrodynamics*. John Wiley & Sons, third ed. edition, 1999.

[88] Leonardo Agudo Jácome, Sebastian Weber, Alois Leitner, Enno Arenholz, Jürgen Bruckner, Heinz Hackl, and Anke Rita Pyzalla. Influence of filler composition on the microstructure and mechanical properties of steel - aluminum joints produced by metal arc joining. *Advanced Engineering Materials*, 11(5):350–358, 2009.

[89] WH Jiang and R Kovacevic. Feasibility study of friction stir welding of 6061-t6 aluminium alloy with aisi 1018 steel. *Proceedings of the Institution of Mechanical Engineers, Part B: Journal of Engineering Manufacture*, 218(10):1323–1331, 2004.

[90] P Jimbert, Iñaki Eguia, MA Gutierrez, B Gonzalez, GS Daehn, Y Zhang, R Anderson, H Sundberg, SO Olsson, and P Brännström. Flanging and hemming of auto body panels using the electro magnetic forming technology. In *Proceedings of the 3rd International Conference on High Speed Forming - ICHSF*, pages 163–172. Citeseer, 2008.

[91] Gordon R. Johnson and William H. Cook. A constitutive model and data for metals subjected to large strains, high strain rates and high temperatures, 1983. ISSN 14710080.

References

[92] Gordon R Johnson and William H Cook. Fracture characteristics of three metals subjected to various strains, strain rates, temperatures and pressures. *Engineering fracture mechanics*, 21(1):31–48, 1985.

[93] K W Jung, Y Kawahito, and S Katayama. Laser direct joining of carbon fibre reinforced plastic to stainless steel. *Science and Technology of Welding and Joining*, 16(8):676–680, 2011.

[94] M Kajihara. Analysis of kinetics of reactive diffusion in a hypothetical binary system. *Acta materialia*, 52(5):1193–1200, 2004.

[95] Angshuman Kapil and Abhay Sharma. Magnetic pulse welding: an efficient and environmentally friendly multi-material joining technique. *Journal of Cleaner Production*, 100: 35–58, 2015.

[96] S Katayama and Y Kawahito. Laser direct joining of metal and plastic. *Scripta materialia*, 2008.

[97] Marian K. Kazimierczuk. *High-Frequency Magnetic Components*. John Wiley & Sons, second ed. edition, 2013. ISBN 1118717732.

[98] E Keller and F Smith. Joining plastics 2006 (2006). 10:1–10.

[99] G Kelly. Quasi-static strength and fatigue life of hybrid (bonded/bolted) composite single-lap joints. *Composite structures*, 2006.

[100] Gordon Kelly. Load transfer in hybrid (bonded/bolted) composite single-lap joints. *Composite structures*, 69(1):35–43, 2005.

[101] C. KHALIL, G. RACINEUX, and AMOSSE Y. Procédé d'assemblage de 2 ou plusieurs pièces de matériaux, 2017.

[102] Hak Sung Kim, Sang Wook Park, et al. Smart cure cycle with cooling and reheating for co-cure bonded steel/carbon epoxy composite hybrid structures for reducing thermal residual stress. *Composites Part A: Applied Science and Manufacturing*, 37(10):1708–1721, 2006.

[103] Hyun Surk Kim, Su Jeong Lee, et al. Development of a strength model for the cocured stepped lap joints under tensile loading. *Composite Structures*, 32(1-4):593–600, 1995.

[104] K Kimapong and T Watanabe. Friction stir welding of aluminum alloy to steel. *Welding journal*, 83(10):277, 2004.

[105] Kittipong Kimapong and Takehiko Watanabe. Lap joint of a5083 aluminum alloy and ss400 steel by friction stir welding. *Materials transactions*, 46(4):835–841, 2005.

[106] N Kleinknecht and SA Halvorsen. High frequency magnetohydrodynamic calculations in comsol multiphysics. *comsol.asia*.

[107] HE. Knoepfel. *Magnetic Fields, A Comprehensive Theoretical Treatise for Practical Use*. John Wiley & Sons, 2000.

[108] Anna Kochan. Magnetic pulse welding shows potential for automotive applications. *Assembly Automation*, 20(2):129–132, 2000.

[109] Sachin D Kore, PN Vinod, Satendra Kumar, and MR Kulkarni. Study of wavy interface in electromagnetic welds. In *Key Engineering Materials*, volume 504, pages 729–734. Trans Tech Publ, 2012.

[110] SD Kore, PP Date, and SV Kulkarni. Effect of process parameters on electromagnetic impact welding of aluminum sheets. *International journal of impact engineering*, 2007.

[111] SD Kore, PP Date, and SV Kulkarni. Electromagnetic impact welding of aluminum to stainless steel sheets. *journal of materials processing technology*, 208(1-3):486–493, 2008.

[112] SD Kore, P Dhanesh, SV Kulkarni, et al. Numerical modeling of electromagnetic welding. *International Journal of Applied Electromagnetics and Mechanics*, 32(1):1–19, 2010.

[113] J.F. Kowalick and D.R. Hay. Proc. 3rd int. conf of the center for high energy rate forming. Denver Research Institute Denver, CO, 1971.

[114] Nilesh Kulkarni, Rajiv S Mishra, and Wei Yuan. *Friction stir welding of dissimilar alloys and materials*. Butterworth-Heinemann, 2015.

[115] S Kundu, D Roy, R Bhola, D Bhattacharjee, B Mishra, and S Chatterjee. Microstructure and tensile strength of friction stir welded joints between interstitial free steel and commercially pure aluminium. *Materials & Design*, 50:370–375, 2013.

[116] Shinichi Kuroda, Kazuyoshi Saida, and Kazutoshi Nishimoto. Microstructure and properties of directly bonded joint of a6061 aluminum alloy to sus316 stainless steel-study on diffusion bonding of aluminum alloy to stainless steel (report 1). *Quarterly Journal of The Japan Welding Society*, pages 17–3, 1999.

[117] Yoshihiro Kusuda. Honda develops robotized fsw technology to weld steel and aluminum and applied it to a mass-production vehicle. *Industrial Robot: An International Journal*, 40 (3):208–212, 2013.

[118] Jin-Hwe Kweon, Jae-Woo Jung, Tae-Hwan Kim, Jin-Ho Choi, and Dong-Hyun Kim. Failure of carbon composite-to-aluminum joints with combined mechanical fastening and adhesive bonding. *Composite structures*, 75(1-4):192–198, 2006.

[119] H Laukant, C Wallmann, M Müller, M Korte, B Stirn, H-G Haldenwanger, and U Glatzel. Fluxless laser beam joining of aluminium with zinc coated steel. *Science and Technology of welding and joining*, 10(2):219–226, 2005.

[120] Chan-Joo Lee, Jung-Min Lee, Ho-Yeon Ryu, Kyung-Hun Lee, Byung-Min Kim, and Dae-Cheol Ko. Design of hole-clinching process for joining of dissimilar materials–al6061-t4 alloy with dp780 steel, hot-pressed 22mnb5 steel, and carbon fiber reinforced plastic. *Journal of Materials Processing Technology*, 214(10):2169–2178, 2014.

[121] Kwang-Jin Lee, Shinji Kumai, Takashi Arai, and Tomokatsu Aizawa. Interfacial microstructure and strength of steel/aluminum alloy lap joint fabricated by magnetic pressure seam welding. *Materials Science and Engineering: A*, 471(1-2):95–101, 2007.

[122] Pierre L'Eplattenier, Grant Cook, Cleve Ashcraft, Mike Burger, Jose Imbert, and Michael Worswick. Introduction of an electromagnetism module in ls-dyna for coupled mechanical-thermal-electromagnetic simulations. *steel research international*, 80(5):351–358, 2009. ISSN 1869-344X.

[123] M Leroy and JY Renaud. Formage électrohydraulique. *Techniques de l'ingénieur. Génie mécanique*, 1980.

[124] Jingjing Li, Qian Yu, Zijiao Zhang, Wei Xu, and Xin Sun. Formation mechanism for the nanoscale amorphous interface in pulse-welded al/fe bimetallic systems. *Applied Physics Letters*, 108(20):201606, 2016.

[125] Yan Li, Hatsujiro Hashimoto, Eiichi Sukedai, Yimin Zhang, and Zenkui Zhang. Morphology and structure of various phases at the bonding interface of al/steel formed by explosive welding. *Microscopy*, 49(1):5–16, 2000.

[126] F.C. Liu, J. Liao, and K. Nakata. Joining of metal to plastic using friction lap welding. *Materials & Design (1980-2015)*, 54:236–244, 2014. ISSN 02613069. doi: 10.1016/j.matdes.2013.08.056.

[127] Xun Liu, Shuhuai Lan, and Jun Ni. Analysis of process parameters effects on friction stir welding of dissimilar aluminum alloy to advanced high strength steel. *Materials & Design*, 59:50–62, 2014.

[128] *LS-DYNA Theory Manual*. Livermore Software Technology Corporation, 7374 Las Positas Road, California 94551, 2015.

[129] *LS-DYNA Keyword User's Manual Volume III*. Livermore software technology corporation (LSTC), r9.0 edition, 2016.

[130] Dmitry Nikolaevich Lysenko, Valerian Vladimirovic Ermolaev, and Anatoly Alexeevich Dudin. Method of pressure welding, July 14 1970. US Patent 3,520,049.

[131] Arun Prasath Manogaran. *Développement du procédé de soudage par point par impulsion magnétique - assemblage hétérogène Al/Fe*. PhD thesis, Ecole Centrale de Nantes, Nantes, France, 2013.

[132] Arun Prasath Manogaran, Prabu Manoharan, Didier Priem, Surendar Marya, and Guillaume Racineux. Magnetic pulse spot welding of bimetals. *Journal of Materials Processing Technology*, 214(6):1236–1244, 2014. ISSN 09240136.

[133] AR Marder. The metallurgy of zinc-coated steel. *Progress in materials science*, 45(3): 191–271, 2000.

[134] R Gomez Martin. Electromagnetic field theory for physicists and engineers: Fundamentals and applications. *Grupo de Electromagnetismo de Granada*, 2006.

[135] M Marya, S Marya, and D Priem. On the characteristics of electromagnetic welds between aluminium and other metals and alloys. *Welding in the World*, 2005.

[136] Kunitaka Masaki, Yutaka S Sato, Masakatsu Maeda, and Hiroyuki Kokawa. Experimental simulation of recrystallized microstructure in friction stir welded al alloy using a plane-strain compression test. *Scripta Materialia*, 58(5):355–360, 2008.

[137] Alexandre Mathieu, Rajashekar Shabadi, Alexis Deschamps, Michel Suery, Simone Mattei, Dominique Grevey, and Eugen Cicala. Dissimilar material joining using laser (aluminum to steel using zinc-based filler wire). *Optics & Laser Technology*, 39(3):652–661, 2007.

[138] Roysuke Matsuzaki, Motoko Shibata, and Akira Todoroki. Evaluation of dimple treatment for gfrp/metal co-cured joint. In *Key Engineering Materials*, volume 326, pages 1729–1732. Trans Tech Publ, 2006.

[139] Ryosuke Matsuzaki, Motoko Shibata, and Akira Todoroki. Improving performance of gfrp/aluminum single lap joints using bolted/co-cured hybrid method. *Composites Part A: applied science and manufacturing*, 39(2):154–163, 2008.

[140] Piotr Matysik, Stanisław Jóźwiak, and Tomasz Czujko. Characterization of low-symmetry structures from phase equilibrium of fe-al system - microstructures and mechanical properties. *Materials*, 8(3):914–931, 2015.

[141] S H McKnight, M McBride, and J W Gillespie. Strength of aluminum and glass reinforced polypropylene sandwich single lap joints. In *PROCEEDINGS-AMERICAN SOCIETY FOR COMPOSITES*, page 419. TECHNOMIC PUBLISHING AG, 1993.

[142] Joseph D Melograna and Joachim L Grenestedt. Improving joints between composites and steel using perforations. *Composites Part A: Applied Science and Manufacturing*, 33(9): 1253–1261, 2002.

[143] Joseph D Melogranaa, Joachim L Grenestedt, and William J Maroun. Adhesive tongue-and-groove joints between thin carbon fiber laminates and steel. *Composites Part A: Applied Science and Manufacturing*, 34(2):119–124, 2003.

[144] MA Meyers. *Dynamic behavior of materials*. 1994.

References

[145] MA Meyers, LE Murr, and KP Staudhammer. Shock-wave and high-strain-rate phenomena in materials. 1992.

[146] Mare Meyers. *Shock waves and high-strain-rate phenomena in metals: concepts and applications*. Springer Science & Business Media, 2012.

[147] M Militzer, WP Sun, and JJ Jonas. Modelling the effect of deformation-induced vacancies on segregation and precipitation. *Acta metallurgica et materialia*, 42(1):133–141, 1994.

[148] MA Miller and EW Mason. Properties of arc-welded joints between aluminum and stainless steel. *Weld. J*, 35:323s–328s, 1956.

[149] RM Miranda, B Tomás, and TG Santos. Magnetic pulse welding on the cutting edge of industrial applications. *Soldagem & Inspeção*, 2014.

[150] RM Miranda, B Tomás, TG Santos, and N Fernandes. Magnetic pulse welding on the cutting edge of industrial applications. *Soldagem & Inspeção*, 19(1):69–81, 2014.

[151] RM Miranda, B Tomás, TG Santos, and N Fernandes. Magnetic pulse welding on the cutting edge of industrial applications. *Soldagem & Inspeção*, 19(1):69–81, 2014.

[152] K. Mori, N. Bay, L. Fratini, F. Micari, and A. E. Tekkaya. Joining by plastic deformation. *CIRP Annals - Manufacturing Technology*, 62(2):673–694, 2013.

[153] M Movahedi, AH Kokabi, SM Seyed Reihani, and H Najafi. Mechanical and microstructural characterization of al-5083/st-12 lap joints made by friction stir welding. *Procedia Engineering*, 10:3297–3303, 2011.

[154] Taichi Murakami, Kazuhiro Nakata, Hongjun Tong, and Masao Ushio. Dissimilar metal joining of aluminum to steel by mig arc brazing using flux cored wire. *ISIJ international*, 43(10):1596–1602, 2003.

[155] Ali Nassiri, Greg Chini, Anupam Vivek, Glenn Daehn, and Brad Kinsey. Arbitrary lagrangian–eulerian finite element simulation and experimental investigation of wavy interfacial morphology during high velocity impact welding. *Materials & Design*, 88:345–358, 2015.

[156] J. C. Nédélec. A new family of mixed finite elements in r3. *Numerische Mathematik*, 50(1): 57–81, Jan 1986. ISSN 0945-3245. doi: 10.1007/BF01389668.

[157] M Ney. Bases de l'électromagnétisme. *Techniques de l'ingénieur. Electronique*, 2004.

[158] University of Denver, editor. *Proceedings of the 4th. International Conference of the Center for High Energy Rate Forming*, Colorado, 1973.

[159] Hatsuhiko Oikawa, Tohru Saito, Takashi Yoshimura, Takao Nagase, and Tadao Kiriyama. Factors influencing spot-weldability of steel to aluminium with an intermediate layer of aluminium clad steel: Dissimilar metal joining of steel to aluminium with intermediate layer (report 2). 1996.

[160] I. Oliveira, P. Teixeira, and A. Reis. Magnetic pulse welding of dissimilar metals: influence of process parameters. In *6th International Conference on High Speed Forming*, 2014.

[161] Australasian Conference on Hydraulics, Fluid Mechanics, A. J. Sutherland, and David Lindley. *Fifth Australasian Conference on Hydraulics and Fluid Mechanics, University of Canterbury, Christchurch, New Zealand, 9-13 December, 1974 : conference proceedings / editors, D. Lindley, A. J. Sutherland*. University of Canterbury [Christchurch, 1974.

[162] HE Otto and R Wittman. Evaluating of nasa-langley research center explosion seam welding. 1977.

[163] Sang Wook Park, Hak Sung Kim, et al. Optimum design of the co-cured double lap joint composed of aluminum and carbon epoxy composite. *Composite structures*, 75(1-4):289–297, 2006.

[164] Robert O Parmley and Robert O Parmley. *Standard handbook of fastening and joining*. McGraw-Hill, 1989.

[165] Liu Peng, Li Yajiang, Wang Juan, and Guo Jishi. Vacuum brazing technology and microstructure near the interface of al/18-8 stainless steel. *Materials research bulletin*, 38 (9-10):1493–1499, 2003.

[166] Mallick P.K. *Materials, design and manufacturing for lightweight vehicles*. Woodhead Publishing Limited and CRC Press LLC, 2010.

[167] Alphonsus V Pocius. *Adhesion and adhesives technology: an introduction*. Carl Hanser Verlag GmbH Co KG, 2012.

[168] R Pretorius, TK Marais, and CC Theron. Thin film compound phase formation sequence: An effective heat of formation model. *Materials Science Reports*, 10(1-2):1–83, 1993.

[169] V Psyk, D Risch, and BL Kinsey. Electromagnetic forming - A review. *Journal of Materials . . .* , 2011.

[170] EM Purcell. *Electricity and magnetism*. Cambridge University Press, second ed. edition, 2013.

[171] Ranfeng Qiu, Chihiro Iwamoto, and Shinobu Satonaka. The influence of reaction layer on the strength of aluminum/steel joint welded by resistance spot welding. *Materials Characterization*, 60(2):156–159, 2009.

[172] Ranfeng Qiu, Chihiro Iwamoto, and Shinobu Satonaka. Interfacial microstructure and strength of steel/aluminum alloy joints welded by resistance spot welding with cover plate. *Journal of Materials Processing Technology*, 209(8):4186–4193, 2009.

[173] Ranfeng Qiu, Shinobu Satonaka, and Chihiro Iwamoto. Effect of interfacial reaction layer continuity on the tensile strength of resistance spot welded joints between aluminum alloy and steels. *Materials & Design*, 30(9):3686–3689, 2009.

References

[174] Ranfeng Qiu, Hongxin Shi, Keke Zhang, Yimin Tu, Chihiro Iwamoto, and Shinobu Satonaka. Interfacial characterization of joint between mild steel and aluminum alloy welded by resistance spot welding. *Materials Characterization*, 61(7):684–688, 2010.

[175] G. RACINEUX, D. PRIEM, J.M. LEBRUN, Y. Amosse, and C. KHALIL. Procédé pour l'assemblage entre une pièce en matériau métallique et une pièce en matériau composite a matrice organique; pièces en matériau composite a matrice organique et ensemble correspondants, June 2016. WO Pub. No. WO/2016/097656.

[176] G. Racineux, C. Khalil, and Y. Amosse. Assembly process of two or more pieces of different materials (metal or organic matrix composites) by deformation and electromagnetic pulse welding, February 2017.

[177] Guillaume Racineux, Didier Priem, Jean-michel Lebrun, Yannick Amosse, and Chady Khalil. Assembly method between a part made of metal material and a part made of organic matrix composite material; corresponding parts made of organic matrix composite material and assembly, February 22 2018. US Patent App. 15/537,556.

[178] KK Ramachandran, N Murugan, and S Shashi Kumar. Effect of tool axis offset and geometry of tool pin profile on the characteristics of friction stir welded dissimilar joints of aluminum alloy aa5052 and hsla steel. *Materials Science and Engineering: A*, 639:219–233, 2015.

[179] G Ramarathnam, T H North, M Libertucci, and R T Woodhams. Ultrasonic bonding of high strength polypropylene to aluminium, 1990.

[180] MJ Rathod and Mm Kutsuna. Joining of aluminum alloy 5052 and low-carbon steel by laser roll welding. *WELDING JOURNAL-NEW YORK-*, 83(1):16–S, 2004.

[181] SR Reid. A discussion of the mechanism of interface wave generation in explosive welding. *International Journal of Mechanical Sciences*, 16(6):399–413, 1974.

[182] SR Reid. Wake instability mechanism for wave formation in explosive welding. *International Journal of Mechanical Sciences*, 20(4):247–253, 1978.

[183] J.L. Robinson. In *Proceedings of the 5th International Conference of the Center for High Energy Rate Forming*, Colorado, 1975. University of Denver.

[184] JL Robinson. The mechanics of wave formation in impact welding. *Philosophical Magazine*, 31(3):587–597, 1975.

[185] E. Rodríguez-Vidal, J. Lambarri, C. Soriano, C. Sanz, and G. Verhaeghe. A Combined Experimental and Numerical Approach to the Laser Joining of Hybrid Polymer and Metal Parts. *Physics Procedia*, 56:835–844, 2014. ISSN 18753892.

[186] Jordan Rotheiser. *Joining of plastics*. Hanser, 1999.

[187] M Roulin, JW Luster, G Karadeniz, and A Mortensen. Strength and structure of furnace-brazed joints between aluminum and stainless steel. *WELDING JOURNAL-NEW YORK-*, 78:151–s, 1999.

[188] VI Ryabov, LB Pervukhin, GA Vol'ferts, and VV Tsitsilin. Effect of explosion welding conditions on the strength and ductility characteristics of steel-aluminium welded joints. *PATON WELDING JOURNAL C/C OF AVTOMATICHESKAIA SVARKA*, 7(12):690–693, 1995.

[189] T Sapanathan, RN Raoelison, E Padayodi, N Buiron, and M Rachik. Depiction of interfacial characteristic changes during impact welding using computational methods: Comparison between arbitrary lagrangian-eulerian and eulerian simulations. *Materials & Design*, 102: 303–312, 2016.

[190] J. Seidt, A. Gilat, J. Klein, and J. Leach. High strain rate, high temperature constitutive and failure models for eod impact scenarios. SEM Annual Conference & Exposition on Experimental and Applied Mechanics, SEM Annual Conference & Exposition on Experimental and Applied Mechanics, 2007.

[191] H SERIZAWA and I SHIBAHARA. Numerical study of joining process in magnetic pressure seam welding. *Transactions of . . .*, 2009.

[192] Rajashekhara Shabadi, Michel Suery, and Alexis Deschamps. Characterization of joints between aluminum and galvanized steel sheets. *Metallurgical and Materials Transactions A*, 44(6):2672–2682, 2013.

[193] LH Shah and M Ishak. Review of research progress on aluminum–steel dissimilar welding. *Materials and Manufacturing Processes*, 29(8):928–933, 2014.

[194] HR Shahverdi, MR Ghomashchi, S Shabestari, and J Hejazi. Microstructural analysis of interfacial reaction between molten aluminium and solid iron. *Journal of materials processing technology*, 124(3):345–352, 2002.

[195] Kum Cheol Shin and Jung Ju Lee. Effects of thermal residual stresses on failure of co-cured lap joints with steel and carbon fiber–epoxy composite adherends under static and fatigue tensile loads. *Composites Part A: Applied Science and Manufacturing*, 37(3):476–487, 2006.

[196] Kum Cheol Shin, Jeong Ok Lim, and Jung Ju Lee. The manufacturing process of co-cured single and double lap joints and evaluation of the load-bearing capacities of co-cured joints. *Journal of materials processing technology*, 138(1-3):89–96, 2003.

[197] V Shribman. Magnetic pulse welding of automotive hvac parts. *rapport technique, Pulsar Ltd*, 2007.

[198] V Shribman. Magnetic pulse welding for dissimilar and similar materials. *Proceedings 3rd International Conference on High Speed Forming*, pages 13–22, 2008.

References

[199] V Shribman and M Blakely. Benefits of the magnetic pulse process for welding dissimilar metals. *Welding journal*, 2008.

[200] Guillaume Sierra. *Étude métallurgique et mécanique de l'assemblage hétérogène acier/aluminium par les procédés laser et TIG*. PhD thesis, Montpellier 2, 2006.

[201] Aude Simar and Marie-Noëlle Avettand-Fènoël. State of the art about dissimilar metal friction stir welding. *Science and Technology of Welding and Joining*, 22(5):389–403, 2017.

[202] R. Smerd, S. Winkler, C. Salisbury, M. Worswick, D. Lloyd, and M. Finn. High strain rate tensile testing of automotive aluminum alloy sheet. *International Journal of Impact Engineering*, 32(1):541 – 560, 2005. ISSN 0734-743X. doi: http://dx.doi.org/10.1016/j.ijimpeng.2005.04.013. Fifth International Symposium on Impact Engineering.

[203] JL Song, SB Lin, CL Yang, and CL Fan. Effects of si additions on intermetallic compound layer of aluminum–steel tig welding–brazing joint. *Journal of Alloys and Compounds*, 488 (1):217–222, 2009.

[204] H Springer, A Kostka, JF Dos Santos, and D Raabe. Influence of intermetallic phases and kirkendall-porosity on the mechanical properties of joints between steel and aluminium alloys. *Materials Science and Engineering: A*, 528(13-14):4630–4642, 2011.

[205] Vijay K Stokes. Joining methods for plastics and plastic composites: an overview. *Polymer Engineering & Science*, 29(19):1310–1324, 1989.

[206] Xin Sun, Elizabeth V Stephens, Mohammad A Khaleel, H Shao, and Menachem Kimchi. Resistance spot welding of aluminum alloy to steel with transition material-from process to performance-part i: experimental study. *WELDING JOURNAL-NEW YORK-*, 83:188–S, 2004.

[207] R Taillard, P Deshayes, C Perdrix, and E Amoris. Durcissement des aciers hsla par re-froidissement accéléré doux. *Revue de Métallurgie*, 91(9):1297–1297, 1994.

[208] Tsutomu Tanaka, Taiki Morishige, and Tomotake Hirata. Comprehensive analysis of joint strength for dissimilar friction stir welds of mild steel to aluminum alloys. *Scripta Materialia*, 61(7):756–759, 2009.

[209] CC Theron, OM Ndwandwe, JC Lombaard, and R Pretorius. First phase formation at interfaces: Comparison between walser-bené and effective heat of formation model. *Materials chemistry and physics*, 46(2-3):238–247, 1996.

[210] Bruno Manuel Coelho Tomás. *Magnetic pulse welding MPW*. PhD thesis, Ph. D. thesis, Department of Mechanical Engineering Universidade Nova de Lisboa, Portugal, 2010.

[211] S. Ucsnik, M. Scheerer, S. Zaremba, and D.H. Pahr. Experimental investigation of a novel hybrid metal and composite joining technology. *Composites Part A: Applied Science and Manufacturing*, 41(3):369–374, 2010.

[212] Camille van der Rest, Pascal J Jacques, and Aude Simar. On the joining of steel and aluminium by means of a new friction melt bonding process. *Scripta Materialia*, 77:25–28, 2014.

[213] P Verleysen, J Peirs, and J Degrieck. Experimental study of dynamic fracture in Ti-6Al-4V. In *4th International Conference on Impact Loading of Lightweight Structures (ICILLS 2014)*, pages 3–6. Cape Town, 2014.

[214] J Verstraete, W De Waele, and K Faes. Magnetic pulse welding: lessons to be learned from explosive welding. *Sustainable Construction and*, 2011.

[215] J Verstraete, W De Waele, and K Faes. Magnetic pulse welding : Lessons to be learned from explosive welding. *Sustainable Construction and Design*, pages 458–464, 2011.

[216] A Vivek, SR Hansen, BC Liu, and Glenn S Daehn. Vaporizing foil actuator: A tool for collision welding. *Journal of Materials Processing Technology*, 213(12):2304–2311, 2013.

[217] JM Walsh, RG Shreffler, and FJ Willig. Limiting conditions for jet formation in high velocity collisions. *Journal of Applied Physics*, 24(3):349–359, 1953.

[218] H Wang, D Liu, G Taber, JC Lippold, and GS Daehn. Laser impact welding-process introduction and key variables. *ICHSF2012*, 255, 2012.

[219] M Watanabe and S Kumai. Interfacial morphology of magnetic pulse welded aluminum/aluminum and copper/copper lap joints. *Materials transactions*, 2009.

[220] M Watanabe, S Kumai, K Okagawa, and T Aizawa. In-situ observation of magnetic pulse welding process for similar and dissimilar lap joints using a high-speed video camera. *Aluminium Alloys*, 2:1992–1997, 2008.

[221] Mitsuhiro Watanabe and Shinji Kumai. Interfacial morphology of magnetic pulse welded aluminum/aluminum and copper/copper lap joints. *Materials transactions*, 50(2):286–292, 2009.

[222] R J Wise and A D H Bates. Ultrasonic welding of pes to aluminium alloy. In *TECHNICAL PAPERS OF THE ANNUAL TECHNICAL CONFERENCE-SOCIETY OF PLASTICS ENGINEERS INCORPORATED*, pages 1203–1207. SOCIETY OF PLASTICS ENGINEERS INC, 1996.

[223] R J Wise and M N Watson. A new approach for joining plastics and composites to metals. In *ANTEC 92-Shaping the future*, pages 2113–2116. Technomic Publishing Co., 1992.

[224] HK Wylie, PEG Williams, and B Crossland. Proc. 3rd int. conf of the center for high energy rate forming. 1971.

[225] Shao Hua Xia, Jia Wang, Jing Tao Wang, and Jin Qiang Liu. Improvement of room-temperature superplasticity in zn–22 wt.% al alloy. *Materials Science and Engineering: A*, 493(1-2):111–115, 2008.

References

[226] M Yasuyama, K Ogawa, and T Taka. Spot welding of aluminium and steel sheet with an insert of aluminium clad steel sheet: dissimilar metal joining of aluminium and steel sheet (1st report). 1996.

[227] M Yılmaz, M Çöl, and M Acet. Interface properties of aluminum/steel friction-welded components. *Materials Characterization*, 49(5):421–429, 2002.

[228] Haiping Yu, Zhidan Xu, Zhisong Fan, Zhixue Zhao, and Chunfeng Li. Mechanical property and microstructure of aluminum alloy-steel tubes joint by magnetic pulse welding. *Materials Science and Engineering: A*, 561:259–265, 2013.

[229] Haiping Yu, Zhisong Fan, and Chunfeng Li. Magnetic pulse cladding of aluminum alloy on mild steel tube. *Journal of Materials Processing Technology*, 214(2):141–150, 2014.

[230] A Zangwill. *Modern electrodynamics*. Cambridge University Press, 2013.

[231] Bing-gang ZHANG, Guo-qing CHEN, Chun-guang ZHANG, and Jia-qiang NI. Structure and mechanical properties of aluminum alloy/ag interlayer/steel non-centered electron beam welded joints. *Transactions of Nonferrous Metals Society of China*, 21(12):2592–2596, 2011.

[232] Guifeng Zhang, Wei Su, Jianxun Zhang, and Zhongxin Wei. Friction stir brazing: a novel process for fabricating al/steel layered composite and for dissimilar joining of al to steel. *Metallurgical and materials transactions A*, 42(9):2850–2861, 2011.

[233] Hongtao Zhang and Jiakun Liu. Microstructure characteristics and mechanical property of aluminum alloy/stainless steel lap joints fabricated by mig welding–brazing process. *Materials Science and Engineering: A*, 528(19-20):6179–6185, 2011.

[234] HT Zhang, JC Feng, Peng He, and H Hackl. Interfacial microstructure and mechanical properties of aluminium–zinc-coated steel joints made by a modified metal inert gas welding–brazing process. *Materials Characterization*, 58(7):588–592, 2007.

[235] MJ Zhang, GY Chen, Y Zhang, and KR Wu. Research on microstructure and mechanical properties of laser keyhole welding–brazing of automotive galvanized steel to aluminum alloy. *Materials & Design*, 45:24–30, 2013.

[236] S Zhang and B Kinsey. Interfacial morphology prediction of impact welding by eulerian method. In *8th International Conference on High Speed Forming*, 2018.

[237] Weihua Zhang, Daqian Sun, Lijun Han, and Yongqiang Li. Optimised design of electrode morphology for novel dissimilar resistance spot welding of aluminium alloy and galvanised high strength steel. *Materials & Design*, 85:461–470, 2015.

[238] Y Zhang, SS Babu, and C Prothe. Application of high velocity impact welding at varied different length scales. *Journal of Materials . . .*, 2011.

[239] Y Zhang, SS Babu, C Prothe, and M Blakely. Application of high velocity impact welding at varied different length scales. *Journal of Materials*, 2011.

[240] Yuan Zhang, Sudarsanam Suresh Babu, Curtis Prothe, Michael Blakely, John Kwasegroch, Mike Laha, and Glenn S. Daehn. Application of high velocity impact welding at varied different length scales. *Journal of Materials Processing Technology*, 211(5):944–952, 2011. ISSN 09240136. doi: 10.1016/j.jmatprotec.2010.01.001.

[241] G Zittel. A historical review of high speed metal forming. *4th International Conference on High Speed*, 2010.

Appendix A

Figures for MPW and MPSW configurations analyses

A.1   MPW overlapping case

A.1.1   Thin sheet metal case ($e_f = 0.5$ mm)

The deformation profiles of thin aluminum 5754-H111 in the MPW overlapping case:
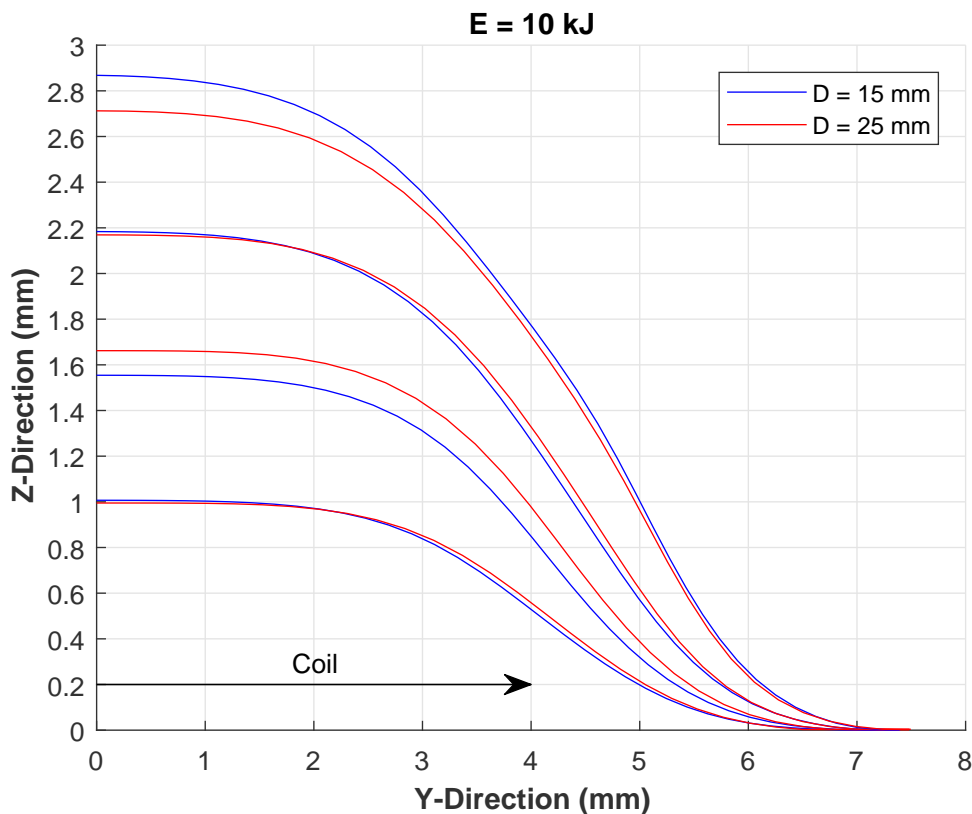
Figure A.1: deformation profile ($e_f = 0.5$ mm, $E = 10$ kJ)
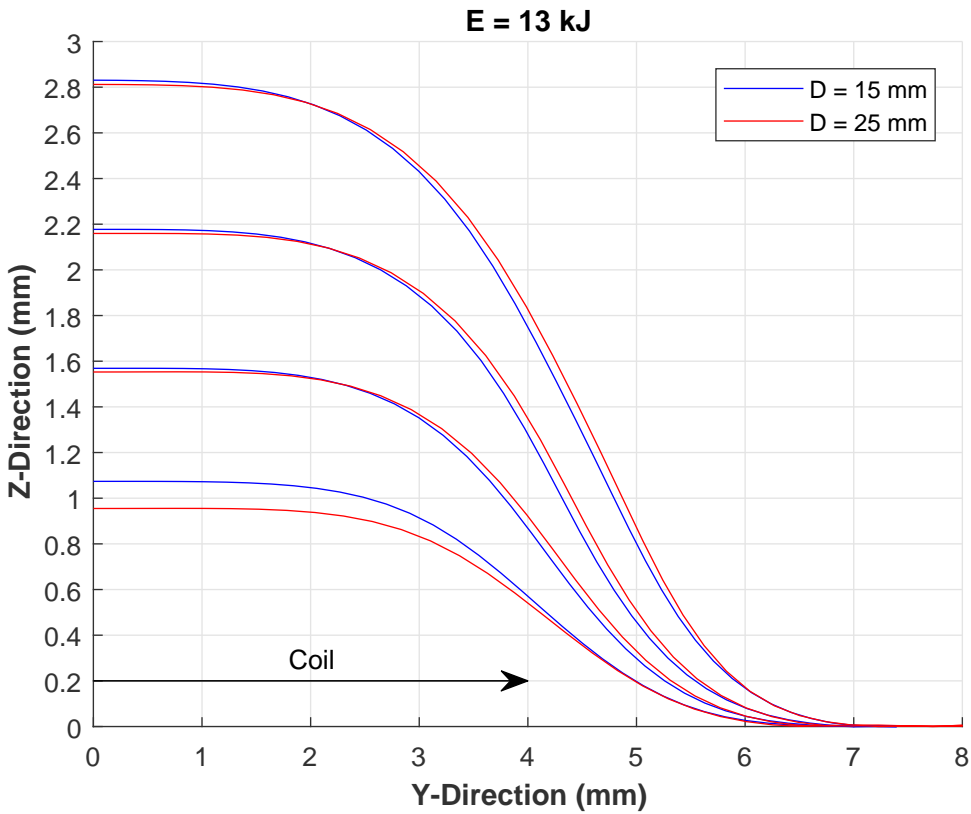
Figure A.2: deformation profile ($e_f = 0.5$ mm, $E = 13$ kJ)
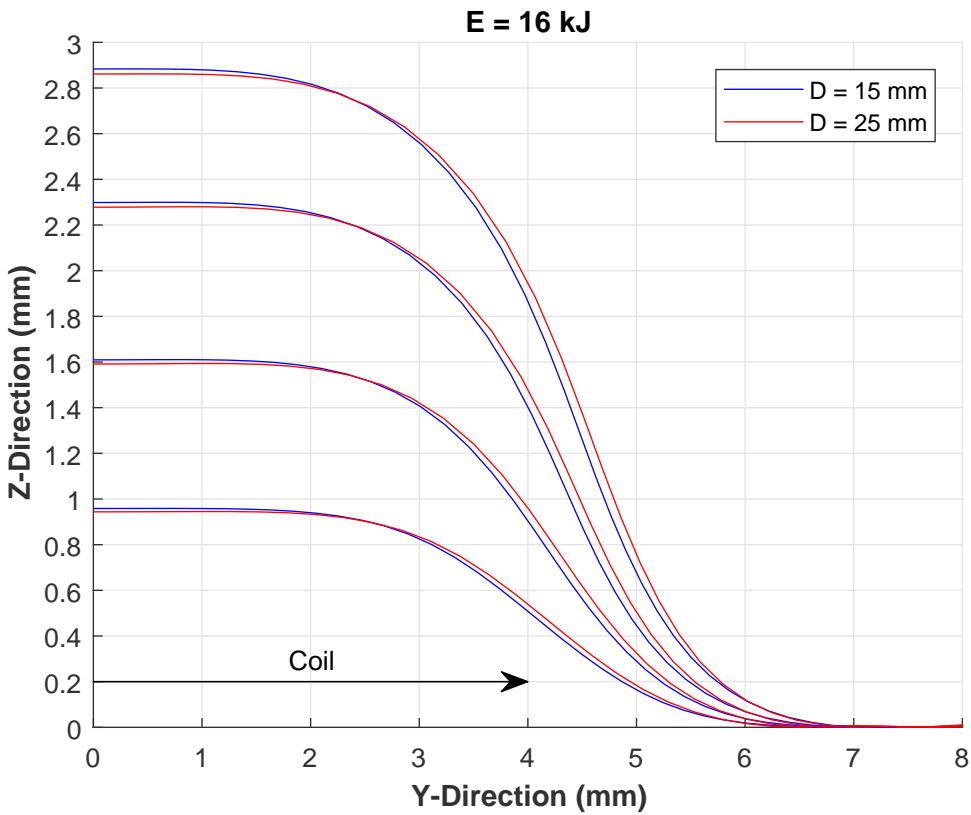
Figure A.3: deformation profile ($e_f = 0.5$ mm, $E = 16$ kJ)

Velocities at the impact moment for different standoff distances at various discharge energies:
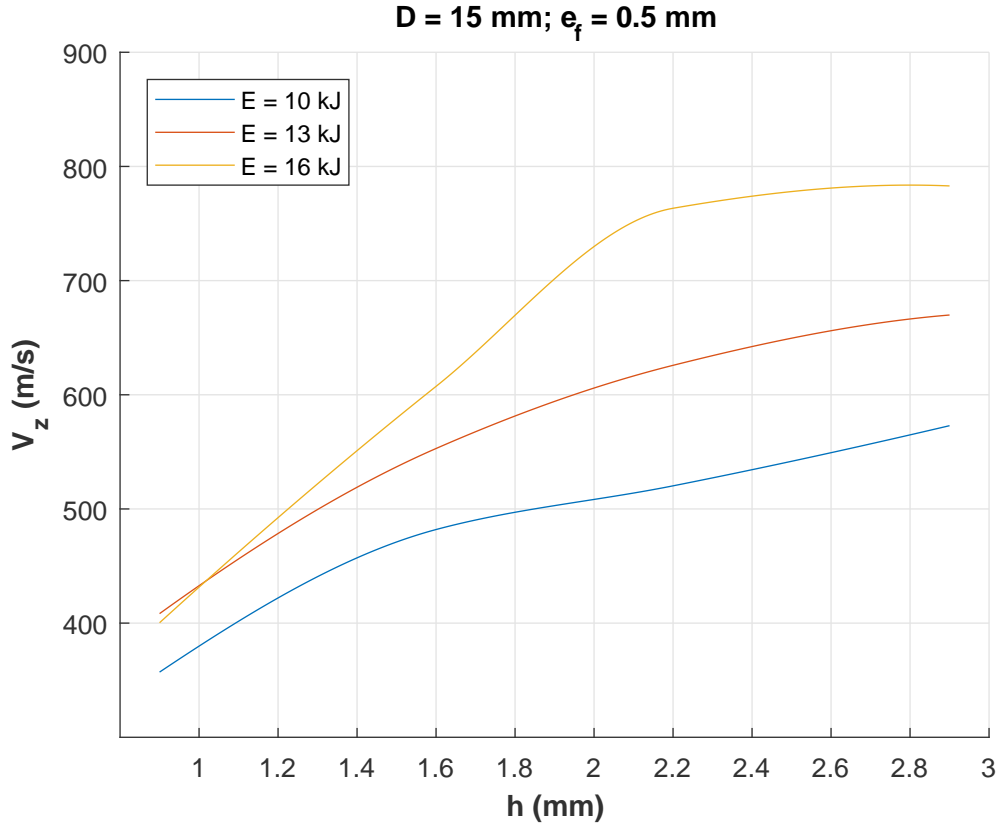
Figure A.4: impact velocities variation ($e_f = 0.5$ mm, $D = 15$ mm)
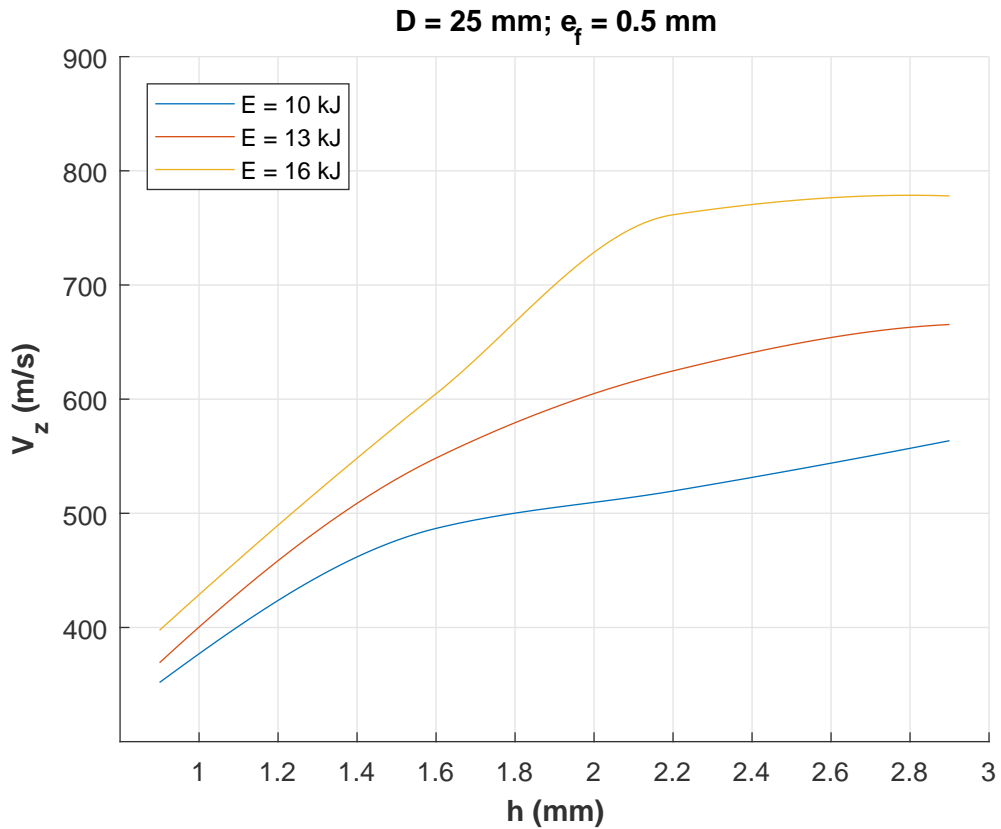
Figure A.5: impact velocities variation ($e_f = 0.5$ mm, $D = 25$ mm)

Figures for MPW and MPSW configurations analyses

The influence of the standoff distance on β_i at different energy levels:
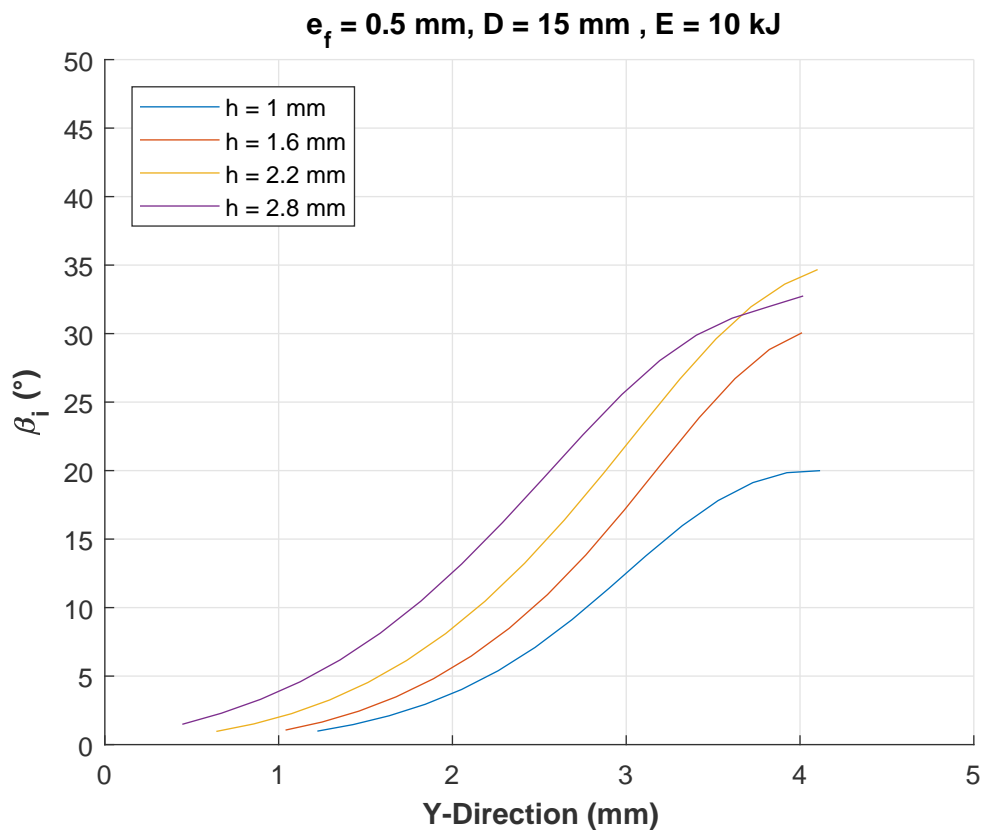
Figure A.6: β_i variation ($e_f = 0.5$ mm, $D = 15$ mm, $E = 10$ kJ)
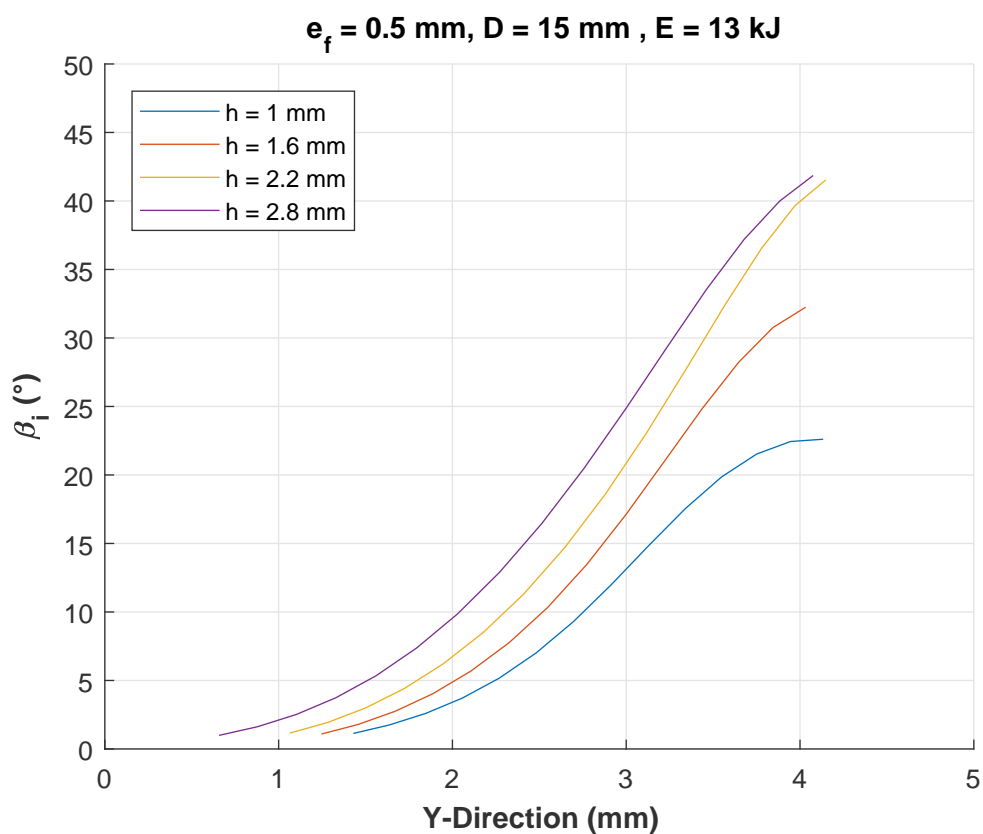
Figure A.7: β_i variation ($e_f = 0.5$ mm, $D = 15$ mm, $E = 13$ kJ)

e$_f$ = 0.5 mm, D = 15 mm , E = 16 kJ
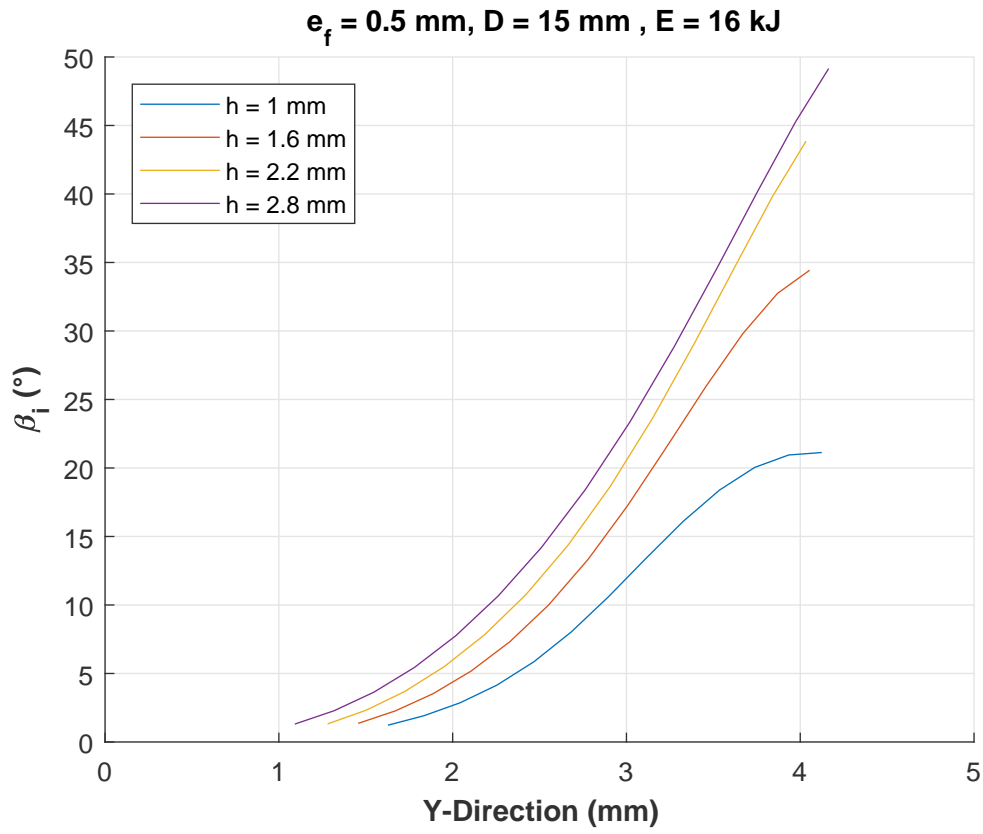
Figure A.8: β_i variation ($e_f = 0.5$ mm, $D = 15$ mm, $E = 16$ kJ)

e$_f$ = 0.5 mm, D = 25 mm , E = 10 kJ
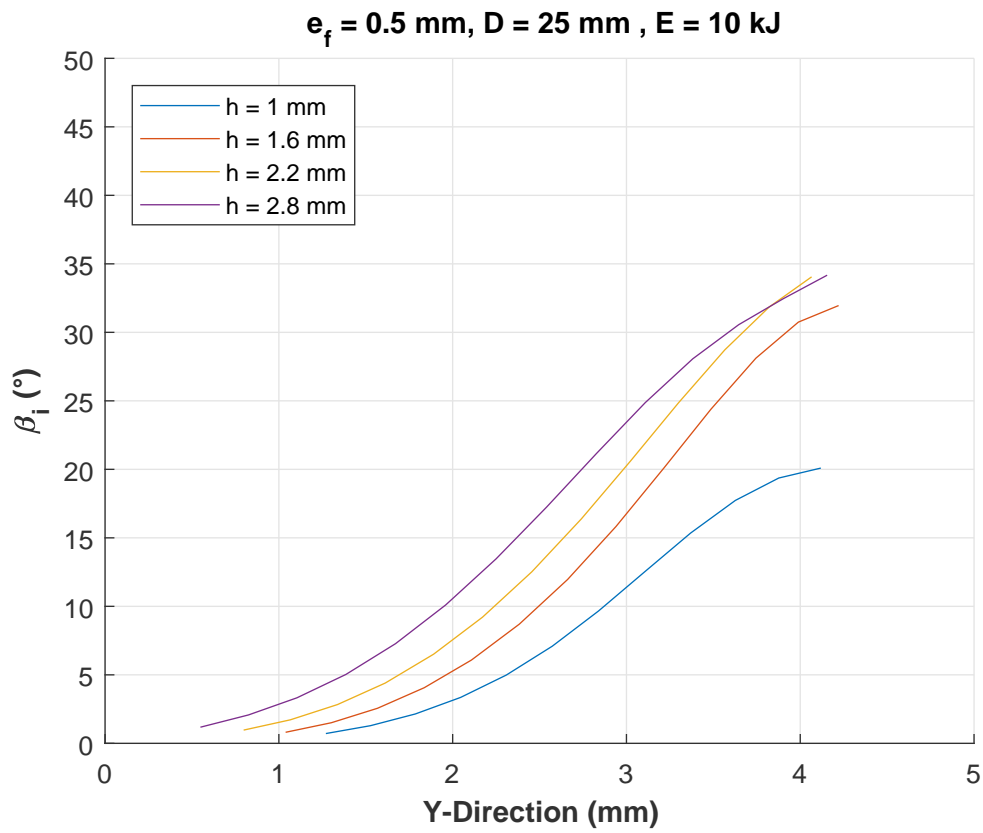
Figure A.9: β_i variation ($e_f = 0.5$ mm, $D = 25$ mm, $E = 10$ kJ)
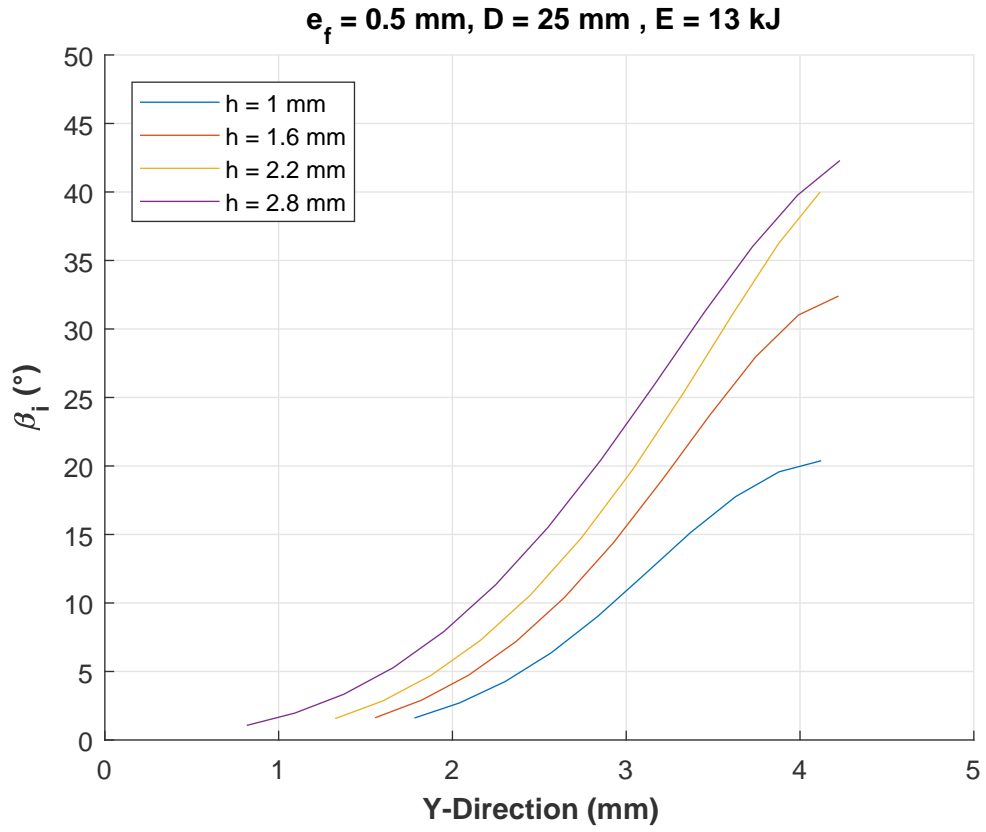
Figure A.10: β_i variation ($e_f = 0.5$ mm, $D = 25$ mm, $E = 13$ kJ)
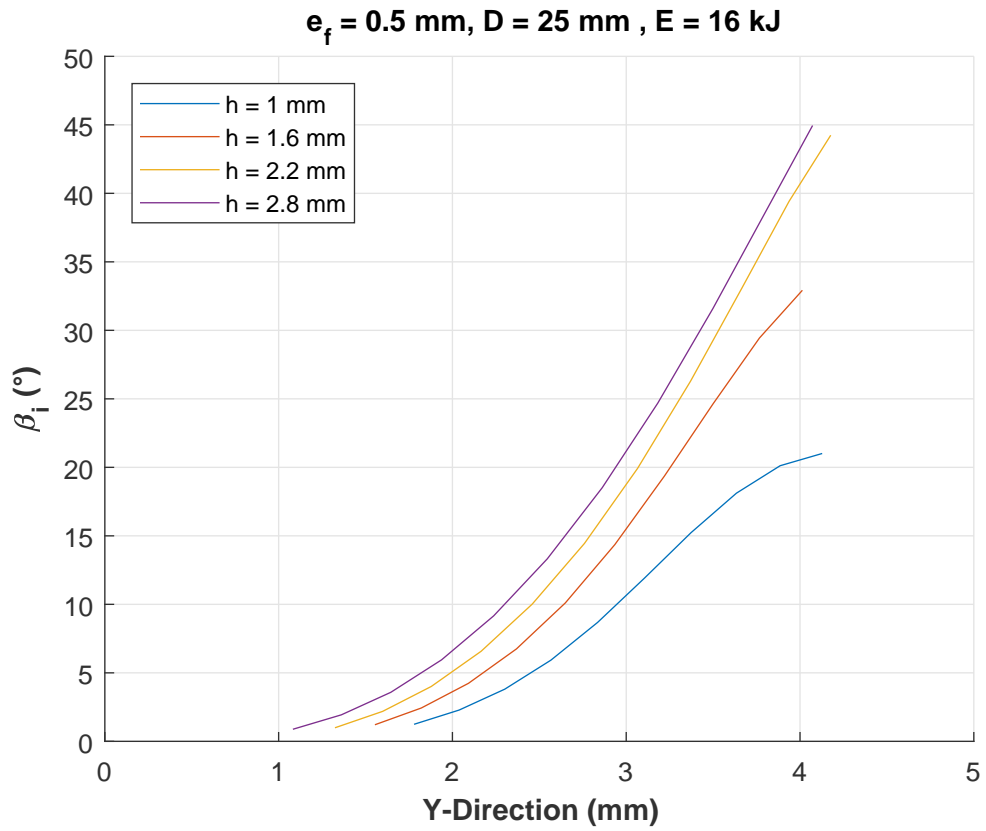
Figure A.11: β_i variation ($e_f = 0.5$ mm, $D = 25$ mm, $E = 16$ kJ)

The influence of the discharge energy on β_i at different standoff distance levels:
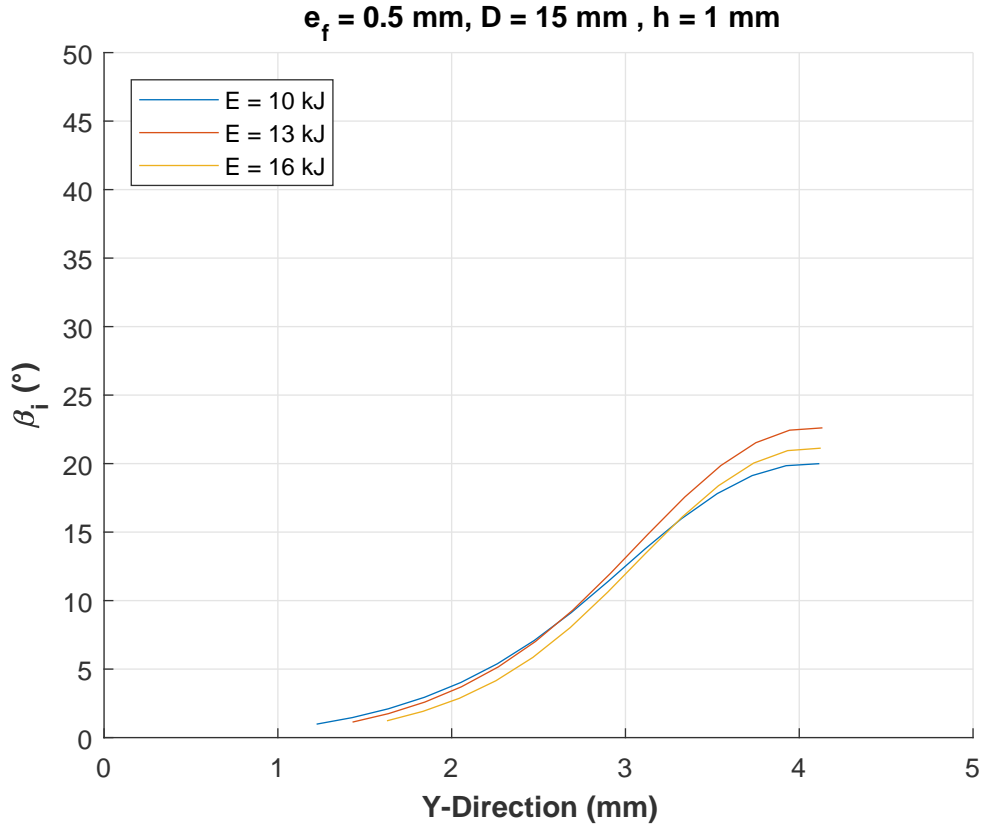
Figure A.12: β_i variation ($e_f = 0.5$ mm, $D = 15$ mm, $h = 1$ mm)
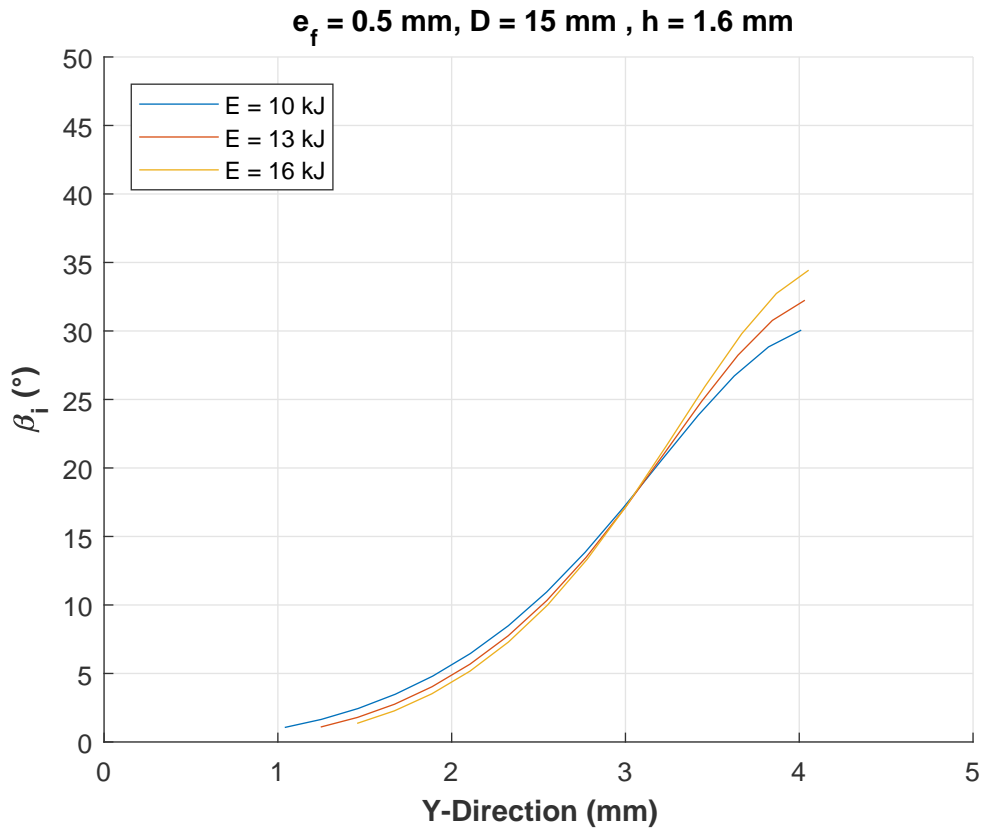
Figure A.13: β_i variation ($e_f = 0.5$ mm, $D = 15$ mm, $h = 1.6$ mm)
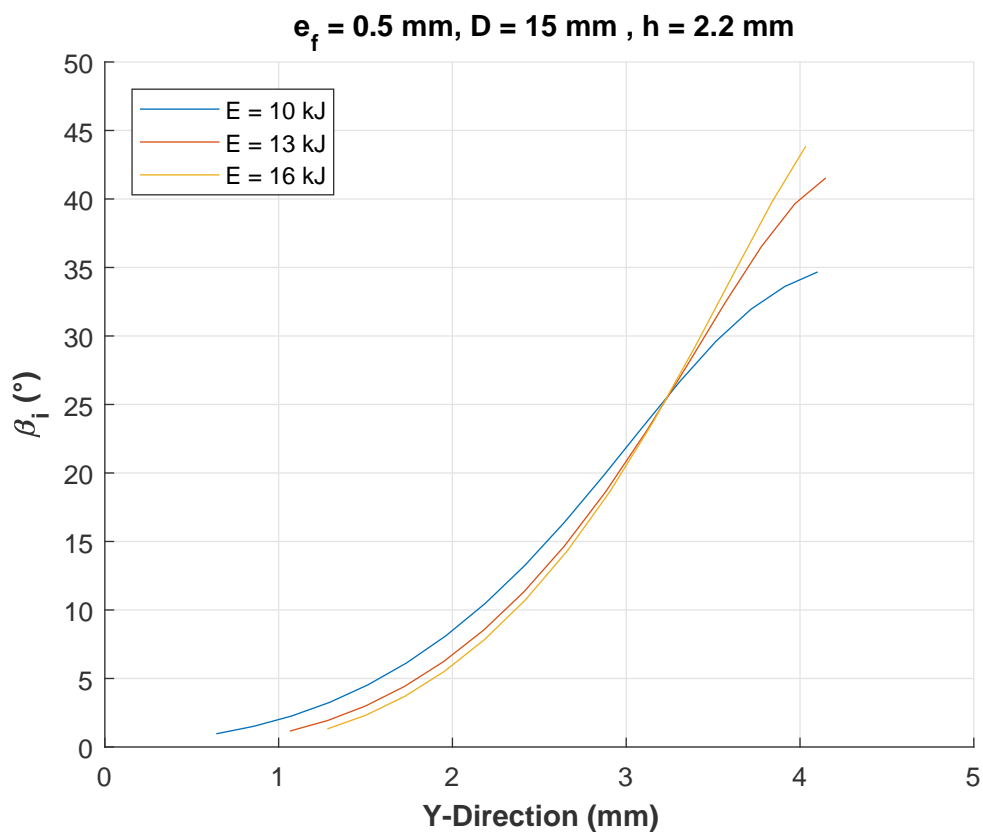
Figure A.14: β_i variation ($e_f = 0.5$ mm, $D = 15$ mm, $h = 2.2$ mm)
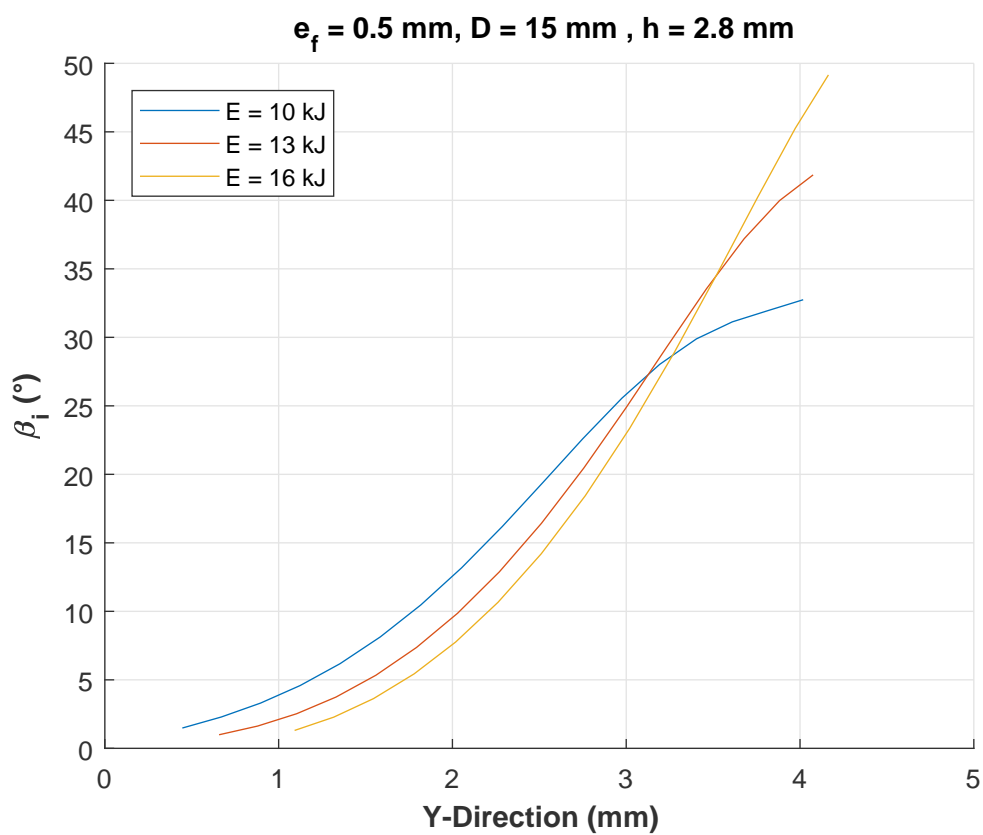
Figure A.15: β_i variation ($e_f = 0.5$ mm, $D = 15$ mm, $h = 2.8$ mm)
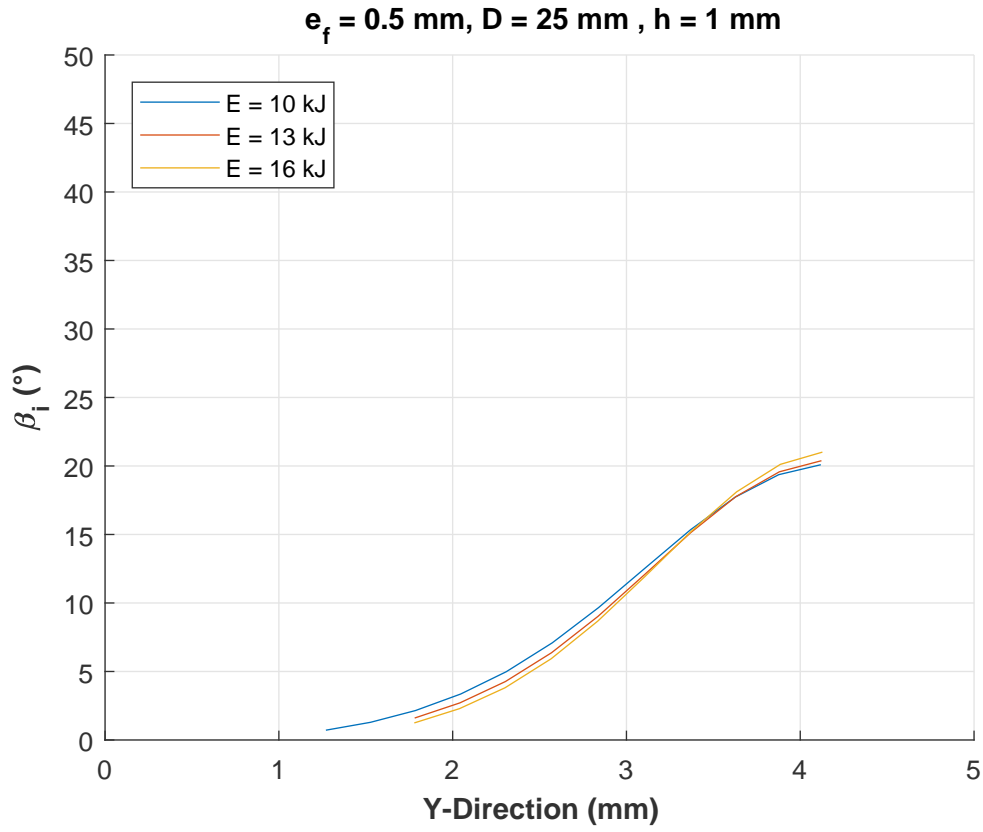
e_f = 0.5 mm, D = 25 mm , h = 1 mm

Figure A.16: β_i variation ($e_f = 0.5$ mm, $D = 25$ mm, $h = 1$ mm)

e_f = 0.5 mm, D = 25 mm , h = 1.6 mm
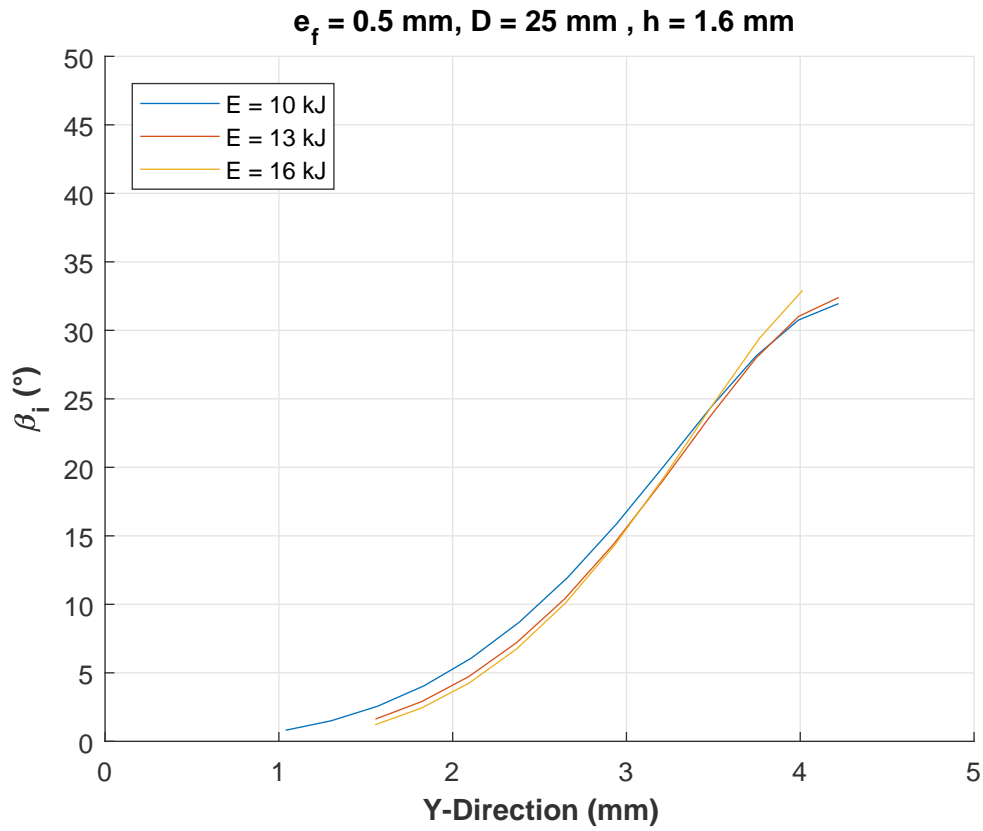
Figure A.17: β_i variation ($e_f = 0.5$ mm, $D = 25$ mm, $h = 1.6$ mm)
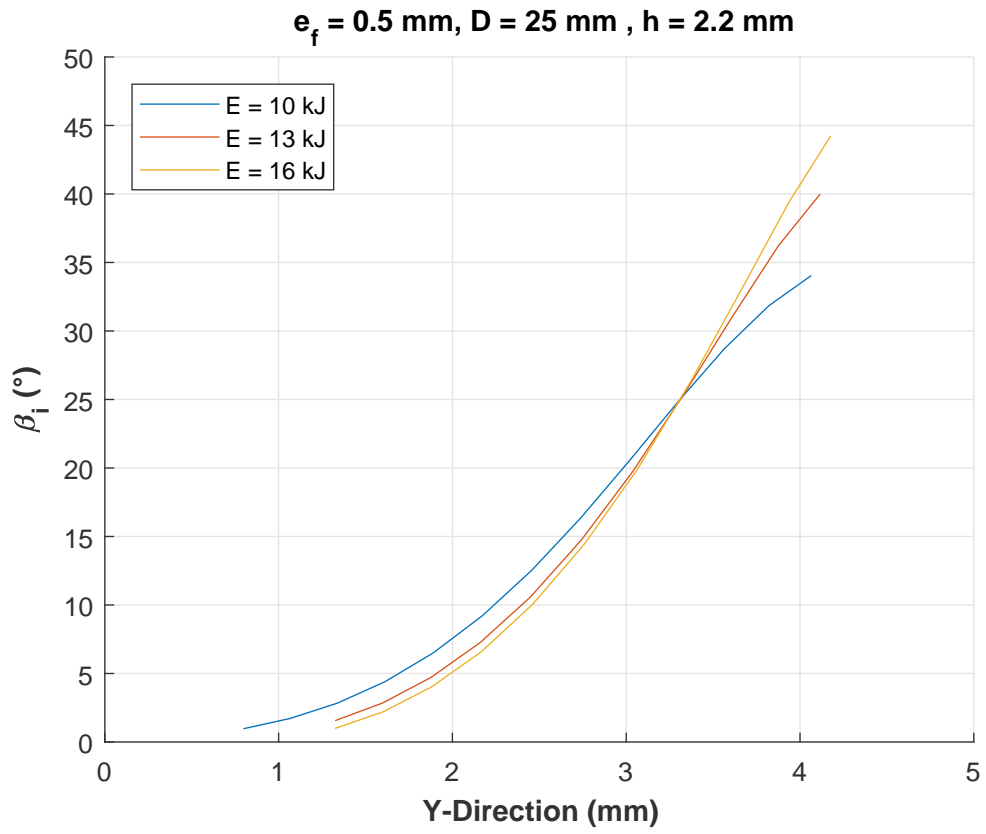
Figure A.18: β_i variation ($e_f = 0.5$ mm, $D = 25$ mm, $h = 2.2$ mm)
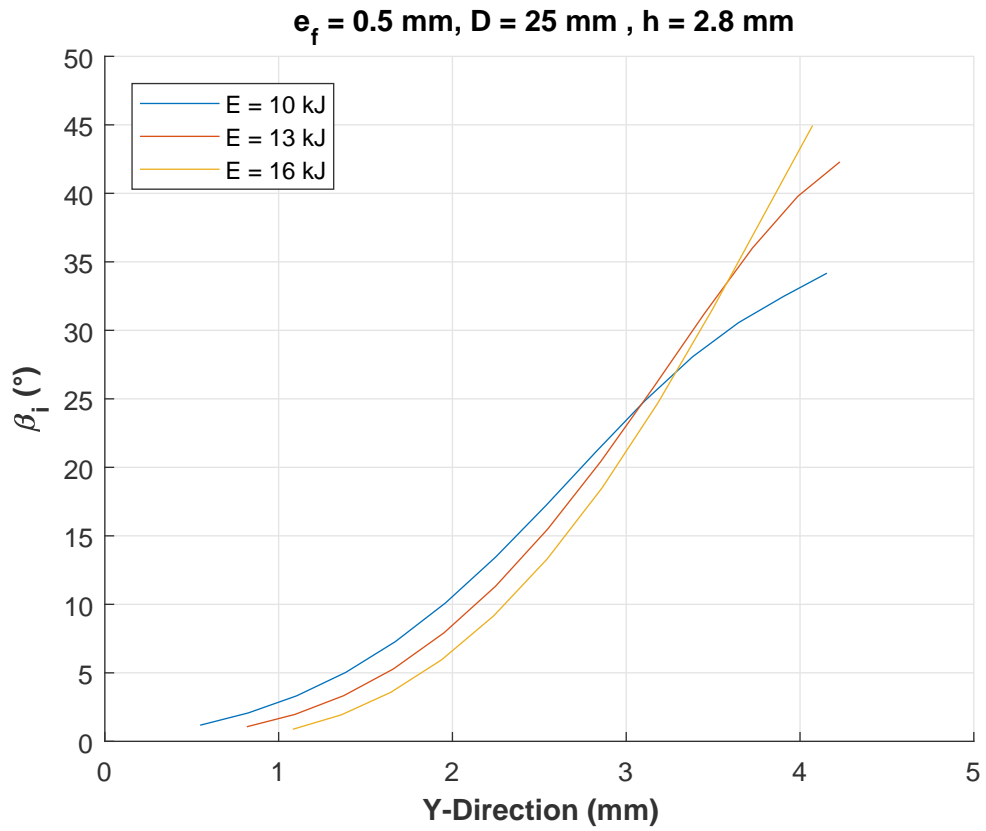
Figure A.19: β_i variation ($e_f = 0.5$ mm, $D = 25$ mm, $h = 2.8$ mm)

The influence of D on the values of β_i for E $= 10$ kJ at different standoff distances:
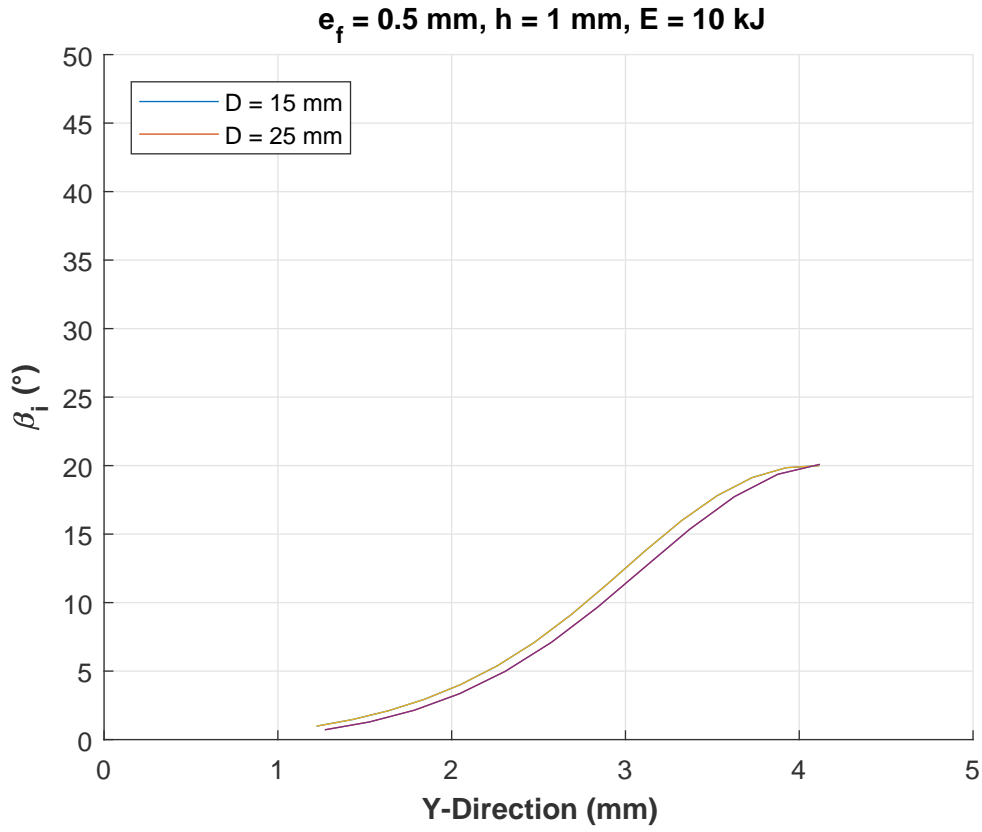
Figure A.20: $\beta_i$variation ($e_f = 0.5$ mm, $E = 10$ kJ, $h = 1$ mm)
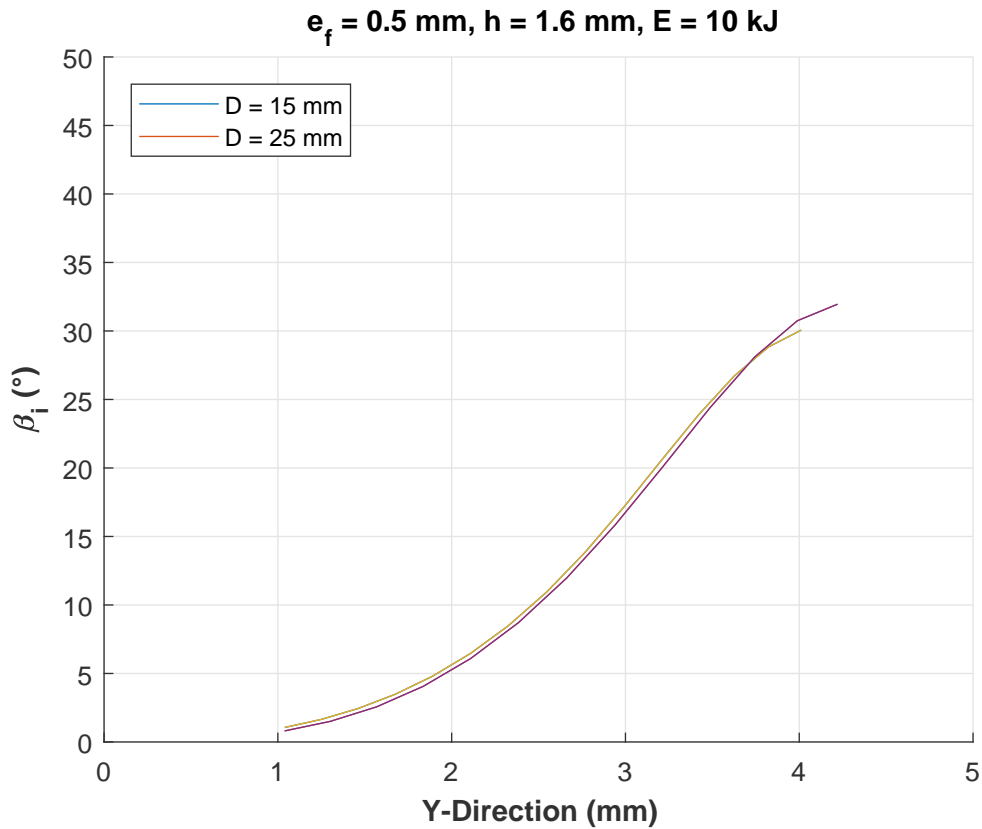
Figure A.21: $\beta_i$variation ($e_f = 0.5$ mm, $E = 10$ kJ, $h = 1.6$ mm)
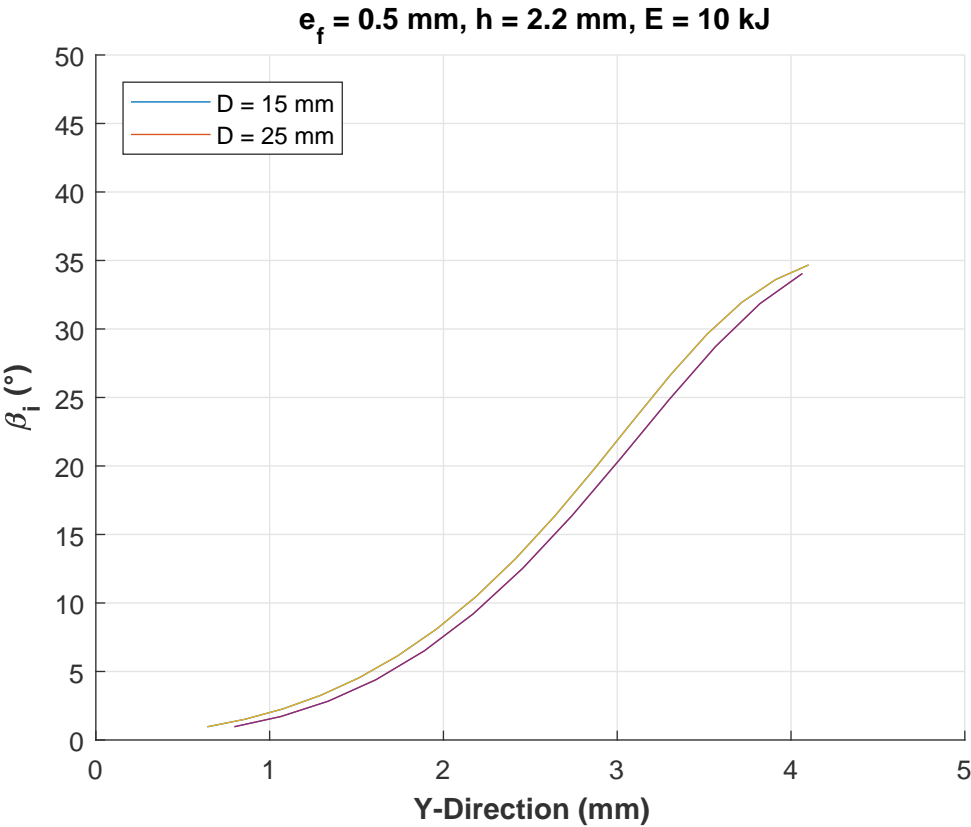
Figure A.22: β_i variation ($e_f = 0.5$ mm, $E = 10$ kJ, $h = 2.2$ mm)
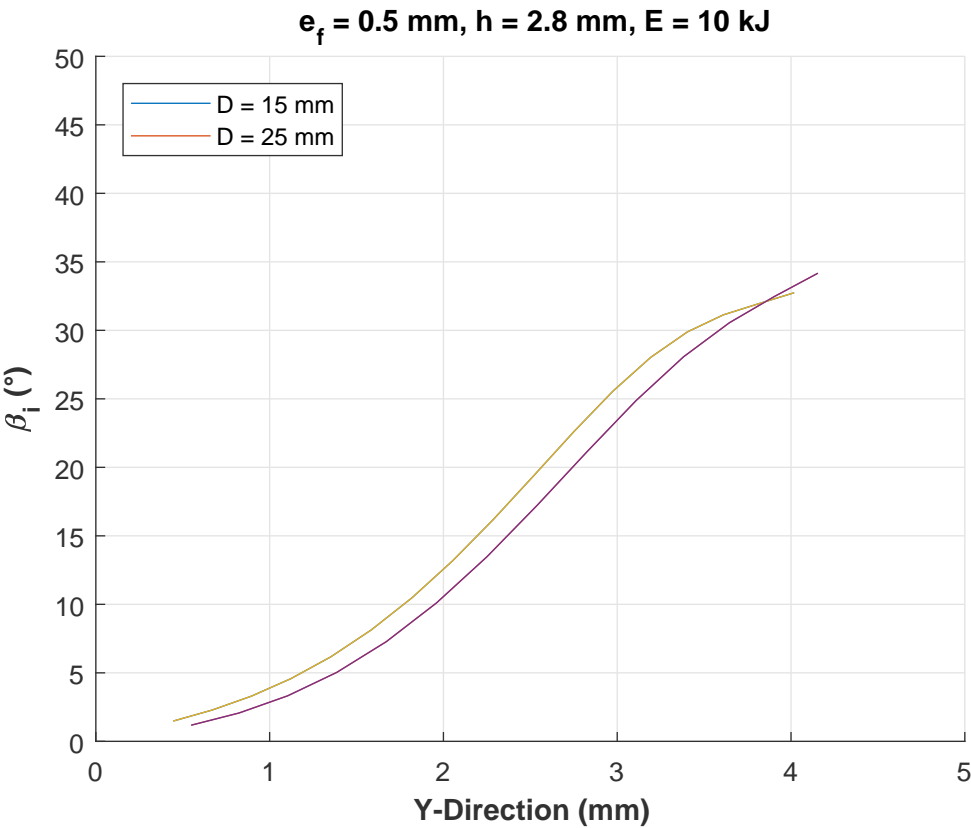
Figure A.23: β_i variation ($e_f = 0.5$ mm, $E = 10$ kJ, $h = 2.8$ mm)

The influence of D on the values of β_i for $E = 13$ kJ at different standoff distances:
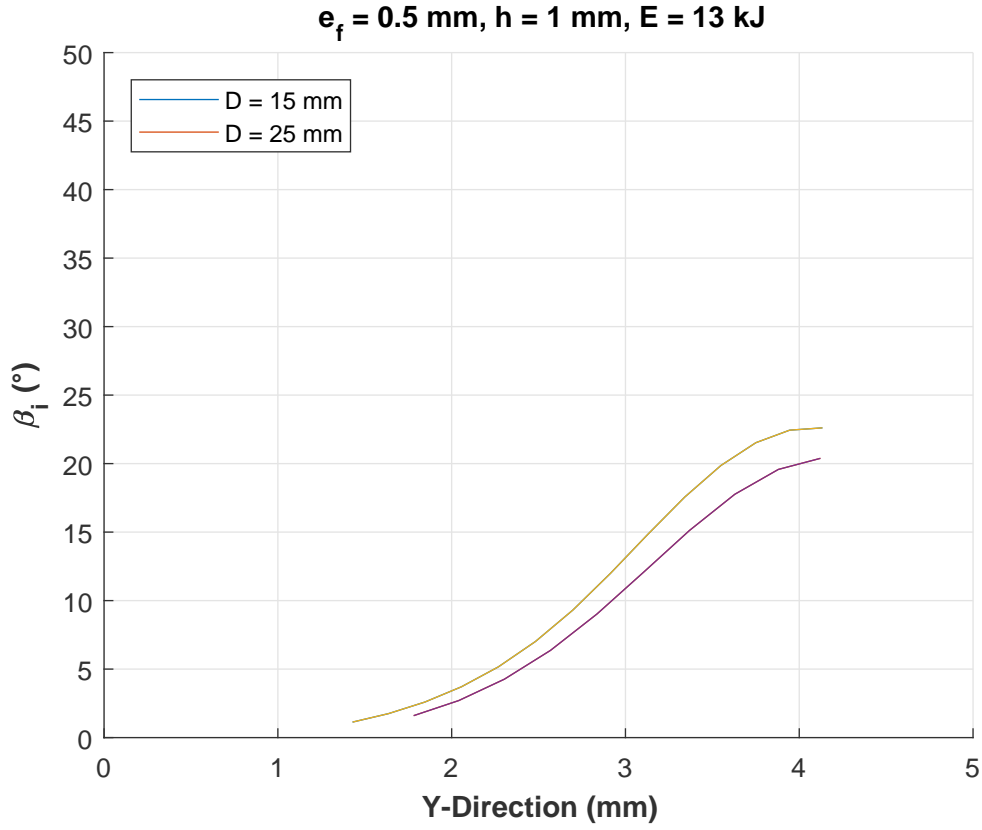

Figure A.24: β_i variation ($e_f = 0.5$ mm, $E = 13$ kJ, $h = 1$ mm
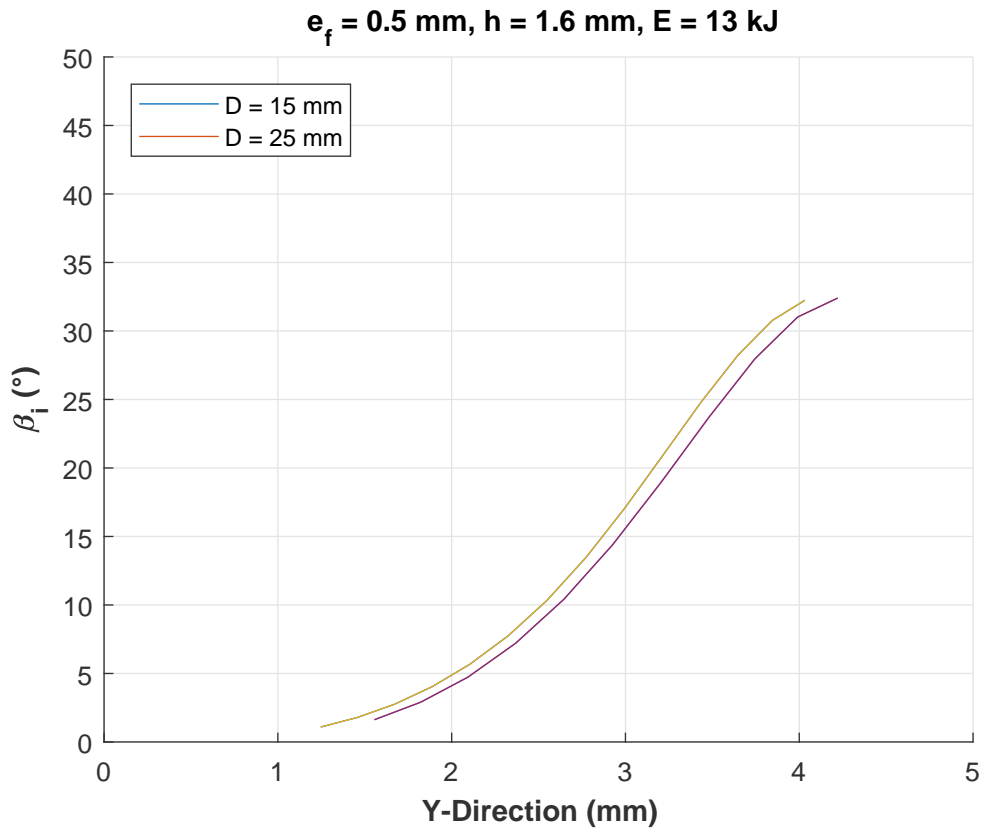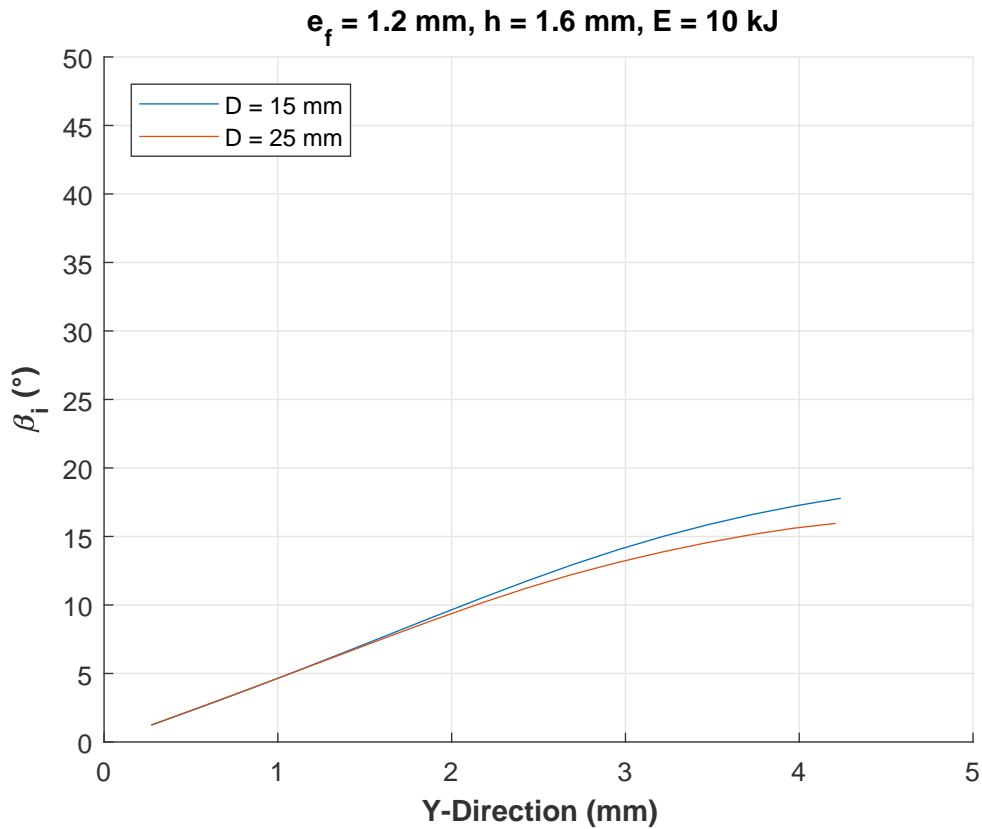

Figure A.25: β_i variation ($e_f = 0.5$ mm, $E = 13$ kJ, $h = 1.6$ mm)
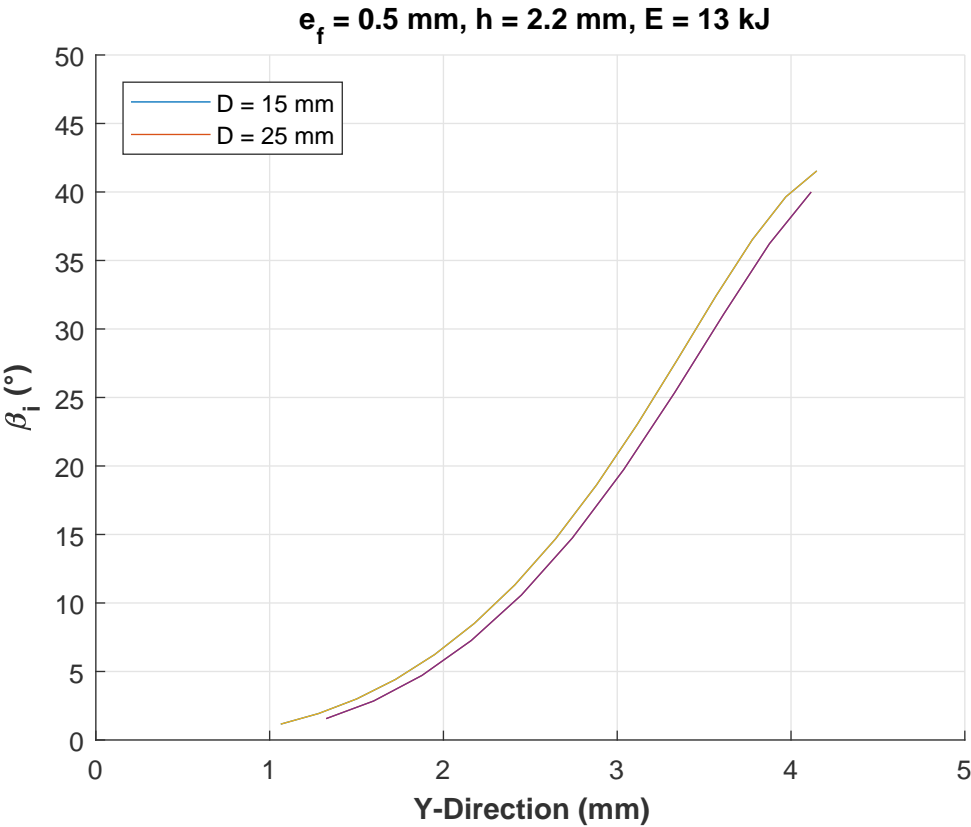
Figure A.26: β_i variation ($e_f = 0.5$ mm, $E = 13$ kJ, $h = 2.2$ mm)
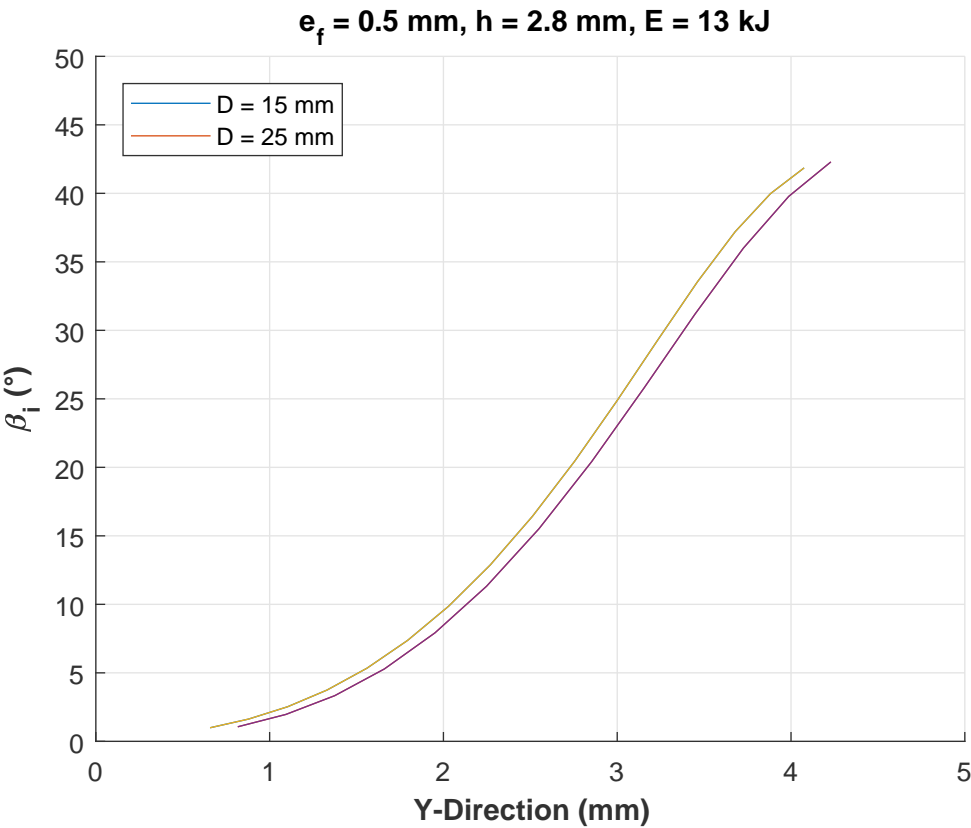
Figure A.27: β_i variation ($e_f = 0.5$ mm, $E = 13$ kJ, $h = 2.8$ mm)

The influence of D on the values of β_i for $E = 16$ kJ at different standoff distances:
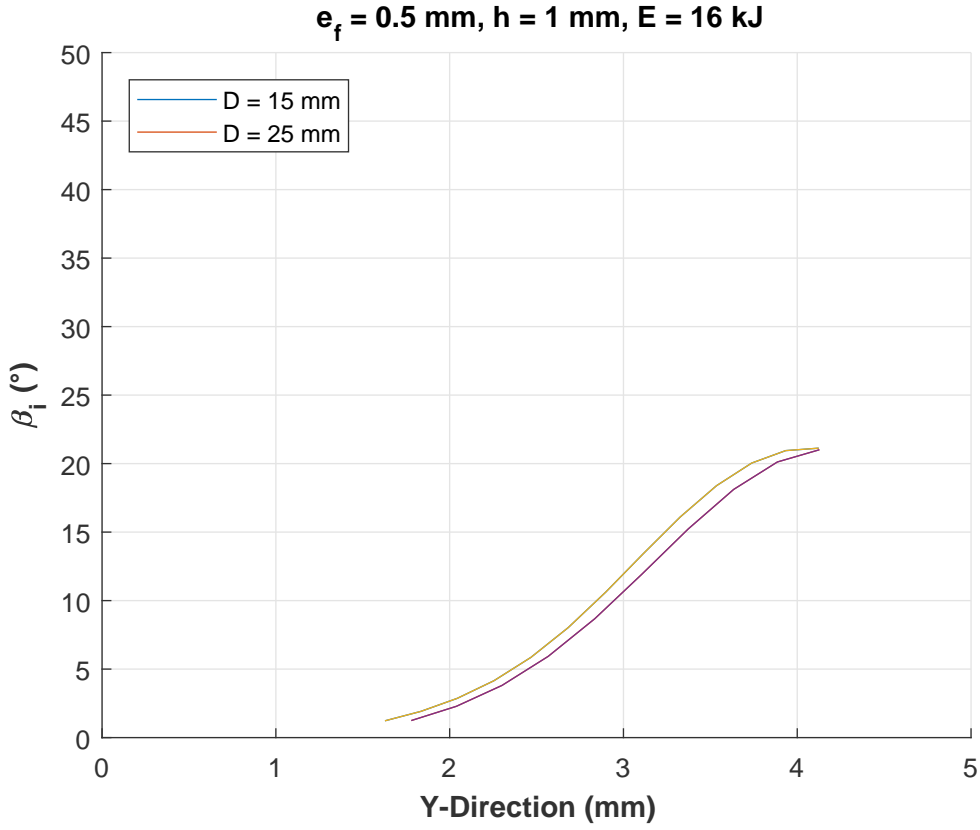
Figure A.28: β_i variation ($e_f = 0.5$ mm, $E = 16$ kJ, $h = 1$ mm)
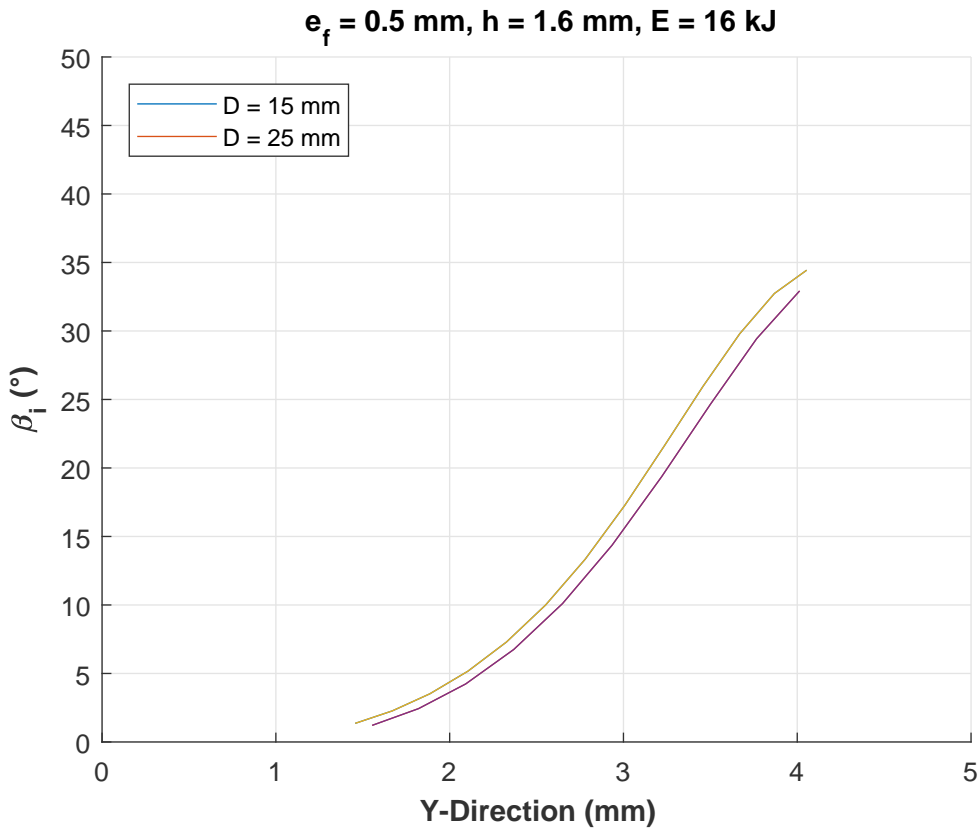
Figure A.29: β_i variation ($e_f = 0.5$ mm, $E = 16$ kJ, $h = 1.6$ mm)
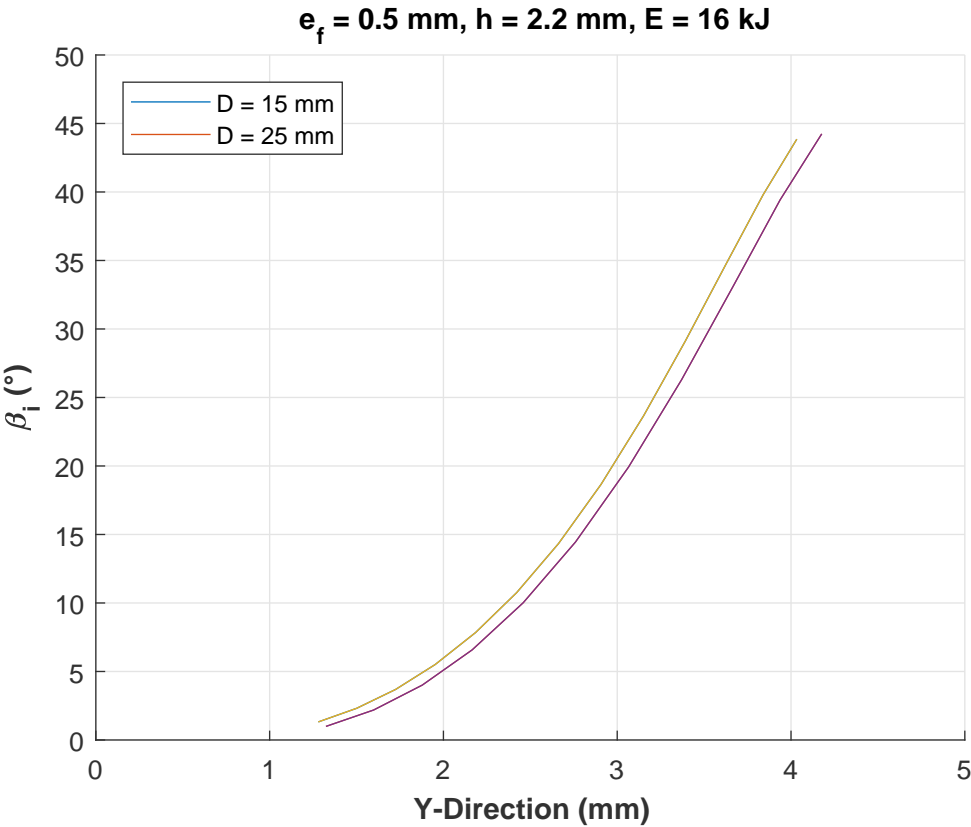
Figure A.30: β_i variation ($e_f = 0.5$ mm, $E = 16$ kJ, $h = 2.2$ mm)
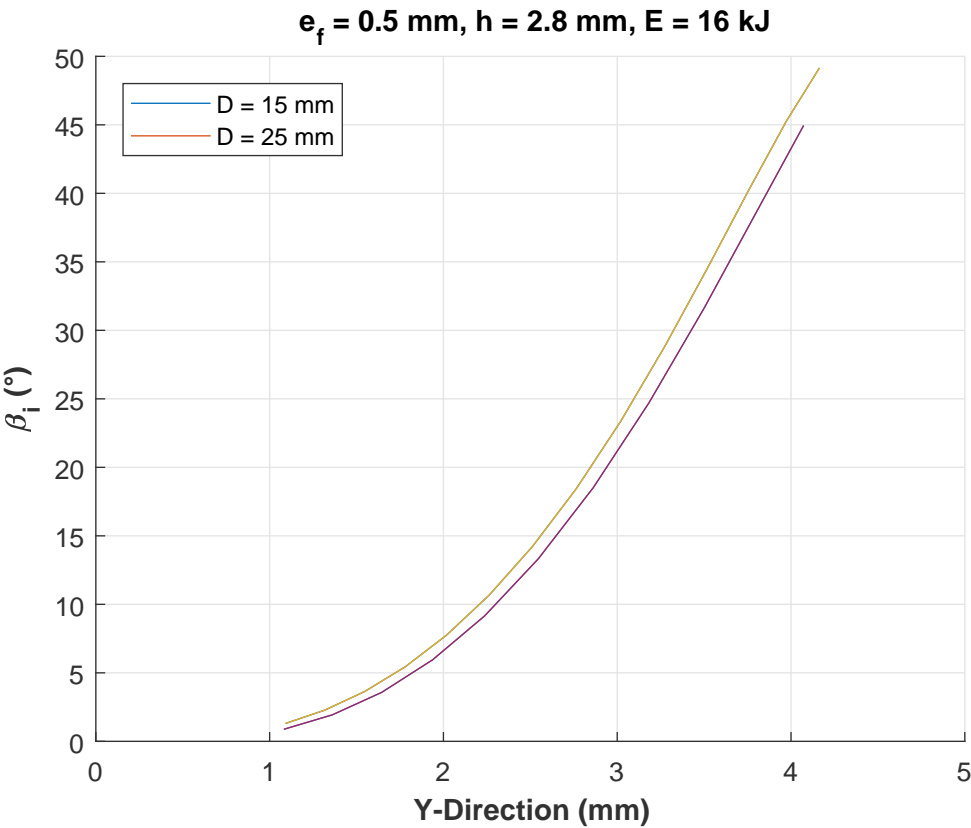
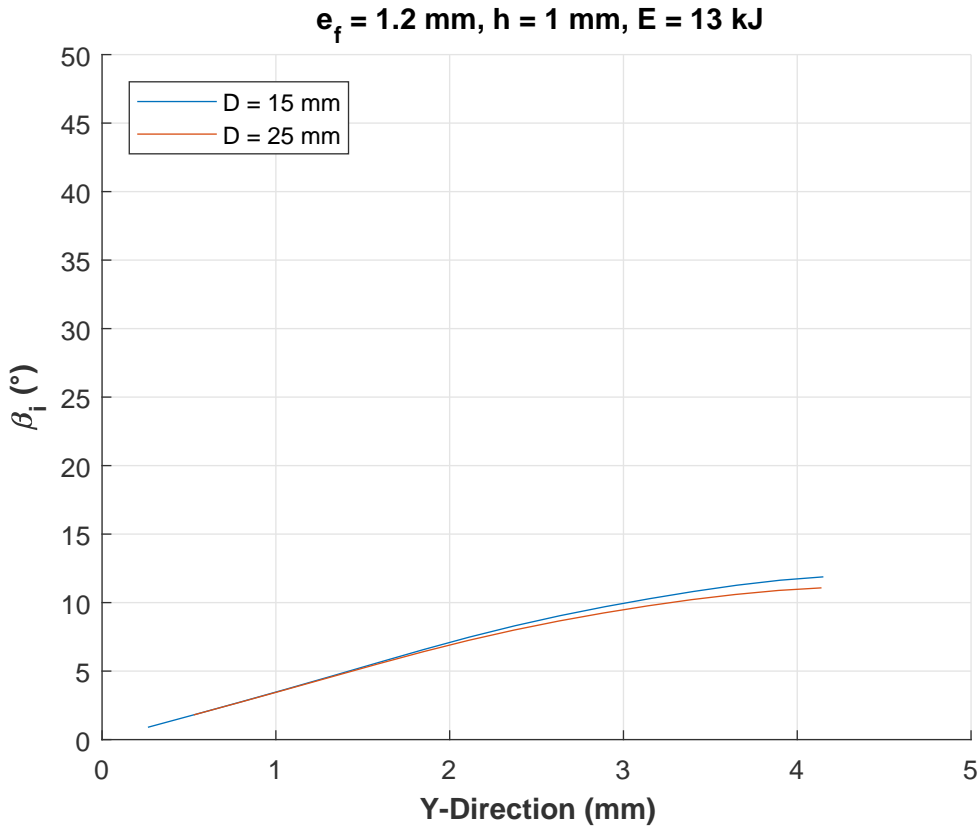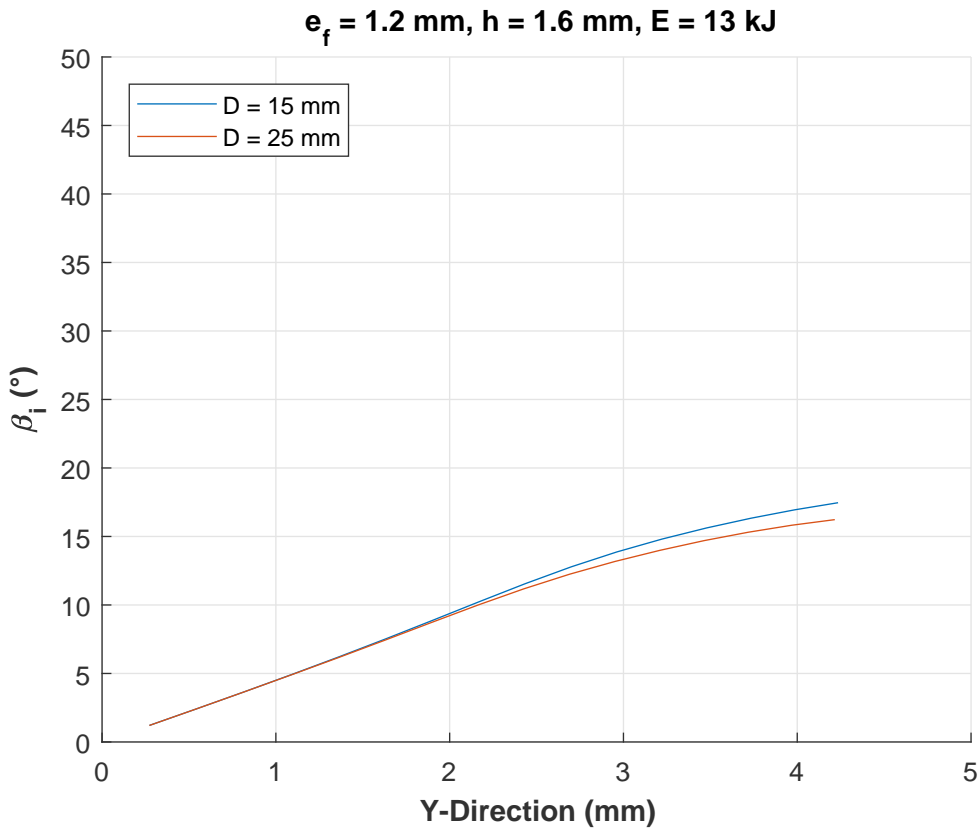Figure A.31: β_i variation ($e_f = 0.5$ mm, $E = 16$ kJ, $h = 2.8$ mm)

A.1.2   Thick sheet metal case ($e_f = 1.2$ mm)

The deformation profiles of the thick aluminum 5754-H111 in the MPW overlapping case:
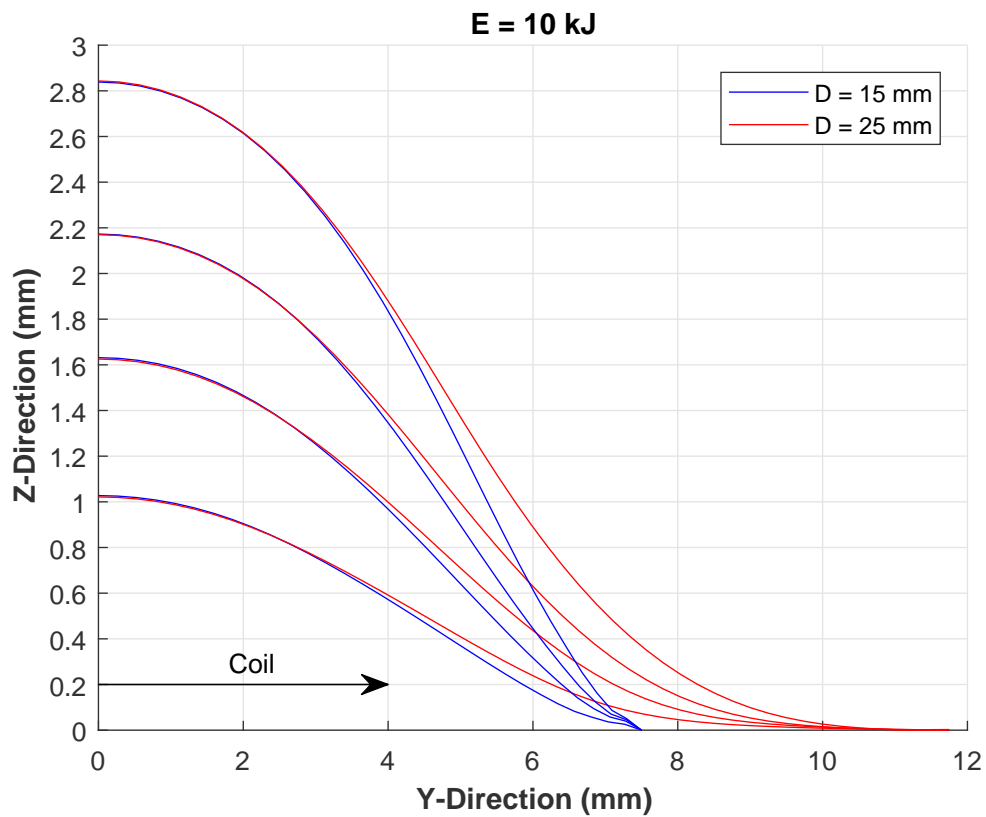
Figure A.32: deformation profile ($e_f = 1.2$ mm, $E = 10$ kJ)
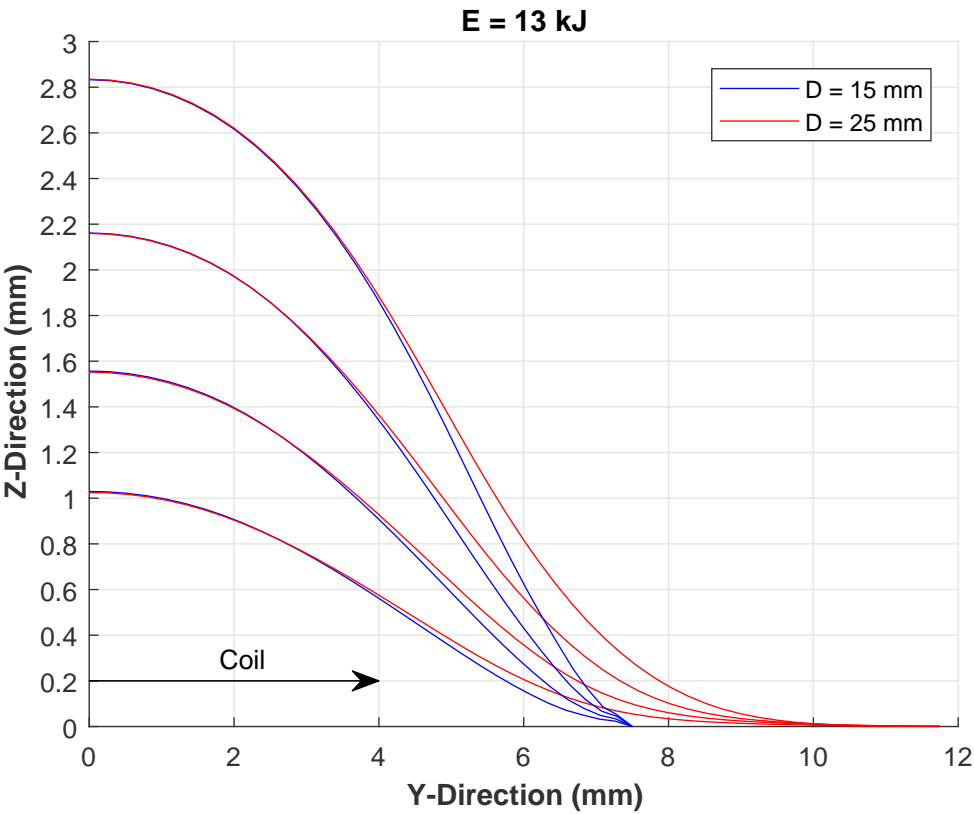
E = 13 kJ

Figure A.33: deformation profile ($e_f = 1.2$ mm, $E = 13$ kJ)
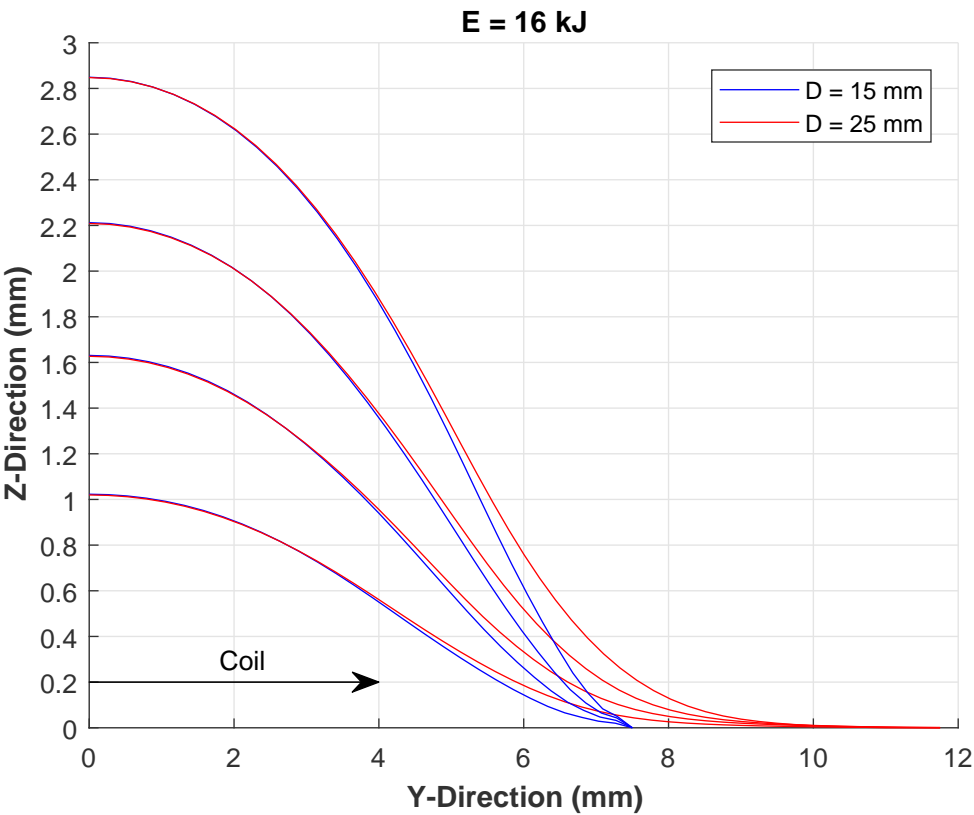
E = 16 kJ

Figure A.34: deformation profile ($e_f = 1.2$ mm, $E = 16$ kJ)

Velocities at the impact moment for different standoff distances at various discharge energies:
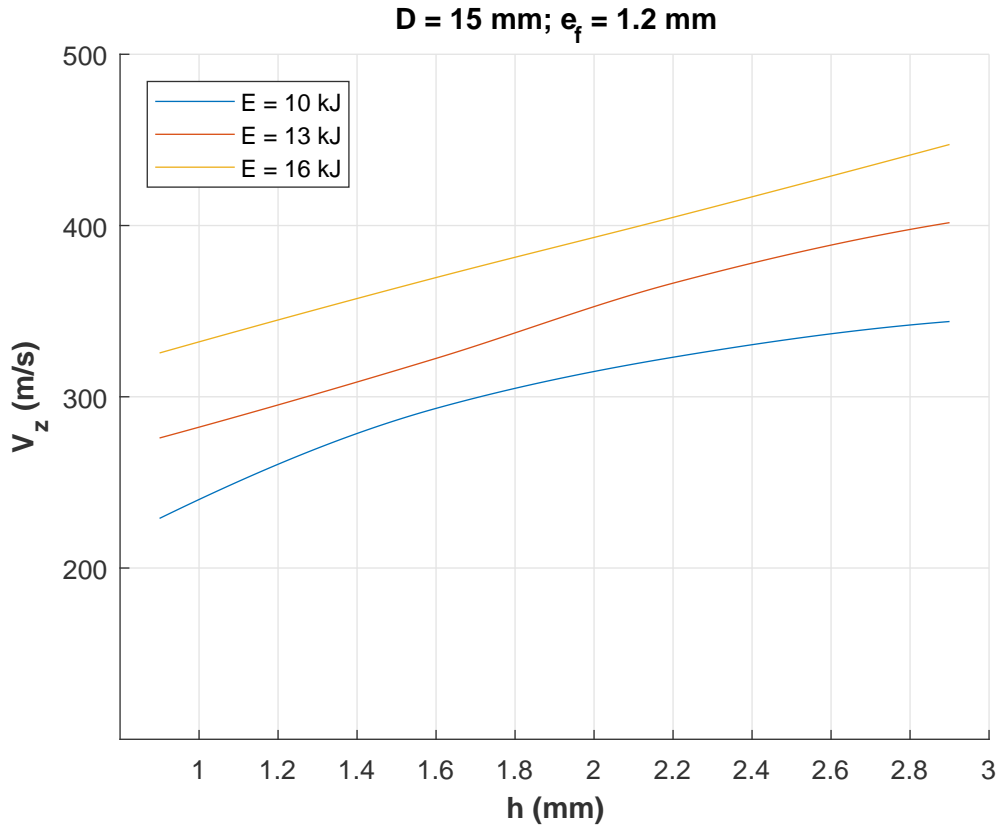
D = 15 mm; e_f = 1.2 mm

Figure A.35: impact velocities variation ($e_f = 1.2$ mm, $D = 15$ mm)
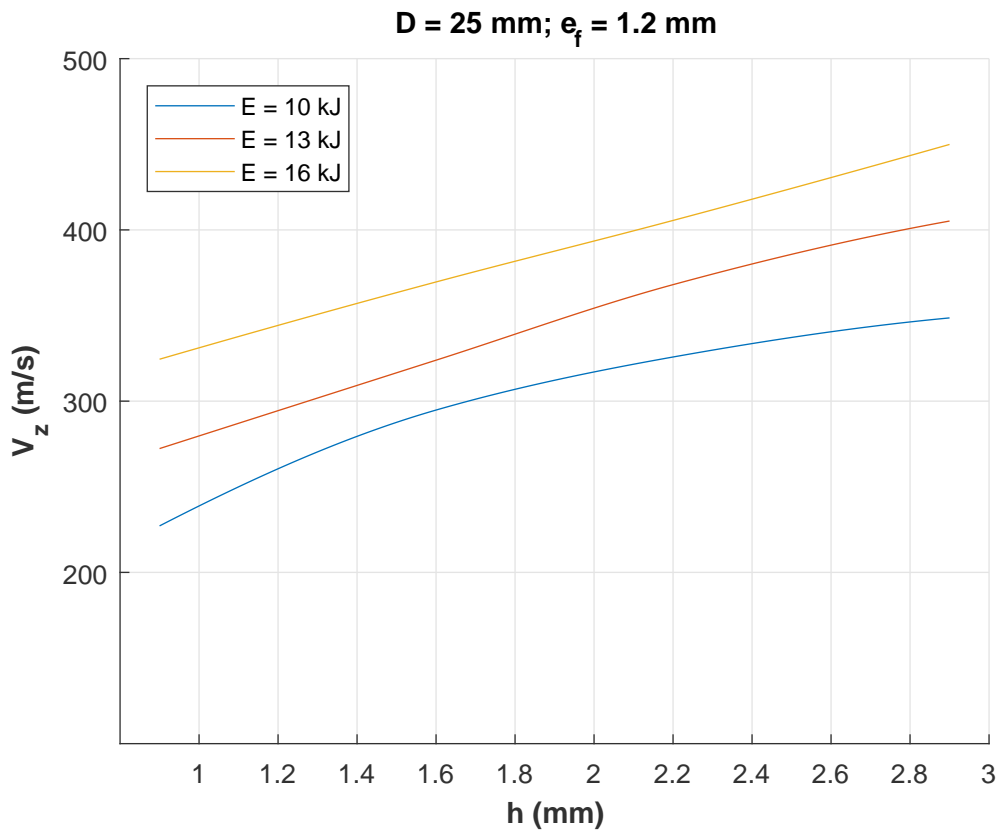
D = 25 mm; e_f = 1.2 mm

Figure A.36: impact velocities variation ($e_f = 1.2$ mm, $D = 25$ mm)

The influence of the standoff distance on β_i at different energy levels:
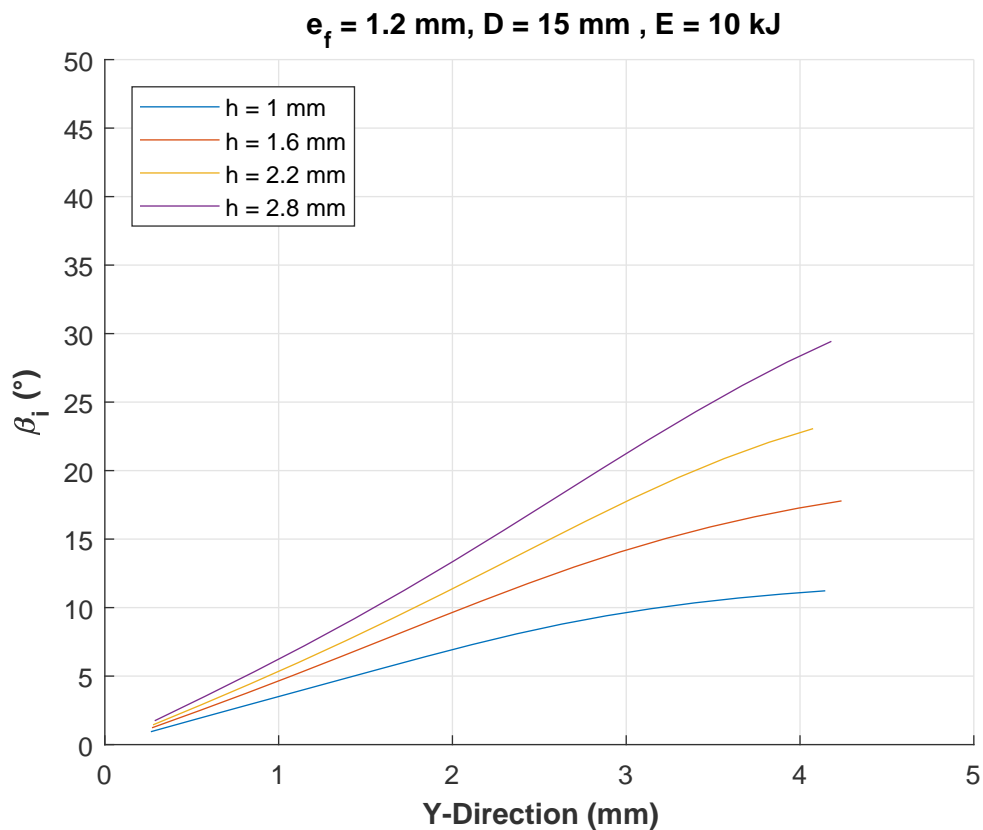
Figure A.37: β_i variation ($e_f = 1.2$ mm, $D = 15$ mm, $E = 10$ kJ)
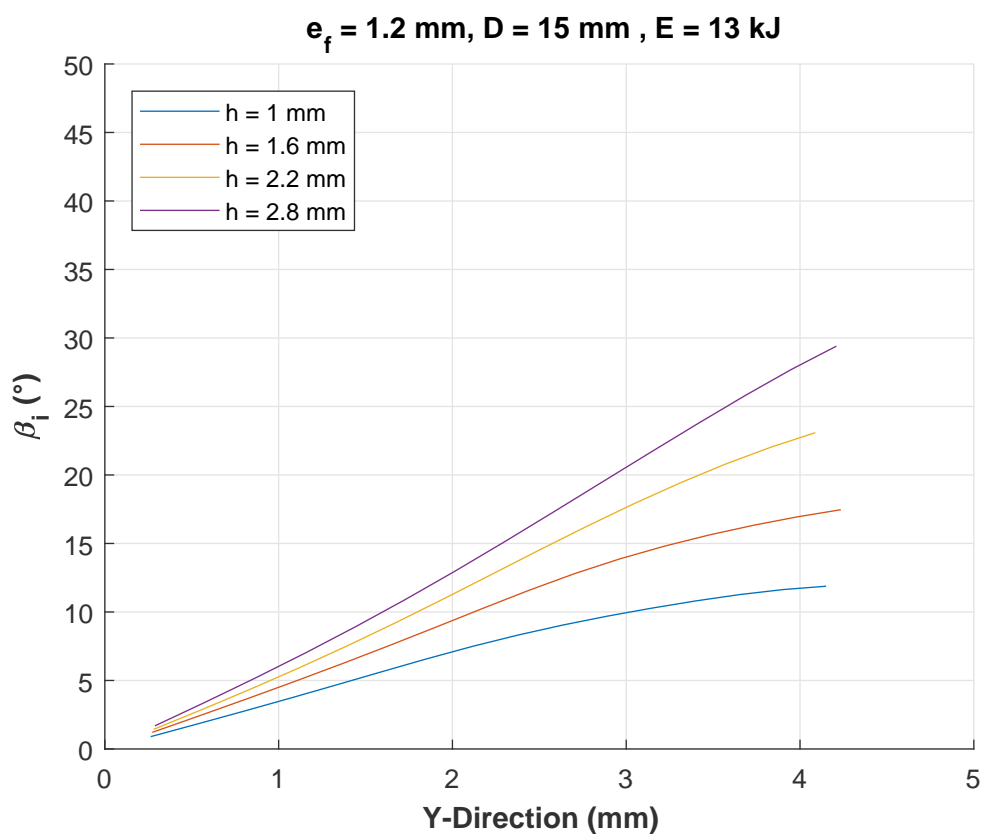
Figure A.38: β_i variation ($e_f = 1.2$ mm, $D = 15$ mm, $E = 13$ kJ)
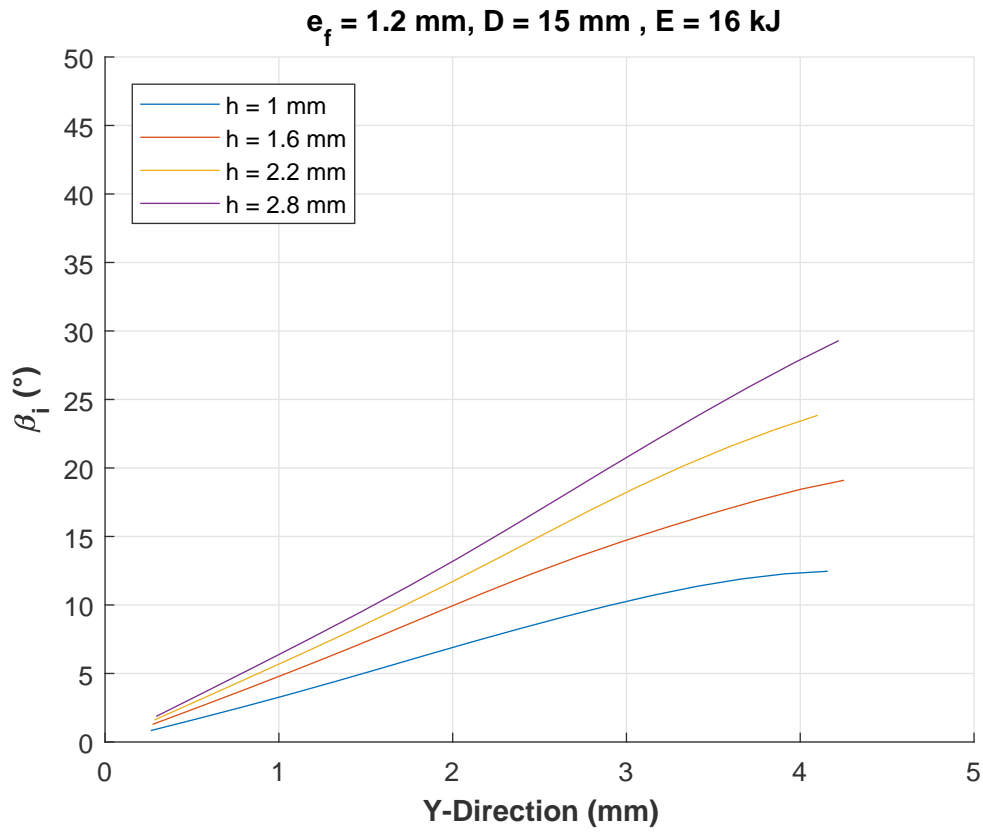
Figure A.39: β_i variation ($e_f = 1.2$ mm, $D = 15$ mm, $E = 16$ kJ)
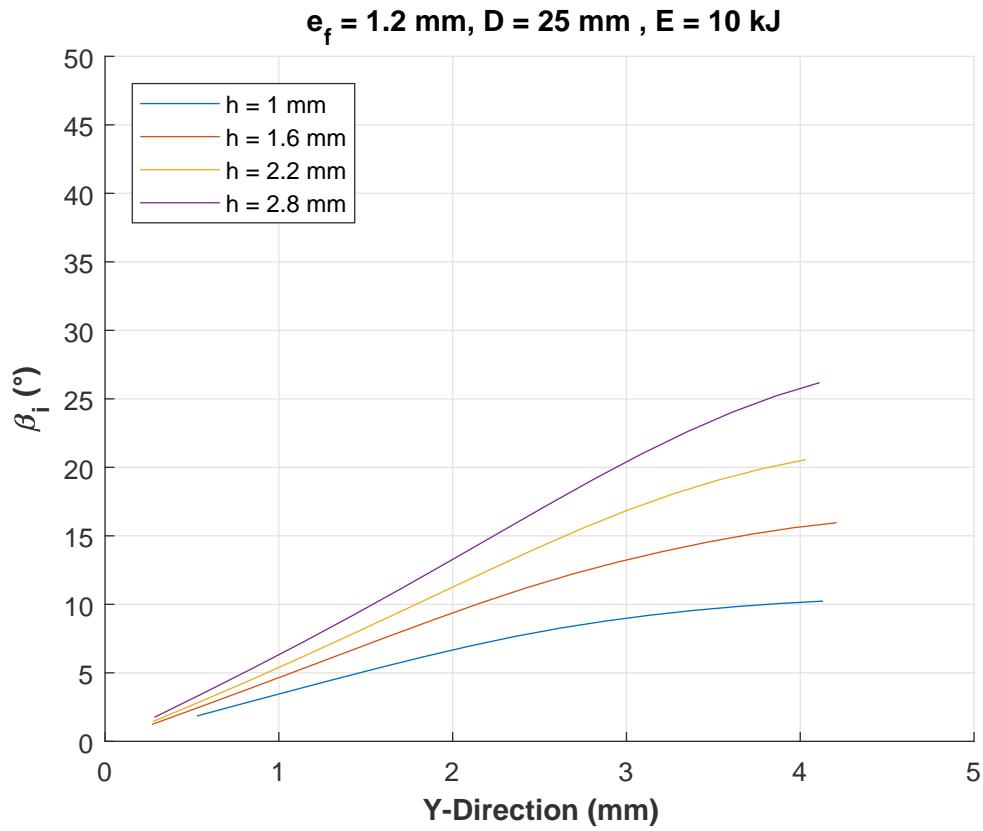
Figure A.40: β_i variation ($e_f = 1.2$ mm, $D = 25$ mm, $E = 10$ kJ)
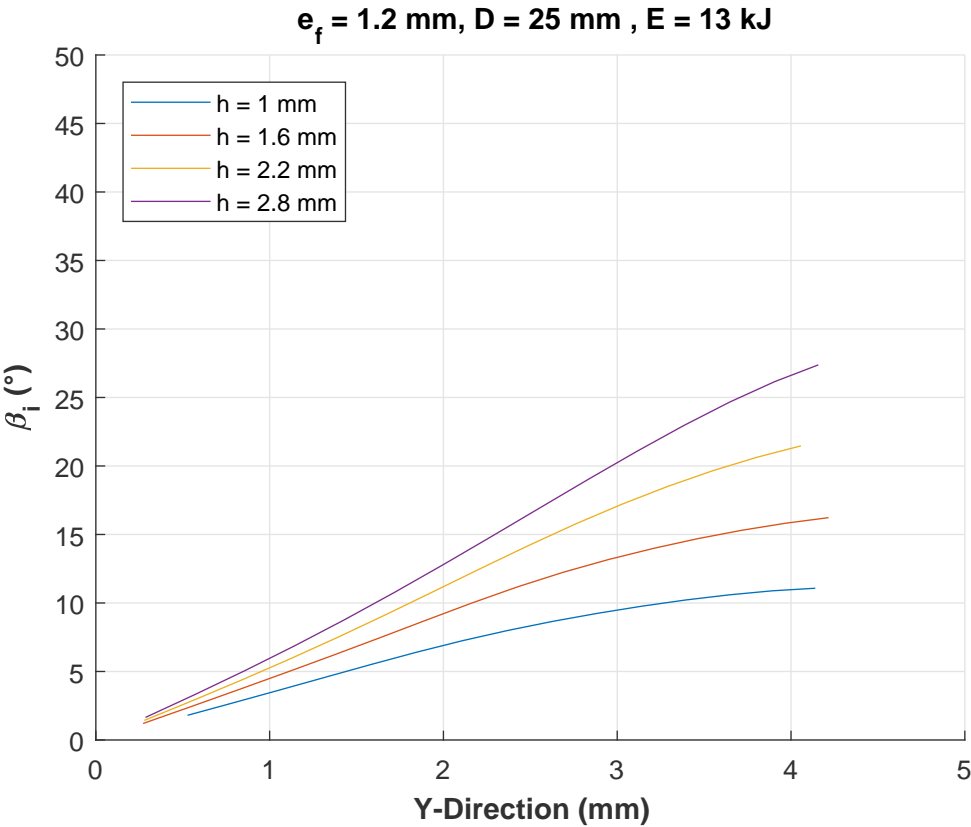
Figure A.41: β_i variation ($e_f = 1.2$ mm, $D = 25$ mm, $E = 13$ kJ)
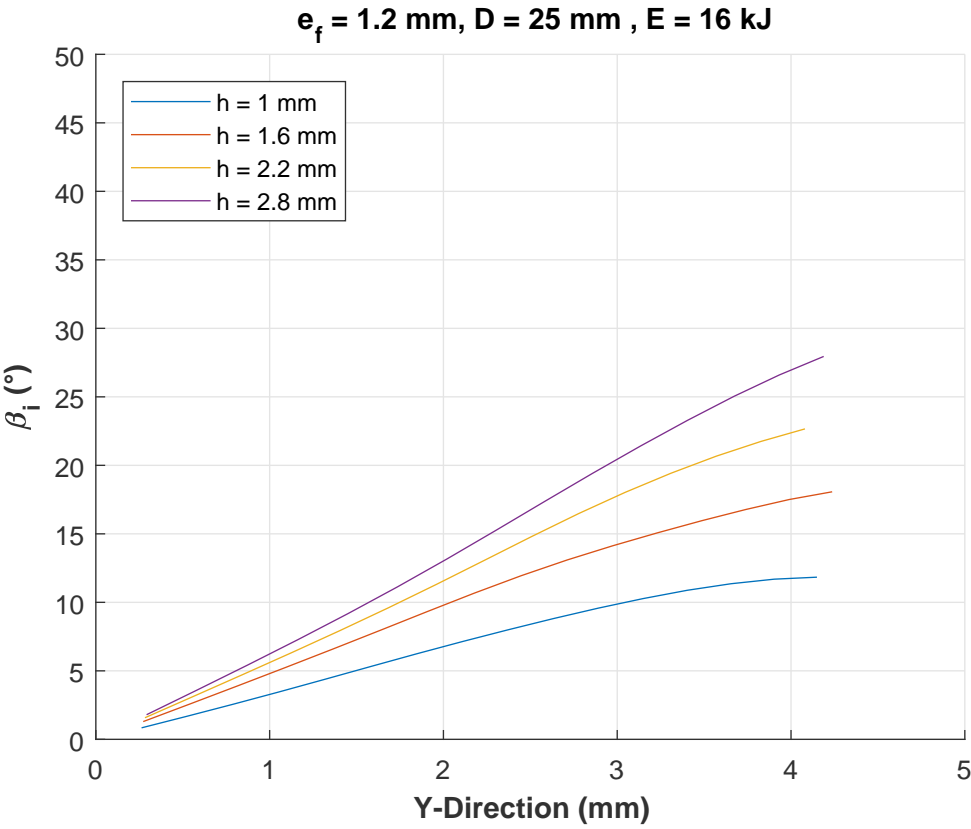
Figure A.42: β_i variation ($e_f = 1.2$ mm, $D = 25$ mm, $E = 16$ kJ)

The influence of the discharge energy on β_i at different standoff distance levels:
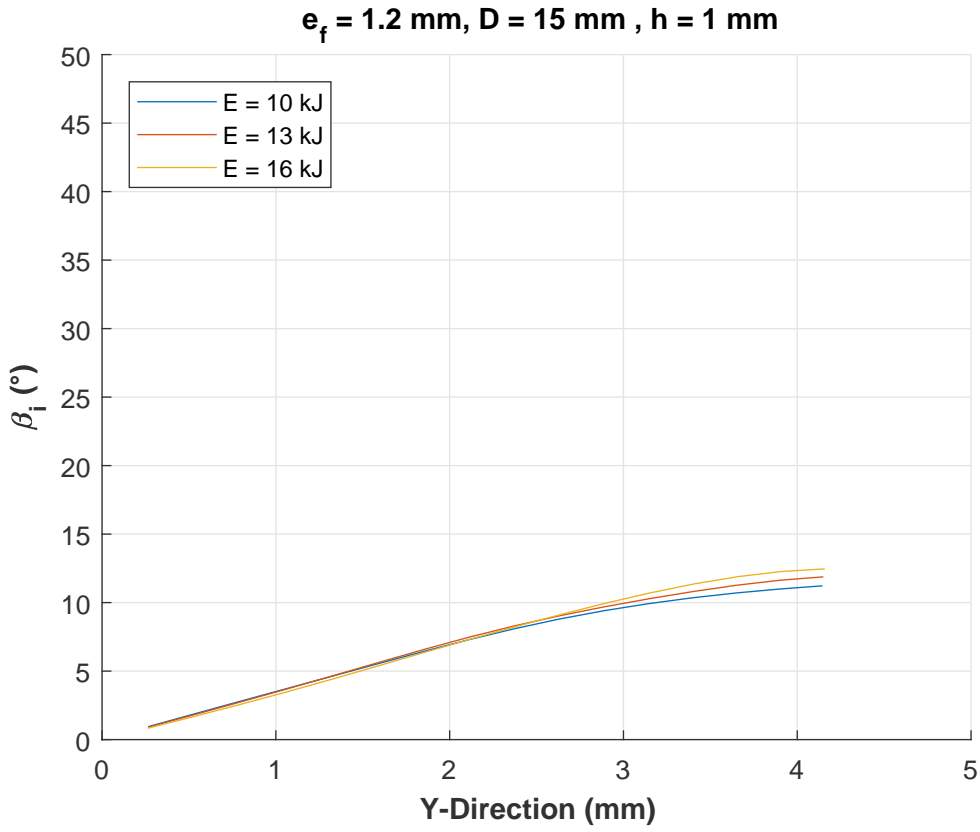
Figure A.43: β_i variation ($e_f = 1.2$ mm, $D = 15$ mm, $h = 1$ mm)
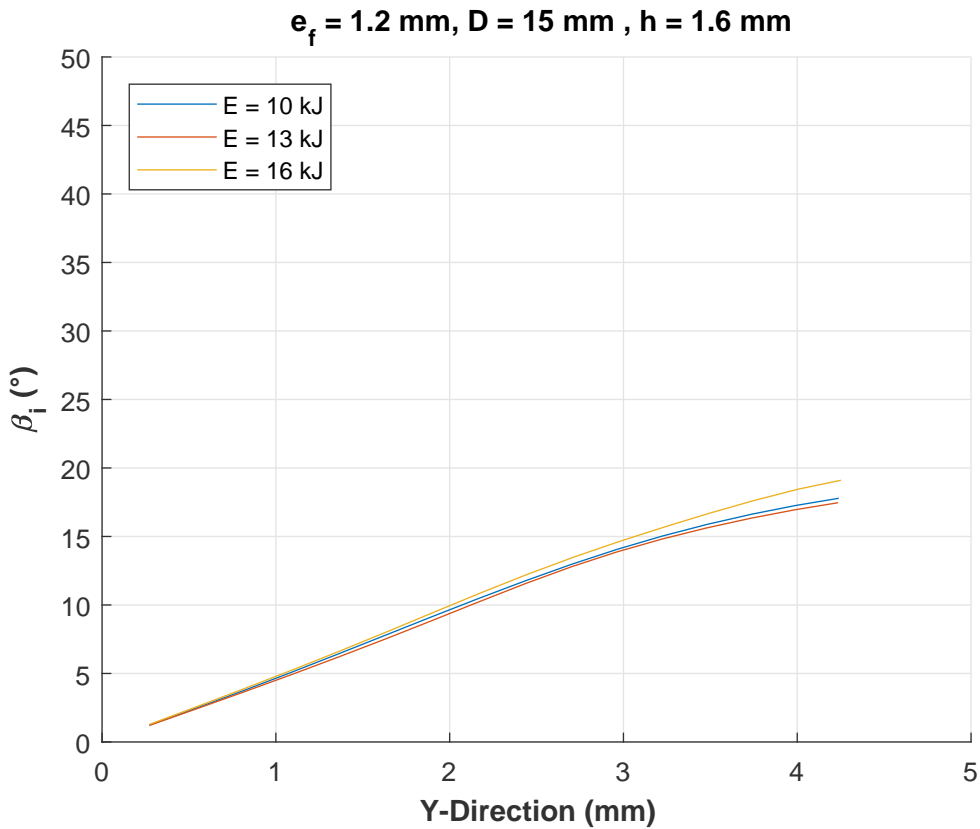
Figure A.44: β_i variation ($e_f = 1.2$ mm, $D = 15$ mm, $h = 1.6$ mm)
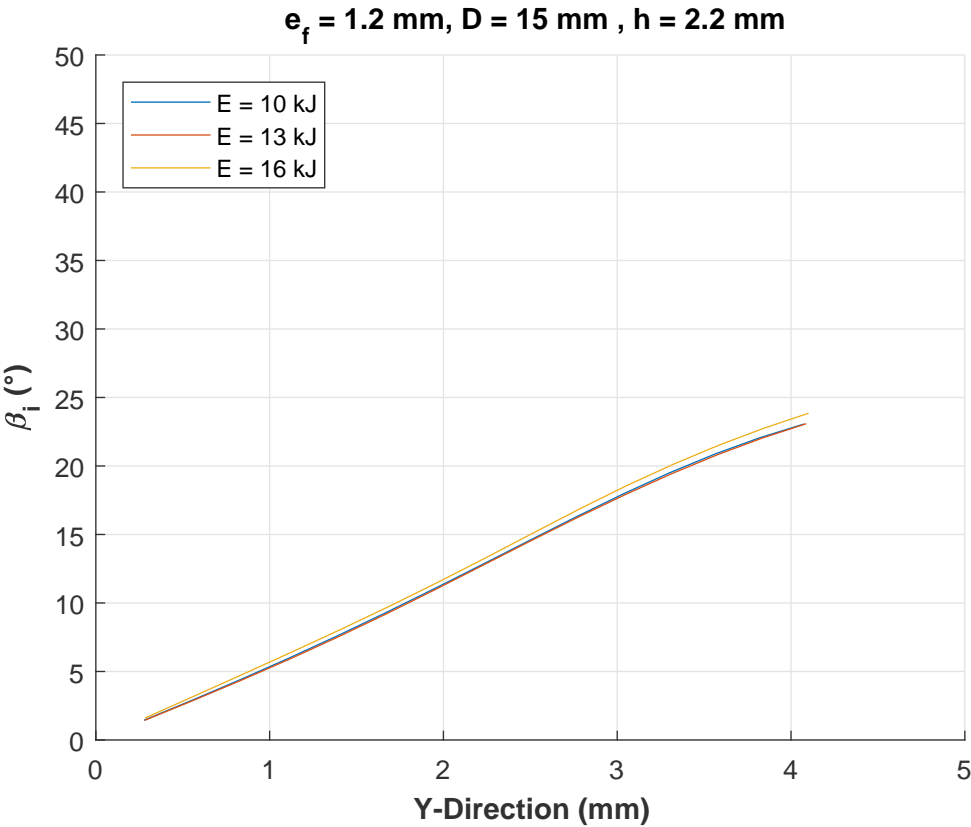
Figure A.45: β_i variation ($e_f = 1.2$ mm, $D = 15$ mm, $h = 2.2$ mm)
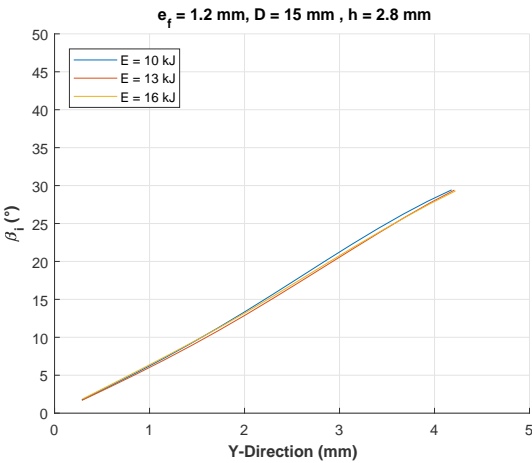
Figure A.46: β_i variation ($e_f = 1.2$ mm, $D = 15$ mm, $h = 2.8$ mm)
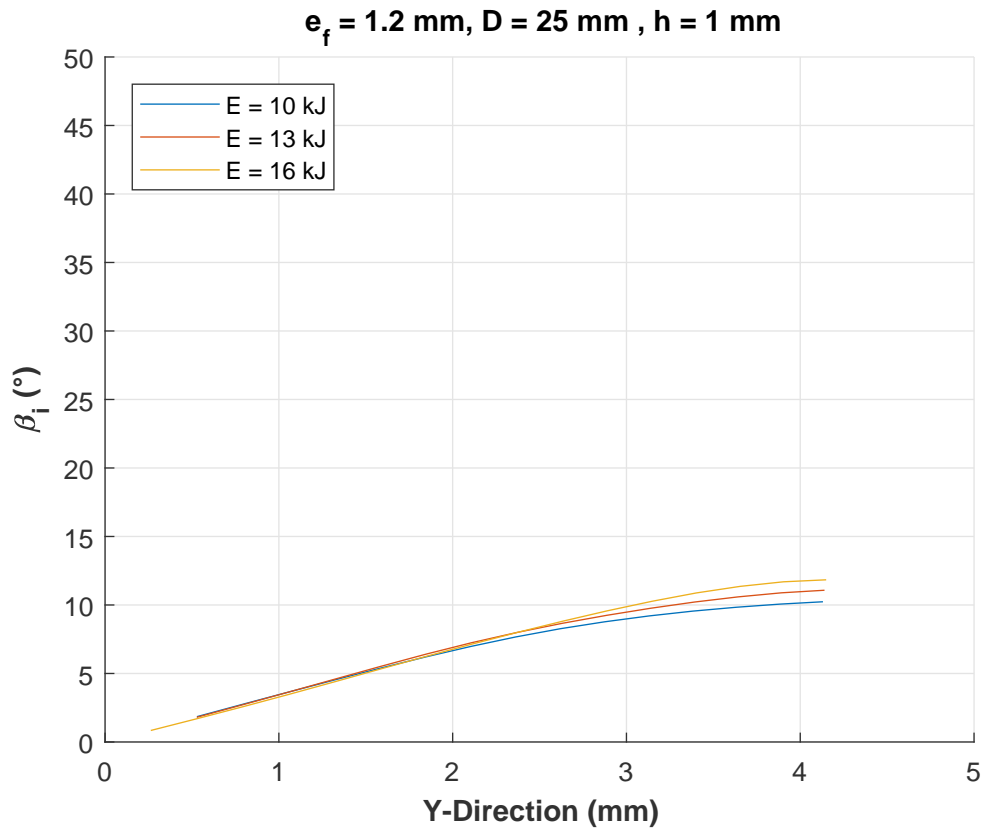
e$_f$ = 1.2 mm, D = 25 mm , h = 1 mm

Figure A.47: $\beta_i$variation ($e_f = 1.2$ mm, $D = 25$ mm, $h = 1$ mm)
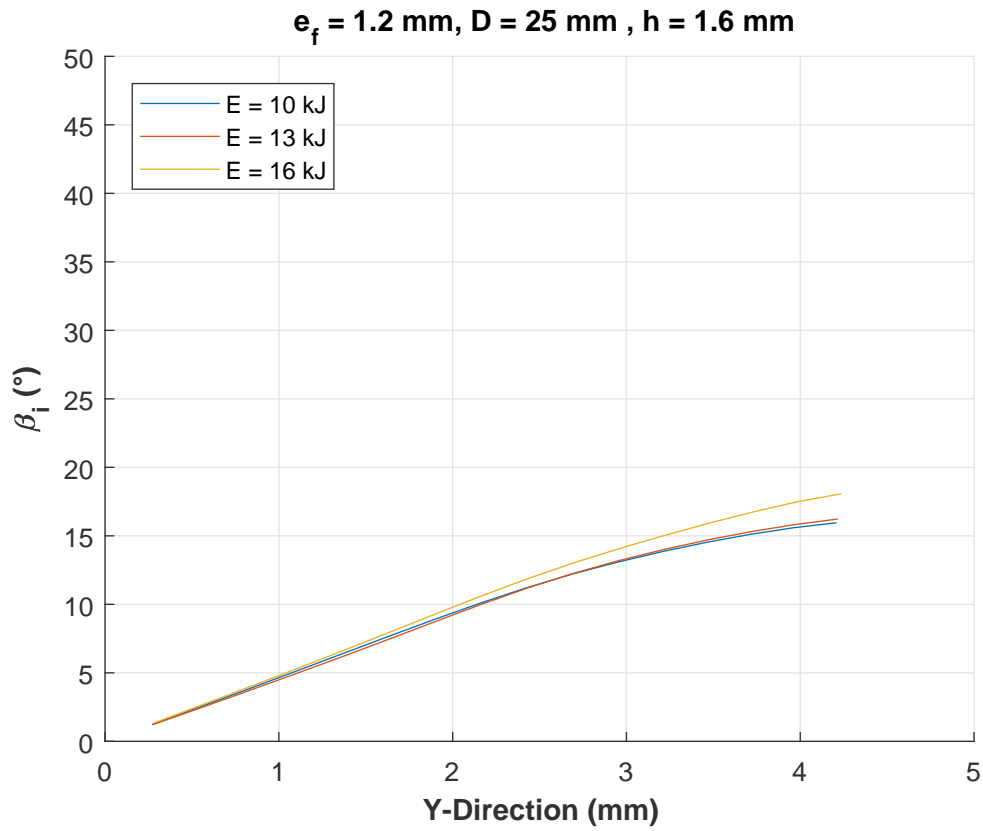
e$_f$ = 1.2 mm, D = 25 mm , h = 1.6 mm

Figure A.48: $\beta_i$variation ($e_f = 1.2$ mm, $D = 25$ mm, $h = 1.6$ mm)
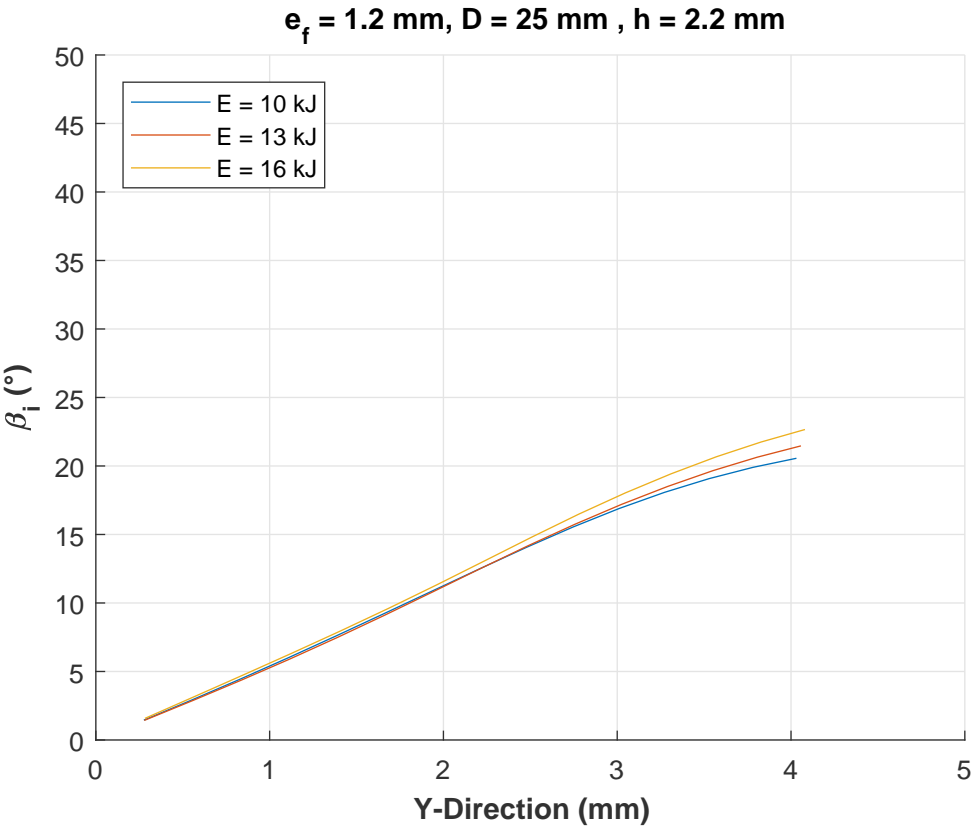
Figure A.49: β_i variation ($e_f = 1.2$ mm, $D = 25$ mm, $h = 2.2$ mm)
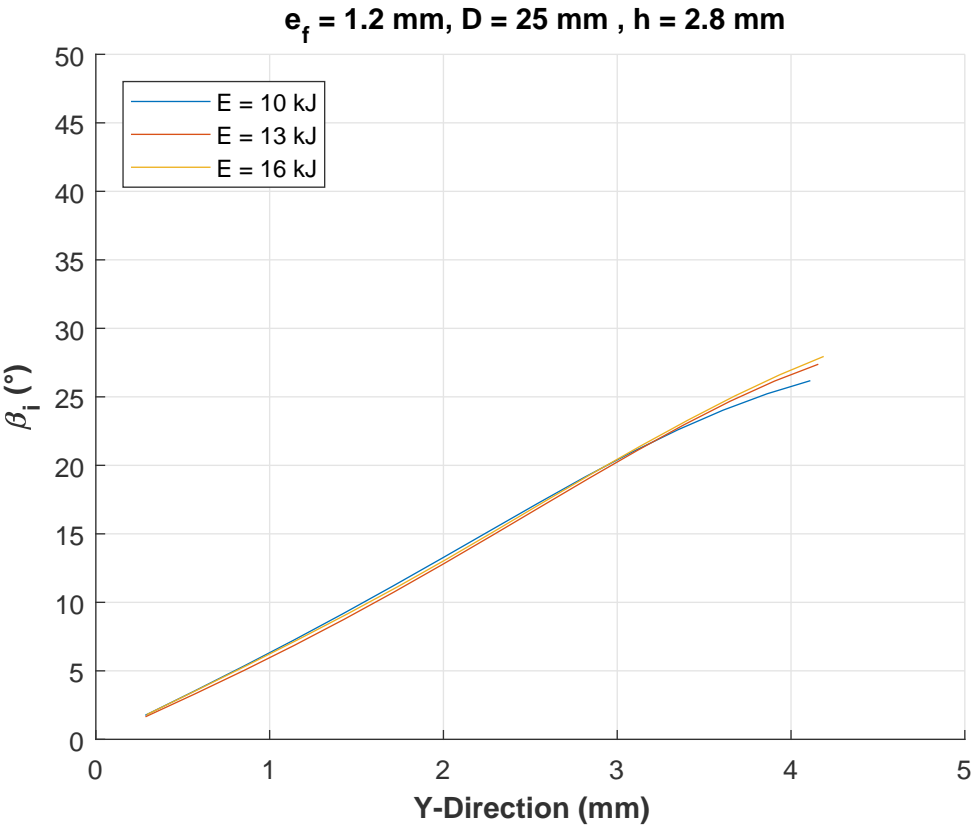
Figure A.50: β_i variation ($e_f = 1.2$ mm, $D = 25$ mm, $h = 2.8$ mm)

The influence of D on the values of β_i for E $=$ 10 kJ at different standoff distances:
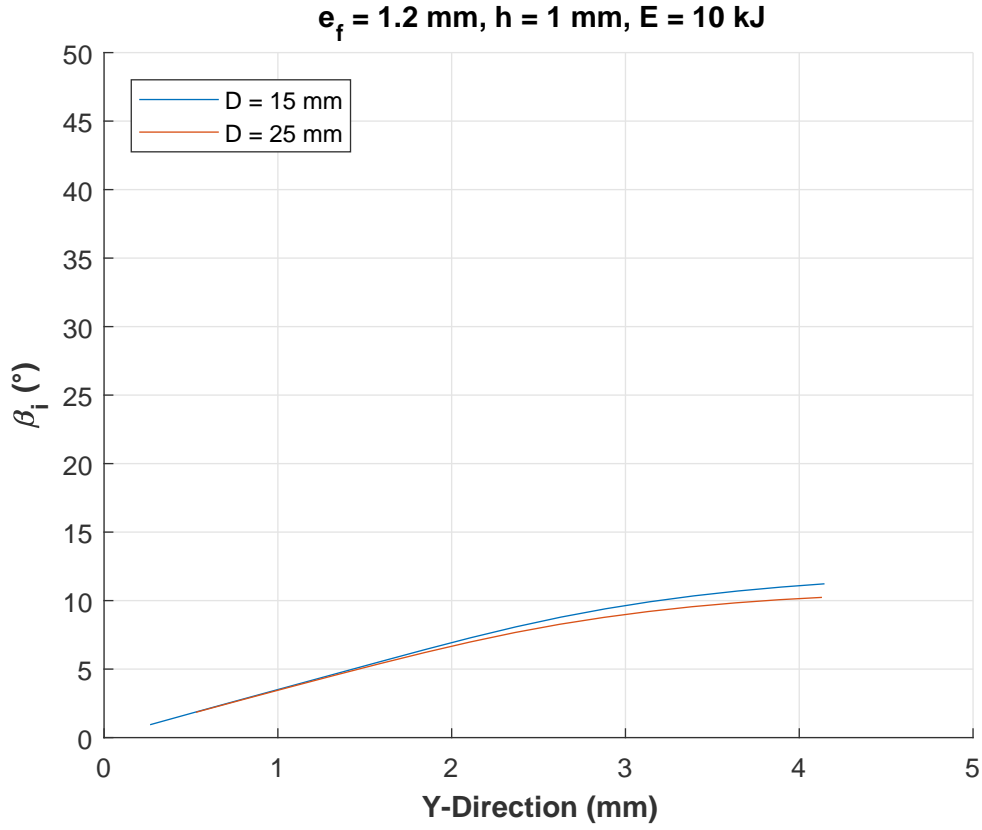
Figure A.51: β_i variation ($e_f = 1.2$ mm, $E = 10$ kJ, $h = 1$ mm)

Figure A.52: β_i variation ($e_f = 1.2$ mm, $E = 10$ kJ, $h = 1.6$ mm)
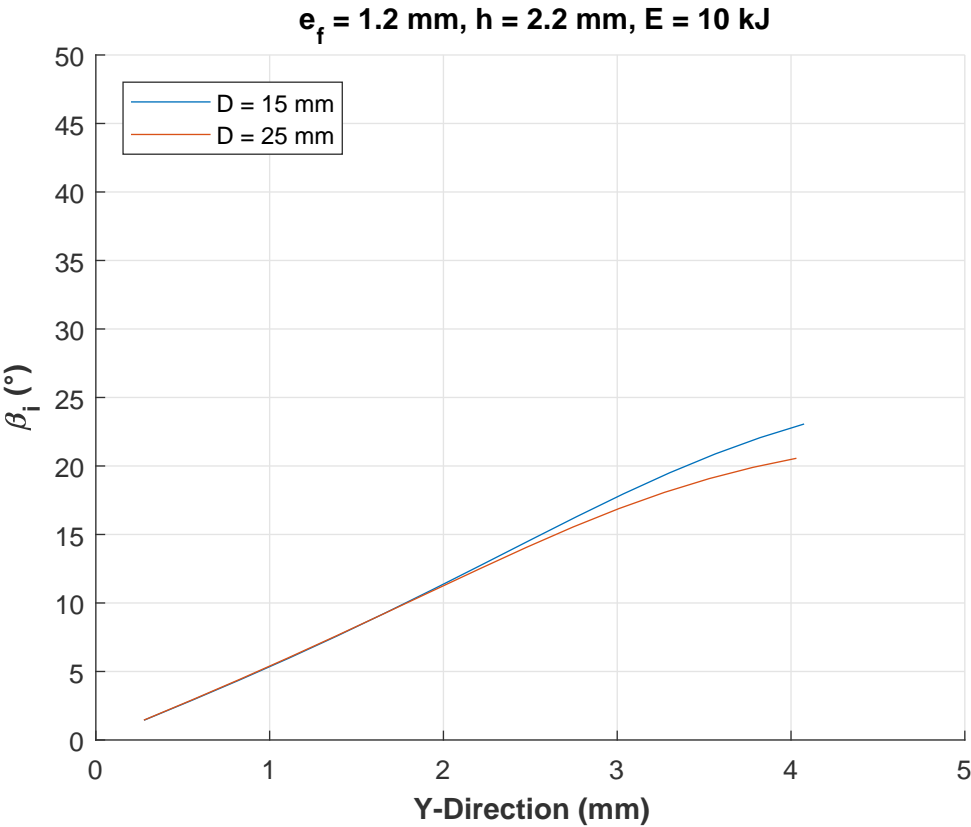
Figure A.53: β_i variation ($e_f = 1.2$ mm, $E = 10$ kJ, $h = 2.2$ mm)
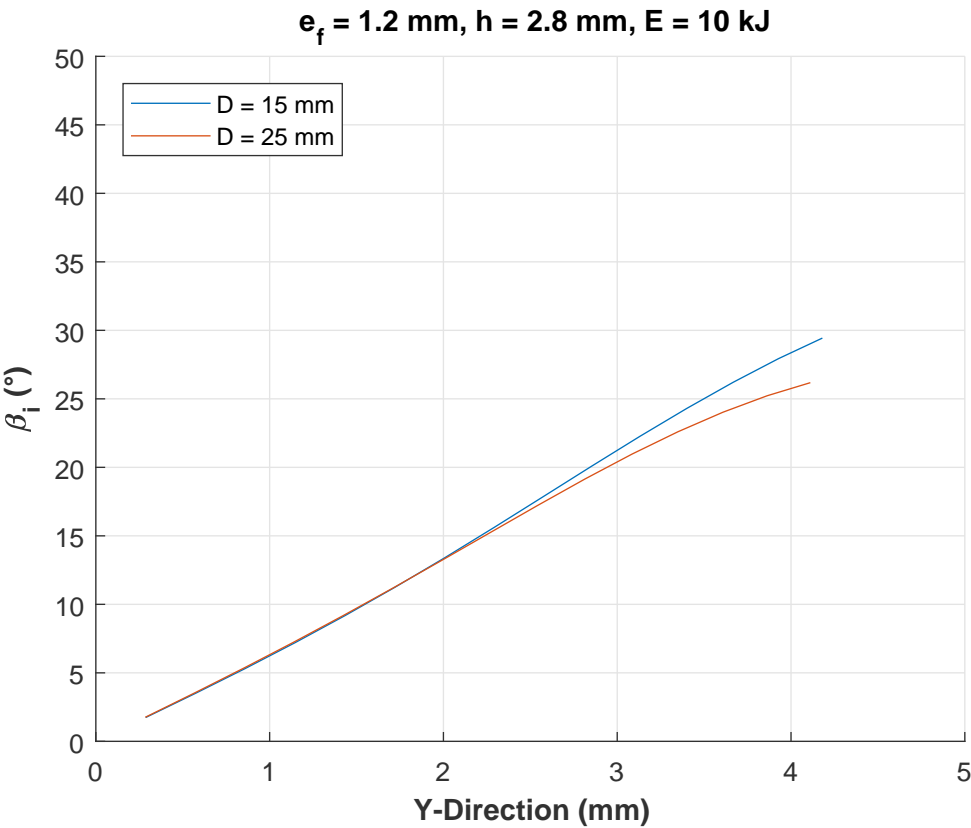
Figure A.54: β_i variation ($e_f = 1.2$ mm, $E = 10$ kJ, $h = 2.8$ mm)

The influence of D on the values of β_i for E $=$ 13 kJ at different standoff distances:

Figure A.55: β_i variation ($e_f = 1.2$ mm, $E = 13$ kJ, $h = 1$ mm

Figure A.56: β_i variation ($e_f = 1.2$ mm, $E = 13$ kJ, $h = 1.6$ mm)
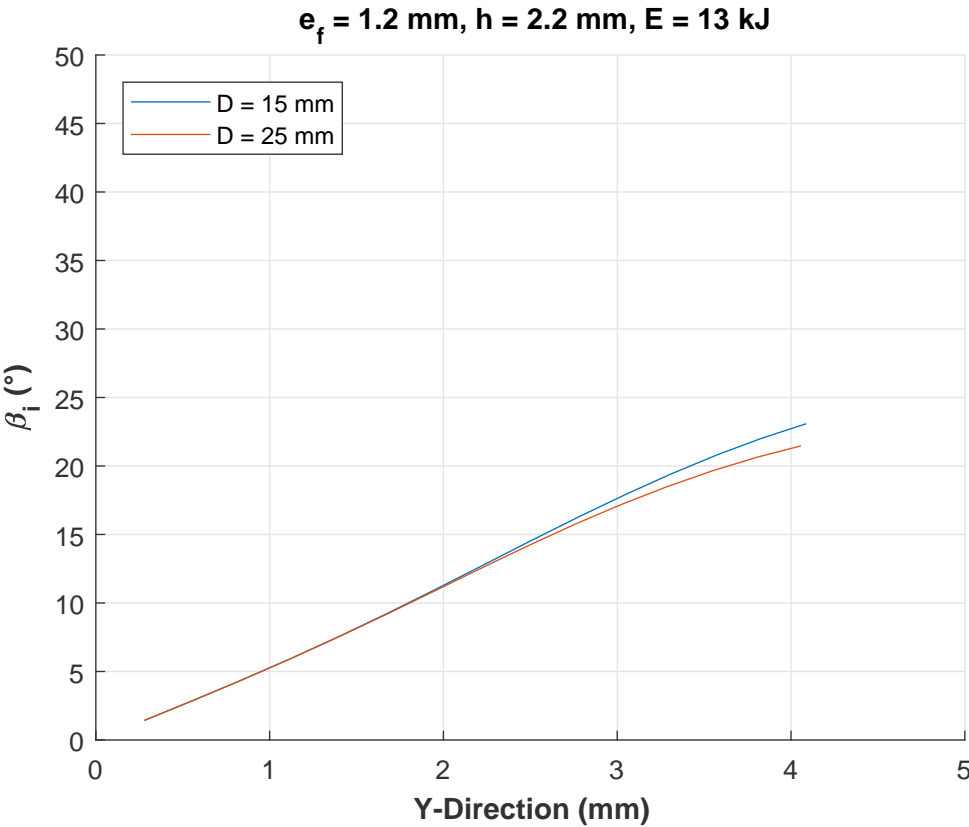
Figure A.57: β_i variation ($e_f = 1.2$ mm, $E = 13$ kJ, $h = 2.2$ mm)
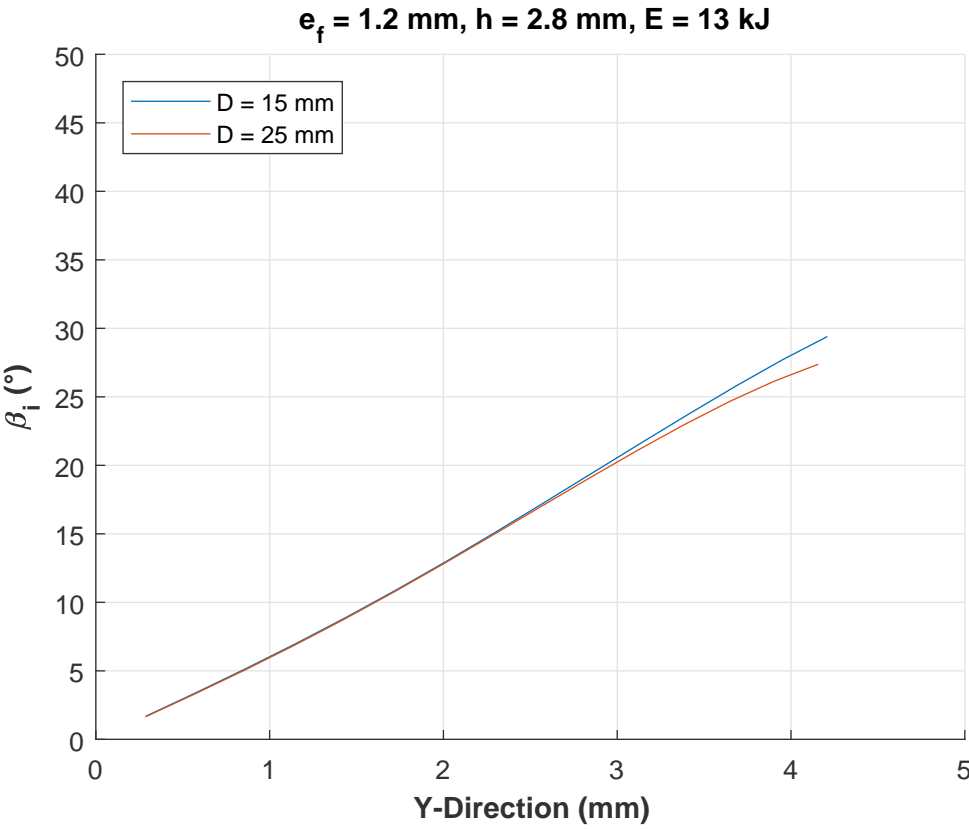
Figure A.58: β_i variation ($e_f = 1.2$ mm, $E = 13$ kJ, $h = 2.8$ mm)

The influence of D on the values of β_i for E = 16 kJ at different standoff distances:
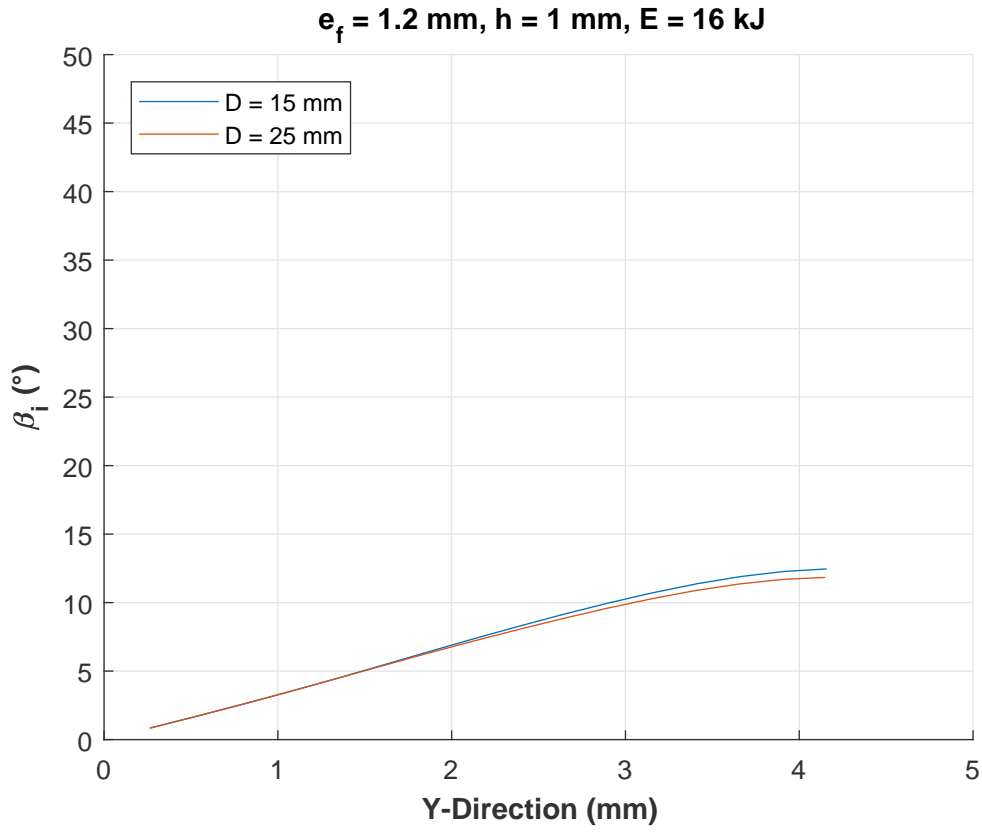
Figure A.59: β_i variation ($e_f = 1.2$ mm, $E = 16$ kJ, $h = 1$ mm)
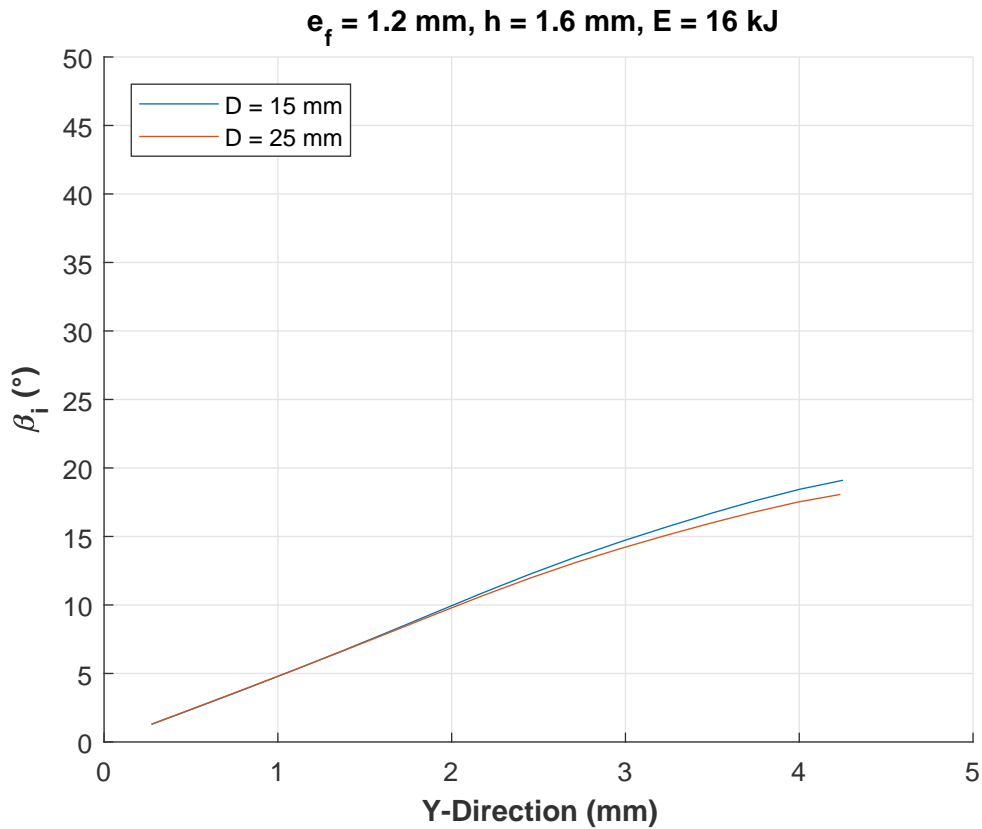
Figure A.60: β_i variation ($e_f = 1.2$ mm, $E = 16$ kJ, $h = 1.6$ mm)
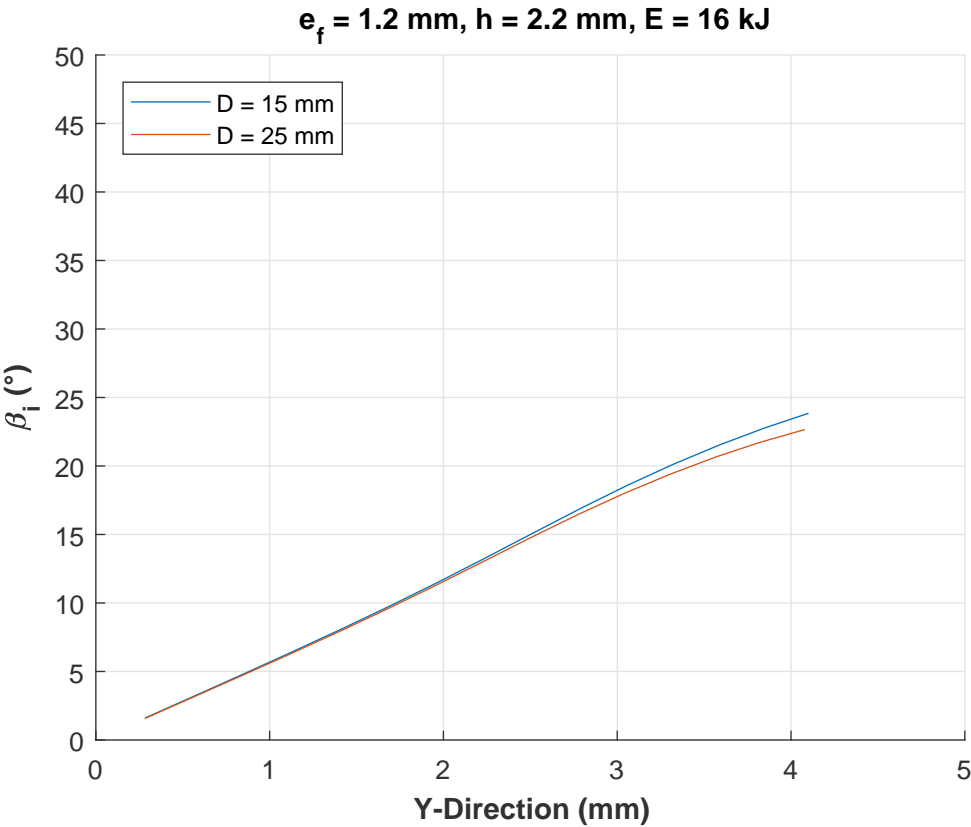
Figure A.61: β_i variation ($e_f = 1.2$ mm, $E = 16$ kJ, $h = 2.2$ mm)
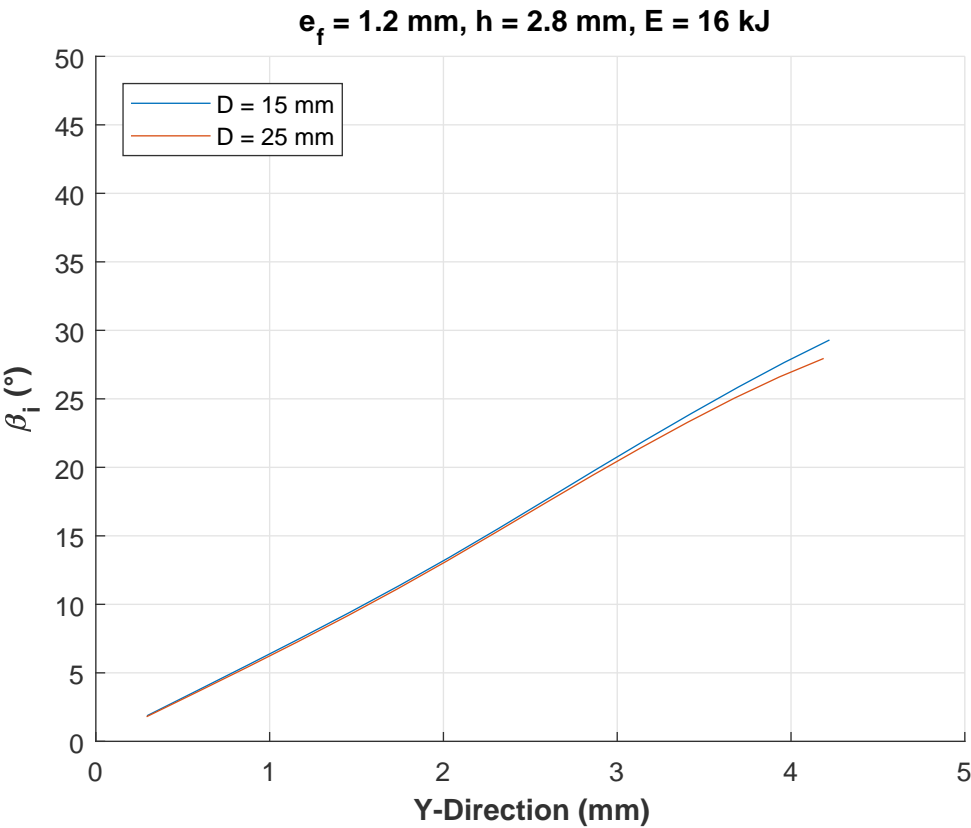
Figure A.62: β_i variation ($e_f = 1.2$ mm, $E = 16$ kJ, $h = 2.8$ mm)

A.2 MPSW case

A.2.1 Thin sheet metal case ($e_f = 0.5$ mm)

The deformation profiles of thin aluminum 5754-H111 in the MPSW case:
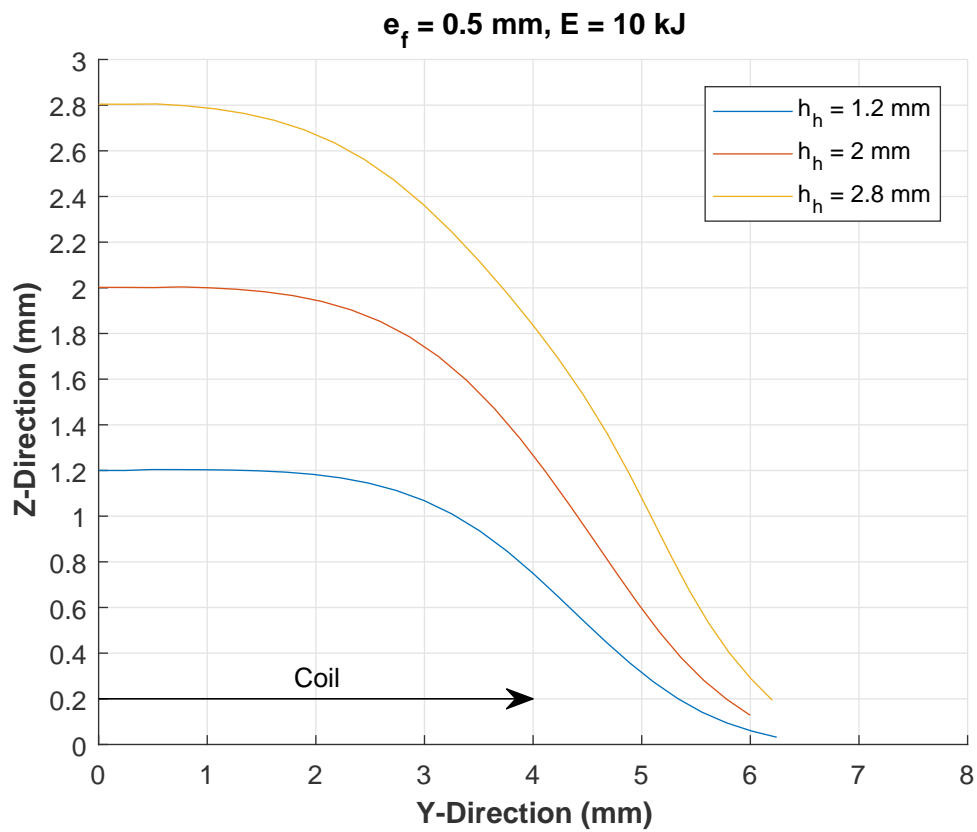
Figure A.63: deformation profile - MPSW ($e_f = 0.5$ mm, $E = 10$ kJ)
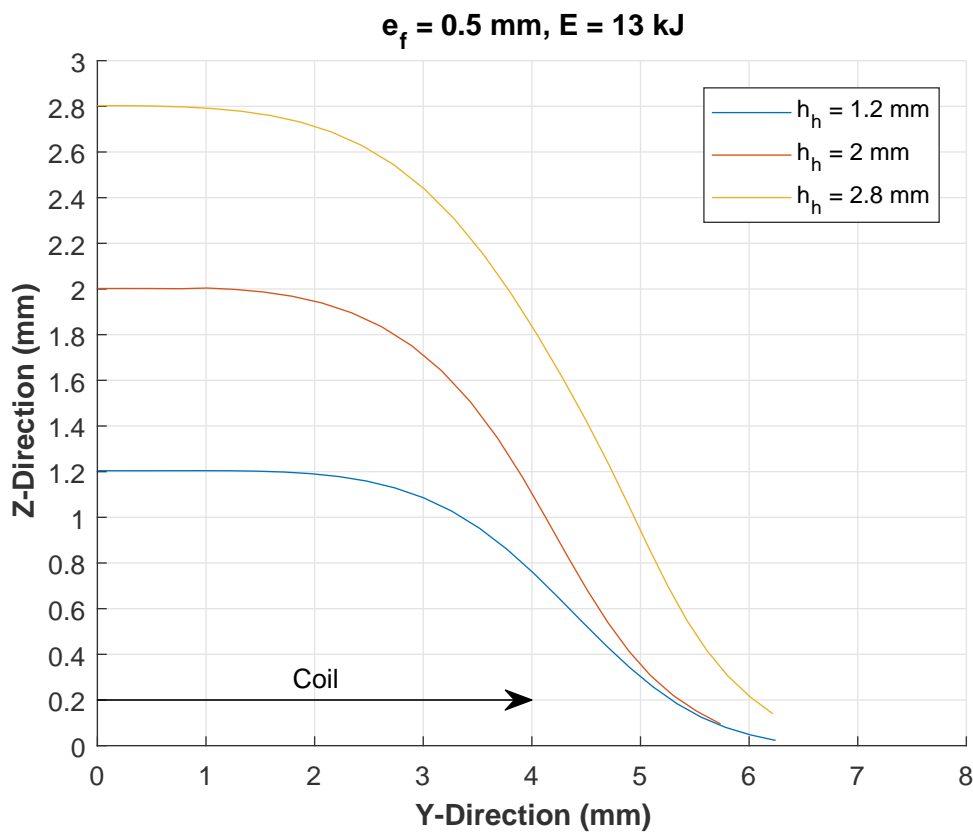
Figure A.64: deformation profile - MPSW ($e_f = 0.5$ mm, $E = 13$ kJ)
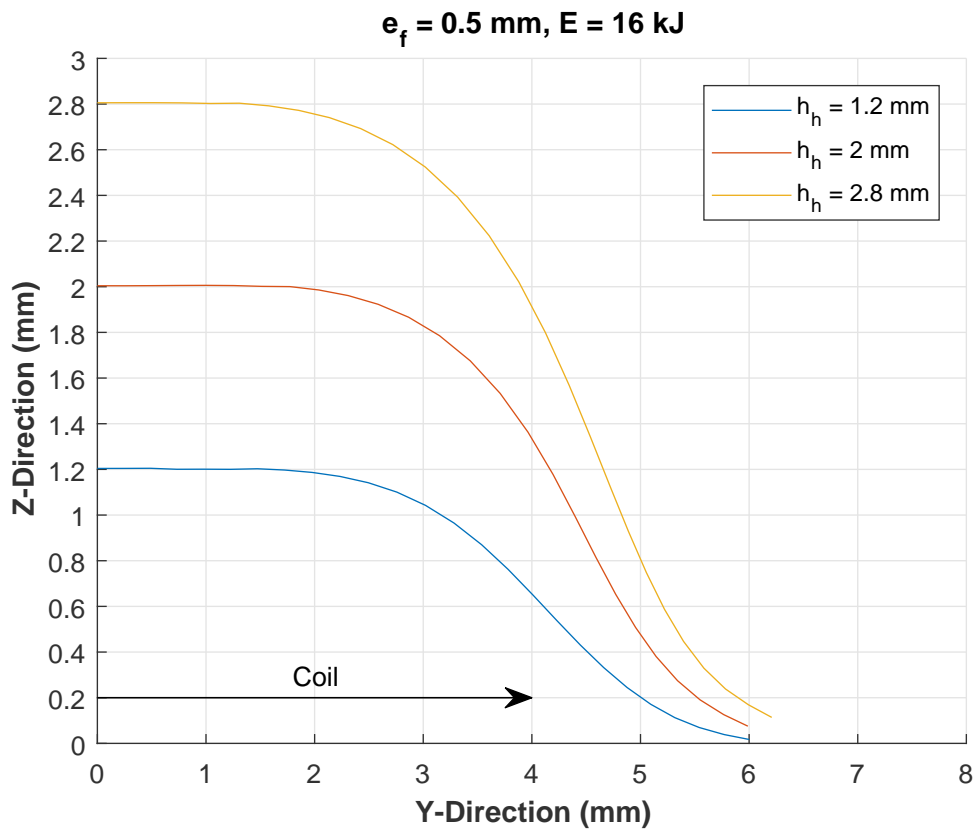
Figure A.65: deformation profile - MPSW ($e_f = 0.5$ mm, $E = 16$ kJ)

The variations of β_i as function of the standoff distances at different energy levels:
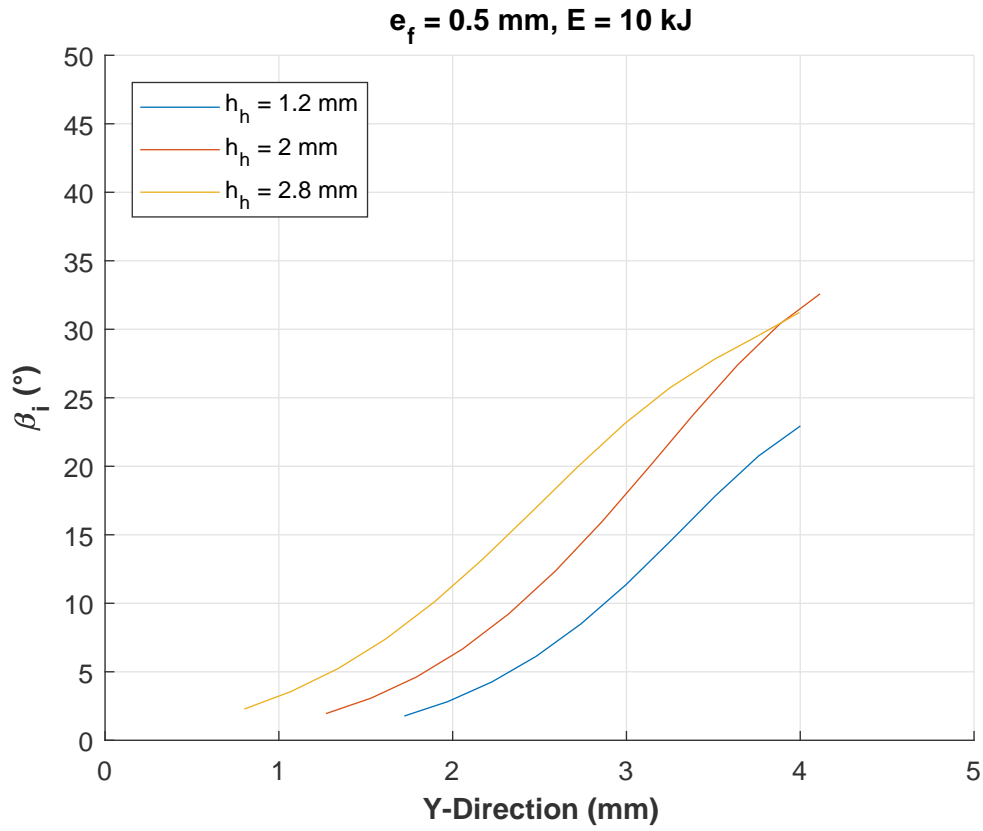
Figure A.66: β_i variation - MPSW ($e_f = 0.5$ mm, $E = 10$ kJ
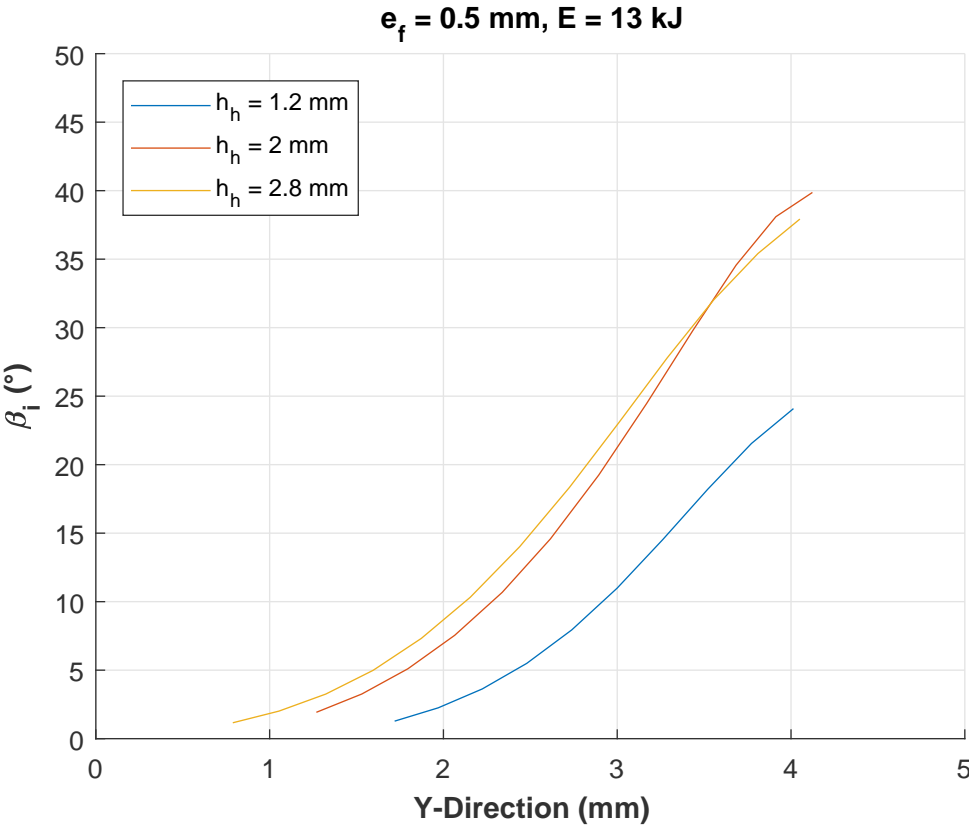
Figure A.67: β_i variation - MPSW ($e_f = 0.5$ mm, $E = 13$ kJ)
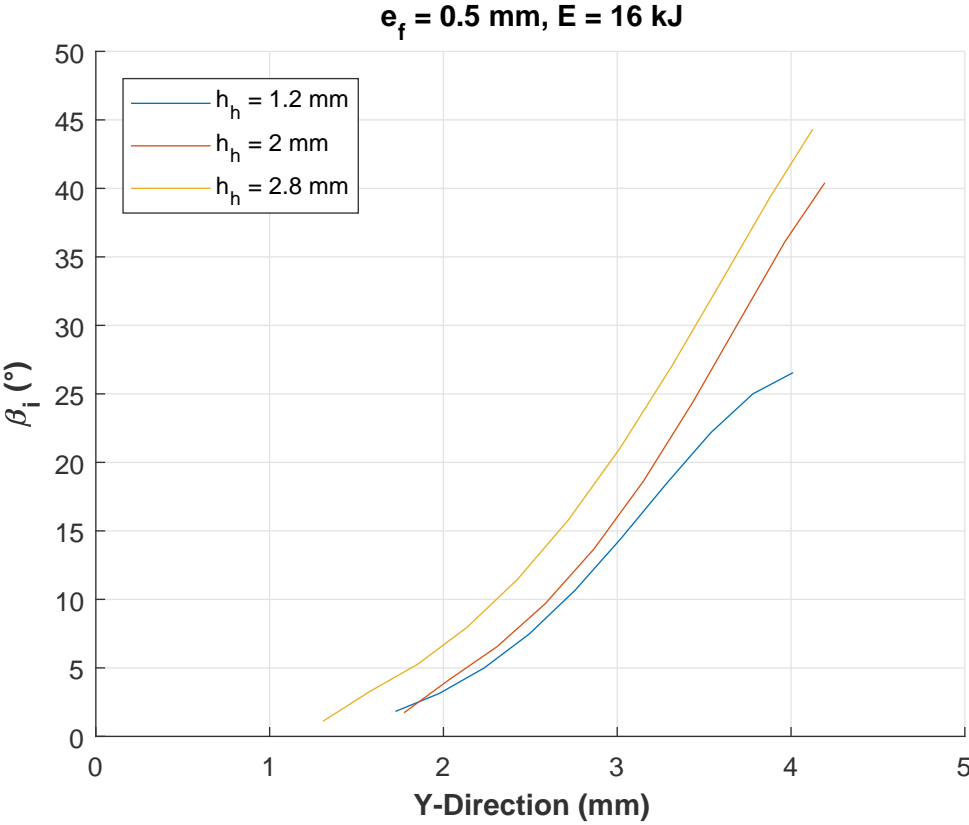
Figure A.68: β_i variation - MPSW ($e_f = 0.5$ mm, $E = 16$ kJ)
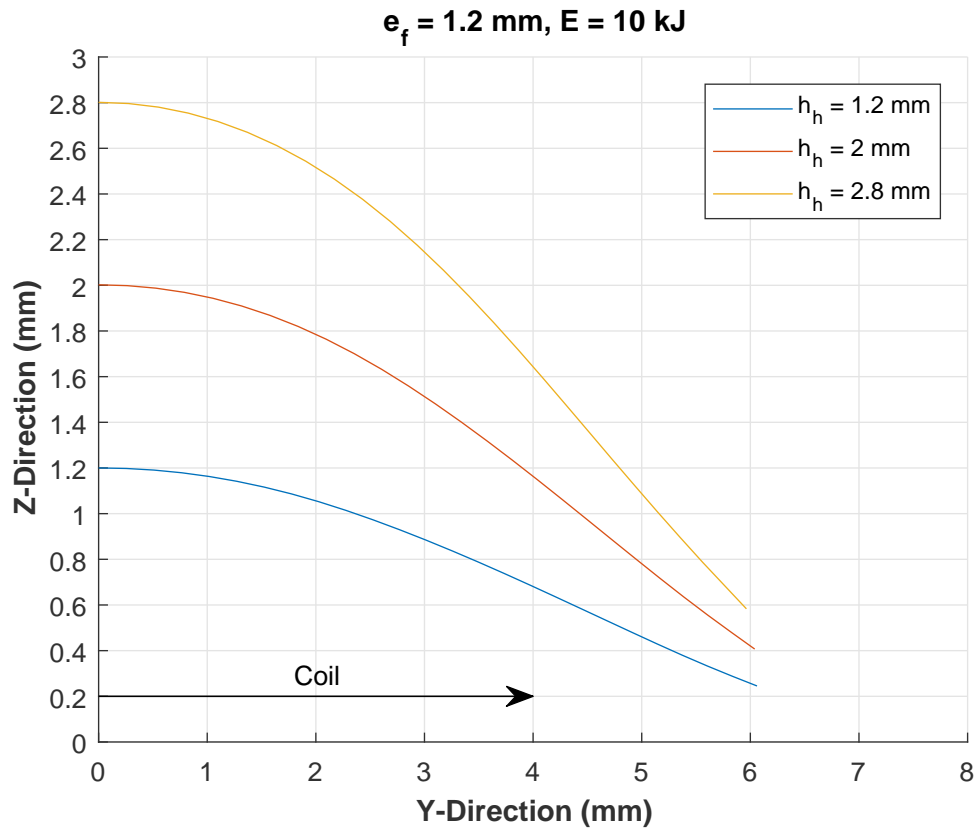
Figure A.69: deformation profiles - MPSW ($e_f = 1.2$ mm, $E = 10$ kJ)

A.2.2 Thick sheet metal case ($e_f = 1.2$ mm)

The deformation profiles of thick aluminum 5754-H111 in the MPSW case:
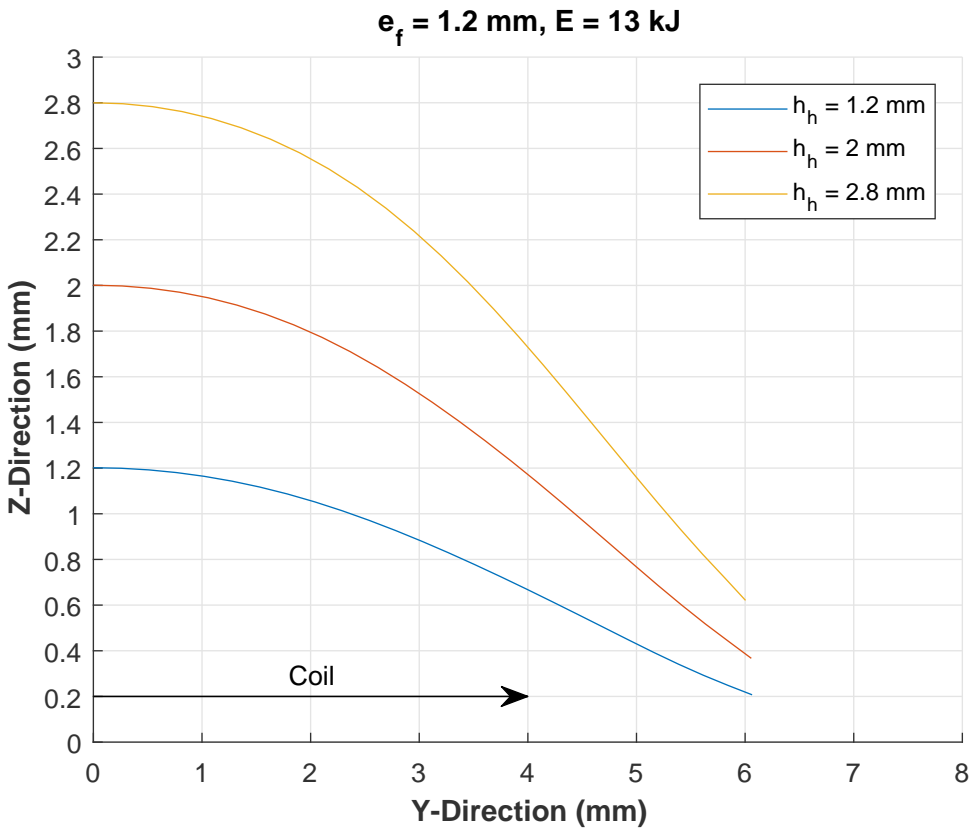
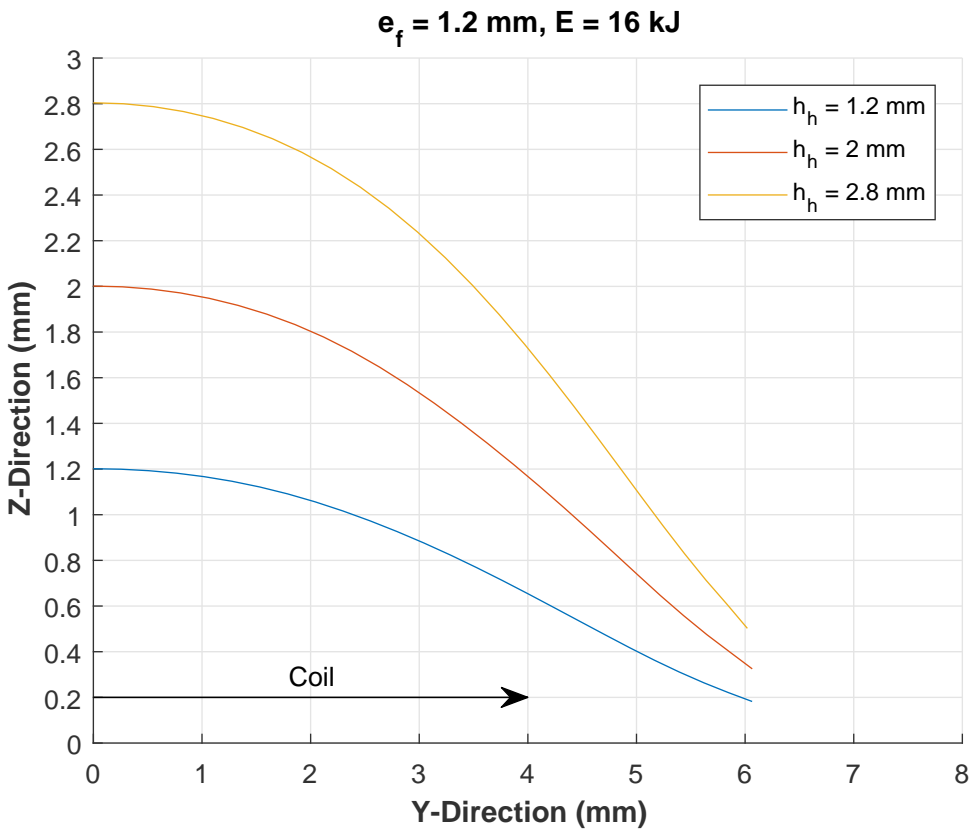Figure A.70: deformation profiles - MPSW ($e_f = 1.2$ mm, $E = 13$ kJ)

Figure A.71: deformation profiles - MPSW ($e_f = 1.2$ mm, $E = 16$ kJ)

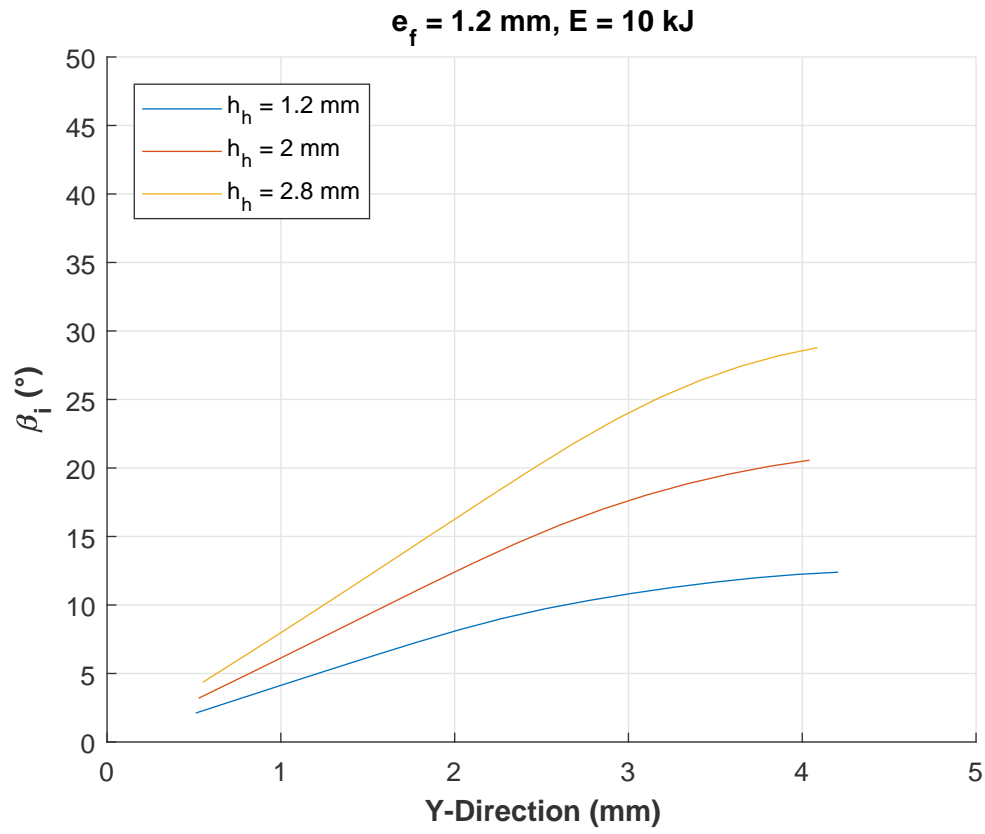Figure A.72: β_i variation - MPSW ($e_f = 1.2$ mm, $E = 10$ kJ)

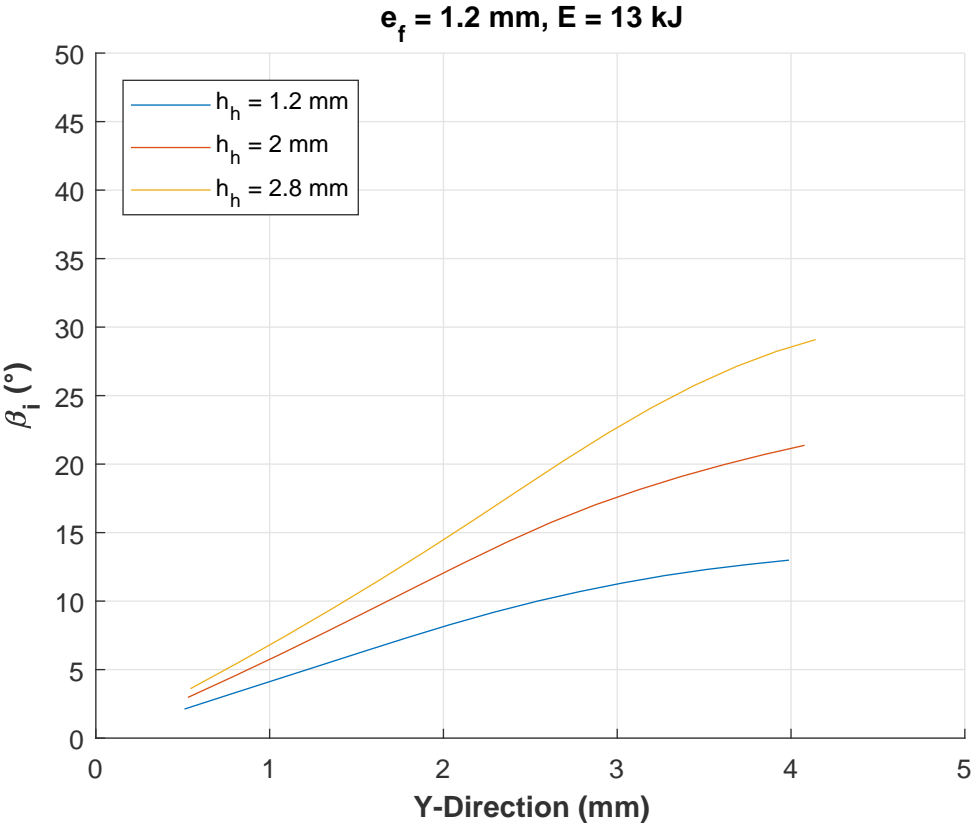The influence of the standoff distance on β_i at different energy levels:

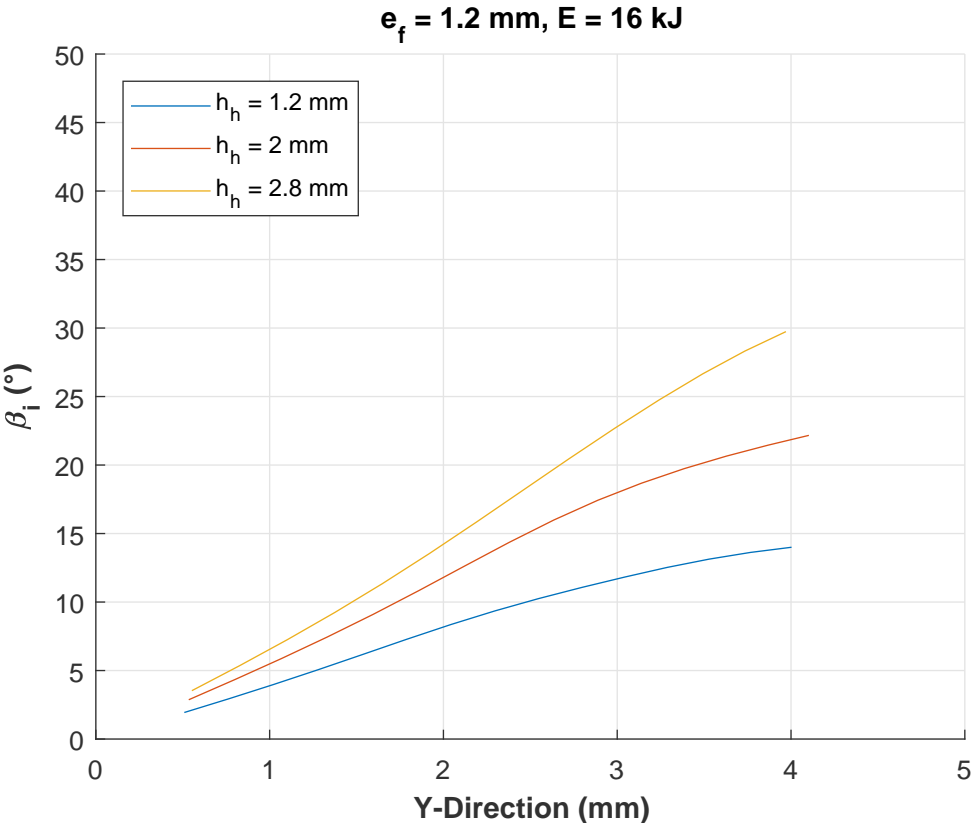Figure A.73: β_i variation - MPSW ($e_f = 1.2$ mm, $E = 13$ kJ)

Figure A.74: β_i variation - MPSW ($e_f = 1.2$ mm, $E = 16$ kJ)

Résumé : La réduction des émissions CO2 et l'amélioration de la performance restent toujours les grands objectifs de l'industrie automobile. Pour atteindre ces objectif, les équipementiers automobiles cherchent toujours à alléger les structures à travers l'emploie des matériaux hétérogènes qui a évolué au cours des dernières décennies où nous trouvons aujourd'hui à la fois des aciers doux, des aciers à très hautes résistances, des alliages légers tels que les alliages d'aluminium et de magnésium ainsi que des composites à fibre de verre ou de carbone.

Cette tendance pose aujourd'hui plusieurs défis concernant à la fois l'assemblage bimétallique et l'assemblage hybride métal/composite. Les difficultés de réaliser ce type d'assemblage est lié surtout à la différence des propriétés mécaniques, thermiques et chimiques des divers matéiaux.

Ces différences limitent l'utilisation des techniques d'assemblage traditionnelles, c'est-à-dire l'assemblage mécanique, le soudage par fusion et le collage, et nécessitent ainsi le développement de nouvelles solutions d'assemblage.

Dans ce contexte, cette étude vise à répondre aux défis des soudages hétérogènes ainsi qu' à développer deux nouvelles solutions originales d'assemblage hybride métal/composite en utilisant le procédé de soudage par impulsion magnétique.

Abstract : Reducing CO2 emissions and improving performance are still the main goals of the automotive industry. To achieve these objectives, automotive suppliers are still seeking to lighten the structures through the use of heterogeneous materials that have evolved in recent decades. We find today in one vehicle mild steels, very high strength steels, light alloys such as aluminum and magnesium alloys as well as fiber reinforces polymeric composites.

The presence of dissimilar materials arises several challenges regarding both the heteregeneous metal assemblies and hybrid metal / composites assemblies.

The differences in the mechanical, thermal and chemical properties of the various materials limit the use of traditional assembly techniques, i.e. mechanical assembly, fusion welding and adhesive bonding, and thus the development of new assembly solutions is required.

In this context, this study aims to meet the challenges of heterogeneous metal welding and aims to develop two new original hybrid metal / composite assembly solutions using the magnetic pulse welding process.